SPARK PLASMA SYNTHESIS AND TRIBOLOGY OF MAX PHASE AND CERAMIC COMPOSITES

BY

CARL MAGNUS

A thesis submitted in accordance with the requirements for the degree of Doctor of Philosophy

This work was carried out under the supervision of Prof Mark Rainforth

Department of Engineering materials

The University of Sheffield

March 2020

ABSTRACT

Synthesis and tribological behaviour of metallo-ceramics and a particulate ceramic composite have been investigated. The microscale deformation mechanisms and effects of intrinsic lubricity of Ti-based MAX phases on their friction and wear behaviour has been investigated. The role of phase transformation toughening and thermal expansion mismatch on the microstructure and wear properties of a TiC particulate-reinforced ceramic composite have been investigated.

The transition in friction and wear observed in MAX phases from low friction and low wear regimes to high friction and high wear regimes was found to the linked to the formation of tribofilms consisting of rutile (TiO_2), titanium oxycarbide (TiO_XC_Y) and graphitic carbon. The low friction and wear regime prior to transition is due to the evolution of easy-shear graphitic material formed at the sliding surface intrinsically. The spallation of the non-adherent frictional heating-induced tribofilms (rutile and oxycarbide) generated over time at the sliding surface led to the transition in friction and wear. The spalled tribofilm constituted an abrasive third-body that led to the removal of the lubricious graphitic layer. The contact between the tribocouple following the removal of the graphitic layer led to the initiation of a series of energy absorbing microscale deformation mechanisms followed by the eventual grain pull-outs and fracture, thus the high friction and wear post transition. An intriguing feature also observed was that the fracture surface can self-heal once the fractured grains becomes pulverized, oxidized and smeared along the sliding direction over time. The healed sliding surface creates a smooth surface necessary for graphitization to bring about a further transition in friction from a high friction regime to a low friction regime. For the Al-based MAX phases, due to their superior oxidation resistance as compared to the Si-based MAX phases, the initiation of graphitization and/or oxidation of the sliding surface took longer and as such the transition in friction and wear proceeded from an initially high friction and wear regime to a low friction and wear regime. Further, due to the larger grain size of the Al-based MAX phases as compared to their Si-based counterpart, this makes them much more susceptible to sliding-induced deformation.

Ancillary TiC formed in situ and/or intentionally added to the Ti_3SiC_2 matrix was found to be beneficial to the tribological behaviour of the Ti_3SiC_2 MAX phase. The presence of TiC as particles in the Ti_3SiC_2 matrix enhances the tribological behaviour of Ti_3SiC_2 MAX phase by improving its oxidation resistance thereby delaying the deleterious formation of non-adherent

rutile as well as acting as load bearing element to further shield the surrounding Ti_3SiC_2 matrix. Also, TiC particles in the matrix acts as reinforcement for the weak Ti_3SiC_2 grain boundaries by impeding grain pull-out as well as inhibiting the propagation of kink-bands (KB) - a deleterious grain-scale deformation mechanism.

The low friction and wear of the monolithic titanium carbide disc was found to be linked to frictional heating-induced tribo-oxidation product preventing direct ball-to-disc contact. As tribo-oxidation product rutile (TiO_2) is non-adherent, it was easily scraped-off by the Al_2O_3 ball, leading to the eventual contact between the Al_2O_3 ball and the TiC sliding surface as evident by the evolution of wear grooves and surface fracture. A wear mechanism involving "oxidation-scrape-re-oxidation" is proposed for the TiC/Al_2O_3 tribocouple.

TiC containing 30 and 50 mol.% SiC particulates exhibited high friction and wear rates against alumina albeit superior fracture toughness in comparison to monolithic TiC. The lower wear resistance is believed to be a result of the incipient stress relaxation caused by the superposition of tensile stress during the sliding contact unto the inherent residual stresses in the composite system. Stress relaxation led to Ti–C bond degradation followed by a systematic mechanical exfoliation of carbon from TiC. A wear mechanism involving the nucleation and propagation of ripplocations – a deformation micromechanism – is proposed for the first time for the SiC-particulate/TiC-matrix ceramic composite.

ACKNOWLEDGEMENTS

I would like to thank Prof Mark Rainforth for his guidance and considerable assistance during my PhD research at the University of Sheffield. I would also express my sincere appreciation to the staffs of the Sorby centre for electron microscopy, most especially Dr Le Ma for her support. Thanks are also due to Dr Ian Ross, Dr Cheryl Shaw and Dr Colm O'Regan for assistance with the electron microscopes. I would also like to specially thank Dr Joanne Sharp for useful discussions as well as taking time to read through all my manuscripts. Discussions with former PhD students, Dr Daniel Cooper, Dr Tom Galvin and Dr Tanagorn Kwamman, were very useful.

The support of the staffs at the Material Science and Engineering student support office is greatly acknowledged. Thanks are particularly due to Mr Andrew Keating, Mrs Ann Newbould and Mrs Lucy Elam, for their considerable help with student related matters throughout the last four years.

To Joanna — Thanks for being there for me in last couple of years, bringing joy, support and love to every bit of my life. For keeping my spirits up, helping me believe in myself and for making the good times so much fun.

To my friends — Moe Elbadawi, Iida Maksimainen, Hussein Asamala, Ellie, and Eduardo & Miriam Pineda — thanks for the support, the great night outs in Sheffield and our memorable Eastern Europe road trip.

To my parents and family — Mum, Dad and Caroline — to whose unwavering love, care and support I owe everything. This thesis is dedicated to my sweet lovely mum – **Gladys Risi Magnus** (R.I.P).

CONTENTS

LIST OF TABLES

LIST OF FIGURES

THESIS

This thesis consists of an extended summary and the following appended peer reviewed papers:

PAPER A	Influence of sintering environment on the spark plasma sintering of Maxthal 312 (nominally—Ti_3SiC_2) and the role of powder particle size on densification. ***Journal of Alloys and Compounds 801 (2019), 208-219***
	https://doi.org/10.1016/j.jallcom.2019.06.076
PAPER B	Synthesis and microstructural evolution in ternary metalloceramic Ti_3SiC_2 consolidated via the Maxthal 312 powder route. ***Ceramic International***
	https://doi.org/10.1016/j.ceramint.2020.03.078
PAPER C	Spark plasma sintering (SPS) synthesis and tribological behaviour of MAX phase composite of the family $Ti_{n+1}SiC_n$ (n = 2). ***Wear 438-439 (2019), 2030662***
	https://doi.org/10.1016/j.wear.2019.203062
PAPER D	The lubricating properties of spark plasma sintered (SPS) Ti_3SiC_2 MAX phase compound and composite. ***Tribology Transactions 1547-3977X (2019)***
	https://doi.org/10.1080/10402004.2019.1657534
PAPER E	Microstructures and intrinsic lubricity of in situ Ti_3SiC_2-$TiSi_2$-TiC MAX phase composite fabricated by reactive spark plasma sintering (SPS). ***Wear (2019), 203169***
	https://doi.org/10.1016/j.wear.2019.203169
PAPER F	Microstructural evolution and wear mechanism of Ti_3AlC_2-Ti_2AlC dual MAX phase composite consolidated by spark plasma sintering (SPS). ***Wear 438-439 (2019), 203013***
	https://doi.org/10.1016/j.wear.2019.203013
PAPER G	Dry sliding friction and wear behaviour of TiC-based ceramics and consequent effect of the evolution of grain buckling on wear mechanism. ***Wear 422-423 (2019), 54-67***
	https://doi.org/10.1016/j.wear.2019.01.026
PAPER H	Wear induced ripplocation during dry sliding wear of TiC-based composite. ***Wear 444-445 (2020), 203121***
	https://doi.org/10.1016/j.wear.2019.203121

The author of this thesis was responsible for the scope and writing of all the manuscripts. Collaboration with co-authors was made partly in some synthesis work and TEM characterizations as directed by me.

LIST OF ABBREVIATIONS

BSE	*Backscattered electron*
CTE	*Coefficient of thermal expansion*
CVD	*Chemical vapour deposition*
DSC	*Differential scanning calorimetry*
ED	*Electron diffraction*
EDS	*Energy dispersive spectroscopy*
EELS	*Electron energy loss spectroscopy*
FIB	*Focused ion beam*
HP	*Hot pressing*
HV	*Vickers hardness*
IKB	*Incipient kink bands*
ISE	*Indentation size effect*
MA	*Mechanical alloying*
OM	*Optical microscopy*
POD	*Pin-on-disc*
PS	*Pressureless sintering*
ROI	*Region of interest*
SE	Secondary electron
SEM	*Scanning electron microscopy*
SHS	*Self-propagating high temperature synthesis*
SPS	*Spark plasma sintering*
TEM	*Transmission electron microscopy*
XRD	*X-ray diffraction*

CHAPTER 1

INTRODUCTION

The demand for self-lubricating tribosystems possessing low wear rates (WRs) and low friction coefficients (µs) across range of temperatures in engineering applications (mechanical and electronic devices) where liquid lubricants are ineffectual or undesirable are of increasing interest in industry [1]. Currently a range of solid lubricant systems in various forms, e.g. laminar solid, soft metal, composite materials, oxides, etc. have been developed and employed [2-4], but the extensive tribological requirement in varying environments as well as limitations of individual material necessitates the development of next generation intrinsically self-lubricating tribological materials.

The interaction between surfaces in mechanical contact can deleteriously affect energy loss, machinery performance and endurance [5]. Employing solid lubricants help to reduce friction and wear which will simultaneously impact on fuel consumption, maintainability and lifetime costs of engineering components [5]. Easy shear ability of solid layered inorganic compounds (such as molybdenum disulphide (MoS_2) and graphite) has led to their use as intrinsic solid lubricants for improved load-bearing capacity and lubricity of surfaces [5, 6]. Their low friction property stems from their anisotropic layered structure that incorporates covalent bonding within adjacent lamellae and weak interlayer Van der Waals forces between them [5]. Thus, during sliding contact, the weak Van der Waals forces enable parallel basal planes to slide over one another via inter and intra-crystalline slip owing to their easy shear [5]. The advantage of these solid lubricants are that they can substitute oil lubricants, function at elevated temperatures due to their thermal stability and/or in vacuum. However, they possess poor adhesion and load-bearing capacity and often degrade in humid air [7]. Further, most solid lubricants fail to work effectively due to degradation of properties above 350 °C [8].

Due to their special nanolaminate hexagonal crystal structure (similar to graphite) and high thermal stability [9], the MAX phases have been speculated to possess solid lubricant properties [10]. Although, there have been a lot of studies on MAX phases, most studies have focused mainly on the synthesis of monolithic phase. It is only recently that potential applications such as in friction and wear are beginning to gain interest. Despite this, little is known about their tribological behaviour and many observations from previous work, most especially, intrinsic lubricity, remains unexplained. For example, the role of frictional heating and the architecture of the tribofilm formed, which play a key role in friction and wear transition is still not fully understood. The role of inevitable ancillary binary phases formed in-situ during the synthesis of MAX phases and their influence on wear behaviour still remains elusive. Given the potential applications of MAX phases in a range of tribological applications, a study on their tribological behaviour necessitates comprehensive research if their full potential as a structural material is to be exploited commercially. A major study of this work is to examine for the first time the near surface microstructure generated by wear by undertaken extensive transmission electron microscopy characterization.

Ceramic composites based on TiC and SiC are promising structural materials for a range of tribological applications. However, the poor fracture toughness of these ceramics in monolithic states has hindered their use in contact-based applications. Previous works have highlighted the importance of fracture toughness in the wear resistance of ceramics [11]. The incorporation of second phase particles into a monolithic phase matrix leading to improved fracture toughness has been demonstrated by investigators [12, 13]. Despite the improved fracture toughness of the resulting composite, the wear rates still remain high and/or in some cases inferior to the monolithic state [14]. No detailed work has been done however, on the role of mismatch in thermal expansion coefficient between the matrix and the second phase particle on deformation processes from the microstructural level and the role on resulting residual stresses on wear behaviour. Thus, the aim of this study was to show for the first time the role of residual stresses owing to thermal expansion mismatch on the wear behaviour of particulate-reinforced ceramic-matrix composites.

Wear testing does not in general quantitatively replicate what may be expected in practical applications. However, a wear test may be seen as a means of investigating the wear mechanisms within each testing condition which includes testing properties such as speed, load, and environment. The understanding of the wear mechanisms can then be used in the understanding of service applications. Thus, emphasis was placed on understanding the microstructural evolution of the worn surface rather than generating large amounts of wear rate data in this work.

A critical assessment of the literature clearly revealed the inadequate chemical and microstructural characterization in the investigation of the wear in ceramic-ceramic composites most notably the analysis of the chemistries of the tribofilm as well as the use of TEM to effectively explain the associated wear mechanism(s). This study has therefore focused on detailed investigation of the worn surfaces rather than exhaustive wear testing in order to effectively answer the following important issues:

For the MAX phase metalloceramic

- Are MAX phases intrinsically self-lubricating?
- During the wear of MAX phases, what is the role of their unique deformation mechanisms, in particular the importance of basal plane slip?
- Are ancillary phases (most notably TiC) inevitably formed during synthesis really detrimental to the tribological behaviour of MAX phases?

For the ceramic composite

- What is the role of thermal expansion mismatch and consequent associated residual stresses on wear?
- What micro-mechanism is responsible for the grain fracture induced wear as previously reported?
- With regard to SiC, what is the role of β→α phase transformation and associated microstructural and residual stress development on wear?
- Is frictional heating during dry sliding wear responsible for the tribochemical-based wear as reported in previous work?

1.1 SCOPE OF THIS WORK

This work investigates the synthesis and tribological behaviour of the $M_{n+1}AX_n$ (MAX) phases of the composition Ti_3SiC_2, Ti_3AlC_2 and Ti_2AlC, respectively. With such self-lubricating and low coefficient of friction properties, MAX phases clearly offer some potential for wear resistant applications. However, if this is to be realized, it is important that some assessment be made of their wear behaviour particularly in dry-sliding and ambient condition. The objective of this research work is to examine the solid lubricity under ambient conditions and wear behaviour of a range of MAX phases in dry sliding conditions in order to understand if these hexagonal layered solids are truly intrinsically self-lubricating and to define the damage and wear mechanisms that govern their tribological behaviour via the investigation of the development of microstructure at the worn surface. Herein, we refer to MAX phases as a layered solid because they exhibit strong plastic anisotropy i.e., their deformation is confined to two dimensions [15] involving dislocation pileups and/or dislocation walls [16].

According to literature survey, the deformation mechanism of MAX phases incorporates a range of micro-plasticity energy absorbing events which makes them unique. Understanding the link between its associated deformation behaviour and wear mechanism(s) will be a core interest in this work. Furthermore, since the microstructural evolution of MAX phase is crucial to their tribological applications as MAX-phases often coexist with ancillary phases such as binary compounds M-X or A-X and/or M-A intermetallics [17], it is crucial that the role of TiC inclusions formed in situ and/or impregnated on their microstructural development and wear behaviour be investigated and discussed. This is because of the discrepancies in reports on the role of ancillary phases (most especially TiC) on the tribological behaviour of MAX phases.

Ceramic materials have been identified to offer promising tribological performance [13, 18]. Monolithic ceramic materials are well suited for a range of engineering applications due to their superior hardness, good chemical resistance, high thermal stability, etc [19]. However, their poor fracture toughness limits their applications in a range of structural applications most notably friction and wear [14, 18, 20]. Ceramic composites with one or more particulate phase are a new generation of engineering materials employed in a wide range of applications [21]. The resulting multiphase microstructures of the ceramic particulates brings about exceptional mechanical properties. The fracture toughness of the ceramic composite with in-situ particulate reinforcement is substantially superior as compared to monolithic ceramics [22].

Friction and wear of ceramics depends essentially on fracture toughness irrespective of the normal load, sliding velocity, temperature and counter surface [23]; the incorporation of a second phase particle into a ceramic matrix may facilitiate the generation of lubricious layer whilst as the same time initiate toughening [18]. Thus, a resulting simultaneous improvement in both the mechanical and tribological performance is expected [23, 24].

CHAPTER 2

LITERATURE SURVEY

This chapter provides a literature review on MAX phases and SiC-based ceramic composites. For the MAX phase material, a detailed review of deformation mechanisms is presented exceptionally as it is understood that, unless a clear understanding of this is achieved, the complex microstructural changes upon wear testing occurring at the worn surface cannot be fully elucidated. In addition, the general properties, synthesis as well as some previous work on the syntheses and tribology of MAX phases have been considered.

For the ceramic-based composites, an extensive literature survey has been carried out preferentially on SiC-based ceramic composites as the poor fracture toughness of SiC in its monolithic state is the main reason for the incorporation of a second phase particle. Furthermore, the role of thermal expansion mismatch and the consequent evolution of residual stresses in the composite system is reviewed as well as some previous work on enhancement of fracture toughness of ceramic composites and wear behaviour. A fairly detailed review of the microstructural evolution during the synthesis of SiC is presented, since it was felt that unless a understanding of the microstructural development which is kinetically aided by surface defects and depends on the consolidation mechanism is fully attained, the complex phase transformation occurring during spark plasma synthesis could not be evaluated.

This literature survey is in general limited in scope to the materials to be studied in this work and may not apply to other materials with similar properties outside of the scope of this work. No emphasis is given on explaining every individual MAX phase family or ceramic composites properties and wear behaviour, rather, a general overview on some of the properties and behaviour typical of these materials are discussed.

2.1. SOLID LUBRICANTS

When present at a sliding surface in most tribological applications, solid lubricants introduce intrinsic lubricity [25]. They shear easily to provide low friction and thus mitigate wear damage. Most inorganic solid lubricants (e.g., molybdenum disulphide, hexagonal boron nitride, graphite) owe their lubricity to a signature lamellar or layered crystal structure. Fig. 1 shows the characteristic crystal structures of MoS_2 and graphite. These layered structures are such that the atoms lying on the same layers tend to be closely packed and strongly covalently bonded to each other, whilst individual layers are actually relatively far apart and bonded by weak Van der Waals forces [25]. When they coexist between sliding surfaces, these layers align themselves parallel to the direction of relative sliding contact and slide over one another with ease, which in turn provides a low friction. Further, the strong interatomic bonding alongside the packing in each layer helps to reduce wear damage [25, 26].

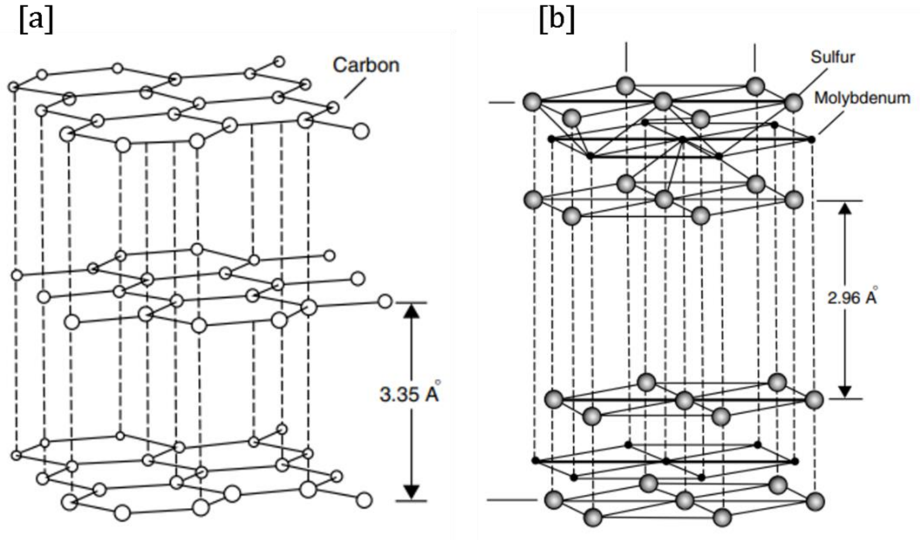

Fig. 1. Schematic showing the characteristic layered crystal structure of (a) graphite and (b) molybdenum disulphide [25].

Some major drawbacks of these solid lubricants include (but are not limited to):

- Poor thermal conductivity, thus inability to transfer heat from the sliding interfaces
- Friction coefficient fluctuates as a function of environment and contact conditions
- Irreversible structural chemistry changes leading to loss of lubricity at high temperature and/or oxidative environments.

In order to lubricate at elevated temperatures and within oxidizing environments, a range of solid tribological materials – for example, composite materials, soft metals, laminar solids, etc – have been developed and employed. Due to their signature nanolaminate crystal structure similar to graphite and MoS_2, the MAX phase metalloceramics have been proposed as a promising tribological materials [27]. Some MAX phases are stable in inert atmospheres above 2200 °C as well as damage tolerant - as they undergo a combination of energy absorbing mechanisms upon deformation. In addition to their lubricious tendency, the TiC particles in situ generated during synthesis is expected to act as reinforcement for the soft MAX phase matrix [28]. From a tribological aspect, TiC-reinforcement is expected to further introduce abrasive and wear resistance due to its high hardness. MAX phase material (notably Ti_3SiC_2) could be a promising solid lubricants owing to their range of properties. Previous study on the properties of Ti_3SiC_2 hypothesized self-lubricating potential [29], and related research on deformation behaviour and self-healing suggests wear resistance capability [30].

However, even though a lot of studies have been conducted on the tribology of MAX phases, the underlying wear mechanism(s) is still not understood, as well as if they are indeed intrinsically lubricating. Some studies have pointed out that, albeit possessing a layered-crystal structure similar to graphite, they are in fact not self-lubricating [31]. Further, a study on the influences of ancillary phase TiC formed in situ during the synthesis of Ti_3SiC_2 showed that it deteriorates its tribological properties [32]. However, an earlier study by Mhyra et al. [27] did indicate friction coeffecient (μ) $< (2\text{-}5) \times 10^{-3}$, whilst ultra-low friction was observed along the planes of easy cleavage with μ below the limits of resolution. Further, due to their high c/a ratio, MAX phases exhibit anisotropic mechanical and tribological properties as reported by Xu et al. [33]. It was found that the textured top surface of Ti_3AlC_2 corresponding to the (0001) plane, had the lowest mean coefficient of friction as compared to those measured on the textured side surface [33].

2.2. MAX PHASE MATERIAL

The polycrystalline solids named as MAX phases stemming from their general formula $M_{n+1}AX_n$ (where $n = 1 – 6$, M is an early transition metal, A is an A-group element and X is C and/or N) are a class of machinable ternary carbide and nitride nanolaminates possessing unusual metal and ceramic properties [28, 34]. These metallo-ceramic properties are linked to previous studies on the electronic structure and bonding properties of MAX phases that revealed a combination of metallic, ionic, and covalent bonds in their layered crystal structure [35]. Like ceramics, they possess relatively low density, high-temperature strength, excellent high-temperature oxidation resistance, high modulus and high melting point [36]. Like metals, they are endowed with high thermal and electrical conductivity, relatively soft (Vickers hardness value range from 1.4 to 8 GPa) thermal shock resistance, and damage resistant [37, 38]. Their characteristic signature property, however, is the ease of machinability of members of the MAX phase family [39]. Fig. 2 shows the periodic table of a list of MAX phase elements.

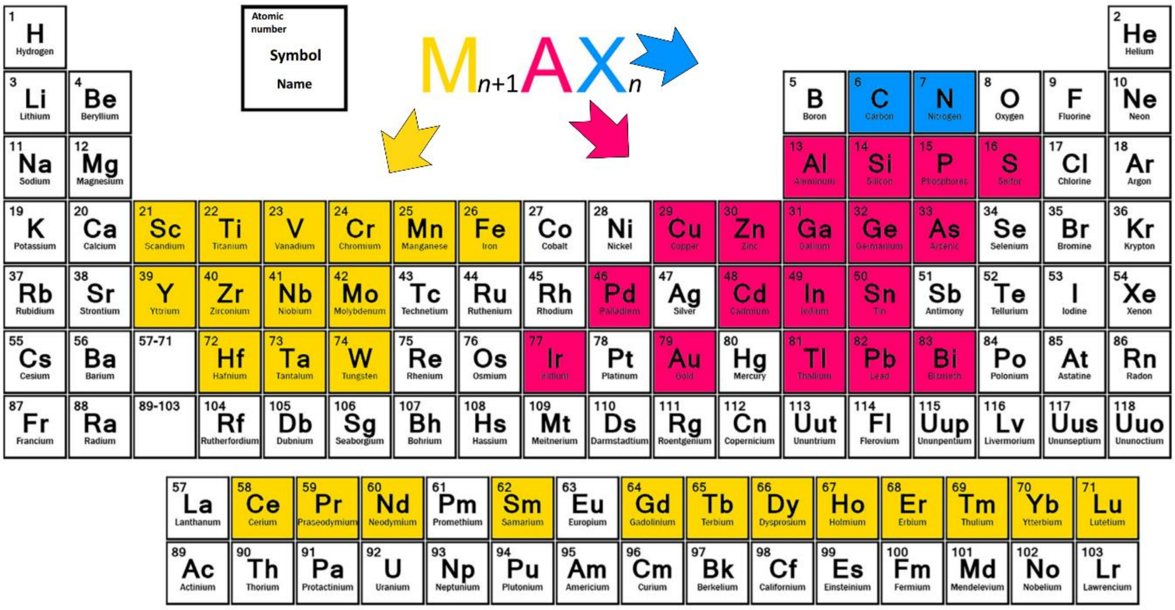

Fig. 2. The periodic table of elements forming ternary and solid solution MAX phases [40].

The growing research interest in MAX phases can be traced back to the properties of Ti_3SiC_2 [29] and the subsequent confirmation that most properties of Ti_3SiC_2 are inherent in all other members of the MAX phase family [41]. The ease at which the chemistry of the MAX phases can be tuned whilst keeping their structure the same, highlights an intriguing feature of these layered compound. They possess an unusual, and sometimes unique, set of properties that stems from their inherent layered nature, as well as the fact that basal slip dislocations are mobile and multiply even at room temperature [42]. Amongst the $M_{n+1}AX_n$ (MAX) family, the most studied are the relatively low density members, such as Ti_3SiC_2 in the $Ti_{n+1}SiC_n$ system, Ti_2AlC and Ti_3AlC_2 in the $Ti_{n+1}AlC_n$ system [29, 43] – all of which are subsets of the $Ti_{n+1}(Si, Al)C_n$ system. The stable members of the $M_{n+1}(Si)X_n$ phases are Ti_3SiC_2 and Ti_4SiC_3 whilst more than a dozen different $M_{n+1}(Al)X_n$ phases have been identified [44].

2.2.1. Crystal Structures

All members of the MAX phase family (≈ 155) adopt the D^4_{6h}-$P6_3/mmc$ symmetry space group with two formula units per unit cell [45] and isomorphous crystal structure consisting of repeating atomic layer sequence of A - M - X - M [46, 47]. The unit cells (Fig. 3) of the MAX phase family (comprising of 211, 312 and 413-phases for n = 1, 2 and 3) consists of $M_{n+1}X_n$ octahedral layers interleaved with layers of pure A-elements [45]. The difference between the crystal structure of these 3-phases is the number of M-layers separating the A-layers in their respective crystal structures which in turn give rise to various compositional forms [45]. In the

M_2AX phase (n = 1), as in e.g., Ti_2AlC, there are two; in the M_3AX_2 phase (n = 2), as in e.g., Ti_3SiC_2, there are three, and in the M_4AX_3 (n = 3), as in Ti_4AlN_3, there are four [42].

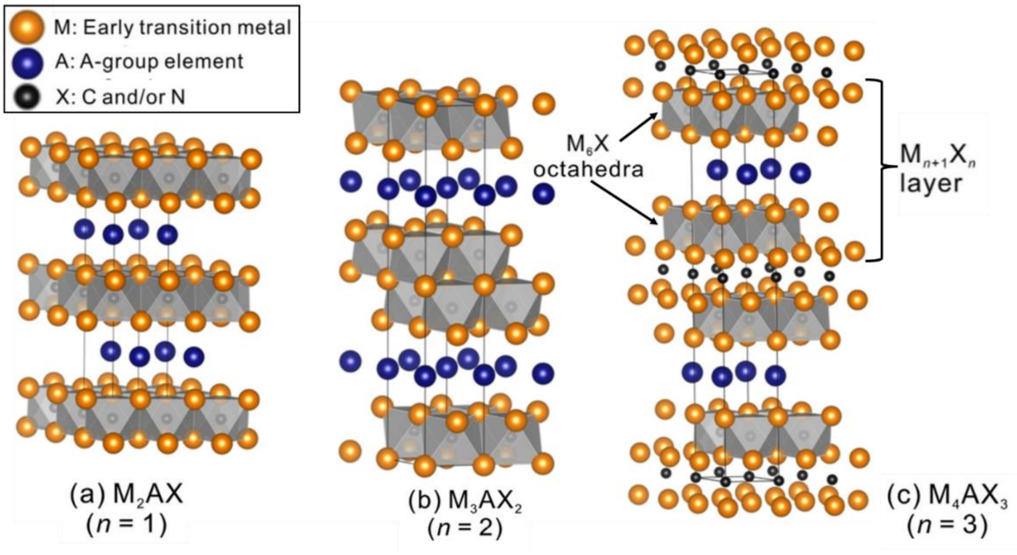

Fig. 3. Typical representative MAX phase units cells left to right for (a) n = 1 (211), (b) n = 2 (312) and (c) n = 3 (413) depicting alternating M_6X octahedral interleafed with A-elements [42].

According to Kisi et al. [48], the $M_{n+1}AX_n$ crystal structure comprises of dissimilar bonding strength, that is, the M – X, X – A, and M – A elements. The bonding between M – X is covalent and much stronger than the bonding between M – A which metallic and relatively weak [34, 46]. These differences in bonding strength is responsible for the following:

- Strength anisotropy as the measured strength in the direction parallel to the basal plane (c-plane) is usually higher than the strength measured in the normal direction [49]
- Reversible deformation and ease of machining [50]
- Irradiation resistance as the A–atomic plane is able to accommodate radiation-induced point defects [46]

2.2.2. Properties of M-A-X Phases

The properties of MAX phases stems from their hexagonal nanolaminated layered structure as well as the dissimilar bonding types integrated in their crystal structure – and these are responsible for its unique physical, chemical and mechanical properties [51]. Some of the properties (Fig. 4) exhibited by MAX phase compounds are: damage tolerance, high stiffness, low thermal expansion coefficient, intrinsic self-healing, ability to deform at room temperature, irradiation resistant, and some are fatigue, creep and oxidation resistant [42]. The ease of machinability amongst other properties is the most characteristic feature of the MAX phases – and this sets them apart from other structural ceramics [42].

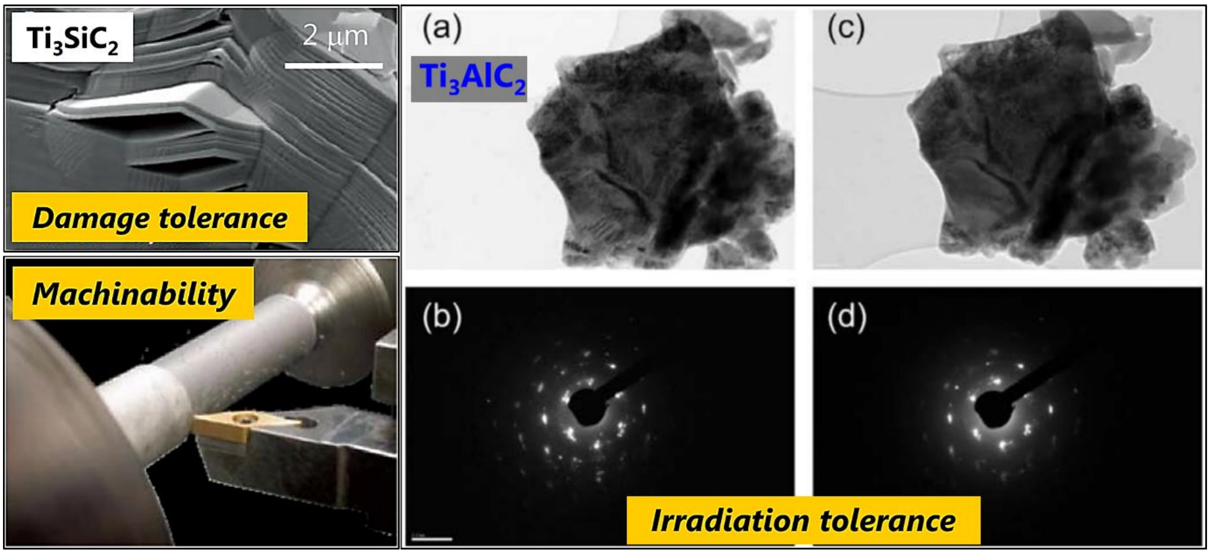

Fig. 4. Properties of M-A-X phases [42, 47]. Note: (a and b) unirradiated Ti_3AlC_2, and (c and d) irradiated Ti_3AlC_2.

Some of the important properties of MAX phases to be explored in this work are highlighted in Table 1.

Table 1. *Typical properties of some MAX phase system [42].*

	Density	*Thermal*	*Mechanical*	
Compound	***g/cm^3***	***CTE/ x10^{-6}K^{-1}***	***E/GPa***	***VH/GPa***
Ti_2AlC	***4.11***	***8.2***	***277***	***4.5***
Ti_3AlC_2	***4.2***	***9.0***	***297***	***3.5***
Ti_3SiC_2	***4.52***	***9.1***	***322***	***4.0***

2.2.2.1. Deformation behaviour and damage tolerance

MAX phases exhibit strong anisotropy in plastic deformation as well as fracture behaviour [52] owing to their complex crystal structure and the lack of five independent slip systems required for ductility [53]. Basal slip is the only operative slip system at room temperature in these layered compounds – thus they deform predominantly via the activation of basal slip, kinking and delamination along the basal planes [54-56]. A study on the deformation of MAX phases revealed these solids deform via a range of energy absorbing micromechanism events (Fig. 5) involving basal-plane slip, grain buckling, kink-band formation, grain pull-outs and eventual crack formation [57]. The initiation and propagation of microcracks has been observed to procced predominantly along the grain boundaries owing to their incomplete slip systems. This makes it difficult for MAX phases to accommodate deformation and highlights the observed pseudoplastic deformation in these compounds [58]. These aforementioned energy-absorbing mechanisms are responsible for the damage tolerance and high fracture toughness in MAX phase compunds [59].

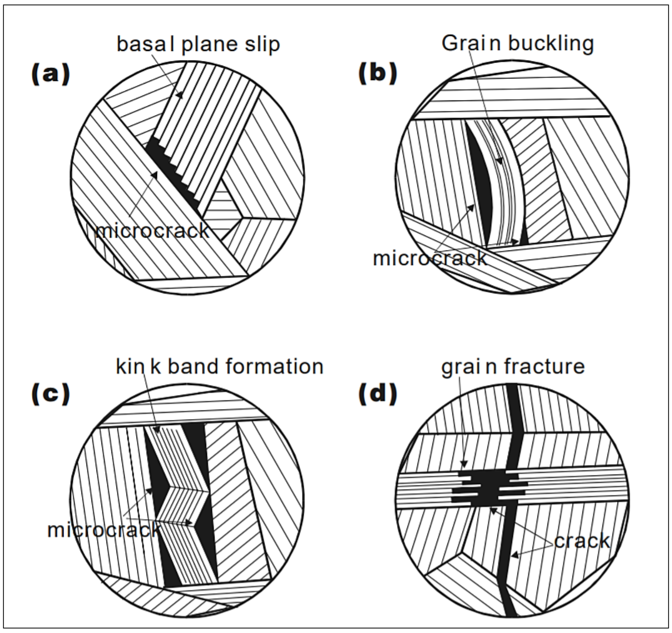

Fig. 5. Schematic highlighting micro-mechanisms involved in the deformation mechanism in Ti_3SiC_2 under compressive loading [57].

The damage tolerance of MAX phases is usually evident by the fact that it is difficult, if not impossible, for cracks to emanate along the diagonals of the indents of Vickers indentation even at high loads up to 500 N; as micro-damage is confined solely around the vicinity of the indentation (Fig. 6) in contrast to TiC with higher hardness but exhibits very low damage tolerance [55, 60].

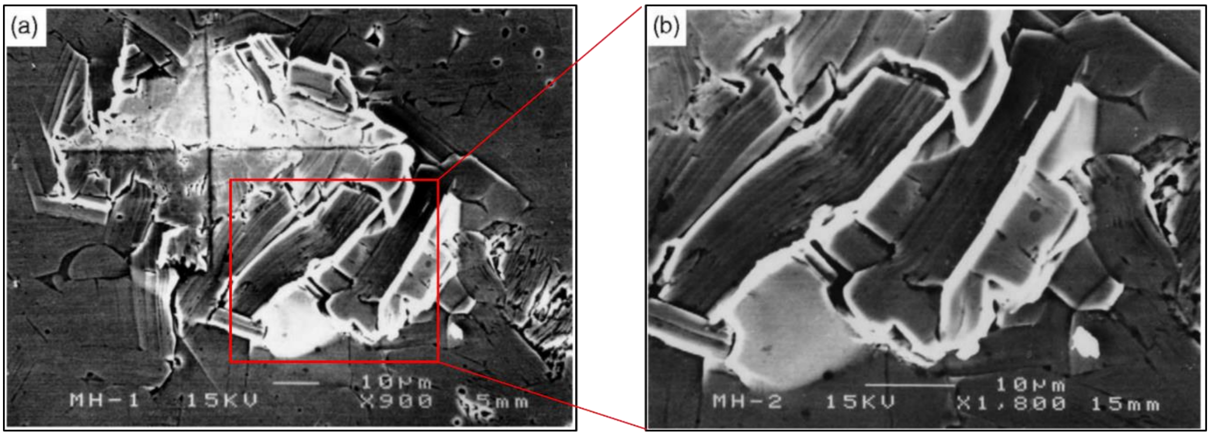

Fig. 6. (a) SEM morphology of indentation on Ti_3AlC_2, and (b) higher magnification of indentation damage in (a) [53].

According to Li et al. [61], MAX phases exhibit unique plasticity even at room temperature as manifested via the evolution of multi energy-absorbing mechanisms such as grain push-out, grain pull-out, grain delamination, kink band formation, buckling of individual grains, crack deflection, and crack branching. Each of these microscale phenomena that have been reported to be responsible for the containment of microdamage during Vickers indentation (Fig. 7) by facilitating stress relaxation and retardation of crack extension [54, 56, 58, 60, 61].

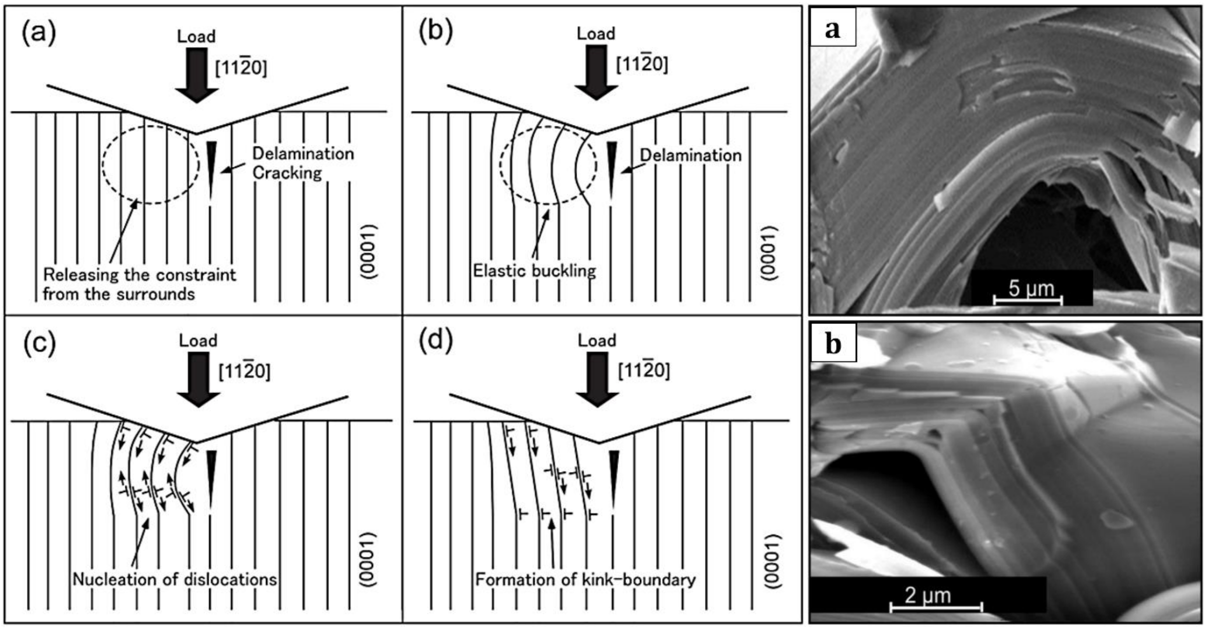

Fig. 7. Schematic of nano-indentation response in Ti$_2$AlC (a-d) [62], and SEM post-fracture micrographs (a-b) of Ti$_2$AlC, showing extensive: (a) buckling, delamination and (b) kink-band formation in nano-layers [63].

2.2.2.2. *Indentation size effect (ISE)*

Nick et al. [64] were the first to notice that the hardness of Ti$_3$SiC$_2$ was anisotropic, low, and higher when loaded along the c-direction. Goto et al. [65] later corroborated the findings and further stated that the hardness of Ti$_3$SiC$_2$ was a function of indentation load (Fig. 8). Both observations have been identified as a characteristic of the MAX phase [16, 54] wherein the measured hardness increases with decreasing indentation load, and below a certain load hardness becomes immeasurable as no indentation impression is visible [42].

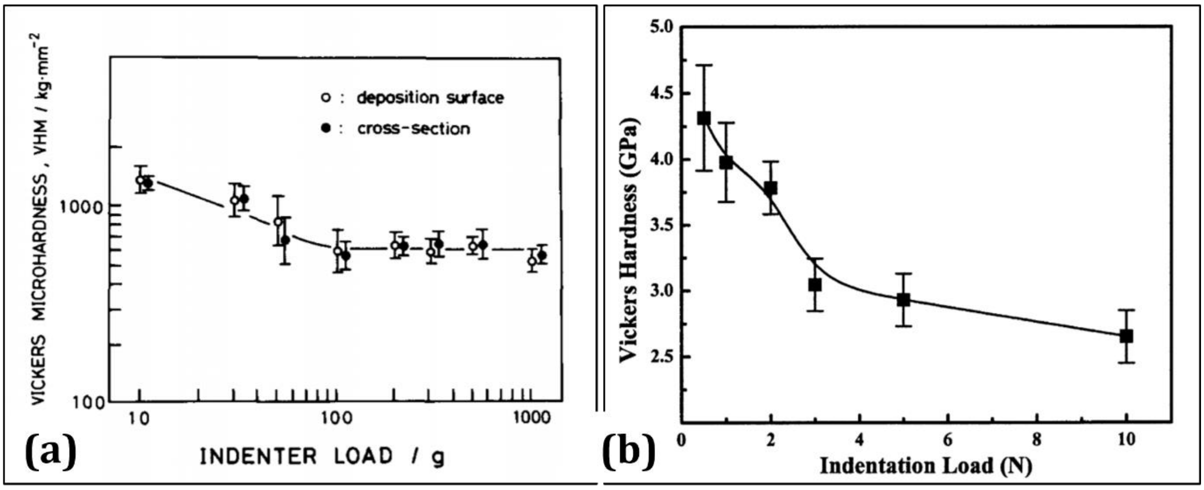

Fig. 8. The dependence of Vickers hardness on indentation load of : (a) CVD-Ti_3SiC_2, and (b) Ti_3AlC_2 [53, 65].

Wang et al. [53] showed that the Vickers hardness of Ti_3AlC_2 was a function of indentation load. They observed that the Vickers hardness decreased with an increase in indentation load from 0.5 to 3 N and reached a constant value of 2.5 GPa when the indentation load further increased to 10 N (Fig. 8(b)). This indentation size effect (ISE) was attributed to the elastic recovery at low indentation load owing to the evolution of incipient kink bands (IKBs) (Fig. 9) bringing about high Vickers hardness value [53, 66].

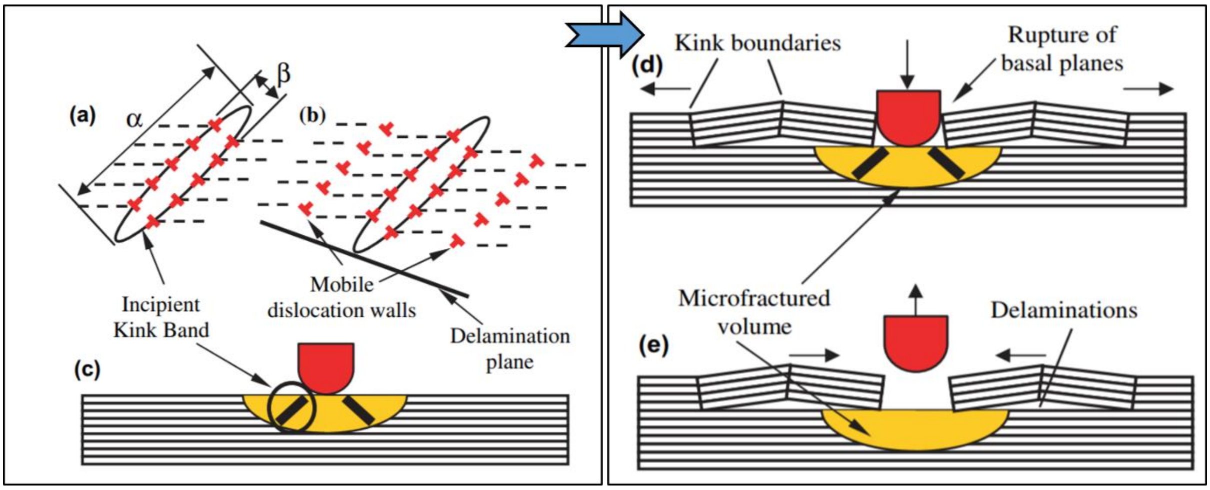

Fig. 9. Schematic of the evolution of incipient kink band (IKB) consisting of two dislocation walls of opposite polarity. A restoring force and eventual relaxation exist as long as the walls remains attached upon retraction of the indenter [66].

This unusual size effect was further elucidated by Murugaiah et al. [67] in their study on spherical nanoindentation and kink bands in Ti_3SiC_2. They showed that the indentation response of Ti_3SiC_2 produces three distinct regimes:

(i) Regime with linear elastic response in the direction normal and parallel to the c-direction.

(ii) Regime of hysteretic response wherein reversible response without microscopic damage is observed due to incipient kink bands formation. Further increase in the load level in this regime led to the evolution of mobile dislocation wall and subsequently the formation of immobile kink bands.

(iii) Regime of plastic response with irreversible damage (delamination and/or microcracking).

According to Kooi et al. [55] when the basal plane is oriented parallel to the surface a higher hardness is measured (Fig. 10 (c)) due to extensive plastic deformation and pile-ups around the indents as compared to perpendicular orientation (Fig. 10). This implies that during low load indentation kink band formation is not constrained thus sideward deflection can easily be initiated during indentation as the basal plane is effectively parallel to the surface.

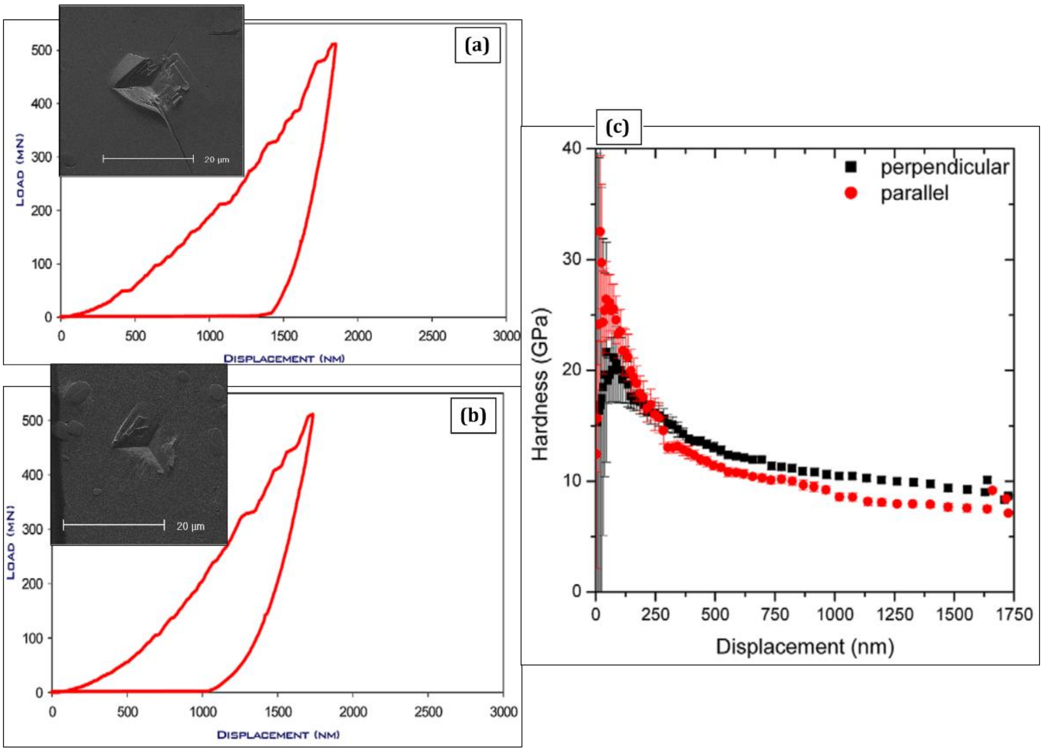

Fig. 10. Load-displacement curve and associated SEM images for an indentation in Ti$_3$SiC$_2$ grain with: (a) basal plane parallel to the surface, and (b) basal place perpendicular to the surface [55]. Note: (c) shows the hardness-displacement curves for both orientations [68].

A complete understanding of the deformation behaviour of MAX phases is critically important, and could extensively influence our current study on their tribological behaviour. This is partly because many aspects of the link between deformation and wear behaviour of MAX phases remain poorly understood.

2.2.2.3. Oxidation behaviour

The only oxide protective scale suitable for extended high temperature application as regards MAX phases is based on that generated by Al-based MAX Phases in the form of alumina. Generally, the overall oxidation of MAX phases follows the reaction [10]:

$$M_{n+1}AX_n + bO_2 = M_{n+1}O_x + AO_y + X_n0_{2b-x-y}$$

The oxidation proceeds by the outward diffusion of the A element followed by an inward diffusion of oxygen [69], whilst the X element is oxidized in-situ [70]. Some members of the aluminium containing MAX phases i.e., ($M_{n+1}AlC_n$), notably Ti_3AlC_2, Ti_2AlC and Cr_2AlC present excellent corrosion resistance owing to the formation of a dense adherent passivating alumina layer [71]. According to a study [72-74] on the oxidation kinetics of Ti_3AlC_2 and Ti_2AlC, their excellent high-temperature oxidation resistance was linked to the continuous Al_2O_3 scale formation during high-temperature oxidation in air. Oxide scale adhesion on the other hand has been identified to be excellent in Ti_2AlC owing to CTE match with α-Al_2O_3 scales (9 x $10^{-6/}$K) which minimized thermal residual stresses [75, 76]. Even though Ti_2AlC is not susceptible to spallation during thermal cycling, its continuous upper temperature use is around 1450 °C [10, 72]; above this temperature a deleterious formation of Al_2TiO_5 (Fig. 11) will induce cracking in the alumina scale [77].

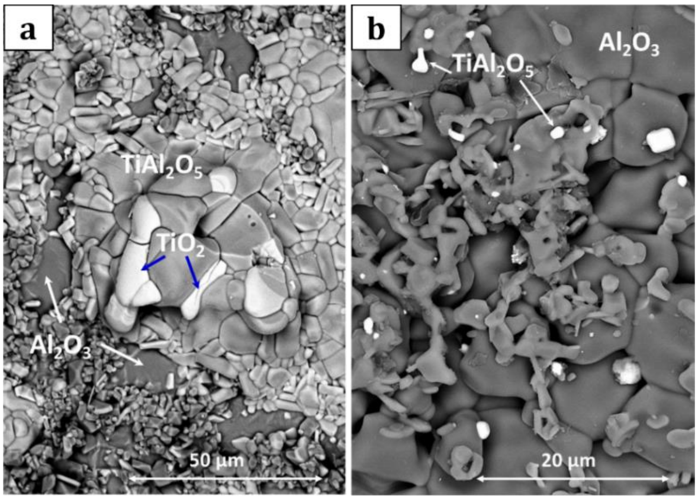

Fig. 11. Oxidation of Ti_2AlC at 1300 °C showing TiO_2 rich scale on top of an Al_2O_3 scale formed at (a) pre-oxidation for 300 h, and (b) subsequent 50 h exposure in High Pressure Burner Rig (HPBR) [78].

A study on the isothermal oxidation of Ti_3AlC_2 in air between 1000 -1400 °C for 20 h showed that Ti_3AlC_2 possessed good oxidation resistance [53]. Even as the temperature reached 1400 °C, the mass gain per unit area was only 3.48 x 10^{-2} kg/m^2 (Fig. 12). The excellent oxidation resistance was attributed solely to the continuous formation of adhesive Al_2O_3 in the oxide scale architecture.

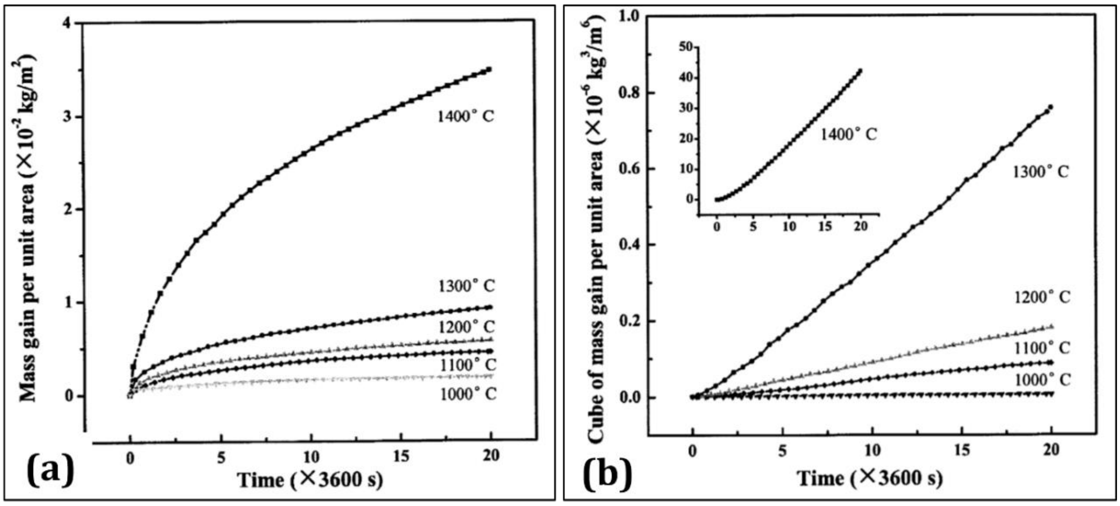

Fig. 12. (a) Plot of mass gain per unit area as a function of time for samples oxidized isothermally at 1000 - 1400 °C, and (b) cubic nature of mass gain per unit area as function of oxidation time [53].

It is worthy to mention that whilst the oxidation resistance of Ti_3SiC_2 is inferior to the Al-containing MAX phases due to the formation TiO_2 scale [79]; it has been reported that impurity phase TiC that accompany its synthesis further disrupt its oxidation kinetics and stability of the oxide scale [76].

2.2.2.4. Self-healing behaviour

Another important characteristic proprty of some $M_{n+1}AX_n$ (MAX) phases linked to their unique oxidation behaviour is autonomous crack healing. Self-healing have been reported for MAX phases e.g., Ti_3AlC_2 and Ti_2AlC [80, 81]. Their self-healing mechanism (Fig. 13) is associated to oxidation mechanism that creates stable adherent reaction products with high relative volume expansion that bonds effectively to crack surfaces – and eventually seals the crack with strong oxidation products with mechanical integrity close to those of the matrix [82]. A crack in Ti_2AlC and Ti_3AlC_2 can autonomously fully repair at high temperature following the formation of fine-grained Al_2O_3 and/or TiO_2 that occupies the crack gap [83, 84]. Some other Al-containing MAX phases that has been deemed as promising for autonomous crack healing includes but are not limited to Ta_2AlC and V_2AlC. Whilst the only Si-containing MAX phase that met the self- healing criteria is Ti_3SiC_2 [82].

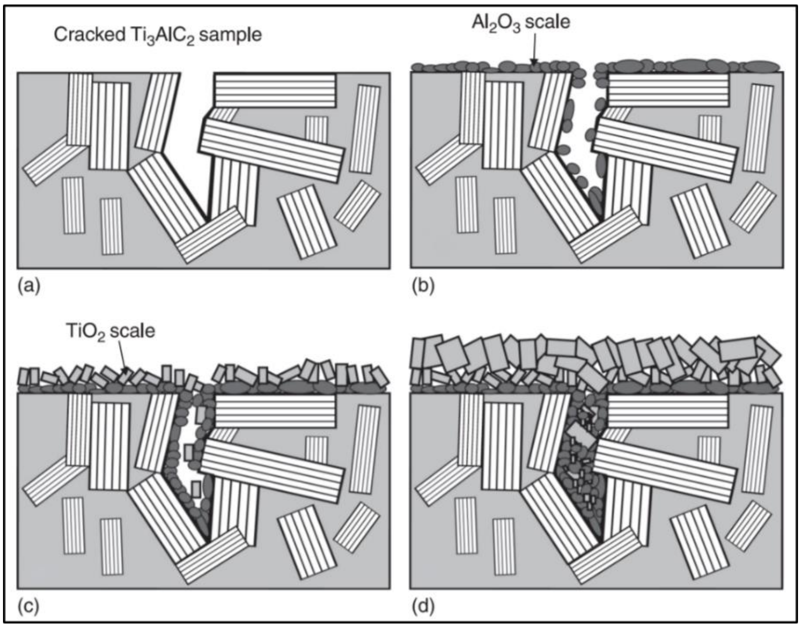

Fig. 13. Schematic of typical autonomous crack healing mechanism observed in MAX phases [83].

MAX phases are generally non-oxidic, as such they preferentially undergo oxidative decomposition at elevated temperatures [82]. Previous work on the $Ti_{n+1}AlC_n$ (n = 1 and 2) compunds revealed that they form a well-adherent protective Al_2O_3 scale at temperatures above 900 °C owing to the fact that the outward diffusion of the weakly bonded Al is easier as compared to the more covalently bonded Ti atoms in the crystal structure [42, 82, 84, 85]. The weak M-A bond as compared to the M-X bond have been identified to favour fast transport of the A-element as a result of higher atom mobility [42, 86]. This is because the strong covalent $M_{n+1}X_n$ layer somewhat helps to inhibit the transport of the transitional metal whilst the A-elements are rendered mobile [82]. In order to guarantee preferential A-element oxidation, it is important to identify M-element for which M-A combination would favour A-oxide formation [82]. Such is the case in formation Al_2O_3 healing products in oxidation of Ti and Cr containing Al-based MAX phases [87, 88]. Anisotropy in atom mobility has been reported both parallel and perpendicular to the basal plane in MAX phases [86].

It is noteworthy that upon the supply of the A-or M-atoms to the reaction surface, at longer times the oxide scale growth is solely governed by the inward diffusion of oxygen [82]. Al_2O_3 has been identified as an excellent inhibitor to further oxidation thus the good oxidation resistance observed in Ti_2AlC and Ti_3AlC_2 as reported elsewhere [37, 73]. Multiple cracking and consequent autonomous repair cycles have been demonstrated for Ti_2AlC (Fig. 14) in a study employing synchrotron X-ray tomographic analysis as well as investigation on microstructure evolution of self-healed cavity in Ti_2AlC [81, 84].

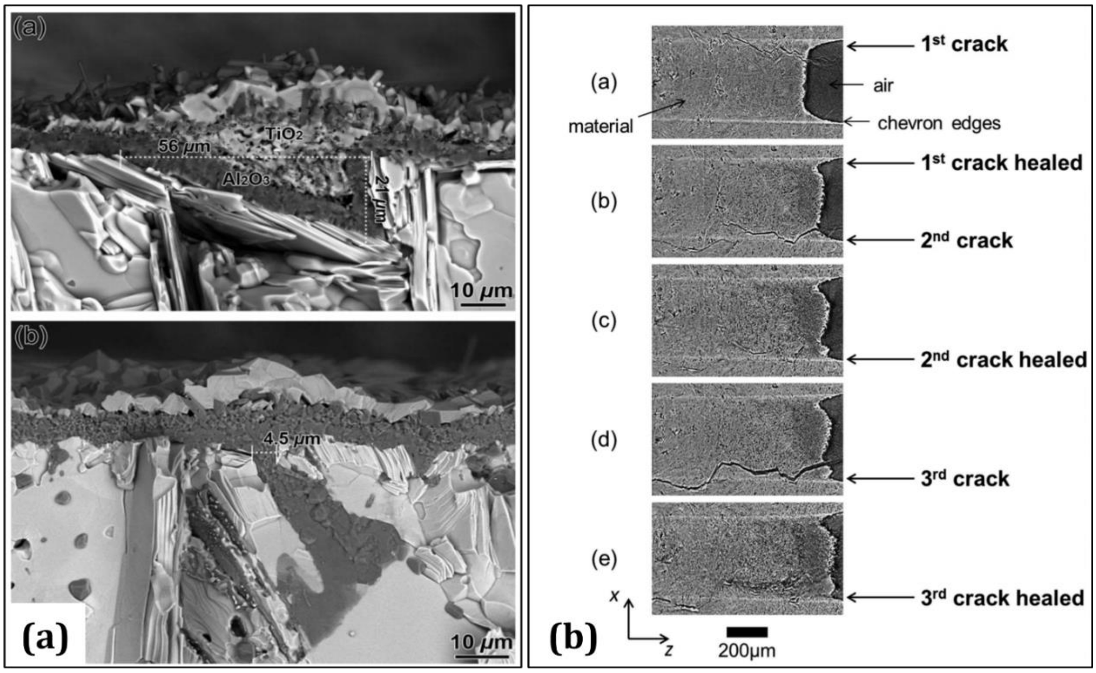

Fig. 14. (a) SEM micrographs (a-b) of microstructural evolution of fracture surface cross-section of self-healed cavity in Ti_2AlC oxidized at 1200 °C for 24 h: (a) V-shaped cavity and (b) L-shaped cavity [84], and (b) Virtual 2D section via tomographic data showing sequential crack growth and repeated crack healing steps in Ti_2AlC [81].

According to van der Zwaag et al. [89] intrinsic self-healing necessitates that the following criteria must be met: (i) healing agent must flow towards the crack, (ii) fill entirely the volume opened by the crack, and (iii) adhere intimately to the crack surface. Since in MAX phases the oxidation product at the crack surface is sufficient for volume expansion, the "flow" requirement is excluded [82]. Farle et al. [82] further postulated that for autonomous self-healing to take place in MAX phases the following criteria must all co-exist: (i) preferential selective oxidation of the A-element, (ii) fast diffusion of the A-element, (iii) volume expansion upon oxidation and adhesion, and (iv) close coefficient of thermal expansion (CTE) of the healing agent with that of the parent MAX phase.

2.2.2.4. Decomposition and thermal stability

$M_{n+1}AX_n$ (M-A-X) phases do not melt but instead will decompose at high temperatures depending on environment and impurities according to the equation [90]:

$$M_{n+1}AX_n(s) \rightarrow M_{n+1}X_n(s) + A(\, g \text{ or } l\,)$$

$$M_{n+1}X_n \rightarrow (n+1)MX_{n/(n+1)}$$

The activity of the out-diffusion of the A-element has been reported to be the predominant factor amongst other things in the decomposition of MAX phases [91]. However, the exact high temperature of decomposition has generated a lot of controversy [90]. Some previous work on Ti_3SiC_2 showed that it is unstable at temperatures above 1400 °C in an inert environment (e.g., vacuum, argon or nitrogen) [92-94]. Whilst a study by Zhang et al. [95] reported that Ti_3SiC_2 became unstable at temperature above 1300 °C in a nitrogen environment. In another study by Gao et al. [96], the decomposition of Ti_3SiC_2 was associated to the vapour pressure of Si which depends on the atmosphere where Ti_3SiC_2 exists.

According to Low et al. [94], the phase stability of MAX phases and possible dissociation depends on the following factors:

(i) The vapour pressure of the A-element; the higher the vapour pressure of the A-element, the more susceptible is the MAX phase to decomposition at high temperature.

(ii) Phase purity, porosity and atmosphere; A highly porous and impure sample will dissociate faster as compared to a dense high purity sample. Employing high vacuum will expedite the rate of phase decomposition due to the high vapour pressure of the A-elements (e.g., Al and Si).

(iii) Heating element used.

(iv) Quality of vacuum employed: at a medium vacuum typically 10^{-3} MPa, MAX phases decompose at 1400 °C. However, when the vacuum is higher than 10^{-3} MPa, MAX phases will decompose below 1400 °C and vice versa in low vacuum environments (Fig. 15).

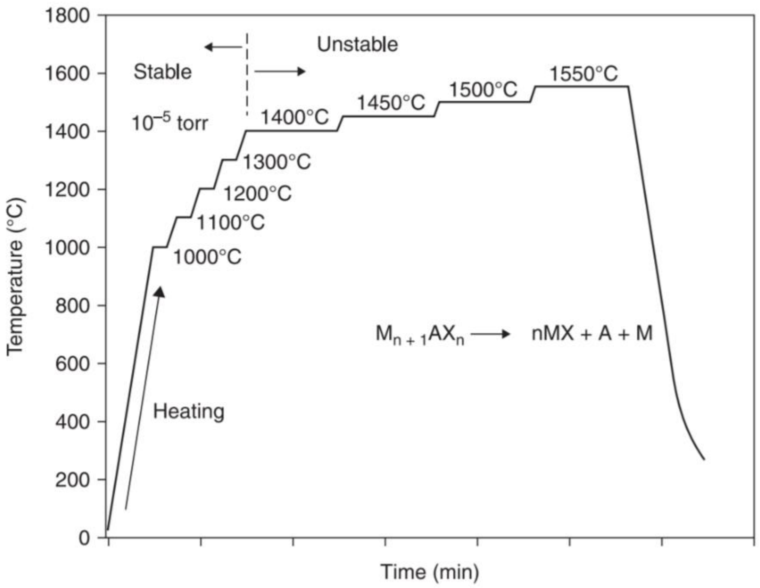

Fig. 15. Thermal stability of $M_{n+1}AX_n$ phases at high temperature in different vacuum conditions [94].

Recault et al. [97] in their work on thermal stability of Ti_3SiC_2 found that polycrystalline Ti_3SiC_2 dissociated in vacuum at 1300 °C triggered by a chemical reaction between the Si and the surrounding carbon rich environment (graphite crucible). This further highlights the importance of the diffusion of the relatively weakly bonded A-element in the decomposition of MAX phases as well as the possible chemical reactions between the MAX phase and the material in contact [91]. Furthermore, Ti_3SiC_2 for example exhibits 2 polymorphs in which Si shifts from 2b to 2d (Wyckoff position) (Fig. 16) at about 1000 K supports the notion of high Si mobility [91].

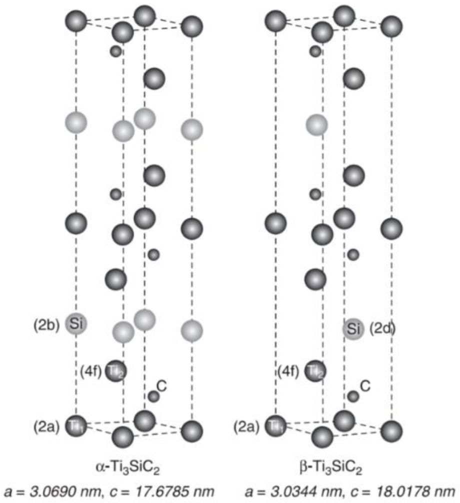

Fig. 16. Crystal structures depiction α-Ti_3SiC_2 and β-Ti_3SiC_2 polymorphs with corresponding lattice parameters [98].

In a study on thermal stability of Ti_3SiC_2 thin films during vacuum annealing by Emmerlich et al. [91], they reported that Ti_3SiC_2 thin films exhibited surface decomposition at 1000 °C via transformation into TiC_x ($x \approx 0.67$) upon Si out-diffusion along the basal planes (Fig. 17). They proposed the following steps in relation to the decomposition mechanisms [91]:

- Stage 1: Si out-diffusion and subsequent evaporation
- Stage 2: Oxygen uptake and subsequent SiO evaporation
- Stage 3: Ti_3C_2 relaxation, detwinning, and eventual $TiC_{0.67}$ formation via C-redistribution leading to void formation.

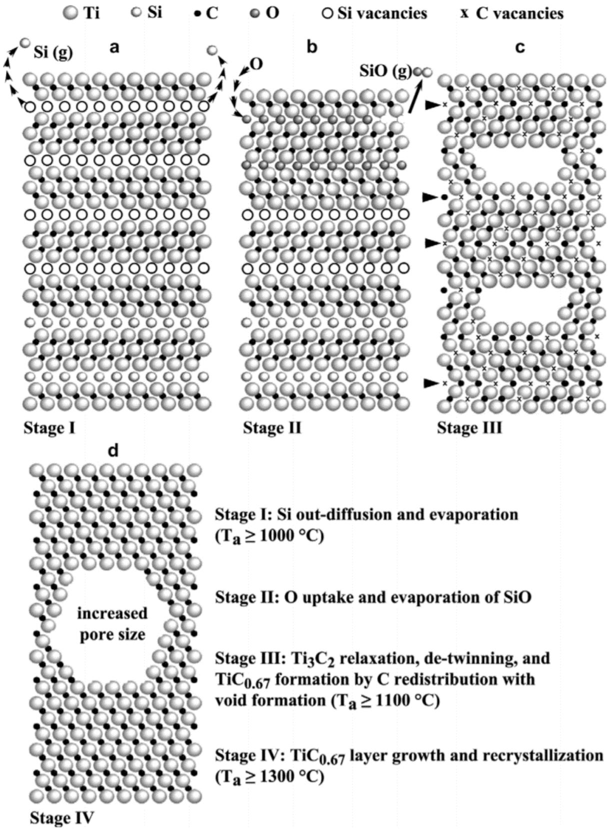

Fig. 17. Schematic depicting various stages of phase transformation during the dissociation of Ti_3SiC_2 (0001) [91].

The difference in decomposition temperature of bulk Ti_3SiC_2 as compared to thin films was attributed to differences in thickness criteria for phase transformation [91].

2.2.3 Potential Application of MAX Phases

MAX phases have been speculated as promising in a range of applications which includes e.g., high temperature structural applications, nuclear and aerospace applications, electrical and biomedical applications [16], where traditional ceramics have been intrinsically disadvantaged owing to brittleness and poor machinability [99]. Some of the potential applications as listed by Barsoum [100] includes but are not limited to: substitutes as machinable ceramics, corrosion and wear protection, heat exchangers, electrical contacts, sensors, tooling for dry drilling, microelectrochemical systems, surface coatings, damping materials and low friction applications to exploit their basal plane lubricity. Some novel heating elements (Fig. 18(a)) as well as gas burners (Fig. 18(b)) based on MAX phases have been developed with properties superior to well-known materials.

Although the MAX phases (typically Ti_3SiC_2) were first synthesized as early as 1960s [101], its potential applications have not been fully exploited mainly because of difficulties associated to fabricating single-phase, bulk, polycrystalline samples as impurity phases have been speculated to degrade some of its exclusive mechanical properties [102]. As shown in later sections herein, this is a misconception as impurity phases could be beneficial to the mechanical properties of MAX phases, most notably tribological properties.

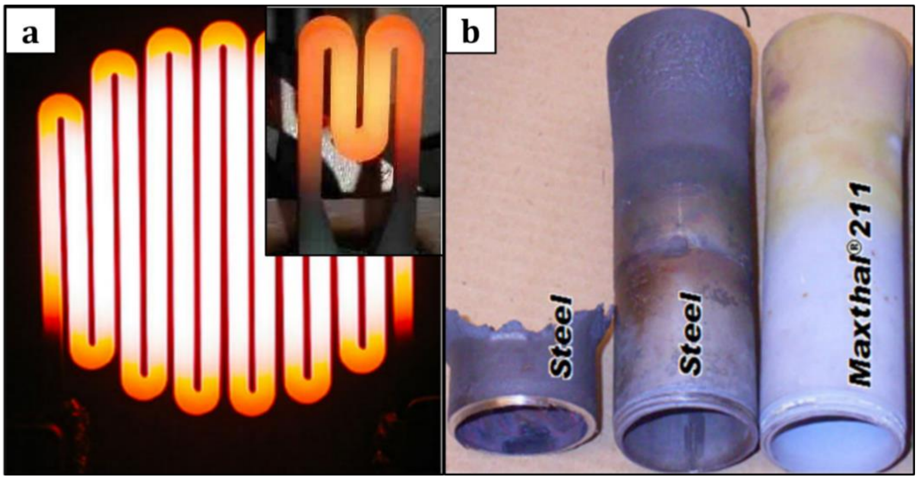

Fig. 18. (a) Heating element based on the Maxthal® 211-phase (Ti_2AlC) glowing at 1350 °C [72], and (b) gas burner nozzles in corrosive environment after a year in a furnace [10].

2.3. SYNTHESIS OF MAX PHASES

More than > 115 MAX phases of different composition sharing similar structure: $M_{n+1}X_n$ interleaved with A-group elements have been successfully synthesized either in bulk, solid solution and thin film form to date after they were first discovered in 1960's in powder form by Nowotny and co-workers [101, 103]. The drive towards the synthesis of MAX phases became more prominent after Barsoum et al. [42] successfully synthesized the first monolithic bulk Ti_3SiC_2 and reported on its unusual properties. Since first synthesized by hot pressing, many other synthesis techniques have been employed over the years to synthesize monolithic

MAX phases. However, most of these synthesis techniques have either failed to be replicable in bulk synthesis or unable to produce monolithic phase [104]. Some of the techniques that have been employed for MAX phase synthesis in powder, bulk and thin films includes; pulsed laser deposition (PLD) [105], chemical vapour deposition [106], magnetron sputtering [107], spark plasma sintering (SPS) [108, 109], pressureless sintering (PS) [110, 111], mechanical alloying (MA) [34, 112], arc melting [113, 114], self-propagating high-temperature synthesis (SHS) [115, 116] and most recently 3D printing [117]. Bulk monolithic MAX phases can be fabricated from starting material powders or pre-synthesized MAX phase powders (such as MAXTHAL$^{(TM)}$) [118]. Assistive pressure incorporation during the synthesis is often needed to facilitate the densification of the final product. Hot pressing, hot isostatic pressing, spark plasma sintering, pressureless sintering are the frequently utilized methods to densify these nanolaminate solids [118]. However, the above-mentioned synthesis methods, besides spark plasma sintering, are all very time consuming and require high temperature and pressure [34, 118]. SPS on the other hand is a more efficient method for synthesizing ceramics owing to its range of controllability of sintering parameters (temperature, pressure, heating rate, cooling rate and dwell time), shorter sintering times, ability to tailor grain size as well as the unique capability of heating sample up with pulse direct current during synthesis [118]. Although in terms of scability it lags behind other traditional consolidation techniques.

2.3.1. Phase Diagram

According to Lin et al. [119] structure and microstructure plays a crucial role as regards determining the physical and mechanical properties of the M–A–X ternary material systems. Minor amounts of M–A or A–X binary phase in the MAX phase matrix has been reported to improve and/or deteriorate the high-temperature oxidation and wear resistance of MAX phases. The presence of ancillary TiC is beneficial to the mechanical properties $Ti_{n+1}AC_n$ ternary phases but detrimental to their oxidation resistance [37]. Whilst the incorporation of Ti_2AlC in TiAl matrix led to an improvement in high-temperature oxidation [120] and wear resistance of TiAl alloys [121]. As the binary phase M–A and/or M–X can be the starting materials, intermediate phases, and ancillaries in the synthesis of MAX phases, understanding the microstructural evolution evolution during synthesis is important for processing and optimizing the properties of MAX phases [119].

The Ti–Si–C and Ti–Al–C ternary phase diagrams are shown in Fig. 19 [37]. According to Yoshida et al. [122], in the synthesis of Ti_3AlC_2 both Ti_2AlC and Ti_3AlC can be found in the ternary system at every temperature in the range 750 °C and 1300 °C. However, Ti_3AlC_2 is not an equilibrium phase at, or below 1000 °C. Thus, the equilibrium relation between 1000 and 1300 °C is the standard for synthesis of Ti_3AlC_2. It is difficult experimentally to synthesize monolithic MAX phases (e.g., Ti_3AlC_2. and Ti_3SiC_2) due to their very narrow stability region as shown in their respective phase diagram which intersects with stable binary or other ternary phases [123]. In the synthesis of Ti_3AlC_2 ancillary phases such as Al_2O_3, TiC, Ti_xAl_y intermetallic [124] and/or Ti_2AlC have always coexisted with the final product [125-127], whilst the synthesis of Ti_3SiC_2 has been reported to be accompanied by a large amount of TiC and titanium silicide (Ti_xSi_y) [39] – this indicated that thermodynamic equilibrium was not always attained [113]. This is indeed true, looking at Ti–Si–C phase diagram, the formation of Ti_3SiC_2 is in equilibrium or in other words intersects with boundaries of $TiSi_2$, TiC_x, SiC, $Ti_5Si_3C_x$, and TiC intermediate phases [93].

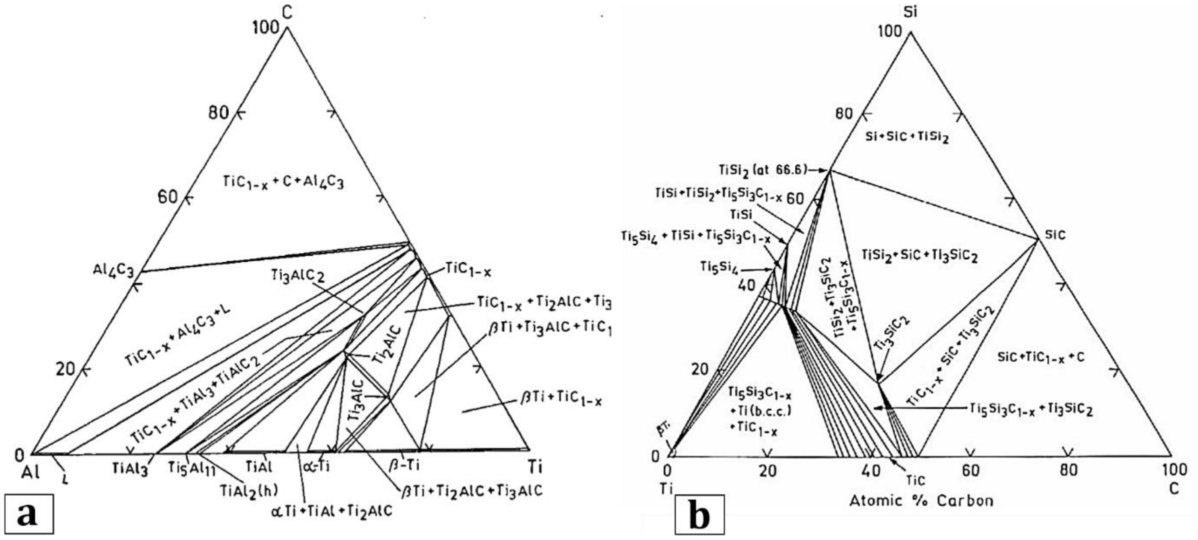

Fig. 19. Isothermal phase diagram sections of (a) Ti-Al-C at 1300 °C and (b) Ti-Si-C at 1250 °C, respectively [128, 129].

2.3.2. Texture in MAX Phases

In powder diffraction sample crystallites have random orientation distribution [130]. However, in a non-random orientation distribution (texture), the integral intensity measured is a function of the samples direction [130]. MAX phases have been reported to exhibit preferred orientation along the [001] direction during synthesis due to pressure incorporation [131]. Lapauw et al. [132] observed a shift in preferred crystallographic orientation from the starting MAX phase powder (Maxthal 312$^{®}$- nominally Ti_3SiC_2) to the spark plasma sintered (SPS) bulk Ti_3SiC_2 disc. Further they reported that the relative intensities of the peaks obtained from the XRD patterns of the raw Maxthal-312 powder corresponds well to those of the reference JCPDS files

– and the (104) peak had the highest intensity. However, in the SPS-ed disc the strongest reflection was in the (008) corresponding to the (001)-direction. The MAX phase grain clearly aligned with the c-axis i.e., the direction parallel to the pressing axis [132]. In another study [133], during the grain growth of Ti_3SiC_2 from the liquid phase during hot-pressing (HP), the basal planes of the Ti_3SiC_2 grains appeared to orient themselves parallel to the pressing surface. This was attributed solely to the characteristic nature of the Ti_3SiC_2 grains. As a result of preferred orientation (Fig. 20), the mechanical properties of MAX phases are expected to depend on crystallographic orientation as their layered nature renders them textured during synthesis [33, 134].

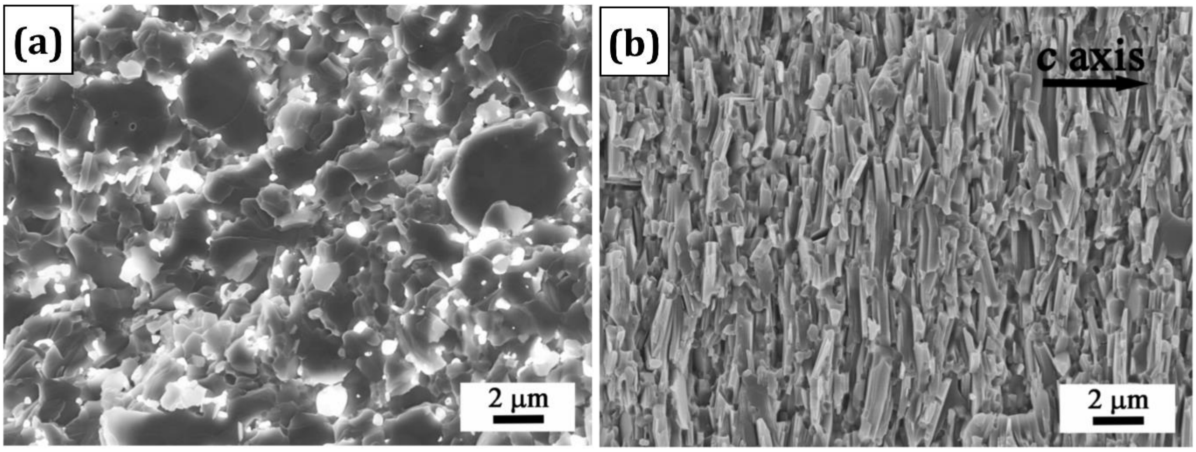

Fig. 20. SEM morphologies of fractured Ti_3AlC_2: (a) along the textured top surface (TTS), and (b) along the textured side surface (TSS). Fracture micrograph showed marked texture along the c-axis [33].

2.3.2.1. Integrated calibration method for phase analysis

As mentioned earlier, it is quite difficult if not impossible to prepare a completely randomly oriented MAX-phase, especially in the case of Ti_3SiC_2 [133]. As a result, phase quantification becomes somewhat difficult due to the exaggerated peak intensity along the c-direction. Thus, phase quantification by Rietveld refinement using the ICSD reference file becomes complex due to preferred orientation. Hence, we employ a theoretical calculation as a standard in cases where the MAX phase is textured as employed herein for phase quantification of the Maxthal-312 sintered compacts.

2.3.2.2. $Ti_{n+1}AlC_n$ – phase quantification by integrated XRD peak intensities

The proportion of constituents phases in a synthesized compact containing Ti_3AlC_2, Ti_2AlC and TiC can be determined using the following equations [135]:

$$W_a = \frac{I_a}{I_a + 0.220 I_b + 0.084 I_c} ; W_b = \frac{I_a}{4.545_a + I_b + 0.382 I_c} ; W_c = \frac{I_a}{11.905 I_a + 2.619 I_b + I_c}$$

Where W_a, W_b and W_c are the weight percentages of Ti_3AlC_2, Ti_2AlC and TiC, respectively. I_a, I_b and I_c on the other hand represent the integrated diffraction intensities of the Ti_3AlC_2 (002), Ti_2AlC (002) and TiC (111) peaks, respectively. The diffraction peaks for quantitative phase analysis were generated from X-ray diffraction peaks for Ti_3AlC_2 Ti_2AlC, and TiC in the range $0^{\circ} < 2\theta < 80^{\circ}$ and with relative intensitities $I/I_0 > 5$ taken from PDF cards (PDF Nos. 2-877, 29-9, and 32-1383), that is, the (002) peak at $2\theta = 9.5^{\circ}$ for Ti_3AlC_2 ($I/I_0 > 26.5$), the (002) peak at $2\theta = 13.0^{\circ}$ for Ti_2AlC ($I/I_0 > 39$), and the (111) peak at $2\theta = 35.9^{\circ}$ for TiC ($I/I_0 > 78$). The method involved mixing powder specimens with unknown amounts of Ti_3AlC_2, Ti_2AlC, and TiC and then collecting a series of XRD patterns followed by calculating the values of C_a, C_b and C_c from the XRD patterns.

From the theory of X-ray diffraction, the diffracted intensity, $I_{hkl,I}$ of the ith phase in a sample is expressed as:

$$I_{hkl,i} = KC_i \frac{\omega_i}{\mu}$$

Where K is a constant and is related to the material and test condition, C_i is a constant corresponding to the ith phase, ω_i is the mass fraction of the ith phase in the sample, and μ is the overall absorption coefficient of the sample. The equation above can then be re-written as the relationship between $I_{hkl,i}$ and ω_i. $I_{hkl,i}$ which can be determined by XRD. This implies that, if the constant KCi and μ are known, the content of the ith phase in the mixture ω_i can be calculated. Further details on how the final equations were derived as well as the experimental procedure are explained explicitly elsewhere [135].

However, for a two-phase compact containing Ti_3AlC_2 and TiC impurity phase, the phase contents in the as-synthesized compacts can be estimated according to the following equation [136]:

$$\omega_{TC} = 1.084/(I_{TAC}/I_{TC} + 1.084)$$

$$\omega_{TAC} = 1 - \omega_{TC}$$

Where ω_{TC} and ω_{TAC} represents the mass percentages of TiC and Ti_3AlC_2, respectively. Whilst I_{TC} and I_{TAC} are the integrated diffraction intensities of TiC (111), and Ti_3AlC_2 (104) peaks, respectively.

2.3.2.3. $Ti_{n+1}SiC_n$ – phase quantification by integrated XRD peak intensities

The purity of Ti_3SiC_2 in a synthesized compact or powder assuming a two-phase mixture of Ti_3SiC_2 and TiC, is estimated using the following equations [137]:

$$W_{TSC} = \frac{1.80}{1.80 + I_{TC}/I_{TSC}} \text{ and } W_{TC} = \frac{I_{TC}/I_{TSC}}{1.80 + I_{TC}/I_{TSC}}$$

Where W_{TSC} and W_{TC} represents the relative weight percentages of Ti_3SiC_2 and TiC, respectively. Whilst I_{TSC} and I_{TC} are the main peak intensities of the Ti_3SiC_2 (104) and TiC (200), respectively.

It is noteworthy that no three-phase equation consisting of Ti_3SiC_2-TiC-$TiSi_2$ currently exists and most Ti_3SiC_2 synthesis reported have largely employed the two-phase equation in a three phase (consisting of small traces of silicides) as the $TiSi_2$ phase that coexists is relatively small and can be neglected in the phase analysis [138, 139].

For a three phase equation consisting of Ti_3SiC_2-Ti_5Si_3-TiC, the experimental calibration for the weight percentages of the three major phases is as follows [126]:

$$W_{TiC} = \frac{I_{TiC}}{1.222\, I_{Ti_3SiC_2} + 5.084 I_{Ti_5Si_3} + I_{TiC}}$$

$$W_{Ti_5Si_3} = \frac{I_{Ti_5Si_3}}{0.240\, I_{Ti_3SiC_2} + I_{Ti_5Si_3} + 0.197 I_{TiC}}$$

$$W_{Ti_3SIC_2} = \frac{I_{Ti_3SiC_2}}{I_{Ti_3SiC_2} + 4.159 I_{Ti_5Si_3} + 0.818 I_{TiC}}$$

Where I_{TiC}, $I_{Ti_5Si_3}$, and $I_{Ti_3SiC_2}$ represents the intensities of non-overlapping peaks of TiC (111), Ti_5Si_3 (102) and Ti_3SiC_2 (104), respectively.

2.3.3. Previous Work on the Synthesis of MAX Phases

The most synthesized and characterized member to date of the MAX phase system is the Ti_3SiC_2 a subset of the $Ti_{n+1}SiC_n$ family. After its first synthesis revealing its unique properties [101], this has since led to the synthesis and further characterization of other members of the $M_{n+1}AX_n$ series. As a representative of the $Ti_{n+1}SiC_n$ phase, Ti_3SiC_2 is the only stable according to the phase diagram [140] – and has layered and anisotropic crystal structure (Fig. 21) incorporating a vertical repetition of two Ti_6C polyhedral layers intercalated by silicon atoms [141].

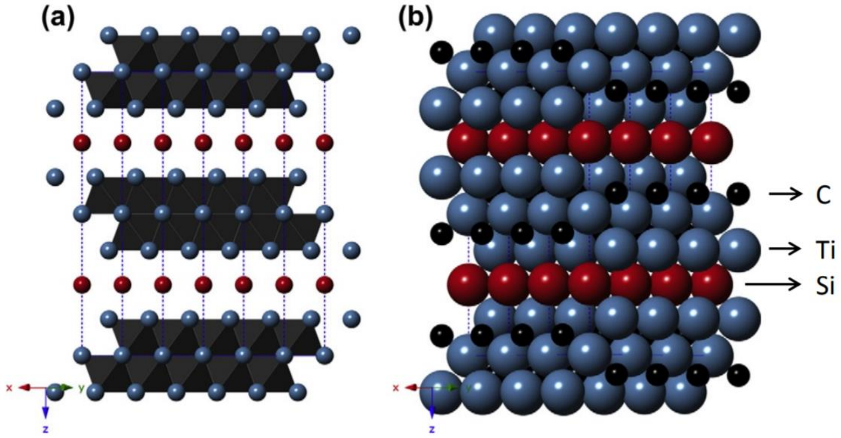

Fig. 21. Unit cell of Ti_3SiC_2: (a) Ti_6C polyhedral intercalated by Si layers and (b) hexagonal crystal structure showing stacking sequence with carbon atoms [142].

Some starting powder combinations commonly employed in the synthesis of bulk Ti_3SiC_2 are Ti/Si/C [113, 143], Ti/Si/TiC [144, 145], and Ti/SiC/C [29, 96]. It is difficult to obtain single phase Ti_3SiC_2 sample as ancillary phases often coexist [146, 147]. The evaporation of silicon during high temperature synthesis has been identified to be responsible for impurity formation [148] – as this detrimentally shifts the phase composition towards the Ti-C region of the phase diagram [149]. Thus, extra silicon is often added to the stoichiometric composition in order to compensate for silicon loss [149, 150]. In addition, the loss of silicon due to high temperature synthesis is also an important factor. Previous work on the thermal stability of Ti_3SiC_2 suggests it is stable up to 1600 °C in vacuum or atmosphere [102]. However, in another study, it was that the decomposition kinetics of Ti_3SiC_2 irrespective of sintering temperature depends on the surrounding medium[151]. The presence of carbon from graphite heating elements (dies, punches and graphite felts) creates carbon-rich environment which detrimentally acts as a driving force for increased Si segregation bringing about decomposition at temperatures way below 1600 °C according to the reaction [97]:

$$\mathrm{Ti_3SiC_2} \rightarrow 3\mathrm{TiC_{0.67}(s)} + \mathrm{Si}(\uparrow)$$

In addition, the reaction mechanism proposed for the formation of Ti_3SiC_2 involves intermediate phase Ti-Si liquid formation and its subsequent reaction with TiC to form Ti_3SiC_2 [152-154]. The formation temperature of Ti-Si eutectic phase is 1333 °C [155], thus the presence or absence of Ti-Si phase in the final product indicates incomplete or complete consumption of the Ti-Si intermediate phase [155]. Table 2 is an overview of some of the previous work on the synthesis of Ti_3SiC_2. The development of MAX phase powder (such as

MAXTHAL® powder) therefore provides an alternative route for synthesis of bulk single-phase MAX phases as well as MAX-phase composites [146].

***Table 2**. Previous work on the synthesis of Ti_3SiC_2 starting with various combinations of reactants [156].*

Starting powder [Ref]	***Synthesis method***	***Ancillary phase***
Ti/Si/C [143]	SHS	TiC
Ti/Si/C [157]	SHS/MA	TiC
Ti/Si/C [158]	Hot pressing	TiC
Ti/Si/C [150]	SPS	TiC, SiC, $TiSi_2$
Ti/Si/C [148]	Hot pressing	TiC, SiC, $TiSi_2$, Ti_5Si_3
Ti/Si/C [159]	MA/P-less	TiC, SiC, $TiSi_2$, Ti_5Si_3
Ti/Si/C [160]	SHS	TiC, Ti_5Si_3
Ti/SiC/C [102]	HP/HIP	---
Ti/SiC/C [161]	Pressureless	TiC_x
Ti/SiC/C [162]	SPS	TiC, Ti_5Si_3
Ti/SiC/C [115]	SHS	TiC_x
Ti/Si/TiC [146]	Vacuum	---
Ti/Si/TiC [163]	Pressureless	---
Ti/Si/TiC [145]	HIP	TiC_x
Ti/Si/TiC [164]	SPS	---
Ti/Si/TiC [165]	Vacuum	---
TiC/Si [166]	Pressureless	SiC, TiC
TiC/Si [167]	Pressureless/HP	SiC, TiC
$TiC_{0.67}$/Si [168]	Pressureless	TiC_x
$TiC_{0.67}$/Si [169]	Pressureless	TiC

--- *indicates no ancillary phases*

Similarly, the MAX phase Ti_3AlC_2 can be synthesized with various combinations of starting reactants: Ti-Al-C, TiH_2-Al-C, Ti-Al-TiC, and Ti-Al_4C_3-TiC [170]. The intermediate phases such as Ti_3Al, TiAl, Ti_3AlC, TiC, and Ti_2AlC are all possible associated phases during the synthesis and reaction formation mechanism of Ti_3AlC_2 [170].

2.3.4. Spark Plasma Sintering (SPS) and Densification Mechanisms

Spark plasma sintering (SPS) is a novel rapid densification technique that employs the use of pressure-driven consolidation and pulsed current (Fig. 22(a)) via a sample that is uniaxially compressed in a graphite die [171]. In principle, a pulse DC current with pulse duration of about 10 ms flows through the punches and dies as well as through the specimen [172]. The ON-OFF pulse current delivers significantly high heat at the contact point between powder particles (Fig. 22(b)) which is in turn dissipated through the entire specimen to allow uniform heat distribution as well as homogeneity [173]. Since the electric discharge takes place on the microscale, this will in turn accelerate material diffusion [174].

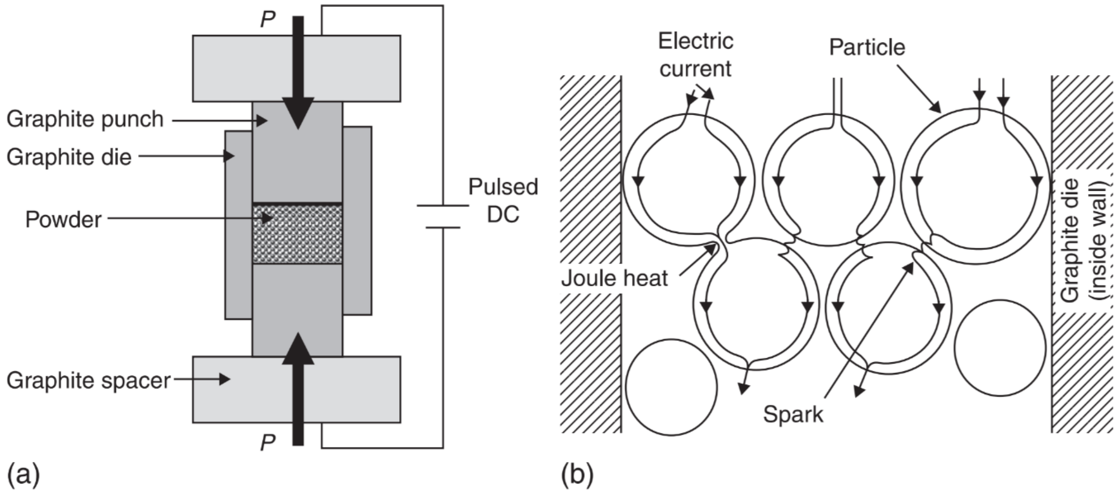

Fig. 22. Schematic depicting (a) spark plasma sintering (SPS), and (b) pulse current flow pattern via powder particles in the SPS die [175].

2.3.4.1. *Densification mechanism*

The mechanical effect of the applied pressure aids to initiate particle re-arrangement (Fig. 23(b)) which in turn breaks down agglomerates (Fig. 23(a)) and helps facilitate surface and grain boundary diffusion during powder consolidation.

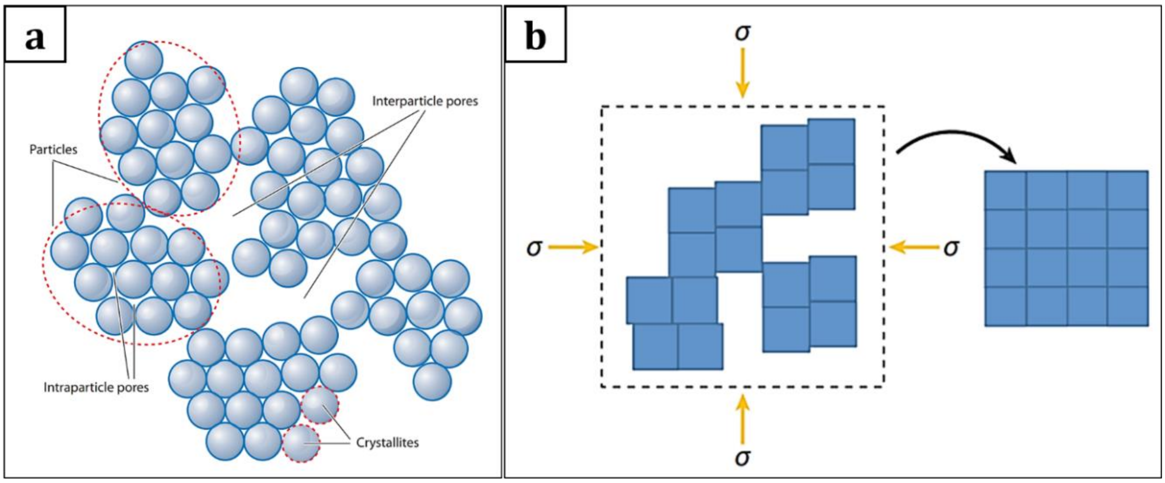

Fig. 23. (a) Schematic depicting pores and agglomerates in powder compact, and (b) particle re-arrangement initiated upon the application of pressure [176].

The microstructure of the final sintered compacts is significantly influenced by the SPS processing parameters [177] (Fig. 24) such as heating rate, holding time, load application rate and on-off current application [176].

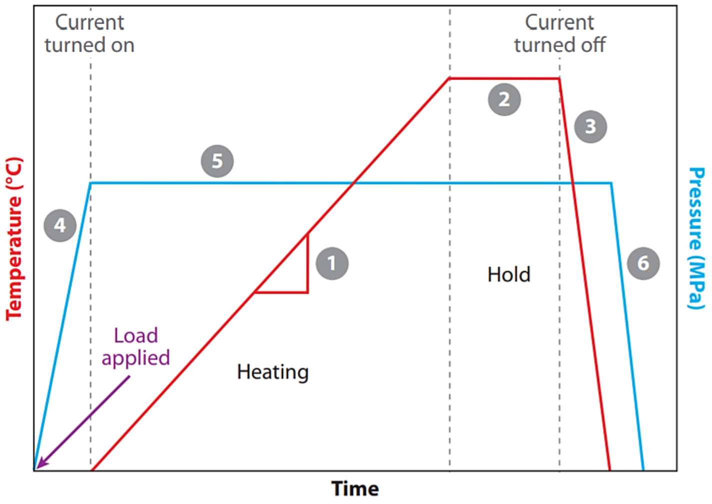

Fig. 24. Schematic of a typical user-defined processing parameters during SPS sintering cycle [176].

The major difference between SPS and other conventional sintering methods is that the incorporation of current expedites mass transport owing to increased concentration of point defects [178]. Mass transport mechanisms such as volume diffusion, evaporation, surface diffusion, and grain boundary diffusion are all known to bring about neck formation during sintering [176]. However, it is known that not all transport mechanisms contribute towards eventual densification i.e., non-densifying mechanisms [176]. A unique advantage of SPS is that the higher heating rate employed delivers additional driving force due to the evolution of large thermal gradient which helps in bypassing the low temperature regime non-densifying mechanism (mechanism (1) and (2)) and proceeds directly to the densifying mechanism (mechanism (3) and (4)) to bring about rapid densification as shown in Fig. 25 [179].

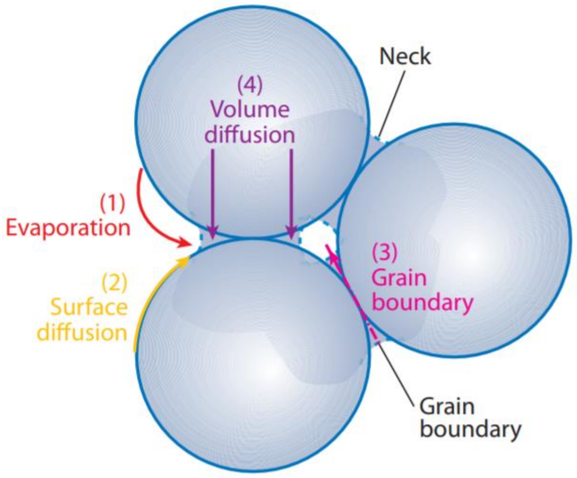

Fig. 25. Schematic showing mass transport mechanisms (1-4): 1 and 2 (non-densifying mechanisms), and 3 and 4 (densifying mechanisms) [176].

2.3.4.2. Spark plasma sintering and MAX phase decomposition

The role of spark plasma sintering in the decomposition of MAX phases at temperatures below their intrinsic temperature of decomposition is explained in relation to the following material and technical requirement of SPS thus:

- Carbon uptake

As the material requirement for the dies and punches employed in spark plasma sintering (SPS) necessitates electrically conductive and good thermal stability at elevated temperatures, the frequently used material for the die and punch is graphite [180, 181]. This choice of material is however of great concern as the powder to be consolidated is usually in direct contact with carbon at high temperature owing to the graphite heating element thus carbon uptake is unavoidable [181]. In addition, graphite foil is often utilized to ease the removal of the sintered sample from the tooling as well as to shield the dies and punches from possible chemical reaction at elevated temperature [180]. All of the aforementioned graphite materials would inadvertently leave carbon “footprints” which will compromise the composition of the subsurface layers of the sintered material [180].

During SPS synthesis of MAX phase, surfaces of the graphite heating element contacting the sample provides carbon contamination which will result in, for example, the decomposition of Ti_3SiC_2 into TiC_x especially in the samples surface by inward diffusion of carbon [155, 182]. The formation and subsequent growth of TiC_x would lead to loss of silicon preferentially by vaporization [97].

Racault et al. [97] in their work suggested the possible formation of SiC at the surface of the sample from free Si and C according to the reaction:

$$\mathrm{Si(g)} + \mathrm{C} \rightarrow \mathrm{SiC}$$

Referring to the Ti-Si-C phase diagram (Fig. 18), during the synthesis of Ti_3SiC_2, the reaction of carbon with Ti_3SiC_2 due to carburization from the graphite tooling will shift the overall composition to the Ti_3SiC_2-TiC-SiC compatibility triangle [182]. As a result, the possible formation of TiC and/or SiC is expected at the surface composition according to the following reaction [182]:

$$\mathrm{Ti_3SiC_2} + (3\mathrm{x} - 1)\mathrm{C} = 3\mathrm{TiC_x} + \mathrm{SiC}$$

However, in the absence of SiC, then a second possible reaction mechanism is consistent with the proposed reaction [182]:

$$\mathrm{Ti_3SiC_2} + (3\mathrm{x} - 2)\mathrm{C} = 3\mathrm{TiC_x}\ (\mathrm{x} > 0.8) + \mathrm{Si}$$

- Vacuum sintering

The use of vacuum during spark plasma sintering (SPS) is intended to aid in drawing out possible impurity elements, for example: oxygen, carbon from heating elements and other impurities [110]. However, during the synthesis of $\mathrm{Ti_3SiC_2}$, owing to the high vapour pressure of silicon, upon the formation of the Ti-Si eutectic liquid the vapour of silicon is drawn away by the vacuum pump which will bring about alteration in stoichiometric composition and consequent impurity formation in the densified compact [110, 163]. On the other hand, employing gas sintering such as the use of argon during the sintering will mitigate against possible Si vapour being drawn away but the diffusion of carbon from the heating element is unimpeded due to the absence of vacuum [110].

2.3.5. MAX Phase Composite

In the synthesis of MAX phases the ancillary phases that often coexist with the final product have been linked to the deterioration of some of is intrinsic attractive properties such as oxidation and chemical resistance [183]. However, mechanical property weaknesses in MAX phases, such as low hardness and poor strength (which may inhibit their potential application as a structural material) have led to a drive towards incorporating a second phase conventional ceramic into MAX phases to form a composite [184]. MAX phases can be strengthened by thermodynamically stable inclusions, such as SiC and TiC, which may readily be formed as ancillary phase(s) during in-situ synthesis or by incorporation in the matrix to bring about MAX–AX and MAX–XA compositions, respectively [60]. For example, in Ti_3SiC_2, the possible reinforcements are Ti_3SiC_2-TiC and Ti_3SiC_2-SiC. However, as TiC has close thermal expansion coefficient to Ti_3SiC_2, it is often employed as a particle reinforcement in Ti_3SiC_2 matrix [185].

In a study involving Ti_3SiC_2-TiC and Ti_3SiC_2-SiC composites, it was found that TiC and SiC incorporation into Ti_3SiC_2 matrix resulted in lower grain boundary mobility in Ti_3SiC_2 [70]. Furthermore, both composites possessed lower flexural strength as compared to unreinforced Ti_3SiC_2 – this suggests the incorpotaion of the second phase deteriotates some of its mechanical properies. The flexural strength was reported to be weaker in the Ti_3SiC_2-SiC as compared to Ti_3SiC_2-TiC composite due fracture induced by thermal expansion mismatch. Tong et al. [186] reported a higher flexural strength in Ti_3SiC_2-30SiC-8TiC (vol.%) composite as compared to monolithic Ti_3SiC_2. The fracture toughness on the other hand was lower than that of monolithic Ti_3SiC_2. This was attributed to the lack of large Ti_3SiC_2 grains in the composite microstructure; as the Ti_3SiC_2 plate-like grain growth was inhibited by the fine SiC particles (Fig. 26) that homogeneously distribute in the composite [186].

Fig. 26. Crack propagation in (a) monolithic Ti_3SiC_2, and (b) Ti_3SiC_2-SiC-TiC composite [186].

2.4. TRIBOLOGICAL BEHAVIOUR

The bonding as well as the crystal structure of MAX phases is similar to well-known solid lubricants such as MoS_2 and graphite [105]. This suggests that some member of the MAX phase family may possess intrinsic self-lubricating properties [187]. According to Barsoum et al. [29], polycrystalline Ti_3SiC_2 felt lubricious during machining with high speed tool and they concluded that Ti_3SiC_2 might possess a self-antifriction properties. This led to Myhra et al. using a lateral force microscope to study its friction properties against a Si_3N_4 counterface. They reported an ultra-low friction coefficient ($2 – 5 \times 10^{-3}$) along the basal planes whilst the friction of the non-basal planes was higher ($\mu \approx 0.1 – 0.25$) [1].

2.4.1. Previous Work on Tribological Behaviour of MAX Phases

The tribology of MAX phases has been extensively studied over the years ever since Myhra et al. [188] on their work on polycrystalline Ti_3SiC_2 revealed ultra-low friction. However, most of the work reported thereafter to date has shown conflicting results with authors indicating poor tribological behaviour [1]. This was attributed to the evolution of complex tribochemistries which led to different tribolayers, thus abrasive third-bodies.

The majority of the previous work on tribological behaviour of MAX phases has been focused on Ti_3SiC_2 and Ti_3AlC_2 [33, 189-191], with a handful of discrepancies in the reported friction and wear behaviour which was reported to be essentially poor at low to moderate temperature [192, 193]. One reason for these discrepancies is the sensitivity of MAX phases to testing conditions such as counterface, applied load, sliding speed, and temperature [192]. However, improvement in tribological behaviour has been at high temperature [187]. Jiqiang et al. [193], studied the tribological behaviour of Ti_3AlC_2 at room and elevated temperature against SiC. In their work, at room temperature, they reported a friction coefficient of 0.34 at steady state whilst the wear rate was 4.24×10^{-4} mm^3/Nm. At high temperature, in the range 600 - 1000 °C, the friction coefficient was in the range 0.60 - 0.80 and the wear rate on the order of 10^{-6} mm^3/Nm. The low wear rate at high temperature was attributed to the compacted continuous oxide layer formed above 600 °C. Souchet et al. [189], observed two distinct friction regimes designated as type I and type II regimes (Fig. 27) in their work on the friction behaviour of fine- and coarse-grained Ti_3SiC_2 against steel and Si_3N_4 balls. Type I was characterized as a relatively low friction coefficient regime and wear rate regime. In this regime, sliding occurs predominantly between a tribofilm on the ball and the Ti_3SiC_2 plane. An analysis of the tribofilm revealed it contained Ti, O, C in the form of TiC_XO_Y (titanium oxycarbide). Type II regime on the other hand was characterized by significant increase in both friction coefficient and wear rate. In this regime, visible wear track can be seen alongside significant wear debris generation in contrast to Type I.

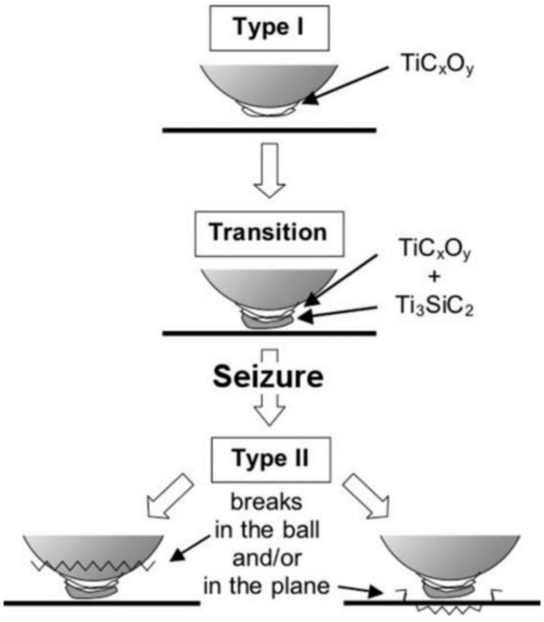

Fig. 27. Schematic illustration of the transition regimes observed in Ti_3SiC_2/steel and Si_3N_4 tribocouples [189].

2.5. SILICON CARBIDE-BASED COMPOSITE

Engineering ceramics are ideal materials for wear-resistant applications under severe environment in a range of applications [194]. Owing to their chemical inertness and high hardness, they are promising wear-resistant tribo-material as compared to metals and polymers [195]. Amongst the ceramics employed in industry, alumina, zirconia and silicon carbide-based ceramics possess the highest application potential [196].

2.5.1. Silicon Carbide

Silicon carbide is a potential candidate for a range of structural engineering applications. However, it has a low fracture toughness which makes it sensitive to damage under contact stress [14, 20, 197]. Hence, improving its fracture toughness via the incorporation of a second phase particle is necessary [13]. However, an increase in its fracture toughness is often accompanied by a drop in hardness [198, 199]. To mitigate the drop in hardness that accompanies an increase in fracture toughness, TiC particles is often used as a reinforcing phase [13]. SiC matrix reinforced with TiC particles ceramic has been reported to retain high hardness whilst its toughness is improved. As an example, SiC-TiC ceramics with hardness > 23 GPa and toughness > 6.0 $MPa.m^{1/2}$ have been reported [12], which demonstrates an improvement as compared to monolithic SiC ceramic with toughness of about 3 – 4 $MPa.m^{1/2}$ [200].

Silicon carbide (SiC) is a high temperature performance ceramic and exhibits polytypic forms which are based on various stacking sequences of a basic structural unit, that is, a 2-layer planar unit of Si and C in tetrahedral coordination [201]. Using the Ramsdell notation [202], 3C represents the cubic symmetry polytype whilst 6H and 15R have hexagonal and rhombohedral symmetry, respectively. 3C is the only cubic polytype and often referred to as β-SiC, and when heated to high temperatures, β-SiC transforms to mixture of hexagonal α-SiC – and it is the only thermodynamically stable form of SiC [202]. Fig. 28 shows a typical crystal structure of hexagonal and rhombohedral polytypes [203, 204]. Cubic SiC undergoes an irreversible phase transformation to hexagonal phase at temperatures above ~1800 °C according to reaction [205]:

$$\beta - SiC \xrightarrow{1800\ °C} \alpha - SiC$$

This phase transformation has been of interest partly because the α-phase that forms in a fine-grained β-phase matrix often occurs as large plates and is linked to the deterioration of mechanical properties [202]. Nonetheless, a unique feature of the β→α transformation according to Shinozaki et al. [202, 206] is the sandwiching of the formed α plates between envelopes of β in a well-defined orientation relation with the α-phase, $[111]_{\beta} \| (0001)_{\alpha}$. According to Mulla et al. [207] this transformation can be exploited to tailor the material's microstructure during liquid-phase sintering. The control of phase transformation and consequent development of plate-like microstructure results in toughened SiC [208]. Bulk samples sintered from β-SiC starting powder typically display an elongated grain structure due to the β to α transformation that brings about improved fracture toughness, whilst the α-SiC starting powder promotes better densification and an equiaxed grain structure [205].

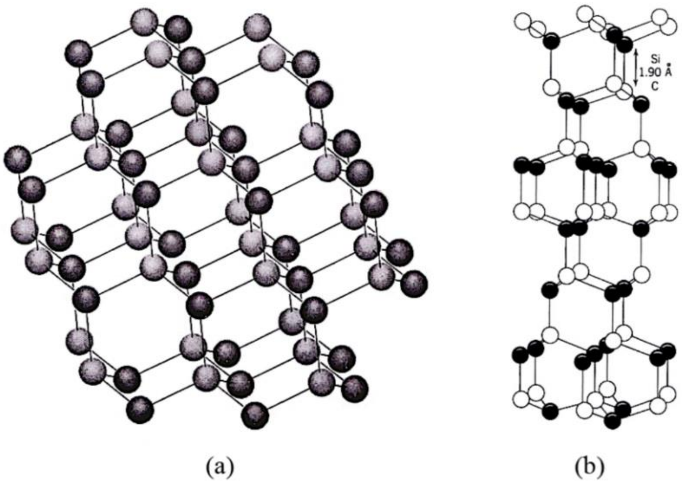

Fig. 28. Crystal structures of (a) β-SiC and (b) α-SiC [209].

Silicon carbide possesses extremely high hardness and wear resistance. Excellent corrosion resistance, oxidation and thermal shock resistance and good high temperature strength which makes it attractive for numerous structural and wear applications such as heat exchangers, electrical systems, nuclear fuel elements and many more. Monolithic phase SiC with little or no grain boundary impurities maintains high temperature strength ~1600 °C with no loss of strength and hardness [210].

2.5.2. Titanium Carbide

Titanium carbide (TiC) exits as a homogeneous face-centred-cubic rock-salt structure depending on the value of x within the limits $0.47 < x < 1.0$ (Fig. 29) [211]. In contrast to SiC, TiC possesses non-stoichiometric composition. As a result, the properties of TiC, crystal structure, thermodynamic and mechanical properties are dependent on the composition, that is, the value of x [212].

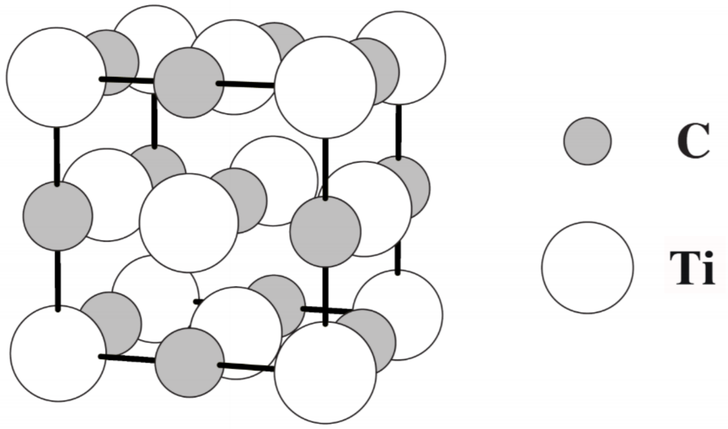

Fig. 29. Titanium carbide rock-salt FCC crystal structure [211].

The room-temperature material properties of TiC and SiC are given in Table 3.

Table 3. *Typical thermomechanical properties of SiC and TiC [212].*

Property	***SiC***	***TiC***
Density (g/cm^3)	**3.21**	**4.93**
Hardness (GPa)	**17-25**	**20-32**
Fracture toughness (MPa.m$^{1/2}$)	**3-5**	**3.8-7.5**
Young's modulus (GPa)	**400-430**	**450-480**
Thermal conductivity (Wm/K)	**60**	**17-31**
Thermal expansion coefficient (°C^{-1})	**4.16×10^{-6}**	**7.12×10^{-6}**
Melting point (°C)	**2830**	**3160**

2.6. TiC-PARTICULATE/SiC-MATRIX COMPOSITE

Several authors have shown that the incorporation of ceramic particles into a ceramic matrix can improve both the mechanical properties and wear resistance [13, 213, 214]. Due to the brittle nature of SiC in its monolithic state, the introduction of TiC particles within SiC matrix have been explored [212]. The advantages of TiC particles as reinforcement for SiC over other possible ceramic particles are [13, 215]: (1) the thermal expansion mismatch as well as the differential cooling from sintering temperature to room temperature will help initiate beneficial residual stresses that improves toughness; (2) the fact that TiC is ductile above 800 °C due to the activation of five independent slip systems, such plasticity will enhance toughness at high temperatures, and (3) chemically compatibility between SiC and TiC at the sintering temperature [13].

Wei et al. [13] reported that the addition of 24.6 vol.% of TiC within SiC matrix increased its fracture toughness by ~50 %, that is, the fracture toughness of the composite reached 6.0 MPa.m$^{1/2}$. The improvement in fracture toughness was linked to thermal expansion coefficients mismatch between SiC and TiC. Incorporation of TiC particles within SiC matrix brings about increased fracture toughness of the resultant composite system via crack deflection mechanism (Fig. 30) [13]. The driving force for crack deflection has been linked to the evolution of residual stress due to mismatch in thermal expansion and differential cooling between TiC and SiC [13]. As a consequence, this will result in residual tensile stresses in the TiC particles whilst the SiC matrix will experience radial tensile and compressive stresses [13].

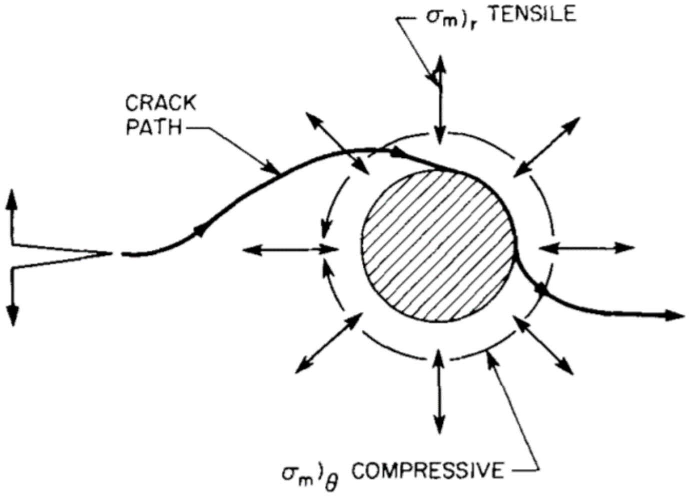

Fig. 30. Schematic of crack deflection by a particle as well as associated matrix stresses [13].

During the cooling phase of the composite TiC particles will shrink faster than the SiC matrix thus creating a tensile hydrostatic stress as shown by Selsing in his work on internal stresses in ceramics [216]. The hydrostatic stress induced during cooling due to difference in thermal expansion of various phases satisfies the relation derived by Selsing et al. [216]:

$$P = \frac{\Delta\alpha \,.\, \Delta T}{\frac{1+\vartheta_m}{2E_m} + \frac{1-2\vartheta_p}{E_p}}$$

Where P is the hydrostatic pressure, Δα is the difference in thermal expansion between the phases, ΔT is the cooling range (i.e., difference between the minimum temperature for plastic deformation and final temperature upon cooling), ϑ is the Poisson's ratio, E is the elastic modulus and subscripts m and p represents matrix and particle respectively. It is however conceivable that since the TiC particles will be under a tensile hydrostatic stress then the SiC matrix will subjected to a compressive stress state [212]. Thus, a propagating crack will be likely deflected around the TiC particles whilst the compressive stress around the SiC matrix would interact with the crack tip stress field thus leading to enhanced fracture toughness [212].

2.6.1. Synthesis of Monolithic TiC and TiC-SiC Composite

The most important feature of SiC is its strong covalent nature which in turns dominates its material properties [217]. However, its covalent nature is responsible for its low self-diffusion coefficients which limits its sinterability [218]. Thus, it is essential to employ sintering aids to enable the densification of SiC material, in both monolithic phase and composite-based forms [218, 219]. The use of sintering aid helps to reduce the sintering temperature as well as reducing the grain growth that proceeds when the sintering temperature is higher than 2000 °C [220]. According to Nadeau et al. [221], using hot pressing (HP), they reported that a sintering temperature as high as 2500 °C and upto 50 MPa of applied pressure is required to obtain a fully dense monolithic SiC. They further stated that, the high sintering temperature led to an exaggerated grain growth which deteriorate its mechanical properties. Thus this necessitates the use of sintering additives such as carbon and boron as they act as a mass transport medium which helps to reduce the sintering temperature [204]. However, such sintering additives should be stable and not react with SiC at high temperature as this might trigger the decomposition of SiC by forming metal oxides [222]. Prochazka et al. [223] obtained up to 96.4 % SiC density using solid-state sintering with sintering additives that required a high sintering temperature of 2100 °C. Irrespective of the use of sintering aids as well as sintering technique employed, the resulting composite properties will depend solely on the microstructural evolution [114]. Intergranular microstructure has been identified to be effective in improving the overall mechanical properties of the resulting composite [224]. Some of the sintering techniques employed in synthesizing SiC-based ceramic are pressureless sintering, reaction sintering, hot-pressing and spark plasma sintering. However, SPS is the best suited amongst all in laboratory scale as it enables very fast sintering and tailoring of microstructure [225].

Spark plasma sintering (SPS) has recently gained prominence in relation to is unique capabilities of synthesizing very hard-to-deform materials requiring elevated temperatures as well as lengthy consolidation times [226]. The introduction of spark plasma sintering for the densification of SiC-based material has helped avoid the use of sintering aids necessary in other sintering methods such as hot pressing (HP) as well as significantly reducing the sintering temperature in the range 200 - 300 °C [217]. Although, this will be the bulk temperature and not the instantaneous flash temperature when DC sparking is triggered. Furthermore, some previous work have shown that very fine and intergranular microstructure can be obtained in SiC - TiC composites with the aid of spark plasma sintering (SPS) [114, 225].

2.6.1.2. Evolution of microstructure during SiC synthesis

The mechanistic features contributing to microstructural evolution, that is, transformation from cubic (fcc) to hexagonal and/or rhombohedral crystal structures in SiC are aided kinetically by surface defects (Such as vacancies, dislocations, stacking faults, twins etc.). These structures can evolve from one another via the rearrangements of as-grown defects (stacking faults or motion of partial dislocations) in the solid state – and represents the dominant mechanistic feature contributing to the microstructure of SiC (Fig. 31(a-d)). However, even though a number of literature links the motion invoked by stacking faults and partial dislocations to this transformation, Warren et al. [208] associated cubic-to-hexagonal SiC transformation to a growth-induced transformation, with the initial growth of beta grain acting as a seed on which the alpha grows subsequently (inset Fig. 31(a-c)).

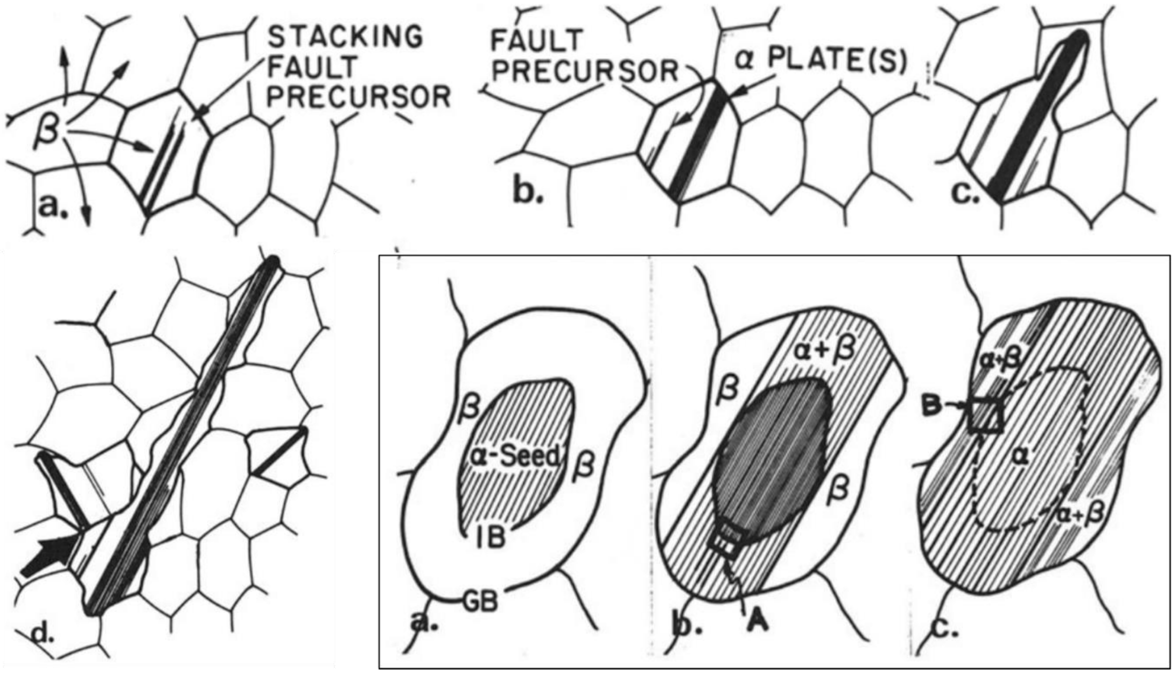

Fig. 31. The sequential morphological development during reaction sintering of SiC [208].

2.6.1.3. Previous work on the tribological behaviour of TiC-SiC composite

The literature on the tribology of TiC-SiC composite is sparse. This makes it difficult to draw conclusions and emphasises how little is known and/or understood on the role of mismatch of coefficient of thermal (CTE) expansion and consequent residual stresses on the tribological properties of this composite system. According to Wasche et al. [13], the dispersion of second phase particles within monolithic ceramics will improve the mechanical properties of the matrix material as well as enhance tribological performance. In addition, the intrinsic properties such as excellent thermal stability and oxidation resistance of the monolithic ceramic (e.g., SiC) are retained [227]. It is well known that TiC can exhibit good friction properties if a titanium oxide layer can form because of its low shear strength [227]. Thus, incorporation of TiC within SiC matrix will enhance the wear resistance of the resulting composite significantly [228, 229]. The reason behind this improvement was solely attributed to tribo-oxidation [228]. In a previous study [18], the introduction of TiC into SiC matrix resulted in wear reduction by a factor of ten. The reduction was attributed to the formation of oxide wear debris transferred to the counterbody, as a result of which the sliding plane was shifted further into the layer. In another study [228], enhanced friction and wear behaviour was reported in a study involving Al_2O_3/TiC-SiC-TiB_2 tribocouples. This was attributed to the evolution of sub-stoichiometric TiO_{2-X} otherwise known as Magneli phase, as well as the presence of carbon due to oxidation of SiC and TiC at the tribo-interface. According to Sharma et al. [230] in their work on wear mechanism in SiC-based ceramic under dry sliding conditions, they reported that the dominant wear mechanisms in SiC-based composites are tribo-oxidation, microcracks induced fracture, grain pull-outs, and compacted oxidized wear debris.

Previous work reported by several authors on SiC-TiC composites mostly focused on maximizing mechanical properties such as hardness and fracture toughness [12, 210, 214, 217], with very limited research on tribology. Even when the tribology of this composite was investigated by few authors [14, 197, 229], the role of residual stresses due to thermal expansion mismatch on the wear behaviour has not been considered.

2.7. TRIBOLOGY

Tribology is the study of friction, wear and lubrication, and encompasses the behaviour of interacting surfaces as well as other tribo-elements in relative motion. It is well known that friction and wear are not inherent material properties. They are in fact responses to a specific tribological system which is influenced by a wide range of testing conditions (i.e., contact pressure, speed, and so forth) [231]. Wear investigations rarely indicate quantitatively what might be expected in practical applications. Instead, wear test may be seen as a method of investigating the wear mechanisms taking place as a function of contact conditions, state of lubricity and environment and relating this to microstructure. Thus, the scope of tribological investigations reported in this research work is dedicated solely to the development of microstructure at the worn surface, rather than exhaustively establishing wear rate data.

2.7.1. Hertzian Contact Pressure

It is well known that when two bodies are in sliding contact the real area of contact consists of a large number of small asperity contacts [232]. As the normal load is increased, a large number of asperities will come together to form a larger area of contact which will support the normal load and thus, responsible for any frictional force generated by the movement.

The maximum contact stress can be estimated from the test parameters thus [233]; given that a ball of radius (R) is in sliding contact with a sample under the application of an normal load (F) (Fig. 32), then the contact radius (a) is given according to the equation:

$$a = \sqrt[3]{\frac{3F_N R}{4E^*}}$$

Where E* is the equivalent Young’s modulus as is given by the equation:

$$E^{*} = \frac{1}{\frac{1-\vartheta^{2}}{E_{sample}} + \frac{1-\vartheta^{2}}{E_{partner}}}$$

Where ϑ represents the Poisson's ratio and E is the Young's modulus of the sample and partner.

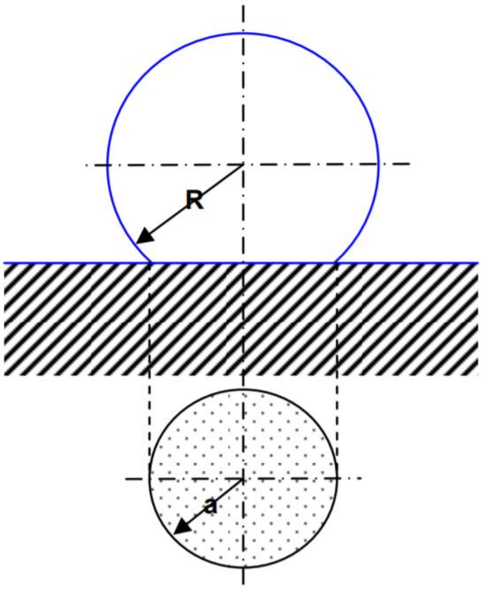

Fig. 32. Schematic representation of idealized spherically shaped single asperity contact [233].

2.7.2. Surface Temperature and Frictional Heating

It is well known that frictional heating during sliding contact plays a critical role in the tribological behaviour of dry sliding systems [232]. This is because the transformation of frictional energy into heat (i.e., frictional heating) is associated to increases in the temperature of sliding counter bodies, especially in the immediate vicinity of the real area of contact [232]. Because of the role frictional heating plays on the tribological behaviour as well as failure of sliding components, surface and near surface temperatures have been of keen interest for years with investigators attempting to measure this temperature both experimentally and analytically. However, irrespective of the different models [234-237] developed for its measurement, the quantitative measurement remains impossible [232].

When two solid surfaces are in contact, there is a work done against friction [234]. The work done against friction is generated as heat at or very close to the surface at which these solids are in contact at all but the slowest speeds of sliding [234]. Associated local changes at the near surfaces such as melting, softening and excessive oxidation as a consequence of interfacial local heating is likely to influence both the friction and wear rate [235, 236].

2.7.2.1. *Surface temperature equation*

When two solids 1 and 2 as shown in Fig. 33 are in sliding contact at a relative velocity V, mated together by the application of a normal force F, with coefficient of friction µ, the maximum local surface heating generated due to sliding at a very small, and severely loaded asperity contacts is calculated by the relationship [235, 237]:

$$T_{Contact} = T_{bulk} + T_{flash}$$

Where T_{bulk} is the bulk temperature of the test sample prior to contact and T_{flash} is known as the flash temperature. The flash temperature is expressed as [238]:

$$T_{flash} = \frac{(\pi/4)\mu H_s r v}{\lambda_1/Z_0 + \lambda r}$$

Where µ is the friction coefficient, H_s is the hardness of the softer material, r is the radius of the contact spot, v is speed, λ_1 is the thermal conductivity of the softer material, λ_r is the relative thermal conductivity i.e. the ratio of the thermal conductivity of the disc to the pin, and Z_0 is given by:

$$Z_0 = \frac{1}{1+V_r/3}$$

Where V_r respresents the relative velocity and is defined as:

$$\frac{V}{\lambda/rdc}$$

Where r is the asperity contact area, d is the density, and c is the specific heat capacity.

The flash temperature which represents the temperature at the initial asperity contact are superimposed into the bulk temperature, and as a consequence, a resultant maximum temperature is established at the asperity contact [237]. According to Kalin et al. [239, 240], this phenomenon can take place even at a very low sliding speed thus, making the magnitude of these temperatures of great tribological importance. The bulk temperature can be determined via direct temperature measurement, but the flash temperature determination is more complicated, due to the fact that the respective areas cannot be assessed easily [240]. The difficulties associated with determining the size and shape of the real contact area makes the temperature calculation models imperfect owing to discrepancies in the results that can be obtained for the same contact situation [239].

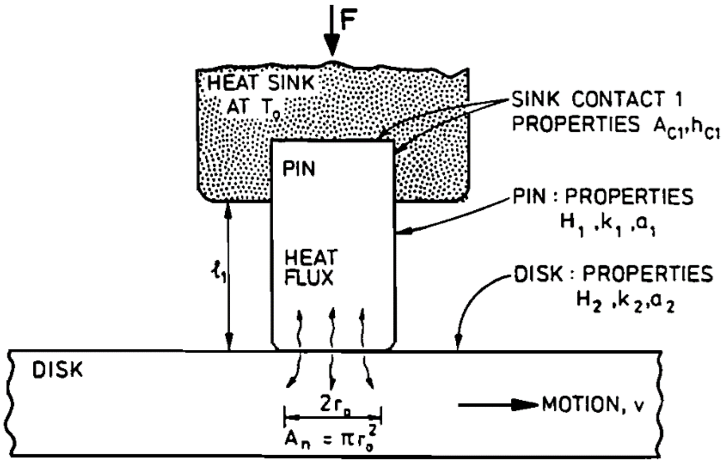

Fig. 33. A pin-on-disk configuration from which temperature estimation was carried out by Ashby et al. [234, 236].

2.8. SUMMARY OF CRITICAL POINTS ADDRESSED IN THIS THESIS

Following the detailed literature review from all studies published on MAX phases and TiC-SiC ceramic composites, the following salient questions provided the basis for the scope of the work carried out in this thesis:

MAX phase and composite

- Majority of the work reported on the synthesis of MAX phases have focussed essentially on optimizing the sintering stoichiometry of the starting elemental power mixture to improve the conversion to monolithic MAX phase. Whilst little attention has been paid to actually understand the mechanisms and/or factors that contributes to the alteration of the starting stoichiometry which in turn shifts the final synthesized composition from a monolithic phase into a two-phase and/or three-phase region. It will be important to simulate the SPS sintering environment by thermal gravimetric analysis using a graphite crucible to fully understand the role graphite-rich SPS evnvironment plays in the decomposition of MAX phase.
- To date majority of the reported work on synthesis of MAX phases has been mostly from elemental powder mixture rather than a prealloyed MAX phase powder. Since during the elemental powder mixing and milling procedure there is often changes in starting powder stoichiometry, it is usually difficult to reproduce the phase content obtained following synthesis. It is therfore conceivable that by using a prealloyed

powder the starting composition will remain fixed and thus improve reproducibility of the final synthesized compact.

- It became immediately clear that the exact sintering temperature leading to monolithic and/or high-yield MAX phase conversion and thus avoid the on-set of the formation of ancillary phases does not exist. This observation is largely because most authors report different sintering temperatures and often it is difficult to replicate their results. Clearly, this necessitates synthesis of MAX phase over a range of temperatures under vacuum and gas sintering conditions so as to delineate the exact temperature above which the on-set of decomposition leading to ancillary phase formation takes place.
- It remains unclear if MAX phases are indeed intrinsically self-lubricating as it has been reported by several authors that whilst the MAX phase possess similar crystal and bonding structure comparable to well known solid lubricants (e.g., graphite) they are actually not lubricious. However, how this conclusion was reached has not been explicitly stated in the reported work – as their hardness and low grain boundary strength were only highlighted as a contributing factors. Even some few authors did report solid lubricant properties, the exact mechanism and formation sequence of the tribofilms was never discussed.
- Whilst most work on the synthesis of MAX phases often try to avoid the ancillary phase TiC formation as it thought this might deteriorate some of the exclusive properties of MAX phases such as friction and wear, little has been done to understand the evolution of TiC from a microstructural point of view and their role as reforcement for the soft MAX phase matrix and if they act as low bearing elements during wear.
- An assessment of the literature has clearly highlighted the lack of TEM characterization in the investigation of wear of MAX phases. The lack of TEM means that it is difficult to understand the role of plastic deformation in the wear process.

<u>TiC-SiC ceramic matrix composite</u>

While wear of ceramics is tradiationally linked to material property such as strength, hardness, microstructure, and toughness, an important property that has not been considered in all the reported literature on the wear of TiC-SiC ceramic matrix composite is the role of the residual stresses trapped in the composite due to mismatch in thermal expansion between the matrix and the particle phase. Thus this study will strive to answer the following key questions:

- Does mismatch in thermal expansion leading to toughening deteriorates wear properties
- What is the role of sliding contact on residual stress relaxation
- Does stress relaxation leads to microstructural evolution

No report on the examination of the near surface microstructure of worn TiC-SiC ceramic composite by TEM has previously been reported. As the wear of ceramics is inextricably linked to microstructure, a major aim of this work is to study the near surface microstructure generated by wear using detailed transmission electron microscopy (TEM).

CHAPTER 3

MATERIALS AND METHODS

A summary of the materials and methods employed in this work is given here and more detailed information can be found in the appended publications. The synthesis of the various MAX phase compositions involved the use of prealloyed MAX phase powder (Maxthal 312® (nominally—Ti_3SiC_2)) and an elemental Powder (Ti, Al, Si, and C) forming the stoichiometric MAX phase compositions Ti_3AlC_2, Ti_2AlC and Ti_3SiC_2, respectively. For the particulate ceramic matrix composite and monolithic TiC ceramic, SiC and TiC powder were employed without sintering aids.

3.1. SYNTHESIS OF MAX PHASES

3.1.1. Elemental Powder Route

In this study, bulk MAX phases of the family type Ti_3SiC_2, Ti_3AlC_2, and Ti_2AlC were synthesized via elemental powder route using homogenous mixtures corresponding to the desired stoichiometry upon ball milling. Milling was carried out dry in a SPEX 8000M mixer with a tungsten carbide vial and two 11.2 mm diameter tungsten carbide balls.

3.1.2. Pre-alloyed Powder Route (MAX phase powder)

Separately, Ti_3SiC_2 (as well as associated composite Ti_3SiC_2-TiC) was synthesized exceptionally via pre-alloyed powder route by using a MAX phase powder (MAXTHAL 312®-nominally Ti_3SiC_2). For the MAX phase-composite, 12 g of MAXTHAL 312 powder was mixed homogenously with 3 g of TiC powder using a rotary mill and zirconia balls.

3.2. COMPACTING PROCEDURE

3.2.1. Elemental and Pre-alloyed Powder

For the MAX phase samples to be synthesized via the elemental powder route, initially graphite papers was first sprayed with boron nitride (BN) to avoid any possible chemical reaction between the graphite paper and the graphite mould. The BN-sprayed graphite paper was then inserted into a 20 mm graphite die followed by the insertion of BN-sprayed graphite punches after which the homogenously mixed powder was then added into the mould. The role of the graphite paper is to ease the removal of the synthesized compact and possibly inhibit graphite diffusion from the graphite heating elements. It is worthy to mention that in the synthesis of the MAXTHAL 312 sample, boron nitride was not employed as the prealloyed powder already contained TiC – thus it was not deemed necessary to shield the sample from carburization.

The graphite mould-powder-punch arrangement (Fig. 34) was then pre-pressed with a load of 641 kg for approximately 3 min prior to the sintering to help facilitate electrical contacts between the punches as well as particle rearrangements. The graphite mould was then covered with graphite felts to inhibit possible heat dissipation during the synthesis thus keep the heat around and within the mould constant during the synthesis.

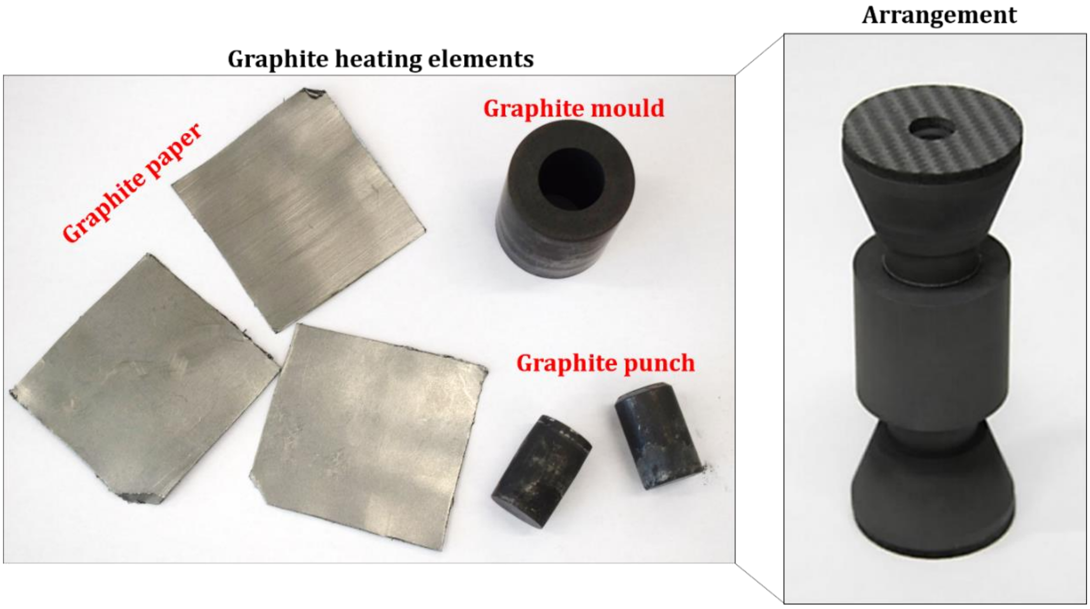

Fig. 34. Graphite heating elements and arrangement prior to spark plasma sintering (SPS).

3.2.1.1. Spark plasma sintering (SPS)

After pre-pressing, the cold compact was then placed in a spark plasma sintering unit (HP D 25 FCT Systeme, GmbH, Germany) as shown in Fig. 35. Heating was carried out under vacuum and/or gas condition whilst the punches acting as electrodes loads the pressure from the upper and bottom surfaces. Joule heat is promptly and efficiently transferred to the powder owing to the good electrical and thermal conductivity of the graphite die and punches. The sintering speed which is a function of the punch displacement is determined by the powder particle size.

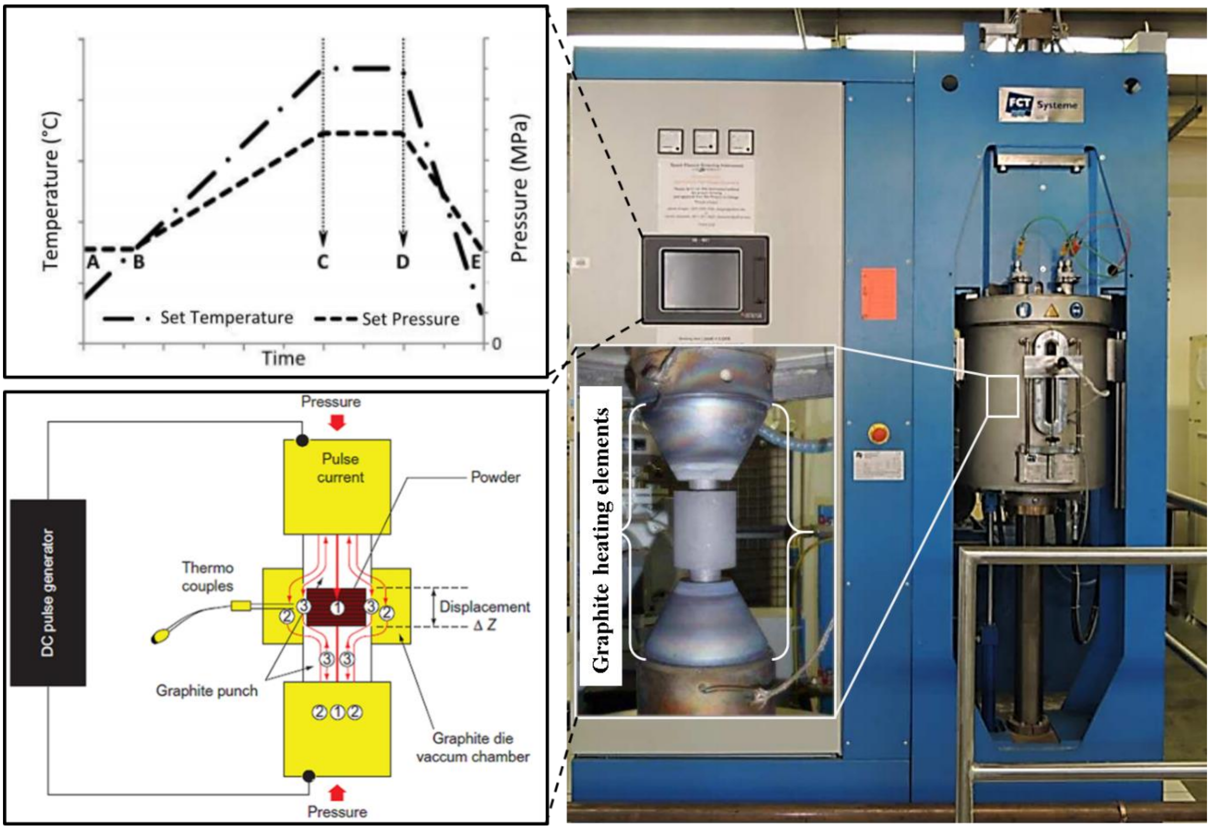

Fig. 35. HP D 25 an FCT Systeme spark plasma sintering (SPS) equipment.

3.3. SYNTHESIS OF MONOLITHIC TiC/TiC-SiC COMPOSITE

3.3.1. Starting Materials

TiC powder (Alfa Aesar 99.5 %) with an average particle size of 2 µm and β-SiC powder (Alfa Aesar 99.8 %) with an average particle size of 1 µm were used to prepare monolithic TiC as well TiC-SiC composites.

3.3.2. Preparation of TiC and TiC-SiC Composites

For the composites, the starting materials were mixed together by isopropanol-based rotary ball mill for 24 h. The powder mixtures were then subsequently dried and sieved using a 200 mesh to eliminate large agglomerates. 7.5 g of the mixed powders were then compacted in a 20 mm cylindrical die using a pre-press pressure of 641 kg for 4 min. Graphite papers were incorporated in the die as well as on the surface of the punches to avoid welding or possible chemical reaction with the die and punches. For the monolithic TiC, the TiC powder were compacted directly into the die without prior milling. Further details on the synthesis are explained in the published paper incorporated in this thesis.

3.4. WEAR TESTING

Non-lubricated ambient wear tests were conducted using Al_2O_3 ball as a counter surface in a ball-on-disc configuration. Tests were conducted in unlubricated condition in order to establish intrinsic lubricity mechanisms as well as self-lubricating tribolayer by selective oxidation induced by frictional heating. Alumina was chosen as counterface because of its relative inertness as it is not expected to react with the bulk material. The normal load and sliding speed employed for wear testing has been carefully chosen to correspond to previous tests in order to aid comparison of results as well as to stay in the mild wear regime according to ceramic wear map as microscale deformation mechanisms are preserved in this regime — this helps to realistically delineate the underlying wear mechanism.

3.4.1. Wear Test Methods and Specimen Preparation

Wear test were carried out in this study using pin-on-disk (POD) tribometers from two different companies; UMT-2 (California, USA), and TRB^3 & NTR^3 (Anton-Paar TriTec AG, Switzerland) - shown in Fig. 36. The TRB^3 is standard tribometer incorporating a dead-weight for load application whilst the NTR^3 is a nano-tribometer which utilizes a cantilever just as the CETR for load application.

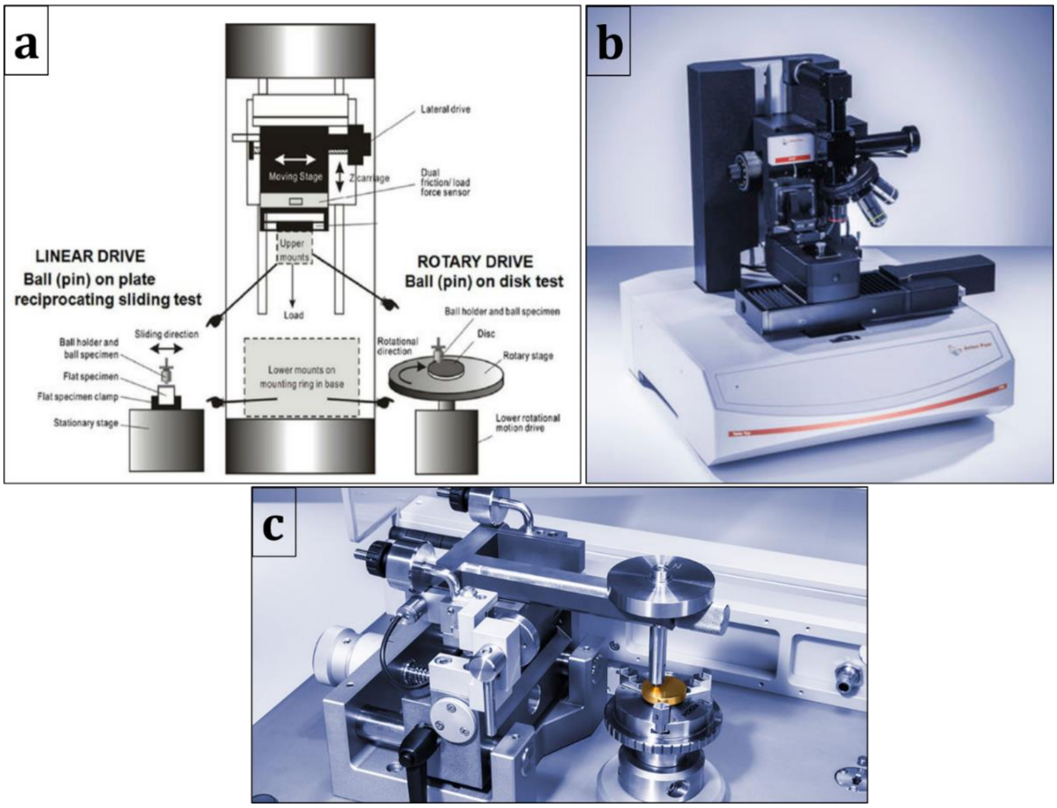

Fig. 36. (a) Schematic of CETR UMT-2 pin-on-disk [241], and (b-c) an Anton-paar nano tribometer (NTR^3) and standard tribometer (TRB^3), respectively.

Prior to the wear test, the surface of the disc was polished down to 0.5 µm diamond paste to ensure the complete removal of any possible reaction layer with graphite during SPS synthesis as well as to ensure a very smooth starting surface for the wear test. Furthermore, the discs and the ball were cleaned with isopropanol before the wear test to ensure all surface contaminants that may interfere with the measurements are all effectively removed. Throughout the testing, similar surface pre-treatment was maintained to ensure little or no variation in results. Friction coefficient was continuously recorded during the test and in some cases tests were interrupted to understand the origin of transition in friction.

The contact load and speed employed for tribological testing in this work was systematically chosen according to the ceramic wear map (for the ceramic composite) [194, 195], whilst multiple trials of a combination of load and speed was used to determine the contact condition for the wear test on MAX phases. For the ceramic composite, it was important to stay in the mild wear regime where micromechanisms are preserved. Whilst for the MAX phases it was essential to choose a combination of parameter(s) to ensure testing was done within the friction transition regime.

3.5. CHARACTERIZATION

3.5.1. Micropreparation

Samples were prepped in several stages using a Buehler Automet. Initial grinding to remove the carburized layer upon SPS was performed with a grit P120 (142 µm) MetPrep Matrix diamond grinding disc until all carburized layer was removed – this was validated visually as well as XRD of the surface which revealed the absence of graphite peaks. This was then followed by grinding with grit P600 (14 µm) Met Prep Matrix and 3 µm Buehler Apex diamond grinding discs, and polishing with a 1 µm Buehler MetaDi™ Combo Monocrystalline Diamond Suspension + Extender diamond suspension on a Microcloth. Lastly, the sample underwent an additional polishing stage with colloidal silica on a Chemomet pad to artificially etch the surface, which in some cases helped to reveal the microstructure without the need of HF. Each grinding stage was performed in 3 min cycles with a 15 N force, 141 rpm platen speed, 60 rpm head speed and complimentary rotation. In some cases, the grinding duration was extended for 5 min cycles as the extent of carbon contamination varied from sample to sample. This implied extending the polishing stage in some cases until all the scratches were removed. The resulting mirror-like polished discs were then sonicated in isopropanol.

3.5.1.1. Density measurement

Density measurements were carried out using Archimedes water immersion method and relative density was calculated by dividing the measured density with the theoretical density of each sample by talking into account the theoretical densities of various phases that coexist in the bulk sample determined by Rietveld refinement and/or XRD integrated intensity calibration (for the textured Maxthal 312 bulk samples).

3.5.1.2. Hardness characterization

Vickers micro indentation was used to determine the bulk hardness from the polished cylindrical discs using DuraScan emcoTest microindentation hardness tester. A range of indentation loads were employed depending on the scope of characterization. Indentation load was varied in some cases to validate indentation size effects (ISE) and/or anisotropic mechanical response in MAX Phases. Indentation was also employed as an analytical model beside just hardness measurements to further describe fracture processes occurring during friction. As previous research has shown that the majority of the micromechanisms occurring during wear can be related to the deformation mechanisms found in an indent using an SEM.

3.5.1.3. X-ray phase analysis

All X-ray analysis was performed on a D2 PHASER Bruker diffractometer equipped with a scintillation counter Cukα radiation and a graphite monochromator. The diffraction patterns were scanned from 5° to 80° 2θ at a scanning rate of 0.02°/min. For the MAXTHAL samples, the phase fraction was determined using integrated calibration method owing to preferred orientation, whilst the phase fraction from the samples synthesized via elemental powder route was determined using Rietveld refinement (GSAS+EXPGUI) upon obtaining diffraction patterns especially using a Panalytical X'PERT PRO diffractometer.

3.5.1.4. Microstructure and chemical analysis

The microstructural development is considered on two levels:

- grain structure: observable on the scale of optical microscopy (OM) and scanning electron microscopy (SEM)
- structure within the grain: observable on the scale of transmission electron microscopy (TEM)

The microstructures of the synthesized and unetched samples upon polishing were then observed analysed using optical microscopy (OM) and scanning electron microscopy (SEM) equipped with an energy-dispersive X-ray spectroscopy (EDS) system. Optical microscopy was also preferentially employed to analyse the pin surfaces after the wear test for possible wear or transfer materials.

3.5.1.5. Focused ion beam (FIB) sample preparation

A focused ion beam microscope (FEI Helios, The Netherlands) equipped with an Omniprobe manipulator was employed to prepare in situ lift-out of electron-transparent TEM specimen from the worn surface perpendicular to the sliding direction in order to analyse the cross-sectional microstructure of the wear tracks. The region of interest (ROI)) on the wear scar was protected from the incident beam bombardment by depositing a Pt cap on the top surface using a gas injection system (GIS). The GIS sytem directs a needle in close proximity to the sample and deposits directly the shielding gas on a defined area on the sample surface. The cross section of the TEM sample is around 15 x 2 µm and thickness after milling is < 100 nm. TEM observation of the microstructural evolution and deformed microstructures was observed using a Philips 420 TEM operated at 120 kV and JEOL 3100Z R005 aberration corrected high-resolution TEM (300 kV).

3.5.1.6. Evolved surface chemistry

Elemental and chemical analysis of the bulk and worn surface were carried using energy-dispersive spectroscopy (EDS), electron energy loss spectroscopy (EELS) and Raman spectroscopy. Raman spectra were collected using a Renishaw inVia Raman microscope equipped with a 514.5 nm argon-ion laser. Raman analysis was performed inside the wear track in air. It was found important to characterize the chemistry of the tribofilm extensively by Raman analysis as it gave more reliable results on the architecture of the tribofilm rather than just elemental distribution.

3.5.1.7. Thermal analysis

Differential scanning calorimetry (DSC) thermoanalysis was carried out on the Maxthal 312 powder in order to simulate the SPS sintering environment to further understand the underlying reaction mechanisms leading to the decomposition of the bulk Ti_3SiC_2 in the graphite-rich SPS environment. Differential scanning thermograms were recorded using a TA Instruments Q1000. About 3 mg of the Maxthal 312 powder was weighed in a graphite crucible and argon employed as the purge gas. Data were collected at a heating rate of 20 °C/min over a temperature range 25-1500 °C.

CHAPTER 4

SUMMARY OF APPENDED PAPERS

The following chapter contains summaries of the appended papers and the contribution of the co-authors.

4.1. PAPER A: Influence of sintering environment on the spark plasma sintering of Maxthal 312 (nominally—Ti_3SiC_2) and the role of powder particle size on densification

This paper investigates the spark plasma sintering (SPS) of Ti_3SiC_2, a member of the MAX phase family using a prealloyed powder route for the first time as compared to the conventional elemental powder mixture route. The role of powder particle size on densification as well as sintering environment on the evolution of ancillary phases is investigated. This paper elucidates the reaction mechanisms leading to the formation of Ti_3SiC_2 and further delineates the optimum sintering conditions to improve the yield of Ti_3SiC_2.

Author contribution

This published article was written entirely by me, aided by comments from co-authors. I also performed the material synthesis and all characterization and data analysis.

4.2. PAPER B: Synthesis and microstructural evolution in ternary metalloceramic Ti_3SiC_2 consolidated via the Maxthal 312 powder route

This paper is a continuation of paper A and it investigates the reaction mechanisms leading to the formation of Ti_3SiC_2, microstructural evolution in Ti_3SiC_2 as well as its Vickers indentation induced deformation microstructure. The role of Si evaporation and/or carburization from the graphite tooling leading to the formation of ancillaries was further investigated. Microstructural and orientation relationship of the compositional phases formed was also elucidated.

Author contribution

This published article was written entirely by me, aided by comments from co-authors. I also performed the material synthesis, characterization and data analysis. The exception is the diffraction patterns and some of the TEM images obtained by Dr Ali Mostaed as directed by me.

4.3. PAPER C: Spark plasma sintering (SPS) synthesis and tribological behaviour of MAX phase composite of the family $Ti_{n+1}SiC_n$ (n = 2)

This paper further investigates the synthesis of Ti_3SiC_2 under vacuum above the optimum sintering temperature delineated in part A. This was undertaken in order to understand the role of carbon diffusion from the graphite heating elements during SPS on the decomposition of Ti_3SiC_2. DSC-TG was done in a graphite crucible on the MAX phase powder to simulate the graphite—rich SPS environment in order to further understand if indeed carbon diffusion is responsible for the decomposition under vacuum sintering or the high vacuum pressure employed in SPS is responsible for drawing out the vapour of Si. The tribological behaviour of the resulting MAX phase composite (Ti_3SiC_2-TiC_X and Ti_3SiC_2-TiC) formed after SPS was investigated under room-temperature dry-sliding conditions for evidence of intrinsic lubricity and to understand the role of TiC ancillary phase on friction and wear behaviour of the composite.

Author contribution

This published article was written entirely by me, aided by comments from co-authors. I also performed the material synthesis, tribological experiments and all characterization and data analysis.

4.4. PAPER D: The lubricating properties of spark plasma sintered (SPS) Ti_3SiC_2 MAX phase compound and composite

This paper is a dedicated study undertaken to understand lubrication mechanism of Ti_3SiC_2 in relation to tribofilm formation and to elucidate the underlying wear mechanisms leading to transition in friction and wear.

Author contribution

This published article was written entirely by me, aided by comments from co-author. I also performed the material synthesis, tribological experiments and all characterization and data analysis.

4.5. PAPER E: Microstructures and intrinsic lubricity of in situ Ti_3SiC_2-$TiSi_2$-TiC MAX phase composite fabricated by reactive spark plasma sintering (SPS)

Following the vague understanding of the wear mechanism in paper C, a tribological investigation was carried out on MAX phase composite synthesized from elemental powder mixture using SPS. Dedicated microstructural and chemical analysis of the worn surface was undertaken to understand the role of deformation microstructure and evolved chemistries on the transition in friction and wear: from low CoF and low wear rate to high CoF and high wear rate. In this paper the underlying wear mechanism in Ti_3SiC_2 and Ti_3SiC2-TiC is fully understood and comprehensively explained for the first time.

Author contribution

This published article was written entirely by me, aided by comments from co-authors. I also performed the material synthesis, tribological experiments and all characterization and data analysis. Exception is the TEM sample made by focused ion beam (FIB) by Dr Le Ma, as well as sample synthesis done in collaboration with Dr Daniel Cooper.

4.6. PAPER F: Microstructural evolution and wear mechanism of Ti_3AlC_2-Ti_2AlC dual MAX phase composite consolidated by spark plasma sintering (SPS)

Aluminium-based dual MAX phase composite (Ti_3AlC_2 – Ti_2AlC) was synthesized for the first time by exploiting the reaction mechanism using elemental powder mixture by spark plasma sintering. In this work microstructural evolution upon synthesis as well as the deformation microstructure following Vickers indentation was investigated. The role of misfit in CTE between Ti_3AlC_2 and Ti_2AlC as well as abnormal grain growth (AGG) on grain fracture and gap formation along the grain boundary was investigated. Further, the dry-sliding room-temperature tribological studies was undertaken for evidence of solid lubrication and to establish the relationship between deformation microstructure upon Vickers indentation and shear-induced deformation microstructure during sliding contact.

Author contribution

This published peer reviewed article was written entirely by me, aided by comments from co-authors. I also performed majority of the sample preparation, tribological testing and all characterization and data analysis. The exception is the EELS analysis and HAADF image collected by Dr Joanne Sharp, as well as sample synthesis done by Dr Daniel Cooper.

4.7. PAPER G: Dry sliding friction and wear behaviour of TiC-based ceramics and consequent effect of the evolution of grain buckling on wear mechanism

This published peer reviewed article investigates the sinterability and densification mechanism of monolithic TiC and TiC/SiC composite without sintering aid using SPS. The tribological behaviour of the SPSed compacts was also investigated as very limited work has been reported on the friction and wear behaviour of TiC-particulate/SiC-matrix ceramic composites at ambient conditions. An interesting observation reported in this work for the first time was the evolution of grain buckling due to sliding contact.

Author contribution

This published peer reviewed article was written entirely by me, aided by comments from co-author. I also performed majority of the sample preparation and all characterization and data analysis. The exception is the TiC-SiC composite synthesized by Dr Tanagorn kwamman.

4.8. PAPER H: Wear induced ripplocation during dry sliding wear of TiC-based composite

Following the work reported in paper F, a comprehensive investigation was further undertaken to understand the micromechanisms leading to grain buckling in the TiC/SiC composite during shear sliding contact. For the first time mechanical exfoliation of carbon normally observed in 3D-materials is reported as the underlying mechanism leading to wear-induced ripplocation in TiC/SiC particulate-matrix ceramic composite.

Author contribution

This published article was written entirely by me, aided by comments from co-authors. I also performed the material synthesis, tribological experiments and all characterization and data analysis. The exception is the diffraction patterns and some of the TEM images obtained by Dr Ali Mostaed as directed by me.

CHAPTER 5

CONCLUSIONS AND FUTURE WORK

This chapter summarizes the main results of the appended papers and provides suggestions for future work. In general the current work has contributed to the synthesis and tribological behaviour of MAX phases and TiC-particulate/SiC-matrix ceramic composite. The use of transmission electron microscopy for cross-sectional examination of evolved microstructure at a worn surface alongside Raman spectroscopy to probe the local chemistries inside the wear track ex-situ have helped fill in gaps left in the solid lubrication behaviour of MAX phases as well as the tribological behaviour of TiC/SiC particulate ceramic composite.

5.1. GENERAL CONCLUSIONS

The key research question on the existence of intrinsic lubricity in MAX phases has been answered comprehensively for the first time using the $Ti_{n+1}[Al, Si]C_n$ MAX phase system. The solid lubrication mechanism has been validated and the formation sequence of self-generating tribofilms consisting of easy shear graphitic layer and frictional heating induced rutile and oxycarbide layers has for the first time elucidated.

The transition from low friction and low wear to high friction and high wear as observed for the Si-based MAX phase is linked to the low grain boundary strength of the Ti_3SiC_2 grains. This facilitates the ease of grain pull-out following the ball-to-disc contact once the tribofilm layer at the interface has been compromised. For the Al-based MAX phase, the initiation of tribofilm layer seems to take longer possibly due to their better oxidation resistance as compared to the Si-based MAX phase. As such, direct ball-to-disc contact takes place almost instantaneously at the onset of the sliding contact, leading to the observed high friction and high wear. As a function of sliding time, the evolution of tribofilm layer takes place which resulted in transition from high friction and high wear rate to low friction and low wear rate. In general the worn surface of the MAX phases can self-heal as observed in “paper D” – and a continuous transition in friction and wear will be observed if the sliding action was to continue infinitely under dry-sliding test condition(s).

It has also been shown in this work that, irrespective of the improved fracture toughness in TiC-SiC particulate ceramic composite, the friction and wear properties are inferior to those of monolithic TiC and SiC at ambient dry-sliding test conditions. The systematic mechanical exfoliation of carbon from the TiC grains has been identified as the main factor deteriorating the room temperature wear properties of TiC-particulate/SiC-matrix ceramic composites. However, at high temperature, this might not be the case following the observation that ripplocations are mobile at high temperature – thus they can nucleate and annihilate leading to surface healing.

5.2. PROPOSALS FOR FUTURE WORK

As TiC can be a starting material, intermediate phase, and an ancillary phase in their matrix in the synthesis of Ti_3SiC_2 and Ti_3AlC_2, further work should be carried out on how to explore the orientation and microstructural relationship between the MAX phase Ti_3SiC_2 and Ti_3AlC_2 and cubic phase TiC to imrprove and/or optimize the conversion into monolithic MAX phase. The following could be useful in the synthesis of monolithic MAX phase:

- An important suggestion is to first synthesize a powder sample containing for example Ti_3AlC_2 ($TiAl_{0.33}C_{0.67}$) and $TiC_{0.67}$, then intercalate Al into the cubic $TiC_{0.67}$ during the bulk synthesis to bring about a phase transformation from cubic $TiC_{0.67}$ to hexagonal $TiAl_{0.33}C_{0.67}$. This will require careful selection of the synthesis method and/or parameter.
- Silicon can inititally be mixed with the MAXthal 312 powder – as the prealloyed powder contains about 8 % TiC, the added Si will intercalate into the ancillary TiC phase during the bulk synthesis thus improving the yield of the MAX phase via cubic to hexagonal phase transformation. The added Si can also compensate for the loss of Si due to the SPS vacuum.

The work carried out in this thesis on the tribology of MAX phase has been undertaken at ambient conditions. Although, intrinsic lubricity signatures has been identified as well as the underlying formation mechanisms of the associated tribo-layers, it will be interesting to see what happens at high terperature if the tribological properties improves or decline at high temperature dry-sliding condition. Especially for the Al-based MAX phase as their good oxidation resistance led to a delay in tribofilm formation that led to increased friction and wear at the start of the sliding action.

Tribological studies on textured MAX phases should also be explored as most work on the tribology of MAX phases has been on non-textured bulk samples – and there are indications that textured sample could give enhanced tribological properties as crack in such samples will be aligned parallel to the sliding direction making grain pull-out – a major factor contributing to three-body wear – extremely diificult.

In general many aspects of the link between deformation and wear of MAX phases remain poorly understood and more work need to be done by carrying out TEM studies in order to fully understanding mechanisms leading to wear in MAX phases.

A further suggestion for future work for both the MAX Phases and the particulate ceramic composite is a high-temperature tribological investigations. Judging from the dry-sliding friction and wear test carried out in this work, it was evident that frictional heating played some important role in the tribological events observed in the wear mechanism of the MAX phase. As such we envisage the case might be different if tribological test is undertaken at high temperature; as the role of frictional-heating induced tribofilm will be fully understood in MAX phases. Also, possible high-temperature healing of the ripple-like features as observed in the particulate ceramic composite during the focused ion beam (FIB) sample preparation for TEM studies will be further understood.

REFERENCES

1. Gupta, S. and M.W. Barsoum, On the tribology of the MAX phases and their composites during dry sliding: A review. Wear, 2011. **271**(9–10): p. 1878-1894.
2. Wang, W., Application of a High Temperature Self-Lubricating Composite Coating on Steam Turbine Components. Vol. 177. 2004. 12-17.
3. Dellacorte, C. and J.A. Laskowski, Tribological Evaluation of PS300: A New Chrome Oxide-Based Solid Lubricant Coating Sliding Against Al_2O_3 from 25° to 650°C. Tribology Transactions, 1997. **40**(1): p. 163-167.
4. Woydt, M., Tribological characteristics of polycrystalline Magnéli-type titanium dioxides. Tribology Letters, 2000. **8**(2): p. 117-130.
5. Domínguez-Meister, S., T.C. Rojas, M. Brizuela, and J.C. Sánchez-López, Solid lubricant behavior of MoS_2 and WSe_2-based nanocomposite coatings. Science and Technology of Advanced Materials, 2017. **18**(1): p. 122-133.
6. Hu, J.J., R. Wheeler, J.S. Zabinski, P.A. Shade, A. Shiveley, and A.A. Voevodin, Transmission Electron Microscopy Analysis of Mo–W–S–Se Film Sliding Contact Obtained by Using Focused Ion Beam Microscope and In Situ Microtribometer. Tribology Letters, 2008. **32**(1): p. 49-57.
7. Khare, H.S. and D.L. Burris, The Effects of Environmental Water and Oxygen on the Temperature-Dependent Friction of Sputtered Molybdenum Disulfide. Tribology Letters, 2013. **52**(3): p. 485-493.
8. Sliney, H.E., Solid lubricant materials for high temperatures—a review. Tribology International, 1982. **15**(5): p. 303-315.
9. Shi, X., W. Zhai, M. Wang, Z. Xu, J. Yao, S. Song, and Q. Zhang, Tribological Behaviors of NiAl-Ti_3SiC_2 Self-Lubricating Composites at Elevated Temperatures. Tribology Transactions, 2014. **57**(4): p. 589-602.
10. Barsoum, M.W., MAX phases : properties of machinable ternary carbides and nitrides. 2013: Weinheim, Germany : Wiley-VCH Verlag GmbH & Co. KGaA, 2013.
11. Evans, A.G. and D.B. Marshall, Fundamentals of Friction and Wear of Materials, in ASM Materials Science Seminar. 1980: Pittsburgh, PA, USA.
12. Endo, H., M. Ueki, and H. Kubo, Microstructure and mechanical properties of hot-pressed SiC-TiC composites. Journal of Materials Science, 1991. **26**(14): p. 3769-3774.
13. Wei, G.C. and P.F. Becher, Improvements in Mechanical Properties in SiC by the Addition of TiC Particles. Journal of the American Ceramic Society, 1984. **67**(8): p. 571-574.
14. Wäsche, R., R. Yarim, D. Klaffke, and M. Hartelt, Oscillating sliding wear behaviour of SiC, TiC, TiB_2, 59SiC–41TiB_2 and 52SiC–24TiC–24TiB_2 materials up to 750°C in air. Tribotest, 2006. **12**(2): p. 99-111.
15. Griggs, J., A.C. Lang, J. Gruber, G.J. Tucker, M.L. Taheri, and M.W. Barsoum, Spherical nanoindentation, modeling and transmission electron microscopy evidence for ripplocations in Ti_3SiC_2. Acta Materialia, 2017. **131**: p. 141-155.
16. Barsoum, M.W. and T. El-Raghy, The MAX Phases: Unique New Carbide and Nitride Materials: Ternary ceramics turn out to be surprisingly soft and machinable, yet also heat-tolerant, strong and lightweight. American Scientist, 2001. **89**(4): p. 334-343.
17. Cui, B., R. Sa, D. Daniel, F. Inam, M. J. Reece, and W. Edward Lee, Microstructural Evolution During High-temperature Oxidation of Spark Plasma Sintered Ti_2AlN Ceramics. Vol. 60. 2012.
18. Wäsche, R. and D. Klaffke, In situ formation of tribologically effective oxide interfaces in SiC-based ceramics during dry oscillating sliding. Tribology Letters, 1998. **5**(2): p. 173.
19. Lafon-Placette, S., K. Delbé, J. Denape, and M. Ferrato, Tribological characterization of silicon carbide and carbon materials. Journal of the European Ceramic Society, 2015. **35**(4): p. 1147-1159.
20. Wäsche, R. and D. Klaffke, Ceramic particulate composites in the system SiC–TiC–TiB_2 sliding against SiC and Al_2O_3 under water. Tribology International, 1999. **32**(4): p. 197-206.
21. Maitra, S., Nanoceramic matrix composites: types, processing and applications, in Advances in Ceramic Matrix Composites, I.M. Low, Editor. 2014, Woodhead Publishing. p. 27-42.

22. Richerson, D.W., Industrial Applications of Ceramic Matrix Composites, in Comprehensive Composite Materials, A. Kelly and C. Zweben, Editors. 2000, Pergamon: Oxford. p. 549-570.
23. Sahoo, P. and J.P. Davim, Tribology of Ceramics and Ceramic Matrix Composites, in Tribology for Scientists and Engineers: From Basics to Advanced Concepts, P.L. Menezes, et al., Editors. 2013, Springer New York: New York, NY. p. 211-231.
24. Carrapichano, J.M., J.R. Gomes, and R.F. Silva, Tribological behaviour of Si_3N_4–BN ceramic materials for dry sliding applications. Wear, 2002. **253**(9): p. 1070-1076.
25. Erdemir, A., Solid lubricants and self-lubricating films. Modern Tribology Handbook, 2001. **2**.
26. Erdemir, A., A crystal-chemical approach to lubrication by solid oxides. Tribology Letters, 2000. **8**(2): p. 97.
27. Myhra, S., J.W.B. Summers, and E.H. Kisi, Ti_3SiC_2—A layered ceramic exhibiting ultra-low friction. Materials Letters, 1999. **39**(1): p. 6-11.
28. Low, I.M., Advances in ceramic matrix composites: an introduction, in Advances in Ceramic Matrix Composites, I.M. Low, Editor. 2014, Woodhead Publishing. p. 1-6.
29. Barsoum, M.W. and T. El-Raghy, Synthesis and Characterization of a Remarkable Ceramic: Ti_3SiC_2. Journal of the American Ceramic Society, 1996. **79**(7): p. 1953-1956.
30. Wang, J., X. Luo, and Y. Sun, Torsional Fretting Wear Properties of Thermal Oxidation-Treated Ti_3SiC_2 Coatings. Coatings, 2018. **8**: p. 324.
31. Zhang, Y., G.P. Ding, Y. Zhou, and B.C. Cai, Ti_3SiC_2-a Self-Lubricating Ceramic. Materials Letters, 2002. **55**: p. 285-289.
32. Zhai, H., Z. Huang, and M. Ai, Tribological behaviors of bulk Ti_3SiC_2 and influences of TiC impurities. Materials Science and Engineering: A, 2006. **435-436**(Supplement C): p. 360-370.
33. Xu, L., D. Zhu, S. Grasso, T.S. Suzuki, A. Kasahara, M. Tosa, B.-N. Kim, Y. Sakka, M. Zhu, and C. Hu, Effect of texture microstructure on tribological properties of tailored Ti_3AlC_2 ceramic. Journal of Advanced Ceramics, 2017. **6**(2): p. 120-128.
34. Qian, X.K., 1 - Methods of MAX-phase synthesis and densification – I A2 - Low, I.M, in Advances in Science and Technology of $M_{n+1}AX_n$ Phases. 2012, Woodhead Publishing. p. 1-19.
35. Yanchun, Z. and S. Zhimei, Electronic structure and bonding properties in layered ternary carbide Ti_3SiC_2. Journal of Physics: Condensed Matter, 2000. **12**(28): p. 457.
36. Wang, X. and Y. Zhou, Solid–liquid reaction synthesis of layered machinable Ti_3AlC_2 ceramic. Journal of Materials Chemistry, 2002. **12**(3): p. 455-460.
37. Wang, X.H. and Y.C. Zhou, Oxidation behavior of TiC-containing Ti_3AlC_2 based material at 500–900 °C in air. Materials Research Innovations, 2003. **7**(6): p. 381-390.
38. Tzenov, N.V. and M.W. Barsoum, Synthesis and Characterization of Ti_3AlC_2. Journal of the American Ceramic Society, 2000. **83**(4): p. 825-832.
39. Zhu, J., B. Mei, X. Xu, and J. Liu, Synthesis of single-phase polycrystalline Ti_3SiC_2 and Ti_3AlC_2 by hot pressing with the assistance of metallic Al or Si. Materials Letters, 2004. **58**(5): p. 588-592.
40. Sokol, M., V. Natu, S. Kota, and M. W. Barsoum, Big Questions in Chemistry - On the Chemical Diversity of the MAX Phases. Trends Chem 2019;1:210-223.
41. Barsoum, M.W., D. Brodkin, and T. El-Raghy, Layered machinable ceramics for high temperature applications. Scripta Materialia, 1997. **36**(5): p. 535-541.
42. Barsoum, M.W. and M. Radovic, Elastic and Mechanical Properties of the MAX Phases, in Annual Review of Materials Research, Vol 41, D.R. Clarke and P. Fratzl, Editors. 2011, Annual Reviews: Palo Alto. p. 195-227.
43. Hoffman, E.N., D.W. Vinson, R.L. Sindelar, D.J. Tallman, G. Kohse, and M.W. Barsoum, MAX phase carbides and nitrides: Properties for future nuclear power plant in-core applications and neutron transmutation analysis. Nuclear Engineering and Design, 2012. **244**: p. 17-24.
44. Fashandi, H., C.C. Lai, M. Dahlqvist, J. Lu, J. Rosen, L. Hultman, G. Greczynski, M. Andersson, A. Lloyd Spetz, and P. Eklund, Ti_2Au_2C and $Ti_3Au_2C_2$ formed by solid state reaction of gold with Ti_2AlC and Ti_3AlC_2. Chemical Communications, 2017. **53**(69): p. 9554-9557.
45. Kanoun, M.B., S. Goumri-Said, and K. Abdullah, 8 - Theoretical study of physical properties and oxygen incorporation effect in nanolaminated ternary carbides 211-MAX phases A2 - Low,

I.M, in Advances in Science and Technology of $M_{n+1}AX_n$ Phases. 2012, Woodhead Publishing. p. 177-196.

46. Xiao, J., T. Yang, C. Wang, J. Xue, and Y. Wang, Investigations on Radiation Tolerance of $M_{n+1}AX_n$ Phases: Study of Ti_3SiC_2, Ti_3AlC_2, Cr_2AlC, Cr_2GeC, Ti_2AlC, and Ti_2AlN. Journal of the American Ceramic Society, 2015. **98**(4): p. 1323-1331.
47. Whittle, K.R., M.G. Blackford, R.D. Aughterson, S. Moricca, G.R. Lumpkin, D.P. Riley, and N.J. Zaluzec, Radiation tolerance of $M_{n+1}AX_n$ phases, Ti_3AlC_2 and Ti_3SiC_2. Acta Materialia, 2010. **58**(13): p. 4362-4368.
48. Kisi, E.H., J.A.A. Crossley, S. Myhra, and M.W. Barsoum, Structure and Crystal Chemistry of Ti_3SiC_2. Journal of Physics and Chemistry of Solids, 1998. **59**(9): p. 1437-1443.
49. Hashimoto, H. and Z.M. Sun, Preparation of TiC-Ti_3SiC_2 Composites by Mechanical Alloying and Hot-Pressing. Materials Transactions, 2008. **49**(7): p. 1572-1578.
50. Barsoum, M.W., T. Zhen, S.R. Kalidindi, M. Radovic, and A. Murugaiah, Fully reversible, dislocation-based compressive deformation of Ti_3SiC_2 to 1 GPa. Nat Mater, 2003. **2**(2): p. 107-111.
51. Magnuson, M. and M. Mattesini, Chemical bonding and electronic-structure in MAX phases as viewed by X-ray spectroscopy and density functional theory. Thin Solid Films, 2017. **621**: p. 108-130.
52. Higashi, M., S. Momono, K. Kishida, N.L. Okamoto, and H. Inui, Anisotropic plastic deformation of single crystals of the MAX phase compound Ti_3SiC_2 investigated by micropillar compression. Acta Materialia, 2018. **161**: p. 161-170.
53. Wang, X.H. and Y.C. Zhou, Microstructure and properties of Ti_3AlC_2 prepared by the solid–liquid reaction synthesis and simultaneous in-situ hot pressing process. Acta Materialia, 2002. **50**(12): p. 3143-3151.
54. El-Raghy, T., A. Zavaliangos, M.W. Barsoum, and S.R. Kalidindi, Damage mechanisms around hardness indentations in Ti_3SiC_2. Journal of the American Ceramic Society, 1997. **80**(2): p. 513-516.
55. Kooi, B.J., R.J. Poppen, N.J.M. Carvalho, J.T.M. De Hosson, and M.W. Barsoum, Ti_3SiC_2: A damage tolerant ceramic studied with nano-indentations and transmission electron microscopy. Acta Materialia, 2003. **51**(10): p. 2859-2872.
56. Low, I.M., Vickers contact damage of micro-layered Ti_3SiC_2. Journal of the European Ceramic Society, 1998. **18**(6): p. 709-713.
57. Sun, Z., Z. Zhang, H. Hashimoto, and T. Abe, Ternary Compound Ti_3SiC_2: Part II. Deformation and Fracture Behavior at Different Temperatures. Materials transactions, 2002. **43**(3): p. 432-435.
58. Barsoum, M.W., L. Farber, and T. El-Raghy, Dislocations, kink bands, and room-temperature plasticity of Ti_3SiC_2. Metallurgical and Materials Transactions A, 1999. **30**(7): p. 1727-1738.
59. Yu, W., S. Li, and W.G. Sloof, Microstructure and mechanical properties of a $Cr_2Al(Si)C$ solid solution. Materials Science and Engineering: A, 2010. **527**(21): p. 5997-6001.
60. Sun, Z.M., Progress in research and development on MAX phases: a family of layered ternary compounds. International Materials Reviews, 2011. **56**(3): p. 143-166.
61. Li, S.B., L.F. Cheng, and L.T. Zhang, Identification of damage tolerance of Ti_3SiC_2 by hardness indentations and single edge notched beam test. Materials Science and Technology, 2002. **18**(2): p. 231-233.
62. Wada, Y., N. Sekido, T. Ohmura, and K. Yoshimi, Deformation Microstructure Developed by Nanoindentation of a MAX Phase Ti_2AlC. Materials Transactions, 2018. **59**(5): p. 771-778.
63. Riddhiman, B., The Deformation Response of Polycrystalline MAX Phases Under High Strain-Rate Loading, in Materials Science and Engineering. 2016, University of Michigan. p. 192.
64. Nickl, J.J., K.K. Schweitzer, and P. Luxenberg, Gasphasenabscheidung im system Ti-Si-C. Journal of the Less Common Metals, 1972. **26**(3): p. 335-353.
65. Goto, T. and T. Hirai, Chemically vapor deposited Ti_3SiC_2. Materials Research Bulletin, 1987. **22**(9): p. 1195-1201.
66. Barsoum, M.W., A. Murugaiah, S.R. Kalidindi, T. Zhen, and Y. Gogotsi, Kink bands, nonlinear elasticity and nanoindentations in graphite. Carbon, 2004. **42**(8): p. 1435-1445.

67. Murugaiah, A., M.W. Barsoum, S.R. Kalidindi, and T. Zhen, Spherical Nanoindentations and Kink Bands in Ti_3SiC_2. Journal of Materials Research, 2011. **19**(4): p. 1139-1148.
68. Kooi, B.J., R.J. Poppen, N.J.M. Carvalho, J.T.M. De Hosson, and M.W. Barsoum, Ti_3SiC_2: A damage tolerant ceramic studied with nano-indentations and transmission electron microscopy. Acta Materialia, 2003. **51**(10): p. 2859-2872.
69. Barsoum, M., L. Ho-Duc, M. Radovic, and T. El-Raghy, Long time oxidation study of Ti_3SiC_2, Ti_3SiC_2/SiC, and Ti_3SiC_2/TiC composites in air. Journal of the Electrochemical Society, 2003. **150**(4): p. B166-B175.
70. MW, B., H.-D. LH, R. M, and E.-R. T, Long time oxidation study of Ti_3SiC_2, Ti_3SiC_2/SiC, and Ti_3SiC_2/TiC composites in air. Journal of the Electrochemical Society, 2003. **150**(4): p. B166-B175.
71. Tallman, D.J., B. Anasori, and M.W. Barsoum, A Critical Review of the Oxidation of Ti_2AlC, Ti_3AlC_2 and Cr_2AlC in Air. Materials Research Letters, 2013. **1**(3): p. 115-125.
72. Sundberg, M., G. Malmqvist, A. Magnusson, and T. El-Raghy, Alumina forming high temperature silicides and carbides. Ceramics International, 2004. **30**(7): p. 1899-1904.
73. Wang, X.H. and Y.C. Zhou, High-Temperature Oxidation Behavior of Ti_2AlC in Air. Oxidation of Metals, 2003. **59**(3): p. 303-320.
74. Wang, X.H. and Y.C. Zhou, Oxidation behavior of Ti_3AlC_2 at 1000–1400 °C in air. Corrosion Science, 2003. **45**(5): p. 891-907.
75. Garg, A. and J.L. Smialek, Microstructure and Oxidation of a MAX Phase/Superalloy Hybrid Interface - NASA/TM-2014-216679. 2014, Sponsoring Organization: NASA Glenn Research Center.
76. Horlait, D., S. Grasso, N. Al Nasiri, P.A. Burr, and W.E. Lee, Synthesis and Oxidation Testing of MAX Phase Composites in the Cr–Ti–Al–C Quaternary System. Journal of the American Ceramic Society, 2016. **99**(2): p. 682-690.
77. Cui, B., D.D. Jayaseelan, and W.E. Lee, Microstructural evolution during high-temperature oxidation of Ti_2AlC ceramics. Acta Materialia, 2011. **59**(10): p. 4116-4125.
78. Smialek, J.L., Environmental resistance of a Ti_2AlC-type MAX phase in a high pressure burner rig. Journal of the European Ceramic Society, 2017. **37**(1): p. 23-34.
79. Radhakrishnan, R., J.J. Williams, and M. Akinc, Synthesis and high-temperature stability of Ti_3SiC_2. Journal of Alloys and Compounds, 1999. **285**(1): p. 85-88.
80. Song, G.M., Y.T. Pei, W.G. Sloof, S.B. Li, J.T.M. De Hosson, and S. van der Zwaag, Oxidation-induced crack healing in Ti_3AlC_2 ceramics. Scripta Materialia, 2008. **58**(1): p. 13-16.
81. Sloof, W.G., R. Pei, S.A. McDonald, J.L. Fife, L. Shen, L. Boatemaa, A.S. Farle, K. Yan, X. Zhang, S. van der Zwaag, P.D. Lee, and P.J. Withers, Repeated crack healing in MAX-phase ceramics revealed by 4D in situ synchrotron X-ray tomographic microscopy. Scientific Reports, 2016. **6**: p. 23040.
82. Farle, A.-S., C. Kwakernaak, S. van der Zwaag, and W.G. Sloof, A conceptual study into the potential of $M_{n+1}AX_n$-phase ceramics for self-healing of crack damage. Journal of the European Ceramic Society, 2015. **35**(1): p. 37-45.
83. Song, G.M., 11 - Self-healing of MAX phase ceramics for high temperature applications: evidence from Ti_3AlC_2 A2 - Low, I.M, in Advances in Science and Technology of $M_{n+1}AX_n$ Phases. 2012, Woodhead Publishing. p. 271-288.
84. Yang, H.J., Y.T. Pei, J.C. Rao, and J.T.M. De Hosson, Self-healing performance of Ti_2AlC ceramic. Journal of Materials Chemistry, 2012. **22**(17): p. 8304-8313.
85. Wang, X.H. and Y.C. Zhou, Layered Machinable and Electrically Conductive Ti_2AlC and Ti_3AlC_2 Ceramics: a Review. Journal of Materials Science & Technology, 2010. **26**(5): p. 385-416.
86. Bai, Y., X. He, Y. Sun, C. Zhu, M. Li, and L. Shi, Chemical bonding and elastic properties of Ti_3AC_2 phases (A=Si, Ge, and Sn): A first-principle study. Solid State Sciences, 2010. **12**(7): p. 1220-1225.
87. Hajas, D.E., M. to Baben, B. Hallstedt, R. Iskandar, J. Mayer, and J.M. Schneider, Oxidation of Cr_2AlC coatings in the temperature range of 1230 to 1410°C. Surface and Coatings Technology, 2011. **206**(4): p. 591-598.

88. Li, S., G. Song, K. Kwakernaak, S. van der Zwaag, and W.G. Sloof, Multiple crack healing of a Ti_2AlC ceramic. Journal of the European Ceramic Society, 2012. **32**(8): p. 1813-1820.
89. van der Zwaag, S., N.H. van Dijk, H.M. Jonkers, S.D. Mookhoek, and W.G. Sloof, Self-Healing Behaviour in Man-Made Engineering Materials: Bioinspired but Taking into Account Their Intrinsic Character. Philosophical Transactions: Mathematical, Physical and Engineering Sciences, 2009. **367**(1894): p. 1689-1704.
90. I. M. Low, W.K.P., Thermal Stability of MAX Phases. Key Engineering Materials, 2014. **617**: p. 153-158.
91. Emmerlich, J., D. Music, P. Eklund, O. Wilhelmsson, U. Jansson, J.M. Schneider, H. Högberg, and L. Hultman, Thermal stability of Ti_3SiC_2 thin films. Acta Materialia, 2007. **55**(4): p. 1479-1488.
92. Low, I.M., Z. Oo, and K.E. Prince, Effect of Vacuum Annealing on the Phase Stability of Ti_3SiC_2. Journal of the American Ceramic Society, 2007. **90**(8): p. 2610-2614.
93. Pang, W., Low, I.M., O'Connor, B.H., Studer, A.J., Peterson, V.K., Palmquist, J.P. Diffraction Study on the Thermal Stability of $Ti_3SiC_2/TiC/TiSi_2$ Composites in Vacuum. in AIP Conference proceedings. 2012. New York.
94. Pang, W.K., Z. Oo, V.K. Peterson, and I.M. Low, 15 - Phase and thermal stability in Ti_3SiC_2 and $Ti_3SiC_2/TiC/TiSi_2$ systems, in Advances in Science and Technology of $M_{n+1}AX_n$ Phases. 2012, Woodhead Publishing. p. 389-413.
95. Zhang, H., Y. Zhou, Y. Bao, and M. Li, Titanium Silicon Carbide Pest Induced by Nitridation. Journal of the American Ceramic Society, 2008. **91**(2): p. 494-499.
96. Gao, N.F., Y. Miyamoto, and D. Zhang, Dense Ti_3SiC_2 prepared by reactive HIP. Journal of Materials Science, 1999. **34**(18): p. 4385-4392.
97. Racault, C., F. Langlais, and R. Naslain, Solid-state synthesis and characterization of the ternary phase Ti_3SiC_2. Journal of Materials Science, 1994. **29**(13): p. 3384-3392.
98. Wang, J.-Y. and Y.-C. Zhou, Polymorphism of Ti_3SiC_2 ceramic: First-principles investigations. Physical Review B, 2004. **69**(14): p. 144108.
99. Zhang, H., X. Liu, and Y. Jiang, Pore Formation Process of Porous Ti_3SiC_2 Fabricated by Reactive Sintering. Materials (Basel, Switzerland), 2017. **10**(2): p. 163.
100. Barsoum, M.W., The $M_{n+1}AX_n$ phases: A new class of solids. Progress in Solid State Chemistry, 2000. **28**(1): p. 201-281.
101. Jeitschko, W. and H. Nowotny, Die Kristallstruktur von Ti_3SiC_2—ein neuer Komplexcarbid-Typ. Monatshefte für Chemie - Chemical Monthly, 1967. **98**(2): p. 329-337.
102. El-Raghy, T. and M.W. Barsoum, Processing and Mechanical Properties of Ti_3SiC_2: I, Reaction Path and Microstructure Evolution. Journal of the American Ceramic Society, 1999. **82**(10): p. 2849-2854.
103. Nowotny, V.H., Strukturchemie einiger Verbindungen der Übergangsmetalle mit den elementen C, Si, Ge, Sn. Progress in Solid State Chemistry, 1971. **5**: p. 27-70.
104. Li, J.-F., T. Matsuki, and R. Watanabe, Combustion Reaction During Mechanical Alloying Synthesis of Ti_3SiC_2 Ceramics from 3Ti/Si/2C Powder Mixture. Journal of the American Ceramic Society, 2005. **88**(5): p. 1318-1320.
105. Hu, J.J., J.E. Bultman, S. Patton, and J.S. Zabinski, Pulsed Laser Deposition and Properties of $M_{n+1}AX_n$ Phase Formulated Ti_3SiC_2 Thin Films. Tribology Letters, 2004. **16**(1): p. 113-122.
106. Jacques, S., H. Di-Murro, M.P. Berthet, and H. Vincent, Pulsed reactive chemical vapor deposition in the C-Ti-Si system from $H_2/TiCl_4/SiCl_4$. Thin Solid Films, 2005. **478**(1): p. 13-20.
107. Palmquist, J.P., U. Jansson, T. Seppänen, P.O.Å. Persson, J. Birch, L. Hultman, and P. Isberg, Magnetron sputtered epitaxial single-phase Ti 3 SiC 2 thin films. Applied Physics Letters, 2002. **81**(5): p. 835-837.
108. Zhou, W., B. Mei, J. Zhu, and X. Hong, Fabrication of high purity dense Ti_2AlC-Ti_3AlC_2 composite by spark plasma sintering method. Journal of Materials Science, 2005. **40**(13): p. 3559-3560.
109. Zhu Jiao-qun, Mei Bing-chu., He Li-ping, Chen Yan-lin, synthesis of Ti_3SiC_2 by spark plasma sintering (SPS) of elemental powders. Trans. Nonferrous Met. Soc. China, 2003. **13**.

110. Li, H., D. Chen, J. Zhou, J.H. Zhao, and L.H. He, Synthesis of Ti_3SiC_2 by pressureless sintering of the elemental powders in vacuum. Materials Letters, 2004. **58**(11): p. 1741-1744.

111. Lu, X. and Y. Zhou, Pressureless Sintering and Properties of Ti_3AlC_2. International Journal of Applied Ceramic Technology, 2010. **7**(6): p. 744-751.

112. Liang, B.Y., S.Z. Jin, and M.Z. Wang, Low-temperature fabrication of high purity Ti_3SiC_2. Journal of Alloys and Compounds, 2008. **460**(1–2): p. 440-443.

113. Sowmya, A. and C.A. H., Synthesis of Titanium Silicon Carbide. Journal of the American Ceramic Society, 1995. **78**(3): p. 667-672.

114. Chen, J., W. Li, and W. Jiang, Characterization of sintered TiC–SiC composites. Ceramics International, 2009. **35**(8): p. 3125-3129.

115. Riley, D.P., E.H. Kisi, T.C. Hansen, and A.W. Hewat, Self-Propagating High-Temperature Synthesis of Ti_3SiC_2: I, Ultra-High-Speed Neutron Diffraction Study of the Reaction Mechanism. Journal of the American Ceramic Society, 2002. **85**(10): p. 2417-2424.

116. Thomas, T. and C.R. Bowen, Effect of particle size on the formation of Ti_2AlC using combustion synthesis. Ceramics International, 2016. **42**(3): p. 4150-4157.

117. Nan, B., X. Yin, L. Zhang, and L. Cheng, Three-Dimensional Printing of Ti_3SiC_2-Based Ceramics. Journal of the American Ceramic Society, 2011. **94**(4): p. 969-972.

118. Zhou, A., 2 - Methods of MAX-phase synthesis and densification – II A2 - Low, I.M, in Advances in Science and Technology of $M_{n+1}AX_n$ Phases. 2012, Woodhead Publishing. p. 21-46.

119. Lin, Z.J., M.J. Zhuo, Y.C. Zhou, M.S. Li, and J.Y. Wang, Microstructural characterization of layered ternary Ti_2AlC. Acta Materialia, 2006. **54**(4): p. 1009-1015.

120. Li, Z., W. Gao, D.L. Zhang, and Z.H. Cai, Oxidation Behavior of a TiAl–$Al_2Ti_4C_2$–TiC–Al_2O_3 in situ Composite. Oxidation of Metals, 2004. **61**(3): p. 339-354.

121. Ramkumar, J., S.K. Malhotra, R. Krishnamurthy, H. Mabuchi, K. Demizu, A. Kakitsuji, H. Tsuda, T. Matsui, and K. Morii, Microstructure and Dry Sliding Wear of Ti-50Al Alloy and Ti-47Al-3W/Ti_2AlC Composite Produced by Reactive Arc-Melting. Materials Transactions, 2003. **44**(9): p. 1861-1865.

122. Yoshida, M., 4 - Microstructural examination during the formation of Ti_3AlC_2 from mixtures of Ti/Al/C and Ti/Al/TiC A2 - Low, I.M, in Advances in Science and Technology of $M_{n+1}AX_n$ Phases. 2012, Woodhead Publishing. p. 81-101.

123. Pietzka, M.A. and J.C. Schuster, Phase equilibria of the quaternary system Ti-Al-Sn-N at 900 °C. Journal of Alloys and Compounds, 1997. **247**(1): p. 198-201.

124. Bei, G.P., V. Gauthier-Brunet, C. Tromas, and S. Dubois, Synthesis, characterization, and intrinsic hardness of layered nanolaminate Ti_3AlC_2 and $Ti_3Al_{0.8}Sn_{0.2}C_2$ solid solution. Journal of the American Ceramic Society, 2012. **95**(1): p. 102-107.

125. Han, J.H., S.S. Hwang, D. Lee, and S.W. Park, Synthesis and mechanical properties of Ti_3AlC_2 by hot pressing TiC_x/Al powder mixture. Journal of the European Ceramic Society, 2008. **28**(5): p. 979-988.

126. Zou, Y., Z. Sun, S. Tada, and H. Hashimoto, Effect of Al addition on low-temperature synthesis of Ti_3SiC_2 powder. Journal of Alloys and Compounds, 2008. **461**(1–2): p. 579-584.

127. Zou, Y., Z.M. Sun, H. Hashimoto, and L. Cheng, Synthesis reactions for Ti_3AlC_2 through pulse discharge sintering TiH_2/Al/C powder mixture. Journal of Alloys and Compounds, 2009. **468**(1): p. 217-221.

128. Bandyopadhyay, D., R.C. Sharma, and N. Chakraborti, The Ti-Al-C system (titanium - aluminum - carbon). Journal of Phase Equilibria, 2000. **21**(2): p. 195.

129. Bandyopadhyay, D., The Ti-Si-C system (Titanium-Silicon-Carbon). Journal of Phase Equilibria and Diffusion, 2004. **25**(5): p. 415-420.

130. Bunge, H.J., Orientation Distributions in Texture Analysis in Materials Science, H.J. Bunge, Editor. 1982, Butterworth-Heinemann. p. 42-46.

131. Istomin, P., E. Istomina, A. Nadutkin, V. Grass, and M. Presniakov, Synthesis of a Bulk Ti_4SiC_3 MAX Phase by Reduction of TiO_2 with SiC. Inorganic Chemistry, 2016. **55**(21): p. 11050-11056.

132. Lapauw, T., K. Vanmeensel, K. Lambrinou, and J. Vleugels, A new method to texture dense $M_{n+1}AX_n$ ceramics by spark plasma deformation. Scripta Materialia, 2016. **111**(Supplement C): p. 98-101.
133. Tang, K., C.A Wang, Y. Huang, Q. Zan, and X. Xu, A study on the reaction mechanism and growth of Ti_3SiC_2 synthesized by hot-pressing. Materials Science and Engineering: A, 2002. **328**(1): p. 206-212.
134. Zhang, H.B., C.F. Hu, K. Sato, S. Grasso, M. Estili, S.Q. Guo, K. Morita, H. Yoshida, T. Nishimura, T.S. Suzuki, M.W. Barsoum, B.N. Kim, and Y. Sakka, Tailoring Ti_3AlC_2 ceramic with high anisotropic physical and mechanical properties. Journal of the European Ceramic Society, 2015. **35**(1): p. 393-397.
135. Wang, C.A., A. Zhou, L. Qi, and Y. Huang, Quantitative phase analysis in the Ti–Al–C ternary system by X-ray diffraction. Powder Diffraction, 2012. **20**(3): p. 218-223.
136. Xu, X.W., C.K. Fu, Y.X. Li, J.Q. Zhu, and B.C. Mei, Fabrication of monolithic bulk Ti_3AlC_2 and impurity measurement by K-value method. Transactions of Nonferrous Metals Society of China, 2006. **16**: p. 490-493.
137. Zhang, Z.F., Z.M. Sun, and H. Hashimoto, Rapid synthesis of ternary carbide Ti_3SiC_2 through pulse-discharge sintering technique from Ti/Si/TiC powders. Metallurgical and Materials Transactions A, 2002. **33**(11): p. 3321-3328.
138. Zhang, Z.F., Z.M. Sun, H. Hashimoto, and T. Abe, A new synthesis reaction of Ti_3SiC_2 from Ti/$TiSi_2$/TiC powder mixtures through pulse discharge sintering (PDS) technique. Material Research Innovations, 2002. **5**(3): p. 185-189.
139. Zhang, Z.F., Z.M. Sun, and H. Hashimoto, Low temperature synthesis of Ti_3SiC_2 from Ti/SiC/C powders. Materials Science and Technology, 2004. **20**(10): p. 1252-1256.
140. Palmquist, J.P., S. Li, P.O.Å. Persson, J. Emmerlich, O. Wilhelmsson, H. Högberg, M.I. Katsnelson, B. Johansson, R. Ahuja, O. Eriksson, L. Hultman, and U. Jansson, $M_{n+1}AX_n$ phases in the Ti-Si-C system studied by thin-film synthesis and ab initio calculations. Physical Review B, 2004. **70**(16): p. 165401.
141. CH Henager, J., TJ Roosendaal, BN Nguyen, W Jiang, KJ Alvine , Y Shin, BA Borlaug, SA Arregum, Nanocrystalline SiC and Ti_3SiC_2 Alloys for Reactor Materials: Annual Report, P.N.N.L. US Department of Energy , Washington, Editor. 2014: Washington USA. p. 41.
142. Whittle, K., M. Blackford, R. Aughterson, S. Moricca, G. Lumpkin, D.P. Riley, and N. Zaluzec, Radiation tolerance of $M_{n+1}AX_n$ phases, Ti_3AlC_2 and Ti_3SiC_2. Acta Materialia, 2010. **58**: p. 4362–4368.
143. Pampuch, R., J. Lis, L. Stobierski, and M. Tymkiewicz, Solid combustion synthesis of Ti_3SiC_2. Journal of the European Ceramic Society, 1989. **5**(5): p. 283-287.
144. Gao, N.F., J.T. Li, D. Zhang, and Y. Miyamoto, Rapid synthesis of dense Ti_3SiC_2 by spark plasma sintering. Journal of the European Ceramic Society, 2002. **22**(13): p. 2365-2370.
145. Gao, N.F., Y. Miyamoto, and D. Zhang, On physical and thermochemical properties of high-purity Ti_3SiC_2. Materials Letters, 2002. **55**(1–2): p. 61-66.
146. Sun, Z., S. Yang, and H. Hashimoto, Ti_3SiC_2 powder synthesis. Ceramics International, 2004. **30**(7): p. 1873-1877.
147. Li, X., M. Zheng, R. Li, and G. Yuan, Effect of heating rate on the purity of the ternary layered compound Ti_3AlC_2 powder synthesized by a low-cost rapid method. Journal of Materials Science: Materials in Electronics, 2018. **29**(13): p. 10942-10948.
148. Li, S.B.X., J.X. ; Zhang, L.T. ; Cheng, L.F., Synthesis and some properties of Ti_3SiC_2 by hot pressing of titanium, silicon, and carbon powders Part 1 - Effect of starting composition on formation of Ti_3SiC_2 and observation of Ti_3SiC_2 crystal morphology. Materials Science and Technology, 2003. **19**(10): p. 1442-1446.
149. Kero, I., R. Tegman, and M.-L. Antti, Effect of the amounts of silicon on the in situ synthesis of Ti_3SiC_2 based composites made from TiC/Si powder mixtures. Ceramics International, 2010. **36**(1): p. 375-379.
150. Zhang, Z.F., Z.M. Sun, H. Hashimoto, and T. Abe, Effects of sintering temperature and Si content on the purity of Ti_3SiC_2 synthesized from Ti/Si/TiC powders. Journal of Alloys and Compounds, 2003. **352**(1): p. 283-289.

151. Kero, I., R. Tegman, and M.-L. Antti, Carbon atmosphere effect on Ti_3SiC_2 based composites made from TiC/Si powders. Ceramics International, 2010. **36**(4): p. 1259-1263.
152. Zhang, Z.F., Z.M. Sun, H. Hashimoto, and T. Abe, Application of pulse discharge sintering (PDS) technique to rapid synthesis of Ti_3SiC_2 from Ti/Si/C powders. Journal of the European Ceramic Society, 2002. **22**(16): p. 2957-2961.
153. Pampuch, R., M. Raczka, and J. Lis, Role of liquid phase in solid combustion synthesis of Ti_3SiC_2. Vol. 10. 1995. 316-324.
154. Sato, F., J. Li, and R. Watanabe, Reaction Synthesis of Ti_3SiC_2 from Mixture of Elemental Powders. Vol. 41. 2000. 605-608.
155. Ghosh, N.C. and S.P. Harimkar, Phase analysis and wear behavior of in-situ spark plasma sintered Ti_3SiC_2. Ceramics International, 2013. **39**(6): p. 6777-6786.
156. Kero, I., Ti_3SiC_2 Synthesis by Powder Metallurgical Methods, Licentiate Thesis, May 2007, in Department of Applied Physics and Mechanical Engineering; Division of Engineering Materials, Luleå University of Technology.
157. Orthner, H.R., R. Tomasi, and W.J. Botta F, Reaction sintering of titanium carbide and titanium silicide prepared by high-energy milling. Materials Science and Engineering: A, 2002. **336**(1–2): p. 202-208.
158. Zhou, Y., Z. Sun, S. Chen, and Y. Zhang, In-situ hot pressing/solid-liquid reaction synthesis of dense titanium silicon carbide bulk ceramics. Material Research Innovations, 1998. **2**(3): p. 142-146.
159. Li, J.-F., T. Matsuki, and R. Watanabe, Mechanical-Alloying-Assisted Synthesis of Ti_3SiC_2 Powder. Journal of the American Ceramic Society, 2002. **85**(4): p. 1004-1006.
160. Yeh, C.L. and Y.G. Shen, Effects of SiC addition on formation of Ti_3SiC_2 by self-propagating high-temperature synthesis. Journal of Alloys and Compounds, 2008. **461**(1): p. 654-660.
161. Wu, E., E.H. Kisi, S.J. Kennedy, and A.J. Studer, In Situ Neutron Powder Diffraction Study of Ti_3SiC_2 Synthesis. Journal of the American Ceramic Society, 2001. **84**(10): p. 2281-2288.
162. Zou, Y., Z. Sun, H. Hashimoto, and L. Cheng, Reaction mechanism in Ti–SiC–C powder mixture during pulse discharge sintering. Ceramics International, 2010. **36**(3): p. 1027-1031.
163. Li, J.T. and Y. Miyamoto, Fabrication of Monolithic Ti_3SiC_2 Ceramic Through Reactive Sintering of Ti/Si/2TiC. Journal of Materials Synthesis and Processing, 1999. **7**(2): p. 91-96.
164. Tian, W., Z. Sun, H. Hashimoto, and Y. Du, Synthesis, microstructure and mechanical properties of Ti_3SiC_2–TiC composites pulse discharge sintered from Ti/Si/TiC powder mixture. Materials Science and Engineering: A, 2009. **526**(1–2): p. 16-21.
165. Yang, S., Z.M. Sun, and H. Hashimoto, Synthesis of Ti_3SiC_2 powder from 1Ti/(1+x)Si/2TiC powder mixtures. Journal of Alloys and Compounds, 2004. **368**(1–2): p. 318-325.
166. Li, S.B., J.X. Xie, L.T. Zhang, and L.F. Cheng, In situ synthesis of Ti_3SiC_2/SiC composite by displacement reaction of Si and TiC. Materials Science and Engineering: A, 2004. **381**(1–2): p. 51-56.
167. Radhakrishnan, R., C.H. Henager, J.L. Brimhall, and S.B. Bhaduri, Synthesis of Ti_3SiC_2SiC and $TiSi_2SiC$ composites using displacement reactions in the Ti-Si-C system. Scripta Materialia, 1996. **34**(12): p. 1809-1814.
168. Hwang, S.S., S.W. Park, and T.W. Kim, Synthesis of the Ti_3SiC_2 by solid state reaction below melting temperature of Si. Journal of Alloys and Compounds, 2005. **392**(1–2): p. 285-290.
169. Panigrahi, B.B., M.C. Chu, A. Balakrishnan, and S.J. Cho, Synthesis and pressureless sintering of Ti_3SiC_2 powder. Journal of Materials Research, 2011. **24**(2): p. 487-492.
170. Zou, Y., Z. Sun, H. Hashimoto, and S. Tada, Low temperature synthesis of single-phase Ti_3AlC_2 through reactive sintering Ti/Al/C powders. Materials Science and Engineering: A, 2008. **473**(1): p. 90-95.
171. Han, Y.H. and T. Nishimura, Spark Plasma Sintering. Advances in Applied Ceramics, 2014. **113**(2): p. 65-66.
172. Sergueeva, A.V., D.M. Hulbert, N.A. Mara, and A.K. Mukherjee, Chapter 3 - Mechanical Properties of Nanocomposite Materials, in Frontiers of Nanoscience, G. Wilde, Editor. 2009, Elsevier. p. 127-172.
173. Aalund, R., Spark Plasma Sintering. Issue of Ceramic Industry, 2008.

174. Guo, J., J. Li, and H. Kou, Chapter 19 - Chemical Preparation of Advanced Ceramic Materials, in Modern Inorganic Synthetic Chemistry, R. Xu, W. Pang, and Q. Huo, Editors. 2011, Elsevier: Amsterdam. p. 429-454.
175. Tokita, M., Mechanism of spark plasma sintering. Vol. 21. 2001. 729-732.
176. Garay, J.E., Current-Activated, Pressure-Assisted Densification of Materials, in Annual Review of Materials Research, Vol 40, D.R. Clarke, M. Ruhle, and F. Zok, Editors. 2010, Annual Reviews: Palo Alto. p. 445-468.
177. Ghosh, N.C. and S.P. Harimkar, 3 - Consolidation and synthesis of MAX phases by Spark Plasma Sintering (SPS): a review, in Advances in Science and Technology of $M_{n+1}AX_n$ Phases, I.M. Low, Editor. 2012, Woodhead Publishing. p. 47-80.
178. Ghosh, N.C. and S.P. Harimkar, 3 - Consolidation and synthesis of MAX phases by Spark Plasma Sintering (SPS): a review A2 - Low, I.M, in Advances in Science and Technology of $M_{n+1}AX_n$ Phases. 2012, Woodhead Publishing. p. 47-80.
179. German, R.M., Sintering theory and practice. Chichester: Wiley, 1996 New York
180. Bokhonov, B.B., A.V. Ukhina, D.V. Dudina, A.G. Anisimov, V.I. Mali, and I.S. Batraev, Carbon uptake during Spark Plasma Sintering: investigation through the analysis of the carbide "footprint" in a Ni-W alloy. RSC Advances, 2015. **5**(98): p. 80228-80237.
181. Mackie, A.J., G.D. Hatton, H.G.C. Hamilton, J.S. Dean, and R. Goodall, Carbon uptake and distribution in Spark Plasma Sintering (SPS) processed Sm(Co, Fe, Cu, Zr)z. Materials Letters, 2016. **171**: p. 14-17.
182. El-Raghy, T. and M.W. Barsoum, Diffusion kinetics of the carburization and silicidation of Ti_3SiC_2. Journal of Applied Physics, 1998. **83**(1): p. 112-119.
183. Konoplyuk, S., T. Abe, T. Uchimoto, and T. Takagi, Ti_3SiC_2/TiC composites prepared by PDS. Journal of Materials Science, 2005. **40**(13): p. 3409-3413.
184. Luo, Y., S. Li, W. Pan, J. Chen, and R. Wang, Machinable and mechanical properties of sintered Al_2O_3-Ti_3SiC_2 composites. Journal of Materials Science, 2004. **39**(9): p. 3137-3140.
185. Ghosh, N.C., Synthesis and Tribological Characterization of In-situ Spark Plasma Sintered Ti_3SiC_2 and Ti_3SiC_2-TiC Composites, S.P. Harimkar, K. Kalkan, and R. Singh, Editors. 2012.
186. Tong, X., T. Okano, T. Iseki, and T. Yano, Synthesis and high temperature mechanical properties of Ti_3SiC_2/SiC composite. Journal of Materials Science, 1995. **30**(12): p. 3087-3090.
187. Torres, H., M. Rodríguez Ripoll, and B. Prakash, Tribological behaviour of self-lubricating materials at high temperatures. International Materials Reviews, 2018. **63**(5): p. 309-340.
188. Alison, C., H.K. Erich, J.W.B. Summers, and M. Sverre, Ultra-low friction for a layered carbide-derived ceramic, Ti_3SiC_2 , investigated by lateral force microscopy (LFM). Journal of Physics D: Applied Physics, 1999. **32**(6): p. 632.
189. Souchet, A., J. Fontaine, M. Belin, T. Le Mogne, J.L. Loubet, and M.W. Barsoum, Tribological duality of Ti_3SiC_2. Tribology Letters, 2005. **18**(3): p. 341-352.
190. Wu, L., J.X. Chen, M.Y. Liu, Y.W. Bao, and Y.C. Zhou, Reciprocating friction and wear behavior of Ti_3AlC_2 and Ti_3AlC_2/Al_2O_3 composites against AISI52100 bearing steel. Wear, 2009. **266**(1): p. 158-166.
191. Wang, S., J. Ma, S. Zhu, J. Cheng, Z. Qiao, J. Yang, and W. Liu, High temperature tribological properties of Ti_3AlC_2 ceramic against SiC under different atmospheres. Materials & Design, 2015. **67**: p. 188-196.
192. Ma, J., F. Li, L. Fu, S. Zhu, Z. Qiao, J. Yang, and W. Liu, Effect of Counterface on the Tribological Behavior of Ti_3AlC_2 at Ambient. Tribology Letters, 2014. **53**(1): p. 311-317.
193. Ma, J., F. Li, J. Cheng, L. Fu, Z. Qiao, W. Liu, and J. Yang, Tribological Behavior of Ti_3AlC_2 Against SiC at Ambient and Elevated Temperatures. Tribology Letters, 2013. **50**(3): p. 323-330.
194. Hsu, S.M. and M.C. Shen, Ceramic wear maps. Wear, 1996. **200**(1): p. 154-175.
195. Adachi, K., K. Kato, and N. Chen, Wear map of ceramics. Wear, 1997. **203-204**: p. 291-301.
196. Medvedovski, E., Wear-resistant engineering ceramics. Wear, 2001. **249**(9): p. 821-828.
197. Wäsche, R., D. Klaffke, R. Yarim, and E. Santner, Tribological Tayloring of Ceramic Composites. Materialwissenschaft und Werkstofftechnik, 2003. **34**(10-11): p. 1008-1013.

198. Kim, Y.W., M. Mitomo, and H. Hirotsuru, Grain Growth and Fracture Toughness of Fine-Grained Silicon Carbide Ceramics. Journal of the American Ceramic Society, 2005. **78**: p. 3145-3148.
199. Hilmas, G.E. and T.Y. Tien, Effect of AlN and Al_2O_3 additions on the phase relationships and morphology of SiC Part I Compositions and properties. Journal of Materials Science, 1999. **34**(22): p. 5605-5612.
200. Blanc, C., F. Thevenot, and D. Goeuriot, Microstructural and mechanical characterization of SiC-submicron TiB_2 composites. Journal of the European Ceramic Society, 1999. **19**(5): p. 561-569.
201. Shaffer, P.T.B., A review of the structure of silicon carbide. Acta Crystallographica, 1969. **B**(25): p. 477-488.
202. Heuer, A.H., G.A. Fryburg, L.U. Ogbuji, T.E. Mitchell, and S. Shinozaki, β→α Transformation in Polycrystalline SiC: I, Microstructural Aspects. Journal of the American Ceramic Society, 1978. **61**(9-10): p. 406-412.
203. Noviyanto, A. and D.H. Yoon, One component metal oxide sintering additive for β-SiC based on thermodynamic calculation and experimental observations. Metals and Materials International, 2012. **18**(1): p. 63-68.
204. Noviyanto, A. and D.H. Yoon, Metal oxide additives for the sintering of silicon carbide: Reactivity and densification. Current Applied Physics, 2013. **13**(1): p. 287-292.
205. Lee, S.K. and C.H. Kim, Effects of α-SiC versus β-SiC Starting Powders on Microstructure and Fracture Toughness of SiC Sintered with Al_2O_3-Y_2O_3 Additives. Journal of the American Ceramic Society, 1994. **77**(6): p. 1655-1658.
206. Shinozaki, S. and K.R. Kinsman, Evolution of Microstructure in Polycrystalline Silicon Carbide, in Processing of Crystalline Ceramics, H. Palmour, R.F. Davis, and T.M. Hare, Editors. 1978, Springer US: Boston, MA. p. 641-652.
207. Mulla, M.A. and V.D. Krstic, Low-temperature pressureless sintering of Low-temperature pressureless sintering of β-silicon carbide with aluminum oxide and yttrium oxide additions Am. Ceram.Soc. Bull 1991. **70**(3): p. 439-443.
208. Moberlychan, W.J., J.J. Cao, C.J. Gilbert, R.O. Ritchie, and L.C. De Jonghe, The Cubic - to - Hexagonal Transformation to Toughen SiC, in Ceramic Microstructures: Control at the Atomic Level, A.P. Tomsia and A.M. Glaeser, Editors. 1998, Springer US: Boston, MA. p. 177-190.
209. Mehregany, M., C.A. Zorman, N. Rajan, and W. Chien Hung, Silicon carbide MEMS for harsh environments. Proceedings of the IEEE, 1998. **86**(8): p. 1594-1609.
210. Khodaei, M., O. Yaghobizadeh, H.R. Baharvandi, and A. Dashti, Effects of different sintering methods on the properties of SiC-TiC, SiC-TiB_2 composites. International Journal of Refractory Metals and Hard Materials, 2018. **70**(Supplement C): p. 19-31.
211. Holt, J.B. and Z.A. Munir, Combustion synthesis of titanium carbide: Theory and experiment. Journal of Materials Science, 1986. **21**(1): p. 251-259.
212. Ahmoye, D., Pressureless Sintering and Mechanical Properties of SiC Composites with in-situ Converted TiO_2 to TiC, in Department of Mechanical and Materials Engineering. 2010, Queen's University Kingston, Ontario, Canada.
213. Kawai, C., K. Suzuki, and K. Tanaka, Fracture Toughness of TiC-SiC Composites Fabricated by CVD and the Mechanism of Toughening. Journal of the Ceramic Society of Japan, 1992. **100**(1162): p. 835-840.
214. Jiang, D.L., J.H. Wang, Y.L. Li, and L.T. Ma, Studies on the strengthening of silicon carbide-based multiphase ceramics I: The SiC-TiC system. Materials Science and Engineering: A, 1989. **109**: p. 401-406.
215. Das, G., K.S. Mazdiyasni, and H.A. Lipsitt, Mechanical Properties of Polycrystalline TiC. Journal of the American Ceramic Society, 1982. **65**(2): p. 104-110.
216. Selsing, J., Internal Stresses in Ceramics. Journal of the American Ceramic Society, 1961. **44**(8): p. 419-419.
217. Kornaus, K., G. Grabowski, D. Zientara, A. Gubernat, and M. Rączka, Mechanical properties of hot-pressed SiC-TiC composites. Vol. 11. 2017. 329-336.

218. Prochazka, S. and R.M. Scanlan, Effect of Boron and Carbon on Sintering of SIC. Journal of the American Ceramic Society, 1975. **58**(1-2): p. 72-72.

219. Gubernat, A., L. Stobierski, and P. Łabaj, Microstructure and mechanical properties of silicon carbide pressureless sintered with oxide additives. Journal of the European Ceramic Society, 2007. **27**(2): p. 781-789.

220. Yamamoto, T.A., T. Kondou, Y. Kodera, T. Ishii, M. Ohyanagi, and Z.A. Munir, Mechanical properties of β-SiC fabricated by spark plasma sintering. Journal of Materials Engineering and Performance, 2005. **14**(4): p. 460-466.

221. Nadeau, J.S., Very high pressure hot pressing of silicon carbide. Am. Ceram.Soc, 1973. **52**: p. 170-174.

222. Negita, K., Effective Sintering Aids for Silicon Carbide Ceramics: Reactivities of Silicon Carbide with Various Additives. Journal of the American Ceramic Society, 1986. **69**(12): p. C-308-C-310.

223. S, P., Hot pressed silicon carbide. 1974: United States.

224. Li, W.J., R. Tu, and T. Goto, Preparation of TiB_2–SiC Eutectic Composite by an Arc-Melted Method and Its Characterization. Vol. 46. 2005. 2504-2508.

225. Cabrero, J., F. Audubert, and R. Pailler, Fabrication and characterization of sintered TiC–SiC composites. Journal of the European Ceramic Society, 2011. **31**(3): p. 313-320.

226. Olevsky, E.A., S.M. Rolfing, and A.L. Maximenko, Flash (Ultra-Rapid) Spark-Plasma Sintering of Silicon Carbide. Scientific Reports, 2016. **6**: p. 33408.

227. Habig, K.H., Friction and wear of sliding couples coated with TiC, TiN or TiB_2. Surface and Coatings Technology, 1990. **42**(2): p. 133-147.

228. Waesche, R., D. Klaffke, M. Woydt, and I. Dörfel, Structure of the Interface in SiC-Based Ceramic Composites Formed by Tribo-Oxidation Under Dry Sliding Conditions. 2012. 401-407.

229. Woydt, M., A. Skopp, and K.H. Habig, Dry friction and wear of self-mated sliding couples of SiC-TiC and Si_3N_4-TiN. Wear, 1991. **148**(2): p. 377-394.

230. Sharma, S.K., B.V. Manoj Kumar, and Y.W. Kim, Tribology of WC reinforced SiC ceramics: Influence of counterbody. Friction, 2018.

231. Sterner, O., R. Aeschlimann, S. Zürcher, K. Osborn Lorenz, J. Kakkassery, N.D. Spencer, and S.G.P. Tosatti, Friction Measurements on Contact Lenses in a Physiologically Relevant Environment: Effect of Testing Conditions on Friction. Investigative Ophthalmology & Visual Science, 2016. **57**(13): p. 5383-5392.

232. Kennedy, F.E., Thermal and thermomechanical effects in dry sliding. Wear, 1984. **100**(1): p. 453-476.

233. CSM Instruments Technical Report, Wear and Friction Analysis of Thin Coatings, in An in-depth study of the tribological properties of thin coatings on stainless steelsubstrates using a CSM Instruments Tribometer. 2009: Switzerland.

234. Archard, J.F., The temperature of rubbing surfaces. Wear, 1959. **2**(6): p. 438-455.

235. Rabinowicz, E., The temperature rise at sliding electrical contacts. Wear, 1982. **78**(1): p. 29-37.

236. Ashby, M.F., J. Abulawi, and H.S. Kong, Temperature Maps for Frictional Heating in Dry Sliding. Tribology Transactions, 1991. **34**(4): p. 577-587.

237. Smith, E.H. and R.D. Arnell, The Prediction of Frictional Temperature Increases in Dry, Sliding Contacts Between Different Materials. Tribology Letters, 2014. **55**(2): p. 315-328.

238. Block, H., General discussion on lubricaton. Inst. Mech. Eng., 1937. **2**: p. 222.

239. Kalin, M. and J. Vižintin, Comparison of different theoretical models for flash temperature calculation under fretting conditions. Tribology International, 2001. **34**(12): p. 831-839.

240. Kalin, M., Influence of flash temperatures on the tribological behaviour in low-speed sliding: a review. Materials Science and Engineering: A, 2004. **374**(1): p. 390-397.

241. Borovanska, I., T. Y, V. Angelov, E. Ivanov, R. Kotsilkova, and S. Djoumaliisky, Tribological Measurements Of Polypropylene Nanocomposites By Scratch And Friction Tests. 2013.

Paper A

Influence of sintering environment on the spark plasma sintering of Maxthal 312 (nominally—Ti_3SiC_2) and the role of powder particle size on densification

Journal of Alloys and Compounds 801 (2019) 208–219

Contents lists available at ScienceDirect

Journal of Alloys and Compounds

journal homepage: http://www.elsevier.com/locate/jalcom

Influence of sintering environment on the spark plasma sintering of Maxthal 312 (nominally-Ti_3SiC_2) and the role of powder particle size on densification

Carl Magnus, William M. Rainforth*

Department of Materials Science and Engineering, University of Sheffield, Sir Robert Hadfield Building, Mappin St, Sheffield, S1 3JD, UK

ARTICLE INFO

Article history:
Received 21 January 2019
Received in revised form
23 May 2019
Accepted 6 June 2019
Available online 7 June 2019

Keywords:
Transitional metal compound
MAX-Phase
Spark plasma sintering
Deformation
Diffusion
Indentation size effect (ISE)

ABSTRACT

Herein, we report on the synthesis of Ti_3SiC_2 via the Maxthal 312 (nominally-Ti_3SiC_2) commercial powder route using spark plasma sintering (SPS). The SPSed bulk samples contained ancillary phases (TiC_X and $TiSi_2$) irrespective of the sintering environment as confirmed by XRD phase analysis. The optimum sintering temperature below which intrinsic decomposition starts appears to be ~1350 °C in vacuum and ~1450 °C in argon atmosphere, respectively. The role of powder particle size on densification during spark plasma sintering (SPS) was investigated. Analysis of the SPS processing parameters (piston movement and piston speed) indicated that the densification of Maxthal 312 powder (nominally-Ti_3SiC_2) can be improved by reduction in particle size, thus promoting the Joule effect, necking, mechanical movement of particles and plastic deformation. Further investigation on the role of graphite heating element as well as environment during the SPS synthesis showed that the graphite paper employed during SPS as well as possible silicon loss during vacuum sintering were responsible for the decomposition at temperature below the melting point of Si and/or shifting of the resultant bulk sample composition away from monolithic phase.

1. Introduction

There is a continuous growing interest in a family of hexagonal layered thermodynamically stable nanolaminates (over 80 + ternary phases, without taking into account quaternary and solid solutions) with composition written as $M_{n+1}AX_n$, where M represents an early transitional metal, A is an A-group element mostly III A and IV A-group elements, X is C or N and $n = [1–3]$; the so called MAX phases [1–5]. This is due to their unusual and sometimes unique set of physical and mechanical properties [2,6]. They possess many similar advantageous features (thermally, elastically, and electrically) of their respective binary carbides or nitrides [6]. Mechanically, they are easily machinable, relatively soft, thermal shock resistant, as well as unusually damage tolerant [6]. They represent the only class of polycrystalline solids that undergoes plastic deformation by a combination of energy absorbing mechanisms such as, kink and shear band formation, alongside with delamination of individual grains [6–10]. Some recently reported advances in MAX phases is the discovery of new A-elements (Au, Ir [4,11], and Zn [12]) as well as expansion of the M-elements (e.g., Zr—Al—C [13], and Hf-Al-C [14]). Furthermore, it has been demonstrated that the A-layers in the 3D MAX phase chemistry can be selectively etched out to form a new class of exciting 2D material known as MXene [3,15].

To date, more than 80 MAX phases have been discovered and successfully synthesized in bulk and thin film forms [3,5,16]. These phases have various compositional formation as a function of their n-values in the form of unit cells M_2AX (211 phases), M_3AX_2 (312 phases), and M_4AX_3 (413 phases) phases, respectively [1]. The main difference between these compositional forms is the number of M layers separating the A layers [1]. Much work has been reported on the synthesis of MAX phases since first synthesized in the late 1960s [17,18]. Initially, the synthesis of MAX phases was plagued by the difficulties associated with the synthesis of monolithic phase without the evolution of undesirable ancillary phases [19–25], such as TiC, SiC, Ti_5Si_3, and $TiSi_2$ [26]. This was attributed to the narrow stable region of Ti_3SiC_2 in the Ti—Si—C system phase diagram which intersects with these binary phases [19,23,26]. However, Barsoum et al. [27] successfully synthesized high-purity Ti_3SiC_2 with less

---

* Corresponding author.
E-mail address: M.rainforth@sheffield.ac.uk (W.M. Rainforth).

https://doi.org/10.1016/j.jallcom.2019.06.076
0925-8388/

than 2 vol% (TiC_X and SiC) ancillary phase using hot isostatic pressing (HIP). Many researchers have since then synthesized highly pure MAX phases by employing various synthesis methods [21,26,28–32]. It is noteworthy to mention that the initial raw material, environment, as well as the synthesis method employed plays a key role on the purity of the synthesized Ti_3SiC_2 powder or bulk sample [19,26,32,33].

As a representative of the $Ti_{n+1}SiC_n$ MAX phase family, Ti_3SiC_2 can be synthesized by various methods such as hot isostatic pressing (HIP) [27], hot pressing (HP) [34], spark plasma sintering (SPS) [35], mechanical alloying (MA) [36], pressureless sintering (PS) [37], chemical vapour deposition (CVD) [38], pulsed electric current sintering (PECS) [39] and more recently molten salt method [40,41]. The synthesis can be carried out by employing stoichiometric, off stoichiometric, and/or Al addition into the starting composition mixtures [42,43], Ti/Si/C [44], Ti/Si/TiC [35,45], Ti/SiC/C [25], Ti/SiC/TiC, Ti/$TiSi_2$/TiC [46], TiH_2/Si/TiC [30,47], and Si/TiC [48]. However, according to Ngai et al. [26] if a stoichiometric composition (molar ratio of Ti:Si:C = 3:1:2) is selected, the possible loss of silicon during the synthesis will push the final reactant composition into a phase region that coexist with TiC as an ancillary phase. It is thus important to dope the composition with excess silicon to compensate for possible silicon loss due to evaporation [26].

Amongst all the synthesis methods, the SPS otherwise known as PDS is a relatively innovative sintering technique that incorporates pressure, temperature and electric current simultaneously for rapid densification via plasma formation which aids mass transportation by enhancing defect mobility [29]. Whilst HP-reactive sintering has been identified as the most realistic way to synthesize high-purity (98–99%) MAX phase, this synthesis route is plagued by the duration (24–72 h) depending on the grain size desired as well as the high energy required [22]. SPS thus provides a unique advantage of faster sintering, low temperature/pressure, and shorter processing time with resultant microstructural evolution depending solely on the SPS processing parameters [49].

In the synthesis of Ti_3SiC_2 by SPS, there are important factors in the sintering process that may play a major role in the purity of the resultant bulk sample especially if the starting composition are of stoichiometric powder mixture [50,51]. These factors are; (a) owing to the high vacuum pressure employed in SPS, the vapour of silicon can easily be drawn away and as a consequence decomposition takes place at temperature below the melting point of Si (i.e., ~1414 °C) the onset of intrinsic Ti_3SiC_2 decomposition [22,35,50], (b) the graphite rich environment in SPS due to graphite tooling (i.e., graphite die & punches and graphite paper) means that there is a tendency of carbon diffusion from graphite tooling which may initiate the carburization of Ti_3SiC_2 [27,43,48,51–53]. According to El-Raghy et al. [53] the reaction of carbon with Ti_3SiC_2 due to carburization from the graphite tooling will shift the overall composition to the Ti_3SiC_2–TiC–SiC compatibility triangle in the Ti–Si–C phase diagram.

Some of the recent works using SPS have reported high purity Ti_3SiC_2 by employing various sintering additives such as Si and Al. Islak et al. [19] synthesized 100% Ti_3SiC_2 using SPS with starting composition 1Ti/1.1Si/2TiC/0.2Al. The high purity was attributed to the excess silicon as well Al addition which helped consumed TiC and expedites the diffusion of Ti and C owing to the liquid phase formed via Al [19,35]. Pourebrahim et al. [43] synthesized high-purity 100% Ti_3SiC_2 using off stoichiometric powder mixture 1Ti/1.2Si/2TiC/xAl with x = 0.2, 0.3, and 0.4 by SPS. They attributed the high-purity of Ti_3SiC_2 even at low sintering temperature to the addition of Al which helps to expedite the diffusion of Ti and Si atoms at low temperatures. Recently, Kozak et al. [22] synthesized Ti_3SiC_2 via the Maxthal 312 (nominally-Ti_3SiC_2) commercial powder route using SPS and obtained a purity of 71.8% Ti_3SiC_2 alongside with TiC and $TiSi_2$ ancillary phases. The ancillary phases were attributed to the initial starting composition as well as Si evaporation from the system.

The scope of this work is thus to investigate the difficulties encountered in the synthesis of high-purity Ti_3SiC_2 from stoichiometric composition using SPS as well as the role of the SPS graphite tooling, sintering temperature, and environment (vacuum or gas) in the sintering process. Furthermore, ways to possibly mitigate against factors that might compromise the purity of the resultant bulk samples will be elucidated.

2. Experimental procedure

2.1. Spark plasma sintering

Commercially available Maxthal 312® (nominally-Ti_3SiC_2) powder precursor (Sandvik AB, Sweden) with particle sizes 2.5 and 7 μm and powder purity 92 wt% Ti_3SiC_2 and 8 wt% TiC were consolidated using Spark Plasma Sintering (SPS) in vacuum as well as in argon atmosphere. Prior to transferring the MAX phase powder inside the die, graphite paper inserts (paper thickness 0.8 mm) were placed inside the graphite die as well as between the punches to prevent sticking during the sintering process and to aid the removal of the sintered compact. The graphite die (20 mm) containing Maxthal powder (7.0 g) was then placed in the sintering chamber and then covered with a graphite felt in order to reduce heat dissipation during sintering. A small window was cut on the graphite felt to enable surface temperature measurement by means of an infrared pyrometer. Finally, graphite spacers were then placed between the graphite punches and the metallic electrode and the sintering cycles carried out in the SPS system as illustrated in Fig. 1. The samples were heated at a rate of 100 °C/min until the requisite temperature of 1250–1500 °C were reached in vacuum sintering

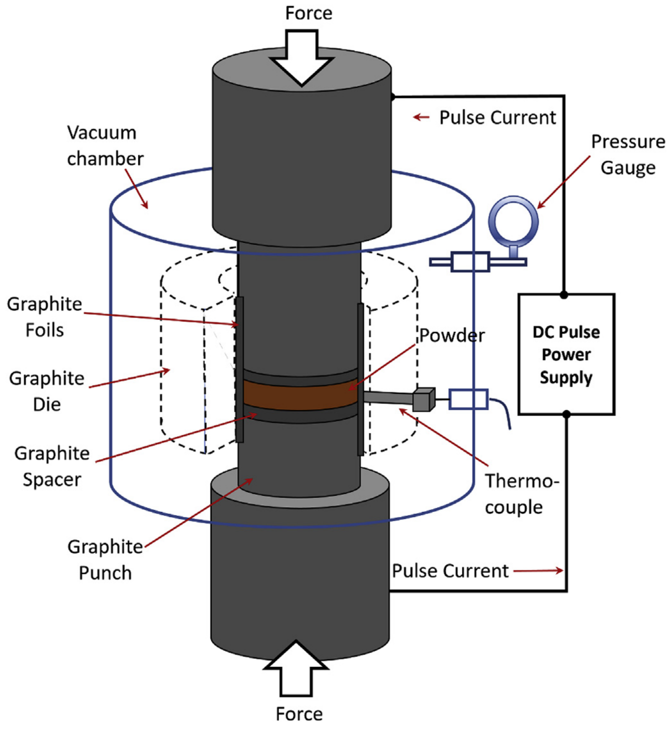

Fig. 1. Schematic of spark plasma sintering configuration. Note graphite foil incorporated to prevent welding of powder with the graphite punch and die [54].

and 1300–1500 °C in argon environment, respectively. The dwell time employed was 10 min and pressure maintained at 50 MPa.

2.2. Analytical methods

X-ray diffraction (XRD) patterns of the synthesized samples were obtained on a D2 diffractometer (Bruker, D2 Phaser) using Cu Kα radiation, step scan 0.02°, 1s/step at 2Θ (5–80°). Peaks were then correlated with the ICSD database using “DIFFRA EVA” program. The density of the polished samples were measured using Archimedes’ method in water at ambient temperature. Whilst Vickers microhardness were measured on the polished samples surfaces using a Durascan microhardness tester (emcoTEST, Prumfmaschinen, GmbH). The indentation load employed was between 1 and 5 kgF and dwell time of 15 s.

Bulk samples microstructure were characterized using optical microscopy and scanning electron microscopy, SEM (FEI inspect F-50, The Netherlands) coupled with an energy-dispersive spectroscope (EDS; EDAX, Oxford Instruments). Further detailed morphological and bulk sample analysis were carried out using TEM (Philips EM420 operating at 120 kV). TEM electron transparent specimen thinning was done using focused ion beam (FIB) milling (FEI Helios NanoLab G3 UC, FEI Company, Netherlands). The chemistry of the synthesized sample and precursor powder were studied using Raman spectroscopy (inVia™, Renishaw., UK) and differential scanning calorimetry (DSC-TG).

3. Results and discussion

3.1. Temperature-time-pressure-punch displacement curve

Typical shrinkage profile recorded for the sample SPSed at 1450 °C for 10 min in argon environment is given in Fig. 2. As seen in the displacement curve, the initial sintering pressure led to powder particle rearrangement as recorded by the positive piston movement A-B. The pre-sintering heating then generated thermal expansion of the powder responsible for the negative piston movement B–C. The piston movement C-D marks the onset of the densification stage due to plastic deformation and necking of the powder particles. The point D-E is when displacement curve plateau as the sintering temperature is reached and all pores are sealed. The last stage E-F is the cooling stage leading to thermal contraction and further positive piston movement.

3.2. Role of particle size on densification mechanism

In order to understand the effect of initial powder particle size on mechanical movement of the particles, the Joule heating effect and plastic deformation necessary for densification, two different particle sizes of Maxthal 312 powders (Fig. 3a) were synthesized by SPS using the same sintering parameter. The results were analysed by investigating the piston movement, piston speed and plastic deformation. Fig. 3b further shows the characteristic layered nature of the MAX phase powder.

The records of the piston movement (i.e., punch displacement) as a function of time for the different particle sizes are reported in Fig. 4. The sintering cycle involving particle rearrangement (mechanical movement), plastic deformation of particles and eventual densification stages are compared for the 2.5 and 7 μm Maxthal powder particle sizes. The clear observable difference between both powders was in the plastic deformation stage. Here, the densification of the 7 μm powder was higher than 2.5 μm powder. However, the order of variation of the piston movement (displacement) was larger for the 2.5 μm powder. It appears that the punch displacement increased sharply for the 2.5 μm powder due to smaller particle size that promotes Joule heating due to more contact area between powder particles for necking.

Fig. 5 shows a plot of the piston speed and sintering temperature as function of time for the different particle size Maxthal powders. The peaks observed in the piston speed plots corresponds to piston movement when the pistons move close together (compaction). The first peak corresponds to the piston movement speed of the

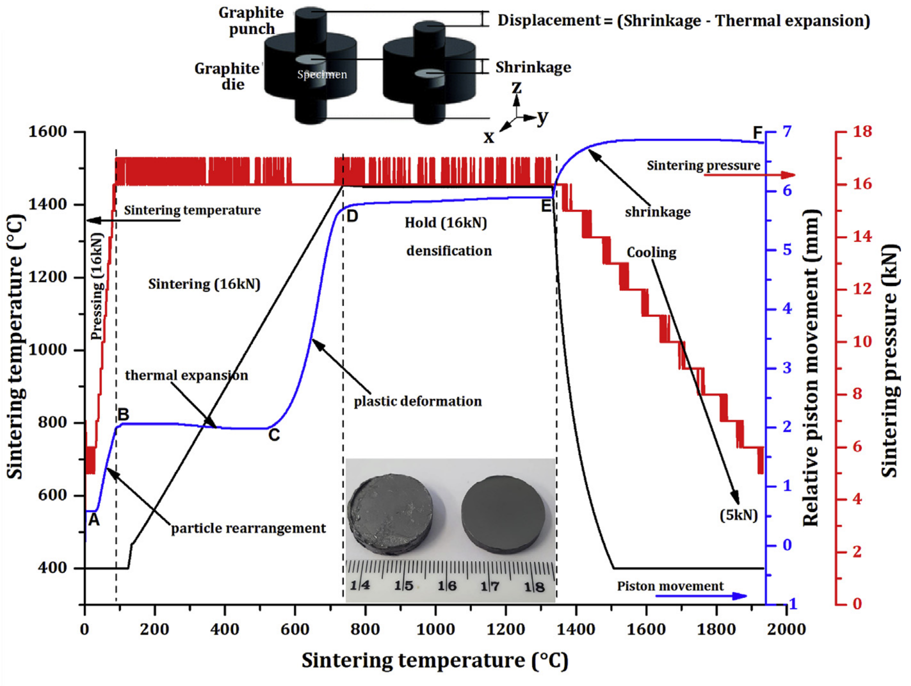

Fig. 2. Shrinkage profile during the SPS of Maxthal 312 (nominally-Ti_3SiC_2): the sample temperature, pressure and piston displacement as a function sintering time.

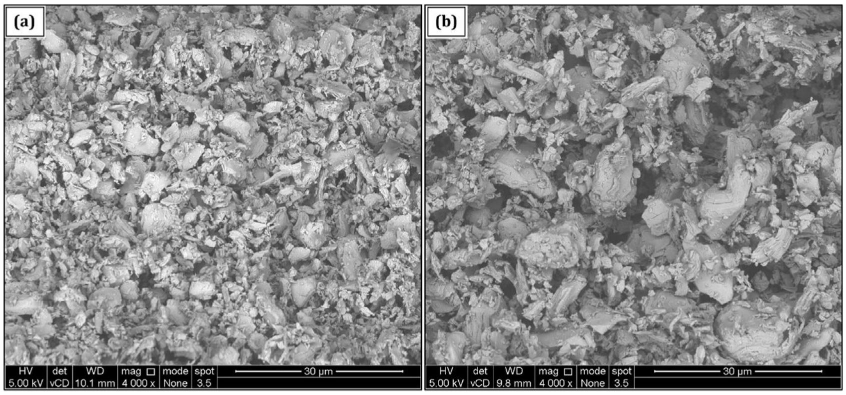

Fig. 3a. Back-scattered electron (BSE) images of Maxthal 312 powder with particle size of (a) 2.5 μm and (b) 7 μm. Note the flake like grains.

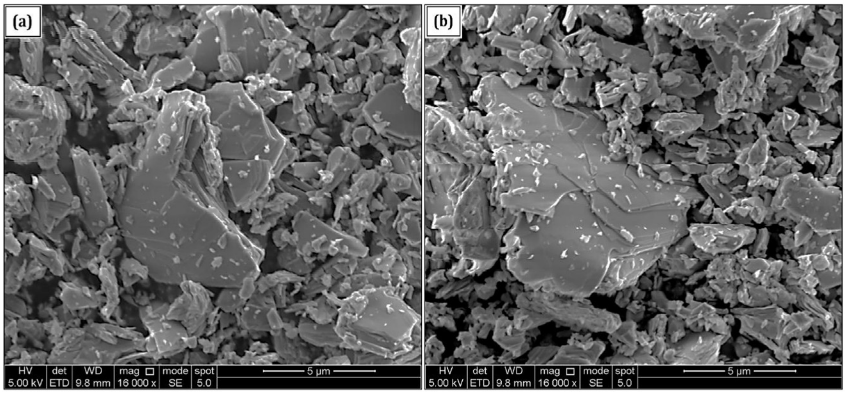

Fig. 3b. Secondary electron (SE) images showing the characteristic inherent nanolaminated nature of the 2.5 μm MAX phase powder. Note the compact and fractured particles.

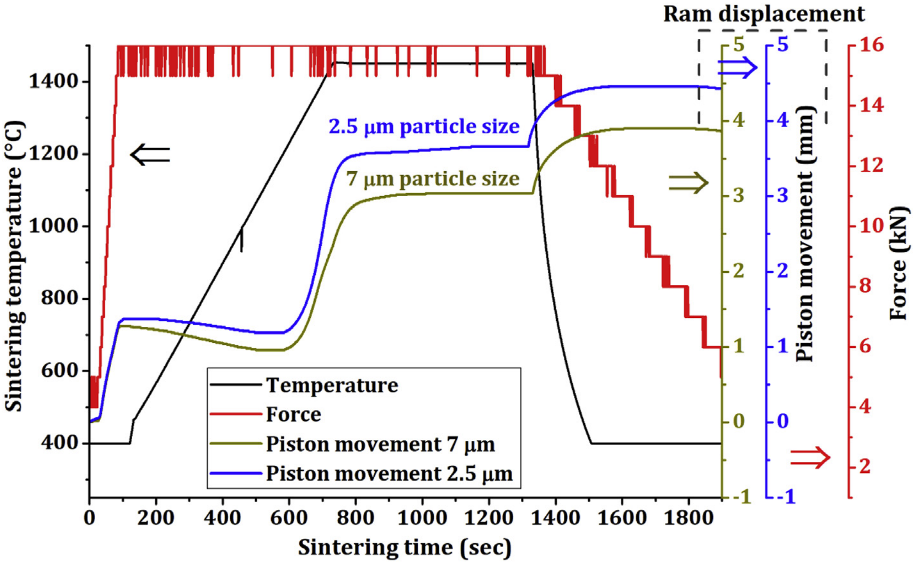

Fig. 4. Ram displacement, temperature and force recorded during the SPS process.

pistons during the initial applied pressure. Whilst the second peak that originates just before the sintering temperature is reached corresponds to pistons movement speed during the majority of the powder densification. The last peak on the other hand corresponds to the piston speed due to contraction during the cooling stage.

Comparing the piston speeds for both powder particle sizes, the first observable difference is the significant lower piston speed recorded for the 7 μm powder in the majority sample densification stage. Since the piston displacement recorded for the 7 μm powder was shorter than the 2.5 μm powder (Fig. 4), it is not surprising that the time to reach the end of densification was shorter as the densification ended even before the sintering temperature was

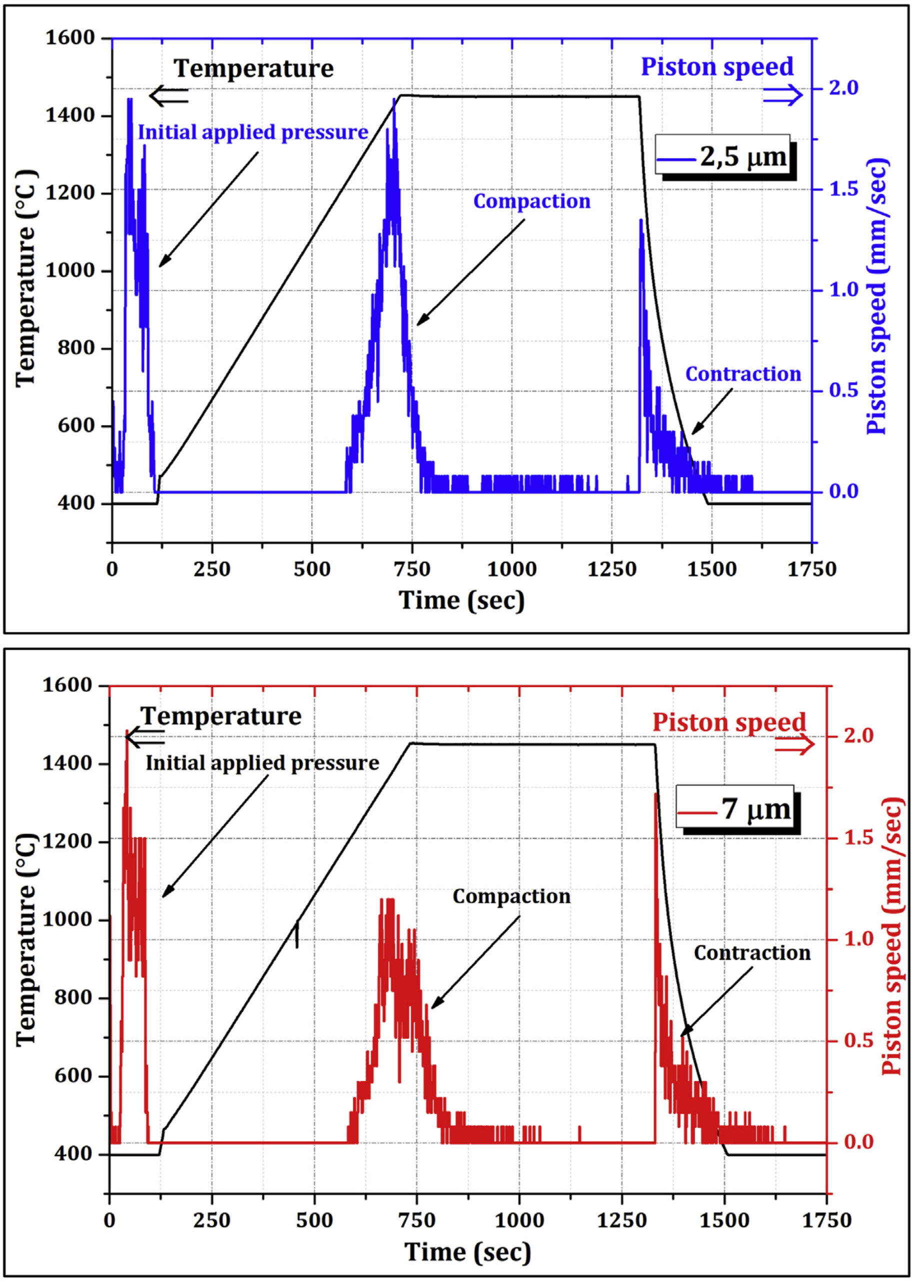

Fig. 5. Variation of piston speed as a function of time for Maxthal powder samples with particle size 2.5 μm (blue) and 7 μm (red), respectively.

reached. For the same sintering parameters, the densification continued even until the maximum sintering temperature for the 2.5 μm powder which explains the reasons for the sharp piston speed during the densification stage. Another evident difference between the powders was the piston speed in the contraction stage. The piston speed for the 2.5 μm powder appeared lower in comparison to the 7 μm powder. An interpretation of this is that a lot of porosity was left behind due to incomplete densification of 7 μm powder and hence contraction speed was higher due to prolonged contraction as a function of time.

Comparing the XRD patterns of the bulk samples of the sintered powders, it can be seen that the XRD pattern of the 7 μm powder contained more TiC_X and $TiSi_2$. This was partly due to the incomplete densification as the majority of the intermediate phases TiC_X and Ti—Si liquid phase have not completely reacted to yield Ti_3SiC_2. Hardness measurements were further carried on the bulk samples to understand quantitatively the influence of particle size on bulk hardness. For the 2.5 μm powder the Vickers hardness was 782 HV, whilst for the 7 μm powder was 1000 HV, respectively. The increase in bulk hardness of the 7 μm powder particle size irrespective of incomplete densification is solely attributed to higher TiC_X content (Fig. 6) as TiC_X has a density which is higher than that of Ti_3SiC_2 (4.93 g/cm^3 vs 4.52 g/cm^3) which explains the reason for higher bulk hardness as compared to the 2.5 μm powder particle size.

3.3. Phase composition analysis

XRD patterns of the top surfaces of the polished samples sintered in vacuum as well as in argon are presented in Fig. 7(a and b). The pattern exhibits peaks primarily assigned to Ti_3SiC_2, and also

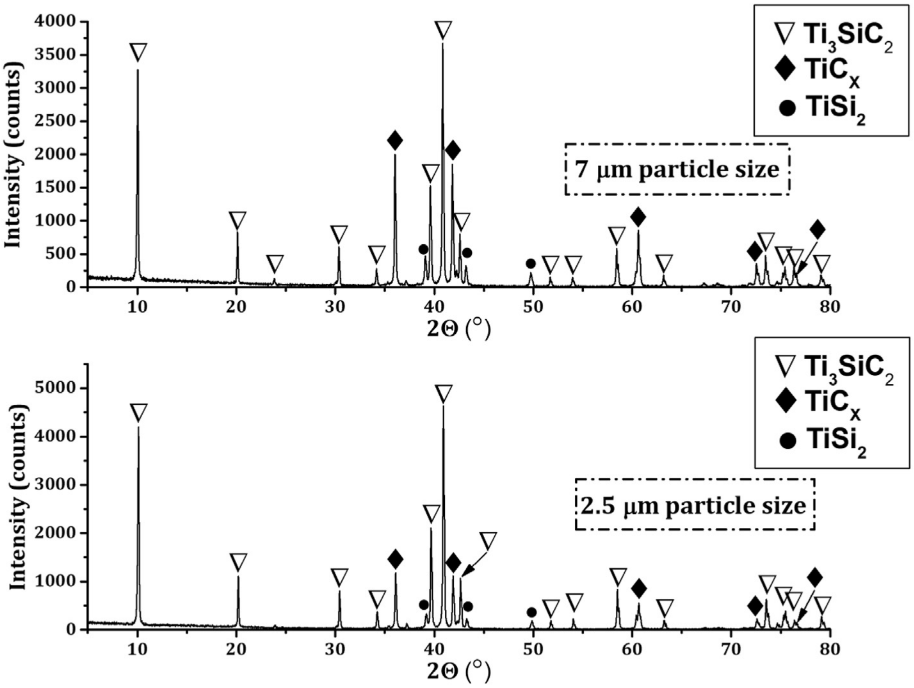

Fig. 6. XRD pattern of sintered bulk samples of Maxthal 312 (powder particle size 2.5 and 7 μm) SPSed at 1450 °C/60 MPa for 10 min.

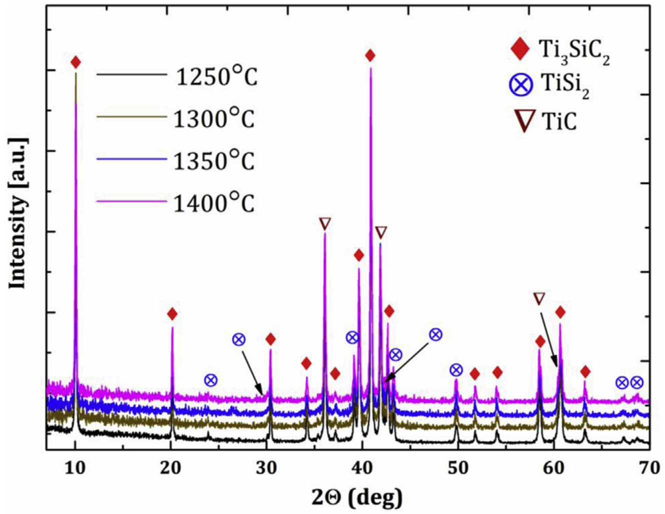

Fig. 7a. XRD phase analysis for the samples sintered under vacuum atmosphere in the temperature range 1250–1400 °C.

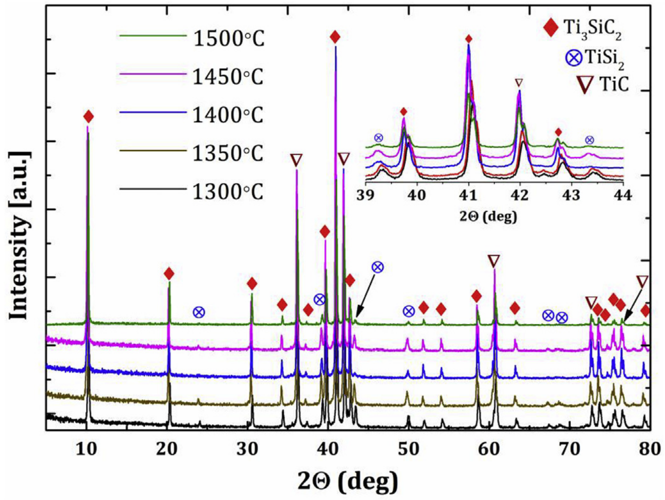

Fig. 7b. XRD phase analysis of the samples sintered under argon environment in the temperature range 1300–1500 °C. Inlet graph shows the silicides were almost completely consumed during argon sintering.

peaks belonging to non-stoichiometric TiC_X. Detailed analysis however showed that a small amount of $TiSi_2$ coexists. In order to determine the phase content as a function of sintering temperature, the integrated calibration method was employed assuming two-phases Ti_3SiC_2 and TiC since the amount of $TiSi_2$ is relatively small and can be ignored according to the formula [55]:

$$W_{TIC} = \frac{I_{TIC}/I_{TSC}}{1.8+I_{TIC}/I_{TSC}} \text{ and } W_{TSC} = \frac{1.8}{1.8+I_{TIC}/I_{TSC}}$$

Where W_{TIC} and W_{TSC} are weight percentages of TiC_X and Ti_3SiC_2, respectively; whilst I_{TIC} and I_{TSC} represent diffraction intensities of TiC (200) and Ti_3SiC_2 (104). Based on the integrated XRD intensity formula employed, the relative content of TiC_X and Ti_3SiC_2 under different sintering environment and temperatures are given in Table 1.

3.4. Densification and microstructural evolution

The microstructure of Maxthal 312 (nominally-Ti_3SiC_2) samples SPS sintered under argon with varying sintering temperature is presented in Fig. 8. At lower temperatures (1250–1350 °C), large area of $TiSi_2$ liquid phase can be seen surround by TiC whilst the Ti_3SiC_2 grows from the silicide melt pool. Ti–Si liquid phase appears to be essential for the growth of Ti_3SiC_2 plates in consistent with observation reported elsewhere [56,57]. At higher sintering temperature (1400–1500 °C), plate-like Ti_3SiC_2 grains (grey phase) continues to grow whilst more TiC_X (dark phase) formation was observed. It appears that at higher sintering temperature most of the Ti–Si liquid phase had been consumed. At optimum sintering

Table 1
Relative phase contents of TiC_X and Ti_3SiC_2 under different sintering conditions.

MAXTHAL-312 Powder	Relative phase contents of the bulk sintered samples (wt. %)			
Sintering Temperature (°C)	SPS Sintering Environment			
	Argon		Vacuum	
	TiC_X	Ti_3SiC_2	TiC_X	Ti_3SiC_2
1250	N/A	N/A	22	78
1300	23	77	23	77
1350	22	78	22	78
1400	25	75	24	76
1450	26	74	N/A	N/A
1500	30	70	N/A	N/A

**Relative phase content determined by integrated calibration method. N/A, not available.*

temperature a duplex microstructure consisting of fine and plate-like Ti_3SiC_2 grains coexist with equiaxed TiC_X grains.

For the various sintering temperatures, average grain size was measured from SEM images using Image-J software. These data are plotted in Fig. 9. It can be seen that both TiC_X and Ti_3SiC_2 grains increased progressively with the sintering temperature (i.e., 1300–1400 °C). The observation agrees well with the conclusion that high sintering temperature accelerates grain growth [46]. However, above 1400 °C there was a sharp decrease in Ti_3SiC_2 grains whilst TiC_X grains continued to grow above 1400 °C. The reason for the decrease in grain size of the Ti_3SiC_2 grains may be possibly linked to intrinsic decomposition owing to the high sintering temperature [58].

TEM micrographs of the as-synthesized bulk sample at 1400 °C in argon are shown in Fig. 10. The characteristic layered nature of the polycrystalline Ti_3SiC_2 grains can be clearly seen with majority of the grains appearing to be defect free i.e., lacking significant dislocation density. However, some grains appear to contain basal dislocations as well as dislocation arrays in consistent with observations reported elsewhere [9,10,59–61].

The phase constitution presented in Table 1 was used in the calculation of the theoretical density. The percentage theoretical density was plotted against sintering temperature for both samples sintered under vacuum and argon environment (Fig. 11(a and b)). This was done in order to reconcile microstructural evolution and densification and to properly delineate the optimum sintering condition. The data plots showed that for samples sintered in vacuum the density curve plateaued at around 1350 °C followed by a subsequent increase in density at temperatures above 1350 °C. Typical behaviour can be observed in the data plot for samples sintered under argon. However, the curve only starts to plateau at 1450 °C with subsequent increase in density at temperatures above 1450 °C. The point where the curves starts to plateau can be attributed to the onset of decomposition, the kinetics which is mainly driven by outward-diffusion and sublimation of the high vapour pressure A-element from the bulk into the vacuum as follows [62]:

$$M_{n+1}AX_n \rightarrow M_{n+1}X_n + A$$

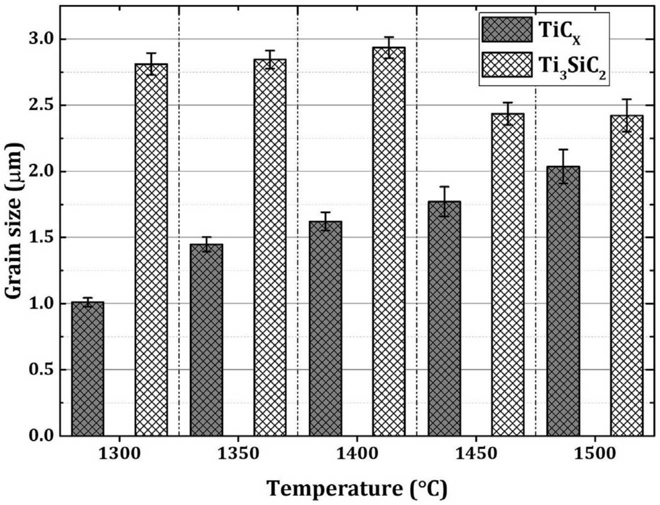

Fig. 9. Average grain size as a function of sintering temperature for Maxthal 312 (nominally-Ti_3SiC_2) sintering under argon in the temperature range 1300–1500 °C for 10 min.

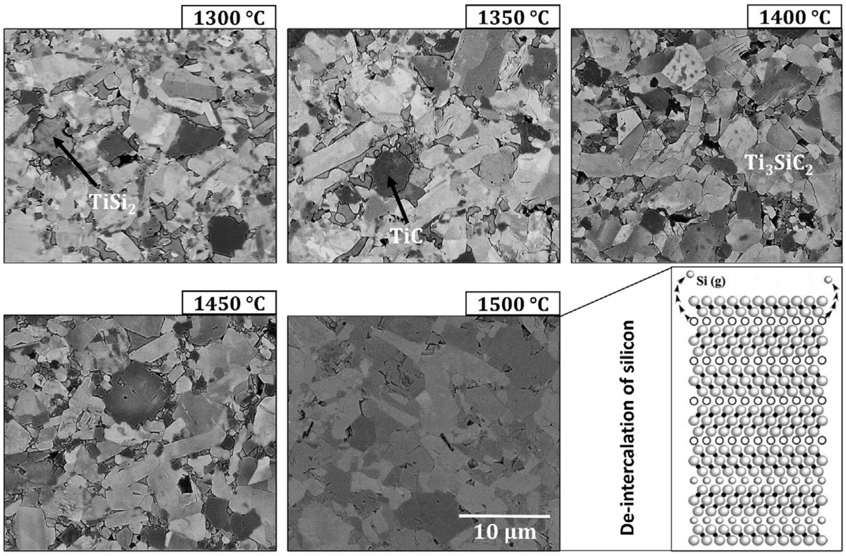

Fig. 8. Evolution of microstructures of samples SPS sintered in argon from Maxthal 312 starting powder. Note the de-intercalation of Si due to evaporation at high sintering temperature resulted in the transformation of hexagonal Ti_3SiC_2 to cubic $TiC_{0.67}$ [16].

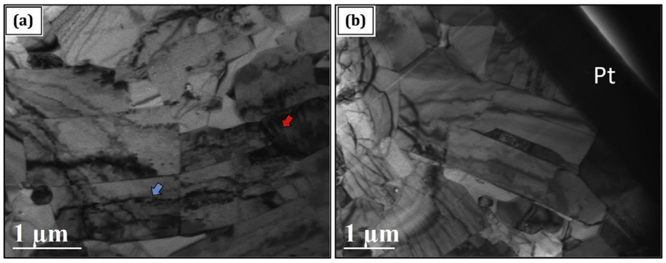

Fig. 10. TEM bright field (BF) image showing the characteristic layered nature of Ti_3SiC_2 taken from bulk sample sintered in argon at 1400 °C. Note red and blue arrow in (a) represents dislocation and dislocation wall. Pt represents the platinum layer deposited to protect the surface during FIB sample preparation. (For interpretation of the references to colour in this figure legend, the reader is referred to the Web version of this article.)

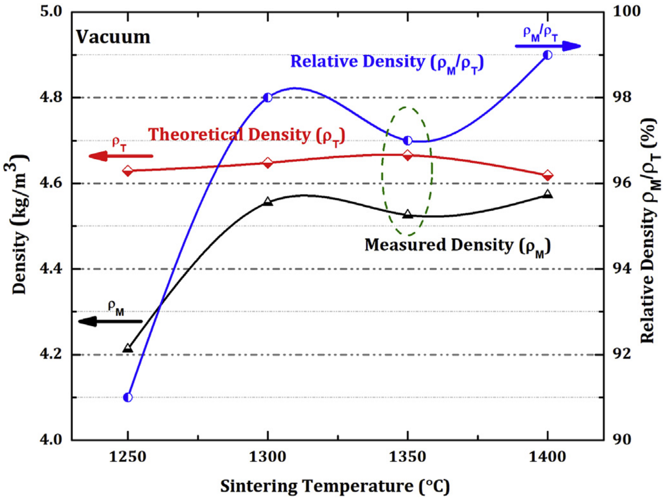

Fig. 11a. Dependence of relative density as a function of temperature during SPS sintering of Maxthal 312 powder (nominally-Ti_3SiC_2) in vacuum.

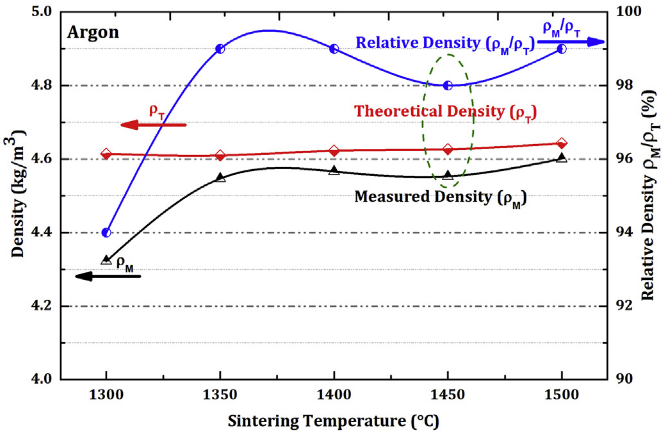

Fig. 11b. Dependence of relative density as a function of temperature during SPS sintering of Maxthal 312 powder (nominally-Ti_3SiC_2) under argon.

Intrinsically, all MAX-phases decomposes at high sintering temperature, the temperature of decomposition will depend on the sintering environment, impurity amongst other things [63]. In this work the early decomposition in vacuum appears to be attributed to the high vapour pressure of silicon which is easily drawn away by the SPS vacuum pressure leading to the de-intercalation of Si and thus the rapid decomposition as compared to sintering under argon [50,64]. The observed subsequent increase in density after the onset of decomposition is solely attributed to more TiC_X formation which possesses a higher theoretical density than Ti_3SiC_2, thus the observed increase in bulk density. Evidence of an increase in TiC_X content can be seen in the microstructures of samples sintered at 1450 °C and 1500 °C, respectively. Bulk density measurement for the sample at the lowest sintering temperature (1300 °C) under argon was about 94% of theoretical value of Ti_3SiC_2 (4.53 g/cm^3) indicating that samples were generally highly dense.

In order to further understand the evolution of bulk hardness as a function of sintering temperature, Vickers hardness indentation plot as a function of sintering temperature for samples sintered under argon is presented (Fig. 12). In consistent to the observed increase in density in Fig. 11b, as well as microstructural evolution in Fig. 8, the measured hardness increased dramatically above 1450 °C. The increase in density due to unique densification capability of the SPS seems to have stopped around 1400 °C (Fig. 11b), thus any subsequent increase in density above 1400 °C is no longer due to the densification imparted by the SPS but instead due to TiC_X decomposition product formation that brings about an overall increase in bulk hardness.

Micro-hardness tests were conducted on the polished sample sintered under argon at 1400 °C using indentation loads of 1, 2, 3, and 5 KgF, respectively. The plot of the Vickers hardness as a function of indentation load showed an increase in hardness with decreasing indentation load (Fig. 13). This response known as indentation-size-effect (ISE) is a typical plasticity at room temperature demonstrated by MAX-phases and has been attributed to a range (some shown in Fig. 14) of energy absorbing mechanism such as kink-band, grain buckling, and delamination of favourably oriented grains due to their anisotropic nature [7].

3.5. Decomposition of Ti_3SiC_2

3.5.1. Role of graphite heating element

To further understand the reason for decomposition of Ti_3SiC_2 leading to TiC_X formation even at low sintering temperatures, a differential scanning calorimetry (DSC) investigation using graphite crucible was carried out to simulate the SPS graphite rich environment. From this plot (Fig. 15), a broad exothermic peak appeared around 862 °C which may be attributed to the low formation

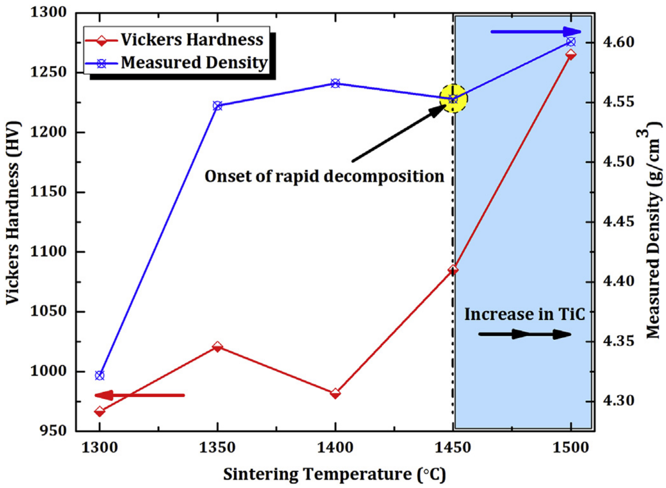

Fig. 12. Dependence of hardness and density as a function of sintering temperature for samples sintered under argon environment.

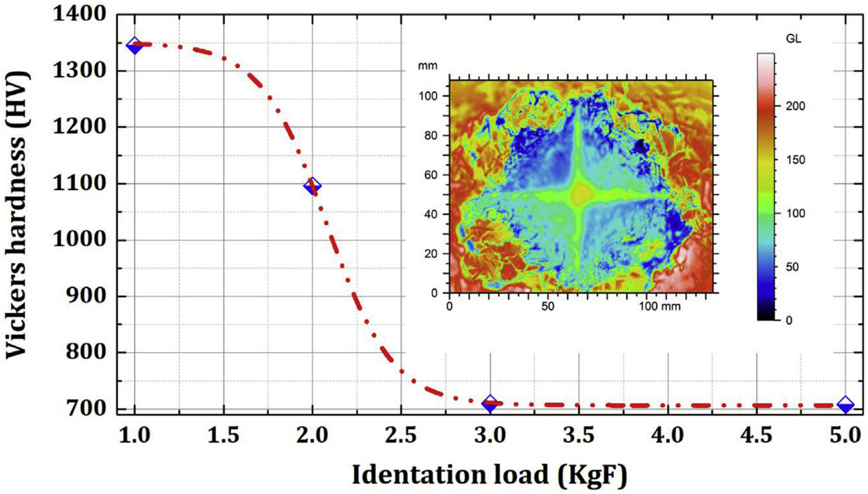

Fig. 13. Vickers hardness versus indentation load (KgF). Inset shows heat map of indentation damage. Note curve fitted using Lorentz function.

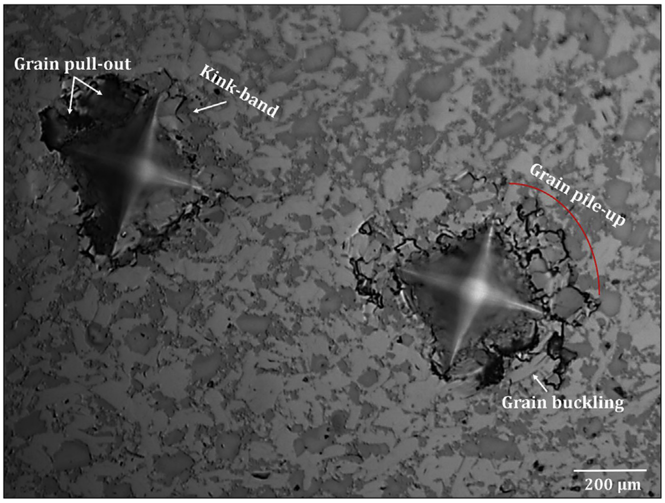

Fig. 14. Optical micrograph of post-mortem damage mechanisms around hardness indentation in SPSed Maxthal 312 (nominally-Ti_3SiC_2).

temperature of Ti_3Si intermetallic according to the Ti–Si phase diagram [65,66] as well as around 1332 °C corresponding to Ti–Si eutectic reactions (Si–$TiSi_2$ and Ti–Ti_5Si_3) [29]. Also, a sharp endothermic peak at about 1466 °C near the melting point of Si appeared on the DSC curve. On the other hand, looking at the TG curve, a slight increase in mass (approx. 1%) corresponding to the exothermic peak due to intermetallic phase formation can be seen. Also, the onset of rapid mass loss (approx. 5.5%) at temperature above 1300 °C corresponds to the melting point of the eutectics according to the Ti–Si phase diagram [65]. The loss of Si will imply loss of purity in the synthesized sample. Also, the absence of endothermic peak below the melting point of Si implies that the graphite crucible did not react with the Ti_3SiC_2 powder.

3.5.2. *Role of graphite foil during sintering*

In order to understand the effect of graphite foil at the die-powder interface before the SPS and the consequent possible carbon diffusion at the graphite foil-sintered Ti_3SiC_2 interface after SPS, microstructural and EDX analysis were further carried out. Fig. 16 is an optical micrograph from the graphite foil/Ti_3SiC_2 interface showing a layer of up to 120 μm diffusion zone of graphite.

Fig. 17 shows the cross-sectional SEM image and EDX elemental map analysis at the interface of the graphite paper and Ti_3SiC_2 sintered sample at 1400 °C. Consistent with the optical micrograph (Fig. 16) a diffusion layer is apparent. EDX map analysis and elemental spectrum from an area in the diffusion zone shows possible SiC layer formation. However, no evidence of SiC was observed in the XRD pattern of the polished bulk sample surface. This will mean that the grinding and polishing process effectively removed all the diffusion layer.

To further ascertain that no SiC layer was present at the surface as SiC and TiC share similar peaks due to their cubic nature [67]. Raman analysis was thus carried out on the polished bulk sample surface of the sample sintered at 1400 °C in argon. The observed Raman peaks (Fig. 18) correspond well with those of Ti_3SiC_2 as reported elsewhere [68].

Carburization due to reaction of the MAX phase powder with the graphite paper will inadvertently shift the overall surface composition to the Ti_3SiC_2–TiC–SiC compatibility triangle following the reaction [53]:

$$Ti_3SiC_2 + (3x - 1)C = 3TiC_X + SiC$$

However, in the absence of SiC, another possible reaction path proposed is given by Ref. [53]:

$$Ti_3SiC_2 + (3x - 2)C = 3TiC_X(x > 0.8) + Si$$

It is thus evident that carburization linked to the use of graphite paper during the SPS of the Ti_3SiC_2 starting powder played an important role in the overall purity of the bulk Ti_3SiC_2.

4. Conclusion

In this study we have shown that near complete densification of Maxthal 312 (nominally-Ti_3SiC_2) can be achieved by using spark plasma sintering at 1350 °C (100 °C/min) in vacuum and 1450 °C (100 °C/min) in argon for 10 min, respectively. Reduction in powder particle size further enhances densification via Joule heating, mechanical movement of particles and plastic deformation. Graphite paper used to isolate the graphite die and powder to aid easy removal of sintered compacts appears to be responsible for the

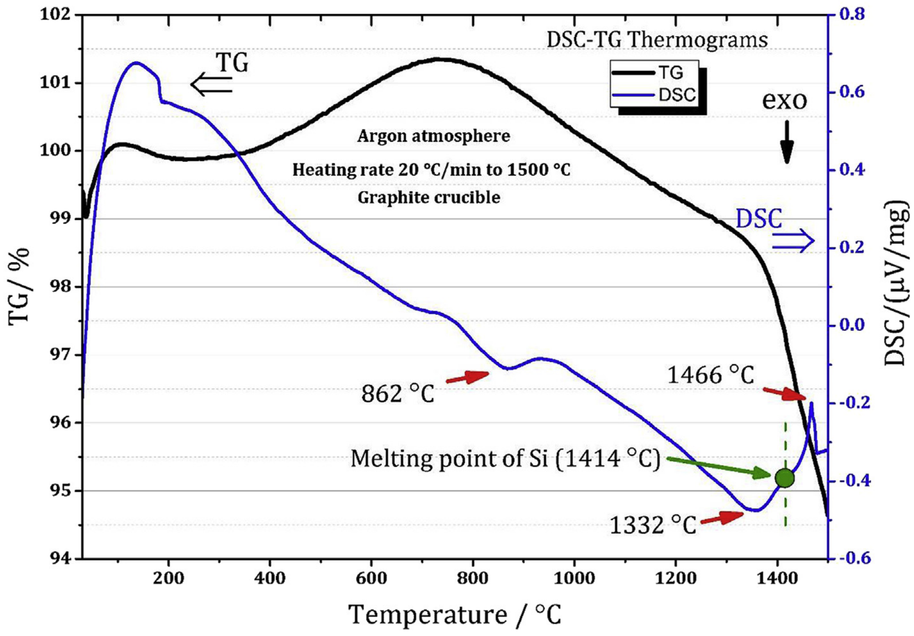

Fig. 15. DSC-TG curve of Maxthal 312 powder (nominally-Ti_3SiC_2) in highly pure argon.

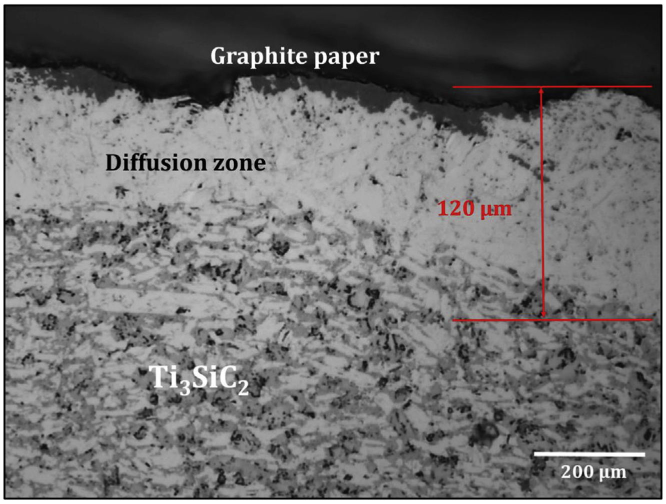

Fig. 16. Optical micrograph of the interface between graphite paper and the MAX-phase after spark plasma sintering.

carbon diffusion into the bulk samples and not necessarily due to the graphite heating elements employed in SPS as evident from the DSC-TG thermogram. Furthermore, the absence of decomposition below the melting point of Si judging from the DSC-TG analysis in flowing Ar implies that the stoichiometry of Si in the MAX phase composition is preserved (i.e., vapour of Si is not drawn out) especially when SPS sintering under argon environment.

It is clear that the graphite tooling (i.e., graphite paper) as well as the sintering environment (i.e., vacuum) plays an important role on the purity of Ti_3SiC_2 irrespective of the sintering temperature and starting composition. One way to inhibit graphite diffusion and/or reaction is the use of boron nitride (BN) spray coatings on the surface of the graphite paper in order isolate the powder and the graphite paper. Also, owing to the loss of Si due to the vapour of Ti—Si eutectics being drawn away easily during vacuum sintering, off-stoichiometric Si in the starting composition is needed to compensate for possible Si loss at low sintering temperature well below the melting point of Si. Hence, a starting Ti_3SiC_2 powder (i.e., Maxthal powder) may not be suitable in obtaining high purity Ti_3SiC_2 during vacuum sintering as Si loss will ultimately push the

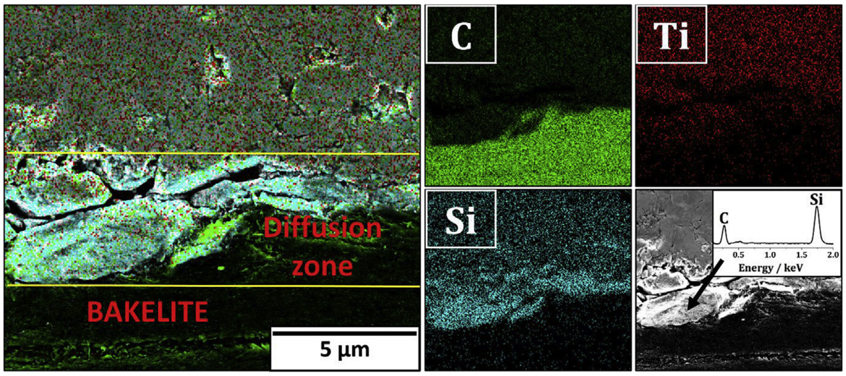

Fig. 17. Cross-sectional SEM image and elemental mapping of C, Ti, and Si at the interface of the graphite paper/Ti_3SiC_2 sintered sample at 1400 °C.

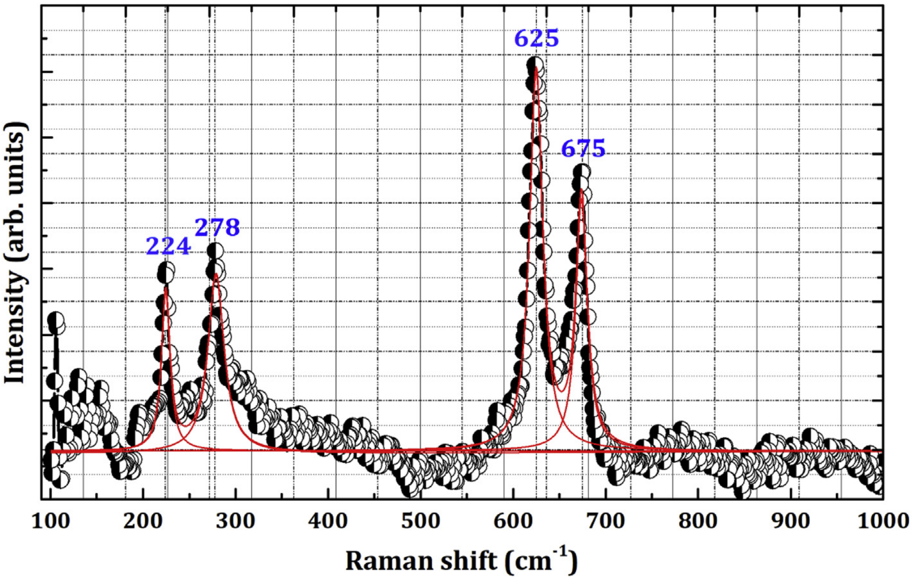

Fig. 18. Raman of bulk spark plasma sintered Maxthal 312 (nominally-Ti_3SiC_2) at 1400 °C. Note curve fitted with Gauss function.

resultant bulk composition into a two-phase or three-phase region according to the Ti–Si–C phase diagram, thus purity is compromised.

References

[1] M.W. Barsoum, M. Radovic, Elastic and mechanical properties of the MAX phases, in: D.R. Clarke, P. Fratzl (Eds.), Annual Review of Materials Research, vol 41, Annual Reviews, Palo Alto, 2011, pp. 195–227.
[2] M. Barsoum, M. Radovic, Mechanical Properties of the MAX Phases, vol. 41, 2011, pp. 195–227.
[3] P. Eklund, J. Rosen, P.O.Å. Persson, Layered ternary Mn+1AXnphases and their 2D derivative MXene: an overview from a thin-film perspective, J. Phys. D Appl. Phys. 50 (11) (2017) 113001.
[4] H. Fashandi, et al., Ti2Au2C and Ti3Au2C2 formed by solid state reaction of gold with Ti2AlC and Ti3AlC2, Chem. Commun. 53 (69) (2017) 9554–9557.
[5] M. Sokol, et al., Big Questions in Chemistry - on the Chemical Diversity of the MAX Phases, 2019.
[6] M.W. Barsoum, The MN+1AXN phases: a new class of solids: thermodynamically stable nanolaminates, Prog. Solid State Chem. 28 (1) (2000) 201–281.
[7] T. El-Raghy, et al., Damage mechanisms around hardness indentations in Ti_3SiC_2, J. Am. Ceram. Soc. 80 (2) (1997) 513–516.
[8] I.M. Low, et al., Contact damage accumulation in Ti3SiC2, J. Am. Ceram. Soc. 81 (1) (1998) 225–228.
[9] M.W. Barsoum, L. Farber, T. El-Raghy, Dislocations, kink bands, and room-temperature plasticity of Ti3SiC2, Metall. Mater. Trans. A 30 (7) (1999) 1727–1738.
[10] B.J. Kooi, et al., Ti 3SiC 2: a damage tolerant ceramic studied with nano-indentations and transmission electron microscopy, Acta Mater. 51 (10) (2003) 2859–2872.
[11] H. Fashandi, et al., Synthesis of Ti3AuC2, Ti3Au2C2 and Ti3IrC2 by noble metal substitution reaction in Ti3SiC2 for high-temperature-stable Ohmic contacts to SiC, Nat. Mater. 16 (2017) 814.
[12] M. Li, et al., Element replacement approach by reaction with Lewis acidic molten salts to synthesize nanolaminated MAX phases and MXenes, J. Am. Chem. Soc. 141 (11) (2019) 4730–4737.
[13] T. Lapauw, et al., Synthesis of the novel Zr3AlC2 MAX phase, J. Eur. Ceram. Soc. 36 (3) (2016) 943–947.
[14] T. Lapauw, et al., Synthesis of MAX phases in the Hf–Al–C system, Inorg. Chem. 55 (21) (2016) 10922–10927.
[15] M. Naguib, et al., Two-dimensional nanocrystals produced by exfoliation of Ti3AlC2, Adv. Mater. 23 (37) (2011) 4248–4253.
[16] J. Emmerlich, et al., Thermal stability of Ti3SiC2 thin films, Acta Mater. 55 (4) (2007) 1479–1488.
[17] M.W. Barsoum, MAX Phases : Properties of Machinable Ternary Carbides and Nitrides, Wiley-VCH Verlag GmbH & Co. KGaA, Weinheim, Germany, 2013, 2013.
[18] V.H. Nowotny, Strukturchemie einiger Verbindungen der Übergangsmetalle mit den elementen C, Si, Ge, Sn, Prog. Solid State Chem. 5 (1971) 27–70.
[19] B.Y. Islak, E. Ayas, Evaluation of properties of spark plasma sintered Ti3SiC2 and Ti3SiC2/SiC composites, Ceram. Int. 45 (2019) 12297–12306.
[20] A. Pourebrahim, et al., Low temperature synthesis of high-purity Ti3SiC2 via additional Si through spark plasma sintering, J. Alloy. Comp. 789 (2019) 313–322.
[21] B. Xu, et al., Synthesis of single-phase Ti3SiC2 from coarse elemental powders and the effects of excess Al, Ceram. Int. 45 (1) (2019) 948–953.
[22] K. Kozak, et al., Influence of composition and grain size on the damage evolution in MAX phases investigated by acoustic emission, Mater. Sci. Eng. A 743 (2019) 114–122.
[23] H. Aghamohammadi, A. Heidarpour, R. Jamshidi, The phase and morphological evolution of Ti3SiC2 MAX phase powder after HF treatment, Ceram. Int. 44 (15) (2018) 17992–18000.
[24] Y. Zhu, et al., Synthesis and Decomposition of Ti3SiC2 under 1-5GPa at 1400°C, vols. 602–603, 2014, pp. 499–502.
[25] H. Abderrazak, et al., Influence of mechanical alloying on Ti3SiC2 formation via spark plasma sintering technique from Ti/SiC/C powders, Ceram. Int. 39 (5) (2013) 5365–5372.
[26] T.L. Ngai, Y. Kuang, Y. Li, Impurity control in pressureless reactive synthesis of pure Ti3SiC2 bulk from elemental powders, Ceram. Int. 38 (1) (2012) 463–469.
[27] M.W. Barsoum, T. El-Raghy, Synthesis and characterization of a remarkable ceramic: Ti3SiC2, J. Am. Ceram. Soc. 79 (7) (1996) 1953–1956.
[28] H. Foratirad, H. Baharvandi, M.G. Maraghe, Effect of excess silicon content on the formation of nano-layered Ti3SiC2 ceramic via infiltration of TiC preforms, J. Eur. Ceram. Soc. 37 (2) (2017) 451–457.
[29] N.C. Ghosh, S.P. Harimkar, Phase analysis and wear behavior of in-situ spark plasma sintered Ti3SiC2, Ceram. Int. 39 (6) (2013) 6777–6786.
[30] X. Liu, et al., Characterization and application of porous Ti3SiC2 ceramic prepared through reactive synthesis, Mater. Des. 79 (2015) 94–98.
[31] X. Liu, et al., Porous Ti3SiC2 Fabricated by Mixed Elemental Powders Reactive Synthesis, vol 35, 2015.
[32] C.L. Zhou, et al., Fabrication and characterization of pure porous Ti3SiC2 with controlled porosity and pore features, Mater. Lett. 131 (2014) 280–283.
[33] J. Qin, D. He, Phase stability of Ti3SiC2 at high pressure and high temperature, Ceram. Int. 39 (8) (2013) 9361–9367.
[34] L. Yongming, et al., Synthesis of high-purity Ti3SiC2 polycrystals by hot-pressing of the elemental powders, Mater. Lett. 52 (4) (2002) 245–247.
[35] W.B. Zhou, B.C. Mei, J.Q. Zhu, Fabrication of high-purity ternary carbide Ti3SiC2 by spark plasma sintering technique, Mater. Lett. 59 (12) (2005) 1547–1551.
[36] C. Li, H.X. Zhai, Synthesis and reaction mechanism of Ti3SiC2 by mechanical alloying of elemental Ti, Si, and C powders 88 (2005) 2092–2098.
[37] H. Li, et al., Preparation and characterization of Ti3SiC2 powder, Ceram. Int. 30 (8) (2004) 2289–2294.
[38] T. Goto, T. Hirai, Chemically vapor deposited Ti3SiC2, Mater. Res. Bull. 22 (9) (1987) 1195–1201.
[39] H. Gao, et al., Structural, physical and mechanical properties of Ti3(Al1−xSix) C2 solid solution with x=0−1, Mater. Sci. Eng. A 676 (2016) 197–208.
[40] T. Galvin, et al., Molten salt synthesis of MAX phases in the Ti-Al-C system, J. Eur. Ceram. Soc. 38 (14) (2018) 4585–4589.
[41] X. Guo, et al., Preparation of Ti3SiC2 powders by the molten salt method, Mater. Lett. 111 (2013) 211–213.
[42] Z. Jiaoqun, M. Bingchu, Effect of aluminum on synthesis of Ti3SiC2 by spark

plasma sintering (SPS) from elemental powders, J. Mater. Synth. Process. 10 (6) (2002) 353–358.
[43] A. Pourebrahim, et al., Effect of aluminum addition on the densification behavior and mechanical properties of synthesized high-purity nano-laminated Ti3SiC2 through spark plasma sintering, J. Alloy. Comp. 730 (2018) 408–416.
[44] N.F. Gao, et al., Rapid synthesis of dense Ti3SiC2 by spark plasma sintering, J. Eur. Ceram. Soc. 22 (13) (2002) 2365–2370.
[45] M.A. El Saeed, F.A. Deorsola, R.M. Rashad, Influence of SPS parameters on the density and mechanical properties of sintered Ti3SiC2 powders, Int. J. Refract. Metals Hard Mater. 41 (2013) 48–53.
[46] Z.-F. Zhang, et al., A new synthesis reaction of Ti3SiC2 from Ti/TiSi2/TiC powder mixtures through pulse discharge sintering (PDS) technique, Mater. Res. Innov. 5 (3) (2002) 185–189.
[47] Y. Zou, et al., Synthesis Reactions for Ti3SiC2 through Pulse Discharge Sintering TiH2/Si/TiC Powder Mixture, vol 43, 2008, pp. 968–975.
[48] F. Turki, et al., SPS Parameters Influence on Ti 3 SiC 2 Formation from Si/TiC: Mechanical Properties of the Bulk Materials, vol 708, 2017.
[49] N.C. Ghosh, S.P. Harimkar, 3 - consolidation and synthesis of MAX phases by spark plasma sintering (SPS): a review, in: I.M. Low (Ed.), Advances in Science and Technology of Mn+1AXn Phases, Woodhead Publishing, 2012, pp. 47–80.
[50] H. Li, et al., Synthesis of Ti3SiC2 by pressureless sintering of the elemental powders in vacuum, Mater. Lett. 58 (11) (2004) 1741–1744.
[51] C. Racault, F. Langlais, R. Naslain, Solid-state synthesis and characterization of the ternary phase Ti3SiC2, J. Mater. Sci. 29 (13) (1994) 3384–3392.
[52] B.B. Bokhonov, et al., Carbon uptake during Spark Plasma Sintering: investigation through the analysis of the carbide "footprint" in a Ni-W alloy, RSC Adv. 5 (98) (2015) 80228–80237.
[53] T. El-Raghy, M.W. Barsoum, Diffusion kinetics of the carburization and silicidation of Ti3SiC2, J. Appl. Phys. 83 (1) (1998) 112–119.
[54] C. Manière, G. Lee, E.A. Olevsky, All-Materials-Inclusive Flash Spark Plasma Sintering, vol. 7, 2017.
[55] Z.F. Zhang, Z.M. Sun, H. Hashimoto, Rapid synthesis of ternary carbide Ti3SiC2 through pulse-discharge sintering technique from Ti/Si/TiC powders, Metall. Mater. Trans. A 33 (11) (2002) 3321–3328.
[56] D.P. Riley, et al., Self-propagating high-temperature synthesis of Ti3SiC2: I, ultra-high-speed neutron diffraction study of the reaction mechanism, J. Am. Ceram. Soc. 85 (10) (2002) 2417–2424.
[57] E.H. Kisi, D.P. Riley, Diffraction thermometry and differential thermal analysis, J. Appl. Crystallogr. 35 (6) (2002) 664–668.
[58] I.M. Low, Z. Oo, K.E. Prince, Effect of vacuum annealing on the phase stability of Ti3SiC2, J. Am. Ceram. Soc. 90 (8) (2007) 2610–2614.
[59] E. Drouelle, et al., Deformation mechanisms during high temperature tensile creep of Ti3AlC2 MAX phase, J. Alloy. Comp. 693 (2017) 622–630.
[60] A. Guitton, et al., Dislocation analysis of Ti 2 AlN deformed at room temperature under confining pressure, Phil. Mag. 92 (36) (2012) 1–11.
[61] L. Farber, Transmission electron microscopy study of a low-angle boundary in plastically deformed Ti3SiC2, Phil. Mag. Lett. 79 (4) (1999) 163–170.
[62] I.M. Low, W.K.P., Thermal stability of MAX phases, Key Eng. Mater. 617 (2014) 153–158.
[63] N.C. Ghosh, S.P. Harimkar, 3 - consolidation and synthesis of MAX phases by spark plasma sintering (SPS): a review A2 - low, I.M, in: Advances in Science and Technology of Mn+1AXn Phases, Woodhead Publishing, 2012, pp. 47–80.
[64] J.T. Li, Y. Miyamoto, Fabrication of monolithic Ti3SiC2 ceramic through reactive sintering of Ti/Si/2TiC, J. Mater. Synth. Process. 7 (2) (1999) 91–96.
[65] Marina, F., N. Flávio Beneduce, and A. Cesar Roberto de Farias, Assessment of the Ti-rich corner of the Ti-Si phase diagram using two sublattices to describe the Ti5Si3 phase. REM: Int. Eng. J.. 70(2): p. 201-207.
[66] T.B. Massalski, et al., Binary Alloy Phase Diagrams, American Society for Metals, Metals Park, Ohio: Metals Park, Ohio, 1986 c1986.
[67] J. Zhong, et al., Synthesis of mesoporous carbon-bonded TiC/SiC composites by direct carbothermal reduction of sol–gel derived monolithic precursor, J. Am. Ceram. Soc. 94 (11) (2011) 4025–4031.
[68] M. Amer, et al., The Raman spectrum of Ti3SiC2, J. Appl. Phys. 84 (10) (1998) 5817–5819.

Paper B

Synthesis and microstructural evolution in ternary metalloceramic Ti_3SiC_2 consolidated via the Maxthal 312 powder route

Ceramics International xxx (xxxx) xxx–xxx

Contents lists available at ScienceDirect

Ceramics International

journal homepage: www.elsevier.com/locate/ceramint

Synthesis and microstructural evolution in ternary metalloceramic Ti_3SiC_2 consolidated via the Maxthal 312 powder route

Carl Magnus[a,*], Tom Galvin[b], Le Ma[a], Ali Mostaed[c], William M. Rainforth[a]

[a] *The Henry Royce Institute and Department of Materials Science and Engineering, The University of Sheffield, Sir Robert Hadfield Building, Sheffield, S1 3JD, UK*
[b] *M&I Materials Ltd, Hibernia Way, Trafford Park, Manchester, M32 0ZD, UK*
[c] *Department of Materials, University of Oxford, 16 Parks Road, Oxford, OX1 3PH, UK*

ARTICLE INFO

Keywords:
Ti_3SiC_2
Metalloceramic
Spark plasma sintering
Reaction mechanism
Microstructure

ABSTRACT

A bulk specimen containing Ti_3SiC_2, $TiSi_2$ and TiC was prepared through an in situ spark plasma sintering/solid-liquid reaction powder metallurgy method using the Maxthal 312 (nominally-Ti_3SiC_2) powder as a starting material. The reaction mechanism, phase constituents and evolution of the microstructure were systematically investigated by X-ray diffraction (XRD), optical microscopy, scanning electron microscopy (SEM) equipped with energy dispersive spectroscopy (EDS) system, transmission electron microscopy (TEM), Raman spectroscopy, differential scanning calorimetry (DSC) and Vickers microhardness testing. Phase analysis and microstructural characterization revealed that the bulk sample contained binary ancillary phases, possibly due to Si evaporation and/or carburization. The deformed microstructure around the indents revealed evidence of plasticity, intrinsic lubricity and toughening. The Microstructural and orientation relationships between the phases contained in the bulk sample are reported.

1. Introduction

Upon the discovery that the ternary metalloceramic compounds with $M_{n+1}AX_n$ (MAX) chemistry (where n = 1–5, M is an early transition metal, A is an A-group and X is C or N) possess an unusual and sometimes unique set of properties, they have been extensively studied [1–3]. The fact that the 2-D materials known as MXenes, which cannot be synthesized directly due to their thermodynamic metastability [4–6] can be synthesized directly from 3-D MAX phases (by taking advantage of the significant difference in strength between the metallic M–A bonding and covalent M–X bonding, which aids in selectively etching out the A-layer to form two-dimensional MXenes) have further attracted extensive interest in MAX phases [7]. Well over 100 MAX phases have now been successfully synthesized, and in some cases ‘hybrid’ MAX phases, consisting of a partial substitution of the M or A elements have also been found to be stable [1–3,8].

MAX phases typically exhibit properties between those of metals and conventional ceramics [1]. They have high electrical and thermal conductivity while also showing creep resistance, high temperature strength, and good resistance to thermal shock and oxidation [9]. They are stiff (Ti_3SiC_2 has around three times the stiffness of titanium with a comparable density [10]) and relatively soft compared to their binary carbide equivalents, so much so that MAX phases are easily machinable with common metalworking tools such as hacksaws or lathes [11]. Due to their layered structure, MAX phases are surprisingly damage tolerant; the layers slide, kink and delaminate to absorb the deformation, causing local hardening at the damage site [12–14]. Currently, MAX phases find applications as furnace tubes and high temperature burner nozzles, as well as electric furnace elements [10]. They have been proposed for use as latex glove formers [10], and, due to some favourable radiation tolerance studies [15–18] MAX phases are also being considered as a potential material for use within current and future designs of nuclear fission reactor [19,20]. Their layered nature and self-lubricating properties make them a candidate for bearings and other sliding applications [21–24].

Titanium silicon carbide (Ti_3SiC_2) is a member of the $M_{n+1}AX_n$ layered compound belonging to the $Ti_{n+1}SiC_n$ system. It is the most stable ternary phase in Ti–Si–C ternary phase system and crystallizes in the space group of $P6_3/mmc$ [25]. However, its formation is compromised by more stable binary phases (TiC, SiC and $TiSi_2$) due to its narrow formation region in the Ti–Si–C Phase diagram [25]. The bonding in Ti_3SiC_2 is anisotropic as well as metallic-covalent-ionic in nature [26]. This unusual bonding characteristics and special crystal structure render the MAX phases with unique properties [27]. Ti_3SiC_2, just like other members of the MAX phases does not melt but instead decomposes into its respective binary phases via the dissociation of Si at

---

* Corresponding author.
E-mail address: mcarl2@sheffield.ac.uk (C. Magnus).

https://doi.org/10.1016/j.ceramint.2020.03.078
Received 10 December 2019; Received in revised form 14 February 2020; Accepted 7 March 2020

Please cite this article as: Carl Magnus, et al., Ceramics International, https://doi.org/10.1016/j.ceramint.2020.03.078

specific temperature in various atmosphere [28]. It is reported to be stable under vacuum or argon atmosphere up to 1600 °C [29]. All these exciting properties makes it a promising next generation material suitable in a range of structural applications as a monolithic phase and/or composite [30]. Some authors have reported that the composite form, Ti_3SiC_2–TiC and Ti_3SiC_2–SiC for example, possesses superior mechanical properties than monolithic Ti_3SiC_2 [31,32].

There are several synthesis routes to produce Ti_3SiC_2. Hot Pressing/Hot Isostatic Pressing (HIP) [33,34], as used by Barsoum and El-Raghy in their initial paper on Ti_3SiC_2 [35], and Spark Plasma Sintering

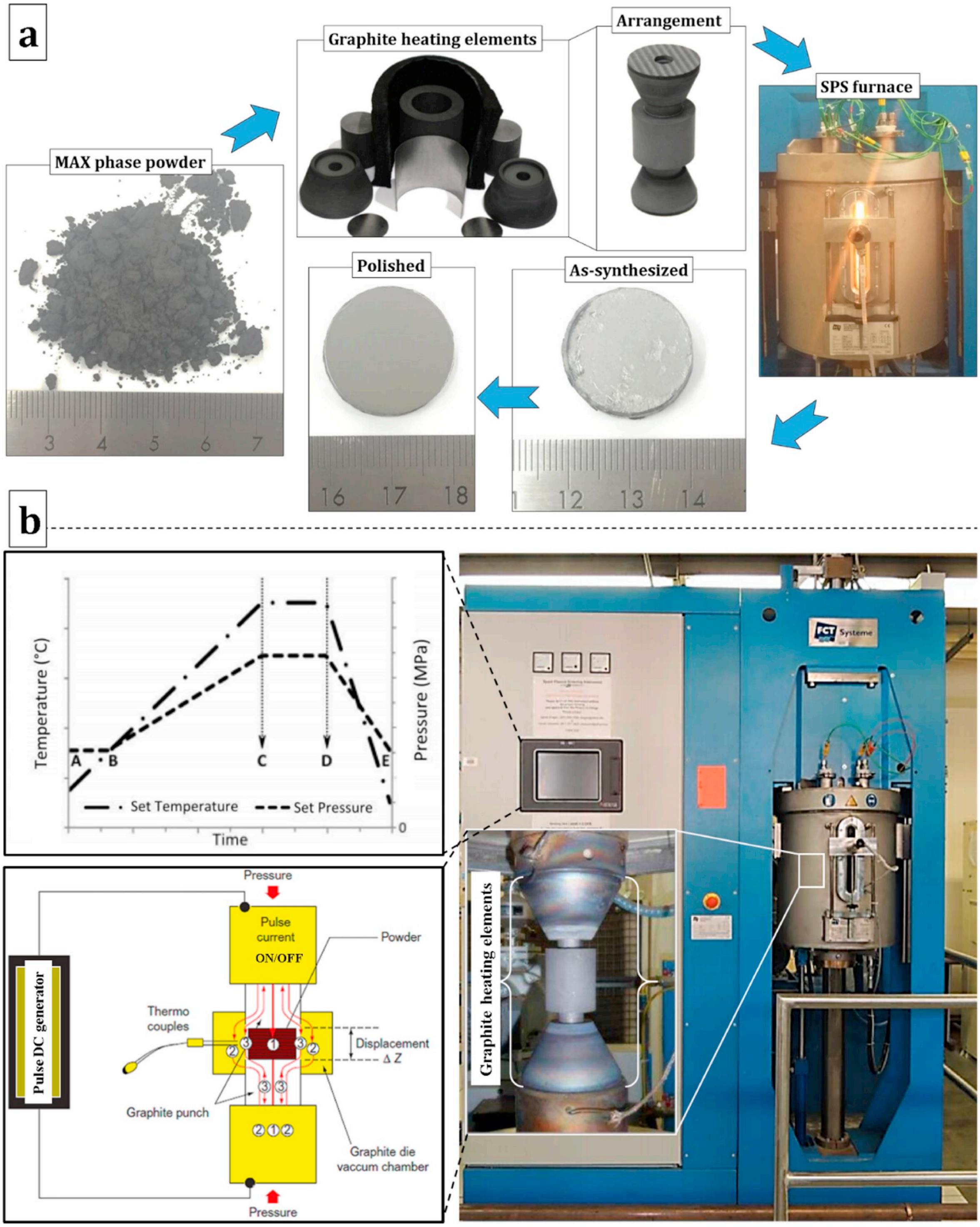

Fig. 1. (a) Punch-powder-die assembly and (b) SPS furnace unit and associated sintering parameters.

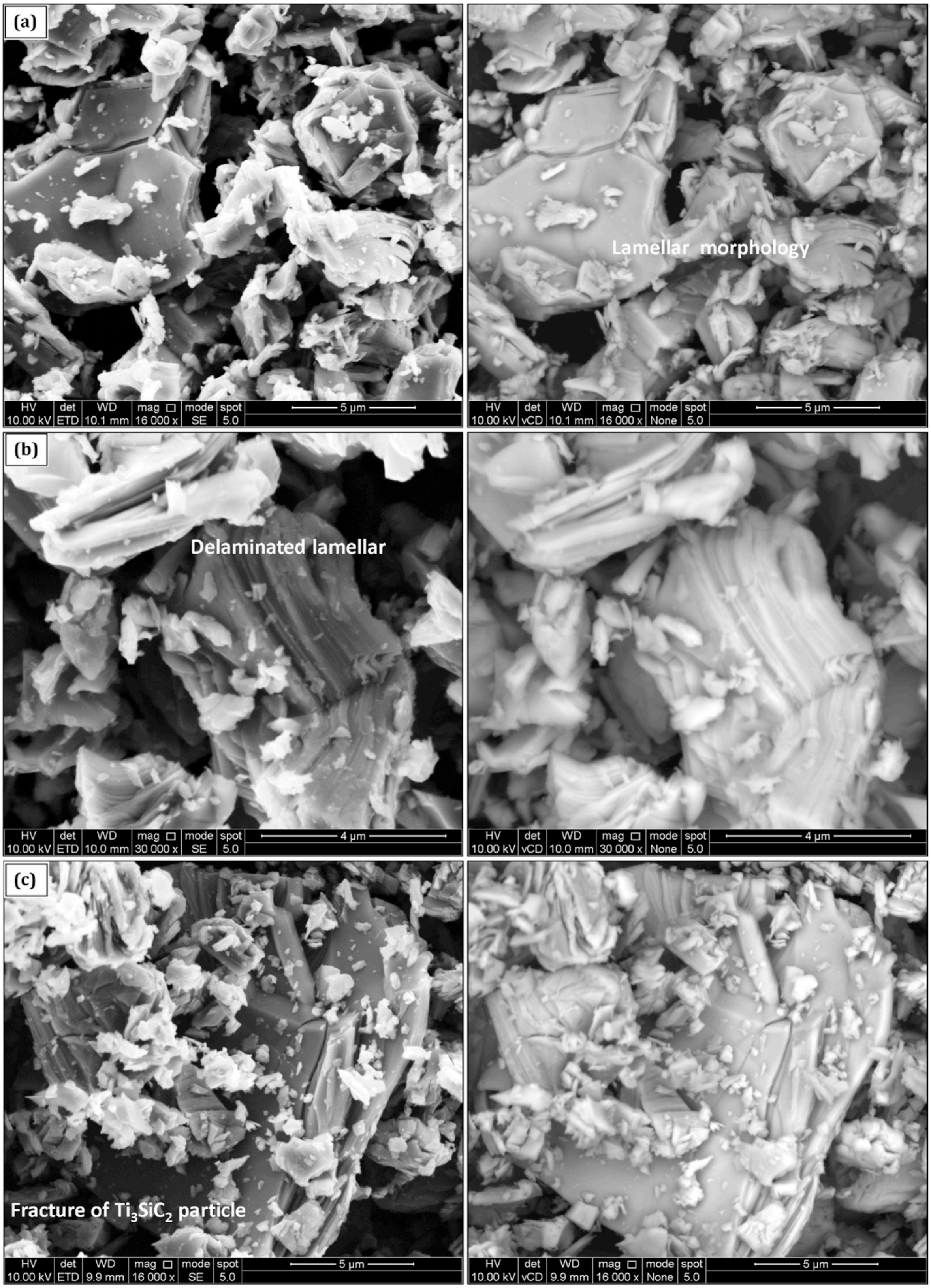

Fig. 2. SEM (SE–BSE) micrographs showing the morphology of the as-received Maxthal 312 (nominally-Ti_3SiC_2) powder.

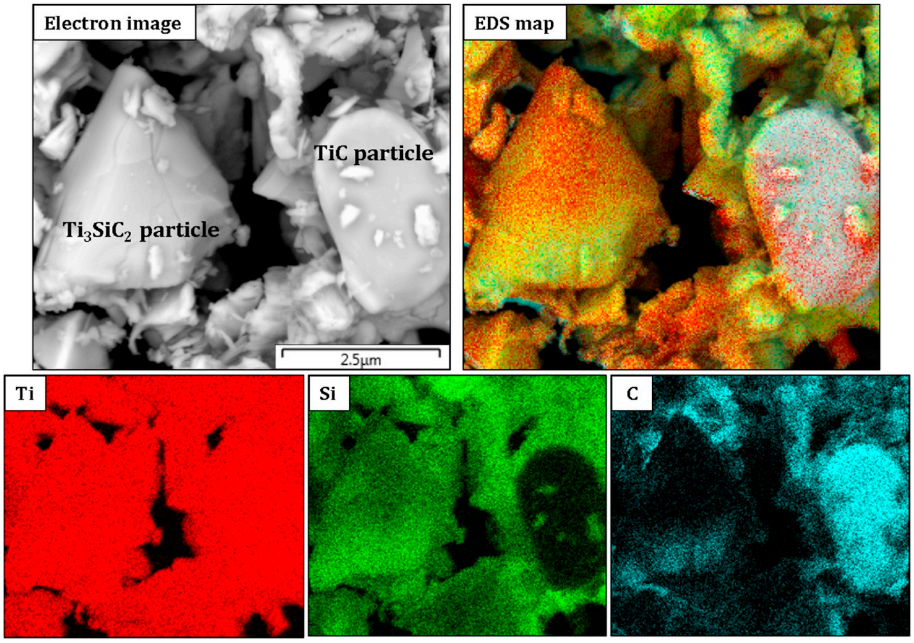

Fig. 3. EDS elemental mapping of the as-received Maxthal 312 (nominally-Ti$_3$SiC$_2$) prealloyed powder.

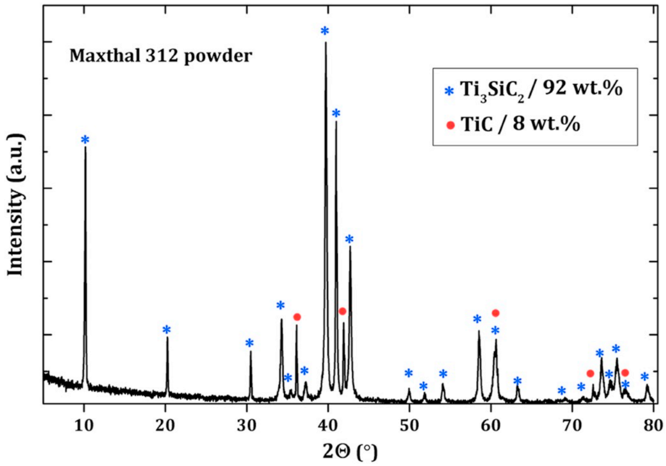

Fig. 4. XRD pattern of the as-received Maxthal 312 (nominally-Ti$_3$SiC$_2$) powder.

[36–39] are common methods, which produce bulk samples. Self-propagating High-temperature Synthesis (SHS) is also employed to produce a low density product, which is commonly crushed to a powder for secondary densification [40–43]. Ancillary phases such as TiC, TiSi$_2$ and SiC are often reported to coexist with Ti$_3$SiC$_2$ during synthesis [24,44,45]. However, the addition of aluminium [36,46] in a controlled amount in the starting powder mixture and/or over-stoichiometric starting powder mixture containing excess silicon [47] has been shown to reduce the ancillary phases produced.

The scope of this study is to investigate the formation of Ti$_3$SiC$_2$ via the prealloyed powder route and determine the reaction mechanism and the resulting microstructural evolution. It is noteworthy that synthesizing high purity Ti$_3$SiC$_2$ is not the aim of this work but instead to further contribute to the metallurgy of Ti$_3$SiC$_2$. Spark plasma sintering (SPS) technique is a synthesis and densification sintering process with the advantage of rapid heating rate and short sintering time. Most especially, the short sintering time is advantageous in suppressing grain growth [48] and the range of controllability of sintering parameters enables tailoring of the evolved microstructure.

2. Material and methods

Pre-reacted commercially available Ti$_3$SiC$_2$ powder (Maxthal 312 (nominally-Ti$_3$SiC$_2$); particle size 2 µm, Kanthal AB, Sweden) was used as starting powder. The composition of the as-received Maxthal 312 powder were 92 wt% Ti$_3$SiC$_2$ and 8 wt% TiC, respectively. The powder was initially cold-pressed in a graphite die (Ø = 20 mm) in between two graphite punches with the inner wall of the die and surface of the punch covered with graphite paper to isolate the powder from the die and punches. The die-powder-punch assembly was then wrapped with graphite felt to minimize possible heat dissipation during the synthesis and subsequently loaded into the SPS furnace unit (HP D 25; FCT Systeme GmbH, Rauenstein, Germany) as shown in Fig. 1. The consolidation was carried out at a requisite sintering temperature of 1400 °C with a hold time of 5 min, the heating rate was 100 °C/min whilst the load (54 MPa) was applied at room temperature and removed at the end of the dwell time. During the synthesis, the chamber was maintained under vacuum (10^{-2} Pa) and the temperature was controlled by a thermocouple that measured the temperature in the interior of the graphite punch. The sintering temperature was selected based on a preliminary test which ensured the bulk composition fell within a three-phase region, as purity of the bulk sample is not the scope of this work.

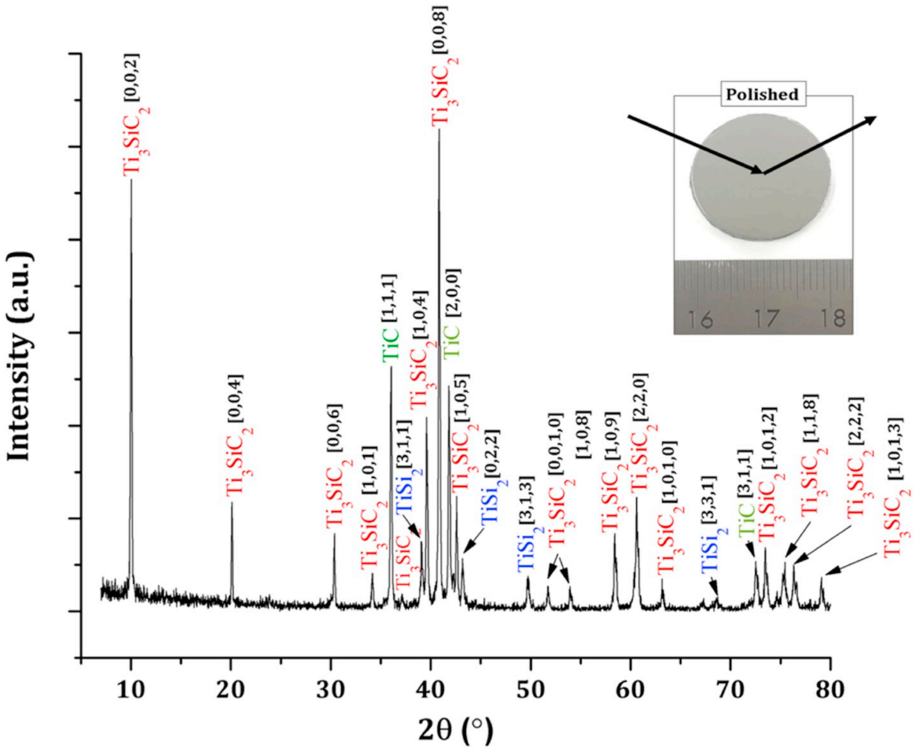

Fig. 5. XRD pattern of the synthesized sample after polishing. Inset shows the pattern was collected from the polished disc.

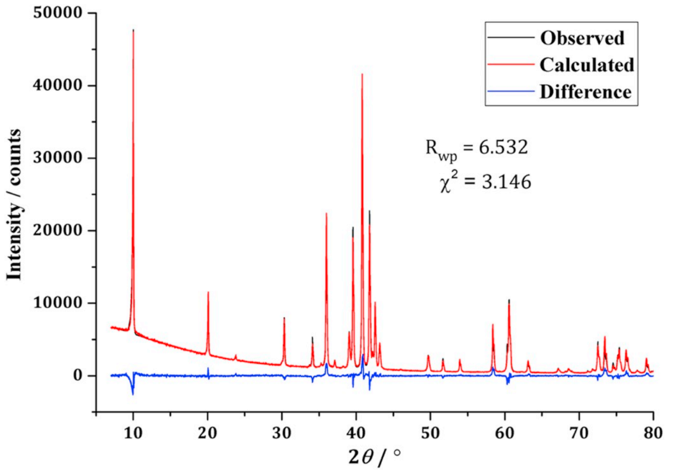

Fig. 6. Rietveld refinement of the XRD pattern of the bulk sample in 2Θ range from 5 to 80°.

2.1. Characterization

X-ray diffraction (XRD) patterns were obtained with a $\theta - 2\theta$ diffractometer (Bruker D2 Phaser, Germany) using Cu Kα radiation source in steps of 0.02° at 1 s/step. The surface layer of the as-sintered disc was removed by grinding prior to XRD analysis. Phase identification was performed using DIFFRAC EVA software suite whilst the phase quantification was obtained by Rietveld refinement (TOPAS) from the diffraction pattern collected in the 5–80° (2Θ) range using X'pert^3 diffractometer (Malvern Panalytical, UK). Microstructural evolution was investigated using scanning electron microscopy (SEM; Inspect F50, FEI The Netherlands) equipped with an EDS detector (Oxford Instruments X-Max/Aztec Nanoanalysis, UK) and transmission electron microscopy (TEM; Philips EM420/120 kV and JEOL JEM-F200/200 kV). TEM electron transparent samples from selected areas were prepared using a focused ion beam (FIB; FEI Helios NanoLab G3 UC, FEI company, The Netherlands). The Vickers hardness (HV) of bulk sample was measured using an indentation load of 19.6 N for 15 s (DuraScan G5 emcoTEST, Austria). The density of the bulk sample was measured (following mirror-like metallographic polishing down to 0.5 μm diamond paste) by the Archimedes' method in water at ambient conditions. Raman analysis was carried out ex-situ on the polished surface by employing a Si-calibrated inVia Raman spectrometer (Renishaw plc, UK) with an Ar laser (λ = 514.5 nm, laser output power 20 mW) and a 50x objective lens (spot size of 2 μm). In order to further understand the phase transformations and reaction mechanisms during synthesis, simultaneous thermal gravimetric analysis (TGA)-differential scanning calorimetry (DSC) experiment was conducted on the Maxthal 312 powder (Q600, TA Instruments) from 25 to 1500 °C in a high purity dynamic nitrogen atmosphere using Al_2O_3 crucible.

3. Results and discussion

3.1. Morphology of Maxthal 312 powder

The morphology of the as-received Maxthal 312 powder is shown in Figs. (2) and (3). Fig. 2 shows the characteristic lamellar nature of the

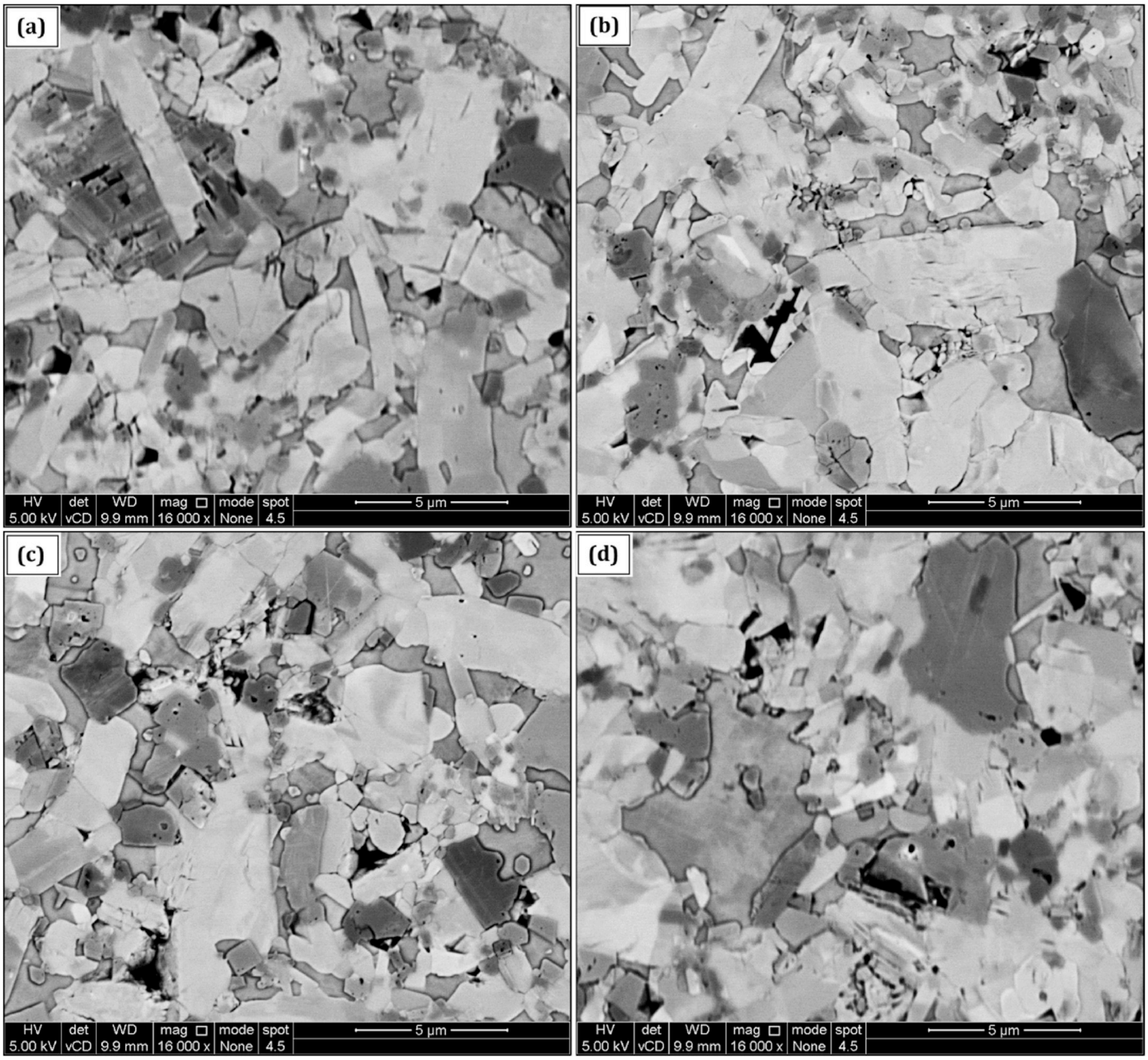

Fig. 7. Backscattered electron (BSE) images of the bulk sample produced by SPS using the Maxthal 312 powder. Note the homogenous dispersion of the in situ formed TiC in the Ti_3SiC_2 matrix.

Ti_3SiC_2 MAX phase compound, whilst Fig. 3 is an EDS elemental map which reveals the coexistence of TiC particle in the as-received prealloyed powder in the form of an ancillary.

3.2. Phase analysis and densification

X-ray diffractogram (XRD) from the as-received prealloyed Maxthal 312 powder confirming Ti_3SiC_2 as a major phase and some minor TiC intermetallic phase is shown in Fig. 4.

The XRD patterns showing the phase evolution of the bulk sample following spark plasma sintering of the prealloyed Maxthal 312 powder is shown in Fig. 5. It can be seen from the diffraction pattern that the bulk sample consists of three phases: Ti_3SiC_2, TiC and $TiSi_2$, respectively. In comparison to the as-received prealloyed powder X-ray diffraction pattern, additional peaks - especially two strong peaks at $2\Theta = 39^\circ$ and 43.2°, corresponding to $TiSi_2$ peaks evolved after synthesis.

Fig. 6 shows X-ray diffraction (XRD) pattern of the bulk sample ($2\Theta = 5^\circ$–80°) alongside Rietveld refinement of the pattern. The Rietveld refined parameters are $R_{wp} = 6.532$ and $\chi^2 = 3.146$, respectively. The bulk sample contained 51.8 wt% Ti_3SiC_2, 36.4 wt% TiC and 11.8 wt% $TiSi_2$, respectively. It is noteworthy that the refinement data showed strong preferred orientation in the 002 direction. This is in agreement with our earlier work which indicated preferred orientation of Ti_3SiC_2 along the pressing direction during the SPS synthesis [24]. The relative density of the polished disc was 99% upon taking into account the phase fraction of the constituent phases and their corresponding theoretical densities, respectively.

3.3. Microstructural evolution and EDS analysis

SEM backscattered electron (BSE) micrographs of the polished unetched bulk sample is shown in Fig. 7. According to the EDS analysis (Fig. 8), the bright phase is the Ti_3SiC_2 phase whilst the dark contrast is

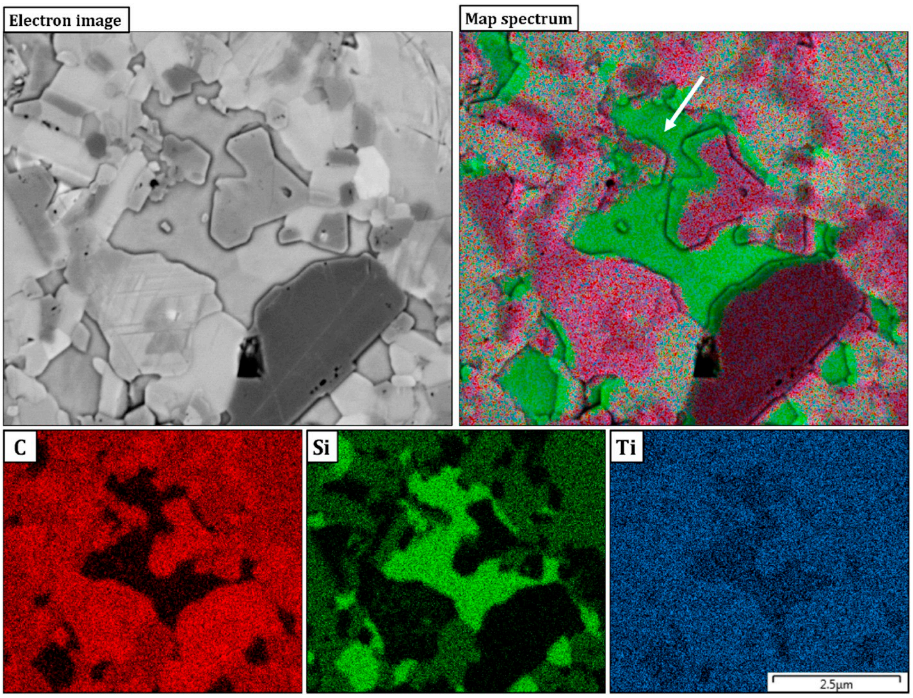

Fig. 8. Identification of particular phases in the bulk sample by EDS elemental map analysis.

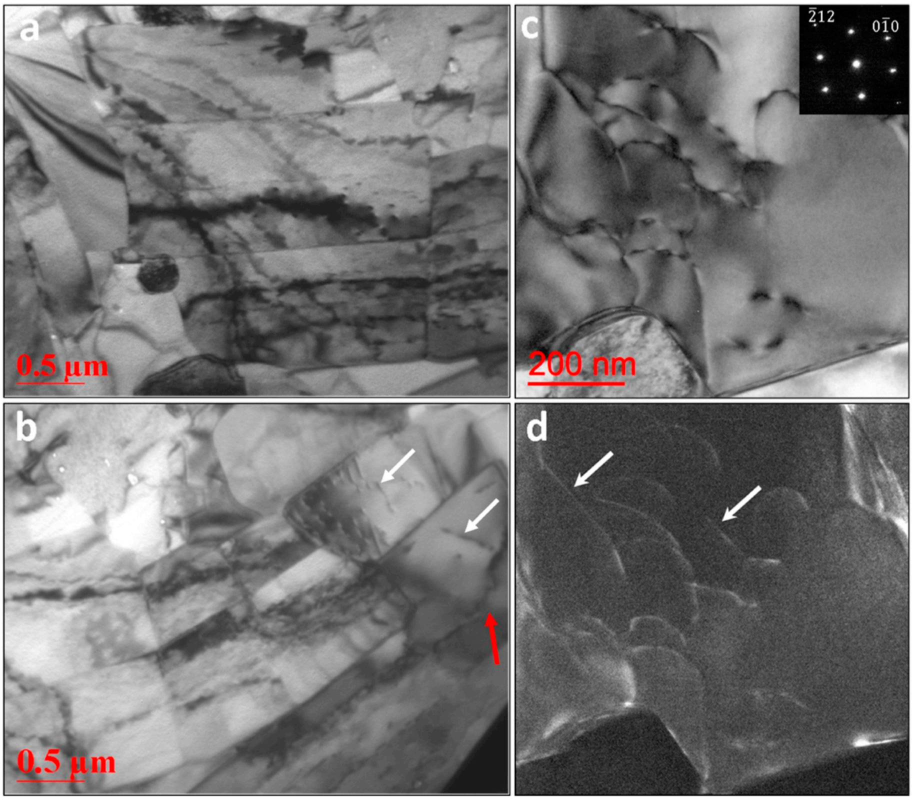

Fig. 9. (a) BF-TEM micrograph showing the plate-like morphology of the Ti_3SiC_2 grains, (b) BF-TEM micrograph showing evidence of basal plane slip (red arrow) and basal plane dislocation (white arrow), (c) BF-TEM image obtained from a Ti_3SiC_2 grain along the [101] direction and (d) DF-TEM image of dislocation shown in (c) imaging with $g = \bar{2}12$ (white arrows show edge-on basal plane dislocations). (For interpretation of the references to colour in this figure legend, the reader is referred to the Web version of this article.)

the TiC phase. Those with the medium contrast are the $TiSi_2$ liquid phase (white arrow in Fig. 8 map spectrum) - an intermediate eutectic liquid phase leading to the formation of Ti_3SiC_2 that has not been fully consumed [49]. According to Ref. [50,51], the reaction mechanism leading to the formation of Ti_3SiC_2 is a solid-liquid reaction partly due to the formation of Ti–Si eutectic liquid (eutectic temperature 1332 °C) and/or liquid Si formation (T_m of Si = 1414 °C).

Fig. 9 shows TEM images obtained from the bulk sample revealing an area containing the Ti_3SiC_2 grains. The plate-like morphology (Fig. 9(a)) typical of MAX phases can be seen alongside with evidence of basal plane dislocation (Fig. 9(b–d)) as reported elsewhere [52]. Basal plane dislocations play a key role during room-temperature

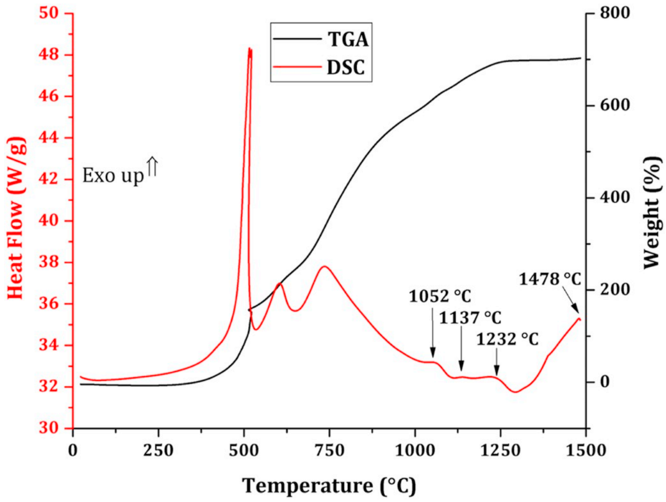

Fig. 10. Typical simultaneous thermogram of TGA/DSC of a Maxthal 312 (nominally-Ti_3SiC_2) powder.

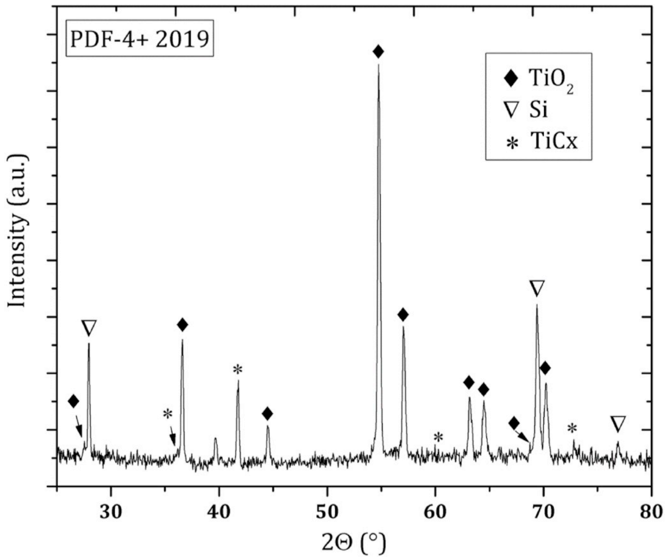

Fig. 12. X-ray (XRD) diffraction pattern of the decomposed powder after TGA/DSC thermal analysis.

deformation of MAX phases as they possess fewer than five slip systems needed for polycrystalline ductility [52,53]. The steps along the grain boundary (red arrow in Fig. 9(b)) is an evidence of slip along the basal planes [10].

3.4. Thermal behaviour of the Maxthal 312 powder

Fig. 10 shows the simultaneous DSC/TGA thermogram recorded during the heating of the Maxthal 312 powder at 20 °C/min from 40 to 1500 °C in flowing Ni. Exothermic peaks (518, 602 and 735 °C) corresponding to anatase and/or rutile TiO_2 layers were detected up to 900 °C. The observed mass increase in this temperature range is linked to the oxidation of titanium in agreement with a previous report [54]. The DSC curve further exhibited three broad overlapped exothermic peaks (1052, 1137 and 1232 °C) as the temperature is further increased. The temperature range of these exothermic peaks when compared to the SEM-EDS analysis revealing the phases in the bulk sample sintered to 1250 °C (Fig. 11), we can reasonable conclude that these peaks

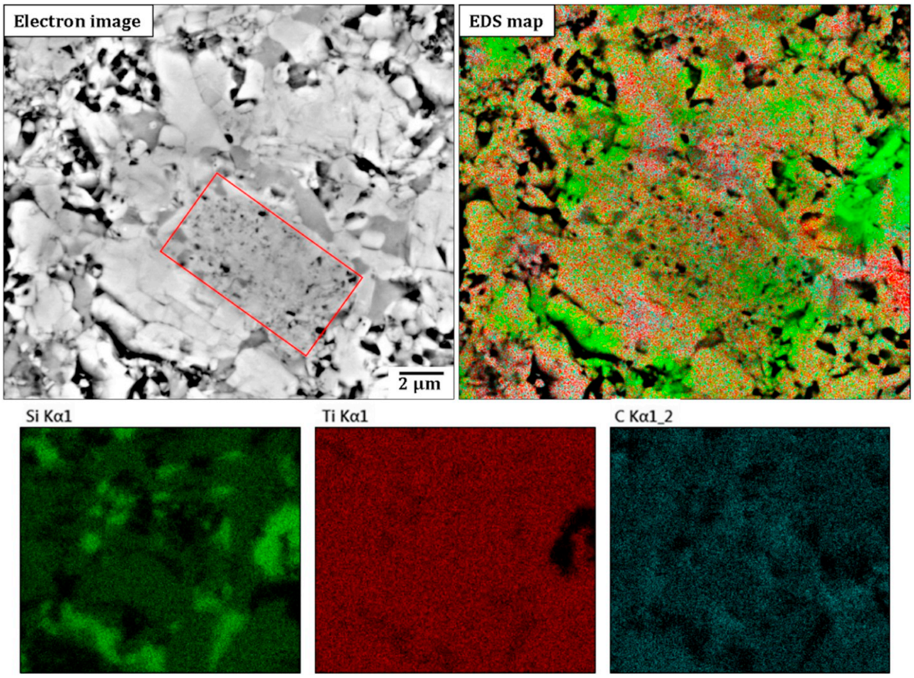

Fig. 11. EDS elemental map showing the evolution of phases in the bulk sample synthesized by SPS to 1250 °C. The highlighted section in the electron image (red rectangle) shows the growth of the Ti_3SiC_2 grains. (For interpretation of the references to colour in this figure legend, the reader is referred to the Web version of this article.)

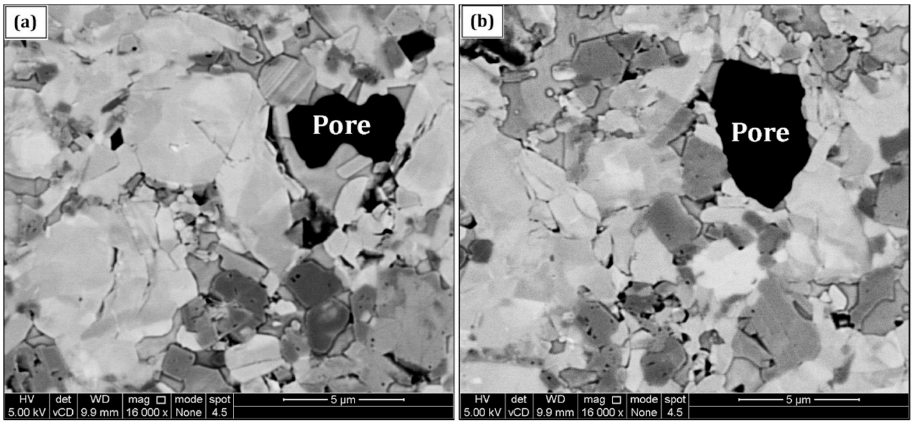

Fig. 13. Pore formation in Ti_3SiC_2 matrix owing to deintercalation of Si under high vacuum pressure.

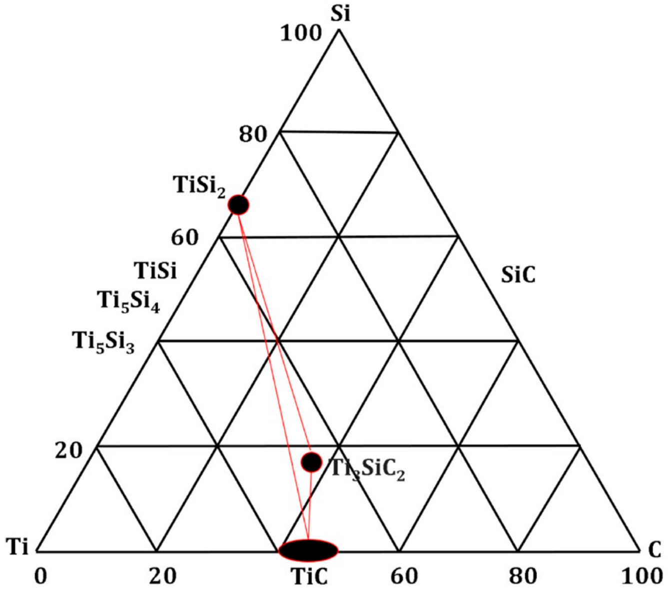

Fig. 14. Compositional diagram in the Ti–Si–C system. The three phases of interest in this work are highlighted using a triangle.

corresponds to the evolution of $TiSi_2$ and Ti_3SiC_2 phases. This is particularly true as the Ti–Si eutectic liquid will provide a direct route for the formation of Ti_3SiC_2 once the pre-existing TiC particles reacts with the Ti–Si liquid phase as proposed by Sato et al. [55] and Zhang et al. [56]. This conclusion is also in agreement with the thermogravimetric results obtained by Kero et al. [49,57], as well as observations in this work revealing the growth of Ti_3SiC_2 takes place within the Ti–Si liquid phase (electron image in Fig. 11). The last exothermic peak at 1478 °C may be attributed to TiC_x formation due to Si evaporation induced Ti_3SiC_2 decomposition as the temperature exceeds the melting point of Si (1414 °C). Fig. 12 shows the XRD pattern obtained from the decomposed Maxthal 312 powder following the thermogravimetric analysis. The phases in the decomposed powder (i.e., TiC_x, TiO_2 and Si) are in good agreement with the exothermic peaks during the thermal analysis.

3.5. Pore formation in Ti_3SiC_2

The pores formed during the synthesis of Ti_3SiC_2 such as those shown in Fig. 13 are derived from the following aspects: the original particle gap; interstitial pores left during the pressing procedure; lack of densification degree; generation of new phase in the sintering process; Si deintercalation linked to the high vacuum pressure during the SPS and/or vapourization during high temperature sintering (i.e., above the melting point of Si). The high vacuum pressure (about 10^{-3}Pa) during the SPS coupled with the high vapour pressure of silicon may have led to decomposition of Ti_3SiC_2 thus promoting pore formation via the outward diffusion of Si from the Ti_3SiC_2 grains. This is supported by observation reported elsewhere [58,59] and the hypothetical deintercalation reaction leading to pore formation given as follows [60]:

$$Ti_3SiC_2 \rightarrow 3TiC_{X=0.67} + Si(vap.)$$

This proposed loss of Si by deintercalation even at sintering temperature below the melting point of silicon (T_m = 1414 °C) contributes significantly to the loss of purity in the synthesized sample during the SPS. Investigators have often compensated for the loss of Si during vacuum sintering by silicon over-stoichiometry [47,61–63] (that is, deviation from 3:1:2 stoichiometric ratio for Ti:Si:C) in the starting mixtures to increase the conversion into Ti_3SiC_2. Another method involves the systematic addition of small amount Al in the starting powder mixture [64–66]. The increase in purity with aluminium addition is as follows: as aluminium has a relatively low melting point (660 °C), molten Al will promote the diffusion of both Ti and Si atoms thus expediting the formation of Ti_3SiC_2 via solid-liquid reaction at low temperature [67]; molten Al also acts as a deoxidation agent which promotes the synthesis of Ti_3SiC_2 [65]. It is worth mentioning that excessive Al may dilute the reactants or react with Ti to form Ti_3Al, thus compromising the phase-purity of Ti_3SiC_2.

On the other hand, pore formation may also result from possible carbon uptake from the graphite tooling (graphite paper/die/punch setup) and its subsequent reaction with Ti_3SiC_2 which will result in bulk compositional shift into a three-phase Ti_3SiC_2–TiC–$TiSi_2$ compositional triangle (Fig. 14) following the decomposition reaction thus [68]:

$$2Ti_3SiC_2 + C \rightarrow 5TiC_X + TiSi_2$$

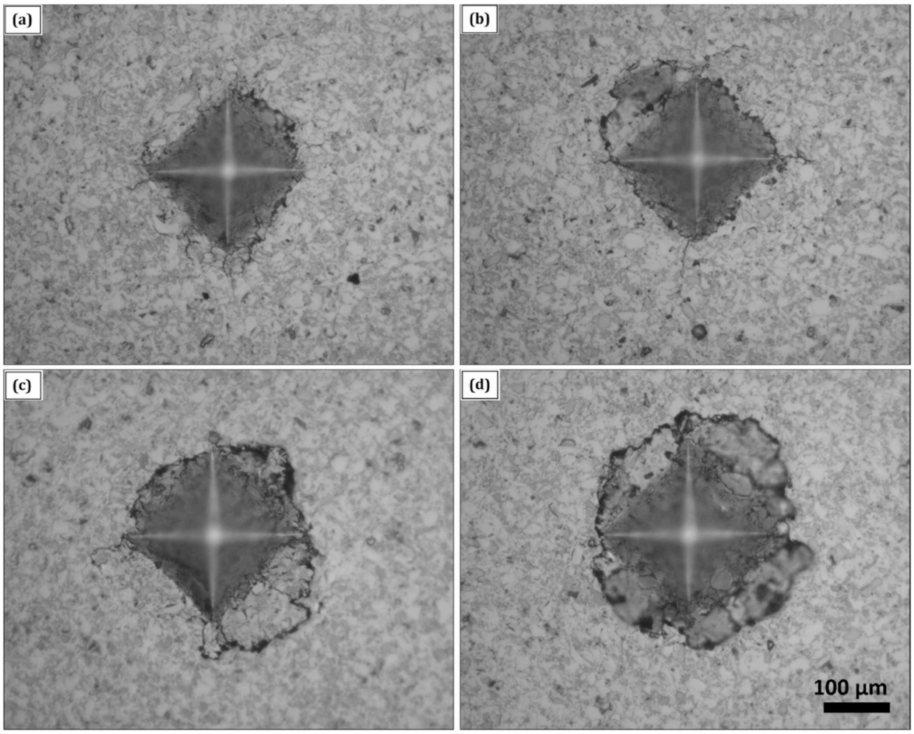

Fig. 15. Optical micrographs showing anisotropic deformation morphology following Vickers indentation.

3.6. Vickers-induced deformation microstructure

Vickers microhardness measured from the polished surface of the SPSed disc was ~5.8 GPa. This value is somewhat higher as compared to the intrinsic hardness of Ti_3SiC_2 reported to be about 4 GPa [12]. The higher hardness as compared to monolithic phase Ti_3SiC_2 may be associated to the finer microstructure introduced by SPS [61] as well as the presence of TiC ancillary in the synthesized sample. Optical micrographs (Fig. 15) obtained from the indents showed no sign of lateral cracks emanating from the indention diagonals as extensive grain pileups around the indents was operative. The ability of Ti_3SiC_2 to contain damage in limited area around the indents is a signature property of the damage tolerance capability reported in MAX phases [12,13,69,70]. Nonetheless, the extent of grain pileup – a microscale deformation mechanism owing to room-temperature plasticity [12] – varied as shown in Fig. 15(a–c) using the same indentation load. According Li et al. [71] asymmetry in the damage zone around indentation is linked to the anisotropic behaviour of Ti_3SiC_2. This is because favourably oriented grains parallel to the surface will deform by the glide of basal plane dislocations [72] to bring about grain push-outs in the vicinity of the indentation once the compressive stresses are released [12,71].

Fig. 16(a) shows the SEM micrographs obtained from the damage zones around the indentation prints on the bulk sample. No indentation-induced cracks were observed around the indentation diagonals as microdamage appears to be confined in the immediate vicinity of the indents - indicating that Ti_3SiC_2 is damage tolerant. However, the morphology of the piled grains around the indent further revealed evidence of additional micro-scale deformation mechanisms as shown in Fig. 16(b–d). The energy of an advancing crack appeared to have been consumed due to the plate-like nature of the Ti_3SiC_2 grains leading to diffuse microcracking as shown in Fig. 16(b). In addition to crack deflection, other micro-scale plasticity events such as, grain pull-out and delamination (Fig. 16(c)); grain buckling and cavitation (Fig. 16(d)) further render Ti_3SiC_2 damage tolerant [12,13]. It is noteworthy that the observed cavitation following indentation induced deformation is due to the lack of five independent slip systems needed for polycrystalline ductility in MAX phases [72,73].

An intriguing observation during the indentation is the evolution of amorphous-carbon films as shown by EDS elemental map analysis (Fig. 17) and Raman spectroscopy (Fig. 18). The evolution of amorphous carbon layer [74,75] following indentation scratch, as well as rutile phase of TiO_2 tribofilm [76] further highlights the intrinsic lubricity of Ti_3SiC_2 as reported elsewhere during tribological studies [21] and machining with cutting tools [9].

In order to clarify that the amorphous carbon films are indeed indentation-induced and not as a result of carburization from the graphite tooling employed during the SPS even though the surface of the bulk sample was polished down to 0.5 µm diamond paste, Raman spectrum was further collected from the as-synthesized surface (Fig. 19) and polished surface (Fig. 20) for validation. For the as-synthesized surface, Raman spectrum collected from the carburized surface corresponded to vibration mode of crystalline graphite [75]. The D/G intensity ratio (I_D/I_G) used as a graphitization index to monitor the deviation from the crystallinity further differentiates the graphitized layer to the amorphous carbon layer [75]. On the other hand, Raman spectrum collected

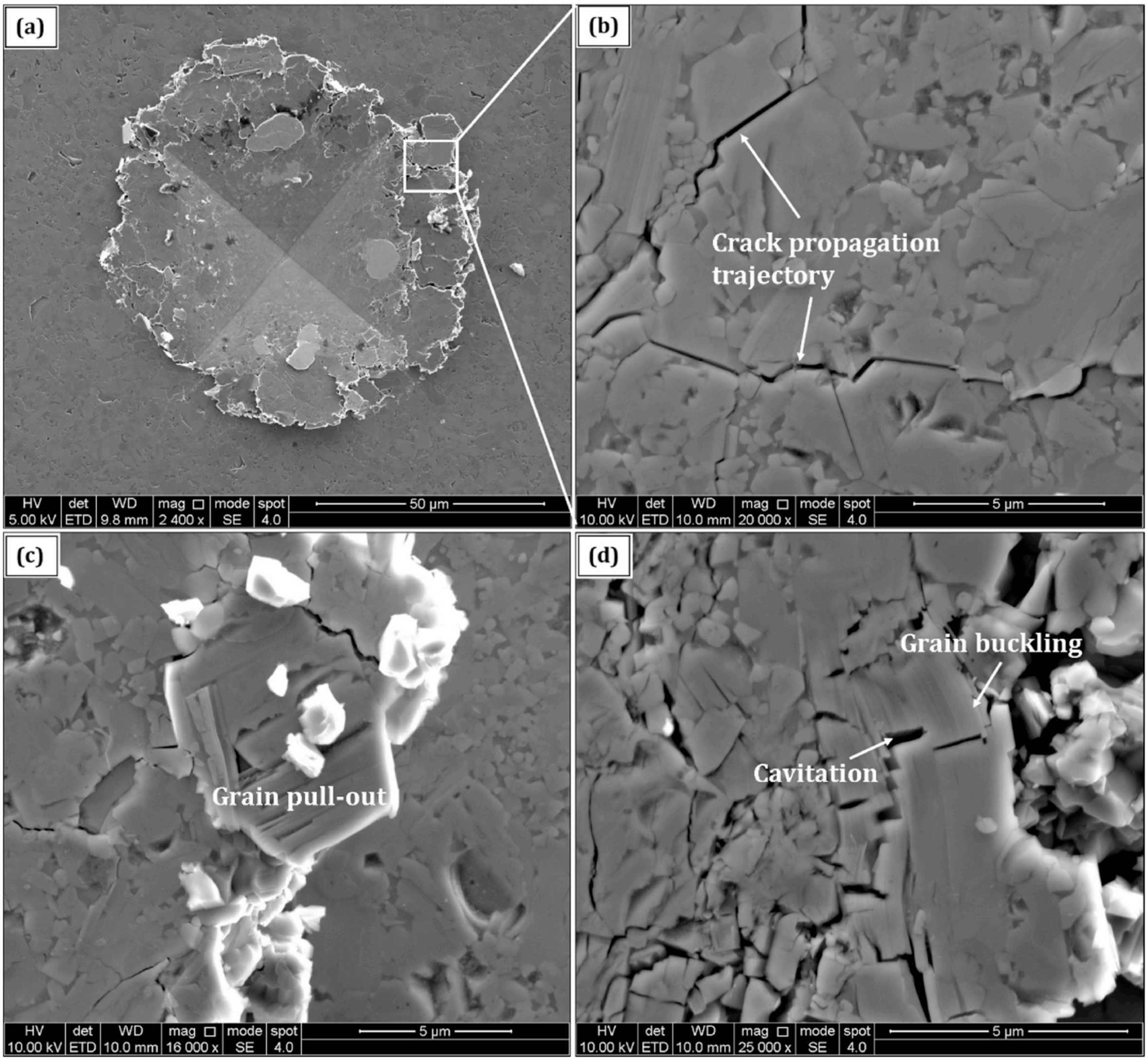

Fig. 16. (a) Scanning electron (SEM) micrographs revealing the morphology around the indent, (b) diffuse microcracking and (c–d) deformation micro-mechanisms in Ti_3SiC_2.

from the polished surface revealed vibrational modes corresponding to essentially Ti_3SiC_2 [77]. No evidence of non-stoichiometric TiC_X which possesses a Raman active mode which might have formed on the surface due to carburization was detected.

4. Microstructural and orientation relationship

An area from the bulk sample analysed by STEM-EDS is shown in Fig. 21(a–e). The EDS data confirmed the presence of all the three phases i.e. Ti_3SiC_2, TiC and $TiSi_2$. The Ti_3SiC_2 phase typically appears as elongated plate-like grains. The TiC and $TiSi_2$ phases are essentially defect-free, also, no cracking were observed at the Ti_3SiC_2–TiC interface due to coefficient of thermal expansion (CTE) mismatch between the two phases as reported elsewhere [78]. The lowest interfacial energy between TiC and Ti_3SiC_2 occurs when (111)TiC is parallel to 001(Ti_3SiC_2), therefore, there is an orientation relationship between TiC and Ti_3SiC_2 in the Ti–Si–C system [79,80]. Here, we observed similar orientation relationship between TiC and Ti_3SiC_2 grains. As illustrated in Fig. 21(f), (111)TiC is parallel to (001)Ti_3SiC_2 at the Ti_3SiC_2–TiC interface.

5. Conclusion

In this work, Ti_3SiC_2 was successfully fabricated in-situ by powder metallurgy spark plasma sintering using the MAX phase prealloyed starting powder. The reaction mechanism leading to the formation, decomposition and microstructural evolution of Ti_3SiC_2 was discussed, and the main conclusions are as follows:

1. The starting composition, carbon uptake and vacuum pressure during SPS plays a crucial role in high Ti_3SiC_2 conversion.
2. A starting powder mixture with excess silicon and deficient carbon

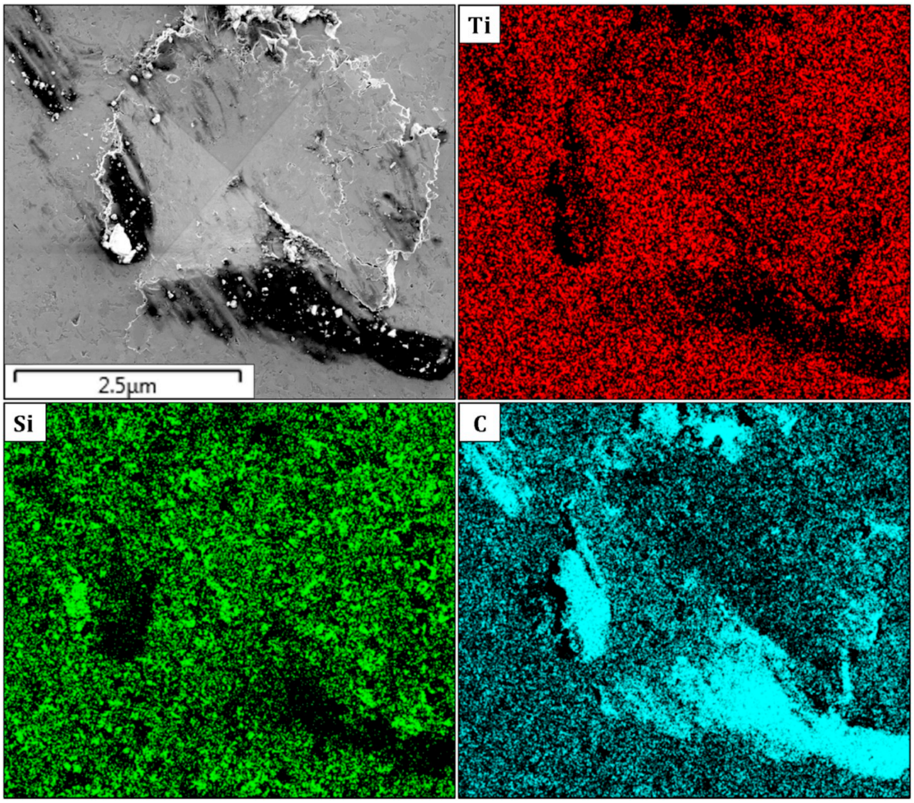

Fig. 17. EDS elemental map of the Vickers indentation print revealing evidence of amorphous carbon around the indent.

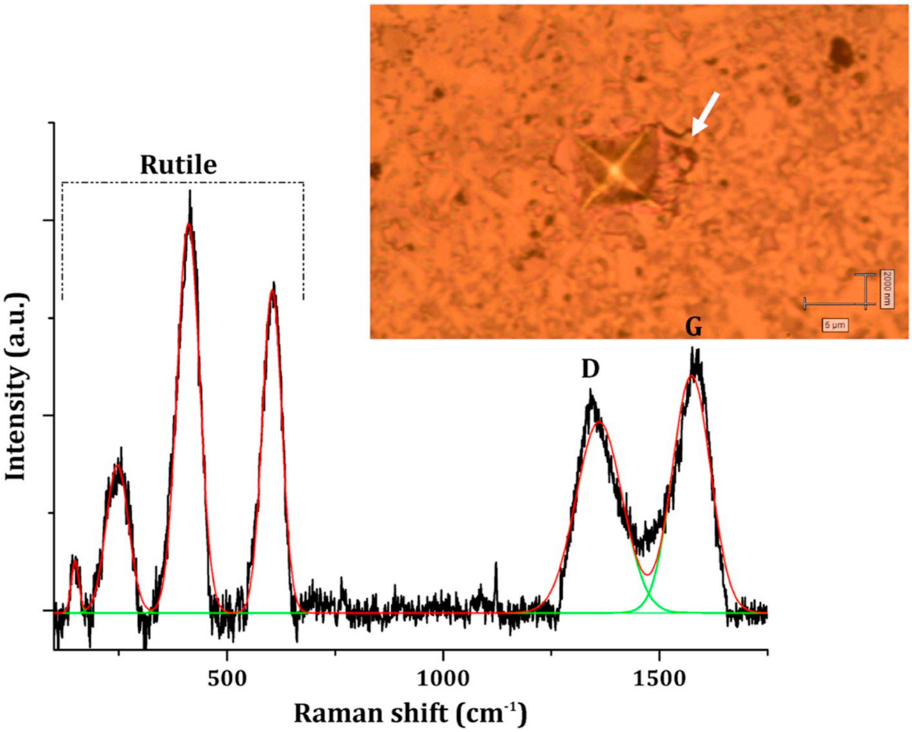

Fig. 18. Raman spectrum collected from the tribofilm region (white arrow) next to the indentation print revealing evidence of tribofilms (rutile (TiO_2) and D & G amorphous carbon Raman vibrational modes).

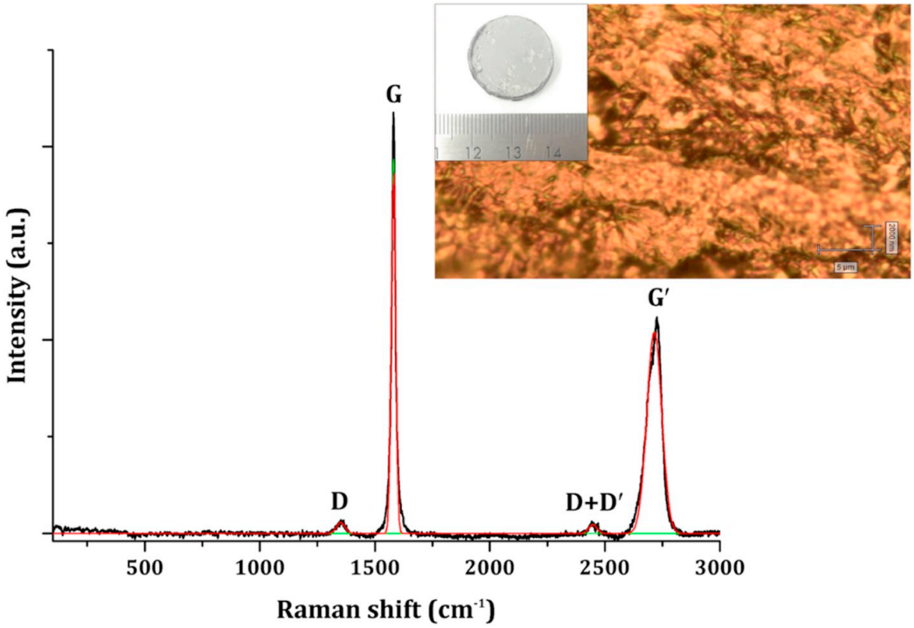

Fig. 19. Raman spectrum collected from the as-synthesized bulk sample surface after SPS. Inset shows the carburized surface where Raman spectrum was collected.

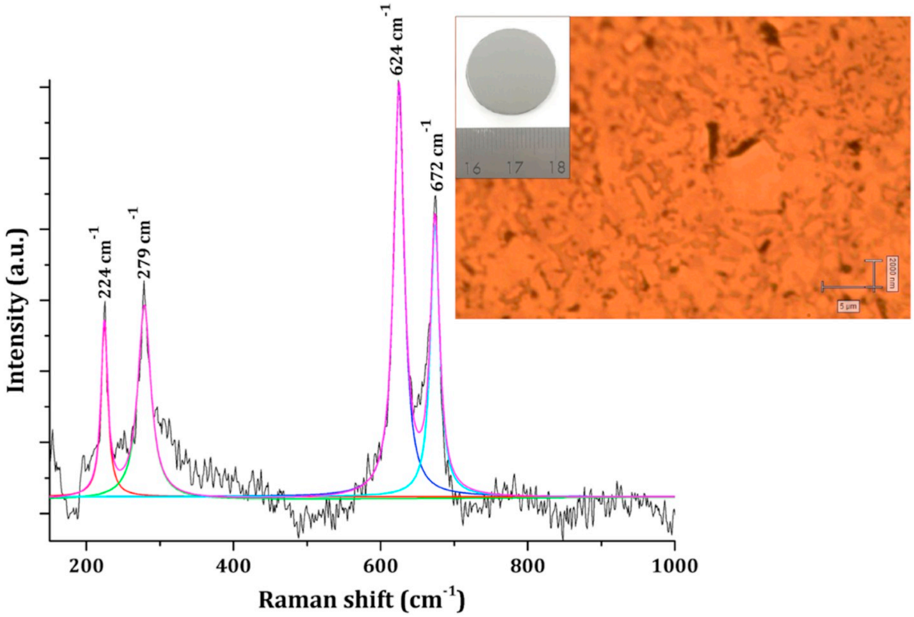

Fig. 20. Raman spectrum collected from the polished surface of the bulk sample. Inset shows the polished surface where the Raman spectrum was collected. Note stoichiometric TiC does not possess any Raman active modes.

(3Ti/(1 + x)Si/(1 - x)C) is needed to compensate for simultaneous Si-loss and carbon uptake, thus leading to high-purity Ti_3SiC_2. The use of boron nitride spray may further help mitigate against carburization from graphite paper.

3. Energy absorbing diffuse microcracking and deformation-induced micromechanisms via basal plane slip renders Ti_3SiC_2 tough and damage tolerant.
4. Ti_3SiC_2 is self-lubricating due to intrinsic rutile and amorphous carbon tribofilm formation.
5. The Maxthal 312 prealloyed starting powder route is suitable in the synthesis of Ti_3SiC_2 if purity of the bulk sample is not of interest such as in the synthesis of MAX phase composites. This is because Si-evaporation will push the overall bulk composition into a two-phase (Ti_3SiC_2–TiC) or three-phase (Ti_3SiC_2–$TiSi_2$–TiC) region with ancillary phases homogeneously distributed in the Ti_3SiC_2 matrix as they formed in-situ and not added as a second phase, thus a reinforcement the MAX phase compound is expected.

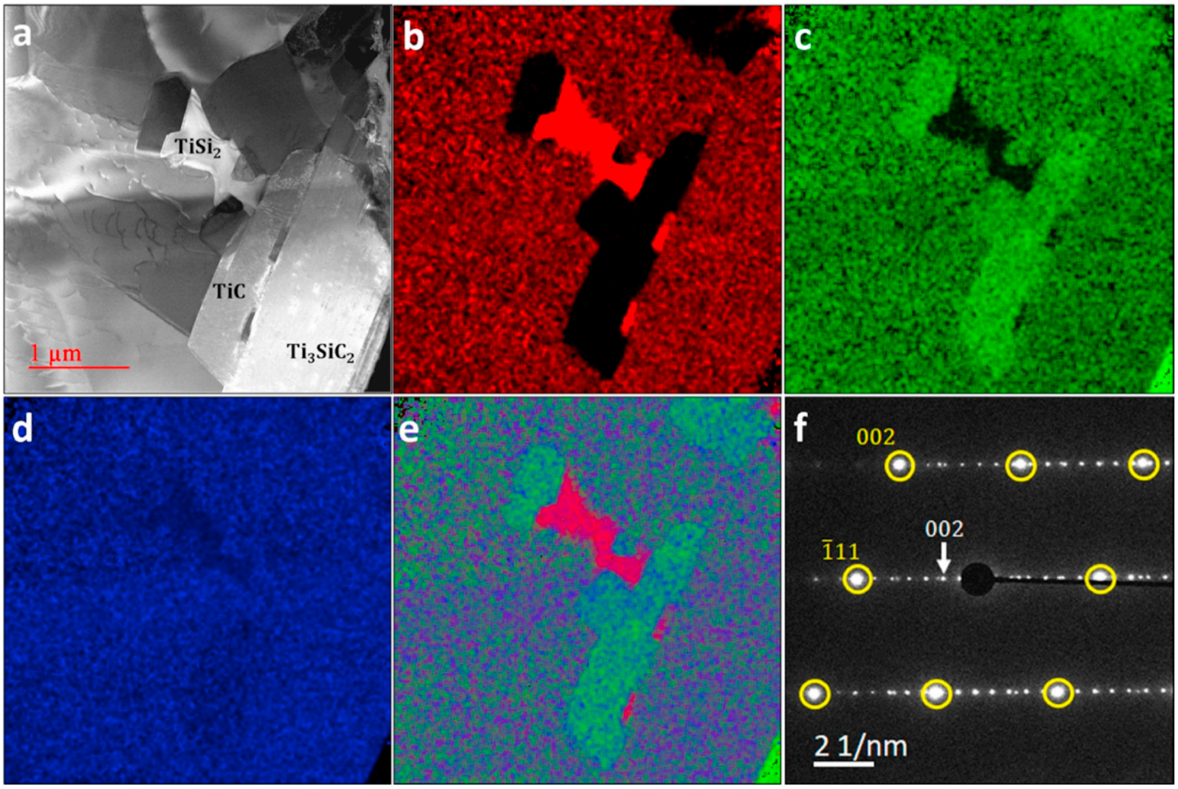

Fig. 21. (a) ADF STEM micrograph obtained from the bulk sample, (b) Si, (c) C and (d) Ti EDS elemental maps from (a). (e) Shows overlay maps of Ti, Si, and C. (f) SAD pattern obtained from the interface of TiC and Ti_3SiC_2 grains where [110]TiC and [100]Ti_3SiC_2 are parallel to the electron beam direction (SAD has been rotated ~ 22° counter-clockwise with regard to (a)). Diffraction spots associated to the TiC grain are highlighted using yellow circles. (For interpretation of the references to colour in this figure legend, the reader is referred to the Web version of this article.)

Declaration of competing interest

We declare no conflict of interest in this work.

References

[1] M. Sokol, et al., Big Questions in Chemistry - on the Chemical Diversity of the MAX Phases, (2019).

[2] H. Fashandi, et al., Synthesis of Ti3AuC2, Ti3Au2C2 and Ti3IrC2 by noble metal substitution reaction in Ti3SiC2 for high-temperature-stable Ohmic contacts to SiC, Nat. Mater. 16 (2017) 814.

[3] H. Fashandi, et al., Ti2Au2C and Ti3Au2C2 formed by solid state reaction of gold with Ti2AlC and Ti3AlC2, Chem. Commun. 53 (69) (2017) 9554–9557.

[4] M. Naguib, et al., Two-dimensional nanocrystals produced by exfoliation of Ti3AlC2, Adv. Mater. 23 (37) (2011) 4248–4253.

[5] B. Anasori, M.R. Lukatskaya, Y. Gogotsi, 2D metal carbides and nitrides (MXenes) for energy storage, Nature Reviews Materials 2 (2) (2017) 16098.

[6] M. Naguib, et al., Two-dimensional transition metal carbides, ACS Nano 6 (2) (2012) 1322–1331.

[7] J. Wang, et al., Discovery of hexagonal ternary phase Ti2InB2 and its evolution to layered boride TiB, Nat. Commun. 10 (1) (2019) 2284.

[8] M. Dahlqvist, B. Alling, J. Rosén, Stability trends of MAX phases from first principles, Phys. Rev. B 81 (2010) 220102.

[9] M.W. Barsoum, T. El-Raghy, The MAX Phases: unique New Carbide and Nitride Materials: ternary ceramics turn out to be surprisingly soft and machinable, yet also heat-tolerant, strong and lightweight, Am. Sci. 89 (4) (2001) 334–343.

[10] M.W. Barsoum, MAX Phases : Properties of Machinable Ternary Carbides and Nitrides, Wiley-VCH Verlag GmbH & Co. KGaA, Weinheim, Germany, 2013 2013.

[11] S. Hwang, et al., Machinability of Ti3SiC2 with layered structure synthesized by hot pressing mixture of TiCx and Si powder, J. Eur. Ceram. Soc. 32 (12) (2012) 3493–3500.

[12] T. El-Raghy, et al., Damage mechanisms around hardness indentations in Ti3SiC2, J. Am. Ceram. Soc. 80 (2) (1997) 513–516.

[13] B.J. Kooi, et al., Ti 3SiC 2: a damage tolerant ceramic studied with nano-indentations and transmission electron microscopy, Acta Mater. 51 (10) (2003) 2859–2872.

[14] I.M. Low, Vickers contact damage of micro-layered Ti3SiC2, J. Eur. Ceram. Soc. 18 (6) (1998) 709–713.

[15] D.J. Tallman, et al., Effect of neutron irradiation on select MAX phases, Acta Mater. 85 (2015) 132–143.

[16] Q. Huang, et al., Irradiation resistance of MAX phases Ti3SiC2 and Ti3AlC2: characterization and comparison, J. Nucl. Mater. 465 (2015) 640–647.

[17] C. Wang, et al., Irradiation-induced structural transitions in Ti2AlC, Acta Mater. 98 (2015) 197–205.

[18] J. Xiao, et al., Investigations on radiation tolerance of Mn + 1AXn phases: study of Ti3SiC2, Ti3AlC2, Cr2AlC, Cr2GeC, Ti2AlC, and Ti2AlN, J. Am. Ceram. Soc. 98 (4) (2015) 1323–1331.

[19] T. Lapauw, et al., Interaction of Mn + 1AXn phases with oxygen-poor, static and fast-flowing liquid lead-bismuth eutectic, J. Nucl. Mater. 520 (2019) 258–272.

[20] K. Lambrinou, T. Lapauw, A. Jianu, A. Weisenburger, J. Ejenstam, P. Szakálos, J. Vleugels, Corrosion-resistant ternary carbides for use in heavy liquid metal coolants, Ceram. Eng. Sci. Proc. 36 (7) (2016) 19–34.

[21] C. Magnus, J. Sharp, W.M. Rainforth, The lubricating properties of spark plasma sintered (SPS) Ti3SiC2 MAX phase compound and composite, Tribol. Trans. (2019) 1–14.

[22] S. Gupta, M.W. Barsoum, On the tribology of the MAX phases and their composites during dry sliding: a review, Wear 271 (9–10) (2011) 1878–1894.

[23] C. Magnus, et al., Microstructural evolution and wear mechanism of Ti3AlC2 – Ti2AlC dual MAX phase composite consolidated by spark plasma sintering (SPS), Wear 438–439 (2019) 203013.

[24] C. Magnus, W.M. Rainforth, Spark plasma sintering (SPS) synthesis and tribological behaviour of MAX phase composite of the family Tin + 1SiCn (n = 2), Wear 438–439 (2019) 203062.

[25] A. Crisan, O. Crisan, Low-temperature formation of 312 phase in Ti-Si-C ternary compound, Digest Journal of Nanomaterials and Biostructures 13 (2018) 155–162.

[26] J.M. Córdoba, et al., Synthesis of Ti3SiC2 powders: reaction mechanism, J. Am. Ceram. Soc. 90 (3) (2007) 825–830.

[27] Z.M. Sun, Progress in research and development on MAX phases: a family of layered ternary compounds, Int. Mater. Rev. 56 (3) (2011) 143–166.

[28] I.M. Low, W.K. Pang, Thermal stability of MAX phases, Key Eng. Mater. 617 (2014) 153–158.

[29] I.-M. Low, An overview of parameters controlling the decomposition and degradation of Ti-based M(n + 1)AX(n) phases, Materials 12 (3) (2019) 473.

[30] S.P. Munagala, MAX phases: new class of carbides and nitrides for aerospace structural applications, in: N.E. Prasad, R.J.H. Wanhill (Eds.), Aerospace Materials and Material Technologies : Volume 1: Aerospace Materials, Springer Singapore, Singapore, 2017, pp. 455–465.

[31] J. Zhang, et al., Microstructure and properties of Ti3SiC2/SiC nanocomposites fabricated by spark plasma sintering, Compos. Sci. Technol. 68 (2008) 499–505.

[32] J. Zhang, et al., Effect of TiC content on the microstructure and properties of Ti3SiC2–TiC composites in situ fabricated by spark plasma sintering, Materials Science and Engineering: A 487 (1–2) (2008) 137–143.

[33] N.V. Tzenov, M.W. Barsoum, Synthesis and characterization of Ti3AlC2, J. Am. Ceram. Soc. 83 (4) (2000) 825–832.

[34] K. Tang, et al., An X-ray diffraction study of the texture of Ti 3SiC 2 fabricated by hot pressing, J. Eur. Ceram. Soc. 21 (2001) 617–620.

[35] M.W. Barsoum, T. El-Raghy, Synthesis and characterization of a remarkable

ceramic: Ti3SiC2, J. Am. Ceram. Soc. 79 (7) (1996) 1953–1956.
[36] J. Zhang, et al., Fabrication of high purity Ti3SiC2 from Ti/Si/C with the aids of Al by spark plasma sintering, J. Alloys Compd. 437 (1–2) (2007) 203–207.
[37] W.B. Zhou, B.C. Mei, J.Q. Zhu, Fabrication of high-purity ternary carbide Ti3SiC2 by spark plasma sintering technique, Mater. Lett. 59 (12) (2005) 1547–1551.
[38] T. Lapauw, et al., A new method to texture dense Mn + 1AXn ceramics by spark plasma deformation, Scripta Mater. 111 (Supplement C) (2016) 98–101.
[39] N.C. Ghosh, S.P. Harimkar, K. Kalkan, R. Singh (Eds.), Synthesis and Tribological Characterization of In-Situ Spark Plasma Sintered Ti3SiC2 and Ti3SiC2-Tic Composites, 2012.
[40] M.A. El Saeed, F.A. Deorsola, R.M. Rashad, Optimization of the Ti3SiC2 MAX phase synthesis, Int. J. Refract. Metals Hard Mater. 35 (2012) 127–131.
[41] V. Gauthier, et al., Self-propagating high-temperature synthesis of Ti3SiC2: study of the reaction mechanisms by time-resolved X-ray diffraction and infrared thermography, J. Am. Ceram. Soc. 89 (2006) 2899–2907.
[42] F. Meng, B. Liang, M. Wang, Investigation of formation mechanism of Ti3SiC2 by self-propagating high-temperature synthesis, Int. J. Refract. Metals Hard Mater. 41 (2013) 152–161.
[43] Y. Khoptiar, I. Gotman, Synthesis of dense Ti3SiC2-based ceramics by thermal explosion under pressure, J. Eur. Ceram. Soc. 23 (1) (2003) 47–53.
[44] W.K. Pang, et al., 15 - phase and thermal stability in Ti3SiC2 and Ti3SiC2/TiC/TiSi2 systems, Advances in Science and Technology of Mn + 1axn Phases, Woodhead Publishing, 2012, pp. 389–413.
[45] Z.F. Zhang, et al., Application of pulse discharge sintering (PDS) technique to rapid synthesis of Ti3SiC2 from Ti/Si/C powders, J. Eur. Ceram. Soc. 22 (16) (2002) 2957–2961.
[46] B. Xu, et al., Synthesis of single-phase Ti3SiC2 from coarse elemental powders and the effects of excess Al, Ceram. Int. 45 (1) (2019) 948–953.
[47] H. Foratirad, H. Baharvandi, M.G. Maraghe, Effect of excess silicon content on the formation of nano-layered Ti3SiC2 ceramic via infiltration of TiC preforms, J. Eur. Ceram. Soc. 37 (2) (2017) 451–457.
[48] C. Qin, et al., Microstructure characterization and mechanical properties of TiSi2-SiC-Ti3SiC2 composites prepared by spark plasma sintering, 47 (2006) 845–848.
[49] I. Kero, R. Tegman, M.-L. Antti, Phase reactions associated with the formation of Ti3SiC2 from TiC/Si powders, Ceram. Int. 37 (7) (2011) 2615–2619.
[50] X. Wang, Y. Zhou, Solid-liquid reaction synthesis and simultaneous densification of polycrystalline Ti 2 AlC, Zeitschrift fuer Metallkunde/Materials Research and Advanced Techniques 93 (2002) 66–71.
[51] X. Wang, Y. Zhou, Solid–liquid reaction synthesis of layered machinable Ti3AlC2 ceramic, J. Mater. Chem. 12 (3) (2002) 455–460.
[52] A. Guitton, et al., Evidence of dislocation cross-slip in MAX phase deformed at high temperature, Sci. Rep. 4 (2014) 6358-6358.
[53] L. Farber, et al., Dislocations and stacking faults in Ti3SiC2, J. Am. Ceram. Soc. 81 (2005) 1677–1681.
[54] X.H. Wang, Y.C. Zhou, Oxidation behavior of Ti3AlC2 powders in flowing air, J. Mater. Chem. 12 (9) (2002) 2781–2785.
[55] F. Sato, J. Li, R. Watanabe, Reaction Synthesis of Ti3SiC2 from Mixture of Elemental Powders vol. 41, (2000), pp. 605–608.
[56] Z.-F. Zhang, et al., A new synthesis reaction of Ti3SiC2 from Ti/TiSi2/TiC powder mixtures through pulse discharge sintering (PDS) technique, Material Research Innovations 5 (3) (2002) 185–189.
[57] I. Kero, M.-L. Antti, M. Odén, Synthesis of Ti3SiC2 by Reaction of TiC and Si Powders, (2009), pp. 21–30.
[58] H. Li, et al., Synthesis of Ti3SiC2 by pressureless sintering of the elemental powders in vacuum, Mater. Lett. 58 (11) (2004) 1741–1744.
[59] J.T. Li, Y. Miyamoto, Fabrication of monolithic Ti3SiC2 ceramic through reactive sintering of Ti/Si/2TiC, J. Mater. Synth. Process. 7 (2) (1999) 91–96.
[60] C. Racault, F. Langlais, R. Naslain, Solid-state synthesis and characterization of the ternary phase Ti3SiC2, J. Mater. Sci. 29 (13) (1994) 3384–3392.
[61] A. Pourebrahim, et al., Low temperature synthesis of high-purity Ti3SiC2 via additional Si through spark plasma sintering, J. Alloys Compd. 789 (2019) 313–322.
[62] M.J. Abu, J.J. Mohamed, Z.A. Ahmad, Effect of excess silicon on the formation of Ti3SiC2 using free Ti/Si/C powders synthesized via arc melting, ISRN Ceramics (2012) 10 2012.
[63] Z.F. Zhang, et al., Effects of sintering temperature and Si content on the purity of Ti3SiC2 synthesized from Ti/Si/TiC powders, J. Alloys Compd. 352 (1) (2003) 283–289.
[64] A. Pourebrahim, et al., Effect of aluminum addition on the densification behavior and mechanical properties of synthesized high-purity nano-laminated Ti3SiC2 through spark plasma sintering, J. Alloys Compd. 730 (2018) 408–416.
[65] Y. Zou, et al., Effect of Al addition on low-temperature synthesis of Ti3SiC2 powder, J. Alloys Compd. 461 (1–2) (2008) 579–584.
[66] Z. Jiaoqun, M. Bingchu, Effect of aluminum on synthesis of Ti3SiC2 by spark plasma sintering (SPS) from elemental powders, J. Mater. Synth. Process. 10 (6) (2002) 353–358.
[67] J.O. Zhu, et al., Effect of aluminum on the reaction synthesis of ternary carbide Ti3SiC2, Scripta Mater. 49 (7) (2003) 693–697.
[68] T. El-Raghy, M.W. Barsoum, Diffusion kinetics of the carburization and silicidation of Ti3SiC2, J. Appl. Phys. 83 (1) (1998) 112–119.
[69] Z.F. Zhang, et al., Micron-scale deformation and damage mechanisms of Ti3SiC2 crystals induced by indentation, Adv. Eng. Mater. 6 (12) (2004) 980–983.
[70] A. Murugaiah, et al., Spherical nanoindentations and kink bands in Ti3SiC2, J. Mater. Res. 19 (4) (2011) 1139–1148.
[71] S.B. Li, J.X. Xie, L.T. Zhang, L.F. Cheng, Synthesis and some properties of Ti3SiC2 by hot pressing of Ti, Si and C powders Part 2 – mechanical and other properties of Ti3SiC2, Mater. Sci. Technol. 21 (9) (2005) 1054–1058.
[72] M. Barsoum, M. Radovic, Mechanical Properties of the MAX Phases vol. 41, (2011), pp. 195–227.
[73] M.W. Barsoum, L. Farber, T. El-Raghy, Dislocations, kink bands, and room-temperature plasticity of Ti3SiC2, Metall. Mater. Trans. 30 (7) (1999) 1727–1738.
[74] F. Tuinstra, J.L. Koenig, Raman spectrum of graphite, J. Chem. Phys. 53 (3) (1970) 1126–1130.
[75] S. Santangelo, et al., Evaluation of crystalline perfection degree of multi-walled carbon nanotubes: correlations between thermal kinetic analysis and micro-Raman spectroscopy, J. Raman Spectrosc. 42 (4) (2011) 593–602.
[76] S. Challagulla, et al., Structure sensitive photocatalytic reduction of nitroarenes over TiO_2, Sci. Rep. 7 (2017).
[77] M. Amer, et al., The Raman spectrum of Ti3SiC2, J. Appl. Phys. 84 (10) (1998) 5817–5819.
[78] A. Dmitruk, et al., Development of pore-free Ti-Si-C MAX/Al-Si composite materials manufactured by squeeze casting infiltration, J. Mater. Eng. Perform. 28 (2019) 6248–6257.
[79] K. Tang, et al., A study on the orientation relationship between Ti3SiC2 and TiC grains, Mater. Lett. 57 (1) (2002) 106–109.
[80] Z.J. Lin, et al., Microstructural relationship between compounds in the Ti–Si–C system, Scripta Mater. 55 (2006) 445–448.

Paper C

Spark plasma sintering (SPS) synthesis and tribological behaviour of MAX phase composite of the family $Ti_{n+1}SiC_n$ (n = 2)

Wear 438–439 (2019) 203062

Contents lists available at ScienceDirect

Wear

journal homepage: http://www.elsevier.com/locate/wear

Spark plasma sintering (SPS) synthesis and tribological behaviour of MAX phase composite of the family $Ti_{n+1}SiC_n$ (n = 2)

Carl Magnus, William M. Rainforth *

Department of Materials Science and Engineering, The University of Sheffield, Mappin Street, Sheffield, S1 3JD, UK

ARTICLE INFO

Keywords:
MAX phases
MAX phase-composite
Decomposition
Dry sliding friction
Deformation
Tribofilms
Frictional heating

ABSTRACT

In this work we report on the spark plasma sintering (SPS) synthesis of Maxthal 312 (nominally-Ti_3SiC_2 but containing ancillary TiC_X) and Maxthal 312-TiC composite as well as their dry sliding room-temperature tribological behaviour. The sintering procedure was further investigated to elucidate the decomposition of Ti_3SiC_2 by replicating the carbon-rich SPS sintering environment using DSC-TG analysis on the Maxthal 312 powder carried out in a graphite crucible. In the SPSed bulk products, Ti_3SiC_2 and TiC_X were the major phases in the sintered Maxthal 312 disc whilst Ti_3SiC_2 and (TiC_X + TiC) were the major phases in the sintered Maxthal 312-TiC composite disc. In addition, some traces of the compulsory intermediate phase ($TiSi_2$) that has not been fully consumed coexisted in relatively small amounts in both bulk samples. Reconciling the SPS synthesis and the DSC-TG analysis, it appears that the formation of TiC_X is attributed mainly to the intrinsic decomposition occurring at temperature above 1350 °C or partly due to the graphite paper used to wrap the powder during the SPS synthesis. Rotary dry sliding tribological behaviour of the sintered discs was then subsequently investigated using Al_2O_3 as a counterface at room temperature. The incorporation of TiC into the Ti_3SiC_2 matrix as well as the in-situ TiC_X formed in the matrix during synthesis appears to improve the tribological behaviour of Ti_3SiC_2 for the tested conditions.

1. Introduction

A family of compounds with chemistry $M_{N+1}AX_N$ known as MAX-phases is emblematic of a class of inherently nanolaminated layered ternary carbides and nitrides crystallizing in the hexagonal crystal system with space group $P6_3/mmc$, where M is an early transition metal, A is an A-group element, X is either C or N [1]. *N* can be 1, 2 or 3 which gives 211, 312 and 413 (Fig. 1) as possible stoichiometries [2,3] with higher *N*-order MAX phases reported recently [4]. A unique feature of these phases is their signature hexagonal layered structure comprising of A and X atoms occupying the interstitial sites between the M atoms [5]. These laminated structures are composed of M – X bonds which possess a combination of ionic-covalent-metallic characteristics whilst the M – A bonds are predominantly metallic in nature. These renders their properties anisotropic and thus they exhibit both metallic and ceramic properties [6,7].

There has been a continuous growing interest in MAX phases most notably because of their unique set of metal and ceramic properties which makes them extraordinarily promising for a range of applications [9]. Like ceramics, they possess high strength, high melting point and thermal stability, as well as good oxidation resistance especially the Al-containing MAX phases [10]. Similar to metals, they are endowed with high thermal and electrical conductivities, damage tolerance, resistant to thermal shock, fatigue resistance and machinability [7,10–13]. They are therefore being considered for potential tribological applications in areas such as the following: (i) electrical contacts owing to their self-lubricity and high electrical conductivity [14]; (ii) applications in high-temperature gas-cooled reactors (HTRs)- as they possess high temperature and radiation-resistance properties alongside with good tribological properties [15]; (iii) self-acting foil bearing rings in turbomachinery based systems [3]; (iv) second phase in polymer matrix to enhance tribological properties of polymer matrix composite [16]; (v) vacuum arc deposited coatings to improve the oxidation and wear resistance of cutting tools [17]; and thin films for sliding electrical contacts [18,19].

The nature of their inherent nano-laminated layered structure suggests that they might possess excellent solid lubricant properties [3]. This is particularly true, stemming from the fact that in the first report

---

* Corresponding author.
E-mail address: m.rainforth@sheffield.ac.uk (W.M. Rainforth).

https://doi.org/10.1016/j.wear.2019.203062
Received 17 April 2019; Received in revised form 11 August 2019; Accepted 20 September 2019

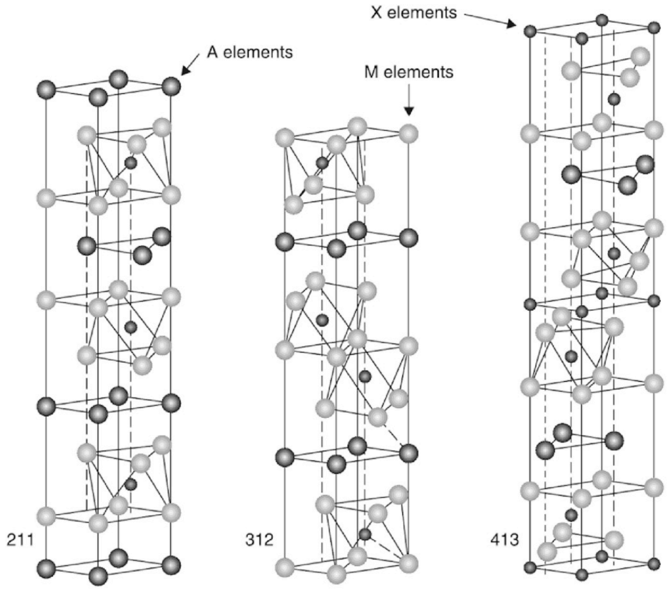

Fig. 1. Crystal structure of M_2AX phase, M_3AX_2 phase, and M_4AX_3 phase [8].

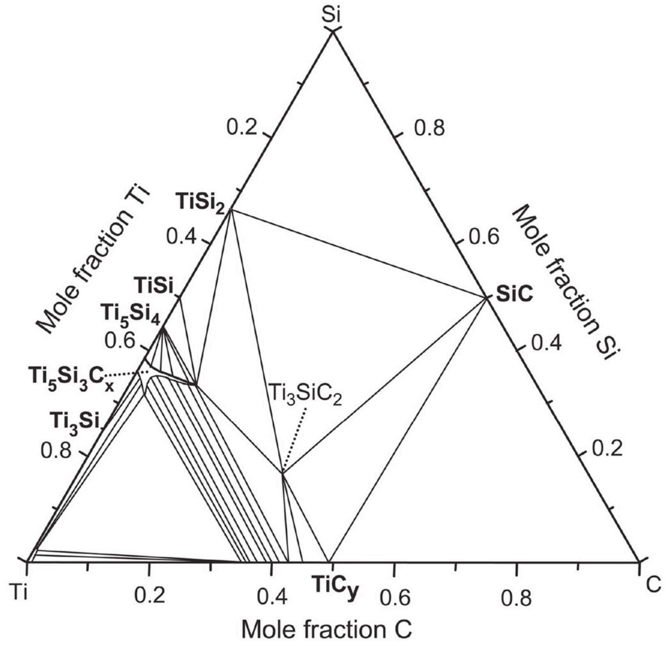

Fig. 2. Isothermal ternary section of the Ti–Si–C system phase diagram at 1100 °C [28].

on the properties of MAX phases, it was reported that Ti_3SiC_2 felt lubricious during machining [12]. However, irrespective of their potential applications, synthesizing a monolithic MAX phase has been a challenge [20–22]. As a monolithic phase is crucial to understanding and effectively characterizing their intrinsic mechanical properties, this step is a major prerequisite for possible future applications [7].

The $Ti_{N+1}SiC_N$ ternary carbide is the most studied amongst the $M_{N+1}AC_N$ (MAX) phase system [12,23]. The only thermodynamically stable member of the $Ti_{N+1}SiC_N$ is Ti_3SiC_2 according to the Ti–Si–C phase diagram. The Ti_3SiC_2 shares a very similar crystal structure with graphite [24], consisting of CTi_6 slabs and a closed packed Si sheet intercalated between the twinned Ti–C layers. It has a Vickers hardness of 4 GPa, elastic modulus of 325 GPa, a room temperature fracture toughness of 7 MPa $m^{1/2}$, and electrical and thermal conductivities are ≈ $4.5\ X10^6 s.m^{-1}$ and 37 W /(m.K) [12,25–27]. Considering the Ti–Si–C phase diagram at 1100 °C in Fig. 2 [28], the Ti_3SiC_2 phase region exists in a very narrow composition range and in equilibrium with TiC and/or possibly (Ti,Si)C [29,30]. Hence, a tie-line can be observed to the Si-rich phases of SiC, $TiSi_2$ and Ti_5Si_3 [31] (Fig. 2.).

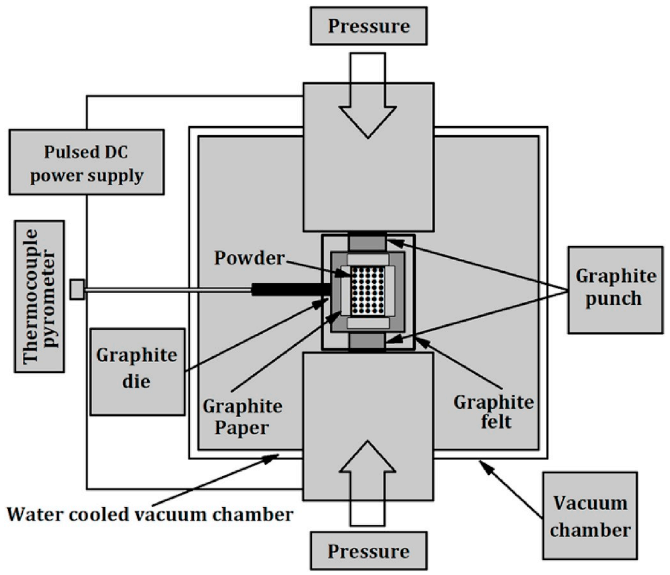

Fig. 3. Schematics of the die-punch-powder configuration and the spark plasma sintering (SPS) set-up.

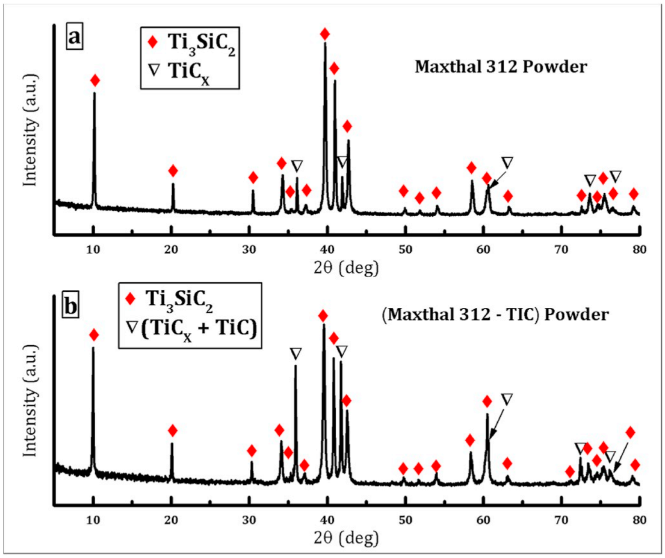

Fig. 4. XRD patterns from the as-received Maxthal 312 powder and mechanically milled Maxthal 312-TiC powder prior to SPS.

Therefore, it is difficult to synthesize a monolithic MAX phase as the evolution of ancillary phases often occurs. In most cases, TiC always accompanies the Ti_3SiC_2 phase because of the close structural relationship between the two compounds [32]. It is thought that these ancillary phases have the tendency to degrade some of the exclusive intrinsic properties of MAX phases [32]. However, the presence of ancillary phases may not be necessarily detrimental [33]. Previous studies [24,34,35] have shown that by effectively controlling the amount of these secondary phases, it is possible to reinforce the MAX phase and thus create a MAX phase composite with improved mechanical properties (i.e., hardness and wear) superior to monolithic MAX phase [33,36].

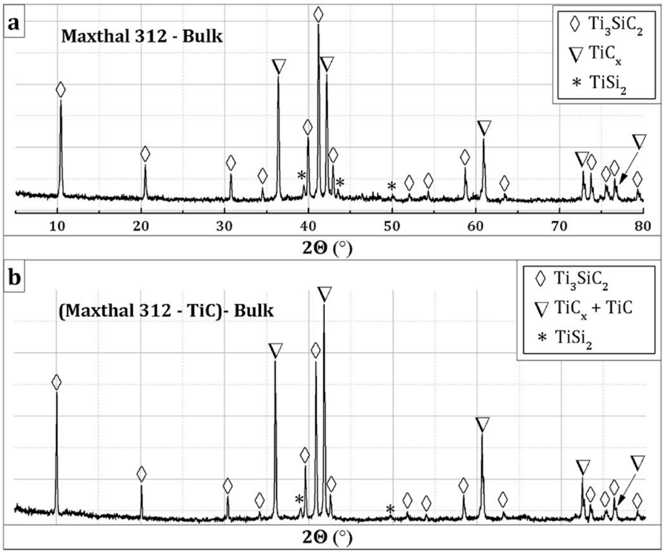

Fig. 5. XRD patterns of the bulk samples: (a) Maxthal 312 and (b) Maxthal 312-TiC after SPS.

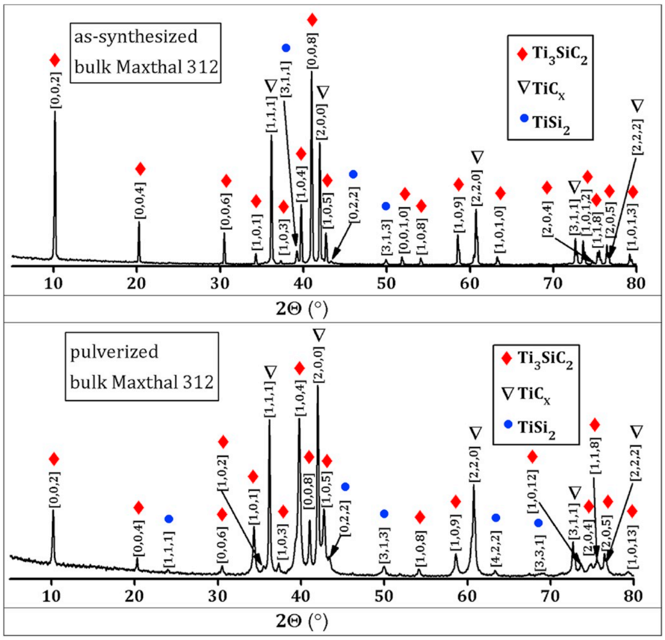

Fig. 6. XRD patterns of the as-synthesized Maxthal 312 disc top surface and pulverized bulk Maxthal 312 showing preferred crystallographic orientation of Ti_3SiC_2.

The purpose of this study is to synthesize fully dense Ti_3SiC_2 and Ti_3SiC_2–TiC via commercially available Maxthal 312 powder route and to study the associated synthesis reaction mechanism(s) as well as the microstructural evolution of the synthesized compositions. Furthermore, detailed investigation will be reported on the tribological behaviour of the synthesized bulk samples and the role of ancillary TiC_X formed in situ during synthesis and the added TiC particles in the Ti_3SiC_2 matrix in the friction and wear behaviour.

2. Experimental details

2.1. Materials

Commercially available Maxthal 312® (nominally-Ti_3SiC_2) powder (Kanthal AB, Sweden) was used as the starting material for the synthesis of Ti_3SiC_2 MAX phase in this work. The as-received powder contained 92 wt% Ti_3SiC_2 and 8 wt% TiC_X as primary constituent starting phases. Separately, 3 g of TiC powder (Alfa Aesar, 2 µm, 99.5%) was mixed with 12 g of the Maxthal 312 powder to further yield an increase in TiC content in the form of Maxthal 312-TiC powder (~3.5 µm).

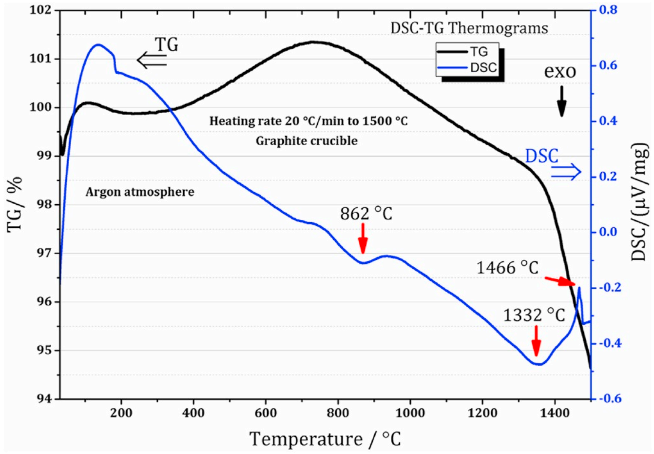

Fig. 7. DSC-TG of the Maxthal 312 powder heated in graphite crucible under flowing argon.

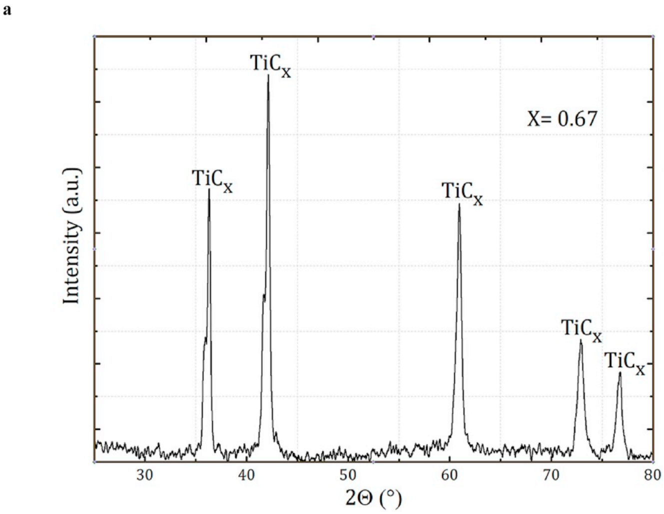

Fig. 8a. XRD pattern of the decomposed Maxthal 312 powder upon TG-DSC analysis.

2.2. Processing

2.2.1. Preparation of Maxthal 312

The powder samples (i.e., 7 g of both Maxthal 312 as well as Maxthal 312-TiC) were poured separately into a graphite die punch set-up (Ø = 20 mm) with graphite foil insert (thickness 0.40 mm) positioned around the powder inside the die (Fig. 3.) to enable easy removal of the sintered compact and to further prevent possible reaction between the graphite heating elements (die-punch) and the powder. The set-up was then initially cold compacted to ensure intimate electrical contact between the punches and the powder during the synthesis. The punch/powder/die set-up was then covered with a graphite felt tied by two graphite wires to reduce heat dissipation during the synthesis. A small hole was cut on the graphite felt to enable direct surface temperature measurement with the aid of a thermocouple. The set-up was then placed in a spark plasma sintering (SPS) furnace unit (HP D25, FCT

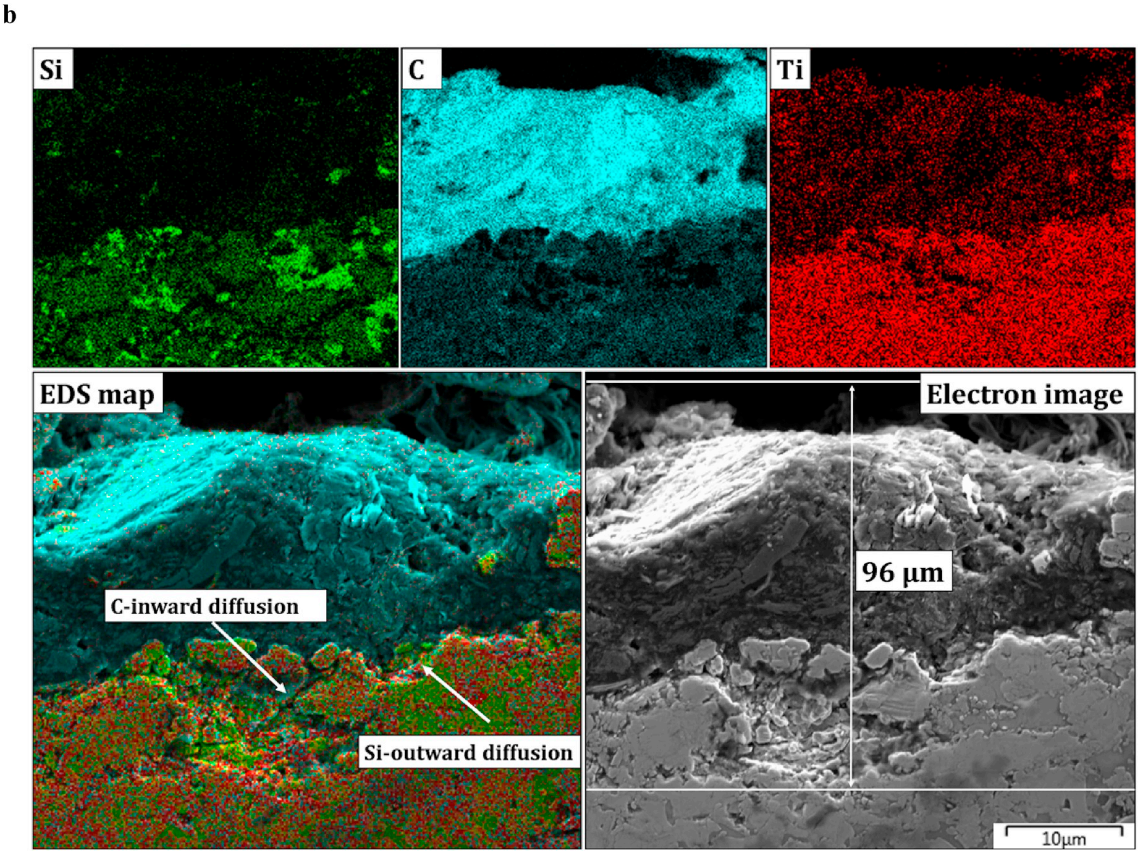

Fig. 8b. SEM-EDX map analysis from the cross-sectioned Maxthal 312 as-synthesized disc. Note: the carbon-rich region is the graphite paper that will normally be peeled off prior to grinding.

Systeme GmbH, Germany) and consolidated under a vacuum environment at a heating rate of 100 °C/min, requisite temperature of 1400 °C, dwell time of 10 min using 16 kN uniaxial pressing pressure. The sintering temperature, the axial pressure and the piston movement were recorded as a function of time in order to monitor the sintering cycle. Upon the completion of the SPS synthesis, the synthesized cylindrical disc was then ground and polished with diamond pastes down to 0.5 µm particle size to ensure the complete removal of any outer reaction layers formed on the disc surface as a result of possible reaction with graphite paper inserts as well as the graphite die. The top surface of the disc was used to acquire X-ray diffraction (XRD) pattern.

2.3. Vickers microhardness and density

The microhardness of the sintered discs were measured on the polished surface (Ra $<$ 0.1) by indentation technique using a Vickers indenter (DuraScan 50, ecos Workflow, EMCO-TEST, GmbH) with a 4.9 N load for 10 s. Six tests were conducted and the mean value was reported. The densities of the sintered discs were measured upon grinding and polishing down to 0.5 µm using the Archimedes method according to the ASTM standard B962-08 [37]. The measured density was determined and translated into relative density by taking into account the intrinsic densities of the phases present in the bulk sample.

2.4. Tribological test

Dry sliding friction and wear tests were conducted on commercially available pin-on-disk tribometer (UMT-1, CETR, California, USA) at room temperature according to the ASTM standard G99-05 [38]. Prior to the friction and wear test, all specimens were cleaned in an ultrasonic bath with isopropanol and subsequently dried in hot air. Dry sliding tests were performed under a normal load of 0.5 N corresponding to a Hertzian contact stress of approximately 296 MPa. A rotational speed of 50 rpm for 60 min and 100 rpm for 30 min were applied. The counterpart material was 4 mm diameter spherical Al_2O_3 (GD-25 alumina, Spheric-Trafalgar., Ltd). Alumina was specifically chosen because it is chemically inert. Tests were conducted at least three times for each condition and the average value used as the evaluated data to ensure repeatability and reliability of the reported data. The specific wear rate was calculated from the equation:

$$k = V_w/F \times S$$

where k (mm^3/Nm) is the specific wear rate, V_w is the worn volume (mm^3), F is the applied load (N), and S is the sliding distance (m), respectively.

2.5. Analyses

X-ray crystal phase analysis of the resultant polished disc surfaces was carried out on a diffractometer (Bruker D2 Phaser, USA) with Cu Kα radiation source using a step size of 0.02° and time per step of 3 s over a 2ϴ range from 5° to 80°. Scanning electron microscopy (SEM) equipped with an energy-dispersive X-ray (EDX) system (FEI Inspect F50, The Netherlands/Oxford Instruments X-Max, AZtec Microanalysis) alongside with transmission electron microscopy (TEM) was used for microstructural characterization of the as-synthesized samples as well as post-mortem worn surface of the discs. Electron transparent TEM samples were prepared by focused ion beam (FIB) (FEI Helios NanoLab G3 UC, FEI Company, The Netherlands) and imaged in bright field using a Philips EM 420 TEM. Additionally, the wear tracks were investigated ex situ by employing a Si-calibrated Raman spectrometer (inVia Renishaw Co., UK) with an Ar laser (wavelength of 514.5 nm, laser output power

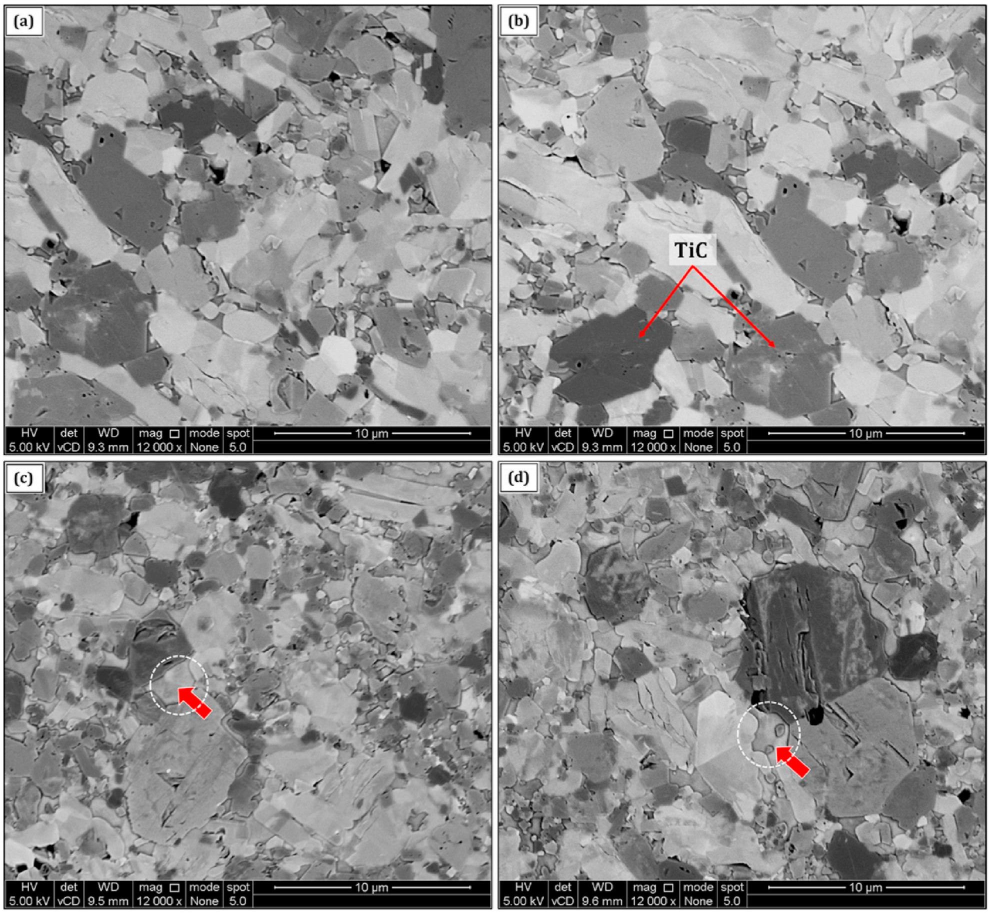

Fig. 9. Back scattered SEM micrographs from the polished unetched surfaces: (a–b) Maxthal 312 and (c–d) Maxthal 312-TiC composite. Note: highlighted section in Fig. 9(c–d) shows the $TiSi_2$ region.

20 mW). From each wear scar, the worn area was determined using an optical profiler (Dektak 150 stylus profiler, Veeco Co., USA) by taking an average of 10 scans. Differential scanning calorimetry (DSC) and thermogravimetry (TG) in an argon environment were used to identify the various reaction temperatures as well as the thermal stability of the Maxthal 312 powder by using a graphite crucible to simulate the graphite rich SPS environment.

3. Results and discussion

3.1. Composition of the powders and bulk samples

The XRD patterns of the Maxthal 312 powder and Maxthal 312-TiC powder before SPS are presented in Fig. 4. Comparing the X-ray diffraction patterns of the as-received Maxthal 312 powder, the ball milled Maxthal 312 powder and the TiC powder (Fig. 4(a and b)), it can be seen that with the incorporation of TiC into the Maxthal 312 powder, the intensities of TiC peaks increased (Fig. 4(b)). Furthermore, no solid state reaction between the Maxthal 312 powder and TiC powder occurred after the ball milling, suggesting a uniform distribution of constituent phases in the mixture prior to SPS.

The XRD patterns from the SPSed Maxthal 312 and Maxthal 312-TiC after SPS at 1400 °C are presented in Fig. 5. After SPS, Ti_3SiC_2 was the main phase in agreement with the JCPDS card (ICDD 34–1383) and some additional peaks corresponding to TiC_X (ICDD 34–1383) alongside some minor $TiSi_2$ (ICDD 34–5425) were also identified. The addition of TiC powder led to an increase TiC and/or TiC_X phase and a corresponding decrease of the Ti_3SiC_2 phase (Fig. 5(b)). It is noteworthy to mention that both stoichiometric and non-stoichiometric titanium carbide (i.e., TiC_X and TiC) both coexist in the Maxthal 312-TiC bulk sample. Non-stoichiometric titanium carbide formed in situ owing to decomposition during the SPS synthesis as well as being present in the starting as-received Maxthal 312 powder composition as an ancillary phase.

3.2. Phase analysis

In order to determine the weight fraction of the phases in the synthesized SPSed bulk samples, the integrated XRD peak intensities was used with experimental calibration according to equation (2) [39], assuming a two phase mixture (Ti_3SiC_2–TiC), since the amount of $TiSi_2$ is relatively small and can be neglected:

$$W_{TSC} = \frac{1.80}{1.80 + \left(I_{TC(200)}/I_{TSC(104)}\right)} \quad \text{and} \quad W_{TC} = \frac{I_{TC(200)}/I_{TSC(104)}}{1.80 + \left(I_{TC(200)}/I_{TSC(104)}\right)} \tag{2}$$

where W_{TC} and W_{TSC} denote the weight percentages of TiC and Ti_3SiC_2, respectively; I_{TC} and I_{TSC} denote the integrated diffraction main peak intensities of TiC (200) and Ti_3SiC_2 (104), accordingly. The weight contents of Ti_3SiC_2 and TiC were calculated according to Eq. (2) for the as-synthesized SPSed bulk Maxthal-312 as well as Maxthal 312-TiC discs after polishing. The Maxthal-312 bulk contained 71 wt% Ti_3SiC_2 and 29 wt% TiC_X, whilst the Maxthal 312-TiC bulk contained 57 wt% Ti_3SiC_2 and 43 wt% (TiC + TiC_X). The XRD data could not be refined for phase fraction by Rietveld analysis as the Maxthal powder was textured during the SPS synthesis. This was evident when the XRD spectrum of the synthesized bulk top surface was compared to that of the pulverized bulk

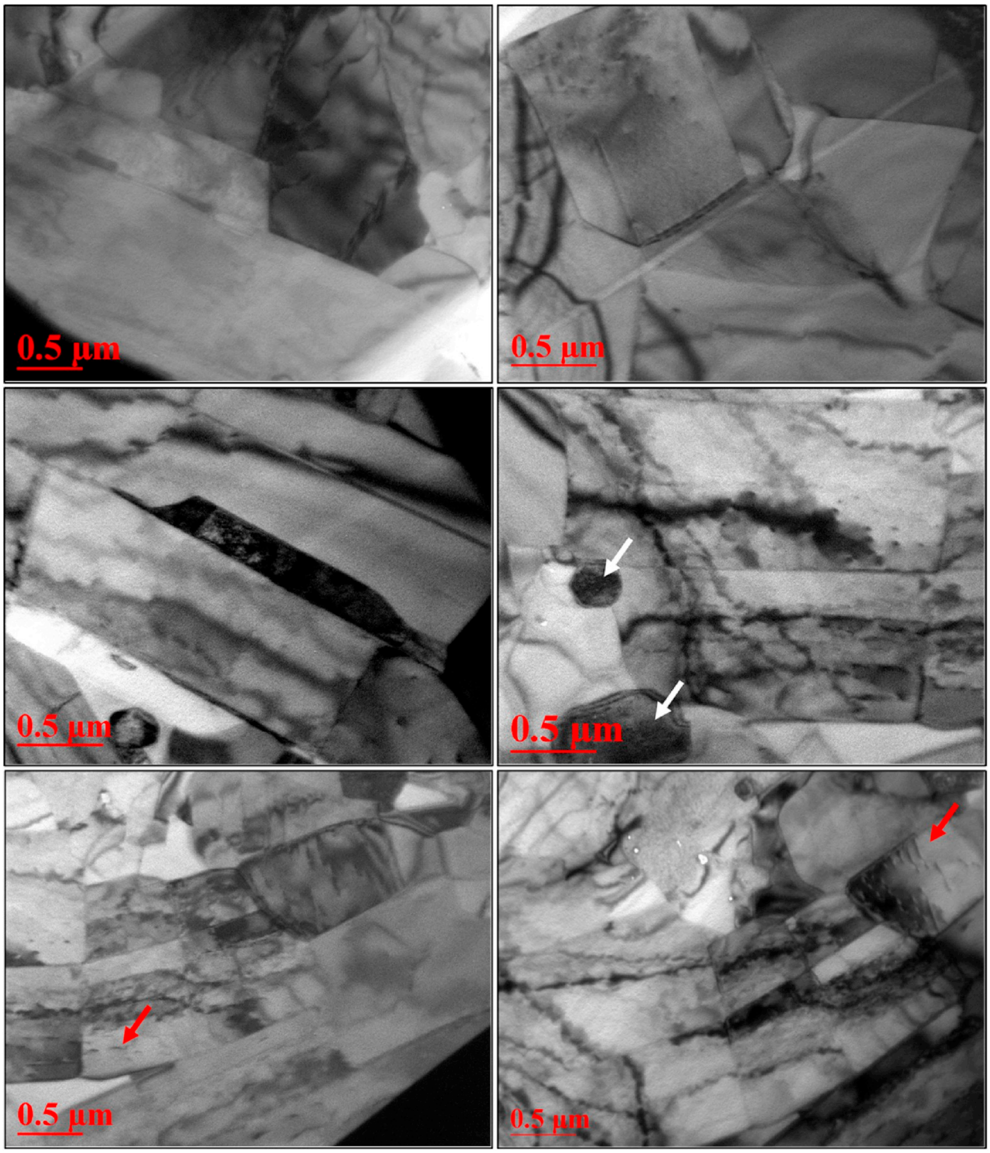

Fig. 10. Bright-field (BF) TEM microstructural evolution of the bulk Maxthal 312 pristine surface after SPS.

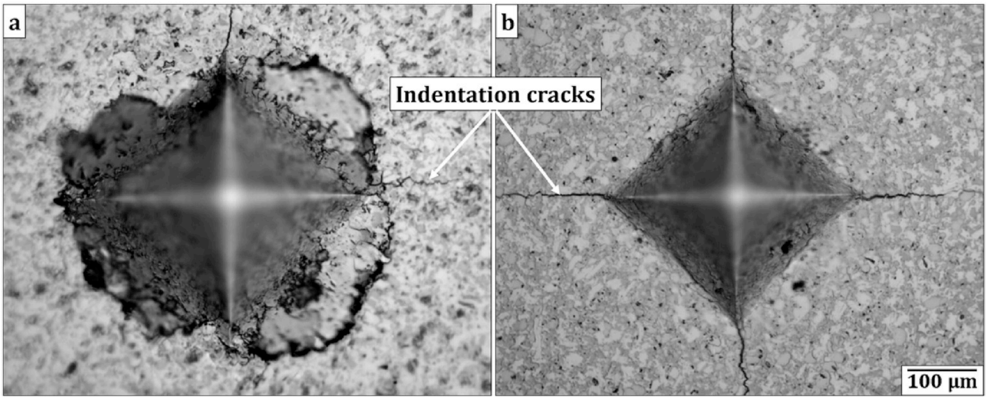

Fig. 11. Optical micrographs of Vickers indentation mark: (a) Maxthal 312 and (b) Maxthal 312-TiC, respectively.

sample as shown in Fig. 6. The strongest diffraction peak of the Ti_3SiC_2 phase appears to have changed from the (008) plane on the top surface in the as-synthesized bulk sample to the (104) plane in the pulverized sample. This suggests that the Ti_3SiC_2 grains in Maxthal 312 bulk sample grew preferentially with the basal planes rotating towards the loading direction in agreement with observations reported elsewhere [40]. Hence, the intensity recorded on the top surface from the XRD analysis is somewhat exaggerated due to texture, thus making Rietveld refinement

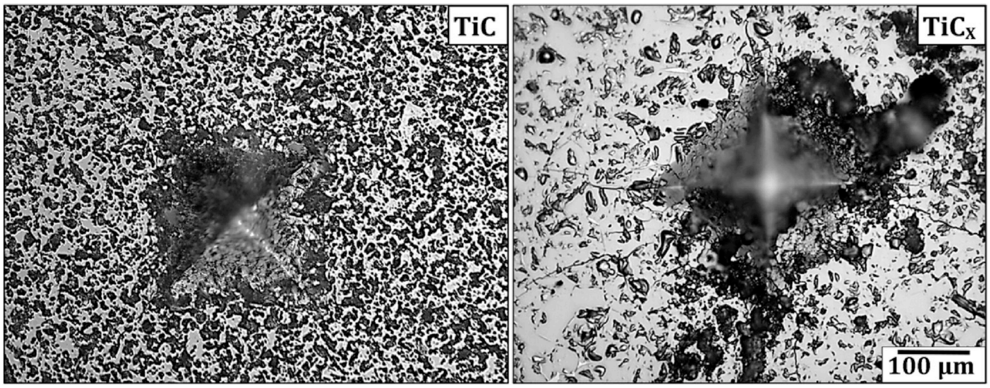

Fig. 12. Optical micrographs showing Vickers indentation-induced fracture behaviour of stoichiometric TiC and non-stoichiometric TiC$_X$ synthesized by spark plasma sintering (SPS).

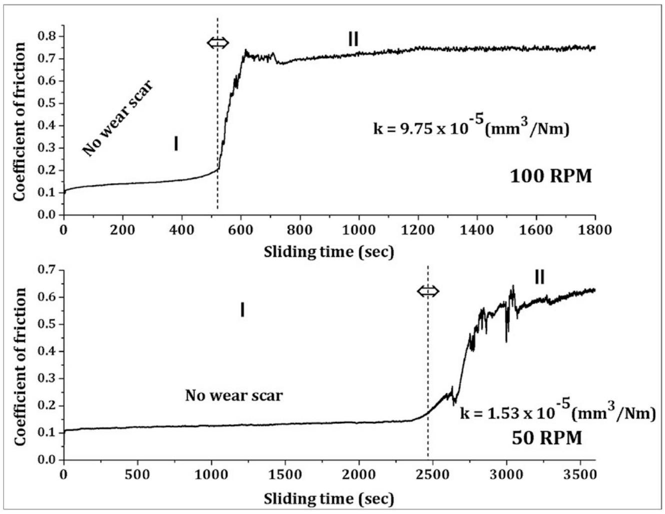

Fig. 13. Dependence of dry-sliding coefficient of friction of Maxthal 312 disc sample with sliding time against Al_2O_3 at 100 rpm for 30 min and 50 rpm for 60 min under a normal load of 0.5 N, respectively.

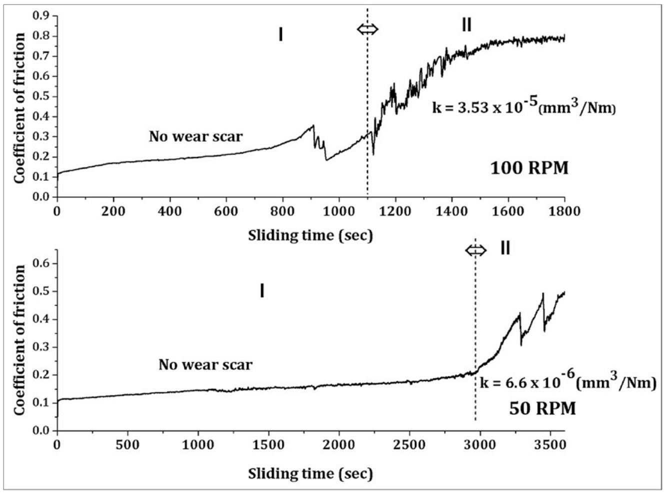

Fig. 14. Dependence of dry-sliding coefficient of friction of Maxthal 312-TiC disc sample with sliding time against Al_2O_3 at 100 rpm for 30 min and 50 rpm for 60 min under a normal load of 0.5 N, respectively.

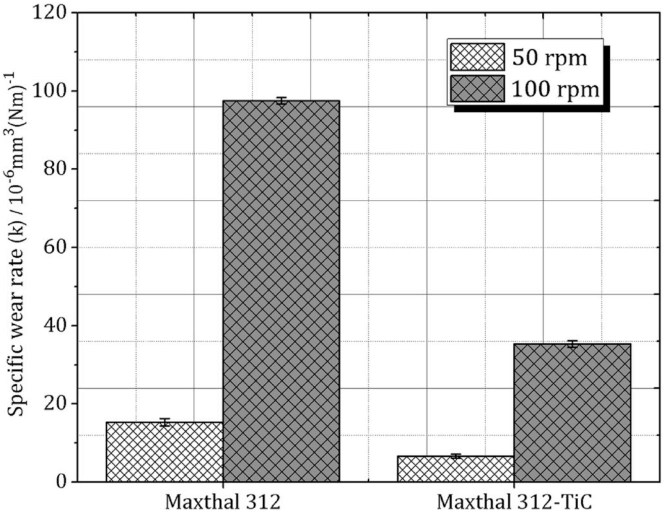

Fig. 15. The dependence of SPSed composition with specific wear rate upon dry sliding against Al_2O_3 at room-temperature.

difficult.

4. Thermal stability of Ti_3SiC_2

4.1. *Thermal stability of Maxthal 312 powder*

In order to understand the decomposition and the phase evolution of the SPSed Maxthal 312 powder, thermal analysis of the Maxthal 312 powder was performed using DSC-TG analysis in a graphite crucible to simulate the graphite environment during the SPS. The heating curves recorded are shown in Fig. 7. The main observable features in the DSC curve are the broad exothermic heat release peak at about 720–964 °C and the sharp endothermic peak at ~1466 °C. Whilst the main features in the TG-curve are the slight increase in mass (approximately 1%) corresponding to the exothermic peak formation temperature in the DSC as well as the onset of the rapid mass loss (~5.5%) from temperature above 1300 °C. Looking at the Ti–Si phase diagram [41], the exothermic peak observed in the DSC appears to coincide with the low formation temperature (862 °C) of Ti_3Si (incongruently melting) intermetallic. Another important feature in the phase diagram is that the melting point of both eutectics is at ~1330 °C whilst the silicon melting point is at 1414 °C. Hence, it is conceivable that the onset of mass loss is primarily due to melting of the eutectics which is followed by the evaporation of silicon at temperature above 1414 °C. The loss of silicon and consequent formation of TiC$_X$ (Fig. 8 (a)) gave rise to the endothermic peak in the

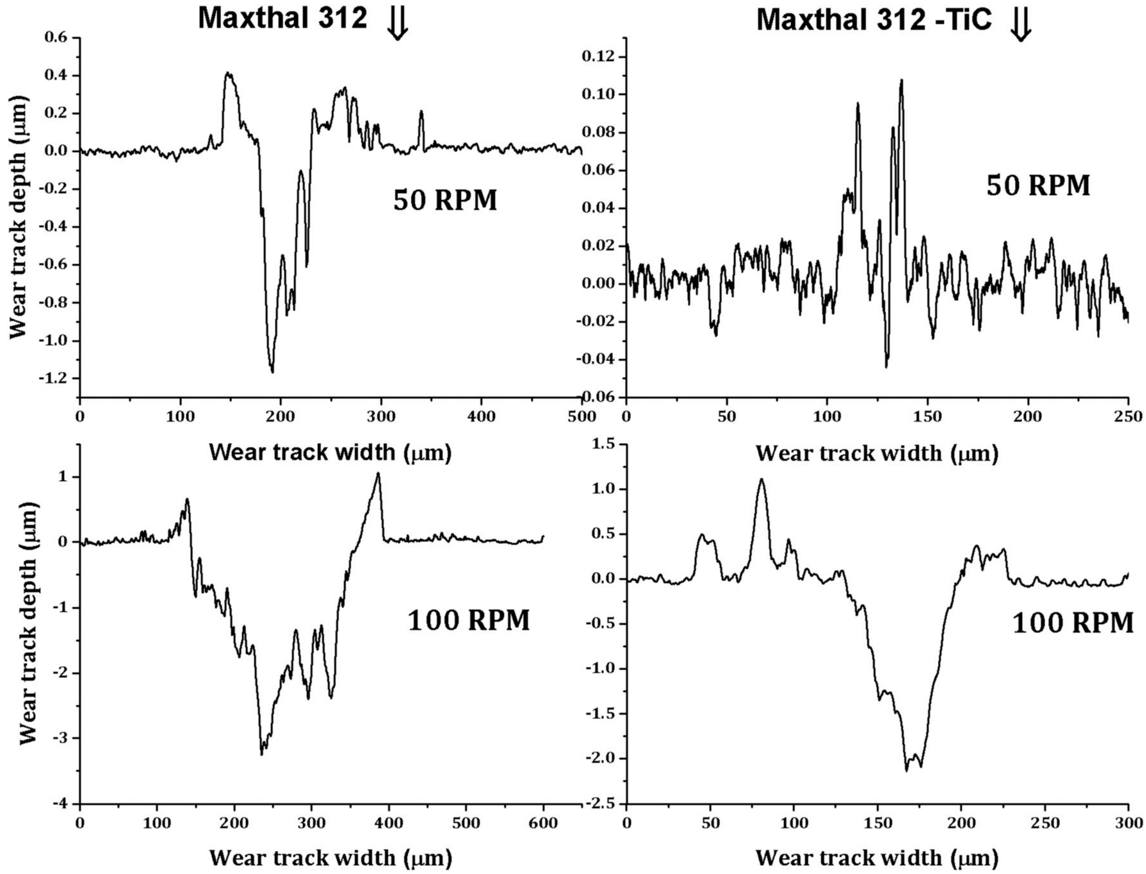

Fig. 16. Cross-sections obtained from profilometry scans of wear tracks of Maxthal 312/Al_2O_3 and Maxthal 312-TiC/Al_2O_3 tribocouples.

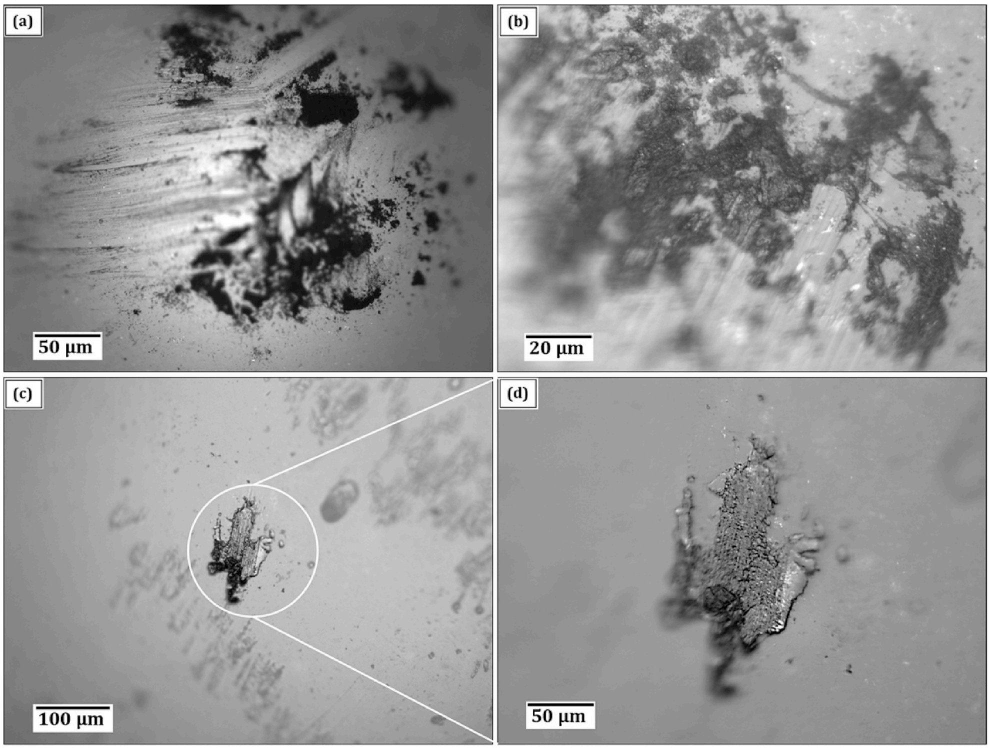

Fig. 17. Optical micrographs of the contact area on alumina ball upon dry sliding: (a–b) Maxthal 312 and (c–d) Maxthal 312-TiC at 100 rpm, respectively.

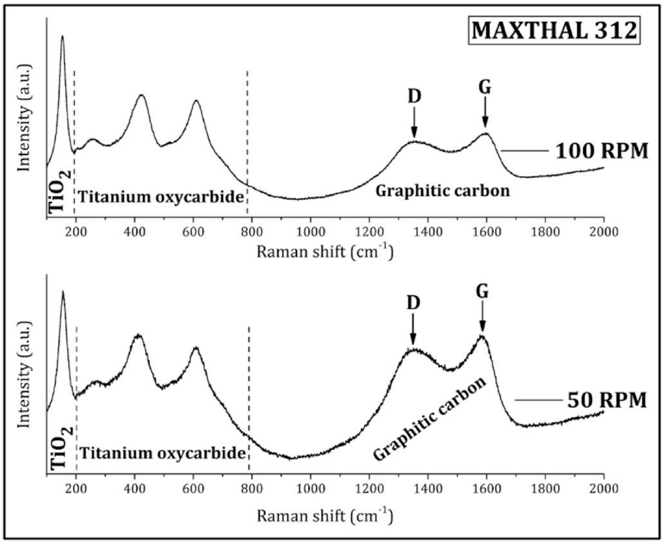

Fig. 18. Raman spectra of the wear track of Maxthal 312 disc upon dry sliding against Al_2O_3 ball at 50 rpm and 100 rpm, respectively.

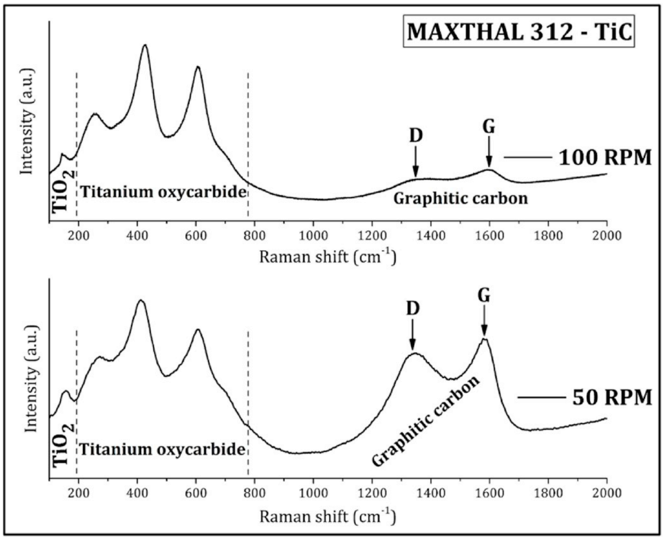

Fig. 19. Raman spectra of the wear track of Maxthal 312-TiC disc upon dry sliding against Al_2O_3 ball at 50 rpm and 100 rpm, respectively.

DSC curve.

The evolution of the secondary phase TiC_X may thus be attributed to two important phenomena taking place during the sintering process:

(1) Problems associated with vacuum sintering and carbon-rich environment

Carbon inward diffusion originating from the use of graphite heating elements will bring about a carburization process as follows [42];

$$Ti_3SiC_2 + (3x\text{-}2)C \rightarrow 3TiC_X + Si(g)$$

Another possible reaction path as proposed by El-Raghy et al. [42] is given by:

$$Ti_3SiC_2 + (3x\text{-}1)C \rightarrow 3TiC_X + SiC$$

However, the problem associated with carbon contamination appears to be less severe when sintering in vacuum compared to sintering under an argon atmosphere. This is because the vacuum pump continuously removes any gas reducing the carbon potential of the atmosphere as proposed by Li et al. [43].

In addition, the possible outward diffusion of Si and subsequent vaporization during vacuum sintering will bring about decomposition. According to Ref. [43], silicon loss is severe in vacuum sintering as its vapour pressure is drawn away upon the formation of the Ti–Si eutectic intermediate phase. The loss of silicon is the main reason why the final composition falls into a two-phase region and not the solubility region as shown in the Ti–Si–C ternary phase diagram [44]. Chen et al. [45] reported that Ti_3AlC_2 will decompose at temperatures as low as 1150 °C in high vacuum ($\sim 10^{-2}$ Pa).

(2) Intrinsic decomposition

At temperatures above 1400 °C most MAX phases will decompose peritectically via the outward diffusion of the A element from the crystal structure, leaving behind a binary phase MX according to the reaction [46]:

$$MAX\ (S) \rightarrow MX\ (S) + A\ (g\ or\ l)$$

However, the relatively small $TiSi_2$ ancillary phase may have originated from the Ti–Si intermediate liquid phase necessary for the formation of Ti_3SiC_2 [47] that has not been fully consumed or a possible decomposition product of Ti_3SiC_2 which is in agreement with the observed increase in $TiSi_2$ content at high sintering temperature reported elsewhere [40].

In order to elucidate the relevant reactions or phase transformation, XRD analysis of the decomposed Maxthal 312 powder was also carried out upon the completion of the DSC–TG analysis shown in Fig. 7. The only phase present after the thermal analysis was non-stoichiometric $TiC_{0.67}$ (Fig. 8(a)) which is consistent with the Ti–Si–C phase diagram as silicon evaporates out of the structure at temperatures above its melting point. This is particularly evident as the loss of silicon through evaporation was visible through deposition on the graphite crucible during the thermal analysis.

SEM-EDX analysis of the cross section of the Maxthal 312 disc (Fig. 8(b)) was performed to analyse the reaction layer owing to possible carbon diffusion at high sintering temperature. According to the EDX elemental map, Si appeared to have diffused outward whilst C diffused inward, thus leading to a reaction layer consisting of SiC by carburization. The high vacuum pressure during vacuum sintering, the high partial pressure of Si at high sintering temperature as well as the sintering temperature relatively close to the melting point of silicon would imply that the vapour of silicon can easily be drawn out [48]. This would consequently lead to the decomposition of Ti_3SiC_2 by carburization [49]. This is, however, evident owing to the increasing amount of TiC_X formed in situ in the matrix, in agreement with observations reported elsewhere [49]. The thickness of the reaction layer was measured using SEM and was around 96 μm. Given that the bulk samples were polished down to 0.5 μm and no evidence of SiC and/or C was found in the XRD data, it is conceivable to believe the reaction layer had been effectively removed during the grinding and polishing performed on the XRD samples.

4.2. Density and microstructures

The relative densities of the SPSed Maxthal 312 and Maxthal 312-TiC composite were determined from the as-synthesized discs after grinding and polishing by considering the theoretical densities of sintered compacts. The theoretical densities were obtained by using the rule of mixtures which takes into account the densities of the two constituent phases $\rho_{Ti_3SiC_2} = 4.53\ g/cm^3$ [50] and $\rho_{TiC} = 4.93\ g/cm^3$ [50], respectively. In the analysis it had to be assumed that the non-stoichiometric titanium carbide produced during the SPS cycle, TiC_X, had the same density as the added stoichiometric TiC. Considering the SPS processing

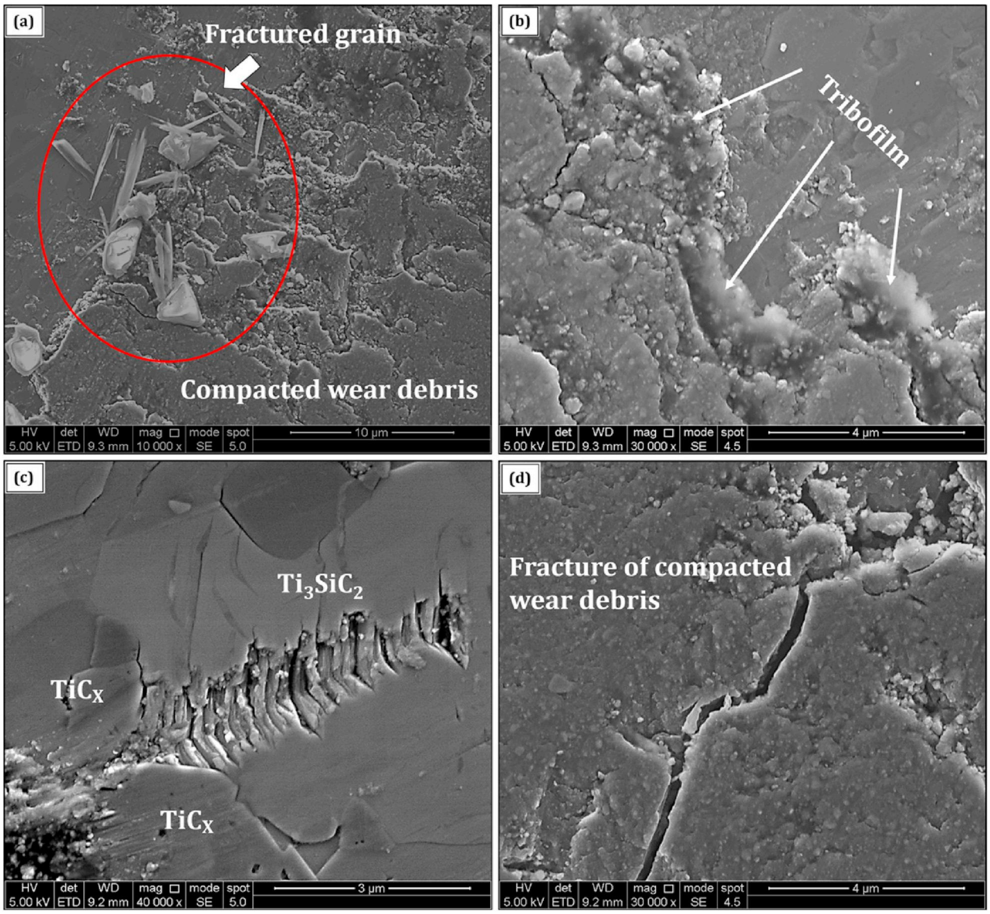

Fig. 20. SEM images obtained from different areas inside the wear track of Maxthal 312 disc at 50 rpm.

parameters utilized, the Maxthal 312 sample (which contained TiC_X but no intentional TiC addition) exhibited sufficient densification in excess of 98%. Similarly, with the same SPS processing parameter, the relative density of the Maxthal 312-TiC composite was 99%.

Fig. 9 shows the SEM microstructures of the polished unetched surfaces of the SPSed bulk Maxthal 312 and Maxthal 312-TiC composites. For the Maxthal 312 bulk sample (Fig. 9(a–b)), the microstructure revealed regions with bright contrast as well grey contrast. The bright contrast area consisted of elongated fine plate-like grains corresponding to Ti_3SiC_2 whilst the grey contrast regions were TiC_X. The TiC_X grains appears to be homogeneously distributed in the matrix with no agglomerates partly due to the fact that it was produced in situ as an ancillary phase rather than being a bulk addition. In addition to the Ti_3SiC_2 and TiC_X grains, small traces of $TiSi_2$ also coexist as the melt region between the Ti_3SiC_2 and TiC grains as shown in Fig. 9(c–d). $TiSi_2$ is an intermediate phase leading to the formation of Ti_3SiC_2 that has not been fully consumed during the synthesis. On the other hand, the microstructure of the Maxthal 312-TiC composite (Fig. 9(c–d)) consisted of mainly plate-shaped Ti_3SiC_2 and coarse (TiC_X + TiC) grains alongside with some traces of $TiSi_2$. Also, the (TiC_X + TiC) in the Maxthal 312-TiC composite in comparison to the in situ TiC_X formation in the Maxthal 312 matrix appears not to be fully homogeneously distributed with some clusters of TiC observed. This is consistent with results obtained elsewhere [51]. It seems that the presence of (TiC_X + TiC) in the bulk Maxthal 312-TiC composite matrix led to an increase in the pinning effect on the growth of the Ti_3SiC_2 grains as they appear to be somewhat smaller as compared to the Ti_3SiC_2 grains in the Maxthal 312 bulk sample. This pinning effect introduced by both TiC_X and TiC in the bulk samples is expected to play a key role in inhibiting grain pull-outs during sliding contact as reported elsewhere [52].

TEM bright field (BF) microstructural analysis of the pristine bulk Maxthal 312 FIBed section is shown in Fig. 10. The characteristic plate-like structure typical of MAX phases alongside some TiC grains (white arrow) can be seen. Some inherent dislocations (red arrow) can be observed in some of the Ti_3SiC_2 grains.

4.3. Microhardness

The comparative Vickers microhardness indentation marks from the bulk Maxthal 312 and Maxthal 312-TiC composite are shown in the optical images in Fig. 11. An average Vickers microhardness value of 9.9 GPa was obtained for the Maxthal 312 whilst for the Maxthal 312-TiC it was 12.4 GPa. The measured Vickers microhardnesses for both bulk samples were rather higher than the intrinsic hardness of monolithic Ti_3SiC_2, which is reported to be about 4 GPa [53]. These differences in hardness as compared to the monolithic phase is however expected as the evolution of the second phase TiC_X during the synthesis as well as the added TiC in the composite would increase the overall bulk hardness. As shown in Fig. 11, the indentation of the Maxthal 312 sample (Fig. 11(a)) resulted in damage areas confined to the vicinity of the indentation where material pile-ups and pull-outs can be observed with little indentation cracking observed around the damage zones. For the Maxthal 312-TiC composite (Fig. 11(b)), however, indentation of the sample led to minimal grain pile-ups of the type typical of MAX phases, as a result of the increase in TiC content. The increase in TiC particles in the Maxthal 312-TiC bulk sample clearly resulted in TiC particles inhibiting the grain growth of Ti_3SiC_2 in the matrix, thus the formation a finer-grained Ti_3SiC_2 matrix than the Ti_3SiC_2 matrix observed in the Maxthal 312 bulk sample (Fig. 11). Thus, the larger the grains are, the easier the deformation is for Ti_3SiC_2 as reported elsewhere [24].

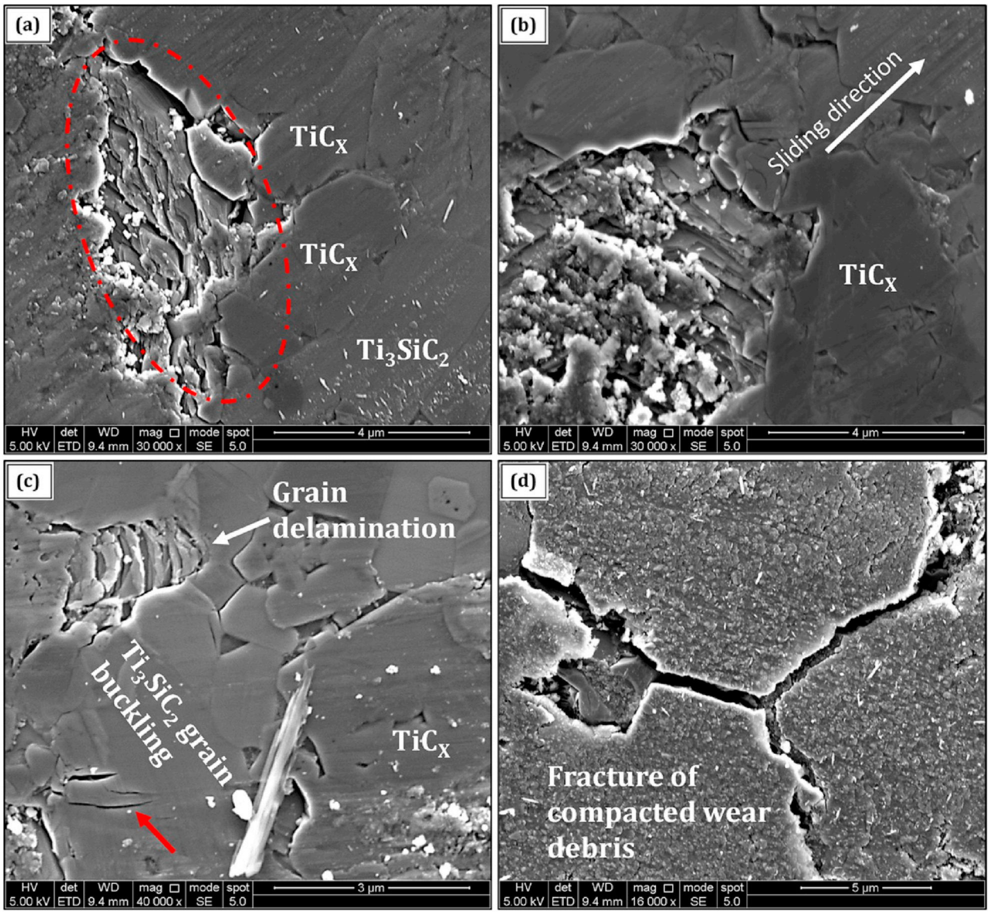

Fig. 21. SEM images obtained from different areas inside the wear track of Maxthal 312 disc at 100 rpm. Note: Red arrow in C indicates buckling induced fracture.

Although radial cracks can be seen emanating from the corners around the indents in both bulk samples, the cracking is severe in the case of the Maxthal 312-TiC sample. Shear deformation appeared to be contained upon indentation on the Maxthal 312-TiC disc owing to the influence of increased TiC particles on the Ti_3SiC_2 matrix; however, the fracture toughness of the bulk sample appeared to have deteriorated due to this increase in TiC content.

To further understand the differences in density and fracture behaviour of stoichiometric TiC and non-stoichiometric TiC_X, a bulk sample of TiC was synthesized by SPS at 1400 °C corresponding to the sintering temperature of the TiC in the Maxthal 312-TiC. A bulk sample of TiC_X was also synthesized at 1300 °C corresponding to the in-situ decomposition temperature of Ti_3SiC_2 to TiC_X. The relative density of the synthesized TiC_X was 90% upon taking into account the calculated density of $TiC_{0.67}$ (4.628 g/cm^3) whilst the relative density of the synthesized stoichiometric TiC was 82% upon taking into consideration the theoretical density of TiC (4.93 g/cm^3). It is however not surprising that the relative density of TiC was only 82% as the intrinsic sintering temperature for a fully dense TiC is reported to be around 2100 °C [54]. Fracture behaviour by Vickers indentation (Fig. 12) showed that for the same indentation load, TiC_X can be fractured much more easily as observed by radial cracks emanating from indentation diagonals of TiC_X in contrast to stoichiometric TiC. This observation may play a significant role in the wear and friction behaviour of TiC_X and TiC in the Maxthal 312 and Maxthal 312-TiC bulk samples.

5. Tribological behaviour

5.1. *Coefficient of friction: two distinct regimes*

Figs. 13 and 14 show the variation of the friction coefficient (μ) versus sliding time of SPSed Maxthal 312 and Maxthal 312-TiC composite. In both cases, μ was initially low and quite stable. This region then transitions as a function of time into a region of high μ and high wear rate. This transition has been linked to the evolution of a third body abrasion arising from the pull-out of MAX phase grains [3,55,56]. Comparatively, μ showed a delayed transition from low μ to high μ during the testing duration for the Maxthal 312-TiC composite as compared to the Maxthal 312. However, in both cases, the coefficient of friction was initially low and subsequently attained a steady state. Gupta et al. [3] named the initial low μ region as regime I, whilst the high μ region is referred to as regime II. Apparently, for both bulk samples, the transition from regime I to regime II appears to be influenced by the TiC content for the same testing condition. According Wu et al. [57], the low μ and wear rate regime is primarily due to relatively smooth worn surfaces as well as the evolution of tribo-oxidation products between the asperity contact of the tribopair. The high μ and high wear rate regime is mostly attributed to rough contact surface due to severe micro-fracture and subsequent grain pull-outs [56,57].

5.2. *Wear rate: regime I and II*

In order to evaluate the extent of material removal, short time tests that stopped before the transition (regime I) as well as after the transition point (regime II) were conducted and the specific wear rates were

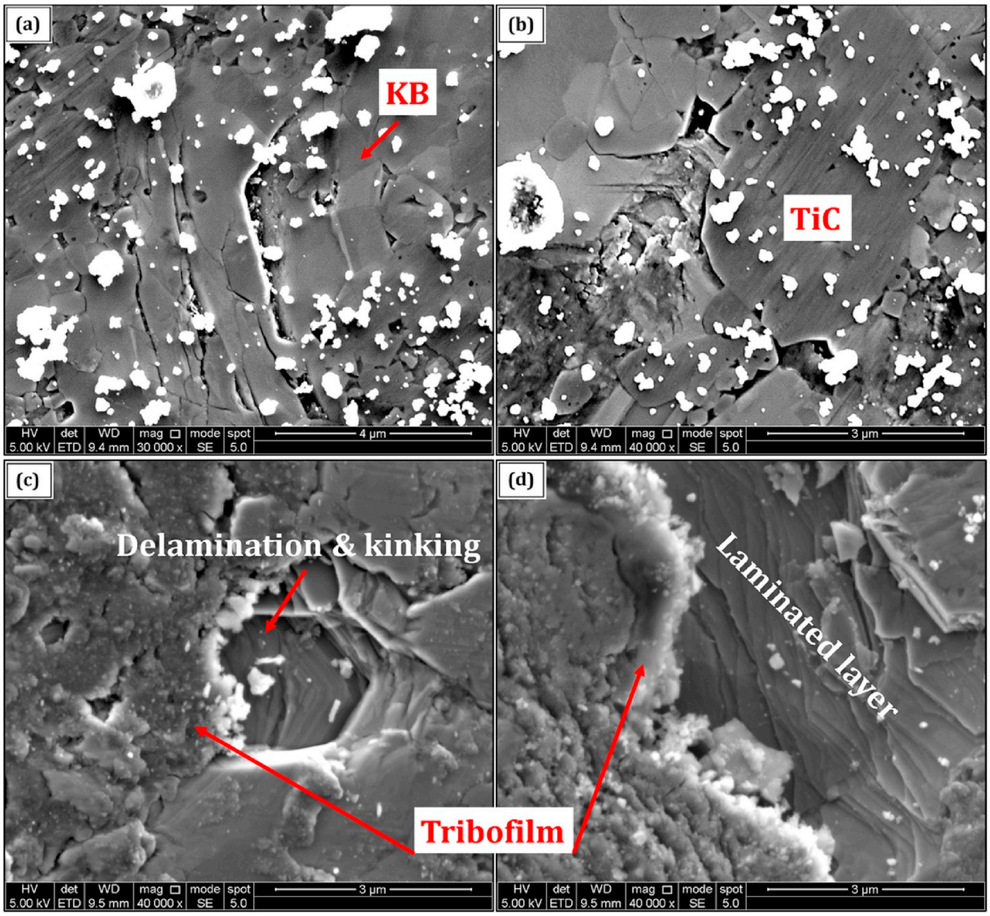

Fig. 22. SEM images obtained from an area inside the wear track of Maxthal 312-TiC disc at 50 rpm.

calculated for both the Maxthal 312 and Maxthal 312-TiC composites. Fig. 15 shows the variation of specific wear rate as a function of composition. The data shows the specific wear rate for the entire duration of the test, as the wear rate for regime I is immeasurable due to the absence of wear scar in this regime for both Maxthal 312 and Maxthal 312-TiC composite. The absence of any visible wear scar and immeasurable wear rate in regime I is consistent with observations reported elsewhere [3,56,58].

Fig. 16 shows the wear scar cross-section for the different material combination and testing combinations for the entire test duration. The stark contrast between the wear track on the Maxthal 312 and Maxthal 312-TiC are consistent with the specific wear rates calculated.

5.3. Alumina counterface

Further analysis of the alumina balls using optical microscopy was carried out preferentially on the tests at 100 rpm to understand the dissimilar tribo-performance between Maxthal 312 and Maxthal 312-TiC as observed in the wear track cross-section profiles (Fig. 17). The worn surface of the alumina balls appeared to be covered with a transfer film with significant scratches observed on the alumina ball worn against the Maxthal 312. These observations are in good agreement with the specific wear rates calculated from the wear track cross sections.

5.4. Study of the wear scars

5.4.1. Raman spectroscopy

The wear scars of the Maxthal 312 and Maxthal 312-TiC discs were investigated by Raman spectroscopy for evidence of intrinsic lubricity. Figs. 18 and 19 shows the spectra of an area inside the wear tracks. Analysis of the spectra was undertaken by comparing with literature data [59–61]. Raman analysis showed that the chemistry of the wear tracks consisted of predominantly TiO_2 (rutile), TiO_XC_Y (titanium oxycarbide) and graphitic carbon. The Raman observations are consistent with the coefficient of friction plots as well as being in good agreement with previous studies [3,56,58] which showed the existence of tribofilm evolution between the pin and the disc during the early stages of sliding. The Raman spectrum from the Maxthal 312-TiC worn section shows that the addition of stoichiometric TiC tends to inhibit TiO_2 formation. This contradicts the results of Barsoum et al. [62] on the oxidation kinetics of TiC_X in Ti_3SiC_2 in the temperature range 875–1200 °C which falls within the possible flash temperature during wear testing. They found that the oxidation resistance of Ti_3SiC_2 was a function of TiC_X content. Samples with less TiC_X were generally found to be more oxidation resistant compared to samples with higher TiC_X in Ti_3SiC_2. In this current work, it appears that the increase in TiC content promotes the growth and stability of the oxycarbide layer formed, the reason of this is unknown at this time. Further work needs to be done to understand the differences in oxidation kinetics of non-stoichiometric titanium carbide (TiC_X) as compared to stoichiometric titanium carbide (TiC).

5.4.2. Scanning electron microscopy (SEM)

Scanning electron microscopy was used to investigate the sliding-induced deformation morphologies of the worn surface of the discs after different testing times at room temperature. The SEM characterization revealed distinct features that have not previously been reported, and also rules out the hypothesis that TiC severely deteriorates the tribological behaviour of MAX phases as previously reported by Hongxiang et al. [63]. Fig. 20 shows the SEM images obtained from different areas inside the wear scar of the Maxthal 312 disc at 50 rpm. The

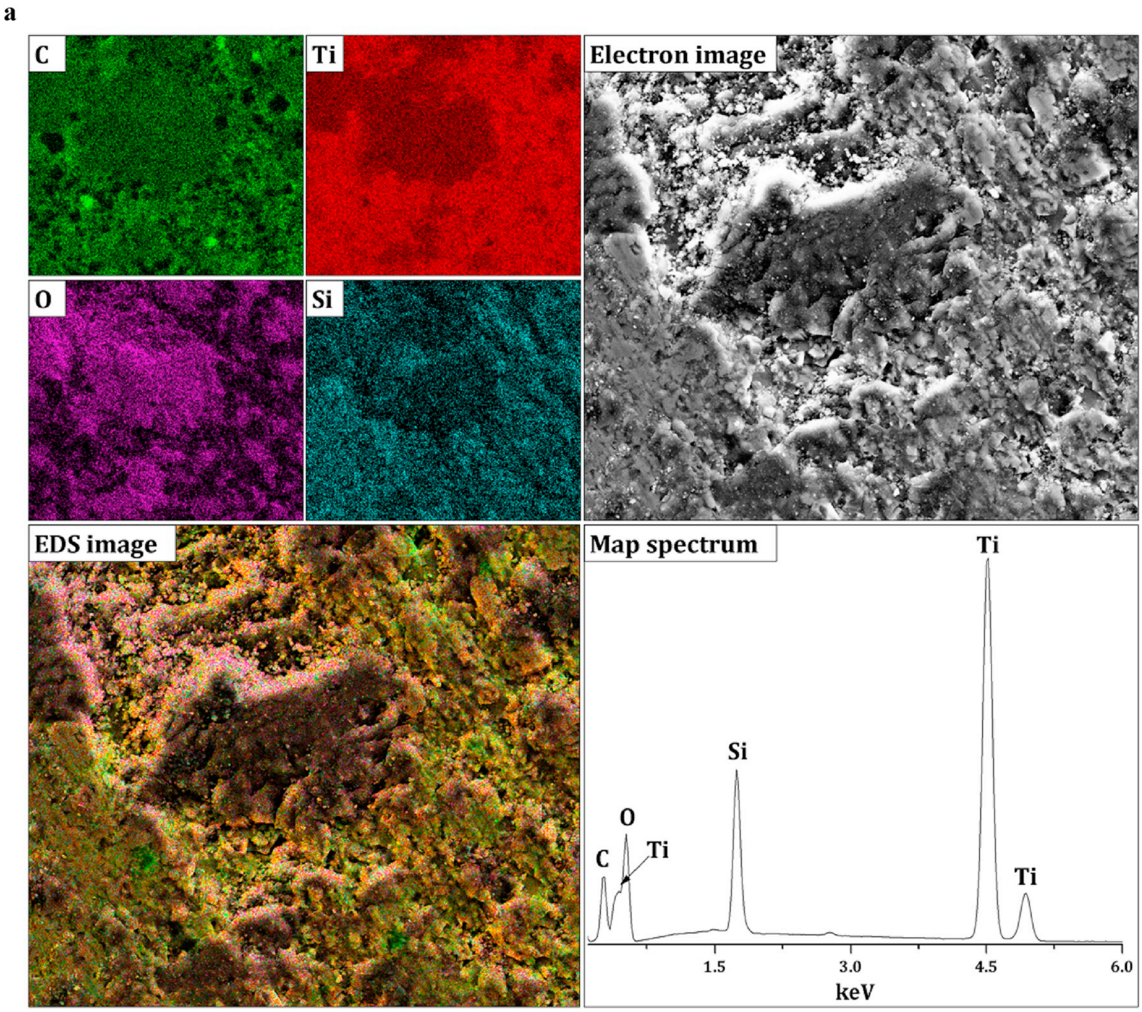

Fig. 23a. EDX elemental map of the wear track of Maxthal 312/Al_2O_3 tribopair at 50 rpm. Note: scale bar is 5 μm.

majority of the worn surface was covered by oxidized wear debris and tribofilm (Fig. 20(b)). Interestingly, the delamination of the Ti_3SiC_2 grains appears to be obstructed by the TiC_X grains (Fig. 20(c)) suggesting that TiC_X grains act as obstacles to Ti_3SiC_2 grain delamination, a major deformation mechanism observed in MAX phases. Some thin sharp wear debris observed in Fig. 20(a) may have originated from grain fractures which were then subsequently pulverized and compacted upon repeated sliding (Fig. 20(d)).

SEM analysis of the wear scar of the Maxthal 312 sliding surface at 100 rpm on the other hand showed similar features to those observed at 50 rpm. However, the extent of damage appears to be more pronounced with severe grain deformation evident (Fig. 21). Furthermore, TiC_X grains can be seen acting as obstacles to Ti_3SiC_2 grain delamination (Fig. 21(a–c)); as a result, deformation is contained. It appears that at higher rotational speed (100 rpm), the tribofilm at the sliding surface was worn off quite rapidly as limited tribolayer was observed in the worn section in contrast to low rotational speed at 50 rpm.

The SEM micrographs taken from the wear scar of the worn Maxthal 312-TiC disc sliding surface at 50 rpm is shown in Fig. 22. Spalled tribofilms can be seen spread over the worn surface (Fig. 22(a and b)) as well as wear debris mixed with tribofilm within the wear track (Fig. 22(c and d)). Grains above the wear track appears to have been deformed as observed in the form of kink band formation (Fig. 21(a)), fractured grains and possibly grain pull-outs. Whilst grains beneath the worn track showed evidence of energy absorbing mechanisms in the form of kinking and delamination (Fig. 22(c)). Again, just as observed in the case of the TiC_X in the wear tracks of the Maxthal 312 disc, the TiC grains wore at a much lower rate than the Ti_3SiC_2, which delaminates, with the TiC grains retaining their morphological integrity at the worn surface. The presence of both TiC_X and TiC hard particles in the matrix of the Maxthal 312-TiC sample appeared to have led to a higher pinning effect on the soft Ti_3SiC_2 grains as compared to just TiC_X in the Maxthal 312 sample. This as a consequence inhibits extensive deformation and pull-outs of the Ti_3SiC_2 grains as observed in the Maxthal 312-TiC worn surface.

Examination of the wear scar of Maxthal 312 disc at 50 rpm by EDX elemental map analysis is shown in Fig. 23(a). In agreement with the Raman data, titanium, silicon, carbon and oxygen were distributed on the worn surface. Furthermore, the oxidized region in the track appeared to be rich in carbon and somewhat titanium, which suggests a possible titanium oxide and/or titanium oxycarbide formation.

EDX analysis performed on the wear track of Maxthal 312-TiC disc at 50 rpm confirmed the presence of titanium, oxygen, silicon, and carbon elemental distribution inside the wear track (Fig. 23(b)). Based on the EDX point spectrum, the oxidized area in the wear track appears to be depleted of silicon. Comparing the EDX data with the Raman spectra, it can be concluded that the evolved tribofilms at the sliding surface were TiO_XC_Y, TiO_2 and a carbonaceous layer.

5.4.3. TEM analysis of the worn surface of Maxthal 312

The FIBed worn surface of the Maxthal 312 disc examined by transmission electron microscopy (TEM) for possible subsurface cracking and deformation is shown in Fig. 24. Grain boundary cracking similar to those observed in the SEM analysis can be seen in the subsurface region (red arrow Fig. 24(a–b)). In addition to grain boundary

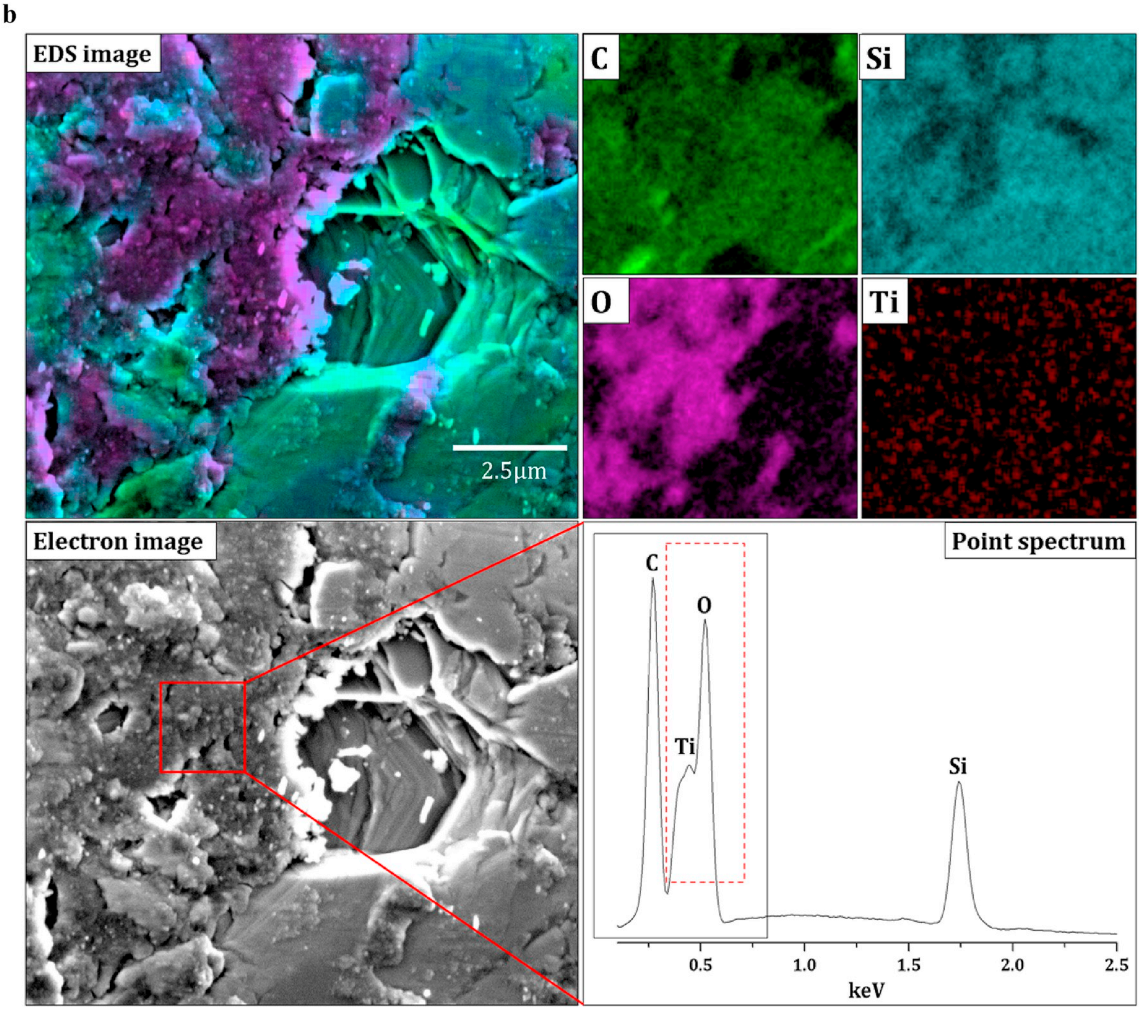

Fig. 23b. EDX elemental map of the compacted oxidized wear debris inside the wear track of Maxthal 312-TiC/Al_2O_3 tribopair at 50 rpm.

cracks, lateral cracks can be seen propagating across the grains with their propagating energy dampened by stacking faults (SFs) (Fig. 24(c)). The evolution of stacking faults in the deformed Ti_3SiC_2 grains might be linked to missing atomic planes due to lattice rotation upon kink band formation [64]. Fig. 24(d) shows dislocations arranged in arrays (green arrow) and dislocation walls (white rectangle). According to Frank et al. [65] dislocation walls are a response to crack nucleation and once forced apart will result in crack formation. Separation of dislocation arrays on the other hand serves as a precursor for kink band (KB) (Fig. 24(b)) and stacking fault (SF) formation [66]. Also, the TiC_X appears to have been slightly deformed with some defect clusters or dislocation debris evident in the TiC_X grains (Fig. 24(e–f)).

5.5. *Role of in situ formed TiC_X and added TiC*

In comparison to Maxthal 312, the friction and wear behaviour of the Maxthal 312-TiC composite exhibited a similar two-stage regimes with an abrupt transition between the two. Both SPSed bulk samples contained secondary binary phases in the form of TiC_X in the Maxthal 312 and (TiC_X + TiC) in the Maxthal 312-TiC. Examination of the worn surfaces of both materials showed that both the in situ formed TiC_X and the addition of TiC played a vital role in extending the mild friction and wear period. This was because they acted as load bearing grains that effectively protected the surrounding Ti_3SiC_2 grains. However, according to the friction and Raman data obtained from the Maxthal 312-TiC worn disc, it appears that the presence of stoichiometric TiC in the Maxthal 312-TiC sample matrix helped in slowing down the oxidation kinetics of Ti_3SiC_2. The slowing in oxidation kinetics suppresses the formation of the brittle TiO_2 tribofilm as observed in Fig. 19 in contrast to the presence of only TiC_X in the Maxthal 312 matrix. Oxygen diffusion within non-stoichiometric TiC_X is easier as compared to stoichiometric TiC due to the presence of carbon vacancies [49]. Barsoum et al. [67] reported on the oxidation of Ti_3SiC_2 in air and found that the presence of TiC_X in Ti_3SiC_2 matrix deteriorates its oxidation kinetics.

6. Wear mechanism

6.1. *Mechanism of transition from mild to severe wear*

A key factor in the performance of these materials was a time dependent transition from low friction and low wear to a much higher friction and higher wear regime. In the pre-transition region, the wear rate was immeasurable. However, post transition, the wear scar exhibited clear wear mechanisms possibly due to the disruption in the tribofilm architecture (e.g., growth of the brittle TiO_2 film that can be easily worn off) or as a result of the tribofilm reaching a critical thickness and subsequently spalling off, thus the evolution of third body abrasives. The wear mechanisms could be subdivided into two i.e., tribo-oxidative wear and surface fracture:

6.1.1. *Tribo-oxidative wear*

In agreement with Raman data as well as the EDX analysis, tribo-

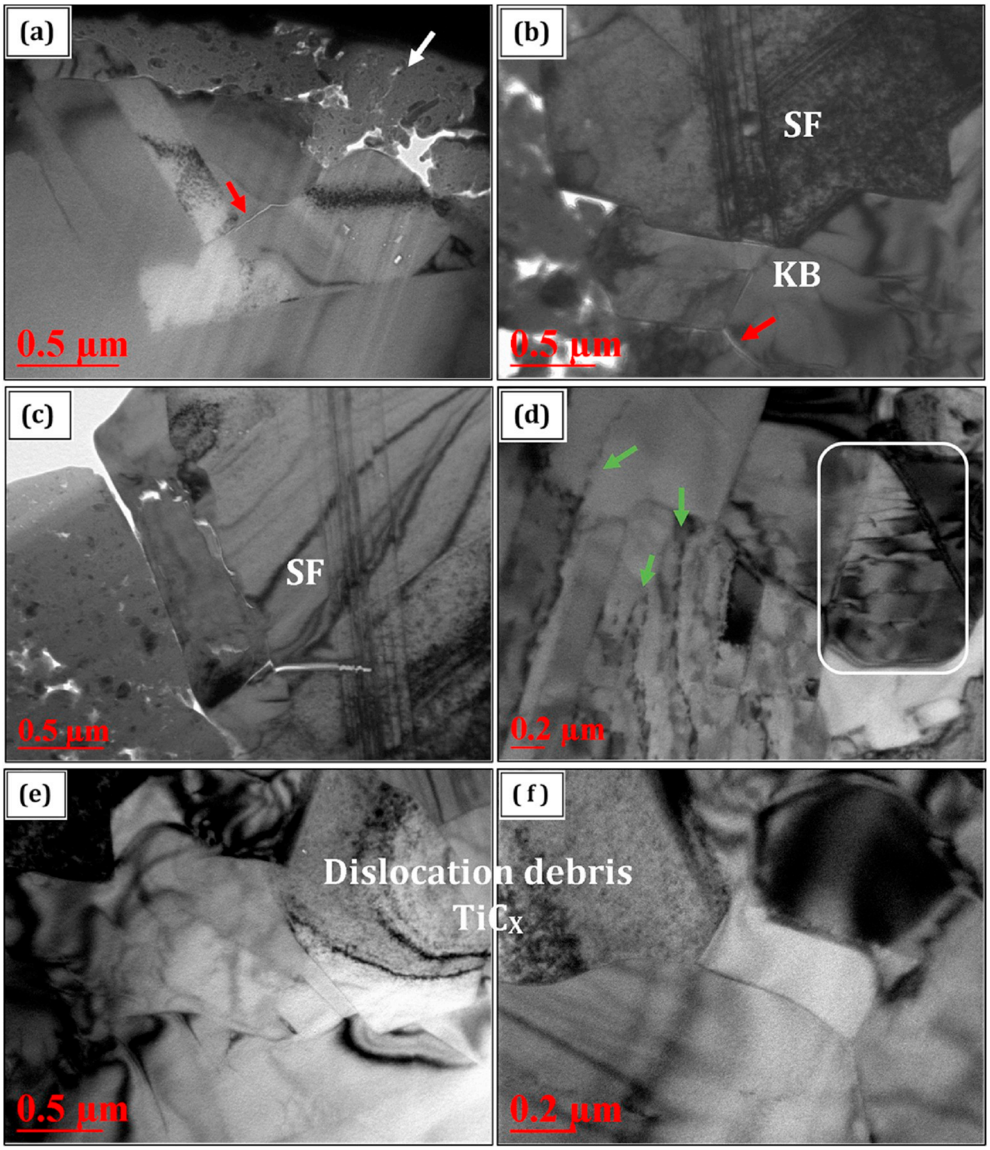

Fig. 24. A collection of bright-field (BF) TEM images from the wear track of the Maxthal 312 disc. Note: white arrow in (a) indicates tribofilm and/or tribofilm mixed with oxidized wear debris.

oxidation was an evident mechanism post transition. It appears that the temperature at the sliding surface during the dry sliding test was high enough to promote tribo-oxidation due to frictional heating. The low friction and insignificant wear in regime (I) can be attributed solely to the formation of a mixed tribofilm consisting of rutile, titanium oxycarbide and graphitic carbon. The structure of this tribofilm suggests that the frictional heating was at least 500 °C. The formation of graphitic carbon is possibly due to the oxidative extraction of titanium and silicon out of Ti_3SiC_2 in agreement with Zhang et al. [68] on the hydrothermal oxidation of Ti_3SiC_2. However, SiO_2 was not detected in the wear track possibly because its detection has always been elusive [69]. Hence, the two-step tribo-oxidative wear mechanism can be explained thus;

1. The disk material oxidizes at the asperity contact and a tribofilm layer grows containing titanium oxide, titanium oxycarbide and graphitic carbon. This leads to a low friction and wear rate in the pre-transition region.
2. The tribofilm layer then breaks down either due to the fact that TiO_2 can easily be worn more or less periodically due to its brittle nature [70], or because the growth of the tribofilm reaches a critical thickness and subsequently breaks up resulting in the formation of abrasive oxide wear debris. The wear debris is deleterious to friction combined with repeated damage accumulation and attrition of the debris between the contacting surfaces, that results in grain microfracture and eventual grain pull-out increasing the friction and wear.

6.1.2. *Fracture dominated wear*

The microstructural investigation of the worn surface suggests that the transition in friction and wear was initiated due to evolution of mild grain boundary cracking caused by accumulation of deformation. Since MAX phases exhibits room temperature ductility [57], during the mild wear regime dislocation slip and twinning occured, which led to dislocation pileup at grain boundaries thus initiating grain boundary fracture. This surface fracture led to the transition in friction and wear and in agreement with investigation by Cho et al. [71], but with a different MAX phase system. According to Cho et al. [71], the mild wear regime is due to grain boundary cracking arising from a combination of slip arrays, dislocation pileup at grain boundaries and twins whilst the severe wear regime was predominantly due to grain fracture.

7. Conclusions

Upon extensive analyses of the friction data and topographical features of the sliding surfaces, the following conclusions are summarized:

- The synthesis of Ti_3SiC_2 via the Ti_3SiC_2 starting powder route (i.e., Maxthal 312) will inevitably lead to ancillary TiC_X and/or $TiSi_2$ formation.
- Ti_3SiC_2 is intrinsically self-lubricating owing to the evolution of graphitic carbon, rutile, and oxycarbides at the sliding surface irrespective of the sliding speed.
- Transition in friction and wear is as a result of the deformation of Ti_3SiC_2 via kinking, grain delamination, grain fracture and eventual grain pull-outs, thus a three-body abrasive wear.
- TiC_X ancillary phase and/or TiC secondary phase inhibits the deformation of the Ti_3SiC_2 soft matrix due to their pinning effect.

References

[1] T. Lapauw, et al., A new method to texture dense Mn+1AXn ceramics by spark plasma deformation, Scr. Mater. 111 (Supplement C) (2016) 98–101.

[2] L. Cai, et al., Fabrication, mechanical properties, and tribological behaviors of Ti2AlC and Ti2AlSn0.2C solid solutions, J. Adv. Ceram. 6 (2) (2017) 90–99.

[3] S. Gupta, M.W. Barsoum, On the tribology of the MAX phases and their composites during dry sliding: a review, Wear 271 (9–10) (2011) 1878–1894.

[4] P. Eklund, J. Rosen, P.O.Å. Persson, Layered ternary Mn+1AXnphases and their 2D derivative MXene: an overview from a thin-film perspective, J. Phys. D Appl. Phys. 50 (11) (2017) 113001.

[5] Z.M. Sun, Progress in research and development on MAX phases: a family of layered ternary compounds, Int. Mater. Rev. 56 (3) (2011) 143–166.

[6] V.M. Hong Ng, et al., Recent progress in layered transition metal carbides and/or nitrides (MXenes) and their composites: synthesis and applications, J. Mater. Chem. 5 (7) (2017) 3039–3068.

[7] X.K. Qian, 1 - methods of MAX-phase synthesis and densification – I A2 - low, I.M, in: Advances in Science and Technology of Mn+1axn Phases, Woodhead Publishing, 2012, pp. 1–19.

[8] M.W. Barsoum, T. El-Raghy, The MAX Phases: unique New Carbide and Nitride Materials: ternary ceramics turn out to be surprisingly soft and machinable, yet also heat-tolerant, strong and lightweight, Am. Sci. 89 (4) (2001) 334–343.

[9] M. Sokol, et al., Big Questions in Chemistry - on the Chemical Diversity of the MAX Phases, 2019.

[10] M.W. Barsoum, M. Radovic, Elastic and mechanical properties of the MAX phases, in: D.R. Clarke, P. Fratzl (Eds.), Annual Review of Materials Research vol. 41, Annual Reviews: Palo Alto, 2011, pp. 195–227.

[11] Y. Liu, J. Chen, Y. Zhou, Effect of Ti5Si3 on wear properties of Ti3Si(Al)C2, J. Eur. Ceram. Soc. 29 (16) (2009) 3379–3385.

[12] M.W. Barsoum, T. El-Raghy, Synthesis and characterization of a remarkable ceramic: Ti3SiC2, J. Am. Ceram. Soc. 79 (7) (1996) 1953–1956.

[13] S. Li, L. Cheng, L. Zhang, Oxidation behavior of Ti3SiC2 at high temperature in air, Mater. Sci. Eng. A 341 (1–2) (2003) 112–120.

[14] R. Grieseler, et al., Copper-MAX-phase composite coatings obtained by electro-co-deposition: a promising material for electrical contacts, Surf. Coat. Technol. 321 (2017) 219–228.

[15] Y. Zhu, et al., Tribological Properties of Ti3SiC2 Coupled with Different Counterfaces, vol. 41, 2015.

[16] S. Gupta, et al., Tribological behavior of novel Ti3SiC2 (natural nanolaminates)-reinforced epoxy composites during dry sliding, Tribol. Trans. 58 (3) (2015) 560–566.

[17] W. Zhenyu, et al., Dense and High-Stability Ti2AlN MAX Phase Coatings Prepared by the Combined Cathodic Arc/sputter Technique, vol. 396, 2016.

[18] P. Eklund, et al., Synthesis and characterization of Ti-Si-C compounds for electrical contact applications, in: Proceedings of the Fifty-First IEEE Holm Conference on Electrical Contacts, 2005, 2005.

[19] J. Emmerlich, et al., Micro and macroscale tribological behavior of epitaxial Ti3SiC2 thin films, Wear 264 (11–12) (2008) 914–919.

[20] B.Y. Islak, E. Ayas, Evaluation of properties of spark plasma sintered Ti3SiC2 and Ti3SiC2/SiC composites, Ceram. Int. 45 (2019) 12297–12306.

[21] Z.F. Zhang, Z.M. Sun, H. Hashimoto, Low temperature synthesis of Ti3 SiC2 from Ti/SiC/C powders, Mater. Sci. Technol. 20 (10) (2004) 1252–1256.

[22] Y. Zhu, et al., Synthesis and decomposition of Ti3SiC2 under 1-5GPa at 1400°C 602–603 (2014) 499–502.

[23] M.W. Barsoum, The MN+1AXN phases: a new class of solids: thermodynamically stable nanolaminates, Prog. Solid State Chem. 28 (1) (2000) 201–281.

[24] S.-B. Li, et al., Mechanical properties and oxidation resistance of Ti3SiC2/SiC composite synthesized by in situ displacement reaction of Si and TiC, Mater. Lett. 57 (20) (2003) 3048–3056.

[25] M.B.-c. ZHU Jiao-qun, H.E. Li-ping, CHEN Yan-lin, synthesis of Ti3SiC2 by spark plasma sintering (SPS) of elemental powders, Trans. Nonferrous Metals Soc. China 13 (2003).

[26] M.W. Barsoum, et al., Thermal properties of Ti3SiC2, J. Phys. Chem. Solids 60 (4) (1999) 429–439.

[27] T. El-Raghy, et al., Damage mechanisms around hardness indentations in Ti_3SiC_2, J. Am. Ceram. Soc. 80 (2) (1997) 513–516.

[28] S. Jacques, et al., Pulsed reactive chemical vapor deposition in the C-Ti-Si system from H2/TiCl4/SiCl4, Thin Solid Films 478 (1) (2005) 13–20.

[29] S.P. Munagala, MAX phases: new class of carbides and nitrides for aerospace structural applications, in: N.E. Prasad, R.J.H. Wanhill (Eds.), Aerospace Materials and Material Technologies : Volume 1: Aerospace Materials, Springer Singapore, Singapore, 2017, pp. 455–465.

[30] A. Garg, J.L. Smialek, Microstructure and Oxidation of a MAX Phase/Superalloy Hybrid Interface - NASA/TM-2014-216679, Sponsoring Organization: NASA Glenn Research Center, 2014.

[31] J. Emmerlich, et al., Thermal stability of Ti3SiC2 thin films, Acta Mater. 55 (4) (2007) 1479–1488.

[32] Y. Zhou, et al., Preparation of TiC free Ti3SiC2 with improved oxidation resistance by substitution of Si with AI, Mater. Res. Innov. 8 (2) (2004) 97–102.

[33] I. Kero, M.-L. Antti, M. Odén, Preparation and Firing of a TiC/Si Powder Mixture, Bristol: IOP Publishing Ltd, Bristol, 2009.

[34] S.-B. Li, et al., In situ synthesis of Ti3SiC2/SiC composite by displacement reaction of Si and TiC, Mater. Sci. Eng. A 381 (1–2) (2004) 51–56.

[35] B. MW, et al., Long time oxidation study of Ti3SiC2, Ti3SiC2/SiC, and Ti3SiC2/TiC composites in air, J. Electrochem. Soc. 150 (4) (2003) B166–B175.

[36] N.C. Ghosh, in: S.P. Harimkar, K. Kalkan, R. Singh (Eds.), Synthesis and Tribological Characterization of In-Situ Spark Plasma Sintered Ti3sic2 and Ti3sic2-Tic Composites, 2012.

[37] B.M. Powders, P. Metal Powder, Standard Test Methods for Density of Compacted or Sintered Powder Metallurgy (PM) Products Using Archimedes' Principle, 2008.

[38] G. Wear, Erosion, Standard Test Method for Wear Testing with a Pin-On-Disk Apparatus, 2010.

[39] Z.F. Zhang, et al., Application of pulse discharge sintering (PDS) technique to rapid synthesis of Ti3SiC2 from Ti/Si/C powders, J. Eur. Ceram. Soc. 22 (16) (2002) 2957–2961.

[40] N.F. Gao, et al., Rapid synthesis of dense Ti3SiC2 by spark plasma sintering, J. Eur. Ceram. Soc. 22 (13) (2002) 2365–2370.

[41] T.B. Massalski, et al., Binary Alloy Phase Diagrams, Metals Park, Ohio : American Society for Metals, Metals Park, Ohio, 1986 c1986.

[42] T. El-Raghy, M.W. Barsoum, Diffusion kinetics of the carburization and silicidation of Ti3SiC2, J. Appl. Phys. 83 (1) (1998) 112–119.

[43] H. Li, et al., Synthesis of Ti3SiC2 by pressureless sintering of the elemental powders in vacuum, Mater. Lett. 58 (11) (2004) 1741–1744.

[44] C.-S. Park, et al., Processing of composites in the Ti-Si-C system, J. Mater. Sci. 36 (13) (2001) 3313–3322.

[45] J.X. Chen, et al., Thermal stability of Ti3AlC2/Al2O3 composites in high vacuum, Mater. Chem. Phys. 104 (1) (2007) 109–112.

[46] L.-O. Xiao, et al., Synthesis and thermal stability of Cr2AlC, J. Eur. Ceram. Soc. 31 (8) (2011) 1497–1502.

[47] I. Kero, R. Tegman, M.-L. Antti, Phase reactions associated with the formation of Ti3SiC2 from TiC/Si powders, Ceram. Int. 37 (7) (2011) 2615–2619.

[48] I. Kero, R. Tegman, M.-L. Antti, Carbon atmosphere effect on Ti3SiC2 based composites made from TiC/Si powders, Ceram. Int. 36 (4) (2010) 1259–1263.

[49] C. Racault, F. Langlais, R. Naslain, Solid-state synthesis and characterization of the ternary phase Ti3SiC2, J. Mater. Sci. 29 (13) (1994) 3384–3392.

[50] M.A. El Saeed, F.A. Deorsola, R.M. Rashad, Influence of SPS parameters on the density and mechanical properties of sintered Ti3SiC2 powders, Int. J. Refract. Metals Hard Mater. 41 (2013) 48–53.

[51] W. Tian, et al., Microstructural evolution and mechanical properties of Ti3SiC2–TiC composites, J. Alloy. Comp. 502 (1) (2010) 49–53.

[52] W. Dang, et al., The tribological properties of Ti3SiC2/Cu/Al/SiC composite at elevated temperatures, Tribol. Int. 104 (2016) 294–302.

[53] S.B. Li, L.F. Cheng, L.T. Zhang, Identification of damage tolerance of Ti3SiC2 by hardness indentations and single edge notched beam test, Mater. Sci. Technol. 18 (2) (2002) 231–233.

[54] C. Magnus, T. Kwamman, W.M. Rainforth, Dry sliding friction and wear behaviour of TiC-based ceramics and consequent effect of the evolution of grain buckling on wear mechanism, Wear 422–423 (2019) 54–67.

[55] T. El-Raghy, P. Blau, M.W. Barsoum, Effect of grain size on friction and wear behavior of Ti3SiC2, Wear 238 (2) (2000) 125–130.

[56] A. Souchet, et al., Tribological duality of Ti3SiC2, Tribol. Lett. 18 (3) (2005) 341–352.

[57] L. Wu, et al., Reciprocating friction and wear behavior of Ti3AlC2 and Ti3AlC2/Al2O3 composites against AISI52100 bearing steel, Wear 266 (1) (2009) 158–166.

[58] S. Gupta, et al., Tribological behavior of select MAX phases against Al2O3 at elevated temperatures, Wear 265 (3) (2008) 560–565.

[59] R.d. Celine, et al., Substrate grain-dependent chemistry of carburized planar anodic TiO2 on polycrystalline Ti, ACS Omega 2 (2) (2017) 631–640.

[60] C.-h. Wu, S.-y. Chen, P. Shen, CH doped anatase nanospheres with disordered shell and planar defects synthesized by pulsed laser ablation of bulk Ti in tetraethyl orthosilicate, CrystEngComm 16 (11) (2014) 2220–2229.

[61] F. Tuinstra, J.L. Koenig, Raman spectrum of graphite, J. Chem. Phys. 53 (3) (1970) 1126–1130.

[62] M. Barsoum, et al., Long time oxidation study of Ti3SiC2, Ti3SiC2/SiC, and Ti3SiC2/TiC composites in air, J. Electrochem. Soc. 150 (4) (2003) B166–B175.

[63] H. Zhai, Z. Huang, M. Ai, Tribological behaviors of bulk Ti3SiC2 and influences of TiC impurities, Mater. Sci. Eng. A 435–436 (Supplement C) (2006) 360–370.

[64] M.W. Barsoum, L. Farber, T. El-Raghy, Dislocations, kink bands, and room-temperature plasticity of Ti3SiC2, Metall. Mater. Trans. A 30 (7) (1999) 1727–1738.

[65] F.C. Frank, A.N. Stroh, On the theory of kinking, Proc. Phys. Soc. Sect. B 65 (10) (1952) 811–821.

[66] B.J. Kooi, et al., Ti 3SiC 2: a damage tolerant ceramic studied with nano-indentations and transmission electron microscopy, Acta Mater. 51 (10) (2003) 2859–2872.

[67] M.W.B.T. El-Raghy, Oxidation of Ti3SC2 in air, J. Electrochem. Soc. 144 (1997).

[68] H.B. Zhang, K.G. Nickel, Hydrothermal Oxidation of Ti3SiC2, 2012, pp. 323–354.

[69] W.K. Pang, et al., 15 - phase and thermal stability in Ti3SiC2 and Ti3SiC2/TiC/TiSi2 systems, in: Advances in Science and Technology of Mn+1axn Phases, Woodhead Publishing, 2012, pp. 389–413.

[70] R. Wäsche, D. Klaffke, In situ formation of tribologically effective oxide interfaces in SiC-based ceramics during dry oscillating sliding, Tribol. Lett. 5 (2) (1998) 173.

[71] S.-J. Cho, et al., The transition from mild to severe wear in alumina during sliding, Acta Metall. Mater. 40 (1) (1992) 185–192.

Paper D

The lubricating properties of spark plasma sintered (SPS) Ti_3SiC_2 MAX phase compound and composite

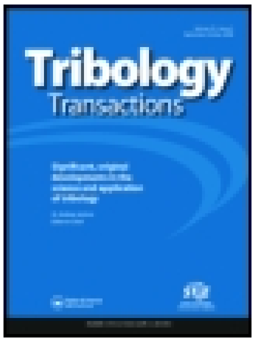

Tribology Transactions

ISSN: 1040-2004 (Print) 1547-397X (Online) Journal homepage: https://www.tandfonline.com/loi/utrb20

The Lubricating Properties of Spark Plasma Sintered (SPS) Ti_3SiC_2 MAX Phase Compound and Composite

Carl Magnus, Joanne Sharp & William M. Rainforth

To cite this article: Carl Magnus, Joanne Sharp & William M. Rainforth (2019): The Lubricating Properties of Spark Plasma Sintered (SPS) Ti_3SiC_2 MAX Phase Compound and Composite, Tribology Transactions, DOI: 10.1080/10402004.2019.1657534

To link to this article: https://doi.org/10.1080/10402004.2019.1657534

TRIBOLOGY TRANSACTIONS
https://doi.org/10.1080/10402004.2019.1657534

stle
Society of Tribologists
and Lubrication Engineers

The Lubricating Properties of Spark Plasma Sintered (SPS) Ti_3SiC_2 MAX Phase Compound and Composite

Carl Magnus, Joanne Sharp, and William M. Rainforth

Department of Materials Science and Engineering, The University of Sheffield, Sheffield, UK

ABSTRACT

MAX phase composites Ti_3SiC_2–TiC_x and Ti_3SiC_2–(TiC_x + TiC) were synthesized and consolidated via a powder metallurgy spark plasma sintering (SPS) technique. The bulk compositions and microstructural evolution of the resulting SPS discs were analyzed using X-ray diffraction, Raman spectroscopy, and scanning electron microscopy (SEM) paired with an energy-dispersive spectroscopy (EDS) system. The tribological behavior of the synthesized discs was investigated at room temperature under dry sliding conditions using an Al_2O_3 ball by employing a ball-on-disc tribometer configuration. Postmortem analyses of the worn surfaces showed that the Ti_3SiC_2 MAX phase exhibited intrinsic self-lubricating behavior due to the evolution of easily sheared graphitic carbon at the sliding surface. The addition of stoichiometric TiC delayed the oxidation kinetics of Ti_3SiC_2, which favors the evolution of graphitic carbon in lieu of rutile and oxycarbide films. Thus, this work shows comprehensively the existence of an intrinsic self-lubricating behavior of Ti_3SiC_2 and the important role of secondary-phase TiC in the Ti_3SiC_2 matrix in its tribological behavior. The wear mechanisms in both composites are dominated by tribo-oxidation triggered by frictional heating. This is then followed by deformation-induced wear upon friction transition.

ARTICLE HISTORY
Received 24 May 2019
Accepted 15 August 2019

KEYWORDS
MAX phases; dry sliding friction; frictional heating; tribofilm

Introduction

The $M_{n+1}AX_n$ phases are metallo-ceramics and are composed of an early transition metal M, an A-group (III, IV, V, or VI) element, where X is C or N, and n ranges from 1 to 6 (Hong, et al. (*1*); Eklund, et al. (*2*); Fashandi, et al. (*3*, *4*); Sokol, et al. (*5*)). These ternary compounds are of interest because of their intercalated hexagonal near-close-packed crystal structure, which forms nanolaminated layered structures (Mo, et al. (*6*); Gupta and Barsoum (*7*)) that impart remarkable properties (Smialek (*8*)). Figure 1 shows the unit cells of typical MAX phases for $n = 1$, $n = 2$, and $n = 3$, thus forming the so-called 312, 211, and 413 phase structures, due to the stoichiometric ratio of the constituent elements.

These phases are important for several reasons:

1. They simultaneously exhibit ceramic and metallic characteristics (Barsoum (*9*); Barsoum and Radovic (*10*)).
2. They possess a crystal structure comparable to that of well-known solid lubricants like graphite and MoS_2 (Zhai, et al. (*11*)).
3. They deform by confining damage to a limited plastically deformed area by combining a range of energy-absorbing mechanisms involving grain buckling, kink band formation, and delamination of individual grains (Le Flem and Liu (*12*); Barsoum, et al. (*13*)). This occurs despite the fact that they lack the five independent slip systems necessary for classic metal ductility (Barsoum (*9*)).
4. They are relatively soft (i.e., hardness ≈ 2–8 GPa) for a transition metal carbide, light (i.e., density ≈ 4.5 g/cm^3), and readily machinable like graphite (Barsoum (*9*)).
5. The have a high fracture toughness (7–9 MPa.m$^{1/2}$; Barsoum and El-Raghy (*14*)).
6. They are damage tolerant and thermal shock resistant, and some are oxidation resistant up to 1400 °C (Al-containing MAX phases: Ti_2AlC, Ta_2AlC, and Cr_2AlC; Haftani, et al. (*15*); Kwakernaak and Sloof (*16*); Shen, et al. (*17*); Farle, et al. (*18*)); in addition, some possess autonomous self-healing properties at high temperature (e.g., Ti_2AlC; Kwakernaak and Sloof (*16*); Shen, et al. (*17*); Qian (*19*); Sloof, et al. (*20*); Farle, et al. (*21*)).

These properties have led to the growing interest in MAX phases for potential structural applications in nuclear, tribological, and high-temperature systems (Gupta and Barsoum (*7*); Le Flem and Liu (*12*); Pang and Low (*22*)). MAX phases possess a hexagonal crystal structure similar to graphite, and previous studies have indicated that they possess lubricating properties (*7*). Therefore, MAX phases have been speculated as candidates in a range of tribological applications (Barsoum (*9*); Sun (*23*)). These applications include (1) electrical contacts, in the case of Cu-MAX phase

---

CONTACT Carl Magnus mcarl2@sheffield.ac.uk

Color versions of one or more of the figures in the article can be found online at www.tandfonline.com/utrb.
Review led by F. Mangolini.

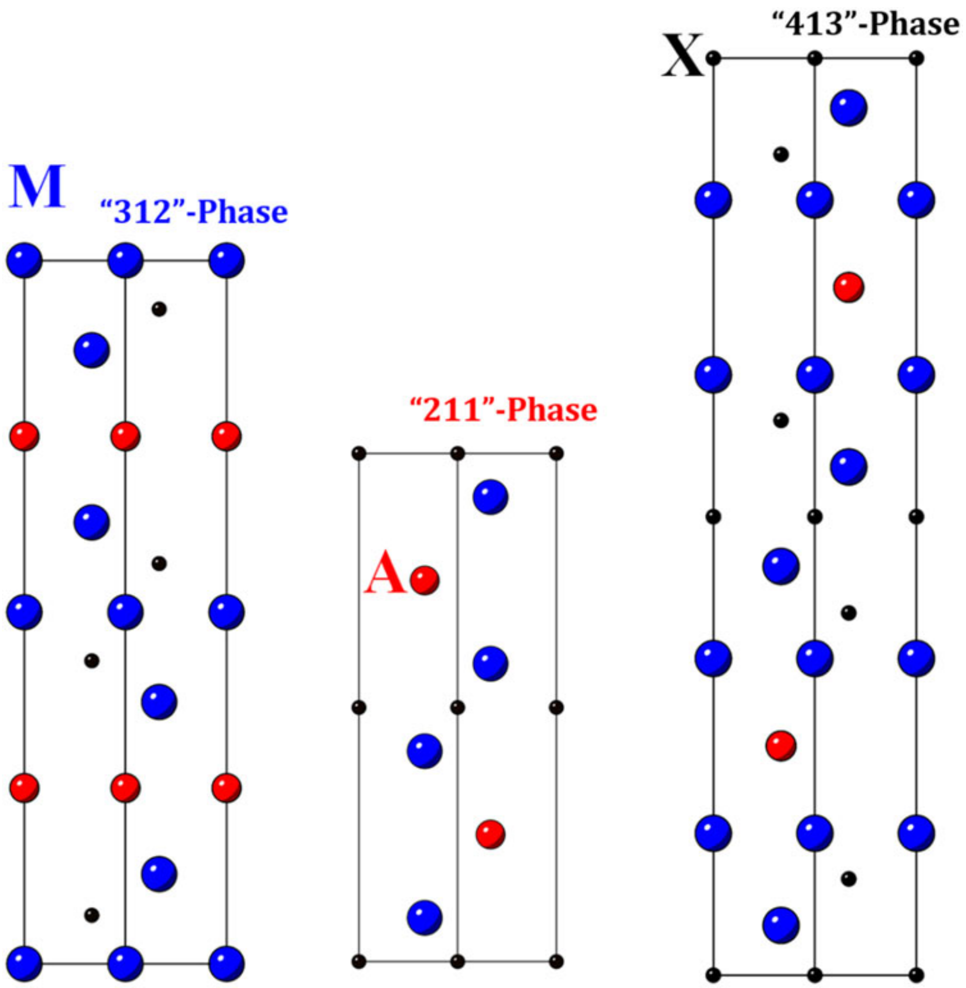

Figure 1. Crystal structure of some MAX phase systems crystallizing in $P6_3/mmc$.

and Ag-MAX phase composite systems (Grieseler, et al. *(24)*); (2) applications in high-temperature gas-cooled reactors (Zhu, et al. *(25)*); and (3) self-acting foil bearing rings in turbomachinery-based systems (Gupta and Barsoum *(7)*).

In a previous work by Souchet, et al. *(26)* on fine-grained and coarse-grained Ti_3SiC_2 sliding against Si_3N_4, they observed two successive regimes. In regime I, both the coefficient of friction μ and wear rate were low. In regime II, μ increased to a range of 0.4 to 0.5 and the wear rate became significant. Sakar, et al. *(27)* studied the fretting wear of Ti_3SiC_2 against steel and concluded that the dominant wear mechanisms were abrasion, tribochemical layer formation, and plastic deformation. Gupta and Barsoum *(7)* stated that the tribological behavior of MAX phases is governed by complex tribochemistries; thus, different tribolayers evolve with architectures dependent on the degree of oxidation as well as the mechanical properties such as adhesion to substrate and hardness. They classified tribofilms based on the triboreactions source into four categories (Gupta and Barsoum *(7)*): Type (I) if the triboreaction occurs mainly at the MAX phase surface; Type (II) if the triboreaction occurs at the countersurface; Type (III) if both the MAX phase and composite phase as well as the countersurface contribute to the tribofilm formation; and Type (IV) if the MAX-phase composite contributes predominantly to the tribofilm formation.

Recent work on the tribology of Ti_3SiC_2 focused on reinforcing the Ti_3SiC_2 matrix by incorporating metal and/or ceramic particles to improve its tribological behavior. Dang, et al. *(28)* studied the tribological behavior of Cu/Ti_3SiC_2 in comparison to monolithic Ti_3SiC_2. They reported that the tribological behavior of Cu/Ti_3SiC_2 was superior to that of Ti_3SiC_2 due to the formation of hard decomposition products (TiC_x, $Ti_5Si_3C_y$, $TiSi_2C_Z$, and Cu_3Si) during synthesis that inhibit abrasive friction and wear. Dang, et al. *(29)* also reported on the tribological behavior of $Ti_3SiC_2/Cu/Al/SiC$ at elevated temperature, showing that the tribological behavior of $Ti_3SiC_2/Cu/Al/SiC$ MAX phase composites was better than that of monolithic Ti_3SiC_2 between room temperature and 200 °C. At higher temperatures, the wear properties of the composite were not better than those of monolithic Ti_3SiC_2. However, the incorporated phases in the Ti_3SiC_2 matrix reinforced the bonding of the Ti_3SiC_2 grains by pinning the surrounding soft Ti_3SiC_2 matrix under cyclic stress. Yang, et al. *(30)* studied the dry sliding friction and wear properties of $(TiB_2 + TiC)/Ti_3SiC_2$ and TiC/Ti_3SiC_2 composites against steel balls with variation in load from 10 to 30 N. The composite TiC/Ti_3SiC_2 exhibited an increase in friction with increasing load, whereas the friction coefficient of the $(TiB_2 + TiC)/Ti_3SiC_2$ was not sensitive to load. Furthermore, the friction and wear rate of the $(TiB_2 + TiC)/Ti_3SiC_2$ composite were reported to be lower than those of TiC/Ti_3SiC_2. This was solely attributed to the pinning effect of the hard TiB_2 and TiC particles on the soft

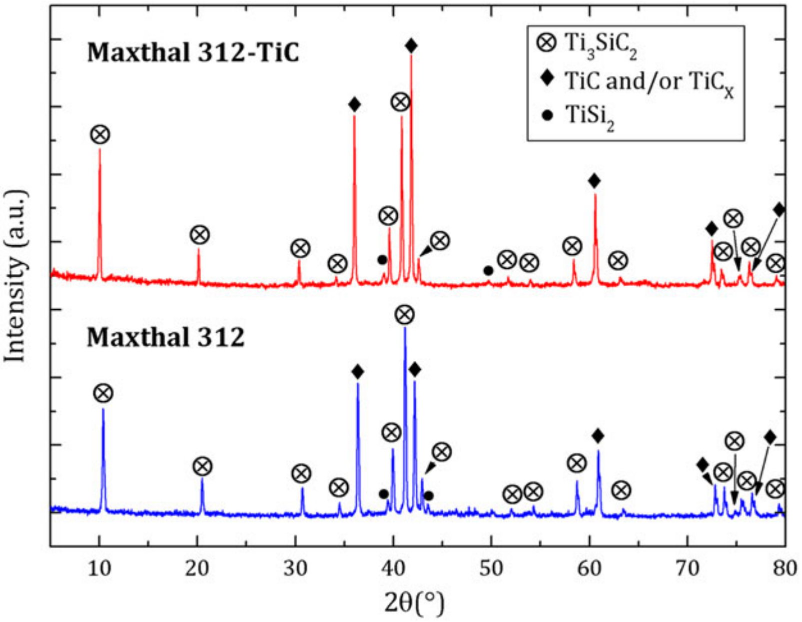

Figure 2. XRD patterns of the synthesized Maxthal 312 and Maxthal 312-TiC polished bulk samples.

Table 1. Density and Vickers hardness of the polished discs after SPS.

Disc samples	Theoretical density (g/cm^3)	Measured density (g/cm^3)	Relative density (%)	Vickers hardness (GPa)
Maxthal 312	4.62	4.54	98	9.4
Maxthal 312-TiC	4.68	4.65	99	12.6

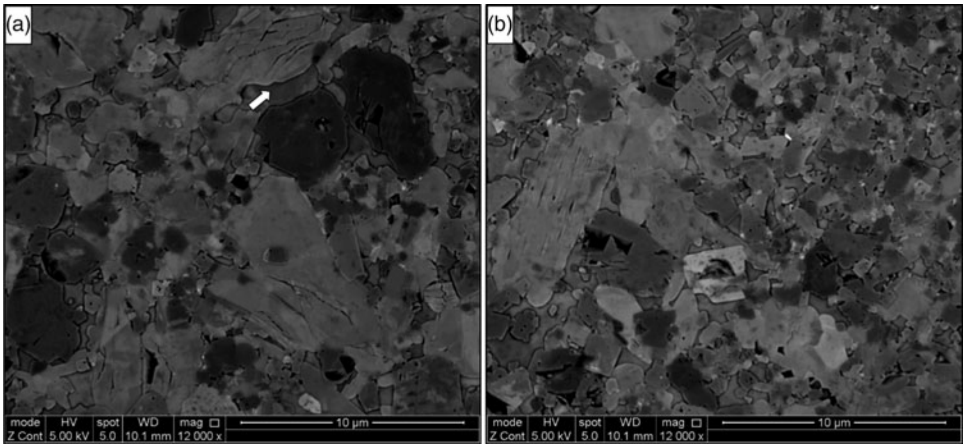

Figure 3. Backscattered SEM micrographs of the bulk Maxthal 312 sample. *Note*: White arrow in (a) shows the silicide region as confirmed by EDS.

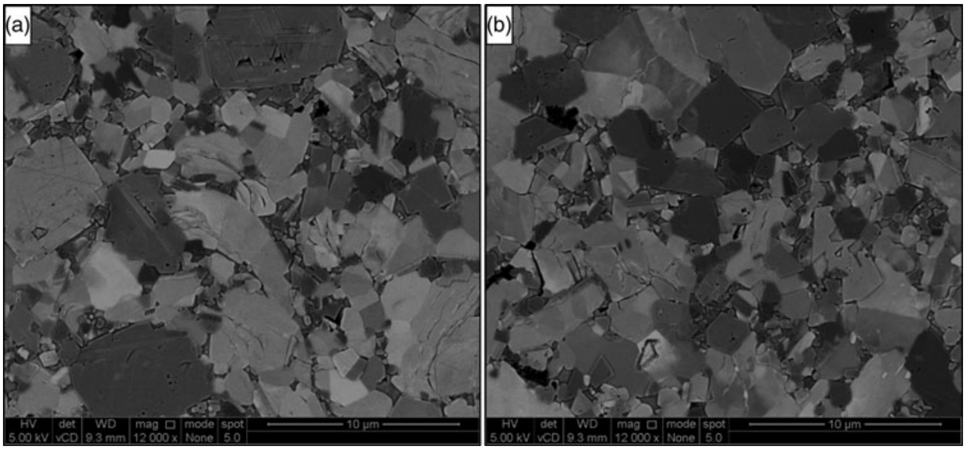

Figure 4. Backscattered SEM micrographs of the bulk Maxthal 312-TiC sample.

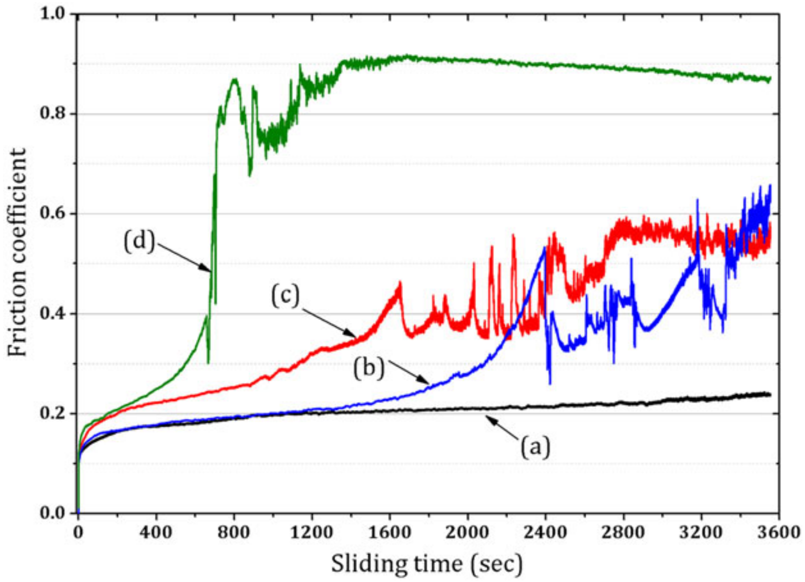

Figure 5. Evolution of the friction coefficient of the bulk samples upon sliding against Al_2O_3 ball using a constant normal load of 0.5 N: (a) Maxthal 312-TiC (50 rpm/60 min), (b) Maxthal 312 (50 rpm/60 min), (c) Maxthal 312-TiC (100 rpm/60 min), and (d) Maxthal 312 (100 rpm/60 min).

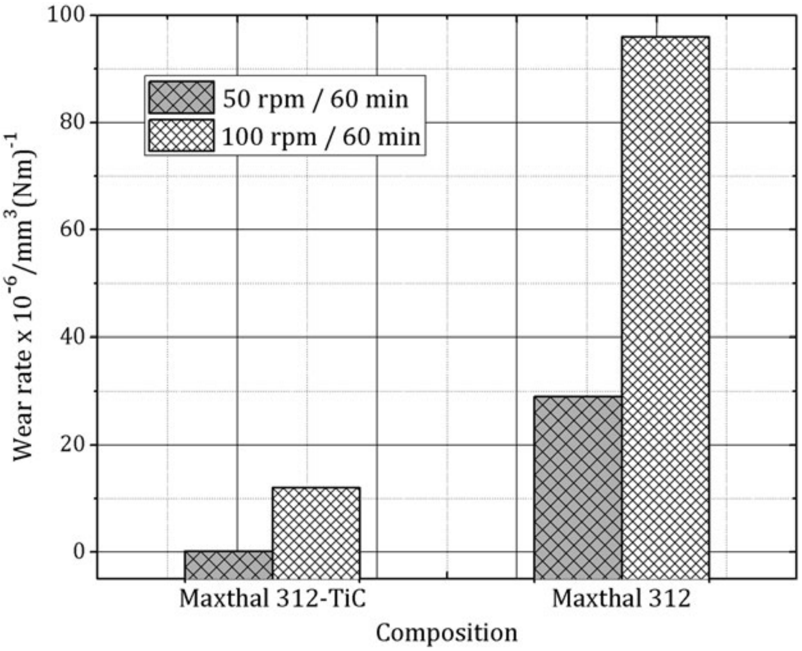

Figure 6. Wear rates of the bulk samples after SPS upon sliding against Al_2O_3 ceramic ball at room temperature.

Ti_3SiC_2 surrounding matrix, which helps to decentralize the shear stresses under the sliding ball.

An important potential application of MAX phases is in aerofoil bearing systems where intrinsic lubricity as well as low friction coefficients (μs) and wear rates (WRs) are required to mitigate friction and wear during engine start-up and shutdown (DellaCorte, et al. *(31)*). In addition, due to the low bearing load capacity of current aerofoil bearings, MAX phase composites consisting of second-phase hard particles can be employed. Such a tribosystem often incorporates Ni-based superalloys as the counterface material. However, in this work, alumina (Al_2O_3) was chosen because it is chemically inert and enables characterization of the intrinsic lubricity of Ti_3SiC_2.

The scope of this work is to synthesize fully dense bulk Ti_3SiC_2 and Ti_3SiC_2-TiC samples via the Maxthal 312 and TiC powder route using spark plasma sintering (SPS) in order to establish the existence of intrinsic self-lubricity in Ti_3SiC_2 during dry sliding contact and to further evaluate them as possible triboactive materials for prospective aerofoil bearing tribological applications through detailed analyses of the worn surfaces. Furthermore, the role of non-stoichiometric TiC_x formed in situ during the synthesis as well as the added stoichiometric TiC in the Ti_3SiC_2 soft matrix were explored. It is noteworthy that the initial starting compositions obtained for tribological investigation contained the ancillary phase TiC_x due to the starting composition of the Maxthal 312 pre-alloyed powder as well as reaction mechanisms explained elsewhere (Magnus and Rainforth *(32)*). Powder synthesis and consolidation were carried out using SPS because it is an inexpensive powder metallurgy process due to relatively short sintering times. SPS has

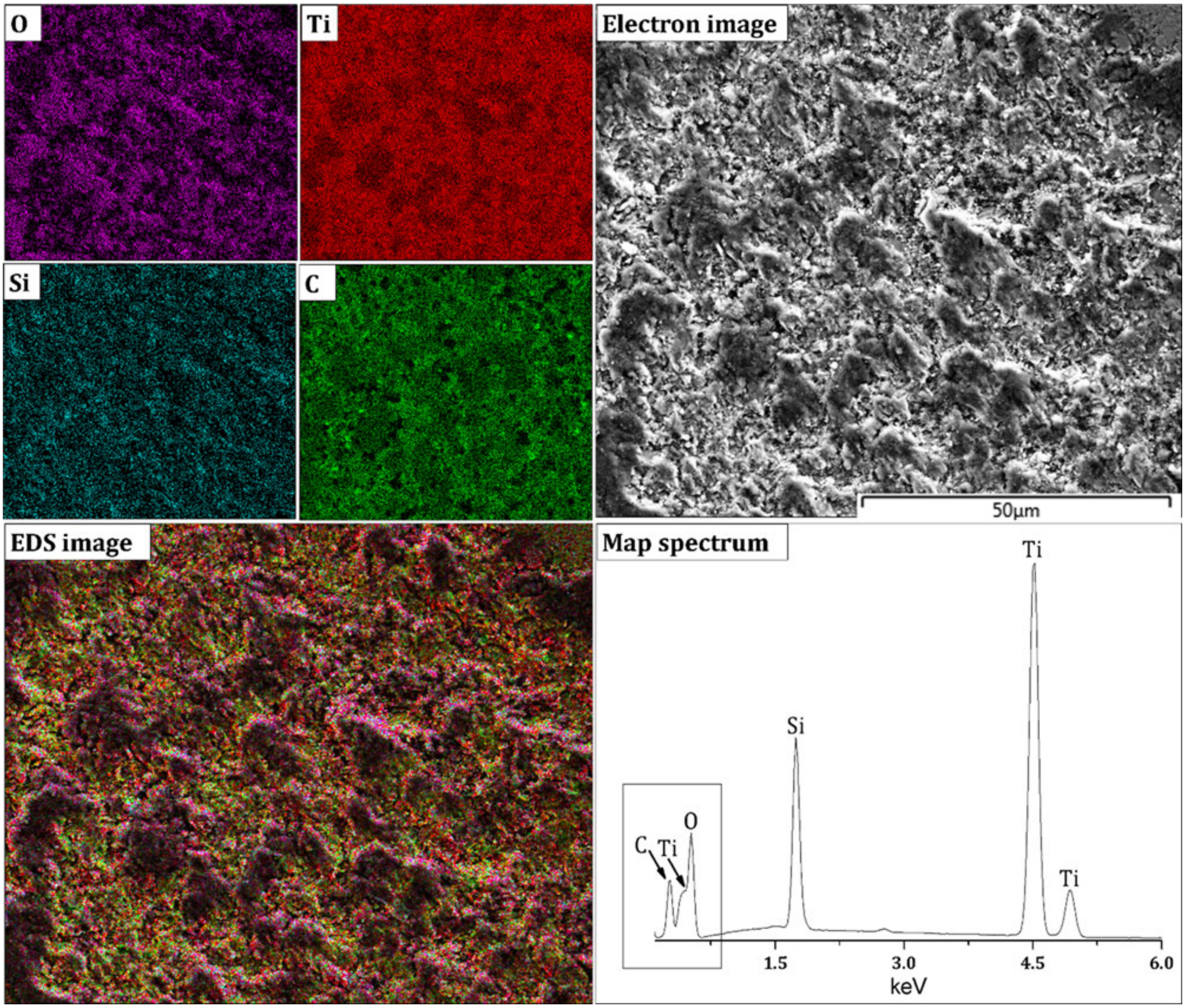

Figure 7. EDS elemental distribution map and spectrum inside the wear track of the Maxthal 312/Al_2O_3 worn section under wear condition 100 rpm/60 min.

unique sintering capabilities that incorporate simultaneous on–off pulse DC electric current via joule heating, temperature, and pressure during powder consolidation (Zhang, et al. (*33*)). The on–off electric current further enables localized high temperature to be transferred and dispersed at fine local areas between powder particles, which reduces the sintering time (Tokita (*34*)). Furthermore, the range of controllability of processing parameters (heating rate, load application rate, cooling rate, holding rate, etc.) makes SPS an extremely versatile process, because microstructures can be easily tailored in comparison to other conventional sintering techniques (Aalund (*35*)).

Experimental details

Materials and sample preparation

Commercially available MAX phase prereacted powder Maxthal 312 (nominally Ti_3SiC_2) with a particle size of 2.5 µm and composition 92 wt% Ti_3SiC_2 and 8 wt% TiC_x as an ancillary phase as well as TiC powder (99.5%, 2 µm particle size) were used as starting powders. To synthesize Ti_3SiC_2-TiC, 3 g of TiC powder was added to 12 g of Maxthal 312 powder, dry ball-milled continuously for 24 h, and then sieved using a 200-mesh sieve. The powder particle size of the resulting Maxthal 312-TiC powder was ~3.2 µm. The Maxthal 312 powder and the resulting Maxthal 312-TiC powder were then synthesized separately using SPS to produce bulk sample discs of Maxthal 312 and Maxthal 312-TiC, respectively. During SPS, the sintering parameters were as follows: 1450 °C sintering temperature, hold time 10 min, sintering pressure 54 MPa ($\approx$ 16 kN), and vacuum sintering environment (5×10^{-2} mbar). Next, disc surfaces were ground with SiC paper and polished with a diamond paste of 0.25 micron particle size to ensure complete removal of the carburized surface.

Vickers hardness and density

The density of the samples was measured using the Archimedes method according to ASTM standard B962-13 (ASTM International (*36*)), and relative density was calculated considering the various phases formed in the bulk samples using the mixture rule. Hardness measurements were done using a Vickers microhardness tester with an indentation load of 4.9 N for 10 s. Five measurements were

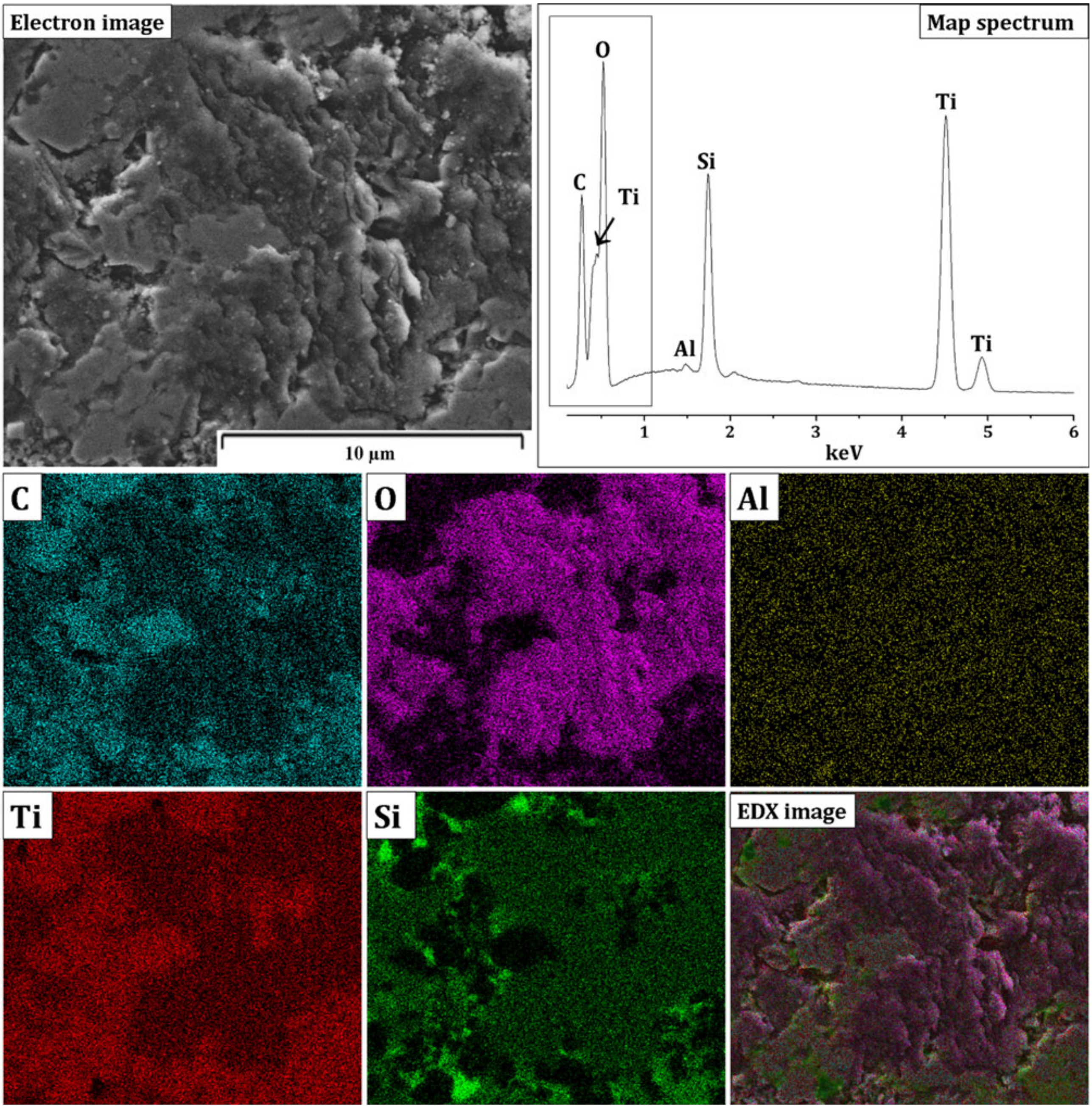

Figure 8. EDX elemental distribution map and spectrum inside the wear track of Maxthal 312-TiC/Al_2O_3 worn section under wear condition 100 rpm/60 min.

taken and their mean value is reported. Separately, to further reveal the role of Vickers induced damage on the deformation microstructures of the synthesized discs, a higher indentation load (49 N) was employed and the resulting Vickers damage was characterized.

Tribological test

Dry sliding room temperature tests (25 °C/29% relative humidity) were carried out using a ball-on-disc configuration with alumina (Al_2O_3, 2 mm ball) employed as the counterface material. The mean surface roughness of the ball and disc were measured using a stylus profilometer. The mean surface roughness (R_a) of the ball was 0.01 µm, and the roughness of the disc after polishing was 0.06 µm. Tribological tests were conducted using a normal load of 0.5 N (~180 MPa Hertzian contact pressure) and rotational speeds of 50 and 100 rpm (corresponding to sliding speeds of 16 and 37 mm/s, respectively), for a total sliding time of 60 min. The coefficient of friction was automatically measured and recorded in real time by the friction tester's computer system. The wear rate was determined by measuring the worn area from profilometric scans across the wear scars and the average wear area was input to the tribometer software to determine the wear rate.

Analyses

The crystal structure of the SPSed bulk Maxthal 312 and Maxthal 312-TiC samples was analyzed with X-ray

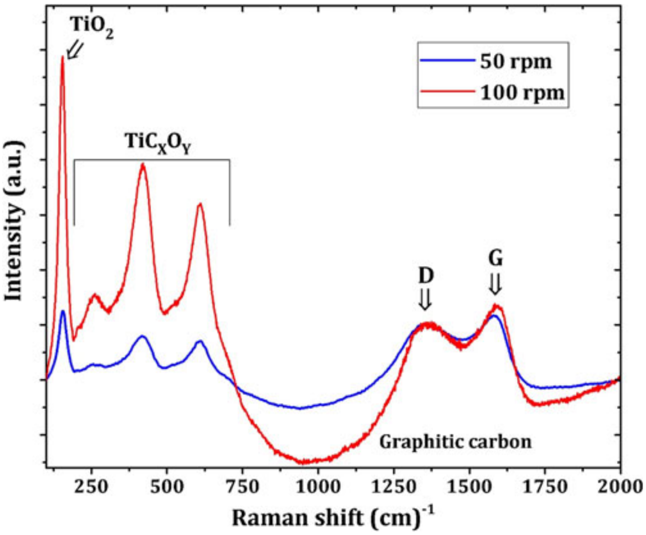

Figure 9. Raman spectra acquired inside the wear track of the Maxthal 312/Al_2O_3 tribocouples.

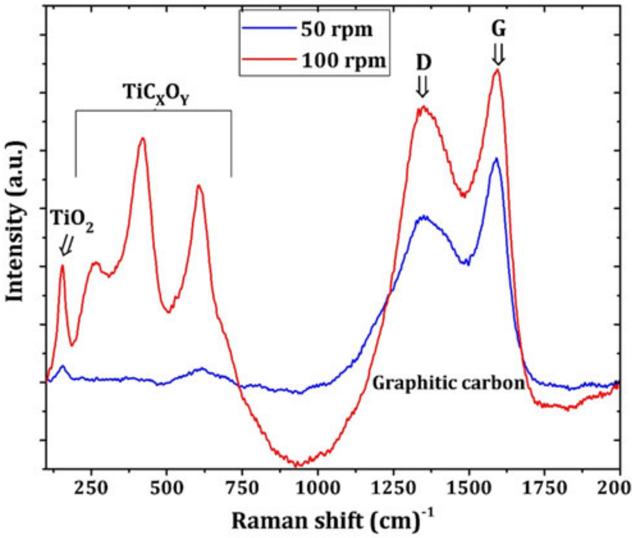

Figure 10. Raman spectra acquired inside the wear track of the Maxthal 312-TiC/Al_2O_3 tribocouples.

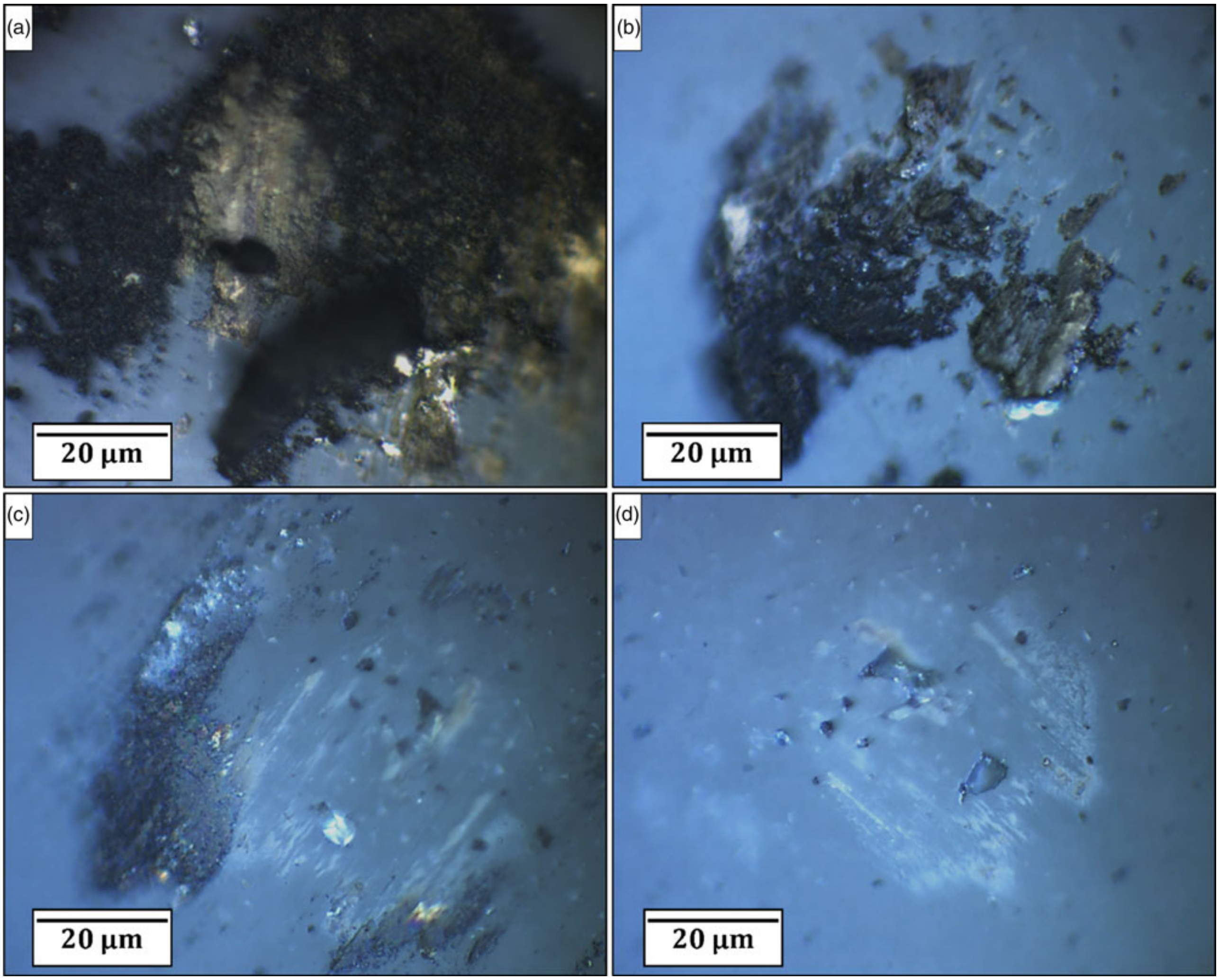

Figure 11. Optical images of the Al_2O_3 ball surface after unlubricated sliding against the Maxthal 312 disc (a) before cleaning and (b) after cleaning and Maxthal 312-TiC disc (c) before cleaning and (d) after cleaning for the contact condition 50 rpm/60 min.

diffractometry (XRD) using Cu Kα radiation. The diffractograms were recorded in the 2Θ range 10° to 80° with a step size 0.02°. The morphologies of the pristine material and wear tracks were analyzed using scanning electron microscopy (SEM) and optical microscopy. The ball surfaces after sliding against the discs were also analyzed using an optical

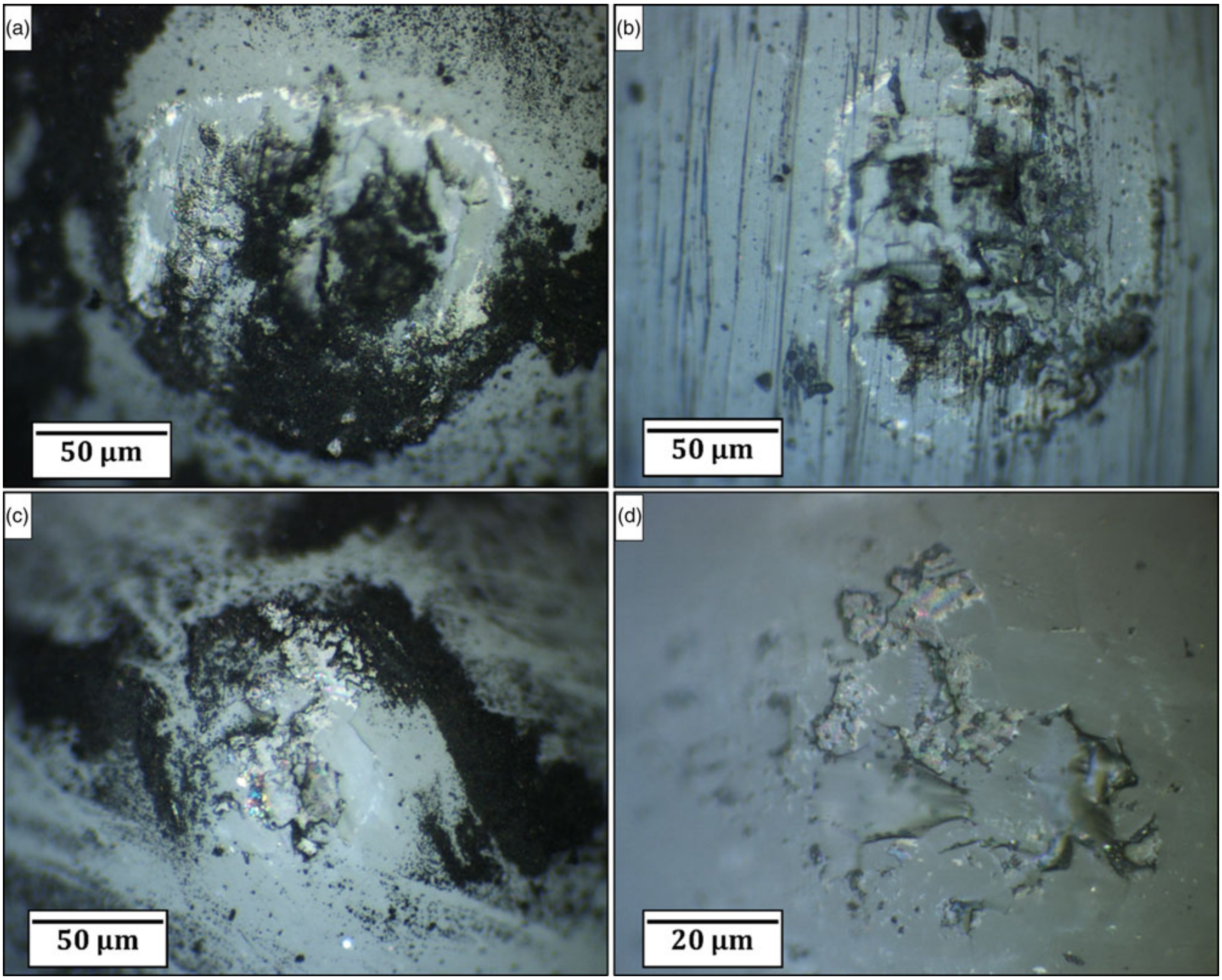

Figure 12. Optical images of the Al_2O_3 ball surface after unlubricated sliding against the Maxthal 312 disc (a) before cleaning and (b) after cleaning and Maxthal 312-TiC disc (c) before cleaning and (d) after cleaning for the contact condition 100 rpm/60 min.

microscope. The evolved surface chemistries was investigated using Raman spectroscopy and quantitative EDS analysis.

Results and discussion

Phase composition, properties, and microstructure

Figure 2 shows the XRD patterns of the synthesized discs after SPS. The main phases are Ti_3SiC_2 and TiC and a small amount of $TiSi_2$. The increase in TiC_x after SPS, especially in the Maxthal 312 bulk sample, is possibly linked to the carburization of Ti_3SiC_2 due to the graphite-rich environment stemming from the graphite tooling employed (i.e., graphite paper, dies, and punches) and/or intrinsic decomposition at high sintering temperature (El-Raghy and Barsoum *(37)*) leading to the formation of TiC_X. The evolution of the $TiSi_2$ phase occurred as it is a compulsory intermediary phase necessary for the formation of Ti_3SiC_2 and was not fully consumed during the synthesis (Kero, et al. *(38)*).

In order to determine the phase content, the integrated calibration for a two-phase Ti_3SiC_2-TiC was employed consistent with other previous work (Zhang, et al. *(39)*). However, it is important to mention that Rietveld refinement phase analysis could not be employed, as the bulk Ti_3SiC_2 had been textured preferentially in the pressing direction during the SPS synthesis, leading to exaggerated intensity. Because the amount of the $TiSi_2$ phase is relatively small, we can sensibly make an approximation by ignoring that phase and perform intensity calibration based on the work by Zhang, et al. *(39)*; thus,

$$W_{TSC} = \frac{1.80}{1.80 + I_{TC}/I_{TSC}} \text{ and } W_{TSC} = \frac{I_{TC}/I_{TSC}}{1.80 + I_{TC}/I_{TSC}},$$

where W_{TSC} and W_{TC} represents the relative weight percentages of Ti_3SiC_2 and TiC, respectively, and I_{TSC} and I_{TC} are the main peak intensities of the Ti_3SiC_2 (104) and TiC (200), respectively.

Using the above relation, the phase content of the Maxthal 312 sample was 76 wt% Ti_3SiC_2 and 24 wt% TiC_x, and for the Maxthal 312-TiC sample the phase content was 61 wt% Ti_3SiC_2 and 39 wt% (TiC_x + TiC). The phase composition shows that nonstoichiometric TiC_x ($x = 0.67$ as indicated by phase identification software) and not stoichiometric TiC formed in situ during the synthesis of both the Maxthal 312 and Maxthal 312-TiC samples due to possible decomposition and/or compositional phase shift according to the Ti-Si-C phase diagram linked to silicon evaporation during the

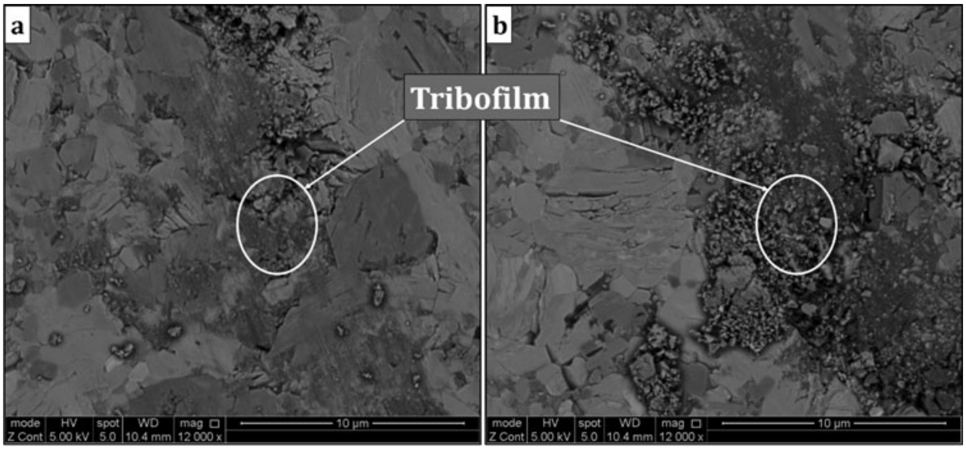

Figure 13a. SEM micrographs of the pretransition phase of the Maxthal 312/Al_2O_3 sliding surface.

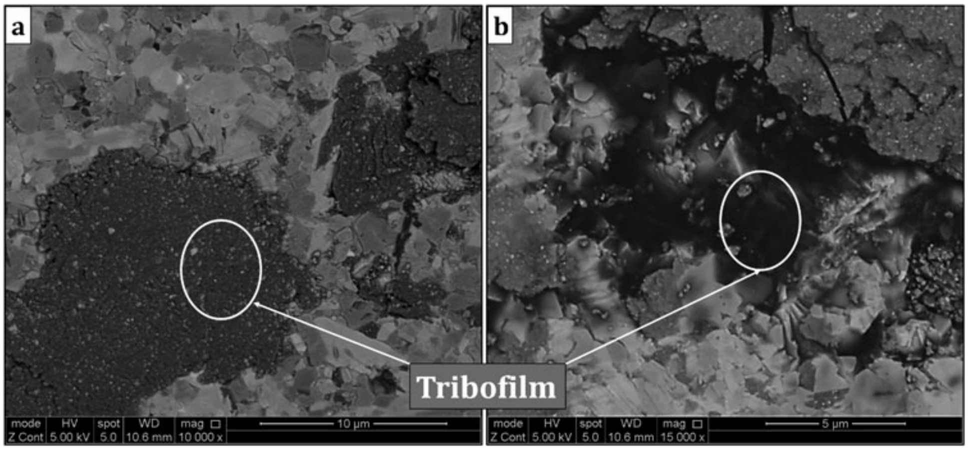

Figure 13b. SEM micrographs of the pretransition phase of the Maxthal 312-TiC/Al_2O_3 sliding surface.

synthesis (El-Raghy and Barsoum (*37*); Kero, et al. (*40*)). However, during the synthesis of the Maxthal 312-TiC, the formation of both TiC_x and TiC occurred due to in situ decomposition (as observed in the Maxthal 312 sample) and TiC powder addition, respectively. The main difference between stoichiometric TiC and nonstoichiometric TiC_x is that TiC possesses a higher density and hardness, superior oxidation resistance, and possibly higher fracture toughness than TiC_x (Zhang, et al. (*41*)). These may therefore lead to differences in the tribological behavior of the TiC_x in the Maxthal 312 disc phase composition and (TiC_x + TiC) in the Maxthal 312-TiC disc phase composition.

Table 1 shows the density and Vickers hardness of the SPSed Maxthal 312 and Maxthal 312-TiC samples. The theoretical densities of the samples are higher than the intrinsic density of Ti_3SiC_2 (4.52 g/cm^3), which can be linked to the evolution of the TiC_x and the addition of TiC phases with density (4.92 g/cm^3). In general, the samples were fully dense with relative density of 98% for the Maxthal 312 sample and 99% for the Maxthal 312-TiC sample. The Vickers hardness of the samples was also higher than the intrinsic hardness of Ti_3SiC_2 (4–5 GPa; Barsoum and Radovic (*10*)) mainly due to the increase in second phases in the matrix.

Backscattered electron images of the polished, unetched synthesized compacts are shown in Figures 3 and 4. The bright phases are the Ti_3SiC_2 phase and the dark phases are the TiC_x and/or TiC phase, and some small pockets of $TiSi_2$ (white arrow) coexist and is consistent with the XRD phase analysis. The microstructures of both Maxthal 312 and Maxthal 312-TiC exhibited a duplex microstructure where large grains are surrounded by a mixture of small grains (Figs. 3b and 4b).

Tribological properties

Friction evolution and wear

Figure 5 shows the evolution of the friction coefficient of the discs against the Al_2O_3 ceramic ball at room temperature. The lowest friction coefficient was obtained from the Maxthal 312-TiC disc (∼0.2) for the test condition 50 rpm/60 min. The friction curve was very stable and no fluctuation was observed. The mean friction coefficient for the Maxthal 312-TiC disc for the test condition 100 rpm/60 min was ∼0.38, exhibiting a transition from a stable low friction regime to an unstable high friction regime. On the other hand, for the Maxthal 312 disc under the test condition 50 rpm/60 min, the friction coefficient was initially very low (∼0.15–0.25) and stable and subsequently underwent a transition to an unstable high friction coefficient regime. The Maxthal 312 disc with test condition 100 rpm/60 min initially had a low friction coefficient (0.2–0.4) for a very short

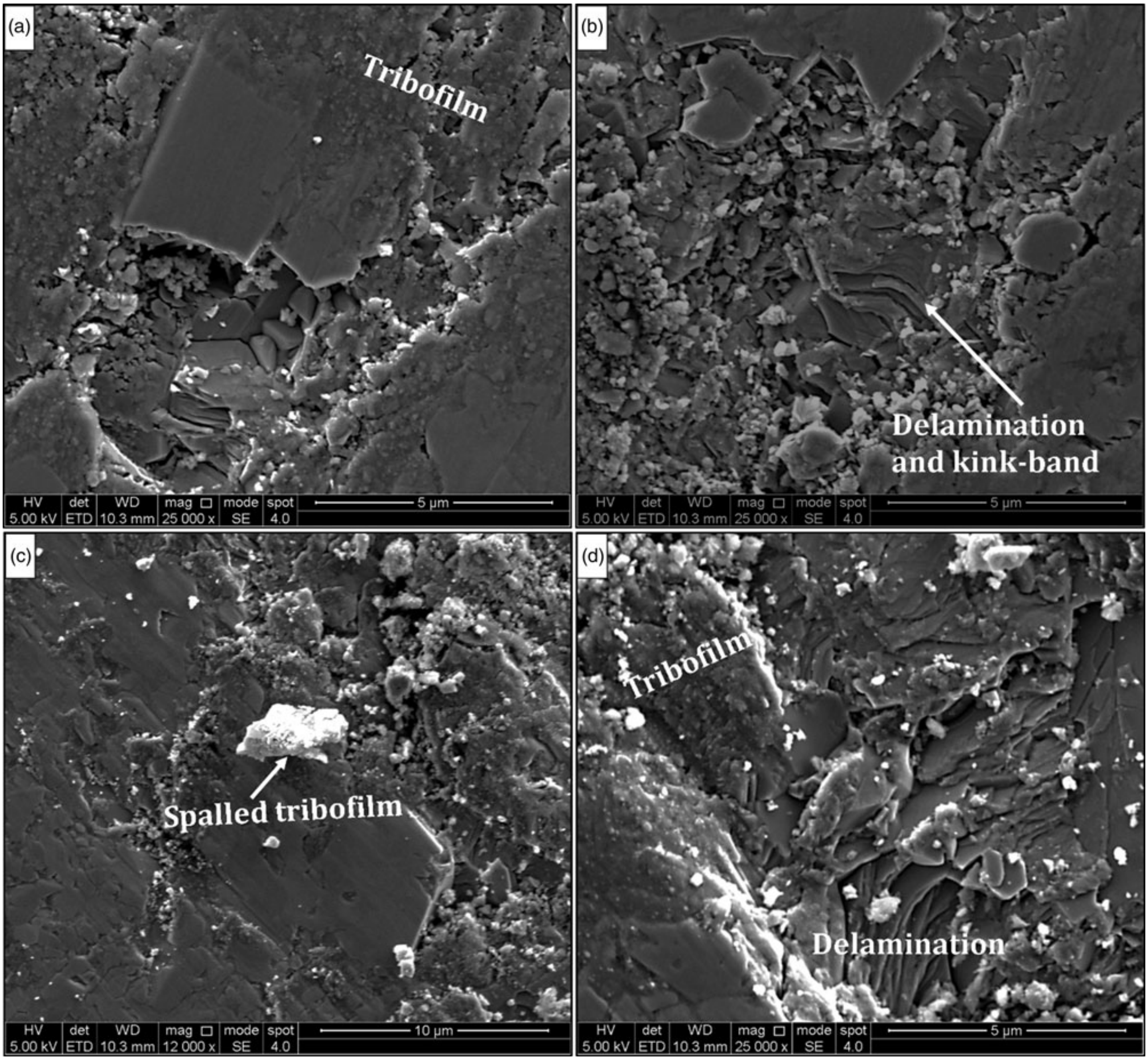

Figure 14. SEM micrographs of the sliding surface of Maxthal 312/Al_2O_3 for the contact conditions (a), (b) 50 rpm/60 min and (c), (d) 100 rpm/60 min. Note: White bits are spalled tribofilms.

time in contrast to the Maxthal 312-TiC sample for the same test condition, and was followed by a transition to a high friction regime (~0.9). The reason for the fluctuations in friction coefficient following the transition in friction as observed in the friction plot is not fully understood; however, the role of the tribofilm and/or wear debris generation cannot be ruled out.

Figure 6 shows the wear rates of the disc samples against the Al_2O_3 ceramic ball. The wear rates of the Maxthal 312-TiC disc for the contact conditions 0.5 N/50 rpm/60 min and 0.5 N/100 rpm/60 min were 2.06×10^{-7} $mm^3/(Nm)$ and 1.26×10^{-6} $mm^3/(Nm)$, respectively. For the Maxthal 312 disc, the wear rates for the contact test conditions 0.5 N/50 rpm/60 min and 0.5 N/100 rpm/60 min were 2.93×10^{-5} $mm^3/(Nm)$ and 9.63×10^{-5} $mm^3/(Nm)$, respectively. The increase in TiC content in the Maxthal 312-TiC seems to play a major role in the friction and wear behavior of Ti_3SiC_2.

Worn surface chemistry

EDX analysis

Figure 7 shows the EDX compositional map of an area from the worn surface of the Maxthal 312 disc for the test condition 100 rpm/60 min. The presence of oxygen in the wear track indicates an oxidation phenomenon triggered by frictional heating due to the dry sliding test condition. The Si-rich area appears to be depleted of oxygen and titanium, whereas the Ti-rich regions have been preferentially oxidized in lieu of Si to form possibly rutile (TiO_2). The absence of Al in the wear track indicates that no transfer of material from the ball onto the sliding surface took place during the test. The wear track seems to be rich in carbon; however, it is not possible using EDX analysis to separate the evolution of a graphitic layer during wear from the intrinsic carbon in the MAX phase composition.

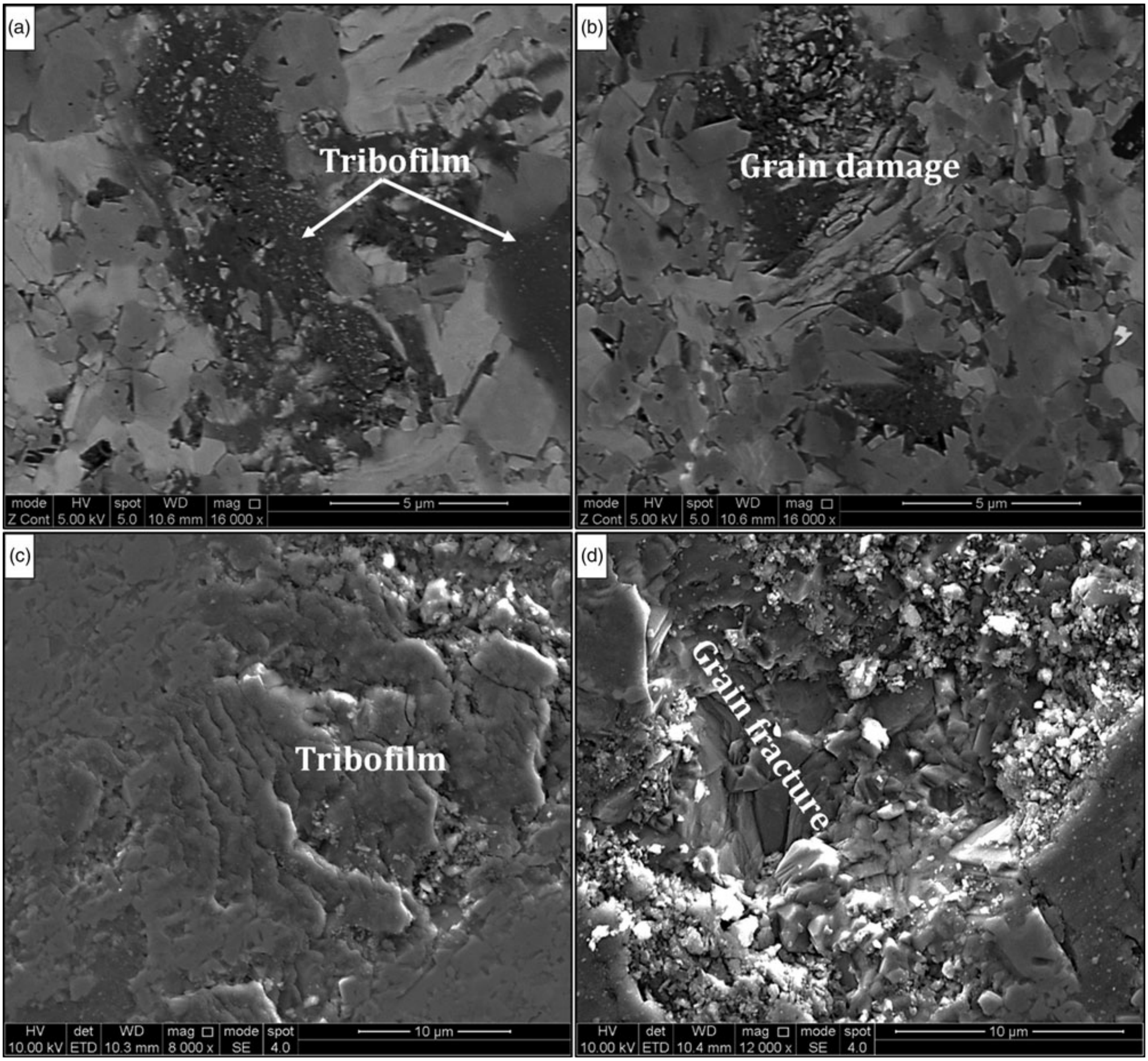

Figure 15. SEM micrographs of the sliding surface of the Maxthal 312-TiC/Al_2O_3 for the contact conditions (a), (b) 50 rpm/60 min and (c), (d) 100 rpm/60 min.

The EDS map acquired from the worn surface of the Maxthal 312-TiC disc (Fig. 8) for the test condition 100 rpm/60 min showed that in addition to the evolution of oxygen consistent with the chemistry of the worn surface of the Maxthal 312 disc, Al coexisted on the worn surface. The presence of Al may be directly linked to the presence of TiC in addition to the TiC_x in the Maxthal 312-TiC bulk sample which might have been abrasive. In addition, the oxygen content in the wear track of the Maxthal 312-TiC was much more significant than that observed in the wear track of the Maxthal 312 disc.

Raman analysis

In order to further probe local changes in chemistry from the wear tracks of the Maxthal 312 and Maxthal 312-TiC discs, Raman analysis was carried out to supplement the EDX analysis. Raman analysis of the Maxthal 312 disc worn surface (Fig. 9) revealed the presence of rutile (TiO_2), titanium oxycarbide (TiC_xO_y), and graphitic carbon. As the sliding speed was increased from 50 to 100 rpm, the rutile and oxycarbide tribofilms tended to grow, whereas the graphitic layer remained unchanged.

Raman analysis of the Maxthal 312-TiC sliding surface (Fig. 10) revealed that at 50 rpm the evolved tribofilm at the sliding surface was essentially graphitic carbon. However, as the sliding speed increased to 100 rpm, the evolution of rutile and oxycarbide can be seen, whereas the graphitic layer grew with increased sliding speed. It appears that the incorporation of TiC into the Ti_3SiC_2 matrix slowed down its oxidation kinetics compared to the presence of TiC_x formed in situ in the matrix. This observation is in agreement with EDX analysis because the higher oxygen content in the Maxthal 312-TiC sliding surface indicated that it formed later compared to Maxthal 312, where the tribofilm formation occurred earlier and was subsequently worn off.

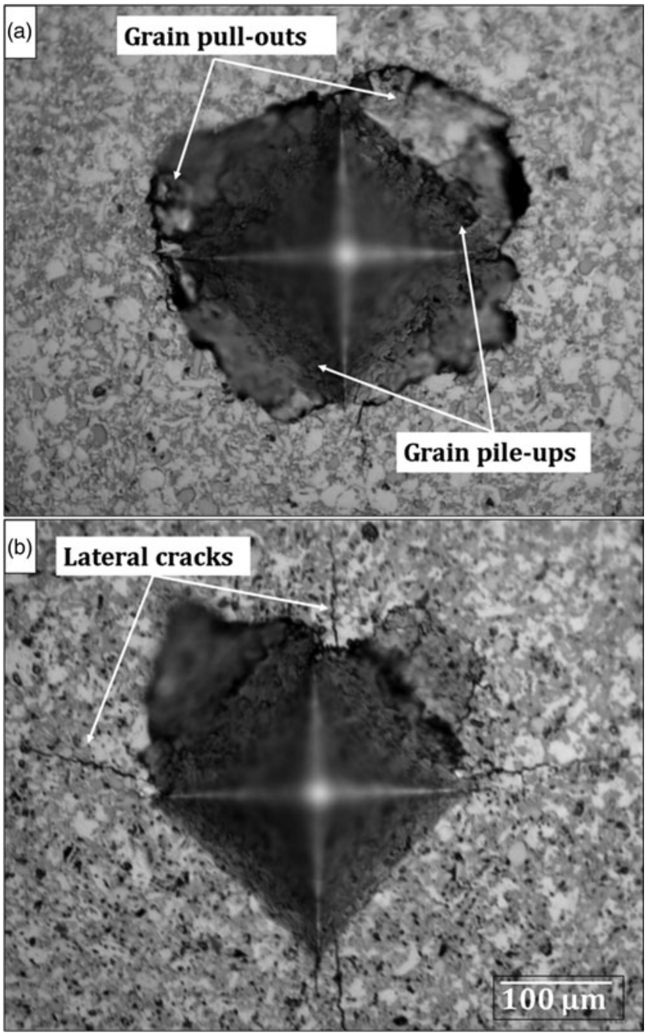

Figure 16. Optical images showing Vickers-induced deformation microstructures using an indentation load of 49 N: (a) Maxthal 312 and (b) Maxthal 312-TiC.

Alumina ball analysis

Figures 11 and 12 show the sliding surface of the Al_2O_3 ball after dry sliding against the Maxthal 312 and Maxthal 312-TiC discs for the contact conditions 50 rpm/60 min and 100 rpm/60 min, respectively. For the test run at 50 rpm/60 min, the Al_2O_3 ball surface after sliding against the Maxthal 312 disc appeared to have been slightly damaged and rough, with some transfer film and a large amount of wear debris evident. On the other hand, the Al_2O_3 ball surface upon sliding against Maxthal 312-TiC was relatively smooth, with some transfer film and slight scratches evident on the surface.

For the contact condition 100 rpm/60 min, a thick adherent layer of wear debris and transfer films were observed on the surface of the pins after sliding against the Maxthal 312 and Maxthal 312-TiC discs, respectively. In addition, the surface of the Al_2O_3 ball was fractured, with severe wear grooves evident on the ball surface after sliding against the Maxthal 312 disc in particular. The lack of elemental Al in the wear track of Maxthal 312/Al_2O_3 seen in EDX analysis (Fig. 7) is surprising due to the severity of the Al_2O_3 ball worn surface at 100 rpm.

Worn surface SEM analysis

Postmortem analyses of the worn surfaces of the discs were carried out using SEM to analyze the sliding surfaces pre- and post-friction transition. Short friction tests were carried out on the Maxthal 312 and Maxthal 312-TiC discs and terminated just before the transition in friction (Fig. 5) to produce pre-transition wear surfaces; the resulting SEM micrographs of the sliding surfaces are presented in Figs. 13a and 13b, respectively. As revealed by SEM, the pretransition sliding surfaces of the Maxthal 312 and Maxthal 312-TiC discs consist of mainly tribofilms with little or no damage at the sliding surfaces.

Analyses of the sliding surfaces of the Maxthal 312 and Maxthal 312-TiC discs posttransition for the entire test duration and contact conditions (Figs. 14 and 15, respectively) showed extensive grain damage, especially on the sliding surface of the Maxthal 312 disc (Fig. 14), which is consistent with the friction evolution curve. It appears that the Ti_3SiC_2 grains in the Maxthal 312 sample can be easily pulled out owing to the limited pinning effect of the TiC_x in the surrounding Ti_3SiC_2 matrix, compared to the extensive pinning effect introduced by the (TiC_x + TiC) on the Ti_3SiC_2 grains in the Maxthal 312-TiC sample, thus limiting pullout of grains and shear deformation of Ti_3SiC_2 during sliding contact, consistent with observations reported elsewhere (Dang, et al. *(28, 29)*; Yang, et al. *(30)*). It appears that the incorporation of TiC particles into the Ti_3SiC_2 matrix deteriorated its fracture toughness, becauses pronounced lateral cracks at the indentation diagonals were observed upon Vickers indentation on the Maxthal 312-TiC disc (Fig. 16b). This is in contrast to the Maxthal 312 disc (Fig. 16a), where little or no lateral cracking was observed, due to extensive deformation of the Ti_3SiC_2 grains, leading to severe grain pileup and pushout around the indentation zone. These microscale energy-absorbing mechanisms involving grain pileup, grain pushout, grain buckling, kink band formation, and eventual grain delamination are responsible for the signature damage tolerance observed in MAX phases (Li, et al. *(42)*). The lack of significant deformation in the Maxthal 312-TiC sample upon Vickers indentation other than cracking implies that the Maxthal 312-TiC sample is less prone to shear deformation by sliding as compared to the Maxthal 312 sample, due to the extensive pinning effect introduced by the (TiC_x and TiC) particles around the Ti_3SiC_2 grains, thus inhibiting deformation.

Friction transition and wear mechanisms

Friction transition

At the start of the experiment—that is, the pretransition regime—easily sheared graphitic carbon formed at the sliding surface as found in the Raman data; thus the low coefficients of friction μ and the low wear rates in this regime as observed from the friction plot of both the Maxthal 312 and Maxthal 312-TiC samples. Over time, as found by SEM-EDX and Raman analyses, the tribofilm architecture then evolved due to frictional heating leading to the formation of TiO_2 and TiC_xO_y subsequently in addition to the graphitic carbon previously formed at the sliding surface. However, it appears that the

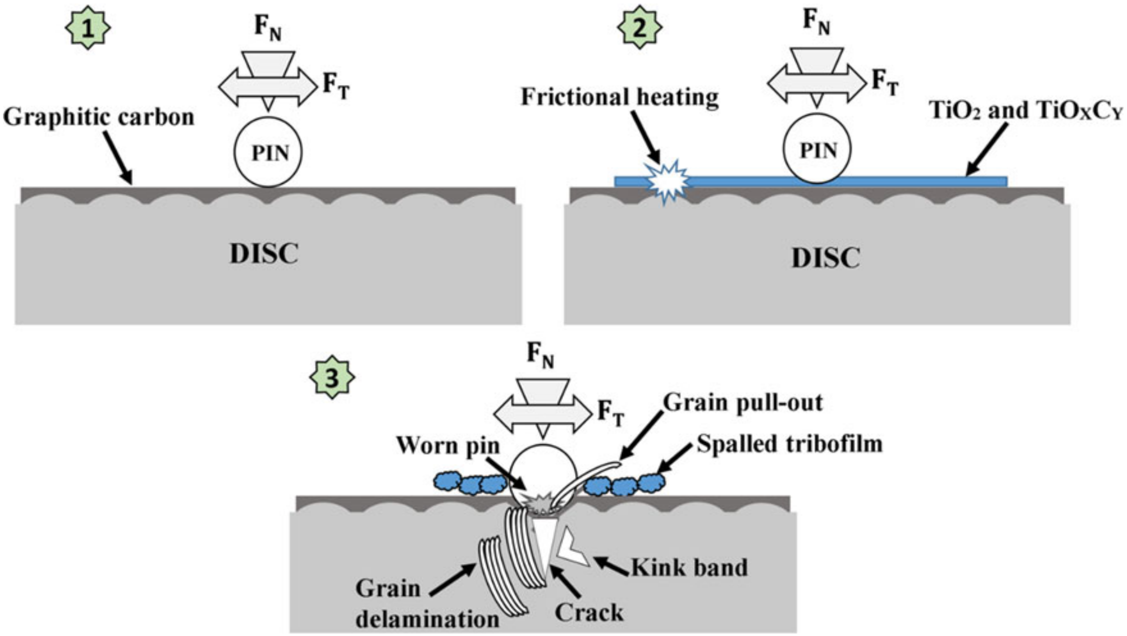

Figure 17. Schematic diagram of the tribo-oxidative to deformation-induced wear transition.

TiO_2 and/or TiC_xO_y was easily worn off the sliding surface, possibly due to their brittle nature or perhaps spalled off upon reaching a critical thickness for spallation, resulting in an abrasive third-body material between the ball and the disc (as evident from the wear grooves on the alumina ball surface); hence the transition in friction from low friction coefficients (μ) and low wear rates (WRs) to high friction coefficients (μ) and high wear rates (WRs) (posttransition). The absence of a transition in friction as observed in the Maxthal 312-TiC/Al_2O_3 at 50 rpm is mainly due to little or no presence of the brittle TiO_2 and TiC_xO_y tribofilms as seen in the Raman data in Fig. 10.

Wear mechanisms

After careful study of the chemistry and morphology of the wear tracks of the Maxthal 312 and Maxthal 312-TiC discs, the wear mechanisms (Fig. 17) are summarized as follows:

- Tribo-oxidative wear (leading to transition): Due to the dry sliding condition, frictional heating resulted in wear-induced oxidation of the sliding surface, which resulted in the evolution of TiO_2 and TiC_xO_y; thus the transition in friction and onset of deleterious wear.
- Deformation-induced wear (posttransition): Upon the transition in friction, direct contact between the Al_2O_3 ball and the discs was initiated, which resulted in microscale deformation (i.e., kink band formation and grain delamination), grain fracture, and eventual grain pullout at the sliding surface. As a result, third-body abrasive wear due to the fracture and pullout of the Ti_3SiC_2 grains dominates the wear mechanism.

Conclusions

The following salient conclusions were reached after exhaustive analyses of the pin and disc surfaces:

- Ti_3SiC_2 MAX phase is indeed intrinsically self-lubricating due to the lubricating effect of the easy shear graphitic carbon as well as the titanium oxycarbide films formed mechanochemically.
- The disruption in tribofilm architecture led to the transition in friction and wear due to the formation of titanium oxide and its subsequent spallation.
- TiC slows the oxidation kinetics of Ti_3SiC_2, thus favoring the presence of easily sheared graphitic carbon at the sliding surface.
- Ti_3SiC_2-TiC might be suitable for air foil bearing systems due to the intrinsic self-lubricity and damage tolerance of Ti_3SiC_2 and the load-bearing capability of second-phase TiC.

References

(1) Hong Ng, V. M., Huang, H., Zhou, K., Lee, P.S., Que, W., Xu, J. Z., and Kong, L. B. (2017), "Recent Progress in Layered Transition Metal Carbides and/or Nitrides (MXenes) and Their Composites: Synthesis and Applications," *Journal of Materials Chemistry A*, **5**(7), pp 3039–3068.

(2) Eklund, P., Rosen, J., and Persson, P. O. Å. (2017), "Layered Ternary $Mn+1AXn$ phases and Their 2D Derivative MXene: An Overview from a Thin-Film Perspective," *Journal of Physics D: Applied Physics*, **50**(11), pp 113001–113014.

(3) Fashandi, H., Lai, C. C., Dahlqvist, M., Lu, J., Rosen, J., Hultman, L., Greczynski, G., Andersson, M., Lloyd Spetz, A., and Eklund, P. (2017), "Ti_2Au_2C and $Ti_3Au_2C_2$ Formed by Solid State Reaction of Gold with Ti_2AlC and Ti_3AlC_2," *Chemical Communications*, **53**(69), pp 9554–9557.

(4) Fashandi, H., Dahlqvist, M., Lu, J., Palisaitis, J., Simak, S. I., Abrikosov, I. A., Rosen, J., Hultman, L., Andersson, M., Lloyd Spetz, A., and Eklund, P. (2017), "Synthesis of Ti_3AuC_2, $Ti_3Au_2C_2$ and Ti_3IrC_2 by Noble Metal Substitution Reaction in Ti_3SiC_2 for High-Temperature-Stable Ohmic Contacts to SiC," *Nature Materials*, **16**, pp 814–818.

(5) Sokol, M., Natu, V., Kota, S., and Barsoum, M. W. (2019), "Big Questions in Chemistry—On the Chemical Diversity of the MAX Phases." *Trends in Chemistry Cell Press Reviews*, **1**(2), pp 210–223.

(6) Mo, Y., Aryal, S., Rulis, P., and Ching, W.-Y. (2014), "Crystal Structure and Elastic Properties of Hypothesized MAX Phase-Like Compound $(Cr_2Hf)_2Al_3C_3$," *Journal of the American Ceramic Society*, **97**(8), pp 2646–2653.

(7) Gupta, S. and Barsoum, M. W. (2011), "On the Tribology of the MAX Phases and Their Composites during Dry Sliding: A Review," *Wear*, **271**(9–10), pp 1878–1894.

(8) Smialek, J. L. (2018), "Oxidation of Al_2O_3 Scale-Forming MAX Phases in Turbine Environments," *Metallurgical and Materials Transactions A*, **49**(3), pp 782–792.

(9) Barsoum, M. W. (2013), *MAX Phases: Properties of Machinable Ternary Carbides and Nitrides*, Wiley-VCH: Weinheim, Germany.

(10) Barsoum, M. W. and Radovic, M. (2011), "Elastic and Mechanical Properties of the MAX Phases," *Annual Review of Materials Research*, **41**, pp 195–227.

(11) Zhai, W., Shi, X., Wang, M., Xu, Z., Yao, J., Song, S., and Zhang, Q. (2014), "Friction and Wear Properties of TiAl-Ti_3SiC_2-MoS_2 Composites Prepared by Spark Plasma Sintering," *Tribology Transactions*, **57**(3), pp 416–424.

(12) Le Flem, M. and Liu, X. M. (2012), "Stability of Ti_3SiC_2 under Charged Particle Irradiation," *Advances in Science and Technology of Mn + 1axn Phases*, Low, I. M. (Ed.), pp 355–387, Woodhead Publishing: Sawston, Cambridge, UK.

(13) Barsoum, M. W., Farber, L., and El-Raghy, T. (1999), "Dislocations, Kink Bands, and Room-Temperature Plasticity of Ti_3SiC_2," *Metallurgical and Materials Transactions A*, **30**(7), pp 1727–1738.

(14) Barsoum, M. W. and El-Raghy, T. (1996), "Synthesis and Characterization of a Remarkable Ceramic: Ti_3SiC_2," *Journal of the American Ceramic Society*, **79**(7), pp 1953–1956.

(15) Haftani, M., Saeedi Heydari, M., Baharvandi, H. R., and Ehsani, N. (2016), "Studying the Oxidation of Ti_2AlC MAX Phase in Atmosphere: A Review," *International Journal of Refractory Metals and Hard Materials*, **61**, pp 51–60.

(16) Kwakernaak, C. and Sloof, W. G. (2018), "Work of Adhesion of Interfaces between M_2AlC (M=Ti, V, Cr) MAX Phases and α-Al_2O_3," *Ceramics International*, **44**(18), pp 23172–23179.

(17) Shen, L., Eichner, D., van der Zwaag, S., Leyens, C., and Sloof, W. G. (2016), "Reducing the Erosive Wear Rate of Cr_2AlC MAX Phase Ceramic by Oxidative Healing of Local Impact Damage," *Wear*, **358–359**, pp 1–6.

(18) Farle, A.-S., Stikkelman, J., Zwaag, S., and Sloof, W. G. (2017), "Oxidation and Self-Healing Behaviour of Spark Plasma Sintered Ta_2AlC," *Journal of the European ceramic society*, **37**, pp 1969–1974.

(19) Qian, X. K. (2012), "Methods of MAX-Phase Synthesis and Densification," *Advances in Science and Technology of Mn + 1axn Phases*, Low, I. M. (Ed.), pp 1–19, Woodhead Publishing: Sawston, Cambridge, UK.

(20) Sloof, W. G., Pei, R., McDonald, S. A., Fife, J. L., Shen, L., Boatemaa, L., Farle, A.-S., Yan, K., Zhang, X., van der Zwaag, S., Lee, P. D., and Withers, P. J. (2016), "Repeated Crack Healing in MAX-Phase Ceramics Revealed by 4D In Situ Synchrotron X-ray Tomographic Microscopy," *Scientific Reports*, **6**, pp 23040–23049.

(21) Farle, A.-S., Kwakernaak, C., van der Zwaag, S., and Sloof, W. G. (2015), "A Conceptual Study into the Potential of Mn + 1AXn-Phase Ceramics for Self-Healing of Crack Damage," *Journal of the European Ceramic Society*, **35**(1), pp 37–45.

(22) Pang, W. K. and Low, I. M. (2014), "Understanding and Improving the Thermal Stability of Layered Ternary Carbides in Ceramic Matrix Composites," *Advances in Ceramic Matrix Composites*, Low, I. M. (Ed.), pp 340–368, Woodhead Publishing: Sawston, Cambridge, UK.

(23) Sun, Z. M. (2011), "Progress in Research and Development on MAX Phases: A Family of Layered Ternary Compounds," *International Materials Reviews*, **56**(3), pp 143–166.

(24) Grieseler, R., Camargo, M. K., Hopfeld, M., Schmidt, U., Bund, A., and Schaaf, P. (2017), "Copper-MAX-Phase Composite Coatings Obtained by Electro-Co-Deposition: A Promising Material for Electrical Contacts," *Surface and Coatings Technology*, **321**, pp 219–228.

(25) Zhu, Y., Zhou, A., Ji, Y., Jia, J., Wang, L., Wu, B., and Qingfeng, Z. (2015), "Tribological Properties of Ti_3SiC_2 Coupled with Different Counterfaces," *Ceramic International*, **41**, pp 6950–6955.

(26) Souchet, A., Fontaine, J., Belin, M., LeMogne, T., Loubet, J.-L., and Barsoum, M. W. (2005), "Tribological Duality of Ti_3SiC_2," *Tribology Letters*, **18**(3), pp 341–352.

(27) Sarkar, D., Kumar, B. V. M., and Basu, B. (2006), "Understanding the Fretting Wear of Ti_3SiC_2," *Journal of the European Ceramic Society*, **26**(13), pp 2441–2452.

(28) Dang, W., Ren, S., Zhou, J., Yu, Y., Li, Z., and Wang, L. (2016), "Influence of Cu on the Mechanical and Tribological Properties of Ti_3SiC_2," *Ceramics International*, **42**(8), pp 9972–9980.

(29) Dang, W., Ren, S., Zhou, J., Yu, Y., and Wang, L. (2016), "The Tribological Properties of Ti_3SiC_2/Cu/Al/SiC Composite at Elevated Temperatures," *Tribology International*, **104**, pp 294–302.

(30) Yang, J., Gu, W., Pan, L. M., Song, K., Chen, X., and Qiu, T. (2011), "Friction and Wear Properties of In Situ (TiB_2+TiC)/Ti_3SiC_2 Composites," *Wear*, **271**(11), pp 2940–2946.

(31) DellaCorte, C., Zaldana, A. R., and Radil, K. C. (2002), "A Systems Approach to the Solid Lubrication of Foil Air Bearings for Oil-Free Turbomachinery," *Journal of Tribology*, **126**, pp 200–207.

(32) Magnus, C. and Rainforth, W. M. (2019), "Influence of Sintering Environment on the Spark Plasma Sintering of Maxthal 312 (Nominally-Ti_3SiC_2) and the Role of Powder Particle Size on Densification," *Journal of Alloys and Compounds*, **801**, pp 208–219.

(33) Zhang, F., Reich, M., Kessler, O., and Burkel, E. (2013), "The Potential of Rapid Cooling Spark Plasma Sintering for Metallic Materials," *Materials Today*, **16**(5), pp 192–197.

(34) Tokita, M. (2001), "Mechanism of Spark Plasma Sintering," *NEDO International Symposium on Functionally Graded Materials*, **21**, pp 729–732.

(35) Aalund, R. (2008), "Spark Plasma Sintering," *Ceramic Industry*.

(36) ASTM International. (2008), *Metal Powder, Standard Test Methods for Density of Compacted or Sintered Powder Metallurgy (PM) Products Using Archimedes' Principle*, ASTM International: Pennsylvania, USA.

(37) El-Raghy, T. and Barsoum, M. W. (1998), "Diffusion Kinetics of the Carburization and Silicidation of Ti_3SiC_2," *Journal of Applied Physics*, **83**(1), pp 112–119.

(38) Kero, I., Tegman, R., and Antti, M.-L. (2011), "Phase Reactions Associated with the Formation of Ti_3SiC_2 from TiC/Si Powders," *Ceramics International*, **37**(7), pp 2615–2619.

(39) Zhang, Z. F., Sun, Z. M., and Hashimoto, H. (2002), "Rapid Synthesis of Ternary Carbide Ti_3SiC_2 through Pulse-Discharge Sintering Technique from Ti/Si/TiC Powders," *Metallurgical and Materials Transactions A*, **33**(11), pp 3321–3328.

(40) Kero, I., Tegman, R., and Antti, M.-L. (2010), "Effect of the Amounts of Silicon on the In Situ Synthesis of Ti_3SiC_2 Based Composites Made from TiC/Si Powder Mixtures," *Ceramics International*, **36**(1), pp 375–379.

(41) Zhang, Z., Geng, C., Ke, Y., Li, C., Jiao, X., Zhao, Y., Tang, H., and Wang, M. (2018), "Processing and Mechanical Properties of Nonstoichiometric TiC_x ($0.3 \leq x \leq 0.5$)," *Ceramics International*, **44**(15), pp 18996–19001.

(42) Li, S. B., Cheng, L. F., and Zhang, L. T. (2002), "Identification of Damage Tolerance of Ti3SiC2 by Hardness Indentations and Single Edge Notched Beam Test," *Materials Science and Technology*, **18**(2), pp 231–233.

Paper E

Microstructures and intrinsic lubricity of in situ Ti_3SiC_2-$TiSi_2$-TiC MAX phase composite fabricated by reactive spark plasma sintering (SPS)

Wear 448-449 (2020) 203169

Contents lists available at ScienceDirect

Wear

journal homepage: http://www.elsevier.com/locate/wear

Microstructures and intrinsic lubricity of in situ Ti_3SiC_2–$TiSi_2$–TiC MAX phase composite fabricated by reactive spark plasma sintering (SPS)

Carl Magnus [a,*], Daniel Cooper [a,b], Le Ma [a], William M. Rainforth [a]

[a] *Department of Materials Science and Engineering, The University of Sheffield, Mappin Street, Sheffield, S1 3JD, UK*
[b] *Seaborg Technologies, Titangade 11, 2200, Copenhagen, Denmark*

ARTICLE INFO

Keywords:
Dry sliding
Microhardness
Frictional heating
Transmission electron microscopy

ABSTRACT

MAX phase composite Ti_3SiC_2–$TiSi_2$–TiC based on the $Ti_{n+1}SiC_n$ system was synthesized by spark plasma sintering (SPS) under vacuum sintering conditions. The microstructural evolution upon synthesis and Vickers indentation contact damage were characterized using scanning electron microscopy (SEM) and optical microscopy (OM). Tribological behaviour of the SPSed MAX phase composite was investigated under dry sliding ambient conditions for evidence of intrinsic lubricity as well as to understand the influence of second phase TiC particles on the wear behaviour of this composite system. Further, the underlying wear mechanisms was elucidated via detailed analyses of the worn surfaces using Raman spectroscopy, SEM-EDS and transmission electron microscopy (TEM). Exhaustive analyses of the worn surface revealed evidence of solid lubrication. Transition in friction and wear is attributed to change in wear mechanism from tribo-oxidative to deformation-induced wear due to the disruption of the tribofilm architecture.

1. Introduction

Early transition-metal ternary metalloceramics composed of hexagonal nanolaminated layered structure with a chemistry $M_{(n+1)}AX_{(n)}$ configuration have attracted a lot of attention [1,2]. Since first discovered in the late 1960s, MAX phases have been recently further explored to investigate their synthesis and structure-property relation owing to their unusual set of metal-like (machinability, stiffness, electrical and thermal conductivities) and ceramic-like (damage tolerance, thermal stability, oxidation resistance) properties [3,4]. The MAX phases are so-called because of their general formula where M are mainly group-4, group-5, and group-6 transition metals (mainly Ti, Zr, Hf, V, Nb, Ta, Cr, and Mo), while A is mainly an A-group element from groups 9 (Ir), 10 (Pd), 11 (Cu, Au), 12 (Cd, Zn), 13 (Al, Ga, In, Tl), 14 (Si, Ge, Sn, Pb), 15 (P, As, Sb, Bi), X is either C or N and $n = 1$–3 and possibly higher [1,5,6]. Fig. 1 shows some of the elements in the periodic table that forms the $M_{n+1}AX_n$ phases.

These ternary phases (80 +) crystallize in a hexagonal structure ($P6_3/mmc$ symmetry) with two formula units per unit cell, where $M_{n+1}X_n$ layers are interleaved with pure A-group atoms thus resulting in a characteristic $(M_{n+1}X_n)A(M_{n+1}X_n)A(M_{n+1}X_n)$ crystal structure [7]. The nature of their characteristic layered structure composed of stacking of n "ceramic" interposed with a "metallic" layer [8], coupled with the mixed covalent-metallic nature of the M–X bonds which are exceptionally strong and the relatively weak M–A bonds, endows the MAX phases with their signature mechanical, chemical, and electrical properties [4,9,10]. They represent the only class of ceramic-like material that deforms plastically via the nucleation and slip of basal dislocations (BDs) [11,12], incorporating a series of energy absorbing micro-scale events such as buckling of individual grains, diffuse micro-cracking, delamination of individual grains, kink and shear band formation followed by eventual grain push-outs and pull-outs [4,10,13–20].

Ti_3SiC_2, a 312 compound, is the most studied representative member of the MAX phase family. It possesses unique metalloceramic properties such as low hardness, low density, high modulus, excellent thermal and electrical conductivity, high fracture toughness, damage tolerance and easy machinability [4,21–23]. Its hexagonal layered crystal structure similar to graphite and MoS_2 [24] suggests it might be an excellent solid lubricant material with a low friction and wear properties suitable in a range of high-temperature structural engineering applications [25,26]. This is supported by the fact that Ti_3SiC_2 felt lubricious during machining as reported by Barsoum et al. [21]. Numerous research have since been conducted on the tribological behaviour of MAX phases for evidence of lubricity [27]. However, some researchers have reported

---

* Corresponding author.
E-mail address: mcarl2@sheffield.ac.uk (C. Magnus).

https://doi.org/10.1016/j.wear.2019.203169
Received 22 October 2019; Received in revised form 22 December 2019; Accepted 23 December 2019

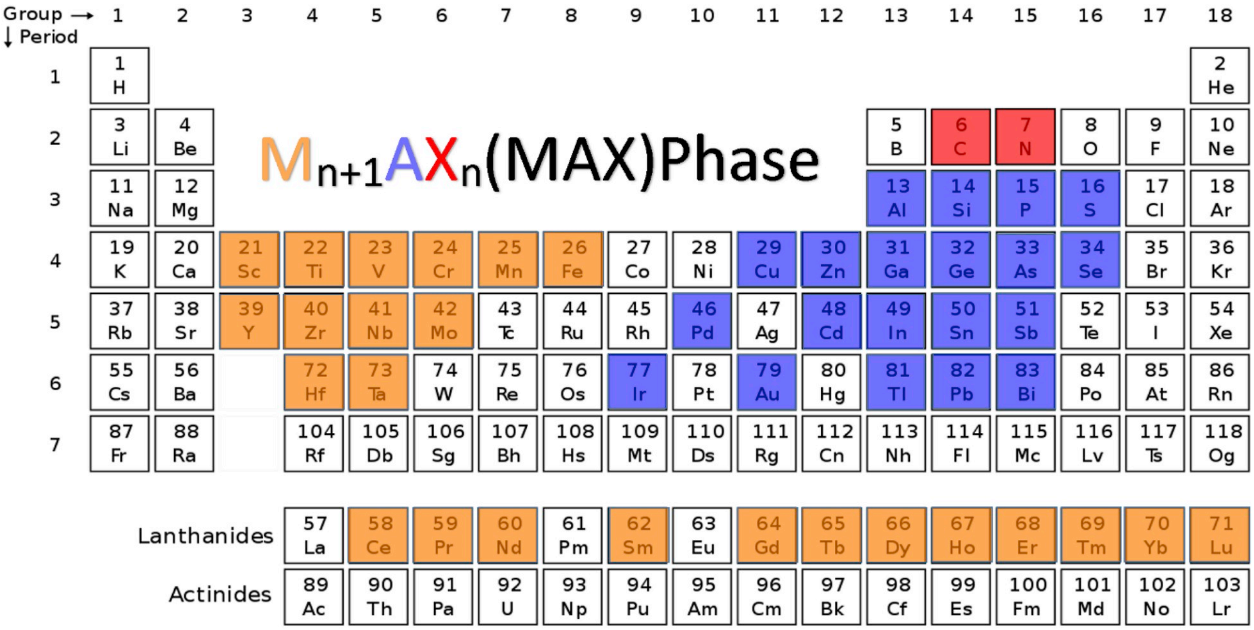

Fig. 1. The periodic table of the M, A, and X elements forming the MAX phases (bulk and thin films) and associated solid-solution MAX phases.

Table 1
Composition, sintering parameters and density of sample sintered by SPS.

Sample	Sintering Parameters				Density	
	Pressure (MPa)	Temperature (°C)	Heating Rate (°C/min)	Hold Time (min)	Actual	Relative
80% Ti_3SiC_2/14% TiC/6% $TiSi_2$	50	1350	50	15	4.437 g/cm^3	98 %

that albeit Ti_3SiC_2 possessing layered hexagonal crystal structure similar to graphite, it is not intrinsically self-lubricating [28]. This was attributed to a three-body abrasive wear that stems from the fracture and pull-out of the Ti_3SiC_2 grains — representing the dominant wear mechanism at room temperature [27,29,30]. The ease of grain fracture and pull-outs has been linked to the weak grain boundary force of the Ti_3SiC_2 grains [31]. In addition, some other authors have highlighted the low hardness and oxidation resistance as the main factors deteriorating the friction and wear properties of monolithic Ti_3SiC_2 [32]. These observations have led to new studies focussing essentially on the incorporation of a second phase hard material in the soft matrix of Ti_3SiC_2 as an effective way to mitigate these weaknesses [32,33]. Some possible reinforcing materials are TiC and TiB_2 as they possess high hardness, excellent oxidation resistance and close coefficient of thermal expansion (CTE) with Ti_3SiC_2 [32,34].

Nevertheless, little is known on the exact wear mechanism(s) as well as the intrinsic self-lubricating behaviour of monolithic Ti_3SiC_2 and Ti_3SiC_2-based material due to the lack of detailed investigation undertaken on the worn surface irrespective of the varying testing conditions reported to date. The scope of this work is to determine comprehensively the wear mechanism sequence of this solid and its associated composites during dry sliding friction at ambient conditions, in order to establish the existence of intrinsic self-lubricating behaviour as speculated [30, 35] and to further elucidate the wear mechanism.

2. Experimental procedure

2.1. Powder preparation

Commercially available titanium powder (100 mesh, 99.7% purity, Aldrich), silicon powder (200 mesh, 99% purity, Acros organics) and graphite powder were used as starting elemental powders. 5.53 g of titanium powder and 0.98 g of graphite powder were dry-milled in a SPEX 8000 mill continuously for 2 h and subsequently mixed with 1.08 g of silicon powder according to a 3:1:2 stoichiometry.

2.2. Consolidation by spark plasma sintering (SPS)

The stoichiometric powder mixture was poured into an electrically and thermally conductive cylindrical graphite mould with an inner

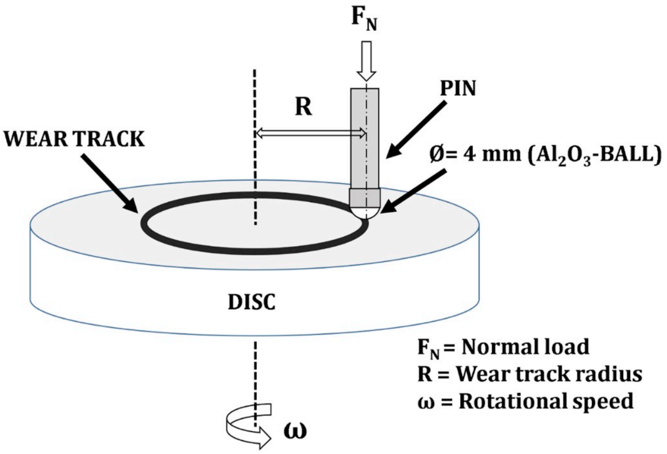

Fig. 2. Schematic of the ball-on-disc rotary configuration employed for the wear test.

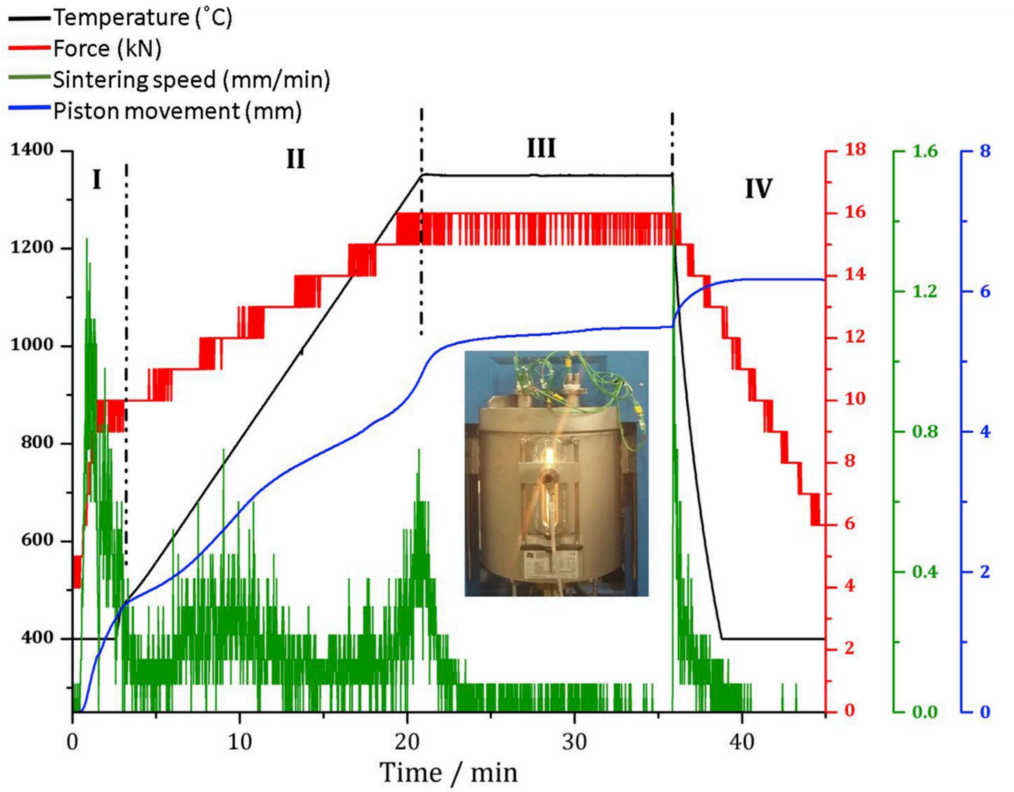

Fig. 3. SPS shrinkage profile during the synthesis of Ti_3SiC_2 metalloceramic under vacuum.

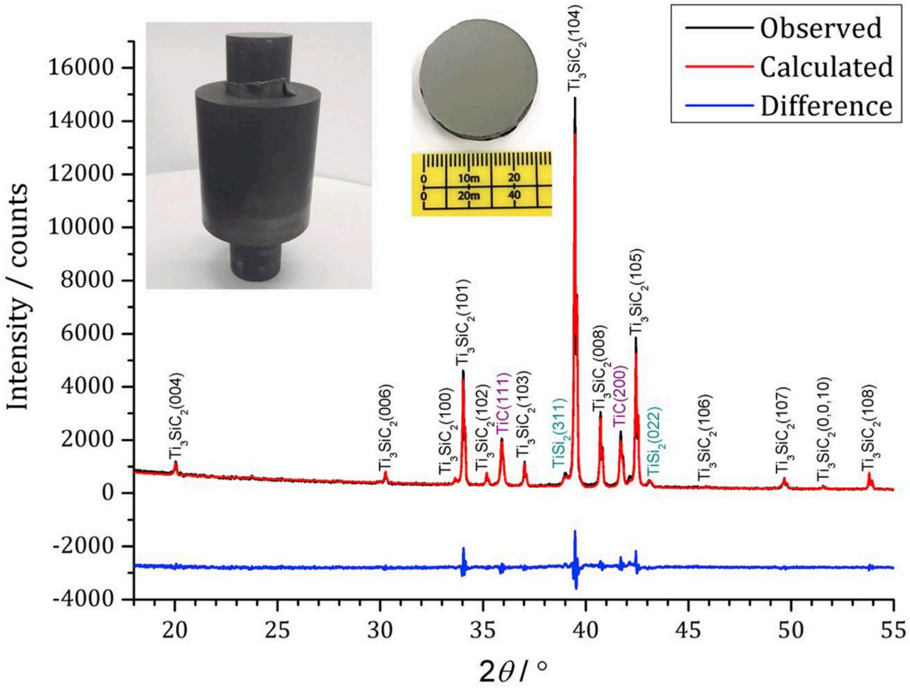

Fig. 4. XRD pattern obtained from the polished surface of the MAX phase composite disc. Inset shows the punch-powder-die set-up.

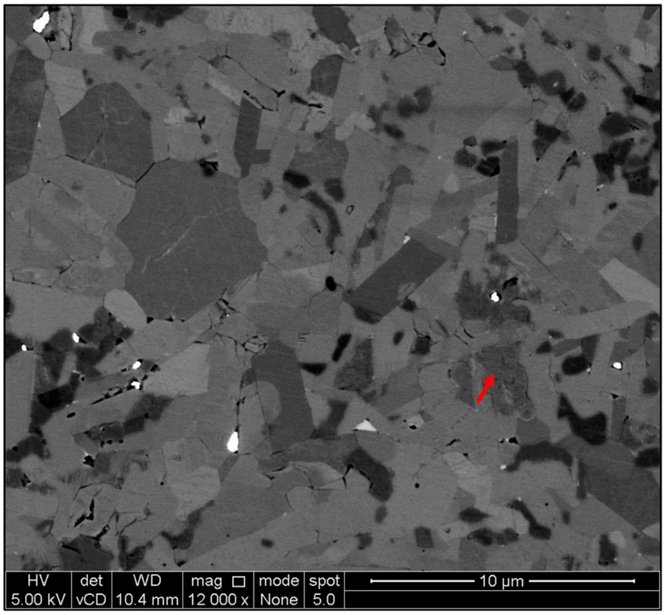

Fig. 5. A backscattered SEM micrograph of the unetched polished bulk sample. Note: white contrast are artefacts from colloidal silica used to reveal the microstructure without etching.

diameter of 20 mm. The powder was isolated from the graphite mould and punches by applying a graphite paper previously sprayed with boron nitride (BN) to ease the removal of the sintered sample from the tooling and to further protect graphite dies and punches from possible chemical reaction with the specimen at high temperature. The die was then subsequently covered with graphite felt and tied with graphite wire in order to reduce heat dissipation during the sintering. The sintering cycle was carried out in-situ in vacuum (10^{-2} Pa) in a SPS furnace unit (HP D 25, FCT Systeme GmbH, Rauenstein, Germany). Details of the SPS synthesis, resulting composition and density of the bulk sample is shown in Table 1.

2.3. Microstructure characterization

The as-synthesized SPSed disc (Ø = 20 mm) was ground and polished down to 0.5 μm using a diamond paste to ensure the complete removal of the graphite layer surrounding the surface after the SPS synthesis. The resultant polished disc surface was analysed by x-ray diffractometry using a Bruker diffractometer (D2 Phaser Bruker AXS, Karlsruhe, Germany) with a Cu Kα radiation source using a step size of 0.02° and time per step of 3 s with diffractometer angle range between $2\Theta = 5°$ to $2\Theta = 80°$. Analysis of the XRD pattern was done with Diffract EVA software. Apparent density was measured by employing the Archimedes water immersion technique. The relative density was determined as a percentage of theoretical density upon determination of the phase fractions by Rietveld refinement of the X-ray diffraction data using GSAS and EXPGUI. The residual values of the refinement (R-weighted pattern (R_{wp}); residual of least-squares (R_p); goodness-of-fit (χ^2)) were evaluated. Scanning electron microscopy (SEM) coupled with an EDS detector (Inspect F50, FEI Company, The Netherlands/X-Max AZtec-Nano-analyis, Oxford Instruments, UK) and transmission electron microscopy (TEM) (Philips EM420 operating at 120 kV/JEOL JEM-F200) were used for microstructural characterization of the pristine sample as well as the post-mortem worn surfaces of the disc. Electron transparent TEM samples were prepared in situ by focused ion beam (FIB) (FEI Helios NanoLab G3 UC, FEI Company, The Netherlands). TEM samples were obtained from the worn surface by preparing FIB cross-sections perpendicular to the sliding direction (across the wear track). Furthermore, point analysis of the evolved chemistry at the worn surface was investigated ex situ by employing a Si-calibrated inVia Renishaw Raman spectrometer (Renishaw plc, UK) with an Ar laser (λ = 514.5 nm, laser output power 20 mW and spot size of 2 μm).

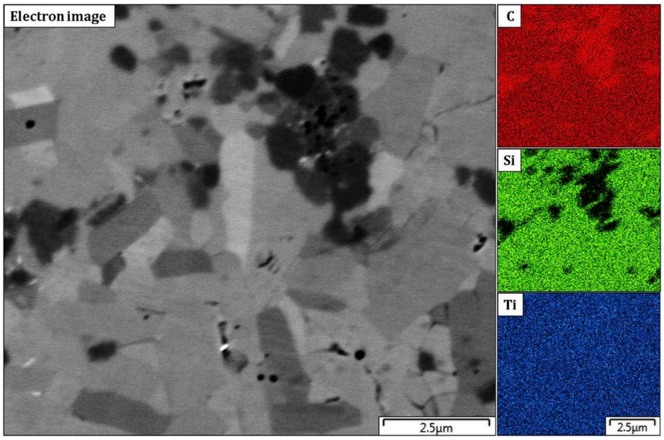

Fig. 6. EDS map showing the TiC regions (dark phase) in the bulk sample. TiC appears to form clusters in some region and moderately distributed in the Ti_3SiC_2 matrix.

2.4. Hardness and tribological testing

Vickers microhardness was measured by indenting the polished surface (Ra = 0.020 μm) of the sintered sample with a microhardness tester (DuraScan 50, ecos Workflow, EMCO-TEST, GmbH) using an indentation load of 4.9 N and a dwell time of 10 s. The indentation load was further increased in order to analyse the resulting change in the indentation zones deformation microstructure. Tribological investigation was undertaken by employing Al_2O_3 ball (99% GD-25 Alumina Spheric Trafalgar, UK) as counterface using a ball-on-disk tribometer (Model CETR UMT-1, USA) under dry sliding ambient test condition (25 °C/22% RH). An Al_2O_3 ball was used as the counterface due to its relative inertness, as it would not be expected to react with the bulk sample. Normal load was kept constant at 0.5 N and disc rotational speed varied at 50 rpm for 60 min and 100 rpm for 30 min, respectively for each test. Low sliding speed and normal load were used to minimize frictional heating due to the dry sliding test condition. Furthermore, the chosen load is in agreement with an earlier work by Souchet et al. [30] and ensures that the test falls within the friction transition region. A schematic diagram of the ball-on-disc rotational wear test configuration is shown in Fig. 2. The coefficient of friction values reported were continuously recorded by the tribometer during the entire duration of the test. Profiles of the wear scars were measured by taking several profilometric scans and the average taken, so as to determine the wear volume as $V = AL$ (where A refers to the wear scar area determined by its profile and L is the length of track (2⍰R). The specific wear rate, which is the measure of wear volume per unit distance and per unit load was then determined thus:

$$K = V/F_n.S_d$$

Where K = specific wear rate (mm^3/Nm), V = wear volume (mm^3), F_n = load (N) and S_d = sliding distance (m), respectively.

2.5. Mechanical and chemical property characterization

The indentation prints created on the pristine surface after Vickers indentation were further analysed by optical microscopy (OM) and scanning electron microscopy (SEM). This was undertaken to characterize the indentation-induced deformation microstructure and crack

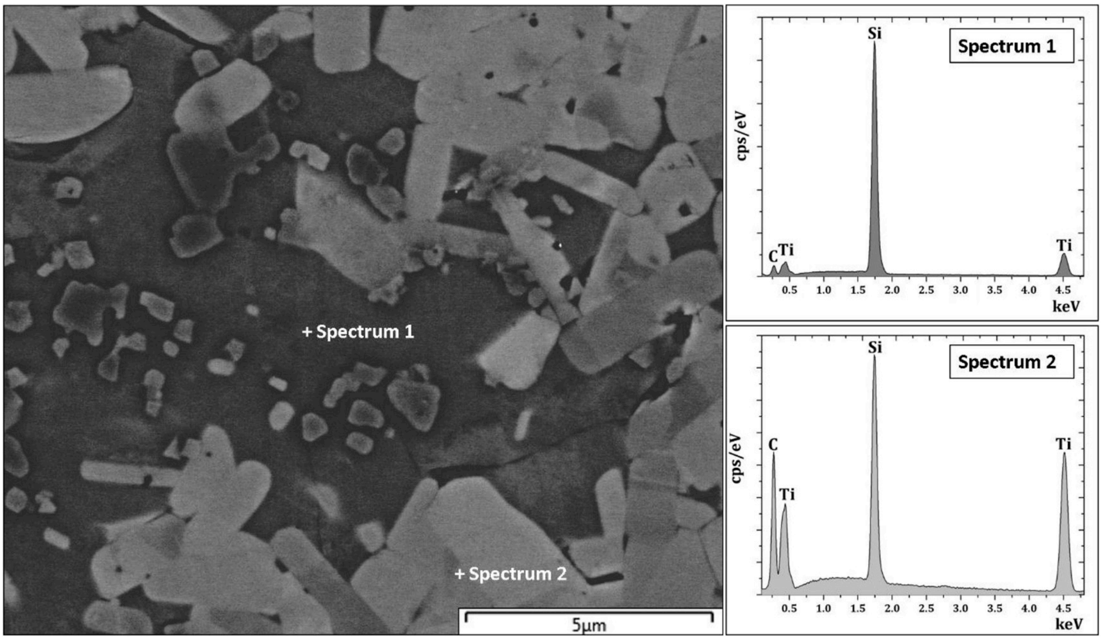

Fig. 7. EDS point spectrums showing the Ti–Si intermediate phase liquid region (spectrum 1) from which the growth of Ti_3SiC_2 (spectrum 2) occurred.

deflection toughening of this MAX phase composite. The evolved chemistries at the sliding surface was probed by SEM-EDS elemental mapping in order to elucidate the evolution sequence of the tribofilms.

3. Results and discussion

3.1. SPS sintering cycle

Fig. 3 shows the variation of temperature, applied force (pressure), punch displacement (piston movement) and sintering speed during the SPS cycle. As shown, the punch displacement has been divided into distinctive segments (I–IV) to represent the respective sintering stages

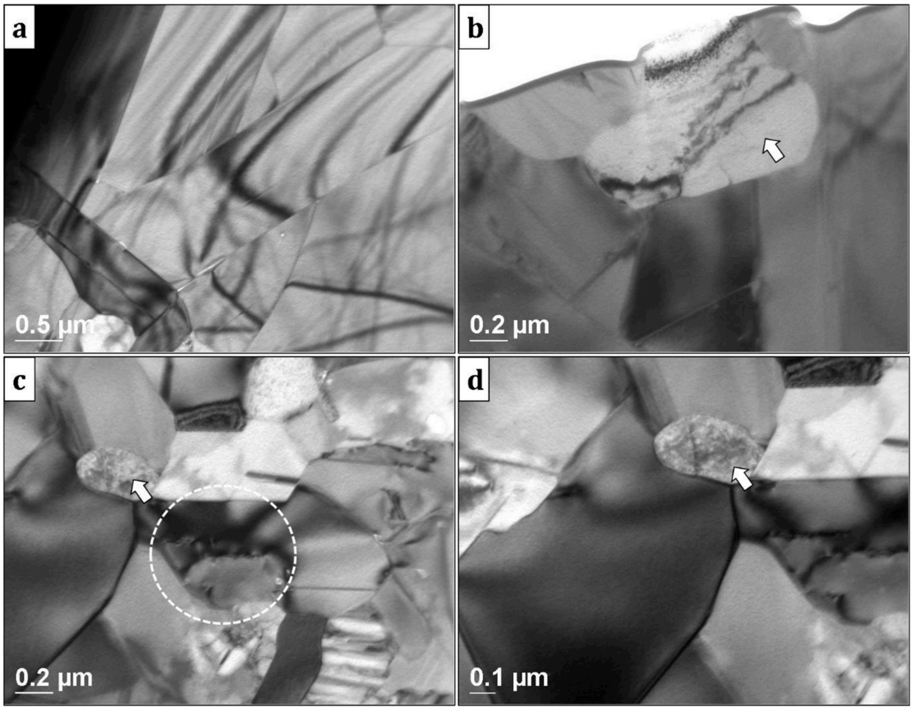

Fig. 8. Bright-field (BF) TEM micrographs showing microstructural evolution in the as-synthesized bulk sample. Fig. 8(d) is a higher magnification of Fig. 8(c) highlighting in situ intergranular formation of TiC particle (white arrow).

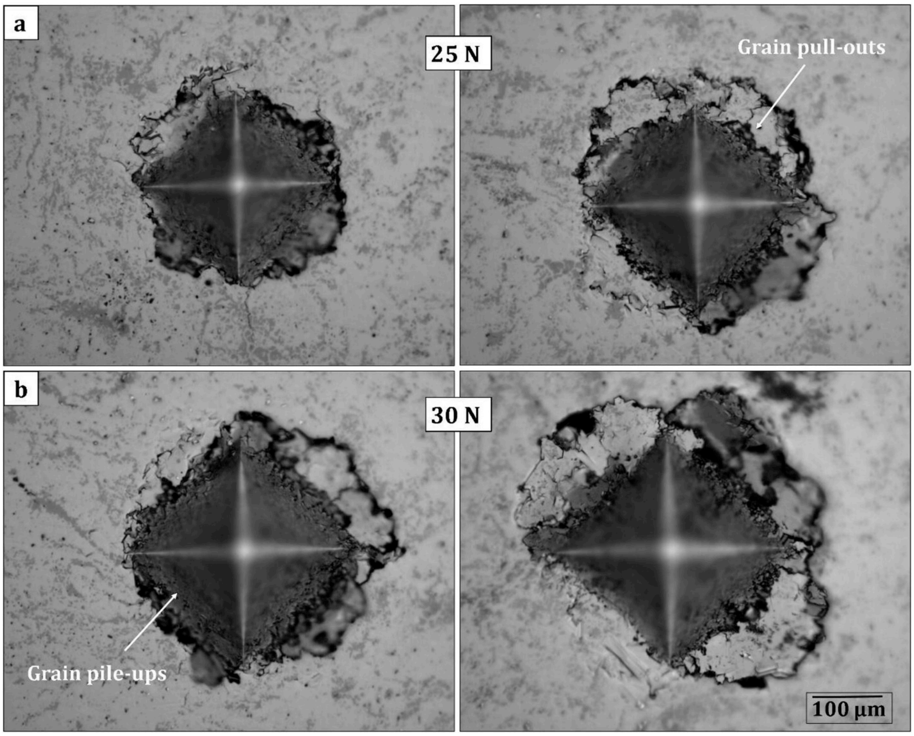

Fig. 9. Optical micrographs taken from the indentation damage prints made by (a) 25 N and (b) 30 N indentation loads, respectively.

and corresponding sintering events. In segment I, particle rearrangement initiated by the applied force resulted in positive punch displacement due to powder compression. A corresponding increase in sintering speed (~ 1.2 mm/min) due to the pistons moving together (compaction) is observed in segment I. In segment II, the densification stage, a slight positive piston displacement at a sintering speed ~ 0.3 mm/min in the temperature range 450–900 °C is observed. This is then followed by a sharp positive piston displacement from 900 °C up to the requisite sintering temperature 1350 °C at an increased sintering speed (~ 0.6 mm/min) owing to necking and plastic deformation of the powder particles. In segment III, the requisite sintering temperature, the piston displacement is relatively constant at this stage as all the pores have been eliminated. The last segment (IV), the cooling stage, further positive piston displacement (~ 1.2 mm/min) due to thermal induced contraction is observed.

3.2. Phase analysis and quantification

The XRD phase identification of the polished disc is shown in Fig. 4. Ti_3SiC_2 is the main phase whilst TiC and $TiSi_2$ exist as the minor phases. The $TiSi_2$ ancillary phase is a compulsory intermediate phase leading to the formation of Ti_3SiC_2 [36]. The phase fractions as determined by Rietveld refinement (χ^2 2.504, R_p 0.0732, R_{wp} 0.0942) indicated 80 wt% Ti_3SiC_2, 14 wt% TiC and 6 wt% $TiSi_2$, respectively.

3.3. Microstructural evolution

A backscattered SEM micrograph obtained from the polished unetched SPSed disc surface is shown in Fig. 5. The bulk sample appears almost fully dense albeit some number of pores were observed. In agreement with XRD phase identification, EDS analysis (Figs. 6 and 7) showed the bulk sample contained the main phase Ti_3SiC_2 (bright contrast) as well as TiC (dark contrast) and $TiSi_2$ (medium contrast (red arrow)) as ancillary phases. According to Sato et al. [37], eutectic Ti–Si liquid forms around the eutectic temperature 1630 K; a compulsory intermediate phase from which Ti_3SiC_2 grows due to the coexistence of the eutectic liquid phase and TiC [38,39] as follows [40]:

$$TiSi_{2(s)} + 2TiC_{(s)} \rightarrow Ti_3SiC_{2(s)} + Si_{(g)}$$

The presence of Ti–Si liquid phase and TiC as ancillaries in the bulk sample may be attributed to incomplete synthesis reaction, as the Ti–Si liquid phase was not fully consumed during the synthesis [41]. It is noteworthy that beside the incomplete reaction that might have led to the formation of ancillary phases, the reactions leading to the formation of Ti–Si and Ti_3SiC_2 are exothermic [42,43]. This implies that the local temperature may have exceeded the melting point of Si ($T_m = 1414$ °C), thus leading to possible Si evaporation. The loss of Si will cause a shift in the overall phase composition of the bulk sample to the Ti_3SiC_2–TiC–$TiSi_2$ three-phase region according to the Ti–Si–C equilibrium phase diagram [38,44].

Fig. 8 shows typical transmission electron micrographs revealing the microstructural evolution of the pristine bulk sample. In agreement with the XRD phase analysis and SEM observation, the majority of the grains were Ti_3SiC_2 (Fig. 8(a)) with some TiC grains (white arrow) distributed in the Ti_3SiC_2 matrix as well as intergranularly (Fig. 8(d)). The in situ intergranular formation of TiC particles at the Ti_3SiC_2 grain boundaries is beneficial partly because it introduces a reinforcement at the TiC–Ti_3SiC_2 interface [33,45]. The grain boundaries are the weakest point in the MAX phase matrix [31], as such, cracks easily nucleate at the grain boundaries, thus expediting grain pull-outs [33]. In addition, some few mobile dislocations (dash circle Fig. 8(c)) can be seen in the Ti_3SiC_2 grains; however, no other planar defects such as stacking faults were evident.

3.4. Densification and hardness

The relative density of the as-synthesized polished disc was ~ 98% upon considering the phase fractions and theoretical densities of Ti_3SiC_2, TiC and $TiSi_2$ in the bulk sample using the mixture rule. Although some pores were seen in the as-synthesized disc as shown in Fig. 5, the bulk sample is nonetheless nearly fully dense. Vickers microhardness obtained from the polished surface of the disc was 7.8 ±

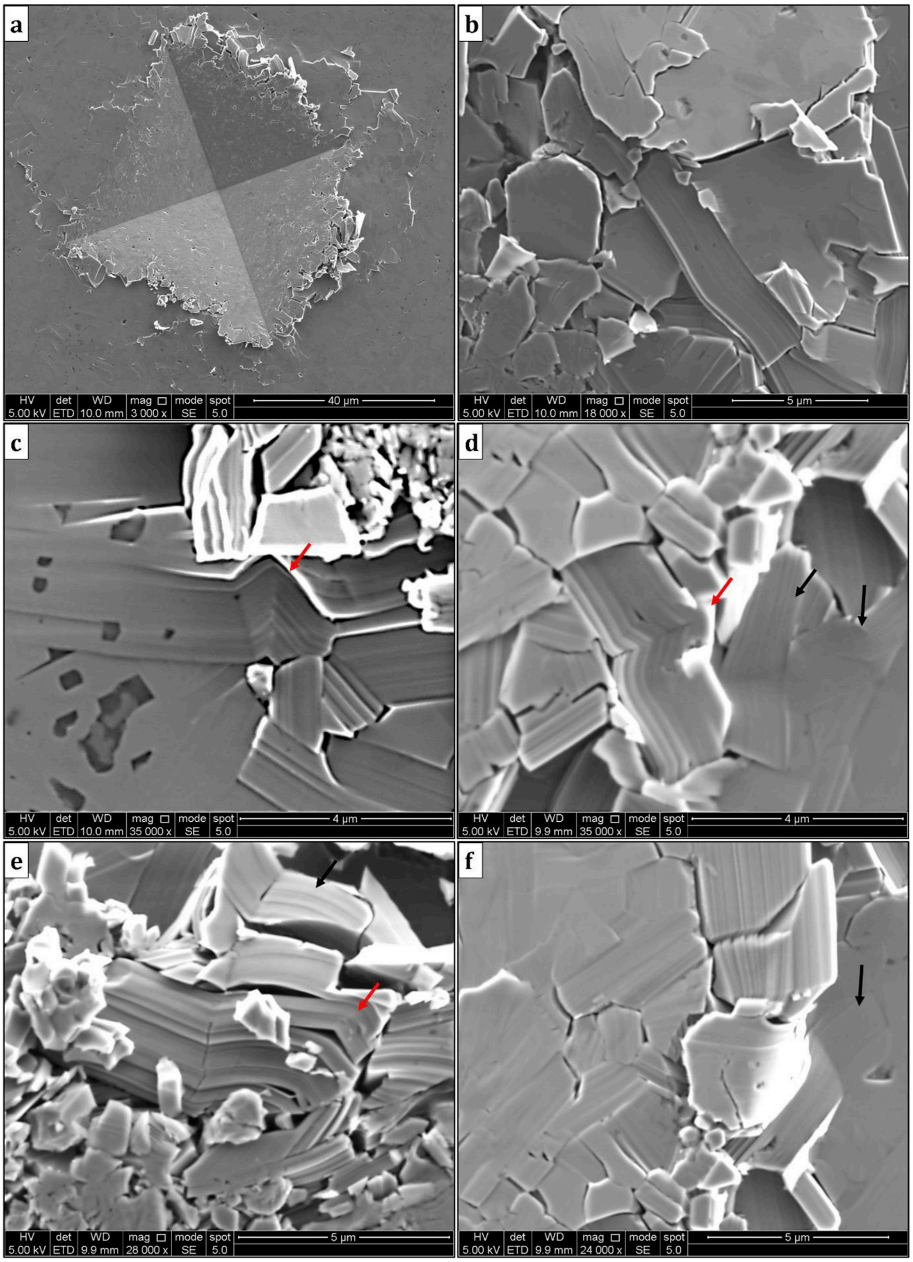

Fig. 10. SEM micrographs revealing the damage micromechanisms around the neighbourhood of the indentation prints created in the Ti_3SiC_2–$TiSi_2$ – TiC composite. Note: In Fig.10(e) cavities are seen to have opened up between layers after extensive kink band formation.

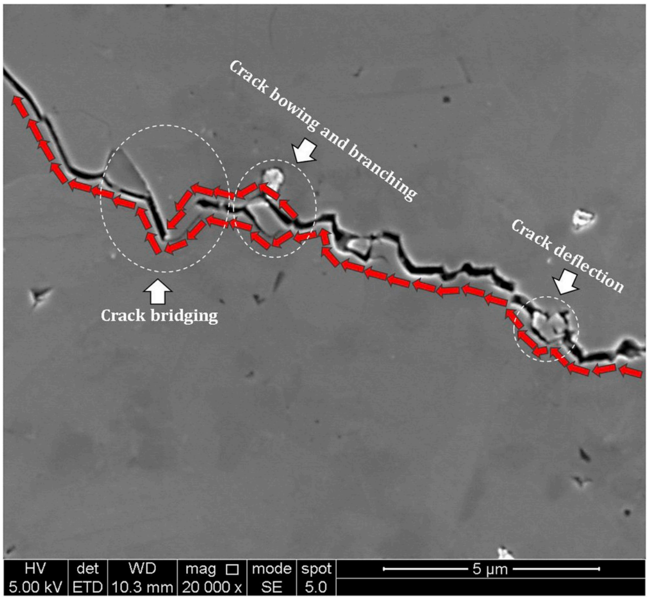

Fig. 11. Secondary electron (SE) SEM micrograph revealing the energy consuming crack propagation path in this composite system.

0.9 GPa. The measured bulk hardness is significantly higher than the reported theoretical hardness of monolithic Ti_3SiC_2 (~ 4 GPa) [46]. This increase can be ascribed solely to the TiC and $TiSi_2$ second phase particles in the bulk sample and is consistent with observations reported elsewhere [44,45,47].

Fig. 9 is an optical micrograph of the Vickers indentation prints and deformation pattern created using different indentation loads. An interesting feature from the observed deformed microstructure is the existence of extensive grain pile-ups and pull-outs around the indentation zones. These microscale plasticity events are examples of some of the typical energy absorbing deformation modes observed in MAX phases [46] contributing to their signature damage tolerance property [4,48]. Furthermore, no radial cracks were seen at the indent diagonals, except for ring cracks around the indents. Such annular ring cracks suggest plastic deformation might be enabled by shear sliding in the bulk sample as reported elsewhere [49]. It is noteworthy that the extent of grain pile-ups and grain push-outs around the indents were different for the same indentation load (Fig. 9) at different points. This asymmetry in the damage zones around the indents for the same indentation load is linked to the anisotropic behaviour of Ti_3SiC_2 [13]. During Vickers indentation, favourably oriented grains parallel to the surface are easily pushed out in the vicinity of the indentation towards the surface as they are relieved of compressive stresses [13,46].

Further, some other microscale plasticity events around the indentation damage zone not visible by optical microscopy were observed using scanning electron microscopy. Secondary electron (SE) micrographs (Fig. 10) shows a range of damage mechanisms such as grain pile-ups (Fig. 10(b)), grain delamination and buckling (black arrow), kink band (KB) formation (red arrow), and eventual cavitation (Fig. 10(e)). The nature of the damage in the neighbourhood of the indentation indicates that Ti_3SiC_2 exhibits microscale plasticity at room temperature [13] albeit lacking the five independent slip systems required for ductility [50], thus the observed cavitation.

Fig. 11 shows the morphology of crack propagation within the fractured section contained in the indentation zone (Fig. 10). A propagating crack was deflected extensively as it met an elongated Ti_3SiC_2 grains. Taking into account the microscale deformation mechanisms around the indentation, as well as the energy consuming crack propagation path within the damage zone, these observations reinforce the conclusion that the Ti_3SiC_2–$TiSi_2$–TiC composite is damage tolerant.

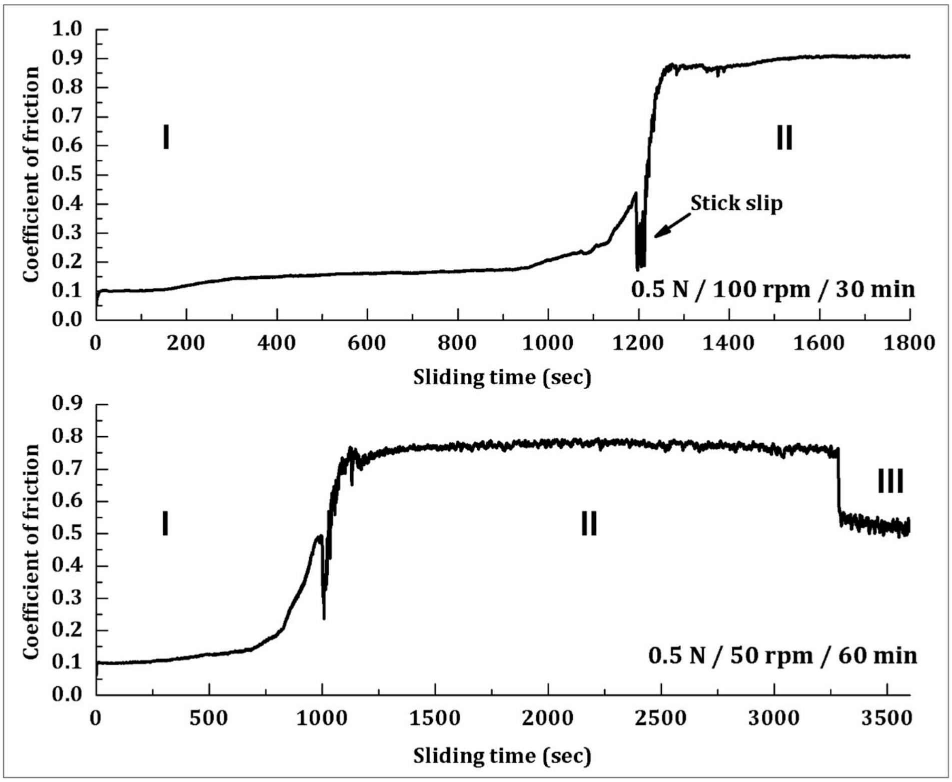

Fig. 12. Evolution of the friction coefficients as a function of sliding time for the test conditions.

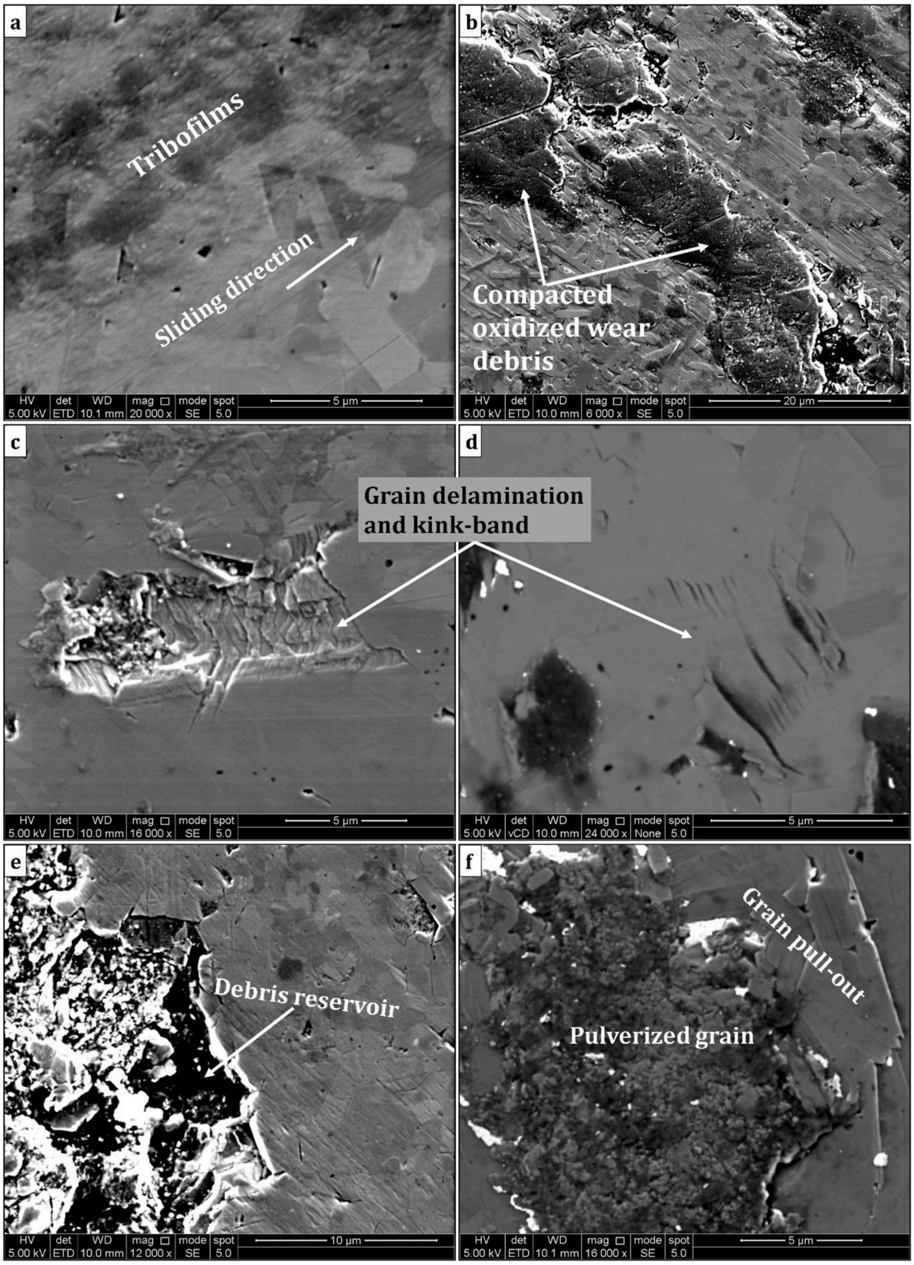

Fig. 13. Secondary electron (SE) SEM micrographs obtained from the worn surface of the disc.

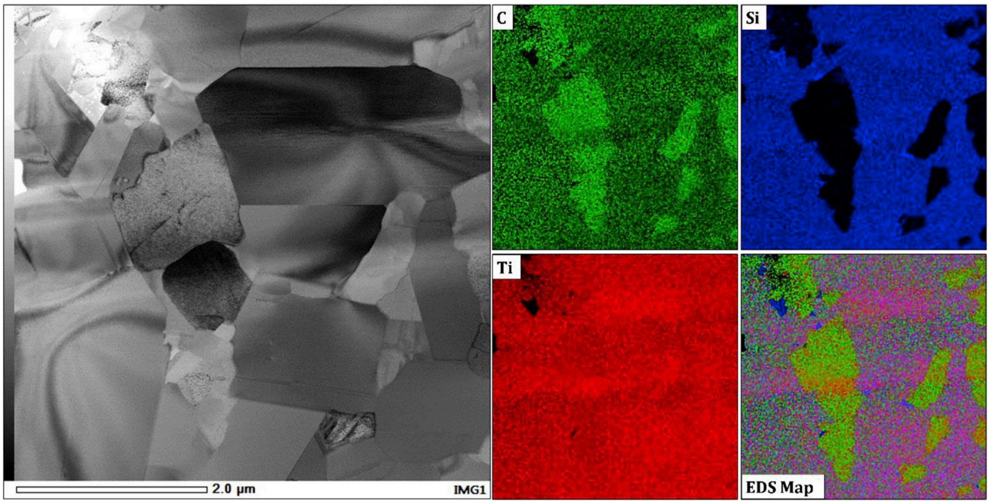

Fig. 14. STEM/EDS chemical mapping of the cross-sectional FIBed section from the worn surface.

4. Tribological behaviour

4.1. Friction and wear

The evolution of friction coefficient as a function of time for the contact condition [0.5 N/50 rpm/60 min] and [0.5 N/100 rpm/30 min] are shown in Fig. 12. The noticeable features of these plots are the friction transition(s) and mild stick-slip phenomenon. The friction plots have been divided into three regimes (I, II, and III). In regime I, the friction was initially very low with no visible wear scar. This was then followed by a transition in friction to a high friction regime II, where the wear scar became visible. For the test condition [0.5 N/50 rpm/60 min], a later transition from high friction (regime II) to a low friction (regime III) is further observed. The transition in friction is consistent with observations reported elsewhere [27,30]. The reason for the transition in friction and wear is not fully understood, however, it may be linked to a possible tribofilm formation and/or spallation taking place at the sliding surface. The stick slip event, on the other hand, may be attributed to possible adhesion between the ball and disc at the friction transition point due to the transfer of oxidized wear debris and/or spalled tribofilm to the ball. The wear rate for the entire test cycles were $(0.74 \pm 0.20)\times 10^{-4}$ $mm^3N^{-1}m^{-1}$ for the test condition [0.5 N/50 rpm/60 min] and $(0.15 \pm 0.35)\times 10^{-3}$ $mm^3N^{-1}m^{-1}$ for the test condition [0.5 N/100 rpm/30 min], respectively. Several attempts were made to measure the wear rate of the disc in regime I, however, the wear track could not be measured using the conventional stylus profiler. Analysis of the disc surface prior to friction transition (regime I) by SEM indicated that the polished surface had remained relatively unchanged. This is possibly because the tribolayer observed at the sliding surface prevented the ball-to-disc contact in this regime leaving the sliding surface relatively undamaged.

4.2. Worn surface analyses

The worn surface from the test conducted at 50 rpm for 60 min was characterized preferentially for evidence of intrinsic lubricity and underlying wear mechanism in the following sections since it exhibited 3 distinct wear regimes (I-III).

4.2.1. Scanning and transmission electron microscopy characterization

SEM micrographs of the deformed microstructure obtained from the worn surface are shown in Fig. 13. Tribofilm formation (Fig. 13(a)) as well as tribofilm mixed with oxidized wear debris (Fig. 13(b)) were evident at the sliding surface. In agreement with the deformation microstructures upon Vickers indentation, grain delamination and kink band formation were also observed from the SEM micrographs of the worn disc surface. A cavity created upon grain pull-outs (Fig. 13(e)) served as a wear debris reservoir for the pulverized fractured grains (Fig. 13(f)).

Fig. 14 shows the cross-sectional bright-field (BF) STEM electron image obtained from inside the wear track alongside with associated EDS map analysis employed to identify the phases. The plate-like grains are all Ti_3SiC_2 grains whilst the equiaxed-like grains are the TiC grains.

A collection of TEM images from the worn surface of the Ti_3SiC_2–$TiSi_2$–TiC composite revealing various shear-induced deformation microstructures are presented in Figs. 15–18. Extensive stacking faults (SFs) running parallel across the Ti_3SiC_2 grains is shown in Fig. 15. The absence of stacking faults in as-SPSed bulk sample supports the reasoning that they are not linked to stacking errors in the layer sequence i.e., the lack of an A-layer and/or insertion of an MX-layer during the SPS synthesis. The stacking faults appears to be a planar defect initiated during the sliding contact in agreement with observation reported elsewhere [3]. According to Barsoum et al. [51], the deformation leading to kink band formation will cause the re-orientation of the basal plane in the kinked region, thus bringing about lattice rotation. This lattice distortion due to kink band (KB) formation possibly led to missing atomic planes and consequently leading to stacking faults in the worn sample. Fig. 15(e) is a bright field STEM image of the deformed Ti_3SiC_2 grain and the corresponding SAED patterns. Corresponding HRTEM image of Fig. 15(e) shows basal plane stacking faults induced by the distortion of the lattice structure and are marked as white arrow in Fig. 15(f).

Fig. 16 shows a range of mechanisms leading to eventual crack formation in the Ti_3SiC_2 matrix. The deformation of the Ti_3SiC_2 matrix as the resolved shear stress exceeds a critical value during sliding contact will result in Ti_3SiC_2 grains shearing away relative to each other. As a consequence, there will be crack formation at the grain boundary such as those observed in Fig. 16 (a and b) [52]. Fig. 16(c) shows an open crack formed owing to continuous shear stresses that have led to the separation of dislocation walls, thus the evolution of kink bands (KBs) in consistent with observations elsewhere [52]. It is not surprising that wear induced deformation of Ti_3SiC_2 led to cavity formation (Fig. 16(c)) as this is consistent with indentation-induced cavitation (Fig. 10(e)) seen around the Vickers indentation prints. Some cracks propagating across the grains such at that shown in Fig. 16(d) were also observed.

Fig. 17 is bright-field TEM micrograph of an area where both the Ti_3SiC_2 and TiC phases coexist in the worn section. As shown, defect clusters in the form of dislocation debris are evident in some of the TiC

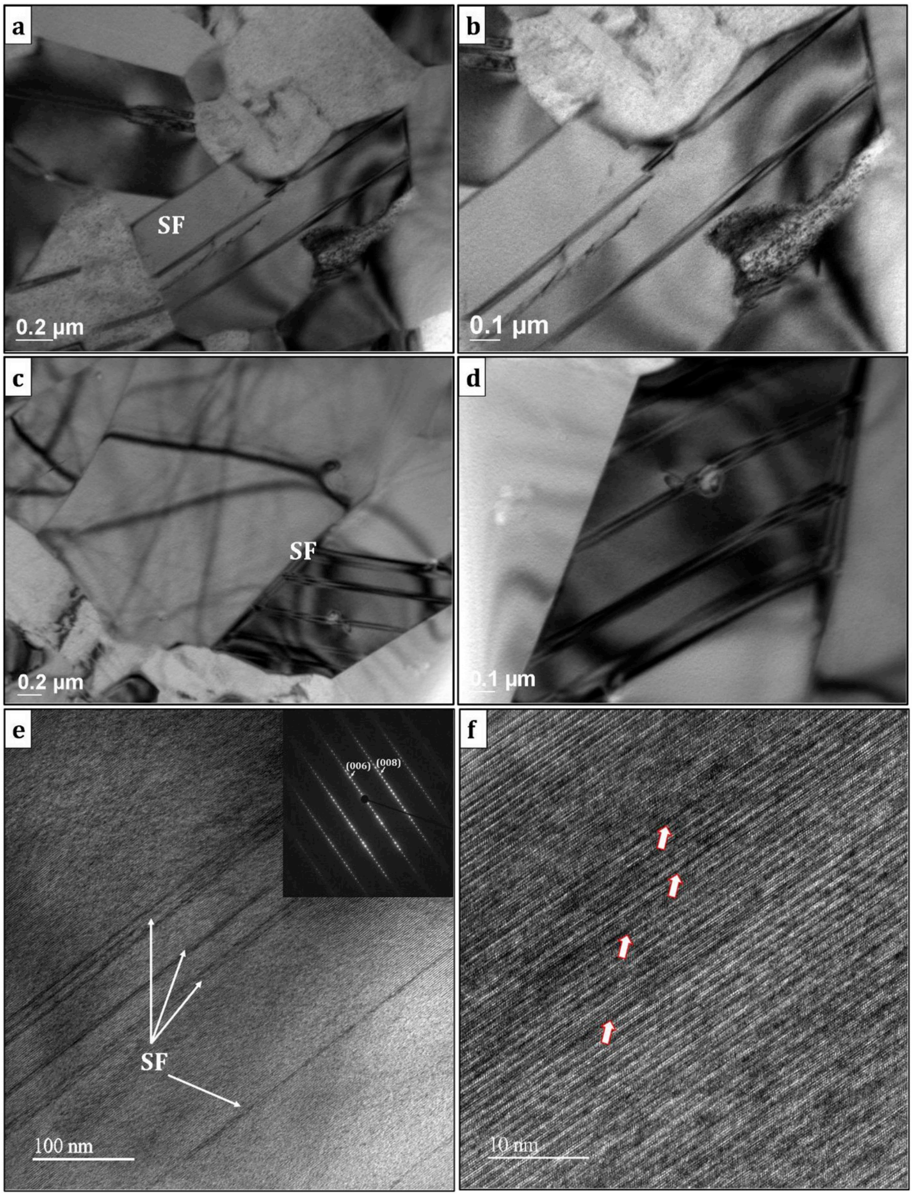

Fig. 15. Bright-field (BF) TEM micrographs showing extensive stacking fault (SF) propagation across the Ti_3SiC_2 grains: (b) is a higher magnification of (a), (d) is a higher magnification of (c), (e) bright-field (STEM) revealing stacking faults across a Ti_3SiC_2 grain with inset showing corresponding SAED pattern and (f) HRTEM image taken from the Ti_3SiC_2 grain.

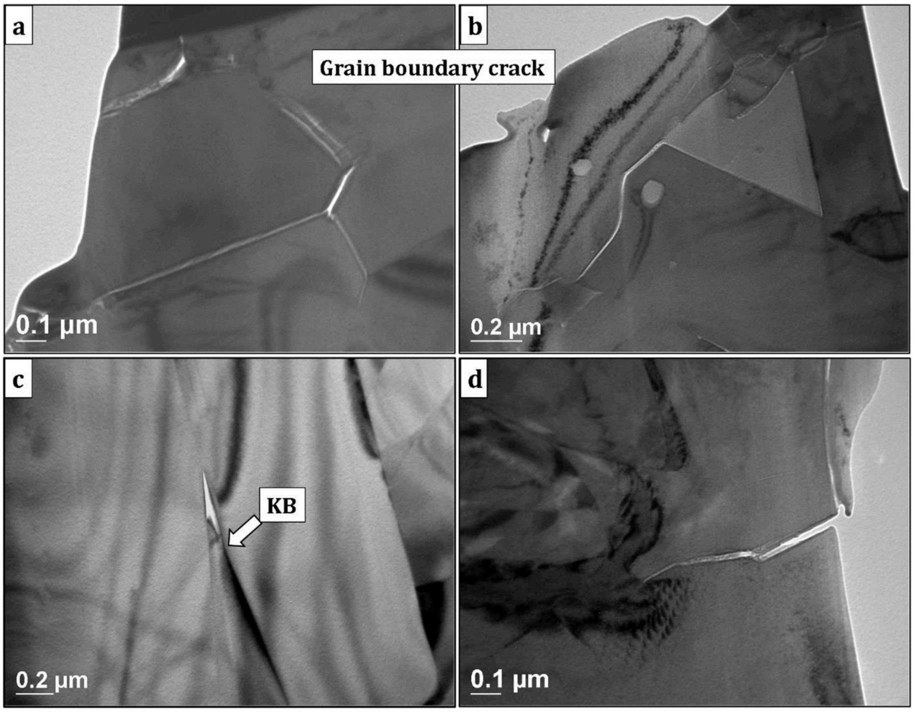

Fig. 16. Bright-field (BF) TEM images showing: (a–b) grain boundary cracks, (c) kink band (KB) containing crack along the kink boundary and (d) crack propagating across the Ti_3SiC_2 grain.

grains (white arrow) and indicates the deformation of TiC phase during the sliding action. It appears the TiC particles shielded the Ti_3SiC_2 matrix by acting as the load-bearing elements. In addition, the TiC particles tends to reinforce the grain boundary in areas where TiC formed intergranularly as no cracks were observed in these worn regions (Fig. 17 (e and f)) in contrast to grain boundary regions where TiC particles are absent such as in Fig. 16 (a and b).

Fig. 18(a) shows the evolution of dislocation walls across the Ti_3SiC_2 grain. The formation and eventual separation of dislocation walls due to shear stresses has been linked to delamination cracks in Ti_3SiC_2 [52,53]. High dislocation density due to dislocation pile-ups can be seen in the Ti_3SiC_2 grain (Fig. 18 (b)), indicating stress concentration prior to grain fracture. It is conceivable that, the observed crack propagation across the Ti_3SiC_2 grains (Fig. 16(d)) is as a result of stress nucleation, concentration and eventual crack formation.

4.2.2. Raman and EDS analyses

Raman spectrum collected from the pristine sample (Fig. 19) displayed peaks corresponding to Raman vibrational modes of Ti_3SiC_2 [54–56] and $TiSi_2$ [57], respectively. It is worthy to mention that TiC peaks were not detected as stoichiometric TiC does not possess Raman-active vibrational modes [54]. Also, the absence of non-stoichiometric TiC_X which possesses Raman active vibrational modes supports the fact that; Ti_3SiC_2 neither decompose at the SPSed requisite sintering temperature (1350 °C) due to Si evaporation nor the possible carbon diffusion from the graphite tooling and subsequent reaction with Ti_3SiC_2 (i.e., carburization) that might have led to TiC_X formation as follows [58]:

$$Ti_3SiC_2 \rightarrow 3TiC_{0.67}(s) + Si(\uparrow) \tag{1}$$

$$Ti_3SiC_2 + (3x-2)C = 3TiC_x(x > 0.8) + Si \tag{2}$$

Raman spectra were further collected from the pre and post-transition worn surface (Fig. 20) in order to elucidate the transition in friction. Raman spectrum collected from the pre-transition worn surface containing an iridescent tribofilm displayed the presence of evolved graphitic carbon at the sliding surface. On the other hand, the post transition worn surface chemistry showed that in addition to the graphitic carbon evolved at pre-transition worn surface, anatase (TiO_2) and titanium oxycarbide (TiC_XO_Y) later evolved at the post-transition sliding surface.

SEM-EDS analysis undertaken to further probe local changes in chemical structure of the wear track is presented in Fig. 21. Oxidation of the worn surface was evident in agreement with Raman analysis. The EDS map further showed depletion of carbon in the oxidized region whilst the Ti and Si-regions were heavily oxidized. A pool of graphite-rich material was seen within the wear track which is again consistent with the Raman analysis pre-transition (Fig. 20) which revealed evidence of graphitization. This wear-induced oxidation can be linked to the flash temperature developed at the asperity contact as well as frictional heating due to the dry sliding condition. Further, evidence of material transfer (Al onto the sliding surface) was seen in the wear track and signifies possible localized adhesive wear. The adhesion between the ball and disc may be responsible for the stick slip events observed at the transition point.

4.3. Friction transition surface evolution and ball analysis

Fig. 22 shows the evolution of surface microstructures corresponding to regime I–III from the friction plot of the test conducted at 50 rpm for an hour. As shown in Fig. 22(a), in regime (I) a very thin layer of graphitic tribofilm evolved at the sliding surface, preventing ball-to-disc contact, as such, the sliding surface was largely undamaged. Regime (II) revealed extensive damage at the sliding surface due to the tribofilms being worn off. The depletion of tribofilm at the sliding surface consequently led to contact between the tribocouple in regime II. In addition, cavities left behind as a result of grain pull-outs upon ball-to-disc contact act as reservoirs for wear debris as highlighted in Fig. 13(e). In regime III, surface smoothing and/or surface healing due to repeated sliding can be seen. This helped create a smooth surface for stable re-graphitization. Fig. 22(b) further highlights the details of the tribofilm architecture leading to friction transition from regime I–II. As shown, smearing of

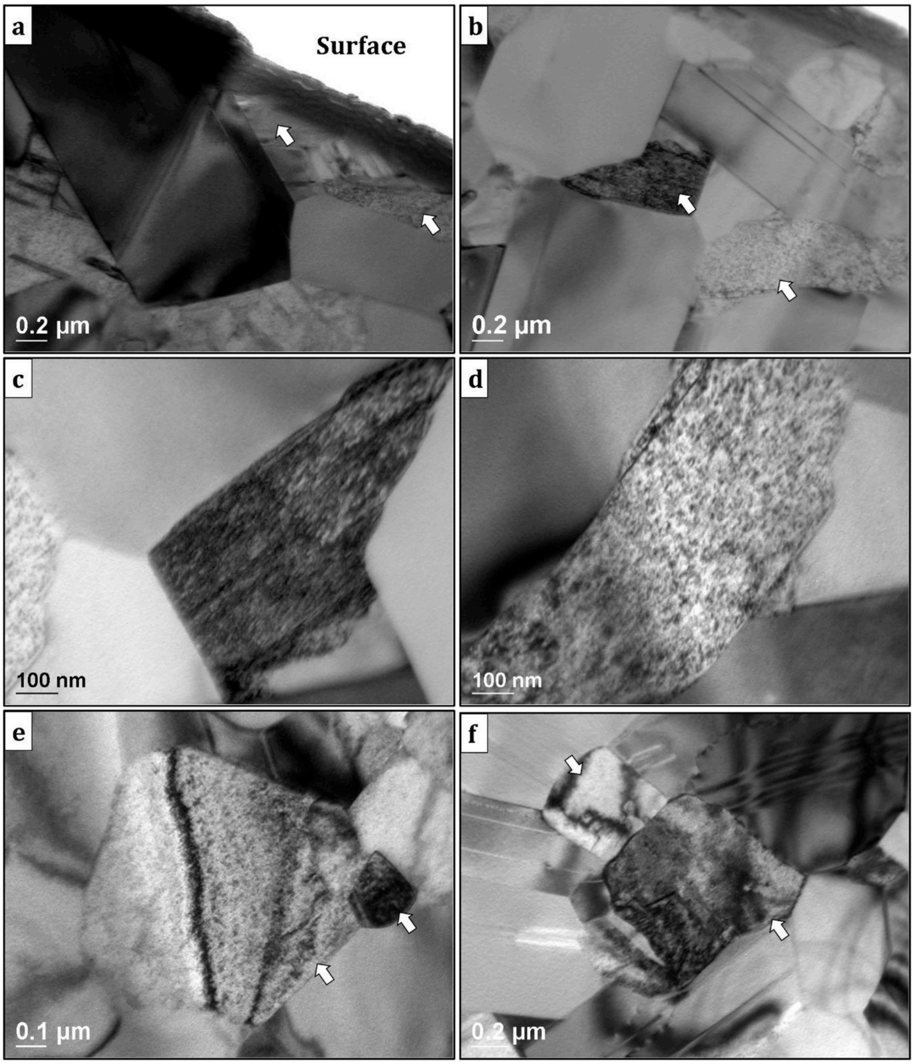

Fig. 17. Bright-field TEM micrographs of the worn surface of the composite showing: (a and b) load-bearing TiC particles (white arrow), (c and d) higher magnification of the TiC particles (white arrows) in (b), and (e and f) shows the absence of grain boundary fracture at the Ti_3SiC_2/TiC deformed grain boundary.

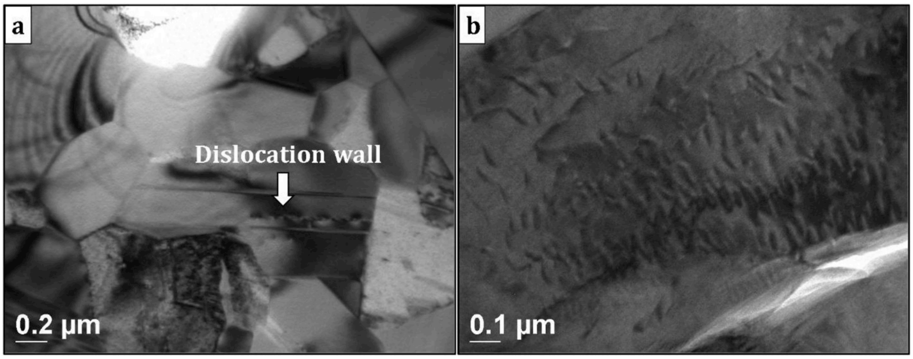

Fig. 18. Bright-field TEM images showing the evolution of: (a) dislocation wall and (b) dislocation multiplication in the Ti_3SiC_2 grains.

tribofilms along the sliding surface took place as the anatase and oxycarbide tribofilms evolved. The smeared layer is then spalled off over time leading to the eventual ball-to-disc contact, thus the generation of abrasive wear debris.

The morphology of the Al_2O_3 ball was observed at the end of the sliding time (that is, test conducted at 50 rpm for 60 min) using an optical microscope and a surface profiler. Evidence of transfer film from the disc to the ball surface is shown in Fig. 23(a). In addition, mild wear grooves (Fig. 23(b)) and scratches (Fig. 23(c)) were observed. This explains the presence of Al in the wear track as revealed by EDS analysis. The presence of hard TiC particles in the Ti_3SiC_2 matrix is possibly responsible for the wear of the Al_2O_3 ball.

5. Wear mechanisms

Following microstructural and chemical analyses before and after the wear tests, the wear mechanisms (Fig. 24) of this MAX phase composite system for the test conditions are designated oxidative–deformation–reoxidation as explained thus:

5.1. Oxidative mechanism

At the beginning of the sliding contact the evolution of graphitic carbon (D and G-bands) at the sliding surface prevented the ball–to–disc contact at the asperities, thus the reduction in friction and wear in regime I. After a certain sliding time required for sufficient surface temperature build-up, oxidation of the surface induced by frictional heat further led to the subsequent evolution of anatase (TiO_2) and titanium oxycarbide (TiC_XO_Y) at the sliding surface.

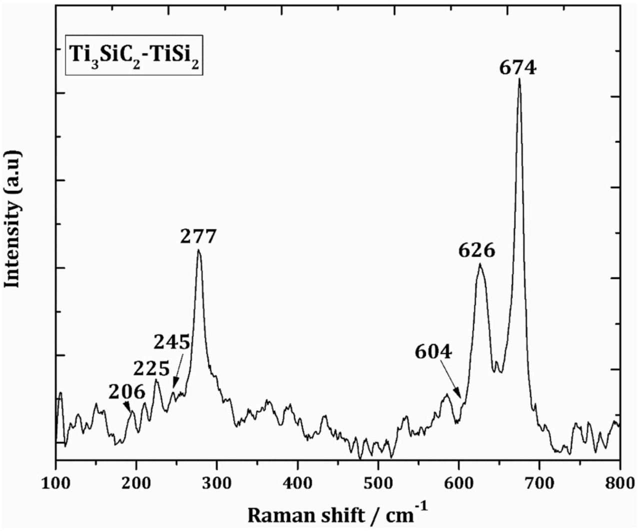

Fig. 19. Raman spectrum collected from the pristine surface of the Ti_3SiC_2–$TiSi_2$–TiC composite. Peaks at 206 cm^{-1} and 245 cm^{-1} correspond to the titanium disilicide vibrational modes.

5.2. Deformation mechanism

Upon repeated sliding contact, both the anatase and titanium oxycarbide tribofilm layers continues to grow until a critical thickness for spallation is reached. Since the anatase (TiO_2) part of the tribofilms is non-adherent and brittle [27], it is easily worn off. The spalled tribofilm at the sliding surface then act as abrasives to the initially formed graphitic layer, thus exposing the underlying bulk surface to wear. The contact between the ball and the disc results in grain pull-outs at the grain boundary. Consequently an abrasive three-body wear dominates the wear process, hence the transition in friction and wear (regime I– II).

5.3. Re-oxidation mechanism

As the sliding contact continues, the fractured grains originating from grain pull-outs are crushed and pulverized at the sliding surface. Over time, the pulverized grains become compacted and smooth enabling initially the reformation of the graphitic layer, followed by the frictional heating induced layer consisting of the anatase and titanium oxycarbide tribofilms. Thus, a further transition from a high friction and high wear regime (II) to a low friction and low wear regime (III).

6. Conclusions

Dense polycrystalline MAX phase composite Ti_3SiC_2–$TiSi_2$–TiC was successfully synthesized by spark plasma sintering via the elemental powder route. The following conclusions can be drawn upon exhaustive characterization of the deformation microstructure and tribological behaviour of this MAX phase composite system:

1. Deformation microstructure revealed evidence of room temperature plasticity, toughening and anisotropy in mechanical response.
2. Evidence of intrinsic solid lubrication was observed due to the evolution of easy shear graphitic carbon alongside with frictional heating induced formation of anatase and titanium oxycarbide tribofilms that lubricates the sliding surface.
3. Second phase TiC particles introduce a pinning effect on the Ti_3SiC_2 grains which helps inhibit grain pull-outs as well as acting as load bearing elements— shielding the Ti_3SiC_2 grains from extensive deformation.

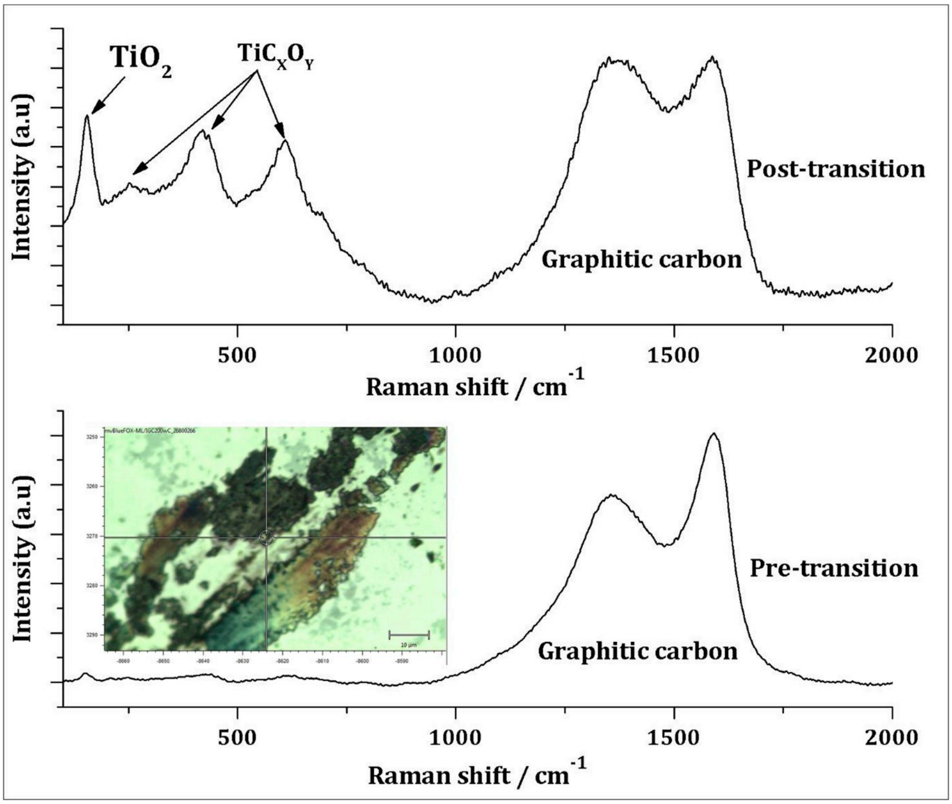

Fig. 20. Raman spectra collected from the pre and post-transition worn surfaces of the disc. In set shows iridescent tribofilm at the pre-transition sliding surface.

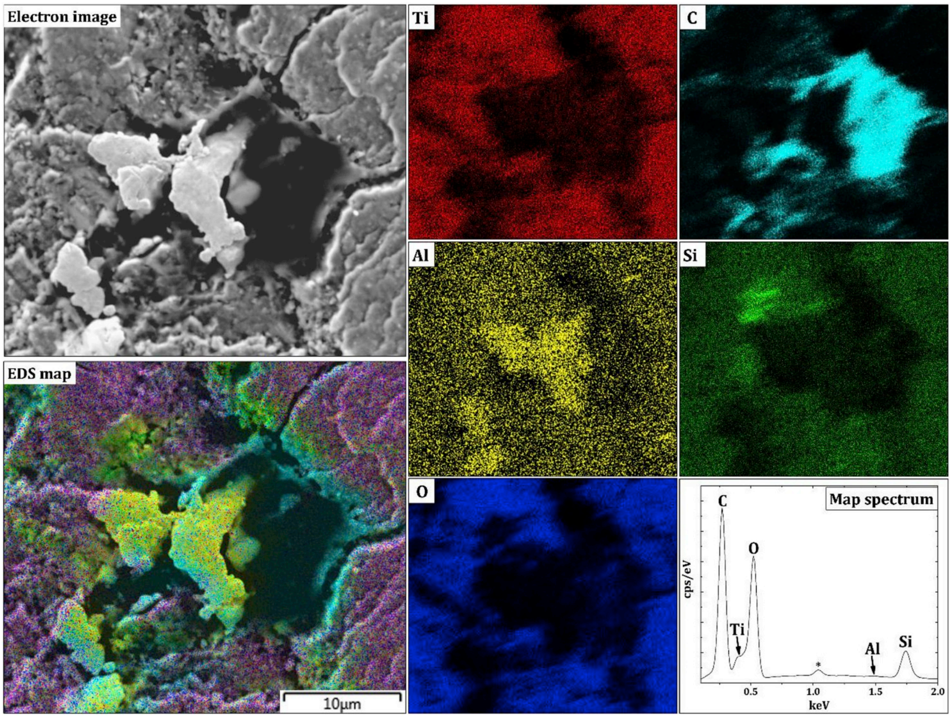

Fig. 21. SEM-EDS chemical map and spectrum taken from inside the wear track of Ti_3SiC_2–$TiSi_2$– TiC/Al_2O_3 tribo-pair for the test condition at 50 rpm.

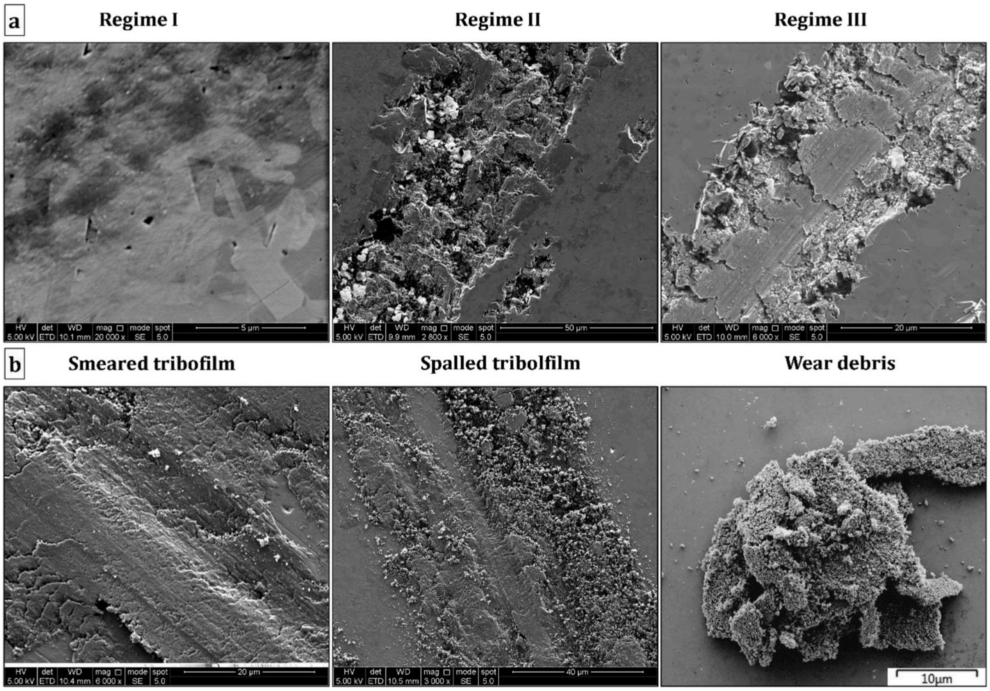

Fig. 22. (a) Evolution of surface microstructures corresponding to regimes I–III, and (b) details of surface microstructure leading to transition from regime I–II as observed in the friction plot for the test conducted at 50 rpm.

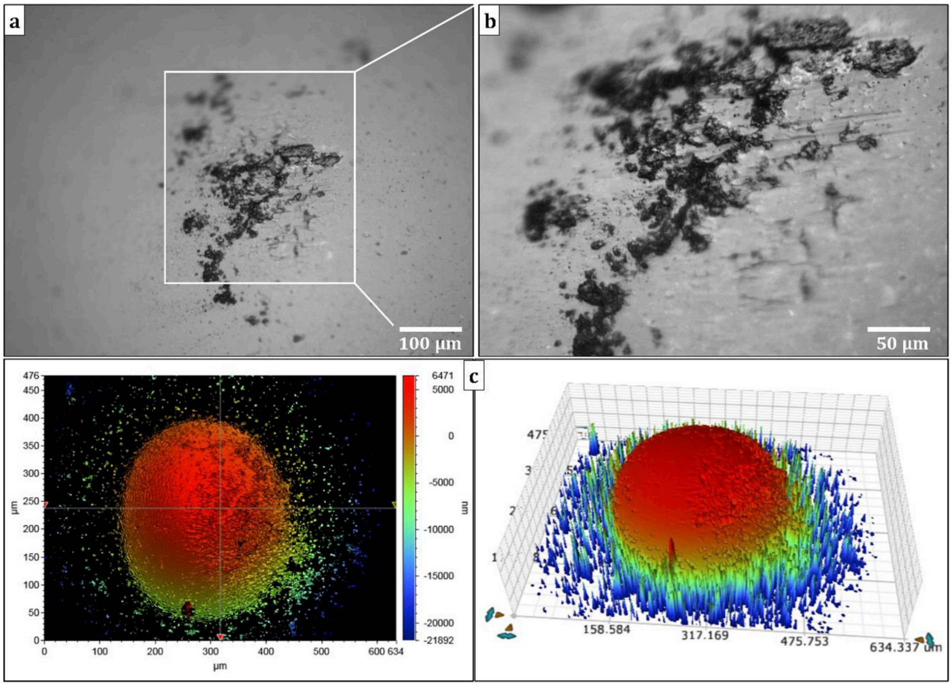

Fig. 23. Optical micrograph (a and b) and (c) 2D – to – 3D ContourGT optical surface profile of the worn surface of the Al_2O_3 ball.

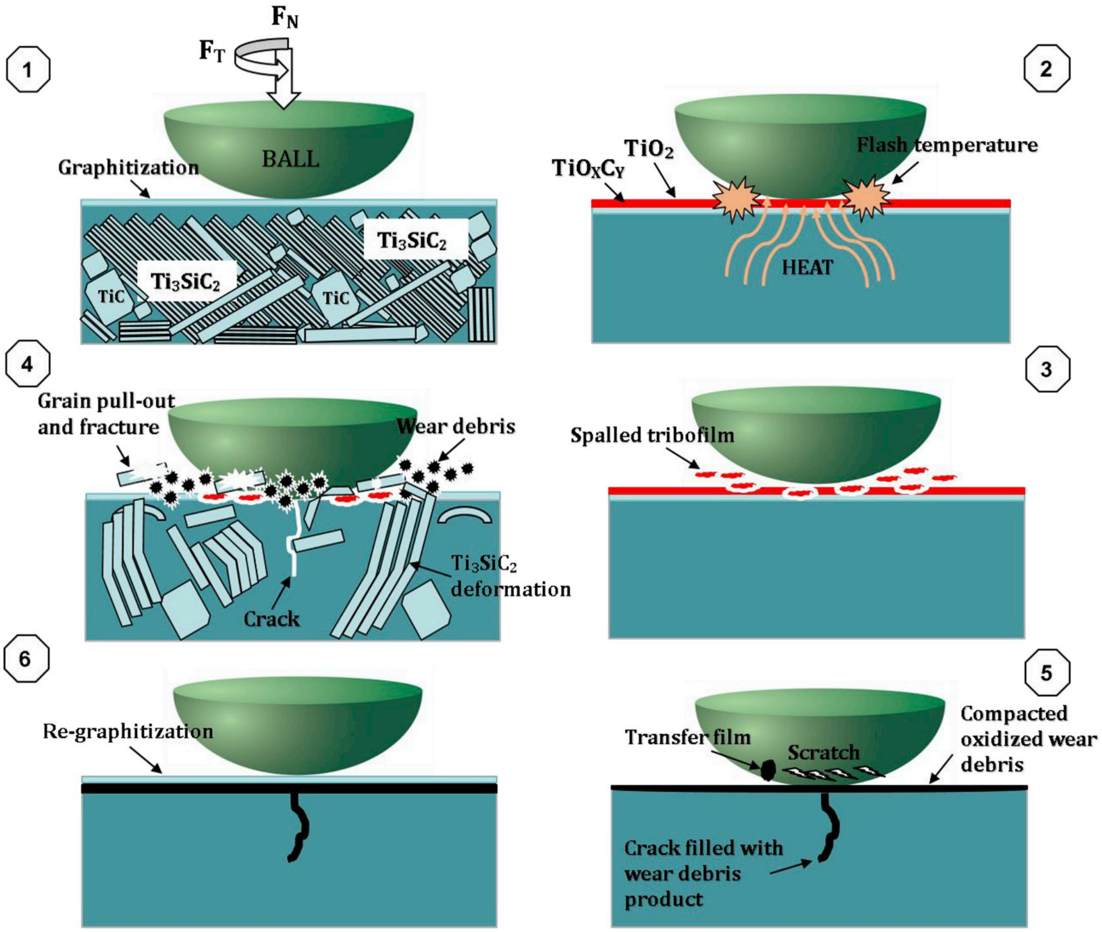

Fig. 24. Schematic presentation (1–6) showing the sequence of wear of the Ti_3SiC_2–$TiSi_2$–TiC MAX phase composite.

Declaration of competing interest

We have no conflict of interest to disclose.

Acknowledgement

We wish to acknowledge the Henry Royce Institute for Advanced Materials for equipment access at Royce@sheffield.

References

[1] W.G. Sloof, et al., Repeated crack healing in MAX-phase ceramics revealed by 4D in situ synchrotron X-ray tomographic microscopy, Sci. Rep. 6 (2016) 23040.

[2] P. Eklund, et al., The Mn + 1AXn phases: materials science and thin-film processing, Thin Solid Films 518 (8) (2010) 1851–1878.

[3] A. Joulain, L. Thilly, J. Rabier, Revisiting the defect structure of MAX phases: the case of Ti4AlN3, Philos. Mag. 88 (9) (2008) 1307–1320.

[4] M.W. Barsoum, M. Radovic, Elastic and mechanical properties of the MAX phases, in: D.R. Clarke, P. Fratzl (Eds.), Annual Review of Materials Research 41, Annual Reviews, Palo Alto, 2011, pp. 195–227.

[5] H. Fashandi, et al., Synthesis of Ti3AuC2, Ti3Au2C2 and Ti3IrC2 by noble metal substitution reaction in Ti3SiC2 for high-temperature-stable Ohmic contacts to SiC, Nat. Mater. 16 (2017) 814.

[6] P. Eklund, J. Rosen, P.O.Å. Persson, Layered ternary Mn+1AXnphases and their 2D derivative MXene: an overview from a thin-film perspective, J. Phys. D Appl. Phys. 50 (11) (2017) 113001.

[7] X. Duan, et al., Synthesis of high-purity, isotropic or textured Cr2AlC bulk ceramics by spark plasma sintering of pressure-less sintered powders, J. Eur. Ceram. Soc. 35 (5) (2015) 1393–1400.

[8] D. Horlait, et al., Synthesis and oxidation testing of MAX phase composites in the Cr–Ti–Al–C quaternary system, J. Am. Ceram. Soc. 99 (2) (2016) 682–690.

[9] M.W. Barsoum, The MN+1AXN phases: a new class of solids: thermodynamically stable nanolaminates, Prog. Solid State Chem. 28 (1) (2000) 201–281.

[10] T. El-Raghy, et al., Processing and mechanical properties of Ti3SiC2: II, effect of grain size and deformation temperature, J. Am. Ceram. Soc. 82 (10) (1999) 2855–2860.

[11] A.K. Kronenberg, S.H. Kirby, J. Pinkston, Basal slip and mechanical anisotropy of biotite, J. Geophys. Res. 95 (B12) (1990) 19257–19278.

[12] M.W. Barsoum, MAX Phases : Properties of Machinable Ternary Carbides and Nitrides, Wiley-VCH Verlag GmbH & Co. KGaA, Weinheim, Germany, 2013, 2013.

[13] T. El-Raghy, et al., Damage mechanisms around hardness indentations in Ti_3SiC_2, J. Am. Ceram. Soc. 80 (2) (1997) 513–516.

[14] Z.-F. Zhang, Z.-M. Sun, H. Hashimoto, Deformation and fracture behavior of ternary compound Ti3SiC2 at 25–1300 °C, Mater. Lett. 57 (7) (2003) 1295–1299.

[15] D. Chen, et al., Cyclic fatigue-crack growth and fracture properties in Ti3SiC2 ceramics at elevated temperatures, J. Am. Ceram. Soc. 84 (12) (2001) 2914–2920.

[16] E. Drouelle, et al., Deformation mechanisms during high temperature tensile creep of Ti3AlC2 MAX phase, J. Alloy. Comp. 693 (2017) 622–630.

[17] M.W. Barsoum, et al., Fully reversible, dislocation-based compressive deformation of Ti3SiC2 to 1 GPa, Nat. Mater. 2 (2) (2003) 107–111.

[18] J.M. Molina-Aldareguia, et al., Kink formation around indents in laminated Ti 3SiC 2 thin films studied in the nanoscale, Scr. Mater. 49 (2) (2003) 155–160.

[19] I.M. Low, Vickers contact damage of micro-layered Ti3SiC2, J. Eur. Ceram. Soc. 18 (6) (1998) 709–713.

[20] B.J. Kooi, et al., Ti 3SiC 2: a damage tolerant ceramic studied with nano-indentations and transmission electron microscopy, Acta Mater. 51 (10) (2003) 2859–2872.

[21] M.W. Barsoum, T. El-Raghy, Synthesis and characterization of a remarkable ceramic: Ti3SiC2, J. Am. Ceram. Soc. 79 (7) (1996) 1953–1956.

[22] M.W. Barsoum, H.I. Y, I.K. Polushina, V.Y. Rud, Y.V. Rud, T. El-Raghy, Electrical conductivity, thermopower, and Hall effect of Ti3AlC2, Ti4AlN3, and Ti3SiC2, Phys. Rev. B 62 (15) (2000) 10194–10198.

[23] M. Barsoum, M. Radovic, Mechanical Properties of the MAX Phases, Vol. 41, 2011, pp. 195–227.

[24] H.-z. Wang, et al., Tribological Performance and Lubrication Mechanism of Alkylimidazolium Dialkyl Phosphates Ionic Liquids as Lubricants for Si 3 N 4 -Ti 3 SiC 2 Contacts 2014, 2014, pp. 1–8.

[25] L. Wu, et al., Reciprocating friction and wear behavior of Ti3AlC2 and Ti3AlC2/Al2O3 composites against AISI52100 bearing steel, Wear 266 (1) (2009) 158–166.

[26] T. Lapauw, et al., A new method to texture dense Mn+1AXn ceramics by spark plasma deformation, Scr. Mater. 111 (Supplement C) (2016) 98–101.

[27] S. Gupta, M.W. Barsoum, On the tribology of the MAX phases and their composites during dry sliding: a review, Wear 271 (9–10) (2011) 1878–1894.

[28] W. Dang, et al., Influence of Cu on the mechanical and tribological properties of Ti3SiC2, Ceram. Int. 42 (8) (2016) 9972–9980.

[29] T. El-Raghy, P. Blau, M.W. Barsoum, Effect of grain size on friction and wear behavior of Ti3SiC2, Wear 238 (2) (2000) 125–130.

[30] A. Souchet, et al., Tribological duality of Ti3SiC2, Tribol. Lett. 18 (3) (2005) 341–352.

[31] Z. Yanchun, S. Zhimei, Electronic structure and bonding properties in layered ternary carbide Ti3SiC2, J. Phys. Condens. Matter 12 (28) (2000) 457.

[32] J. Yang, et al., Friction and wear properties of in situ (TiB2+TiC)/Ti3SiC2 composites, Wear 271 (11) (2011) 2940–2946.

[33] W. Dang, et al., The tribological properties of Ti3SiC2/Cu/Al/SiC composite at elevated temperatures, Tribol. Int. 104 (2016) 294–302.

[34] S. Konoplyuk, et al., Synthesis of Ti3SiC2/TiC composites from TiH2/SiC/TiC powders, Mater. Lett. 59 (18) (2005) 2342–2346.

[35] S. Gupta, et al., Tribological behavior of select MAX phases against Al2O3 at elevated temperatures, Wear 265 (3) (2008) 560–565.

[36] I. Kero, R. Tegman, M.-L. Antti, Phase reactions associated with the formation of Ti3SiC2 from TiC/Si powders, Ceram. Int. 37 (7) (2011) 2615–2619.

[37] F. Sato, J. Li, R. Watanabe, Reaction Synthesis of Ti3SiC2 from Mixture of Elemental Powders, Vol. 41, 2000, pp. 605–608.

[38] H. Hashimoto, et al., Synthesis of Ti3SiC2 from powder blend of Ti, Si and TiC, J. Alloy. Comp. 426 (2006) 263–267.

[39] E. Wu, et al., Intermediate phases in Ti3SiC2 synthesis from Ti/SiC/C mixtures studied by time-resolved neutron diffraction, J. Am. Ceram. Soc. 85 (12) (2002) 3084–3086.

[40] W.K. Pang, et al., 15 - phase and thermal stability in Ti3SiC2 and Ti3SiC2/TiC/TiSi2 systems, in: Advances in Science and Technology of Mn+1axn Phases, Woodhead Publishing, 2012, pp. 389–413.

[41] W.K. Pang, et al., Effect of vacuum annealing on the thermal stability of Ti3SiC2/TiC/TiSi2 composites, J. Aust. Ceram. Soc. 45 (2009) 72–77.

[42] P.J. Counihan, A. Crawford, N.N. Thadhani, Influence of dynamic densification on nanostructure formation in Ti5Si3 intermetallic alloy and its bulk properties, Mater. Sci. Eng. A 267 (1) (1999) 26–35.

[43] J. Lis, et al., Ti3SiC-based materials prepared by HIP-SHS techniques, Mater. Lett. 22 (3) (1995) 163–168.

[44] C. Magnus, W.M. Rainforth, Influence of sintering environment on the spark plasma sintering of Maxthal 312 (nominally-Ti3SiC2) and the role of powder particle size on densification, J. Alloy. Comp. 801 (2019) 208–219.

[45] C. Magnus, W.M. Rainforth, Spark plasma sintering (SPS) synthesis and tribological behaviour of MAX phase composite of the family Tin+1SiCn (n = 2), Wear 438–439 (2019) 203062.

[46] S.B. Li, J.X. X, L.T. Zhang, L.F. Cheng, Synthesis and some properties of Ti3SiC2 by hot pressing of Ti, Si and C powders Part 2 – mechanical and other properties of Ti3SiC2, Mater. Sci. Technol. 21 (9) (2005) 1054–1058.

[47] C. Magnus, J. Sharp, W.M. Rainforth, The lubricating properties of spark plasma sintered (SPS) Ti3SiC2 MAX phase compound and composite, Tribol. Trans. (2019) 1–14.

[48] Z.M. Sun, Progress in research and development on MAX phases: a family of layered ternary compounds, Int. Mater. Rev. 56 (3) (2011) 143–166.

[49] J. Xu, et al., Synergistic Toughening of Hard, Nacre-Mimetic MoSi2 Coatings by Self-Assembled Hierarchical Structure, Vol. 4, 2014, p. 4239.

[50] Z. Sun, et al., Ternary compound Ti3SiC2: Part II. Deformation and fracture behavior at different temperatures, Mater. Trans. 43 (3) (2002) 432–435.

[51] M. Barsoum, T. El-Raghy, Room-temperature ductile carbides, Metall. Mater. Trans. A 30 (2) (1999) 363–369.

[52] M.W. Barsoum, L. Farber, T. El-Raghy, Dislocations, kink bands, and room-temperature plasticity of Ti3SiC2, Metall. Mater. Trans. A 30 (7) (1999) 1727–1738.

[53] F.C. Frank, A.N. Stroh, On the theory of kinking, Proc. Phys. Soc. Sect. B 65 (10) (1952) 811–821.

[54] M. Amer, et al., The Raman spectrum of Ti3SiC2, J. Appl. Phys. 84 (10) (1998) 5817–5819.

[55] F. Mercier, et al., Raman scattering from Ti3SiC2 single crystals, Appl. Phys. Lett. 98 (8) (2011), 081912.

[56] E. Jonathan, S.G. Spanier, S. Maher, Amer and Michel W. Barsoum, vibrational behavior of the Mn+1AXn phases from first-order Raman scattering (M=Ti,V,Cr, A=Si, X=C,N), Phys. Rev. B Condens. Matter Mater. Phys. 71 (1) (2005), 2005.

[57] I. Jauberteau, et al., Silicides and nitrides formation in Ti films coated on Si and exposed to (Ar-N2-H2), Expanding Plasma 7 (2017) 23.

[58] T. El-Raghy, M.W. Barsoum, Diffusion kinetics of the carburization and silicidation of Ti3SiC2, J. Appl. Phys. 83 (1) (1998) 112–119.

Paper F

Microstructural evolution and wear mechanism of Ti_3AlC_2-Ti_2AlC dual MAX phase composite consolidated by spark plasma sintering (SPS)

Wear 436-437 (2019) 203013

Contents lists available at ScienceDirect

Wear

journal homepage: www.elsevier.com/locate/wear

Microstructural evolution and wear mechanism of Ti_3AlC_2 – Ti_2AlC dual MAX phase composite consolidated by spark plasma sintering (SPS)

Carl Magnus[a,*], Daniel Cooper[a,b], Joanne Sharp[a], William M. Rainforth[a]

[a] *Department of Materials Science and Engineering, University of Sheffield, Sir Robert Hadfield Building, Mappin St, Sheffield, S1 3JD, UK*
[b] *Seaborg Technologies, Titangade 11, 2200, Copenhagen, Denmark*

ARTICLE INFO

Keywords:
MAX phases
Deformation
Frictional heating
Wear mechanism
Grain buckling

ABSTRACT

In this work, we report the synthesis, deformation and tribological behaviour of a novel Ti_3AlC_2 – Ti_2AlC MAX phase composite metallo-ceramic. The dual MAX phase composite was synthesized by spark plasma sintering (SPS) under a vacuum environment using Ti, Al, and C precursor powders. The layered composite deformation mechanism and tribological behaviour were studied and analyzed by SEM, TEM, and Raman spectroscopy. The transition in friction and wear as well as the operative wear mechanisms involved were further discussed. Detailed analyses of the worn surface showed that Ti_3AlC_2 – Ti_2AlC dual MAX phase composite is intrinsically self-lubricating.

1. Introduction

The nanolaminates known as the $M_{n+1}AX_n$ phases (MAX phases), are highly anisotropic hexagonal layered ternary machineable carbides and nitrides, where M represents an early transition metal, A is an A-group element (mostly from group 13 and 14), X is either C and/or N, and n ranges from 1 to 6 [1]. According to their n-values, the hexagonal crystal structure crystallizing in $P6_3/mmc$ space group can be further categorized as “211-phase” for M_2AX (n = 1), “312-phase” for M_3AX_2 (n = 2) and “413-phase” for M_4AX_3 (n = 3), etc [2,3]. The major difference between the crystal structure of these phases is the number of M-layers separating the A-layers. In the “211 phase” there are two, in the “312 phase” there are three, whilst in the “413 phase” there are four [4]. These class of materials combine some attractive properties of ceramics and metals simultaneously which endow them with unusual and exceptional electrical, thermal, elastic, chemical and mechanical properties [5,6]. The chemical bonding in MAX phases is anisotropic and metallic-covalent-ionic in nature [7], with the metallic and covalent contribution playing a very significant role [8]. Mechanically, they represent the only class of polycrystalline solids that deform by a range of energy absorbing mechanisms such as grain buckling, kink band formation and delamination of individual grains which in turn renders them extremely damage tolerant [2,5,9,10]. Some important properties of this family of metallo-ceramics are high melting point, damage tolerance at room temperature, high thermal and electrical conductivity, good high-temperature-oxidation resistance, autonomous self-healing at high temperature and machinability [7].

Ti_3AlC_2 and Ti_2AlC are both layered ceramics belonging to a series generated from the MAX phase family $Ti_{n+1}AlC_n$ (n = 1–2). Fig. 1 shows the crystal structures of Ti_3AlC_2 and Ti_2AlC with atomic configuration in the unit cells. Previous works [11–13] have shown that it is difficult to synthesize monolithic phase Ti_3AlC_2 or Ti_2AlC, as in most cases the fabrication of either of these phases has always led to the formation of the other alongside as an ancillary phase due to the reaction mechanisms. It is also common to have TiC coexisting with these phases during synthesis; this has however been linked to the reaction mechanism, possible decomposition at high sintering temperature, as well as the synthesis method [11,14–16]. Thus the reaction mechanism(s) can be exploited to aid the fabrication of a 100 % layered composite.

The purpose of this work is to attempt to fabricate a dual MAX phase Ti_3AlC_2 – Ti_2AlC composite via the elemental powder route using spark plasma sintering (SPS) and characterize the resulting layered composite microstructural evolution as well as its deformation microstructure upon indentation. This work further aims to evaluate the friction and wear behaviour of this unique layered microstructure via detailed chemical and microstructural analyses of the worn surface in order to elucidate the underlying wear mechanism(s). However, it is important to mention that, the mismatch in coefficient of thermal expansion (CTE) between Ti_2AlC ($8.2 \times 10^{-6}\,K^{-1}$) and Ti_3AlC_2 ($9.0 \times 10^{-6}\,K^{-1}$) although small [17,18], might be enough to trigger some shrinkage cracking that might impair the unique mechanical properties of this composite system.

---

[*] Corresponding author.
E-mail address: mcarl2@sheffield.ac.uk (C. Magnus).

https://doi.org/10.1016/j.wear.2019.203013
Received 26 April 2019; Received in revised form 7 August 2019; Accepted 16 August 2019

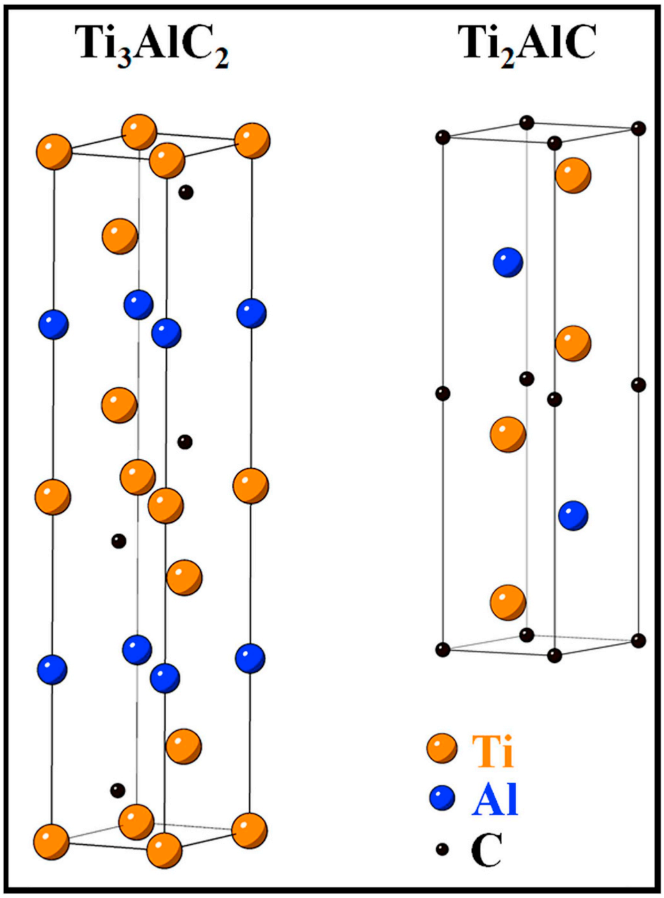

Fig. 1. Crystal structures of Ti_3AlC_2 and Ti_2AlC with atomic configuration in the unit cells.

2. Experimental procedure

2.1. Materials and methods

Commercially available Ti (titanium metal), Al (aluminium metal) and C (graphite) powder precusors were used as starting materials. The powder characteristics of the as-received powders are presented in Table 1. The powder mixture was mixed in a planetary ball mill according to the molar ratio described in Table 1 and then poured in a 20 mm graphite die. The graphite die was then placed in a spark plasma sintering (SPS) furnace (Fig. 2) and sintered at 1100 °C for 8 min with a pressure of 30 MPa under vacuum. The sample was heated at a rate 50 °C/min with surface temperature continuously monitored with the aid of a thermocouple.

2.2. Analytical methodology

Phase composition of the sintered sample was determined using X-ray diffraction (Bruker D2 Phaser, $5^\circ \le 2\Theta \le 80^\circ$, 0.02° step size, Cu kα source) and phase fractions obtained by Rietveld refinements using GSAS and EXPGUI. The microstructure was analyzed with SEM (FEI Inspect F50, The Netherlands) equipped with an EDS detector (Oxford Instruments X-Max, UK), TEM (JEOL 2010F operating at 200 kV (JEOL Ltd, Japan); Philips EM420 operating at 120 kV) and Raman spectroscopy ex situ by employing a Si-calibrated Raman spectrometer (inVia Renishaw Co., UK) with an Ar laser (wavelength of 514.5 nm (green) / 50 × objective lens, laser output power 20 mW). A focused ion beam (FIB) instrument (FEI Helios NanoLab G3 UC, FEI company, The Netherlands) was used to prepare samples for cross-sectional transmission electron microscopy with Pt layer deposited to protect the area of interest.

The density of the sintered sample was measured using the Archimedes method with distilled water used as the immersion medium and relative density calculated by taking into consideration the theoretical density of Ti_3AlC_2 (4.25 g/cm^3) [14] and Ti_2AlC (4.11 g/cm^3) [19]. Hardness testing was carried out using Vickers microindentation (DuraScan G5, emco TEST) using a 4.9 N load with a dwell time of 15 s. Five readings were taken at different locations which were then averaged to get the final hardness value. The deformation microstructure upon contact damage by Vickers indentation was observed using optical microscopy and scanning electron microscopy.

Friction and wear tribological testing was conducted in a pin-on-disk rotary tribometer (CETR, UMT-1), using a 4 mm-diameter Al_2O_3 ball counterpart in ambient air (27 °C/32% RH) under dry sliding condition. The rotational speed was 50 rpm, and the normal load was 0.5 N producing a wear track length of ~7 mm. The worn area was measured by employing a surface profilometer (Veeco, Dektak 150) to obtain the worn volume and specific wear rates calculated using the equation:

$$K = V/L \text{ x } N$$

where K, V, L, and N represent specific wear rate, volume, sliding distance and load, respectively. Wear volume (V) is calculated by determining the cross-sectional area of the wear track and multiplying by the wear track length. The worn surface morphology was characterized by scanning electron microscopy and the chemistry at the sliding surface was probed for evolved tribofilms using Raman spectroscopy and electron energy loss spectroscopy (TEM/EELS).

3. Results and discussion

3.1. XRD patterns and phase fraction

Fig. 3 shows the characteristic XRD patterns of the resulting dual MAX phase composite after SPS. It can be seen that two phases, Ti_3AlC_2 and Ti_2AlC were the only phases present. More importantly, no presence of TiC was observed in the sintered sample, which implies that all TiC intermediary phase was consumed during the synthesis. Rietveld refinement confirmed that Ti_3AlC_2 is the main crystalline phase with weight fraction 68 % whilst 32 % of the residual phase was Ti_2AlC, thus 100 % MAX phase composite was formed.

3.2. Microstructure characterization

SEM micrographs of the polished unetched surface of the as-synthesized Ti_3AlC_2 – Ti_2AlC MAX phase composite are shown in Fig. 4.

Table 1
Powder characteristics and precursor formulation.

Powder	Supplier	Purity (%)	Particle size	Starting powder (g)	Comments
Ti	Aldrich	99.7	− 100 mesh	5.17	All powders were milled together in one step for 10 min
Al	Acros Organics	99	− 200 mesh	1.68	
C	Fischer- Chemicals	General purpose grade	n/a	0.65	

**Milled powder was then subsequently SPSed under vacuum sintering condition*

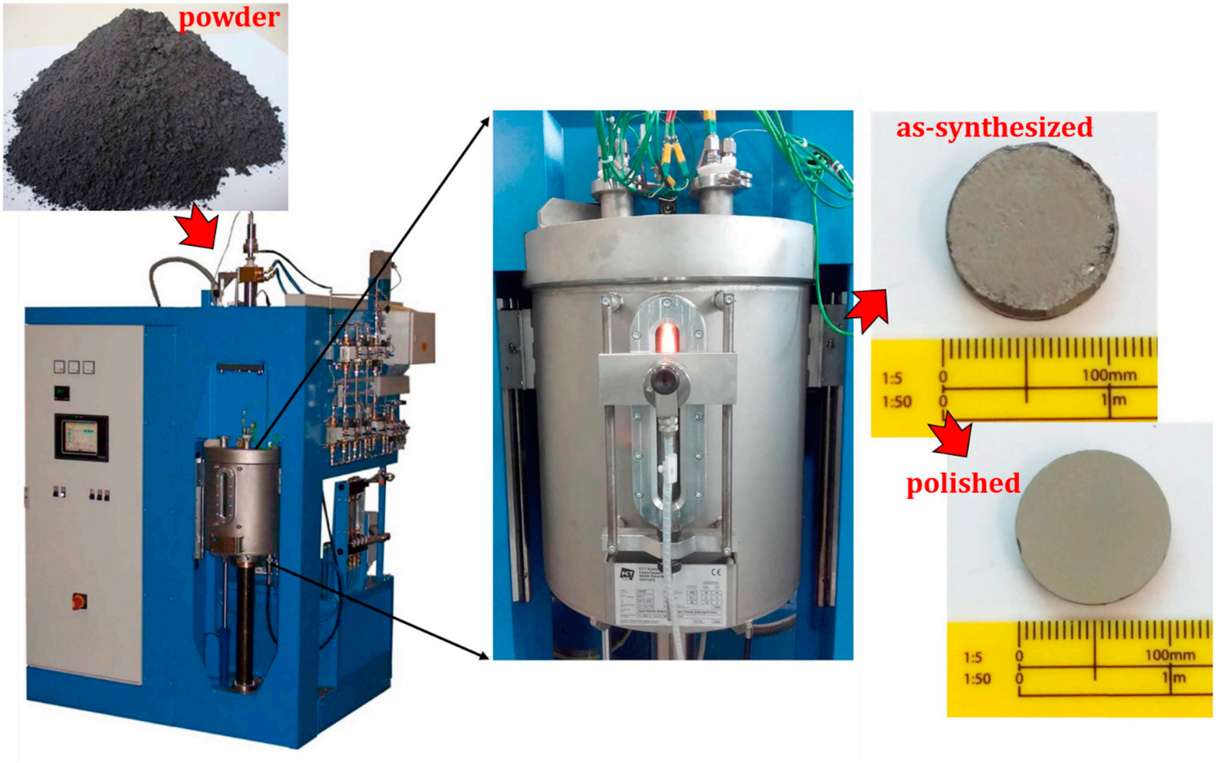

Fig. 2. HP D 25 spark plasma sintering (SPS) set-up and the resulting synthesized bulk sample.

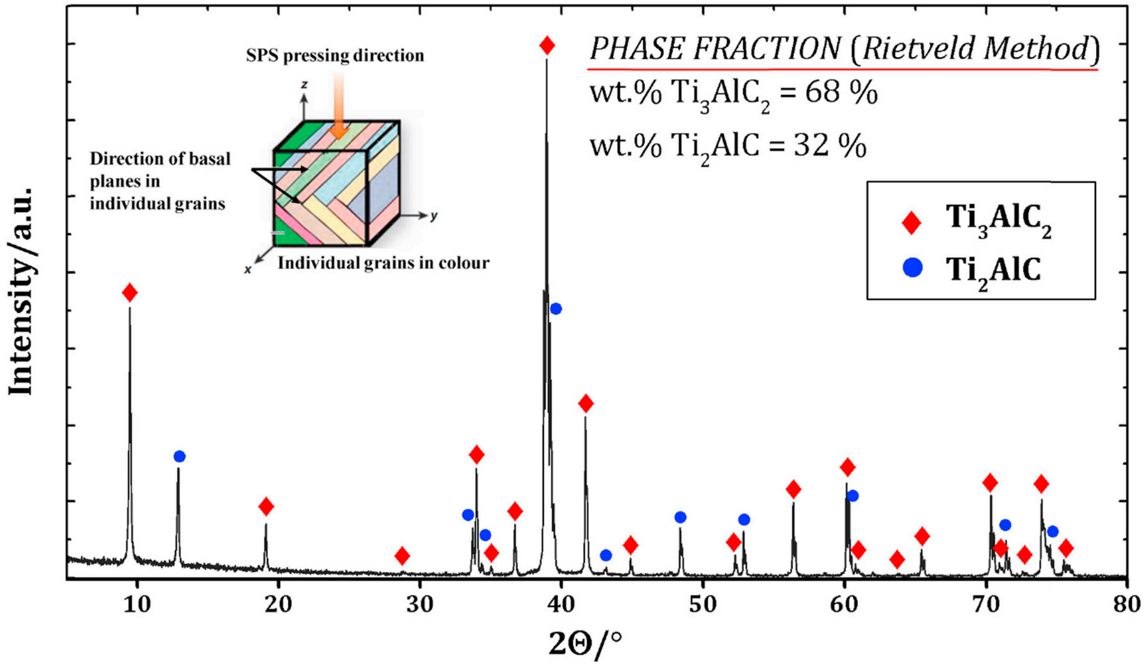

Fig. 3. XRD patterns of the resulting bulk MAX phase composite obtained by in-situ SPS of elemental Ti, Al and C powder mixture.

The microstructure depicts the characteristic plate-like nature of MAX phases and conforms well with the relative density measurement as there is no evidence of porosity which indicates complete densification. It is interesting that no Al_3Ti intermetallic phase coexist with the MAX phase composite, as previous studies carried out at this sintering temperature led to the formation of Al_3Ti which later disappeared at sintering temperatures above 1200 °C [20].

Further analysis by SEM-EDS to identify the phases was done as shown in Fig. 5. Based on the intensity of the peaks, it is clear that the bright phase is the Ti_3AlC_2 phase whilst the dark phase is the Ti_2AlC phase. Phase identification was necessary as it helps to understand the deformation behaviour of these MAX phases.

Abnormal grain growth (AGG) of the Ti_3AlC_2 and Ti_2AlC grains was observed in some areas in the matrix (Fig. 6). The implication of this is not fully understood at this time but such abnormal grain growth has been reported to be detrimental to hardness and fracture toughness due to crack nucleation [21].

A deleterious contribution of the abnormal grain growth is the role

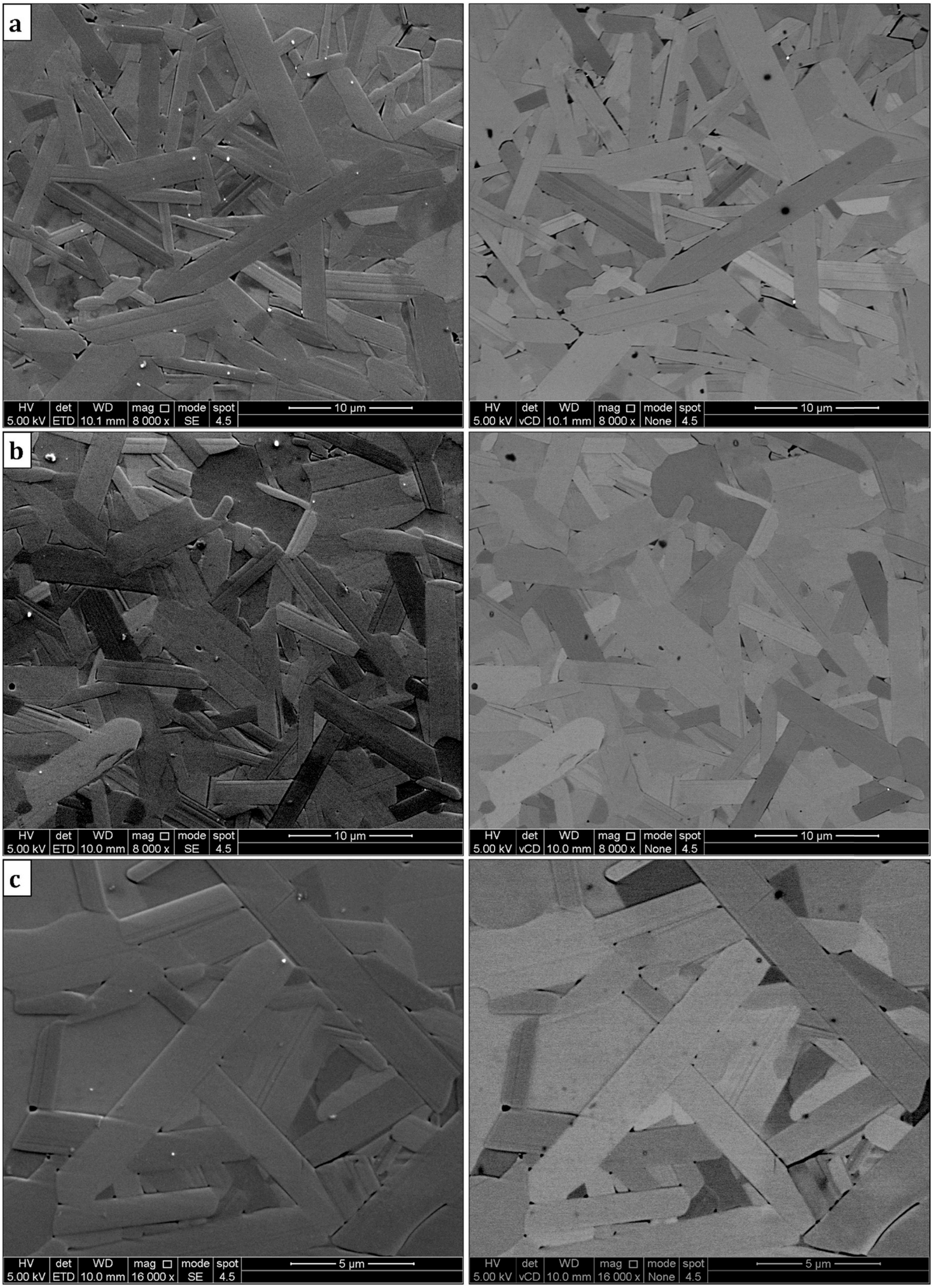

Fig. 4. Secondary electron (SE) and backscattered electron (BSE) SEM micrographs of the polished unetched Ti_3AlC_2 – Ti_2AlC MAX phase composite obtained by SPS.

it plays in gaps and cracking as observed in this composite system (Fig. 7). Since the thermal expansion coefficient (TEC) of Ti_3AlC_2 is higher than that of Ti_2AlC, compressive stress will be imposed on Ti_2AlC, and a tangential tensile stress in Ti_3AlC_2. During cooling from the requisite sintering temperature of the composite, spontaneous radial microcracking would initiate if the dimension of the Ti_2AlC exceeds

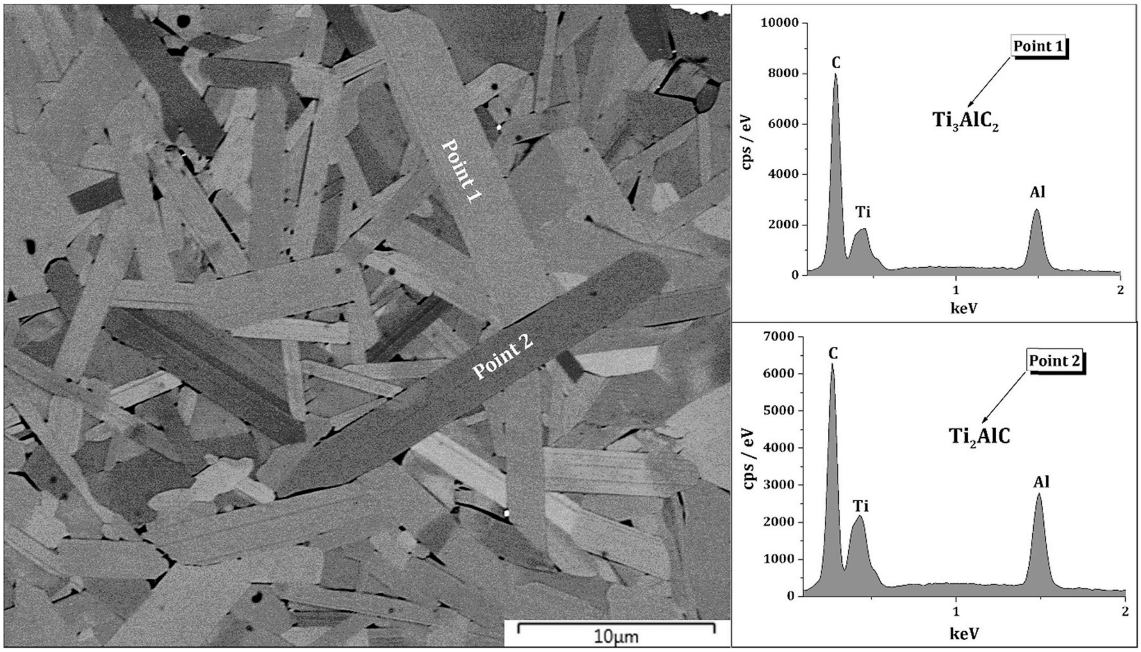

Fig. 5. EDS point spectrum collected from the different phase contrast point 1 and point 2.

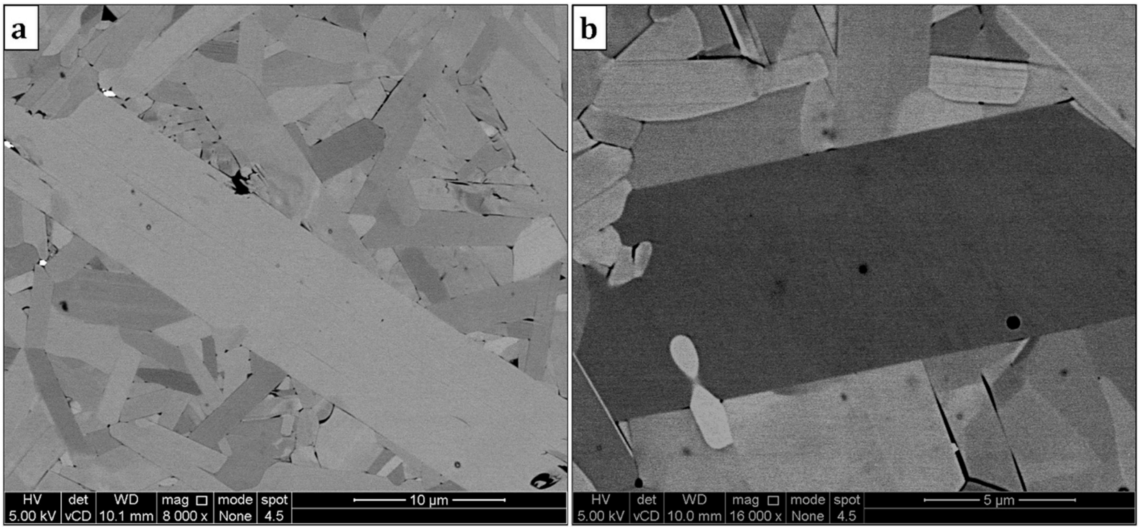

Fig. 6. Abnormal grain growth (AGG) of (a) Ti_3AlC_2 and (b) Ti_2AlC grains in the Ti_3AlC_2 – Ti_2AlC composite matrix.

the critical size based on the Selsing's model [22]. It is conceivable to attribute the cracking observed in this composite system to the thermal expansion coefficient mismatch as well as the abnormal grain growth. The majority of the cracks observed present themselves in the form of gaps along the grain boundary as the boundaries between the grains are inherently the weakest point. In some cases cracks were deflected along the grains upon meeting a plate shape grain.

Other synthesis routes discussed in literature such as hot presssing (HP) as an example, have often led to intergrown structures such as Ti_3AlC_2 – TiC – Ti_2AlC [23], Ti_3AlC_2 – TiAl [24], and Ti_3AlC_2 – TiAl – Ti_2AlC [25]. These composite structures may possess superior flexural strength as well as minimal spontaneous microcracking as the binary phase often segregate preferentially along the grain boundary, thus creating a pinning effect on the grain growth of the Ti_3AlC_2 and Ti_2AlC grains as reported elsewhere [16].

The characteristic lamellar plate-like microstructure of the polycrystalline Ti_3AlC_2 – Ti_2AlC dual MAX phase composite is further shown in the TEM images (Fig. 8). The grains are essentially planar defect-free with no dislocations and/or stacking faults observed in the as-synthesized composite. Both the Ti_3AlC_2 and Ti_2AlC grains crystallize in the form of two distinct laminated slab layers (Fig. 8(a)). Fig. 8(b) shows the selected area electron diffraction pattern (SAED) obtained from the different layers (layer 1 and layer 2) in the composite.

3.3. Density and vickers hardness

Table 2 is a summary of some of the mechanical properties of $TiAl_3$, Ti_3AlC_2 and Ti_2AlC for comparison. Particularly, it is important to include the properties of $TiAl_3$, a possible intermetallic phase which often crystallizes from the decomposition of Ti_3AlC_2 and has been found to enhance the flexural strength and hardness of Ti_3AlC_2 and Ti_2AlC [16,24].

The density of the Ti_3AlC_2 – Ti_2AlC bulk composite fabricated by SPS was 4.16 g/cm^3, which is ~ 99 % of the combined theoretical values upon considering the phase fraction and theoretical density of Ti_3AlC_2 and Ti_2AlC. It indicates that dual Ti_3AlC_2 – Ti_2AlC MAX phase

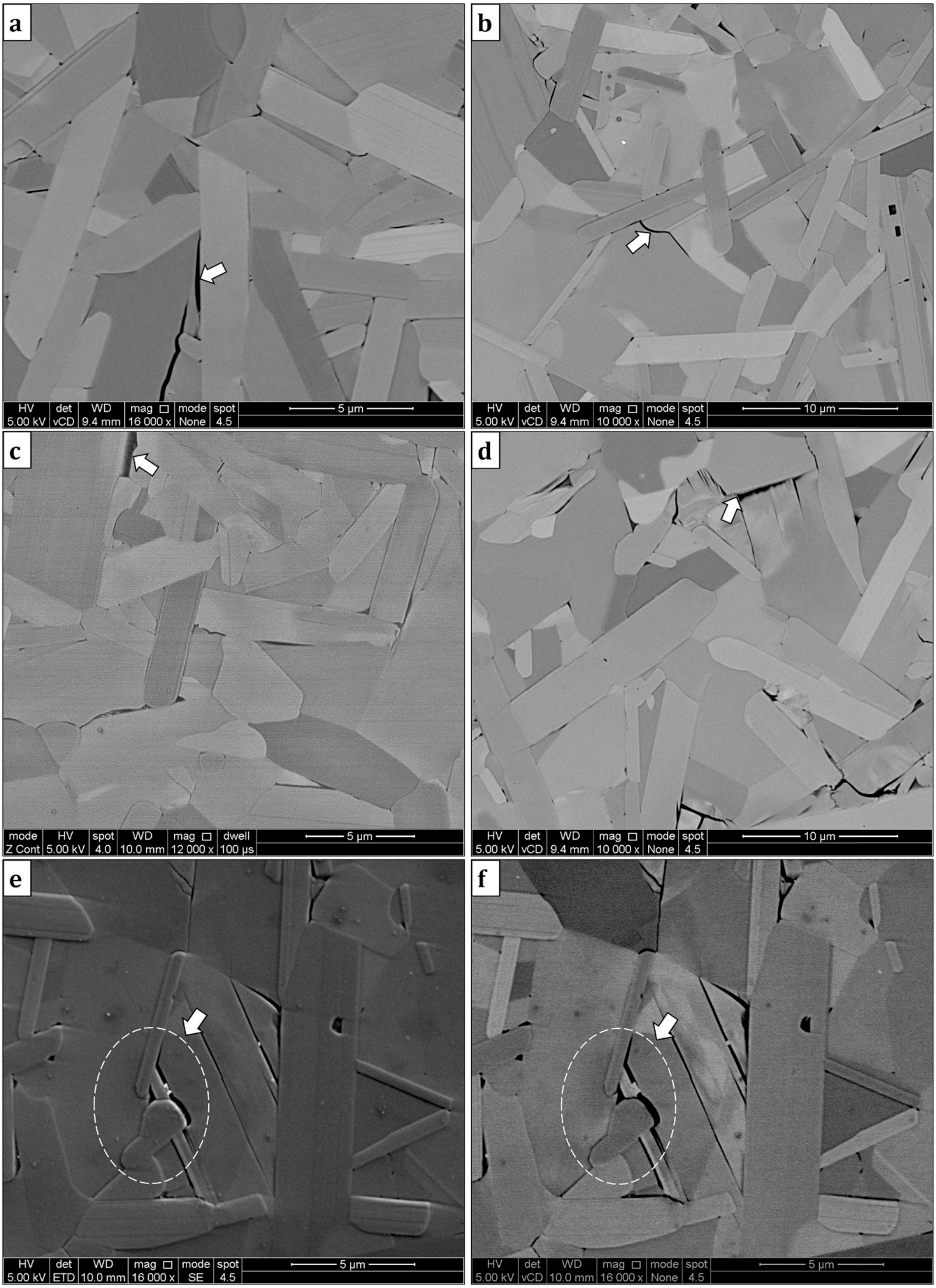

Fig. 7. A collection of SEM micrographs showing gaps and/or microcracking along the grains and grain boundaries.

composite can be synthesized by the SPS technique at relatively low temperature for short dwell times to obtain high purity and complete densification in contrast to other sintering techniques such as hot pressing (HP) where intermediate phases often still exist at low temperatures owing to incomplete densification as reported elsewhere [16,25]. The Vickers microhardness was measured as ~ 2.9 GPa, which

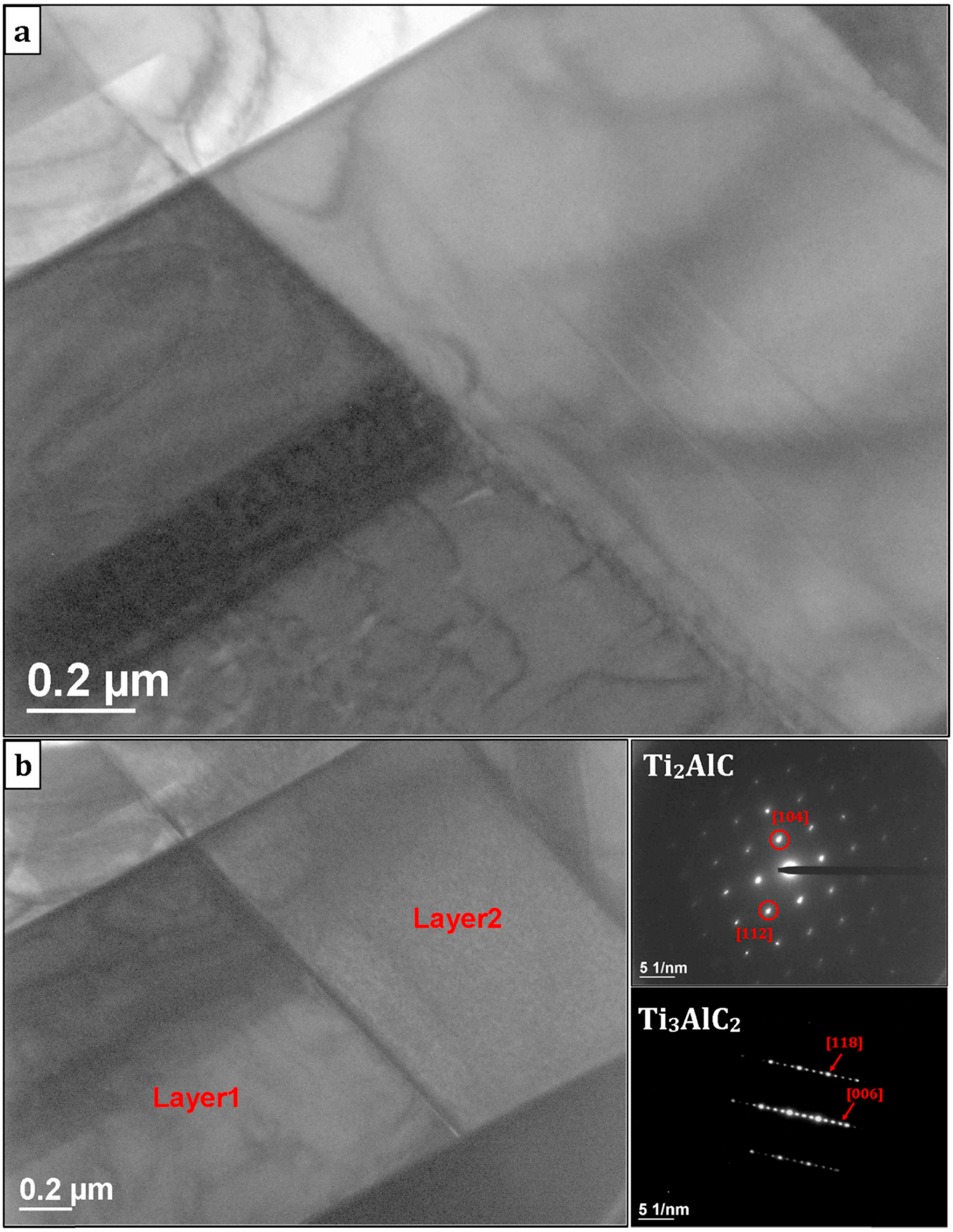

Fig. 8. TEM bright-field (BF) images showing (a) Ti_3AlC_2 – Ti_2AlC layers and (b) Ti_3AlC_2 – Ti_2AlC layers as well as the corresponding selected area electron diffraction (SAED) patterns of layer 1 (Ti_2AlC) and layer 2 (Ti_3AlC_2), respectively.

Table 2
Comparison of some mechanical properties of $TiAl_3$, Ti_3AlC_2 and Ti_2AlC.

Properties	$TiAl_3$	Ti_3AlC_2	Ti_2AlC
Density (g/cm^3)	3.3	4.2	4.1
Vickers hardness (GPa)	6	3.5	4.5
Flexural strength (MPa)	162	375	384
Fracture toughness ($MPa.m^{1/2}$)	2	7.2	5.37
Sources	[27]	[26]	[28]

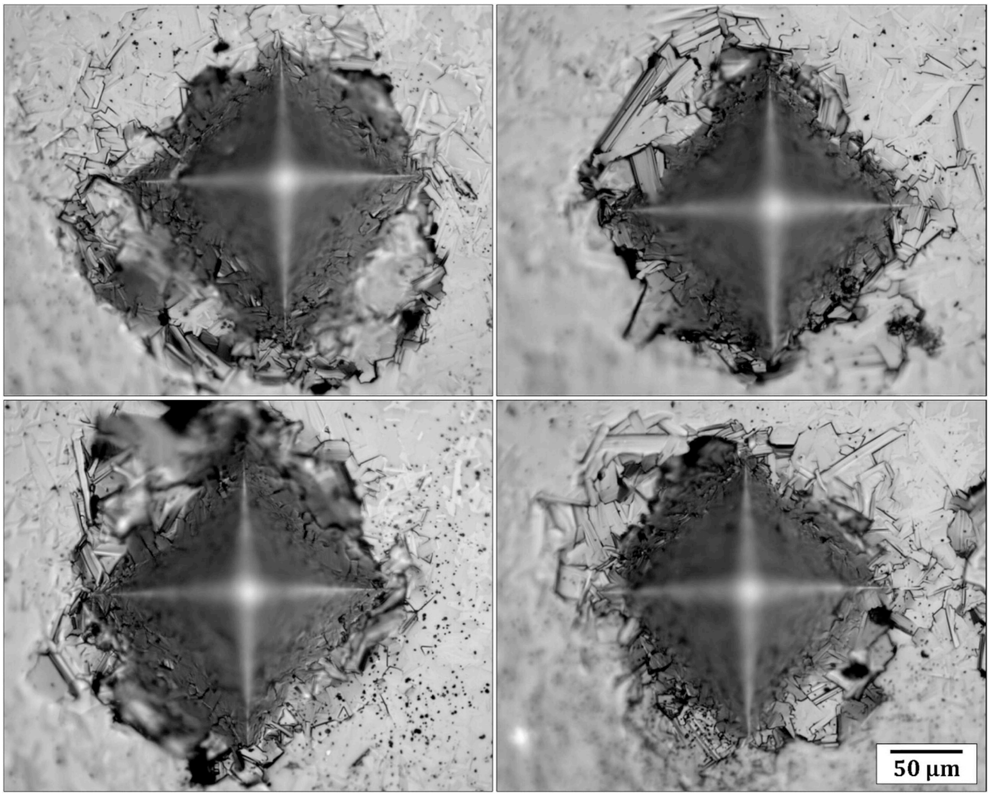

Fig. 9a. Optical micrographs showing Vickers indentation damage around the indents. Note the absence of indentation crack from the corners of the indents as well as pile-ups around the indent.$_3$AlC$_2$ – Ti$_2$AlC MAX phase composite.

is in the range of the intrinsic hardness of monolithic phase MAX phases reported to be in the range of 2–8 GPa [5] but lower than that of Ti_3AlC_2 (3.5 GPa [26]) and Ti_2AlC (4.5 GPa [17]). However, it is not surprising that the Vickers hardness of the composite was lower than the intrinsic hardness of Ti_3AlC_2 and Ti_2AlC as the presence of voids at cracked grain boundaries as shown in Fig. 7 will result in decreased hardness and flexural strength as reported elsewhere [16].

Contact damage by Vickers indentation (Fig. 9(a) and Fig. 9(b)) revealed extensive energy absorbing mechanisms such as grain pile-ups, delamination of laminated grains, crack deflection, grain buckling and grain pull-out in agreement with the damage mechanism observed in Ti_3SiC_2 [10,29–33]. The optical micrographs (Fig. 9(a)) confirm the evidence of indentation-induced damage with grain pull-out and push-out clearly seen alongside with extensive grain pile-ups. No evidence of indentation cracks emanating from the indentation diagonals was observed as damage appeared to be contained in consistent with other MAX phases [9,17,34].

In order to obtain a deeper insight into the damage resistance of the Ti_3AlC_2 – Ti_2AlC layered composite, the indents created by the Vickers indenter were further examined by SEM (Fig. 9(b)). A range of deformation modes such as grain pile-ups (Fig. 9b(a)), chevron fold (Fig. 9b(b)), delamination and kink band formation (Fig. 9b(c-d)) can be observed upon indentation. This suggests that plastic deformation might be enabled by shear sliding in this composite system.

Furthermore, the indentation damage zone was characterized by using a 3D –image analysis software (MountainsMap® SEM Topo, Digital Surf, France) to reconstruct the backscattered SEM image using stereo pairs. Some energy absorbing mechanisms (Fig. 10) not readily observed in the optical micrographs such as grain buckling, grain delamination, kink band formation and grain boundary cracking can be clearly seen. This damage tolerance is a hallmark of the MAX phases and has been attributed to basal slip activation as reported elsewhere [35,36]. In practical applications, the importance of this high-damage tolerance phenomemon i.e., ability of this composite to confine damage to small area around indentations cannot be overemphasized.

3.4. Friction coefficient and wear characteristics

The variation of friction coefficient as a function of sliding time under the dry sliding contact condition at room temperature is shown in Fig. 11. The friction curve exhibits a typical break-in curve as described by Blau [37]. The initial coefficient of friction was high and around ~ 0.75 and later attained a steady state around ~ 0.85 when all sharpest asperities are worn off and surface becomes smoother. However, at about 2500 cycles, a transition in friction occurs which further led to a drop in friction coefficient to about ~ 0.35. The reason behind this sharp transition in friction is not fully understood. It might, however, be attributed to the evolution of oxide films that have grown over time thus becoming tenacious and protective.

The calculated specific wear rate of the composite was of the order of $10^{-4}\,mm^3(N.m)^{-1}$ which is somewhat lower in comparison with that recorded for Ti_3SiC_2 sliding against steel which was of the order $10^{-3}\,mm^3(N.m)^{-1}$ [38].

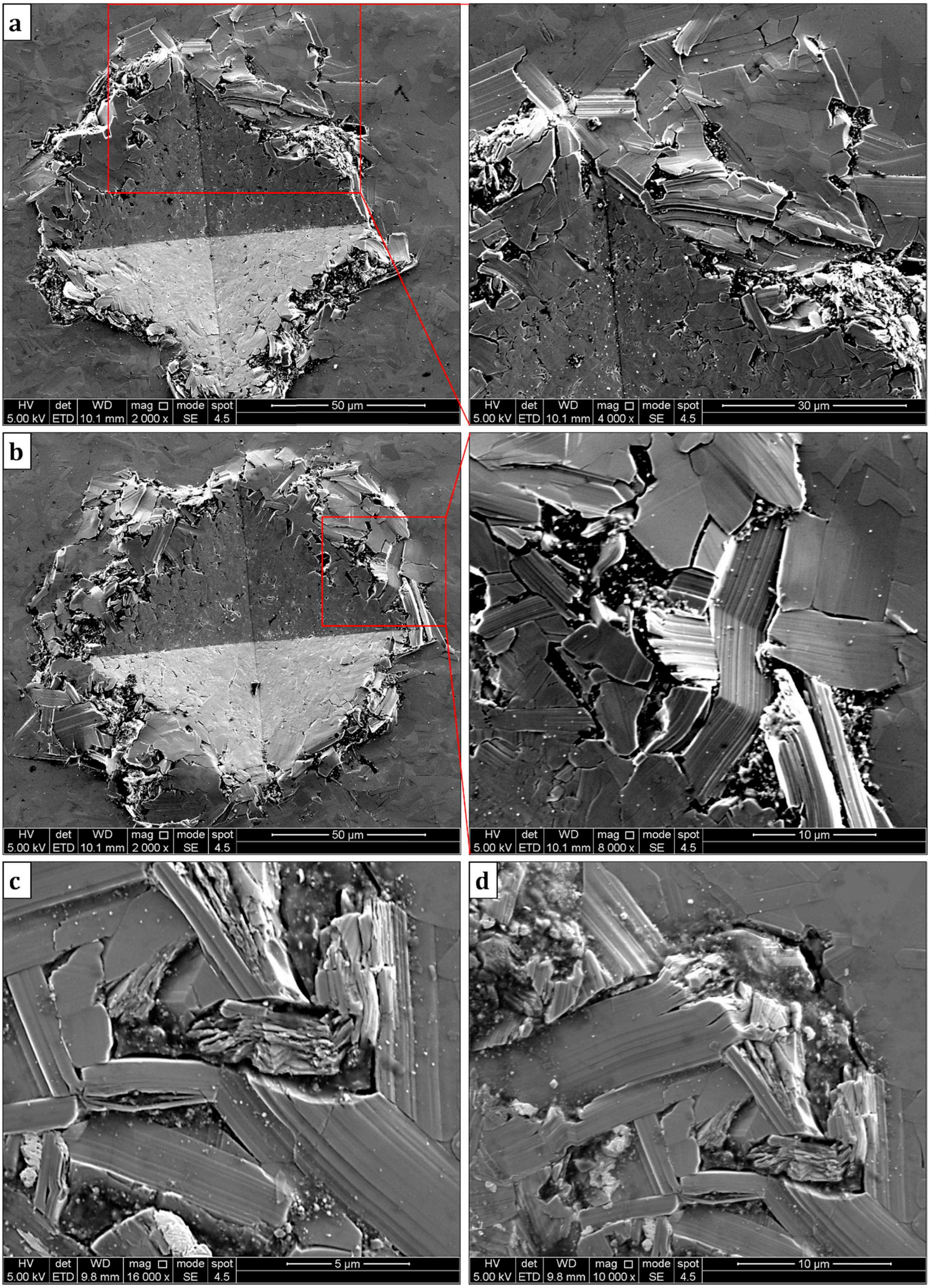

Fig. 9b. Scanning electron micrographs (SEM) of the Vickers indentation patterns created on Ti_3AlC_2 – Ti_2AlC MAX phase composite.

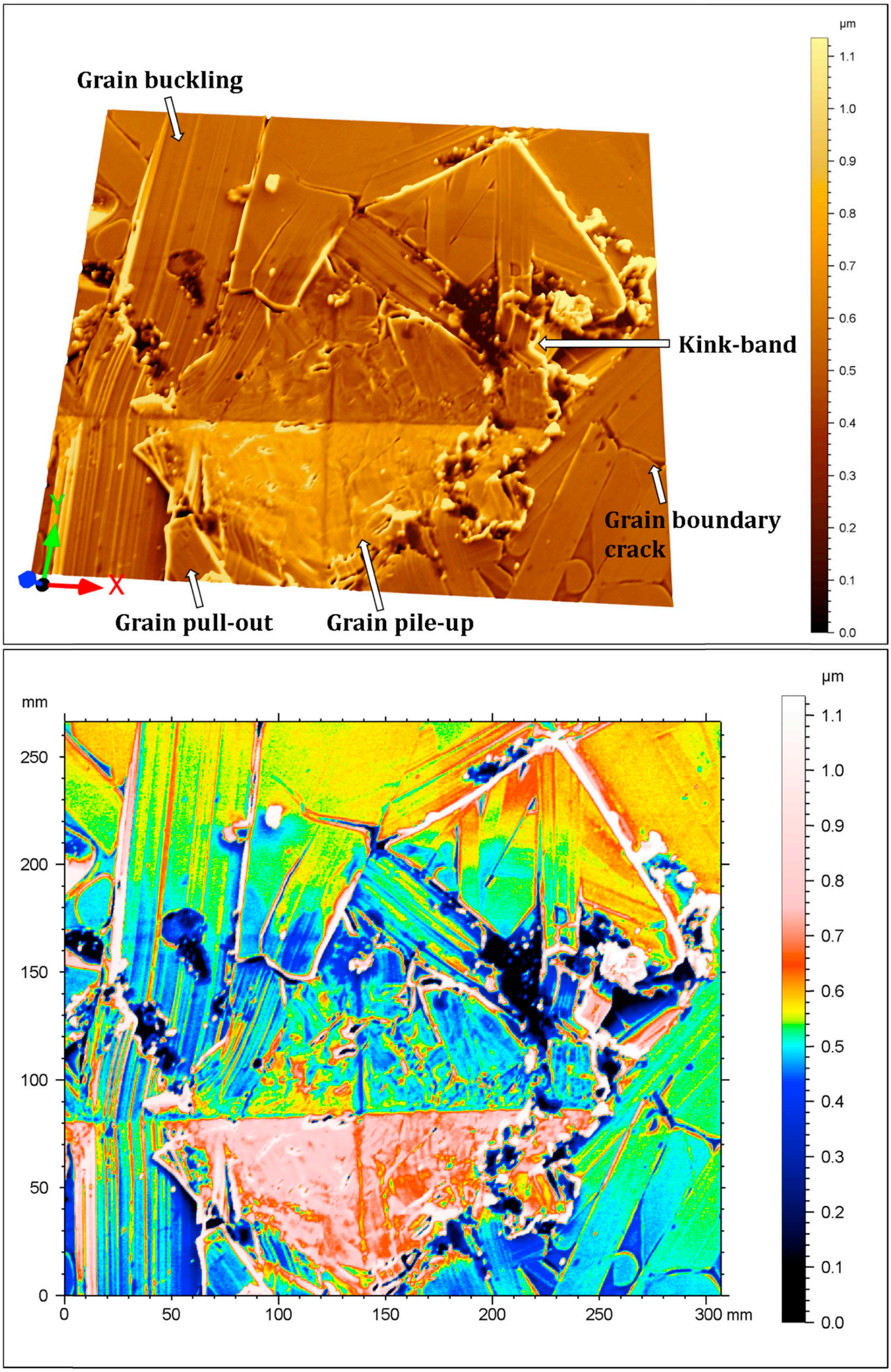

Fig. 10. 3D reconstruction of backscattered scanning electron micrograph showing Vickers-induced damage in Ti_3AlC_2 – Ti_2AlC dual MAX phase composite.

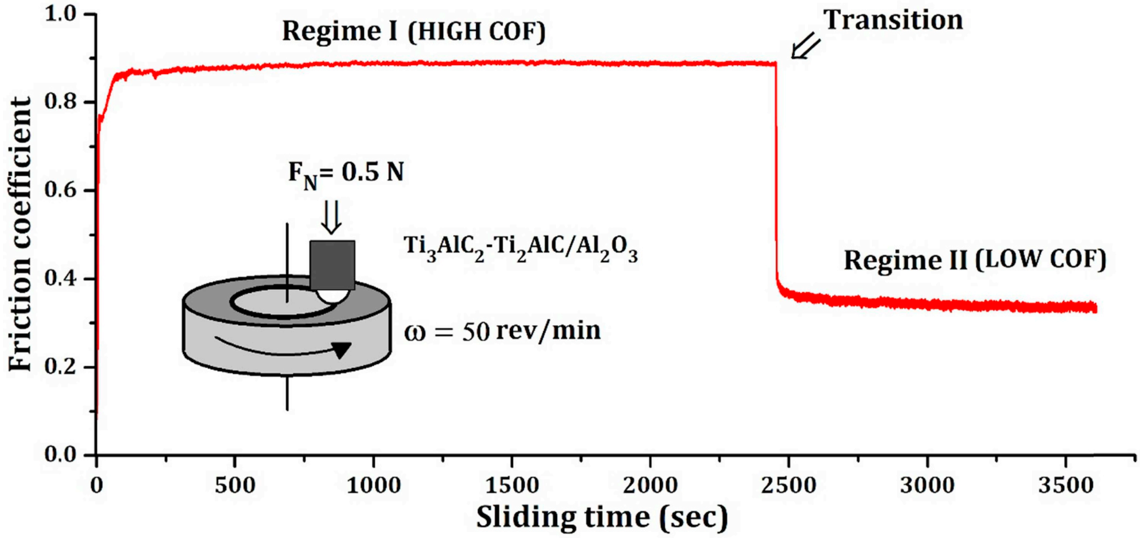

Fig. 11. Dependence of the coefficient of friction as a function of sliding time.

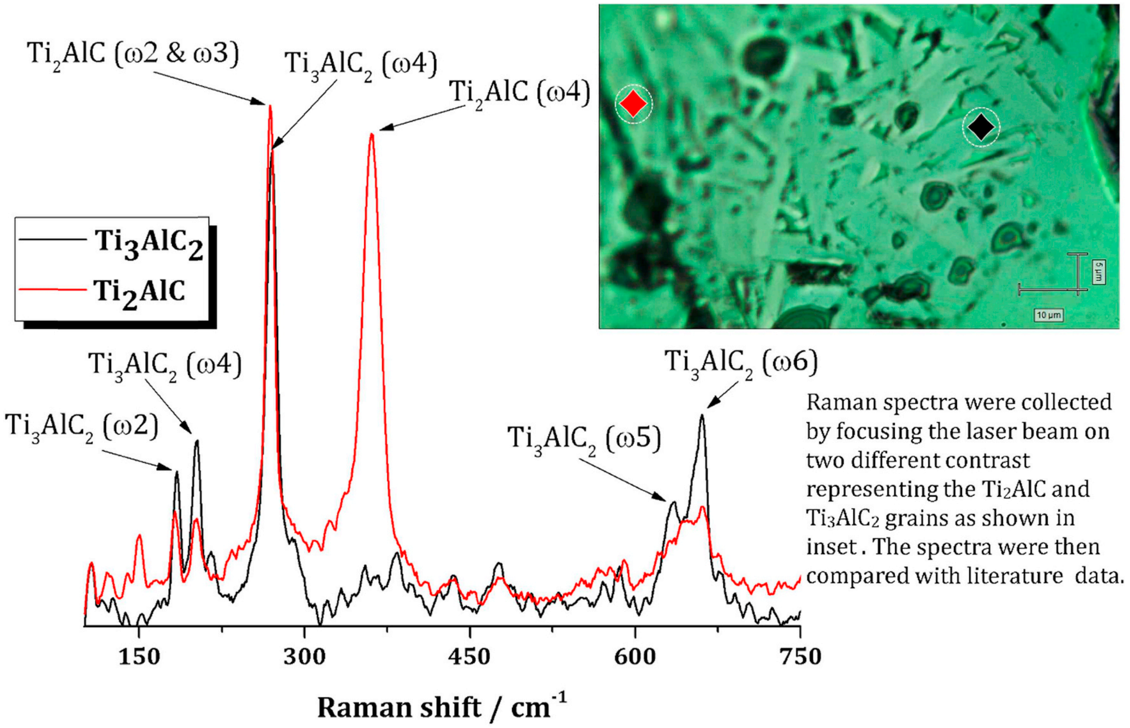

Raman spectra were collected by focusing the laser beam on two different contrast representing the Ti_2AlC and Ti_3AlC_2 grains as shown in inset. The spectra were then compared with literature data.

Fig. 12. Raman spectra collected from the polished as-synthesized Ti_3AlC_2 – Ti_2AlC MAX phase composite.

3.5. *Wear track characterization*

3.5.1. *Raman analysis*

The Raman spectra obtained from the pristine surface of Ti_3AlC_2 – Ti_2AlC MAX phase composite and wear track of the Ti_3AlC_2 – Ti_2AlC/Al_2O_3 tribocouple are shown in Fig. 12 and Fig. 13, respectively. The spectra recorded show peaks corresponding solely to Ti_3AlC_2 and Ti_2AlC [39,40] for the pristine sample whilst titanium oxide (TiO_2) [41,42], titanium oxycarbide (TiO_xC_y) [43], as well as vibrational modes originating from graphitic carbon [44] were recorded from the wear track. The presence of TiO_2 shows that the surface temperature due to dry sliding increased in the range 500–600 °C, the formation temperature range of anatase and possible anatase to rutile transformation [45,46]. The formation mechanism resulting in the evolution of TiO_xC_y is not fully understood; however its evolution is consistent with results reported elsewhere, and is speculated to be due to self-generating triboreaction [47,48]. The D and G graphitic carbon signatures in the wear track on the other hand may be due to possible outward diffusion of Ti and Al owing

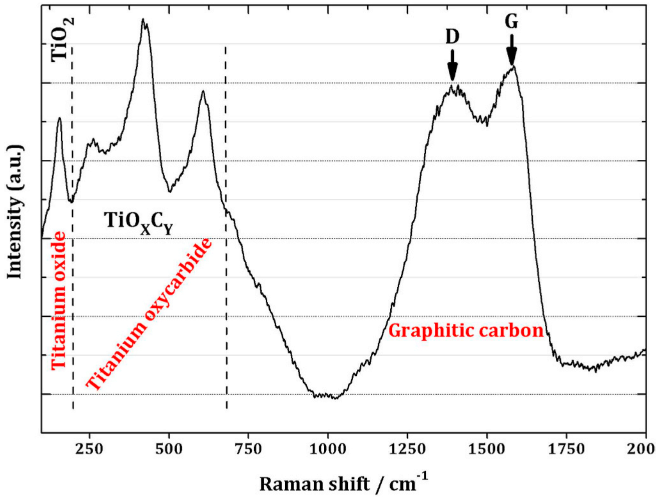

Fig. 13. Raman spectrum of an area inside the wear track of Ti_3AlC_2 – Ti_2AlC/Al_2O_3 tribocouple.

to frictional heating and their subsequent reaction with the inward diffusion of oxygen to form TiO_2 and Al_2O_3 respectively, thus leaving behind carbon which possess poor affinity to oxygen [46]. The weak covalent interaction between the Ti and Al layers as well as the layered nature of the MAX phase grains enhances the diffusion [46]. It is noteworthy to mention that the Raman analysis of the wear track did not reveal the coexistence of Al_2O_3 in the tribofilm architecture.

3.5.2. Scanning electron microscopy

Fig. 14 shows the scanning electron microscopy (SEM) micrographs of the wear track after dry sliding. Majority of the grains in and around the wear track have been fractured (Fig. 14(a–b)), pulverized and subsequently compacted inside the wear track. Also, loose wear debris can be seen distributed inside the wear track. Tribofilms are visible inside the wear track as patches (arrows in Fig. 14(e–f)) and mixed with the compacted wear debris (Fig. 14(e–f)). The grains appear to have been deformed with extensive grain delamination evident (Fig. 14(c–d)). The observed deformation microstructure after dry sliding contact is consistent with indentation-induced deformation microstructure as shown in Fig. 9(b).

3.6. SEM-EDS analysis

EDS elemental map was collected (Fig. 15) to further understand the chemistry of the worn surface. As observed, the arrows (electron image and also in Fig. 14(e–f)) correlates essentially to graphite-rich regions. Also, the compacted wear debris have been heavily oxidized due to wear-induced oxidation and consequently led to the evolution of TiO_2 and/or TiO_XC_Y on the compacted wear debris surface to further create a lubricious layer.

3.6.1. Transmission electron microscopy

STEM images of the FIBed section from the wear track showing the deformed grains as well as the EELS analysis of the tribofilm formed on the worn surface after dry sliding at room temperature is presented in Fig. 16. The grains appear to have buckled with grain cracking evident along the grain boundary and intergranularly (red arrow) as shown in Fig. 16(a) and highlighted in higher magnification. The worn surface deformation microstructure is consistent with that reported elsewhere [31]. Since the grain boundary is relatively weak it will thus facilitate the nucleation of intergranular cracks [31]. According to Ref. [49], the grain buckling of nanolayers within the grains serve as a precursor for the evolution of cavities as well as kink bands. EELS analysis (Fig. 16(b)) of the tribofilm revealed strong C-K, Ti-$L_{2,3}$, and O-K suggesting the coexistence of titanium, oxygen and carbon in the form of titanium oxide (TiO_2) and titanium oxycarbide (TiO_XC_Y) in agreement with the Raman analysis.

Bright-field TEM observation of the sliding surface (Fig. 17) revealed that in addition to grain fracture and buckling, some stacking faults exist in response to the sliding deformation. The reason behind the stacking fault formation is not fully understood at this time but the evolution might be linked to possible missing atomic planes owing to lattice rotation triggered by kink band formation upon separation of dislocation walls as reported elsewhere [29].

Bright-field conventional TEM (Fig. 18) further shows that dislocations multiplied and arranged themselves in the form of dislocation walls as a response to grain buckling following extensive deformation. It is important to mention that no kink bands were observed other than delamination. This is possibly due to the fact that grain buckling due to sliding deformation did not lead to extensive damage or the FIBed section did not contain all the deformation mechanisms.

4. Alumina (Al_2O_3) ball analysis

Analysis of the alumina ball upon dry sliding against the MAX phase composite showed evidence of material transfer to the ball (Fig. 19). Tribofilm(s) as well as oxidized wear debris can be seen from the optical images taken from the Al_2O_3 ball sliding surface before cleaning. The ball also appeared to have been scratched slightly post cleaning (Fig. 19(d)).

5. Wear mechanism

The wear mechanism is dominated by a wear transition from deformation induced wear to oxidative controlled wear owing to the evolution of triboreaction products triggered by frictional heating. The wear mechanisms are further explained thus:

5.1. Deformation induced wear

Plastic deformation at the sliding interface induced on the asperity contact scale, as well as deformation induced by basal plane slip [50], will lead to microfracture and subsequent generation of wear debris, which acts as an abrasive third-body - thus the observed sharp increase in CoF in the early stage (regime I). The deformation morphology shows that grain buckling, initiated possibly by basal plane slip, led to grain cracking because the shear strains between the bent and the unbent layers are incompatible, thus leading to grain delamination in agreement with the deformation mechanism reported in MAX phases [31]. It is apparent that basal slip induced grain buckling is the main deformation mechanism for this composite. As a result, there are two damage modes i.e., delamination and grain fracture, both of which are induced by buckling. According to Yanchun et al. [50], during deformation by basal slip, dislocations will move throughout the entire grain and preferentially pileup at grain boundaries to bring about grain boundary cracking. In general, extensive micro-deformation mechanisms incorporating basal plane slip, grain buckling, delamination, kink

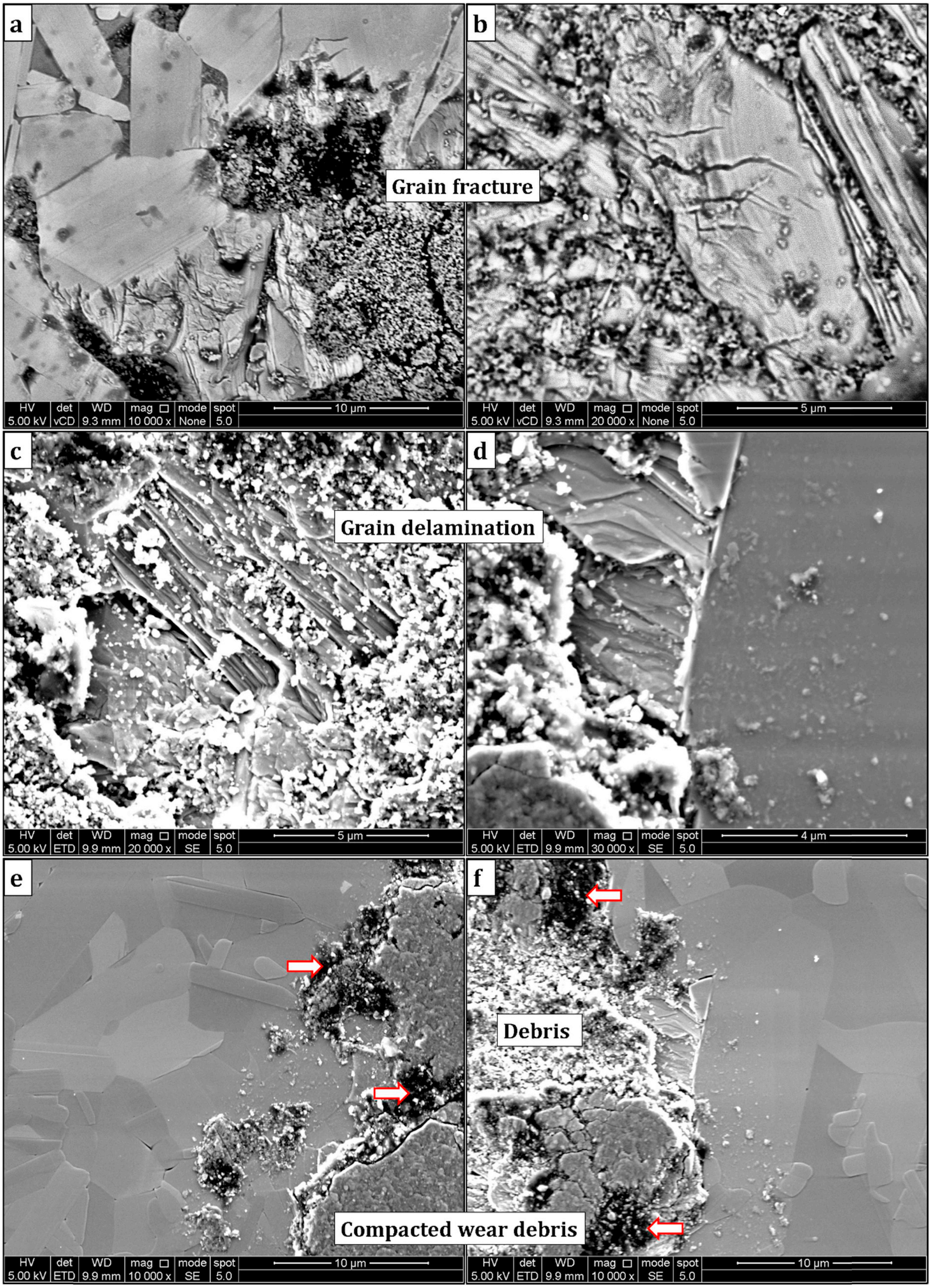

Fig. 14. SEM micrographs of the worn surface showing associated deformation microstructure of Ti_3AlC_2 – Ti_2AlC MAX phase composite upon dry sliding. Note: arrows in (e–f) show tribofilms.

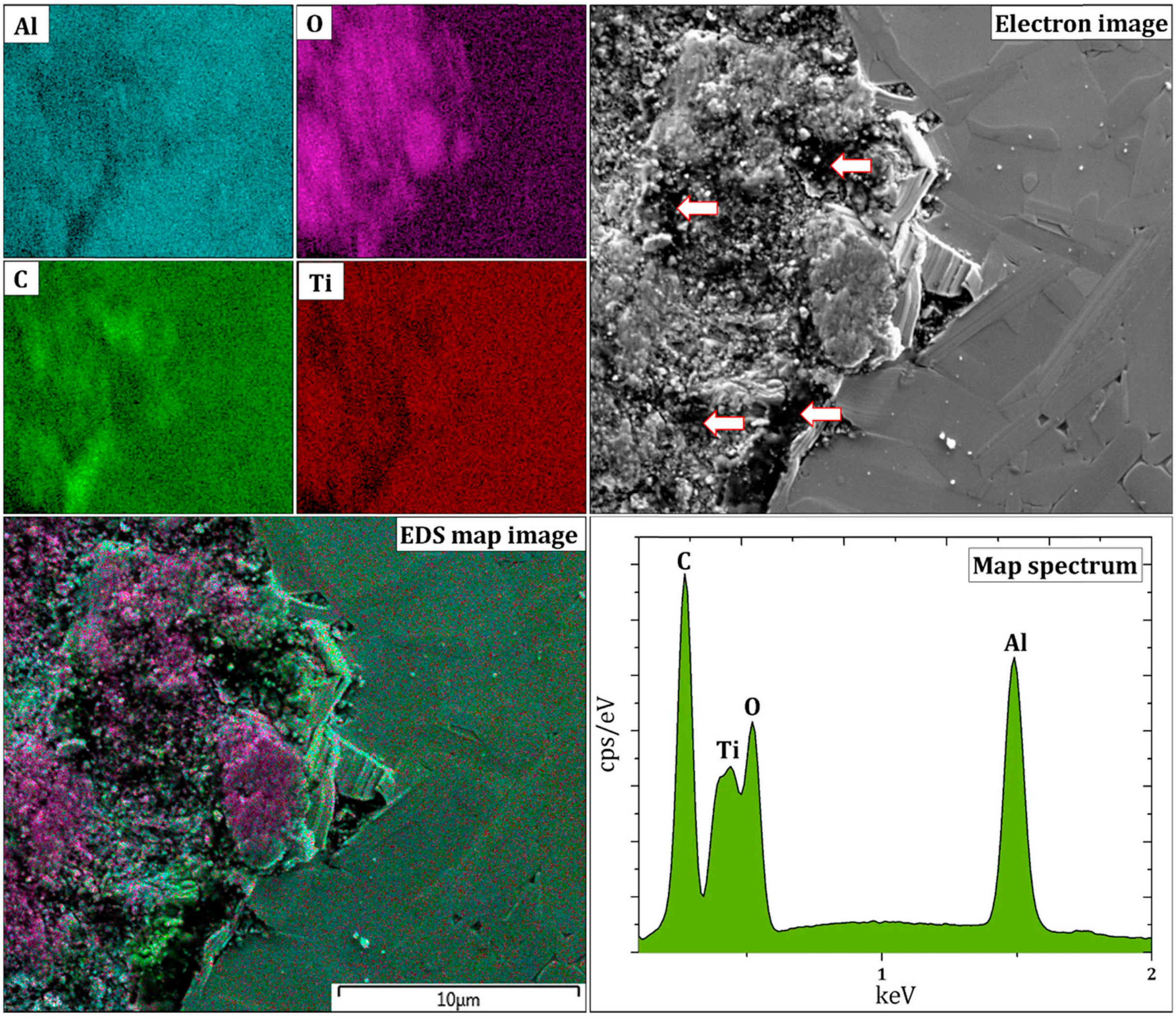

Fig. 15. EDS elemental map collected from the wear track of Ti_3AlC_2 – Ti_2AlC after dry sliding against Al_2O_3 at room temperature.

band formation and fracture of layers have been reported as operative deformation mechanisms in MAX phases. Nonetheless, it is noteworthy to highlight that the presence of gaps in the matrix will expedite grain pull-outs which might have also played a major role in the high COF observed in regime I.

5.2. Tribo-oxidative wear

According to the coefficient of friction plot, after a certain sliding time (probably necessary for sufficient oxide film generation), a transition from a deformation induced wear mechanism to a different wear mechanism characterized by a lower friction coefficient took place, thus highlighting the influence of tribofilm evolution. Raman and EELS analyses of the wear track clearly indicated that, after the transition, the wear mechanism changed from deformation-induced to a tribo-oxidative wear mechanism. The tribo-oxidative wear mechanism was triggered by frictional heating as a result of the dry sliding contact, thus the increase in contact temperature as a function of time. The reduction in friction coefficient (regime II) was therefore due to the lubricating action initiated by the tribofilms. It is believed that the fractured grains at the sliding surface were pulverized inside the wear track, thus generating wear debris that subsequently become compacted due to repeated sliding contact. The compacted wear debris is then oxidized due to frictional heating to generate protective tribofilms at the sliding surface, thus the wear transition from deformation induced (regime I) to tribo-oxidative wear (regime II).

6. Conclusion

Fully dense polycrystalline Ti_3AlC_2 – Ti_2AlC dual MAX phase composite was successfully synthesized by spark plasma sintering (SPS). The microstructural evolution and tribological properties of the as-synthesized sample was studied, and the following salient conclusions can be drawn:

(1) The Ti_3AlC_2 – Ti_2AlC MAX phase composite microstructure displayed a nanolaminated structure typical of laminated carbides and nitrides with exaggerated grain growth of the phases observed. The

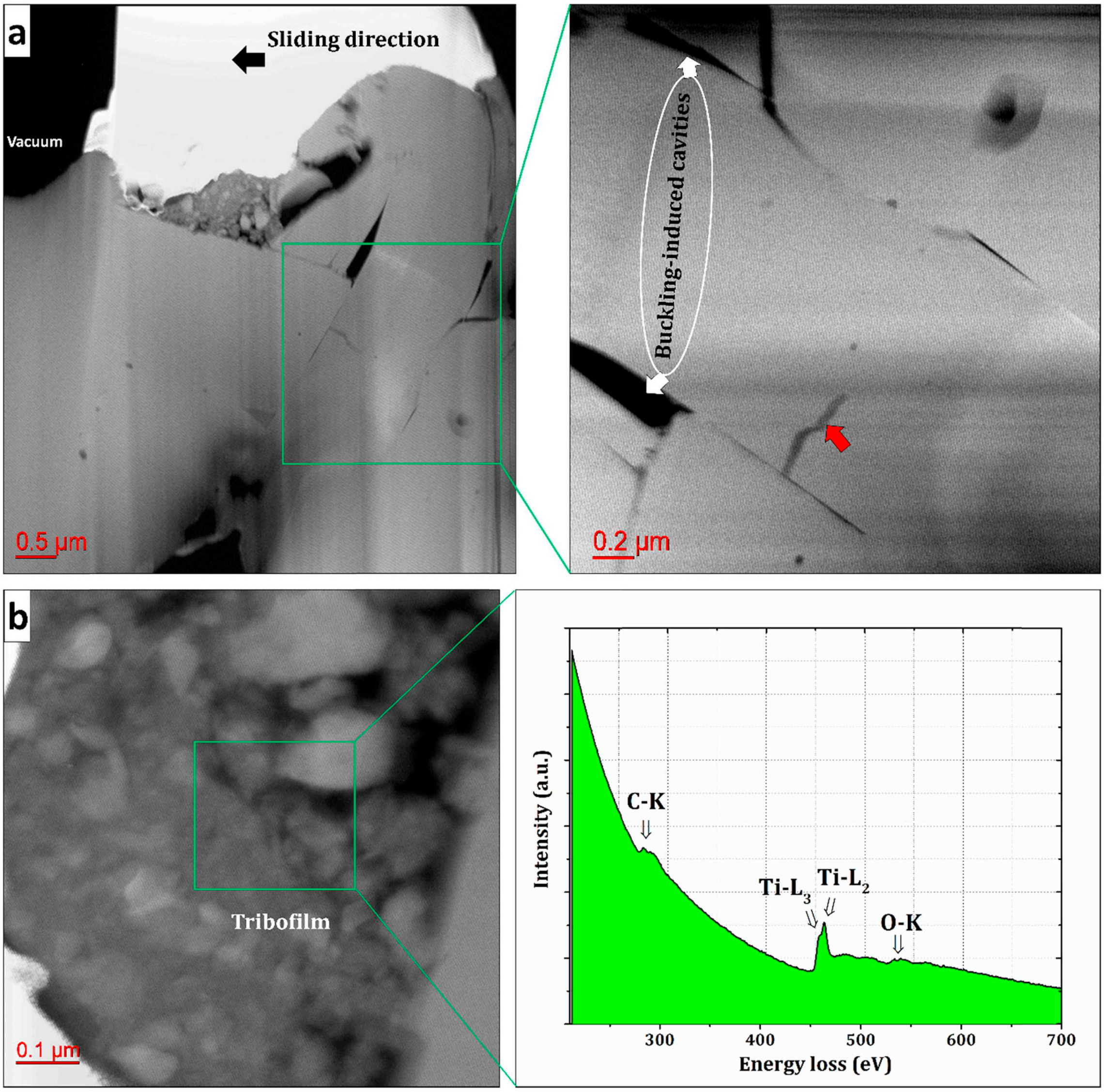

Fig. 16. Cross-sectional HAADF-STEM images of the Ti_3AlC_2 – Ti_2AlC worn surface showing (a) sliding induced deformation as well as the higher magnification of highlighted section, and (b) EELS microanalysis of the evolved tribolayer.

deformation microstructure upon Vickers indentation revealed micro-scale plasticity involving a range of energy absorbing mechanisms such as grain buckling, delamination, kink band formation, chevron fold, grain push-out and pull-out and eventual grain fracture.

(2) The lubrication and wear phenomena of the Ti_3AlC_2 – Ti_2AlC MAX phase composite is fundamentally dependent on the tribo-oxidation transfer film formed at the sliding surface. However, owing to the good oxidation resistance of these Al-containing MAX phases, tribo-oxidation is delayed. Since tribo-oxidative layer formation at the sliding surface is delayed, then a three-body abrasive wear that originates from the direct contact between the counterparts leading to pull-out of grains and subsequent fracture will dominate the wear mechanism.

(3) The wear rate of the composite was particularly high due to the low hardness and ease of grain pull-outs. A possible way to improve the wear rate is to consider appropriate interface combination and reinforcement with TiAl intermetallics which will enhance simultaneously both the composites hardness as well as the flexural strength by filling the voids and/or gaps in the matrix. It is noteworthy to mention that the presence of intermetallic phase particles in the matrix might also help to deteriorate the good oxidation resistance these Al-containing MAX phases, thus expediting the formation of transfer film via tribo-oxidation.

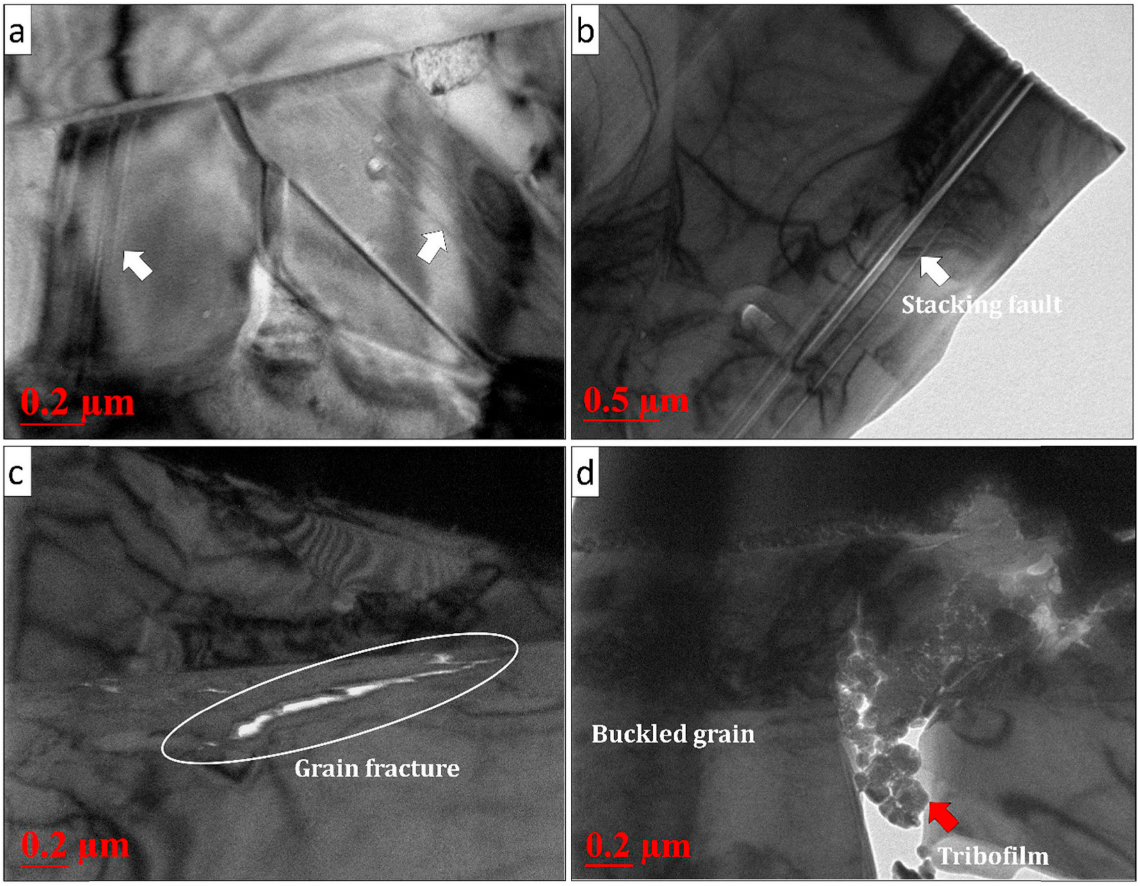

Fig. 17. Bright field TEM images of the sliding contact-induced deformation morphology showing (a–b) stacking faults (white arrow), (c) grain fracture and (d) grain buckling and tribofilms at the worn surface of the Ti_3AlC_2 – Ti_2AlC/Al_2O_3 tribocouple.

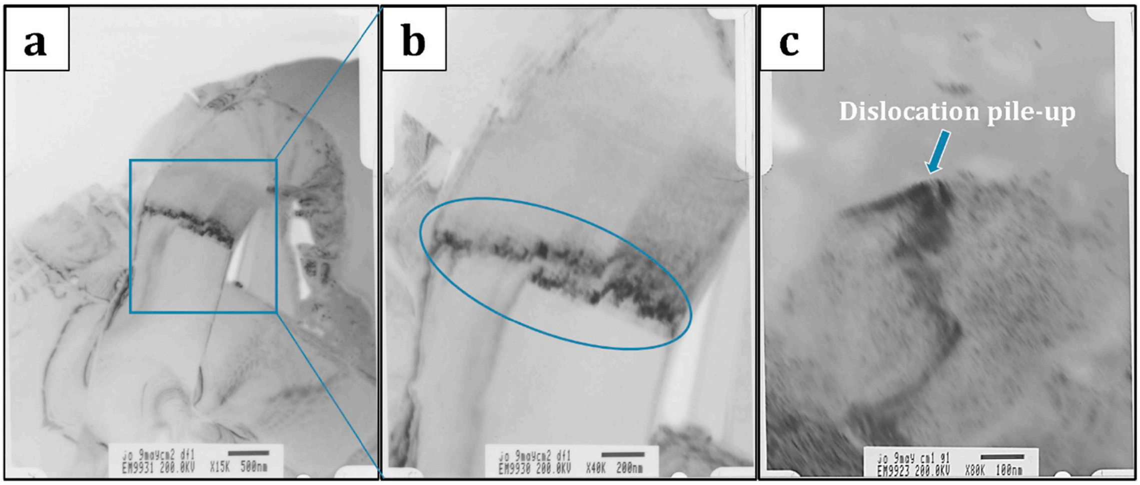

Fig. 18. Bright-field conventional TEM images showing (a) buckled grain with dislocation walls, (b) enlarged region of square outlined in (a) with blue highlight showing dislocation wall and (c) dislocation pile-ups along the grain. (For interpretation of the references to colour in this figure legend, the reader is referred to the Web version of this article.)

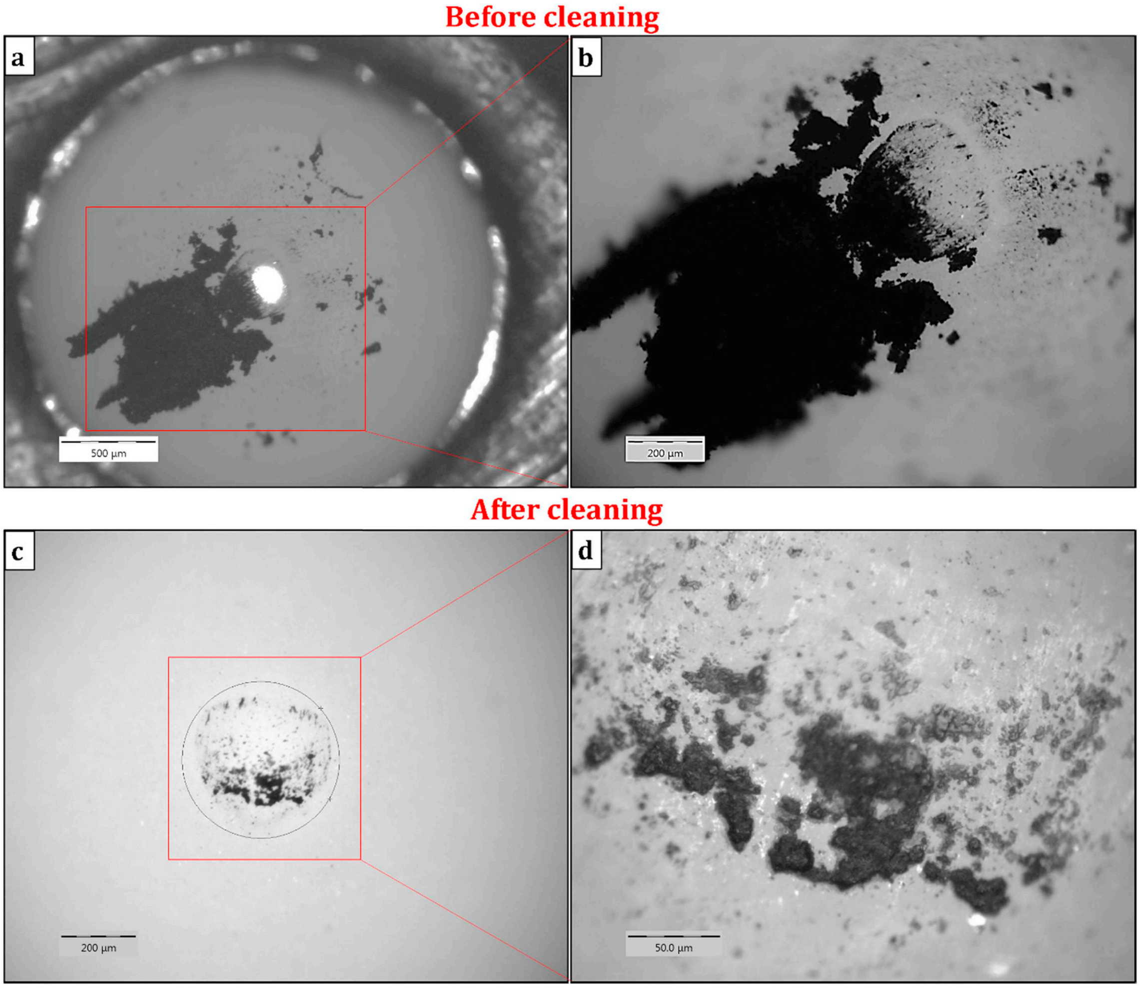

Fig. 19. Optical images of the Al_2O_3 ball after dry sliding wear test against the Ti_3AlC_2 – Ti_2AlC MAX phase composite.

References

[1] M.W. Barsoum, MAX Phases : Properties of Machinable Ternary Carbides and Nitrides, Wiley-VCH Verlag GmbH & Co. KGaA, Weinheim, Germany, 2013 2013.

[2] M.W. Barsoum, The MN+1AXN phases: a new class of solids, Prog. Solid State Chem. 28 (1) (2000) 201–281.

[3] C. Hu, et al., New phases' discovery in MAX family, Int. J. Refract. Metals Hard Mater. 36 (2013) 300–312.

[4] M.B. Kanoun, S. Goumri-Said, K. Abdullah, 8 - theoretical study of physical properties and oxygen incorporation effect in nanolaminated ternary carbides 211-MAX phases A2 - low, I.M, Advances in Science and Technology of Mn+1axn Phases, Woodhead Publishing, 2012, pp. 177–196.

[5] M.W. Barsoum, M. Radovic, Elastic and mechanical properties of the MAX phases, in: D.R. Clarke, P. Fratzl (Eds.), Annual Review of Materials Research, vol. 41, Annual Reviews: Palo Alto, 2011, pp. 195–227.

[6] P. Eklund, et al., The Mn + 1AXn phases: materials science and thin-film processing, Thin Solid Films 518 (8) (2010) 1851–1878.

[7] Y. Zhou, Z. Sun, Electronic structure and bonding properties layered machinable Ti2AlC and Ti2AlN, Phys. Rev. B 61 (2000) 75120-12573.

[8] J.M. Córdoba, et al., Synthesis of Ti3SiC2 powders: reaction mechanism, J. Am. Ceram. Soc. 90 (3) (2007) 825–830.

[9] T. El-Raghy, et al., Damage mechanisms around hardness indentations in Ti_3SiC_2, J. Am. Ceram. Soc. 80 (2) (1997) 513–516.

[10] I.M. Low, Vickers contact damage of micro-layered Ti3SiC2, J. Eur. Ceram. Soc. 18 (6) (1998) 709–713.

[11] A. Zhou, C.-a. Wang, Y. Huang, A possible mechanism on synthesis of Ti3AlC2, Mater. Sci. Eng., A 352 (1) (2003) 333–339.

[12] C. Peng, et al., A novel simple method to stably synthesize Ti3AlC2 powder with high purity, Mater. Sci. Eng., A 428 (1) (2006) 54–58.

[13] M. Akhlaghi, et al., Self-propagating high-temperature synthesis of Ti3AlC2 MAX phase from mechanically-activated Ti/Al/graphite powder mixture, Ceram. Int. 44 (8) (2018) 9671–9678.

[14] M.A. Pietzka, J.C. Schuster, Phase equilibria of the quaternary system Ti-Al-Sn-N at 900 °C, J. Alloy. Comp. 247 (1) (1997) 198–201.

[15] L. Chlubny, et al., Processing and properties of MAX phases - based materials using SHS technique, Arch. Metall. Mater. 60 (2) (2015) 859–863.

[16] T. Ai, et al., Microstructural and mechanical properties of dual Ti3AlC2–Ti2AlC reinforced TiAl composites fabricated by reaction hot pressing, Ceram. Int. 40 (7) (2014) 9947–9953 Part A.

[17] M.W. Barsoum, T. El-Raghy, M. Ali, Processing and characterization of Ti2AlC, Ti2AlN, and Ti2AlC0.5N0.5, Metall. Mater. Trans. A 31 (7) (2000) 1857–1865.

[18] S.R. Kulkarni, A.V.D.K.-H. Wu, Synthesis of Ti2AlC by spark plasma sintering of TiAl–carbon nanotube powder mixture, J. Alloy. Comp. 490 (1) (2010) 155–159.

[19] C. Wang, et al., Irradiation-induced structural transitions in Ti2AlC, Acta Mater. 98 (2015) 197–205.

[20] W. Zhou, et al., Fabrication of high purity dense Ti2AlC-Ti3AlC2 composite by spark plasma sintering method, J. Mater. Sci. 40 (13) (2005) 3559–3560.

[21] T.A. Furnish, et al., The onset and evolution of fatigue-induced abnormal grain growth in nanocrystalline Ni–Fe, J. Mater. Sci. 52 (1) (2017) 46–59.

[22] J. SELSING, Internal stresses in ceramics, J. Am. Ceram. Soc. 44 (8) (1961) 419-419.

[23] Z.J. Lin, et al., Microstructural characterization of layered ternary Ti2AlC, Acta Mater. 54 (4) (2006) 1009–1015.

[24] T. Ai, et al., Processing, microstructural characterization and mechanical properties of in situ Ti3AlC2/TiAl3 composite by hot pressing, Mater. Sci. Eng., A 610 (2014) 297–300.

[25] M.B. Rahaei, et al., Manufacturing of high volume fraction of Ti3AlC2-Ti2AlC metallic ceramics as nano-multilayered structures through high energy milling, hot pressing and liquid phase sintering, Mater. Char. 128 (2017) 176–183.

[26] N.V. Tzenov, M.W. Barsoum, Synthesis and characterization of Ti3AlC2, J. Am. Ceram. Soc. 83 (4) (2000) 825–832.

[27] Y.V. Milman, et al., Mechanical behaviour of Al3Ti intermetallic and L12 phases on its basis, Intermetallics 9 (9) (2001) 839–845.

[28] P. Wang, et al., Synthesis of Ti2AlC by hot pressing and its mechanical and electrical properties, Trans. Nonferrous Metals Soc. China 17 (5) (2007) 1001–1004.

[29] M.W. Barsoum, L. Farber, T. El-Raghy, Dislocations, kink bands, and room-temperature plasticity of Ti3SiC2, Metall. Mater. Trans. A 30 (7) (1999) 1727–1738.

[30] S.B. Li, L.F. Cheng, L.T. Zhang, Identification of damage tolerance of Ti3SiC2 by hardness indentations and single edge notched beam test, Mater. Sci. Technol. 18 (2) (2002) 231–233.

[31] Z.F. Zhang, et al., Micron-scale deformation and damage mechanisms of Ti3SiC2 crystals induced by indentation, Adv. Eng. Mater. 6 (12) (2004) 980–983.

[32] T.A. Prikhna, et al., Mechanical properties of materials based on MAX phases of the Ti-Al-C system, J. Superhard Mater. 34 (2) (2012) 102–109.

[33] Z. Sun, et al., Ternary compound Ti3SiC2: Part II. Deformation and fracture behavior at different temperatures, Mater. Trans. 43 (3) (2002) 432–435.

[34] T. El-Raghy, et al., Processing and mechanical properties of Ti3SiC2: II, effect of grain size and deformation temperature, J. Am. Ceram. Soc. 82 (10) (1999) 2855–2860.

[35] E. Drouelle, et al., Deformation mechanisms during high temperature tensile creep of Ti3AlC2 MAX phase, J. Alloy. Comp. 693 (2017) 622–630.

[36] S. Amini, M.W. Barsoum, T. El-Raghy, Synthesis and mechanical properties of fully dense Ti2SC, J. Am. Ceram. Soc. 90 (12) (2007) 3953–3958.

[37] P.J. Blau, Interpretations of the friction and wear break-in behavior of metals in sliding contact, Wear 71 (1) (1981) 29–43.

[38] T. El-Raghy, P. Blau, M.W. Barsoum, Effect of grain size on friction and wear behavior of Ti3SiC2, Wear 238 (2) (2000) 125–130.

[39] V. Presser, et al., First-order Raman scattering of the MAX phases: Ti2AlN, Ti2AlC0.5N0.5, Ti2AlC, (Ti0.5V0.5)2AlC, V2AlC, Ti3AlC2, and Ti3GeC2, J. Raman Spectrosc. 43 (1) (2012) 168–172.

[40] E. Jonathan, S.G. Spanier, S. Maher, Amer and Michel W. Barsoum, vibrational behavior of the Mn + 1AXn phases from first-order Raman scattering (M = Ti,V,Cr, A = Si, X = C,N), Phys. Rev. B Condens. Matter Mater. Phys. 71 (2005) 1 2005.

[41] O. Frank, et al., Raman spectra of titanium dioxide (anatase, rutile) with identified oxygen isotopes (16, 17, 18), Phys. Chem. Chem. Phys. 14 (42) (2012) 14567–14572.

[42] U. Balachandran, N.G. Eror, Raman spectra of titanium dioxide, J. Solid State Chem. 42 (3) (1982) 276–282.

[43] C.-h. Wu, S.-y. Chen, P. Shen, CH doped anatase nanospheres with disordered shell and planar defects synthesized by pulsed laser ablation of bulk Ti in tetraethyl orthosilicate, CrystEngComm 16 (11) (2014) 2220–2229.

[44] F. Tuinstra, J.L. Koenig, Raman spectrum of graphite, J. Chem. Phys. 53 (3) (1970) 1126–1130.

[45] W.K. Pang, et al., 12 - oxidation characteristics of Ti3AlC2, Ti3SiC2 and Ti2AlC, Advances in Science and Technology of Mn + 1AXn Phases, Woodhead Publishing, 2012, pp. 289–322.

[46] H.B. Zhang, K.G. Nickel, Hydrothermal Oxidation of Ti3SiC2, (2012), pp. 323–354.

[47] A. Souchet, et al., Tribological duality of Ti3SiC2, Tribol. Lett. 18 (3) (2005) 341–352.

[48] S. Gupta, M.W. Barsoum, On the tribology of the MAX phases and their composites during dry sliding: a review, Wear 271 (9–10) (2011) 1878–1894.

[49] M.W. Barsoum, et al., Kinking nonlinear elastic solids, nanoindentations, and geology, Phys. Rev. Lett. 92 (25) (2004) 255508.

[50] Y. Zhou, Z. Sun, Micro-scale plastic deformation of polycrystalline Ti3SiC2 under room-temperature compression, J. Eur. Ceram. Soc. 21 (8) (2001) 1007–1011.

Paper G

Dry sliding friction and wear behaviour of TiC-based ceramics and consequent effect of the evolution of grain buckling on wear mechanism

Wear 422–423 (2019) 54–67

Contents lists available at ScienceDirect

Wear

journal homepage: www.elsevier.com/locate/wear

Dry sliding friction and wear behaviour of TiC-based ceramics and consequent effect of the evolution of grain buckling on wear mechanism

C. Magnus, T. Kwamman, W.M. Rainforth*

Department of Materials Science and Engineering, The University of Sheffield, Mappin Street, Sheffield S1 3JD, UK

ARTICLE INFO

Keywords:
Spark plasma sintering
High temperature ceramics
Dry sliding friction
Residual stresses

ABSTRACT

In this study, the dry sliding tribological behaviour of TiC-based ceramics against alumina is elucidated. Monolithic TiC as well as TiC-SiC composites were successfully densified by spark plasma sintering (SPS) using TiC and SiC powders as starting materials. Friction tests were performed using a pin-on-disk-type friction tester wherein alumina was used as counterpart material in an unlubricated condition at room temperature. The friction coefficient for the TiC-based ceramics dry sliding against alumina all initially increased and attained steady state after the first 200 s. The coefficient of friction in the case of monolithic TiC attained steady state earlier than the composites and exhibited the lowest friction coefficient. The specific wear rate of the TiC-based ceramics increased with increasing SiC content; it was lowest when sliding against monolithic TiC. The increase in wear rate in the composites is linked to grain buckling induced fracture owing instability arising from residual compressive stresses inherent in the composite due to mismatch in thermal expansion coefficients between TiC and SiC. The wear mechanism in general appears to be primarily dominated by third-body wear triggered by grain fracture and subsequent grain pull-out.

1. Introduction

Ultra-high temperature ceramics (UHTCs) based on titanium carbide (TiC) and silicon carbide (SiC), as well as their composites, have been extensively studied due to their fascinating range of properties [1]. They possess outstanding high temperature stability, exceptional hardness, and good oxidation and wear resistance [2–5]. However, a major limiting mechanical property especially in structural application is that TiC and SiC possess intrinsically low fracture toughness values in the range (3–4 MPa $m^{1/2}$) in their monolithic state [2,6,7]. As a consequence, they are preferentially employed as a second dispersive phase to improve the mechanical properties of composite ceramic materials [6,8,9]. It has been reported that the addition of titanium carbide particles to silicon carbide matrix will increase the mean fracture toughness of the resulting composite [6,7,10,11] in comparison to monolithic TiC and SiC ceramic [6,12,13]. The improved fracture toughness is mainly attributed to the following reasons [6,8]:

- The TiC particles toughens the SiC matrix by crack deflection (Fig. 1), owing to the mismatch in thermal expansion coefficient ($\Delta\alpha = \sim 2.6 \times 10^{-6}\ ^{\circ}C^{-1}$) as well as elastic moduli (E) between TiC and SiC which brings about residual stresses in the particle and surrounding matrix which contributes to the enhancement of fracture toughness.
- The mismatch in thermal expansion, as well as cooling from the high sintering temperature to ambient, results in a residual hydrostatic tension in TiC particles whilst the SiC matrix will be subjected to both hoop compression and radial tension.
- TiC undergoes severe plastic deformation at temperature above 800 °C due to its five independent slip systems which is aided by high temperature sintering as well as possible $\beta \rightarrow \alpha$ phase transformation of SiC. Such plasticity will initiate deformation in the crack-tip zone to bring about toughening at high temperature.
- TiC is chemically compatible to SiC at the spark plasma sintering temperatures.

Additionally, it has been reported that the addition of SiC particles into TiC matrix will bring about increased fracture toughness due to refinement of the TiC matrix [14]. While the addition of TiC particles into SiC matrix on the other hand increases the density as well as the flexural strength of the resulting composite system [15]. However, owing to the highly covalently bonded nature of TiC and SiC in TiC-SiC composites [5], the use of sintering aid is needed in most sintering methods [4,16–18]. A major disadvantage of sintering aids is that their relatively low melting point limits the application of these ceramic composites at higher temperatures [2]. Hence, it is imperative to consolidate TiC-SiC composite without sintering aid. Recently, composites

---

* Corresponding author.
E-mail address: m.rainforth@sheffield.ac.uk (W.M. Rainforth).

https://doi.org/10.1016/j.wear.2019.01.026
Received 1 August 2018; Received in revised form 4 January 2019; Accepted 6 January 2019

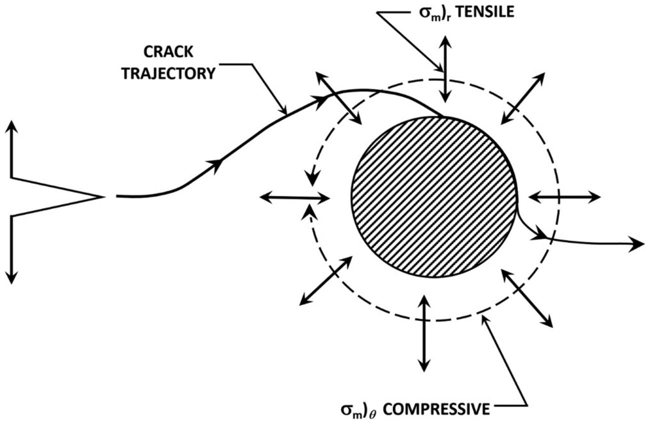

Fig. 1. Schematic of crack deflection mechanism. A crack propagating in a plane of particle (α_p (thermal expansion of particle) > α_m (thermal expansion of matrix)) will be first deflected (compressive stress hoop axis in the matrix is normal to the crack propagating plane). As the crack traverses further around the particle it can be subsequently attracted to the particle interface (tensile radial stress axis) [6].

Table 1
Starting compositions and preparation conditions of TiC and TiC–SiC composites.

Material	*Phase composition (mol%)*		*Temperature (°C)*	*Heating rate (°C/min)*	*Holding time (min)*	*Environment*
	TiC	*SiC*				
TiC	100	–	1400	100	10	Argon
TiC	100	–	2100	100	10	Argon
TiC-SiC	50	50	2100	100	15	Argon
TiC-SiC	70	30	2100	100	15	Argon

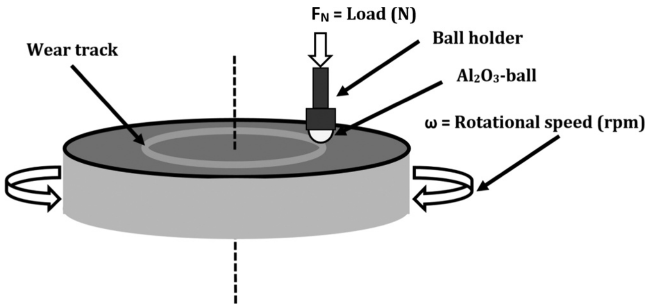

Fig. 2. Schematic illustration of the rotary Pin – on – Disk dry sliding wear test.

of SiC–TiC have been fabricated by spark plasma sintering (SPS) without sintering aid to nearly full densification at temperatures up to 1800 °C and above [7,19], irrespective of the low self-diffusion of SiC in TiC as observed in other sintering techniques [7]. In general, spark plasma sintering has emerged as outstanding sintering technique to synthesize and consolidate powders close to the theoretical density owing to range of controllability of processing parameter's [20].

As shown in several publications, monolithic TiC and SiC as well as TiC-SiC ceramic-matrix composite are of increasing interest as candidate materials for tribological applications [21–25]. Recent findings, confirmed by Wasche et al. [25] indicates that incorporation of particles of a second phase into monolithic ceramic can significantly improve the mechanical properties of the matrix and as result improve the friction and wear behaviour. It has been shown in previous publications [22–26] that the wear behaviour of monolithic SiC can be essentially improved by adding TiC to the phase composition thus creating a ceramic particulate composite material [24]. The improved tribological behaviour can be attributed to the formation of soft and malleable multi-oxide film formation at the interface during dry sliding conditions [22].

Very limited data are available on the dry sliding tribological behaviour of monolithic TiC and SiC as well as their particle-matrix composites. In this work monolithic TiC as well as TiC-SiC composites have been synthesized by spark plasma sintering and resulting microstructures fully characterized. The goal of this present work however is focused on the dry sliding tribological behaviour of the fully densified targets at room temperature. It is well known that the tribological behaviour of ceramic based composites depend on a range of different parameters. In particular, tribochemical reactions play a vital role during dry sliding conditions as chemical reactions with either the surrounding atmosphere or among the tribocouples will be initiated by frictional heating into the contacting asperities [22]. Hence, a key understanding of these phenomena is crucial to the understanding of the plausible tribological behaviour and performance of the material system.

2. Experimental details

2.1. Materials

Commercially available powders TiC (Alfa Aesar, 99.5%, 2 µm powder) and β-SiC (Alfa Aesar, 99.8%, 1 µm powder) was used for preparing monolithic TiC as well as TiC-SiC composites, respectively. The composition of starting powder mixtures and preparation procedures used are detailed in Table 1. The required quantities of powders in accordance with composition in Table 1 were mixed using a rotary mill driven by a 0.09 kW variable speed motor using a zirconia ball in order to ensure a controlled purity and phase content in a medium of isopropanol for 24 h. After drying these mixtures at 90 °C, the powders were sieved using a 200-mesh sieve in order to eliminate hard, large agglomerates which were not comminuted during milling. Next, 7.5 g of each powder composition were compacted into a 20 mm cylindrical graphite die with graphite foils (0.40 mm-thickness) incorporated internally. The role of the graphite paper inside the mould as well as either sides of the powder surface in contact with punches was to prevent the direct interaction of the powder with the graphite punches and mould at high temperatures and to ease the removal of the SPSed samples from the mould. The measured powder in the mould were first pre-pressed using a load of 641 kg, this was done to ensure that, electrical contact between the graphite punches will be established during SPS synthesis. The pre-compacted powder in the graphite mould was then placed in a spark plasma sintering (SPS) furnace unit (HPD-25, FCT Systeme, Germany) and subsequently sintered in an argon and vacuum environment as shown in Table 1. The sintering temperature was accurately measured with the aid of an optical pyrometer focused on the die surface. In general, sintering parameters: temperature, applied load, shrinkage were monitored throughout the densification cycle in order to have a full-scope of the sintering profile.

2.2. Density and Vickers' hardness

The densities of the SPSed samples were obtained by the Archimedes' water displacement method. The relative densities of the synthesized compacts were evaluated by taking into consideration the theoretical densities of TiC and SiC as 4.93 g/cm^3 and 3.21 g/cm^3, respectively [27]. The hardness of each as-synthesized samples were obtained by Vickers microhardness (DuraScan 50, emco-TEST Co., Austria). An indentation load of 0.5 kgF ($HV_{0.5}$) was employed and dwell times maintained at 10 s. Up to ten measurements were conducted on each sample and the mean value given for the data analysis.

2.3. Friction and wear test

Dry sliding tribological test at RT was conducted on a commercially available pin-on-disk tribometer (UMT-2, CETR, California, USA), as shown in Fig. 2. Frictional and wear test were conducted using a normal

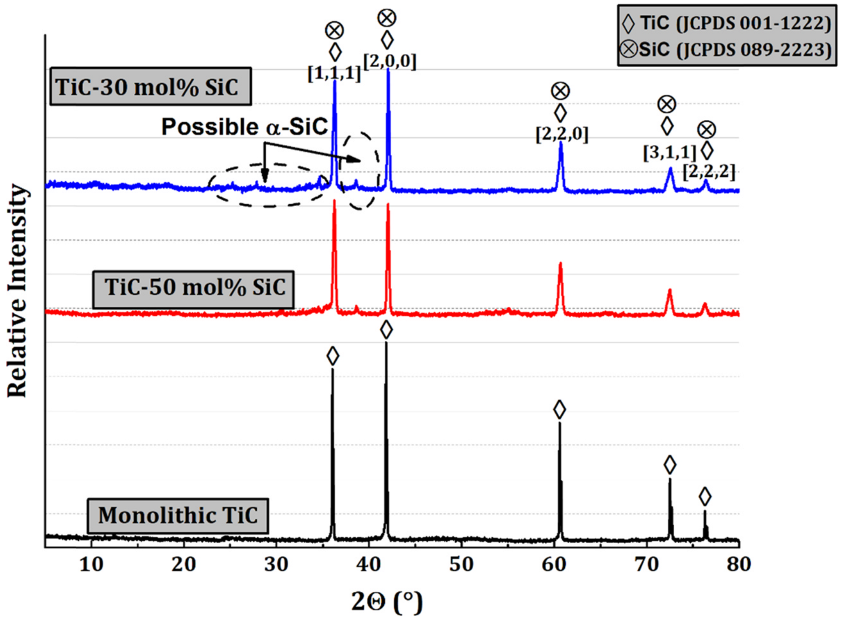

Fig. 3. X-ray diffraction patterns of the synthesized TiC-based ceramics compositions.

load of 2 N, rotational speed of 200 rpm, and a sliding distance of 207 km for a period 60 min. All test were conducted at room temperature (25 ± 3 °C) in laboratory air using spherical Al_2O_3 (99%) ball (GD-25 ALUMINA, Spheric-Trafalgar., Ltd). Normal load and friction force were continuously monitored by a load cell, and the coefficient of friction (μ) was recorded in real time during the test.

Volumetric wear losses were determined by carrying out several profilometric scans across the wear track using a stylus profilometer (Dektak 150 stylus profiler, Veeco Co., USA), and then converting the profiles into worn volume by multiplying the track length by the average cross-section area. The specific wear rate (k), defined as the wear volume per unit normal force per unit sliding distance ($mm^3(Nm)^{-1}$) i.e., a measure of the wear damage was calculated from Eq. (1),

$$k = W_v/F_N \times d \tag{1}$$

where W_V is the worn volume, and F_N and d represents the normal load and the sliding distance, respectively.

The friction and wear test were performed at least twice for each material combination in order to ascertain repeatability and replicability, and average value used for analysis. Post-mortem wear track characterization was then carried out in order to elucidate the tribological process.

3. Analysis

Prior to characterization, the as-synthesized samples were ground and polished using a classical metallographic route (grinding with SiC disc and polishing up to 1 μm without etching). The crystalline phases present were analysed using X-ray diffractometer (XRD) operating with Cu Kα radiation (D2 Phaser, Bruker Co., Germany). The phase present were identified using the EVA software which contained JCPDS ICDD files database. The morphologies and compositions of the as-synthesized samples, and indentation cracks were examined and analysed by SEM (Inspect–F50, FEI Co., Netherlands), as well as optical microscopy. The morphology of the worn surfaces were also analysed with SEM and quantitatively with Raman spectroscopy (inVia Renishaw Co., UK) in order to further understand the friction and wear mechanism.

4. Results

4.1. Phase composition

Fig. 3 shows the XRD diffraction patterns of the sintered compacts for monolithic TiC and TiC-SiC composites synthesized at 2100 °C, respectively. TiC and SiC were the only crystalline phases present and no evidence of the reaction between TiC and SiC or any new phase was detected. Nevertheless, the peaks of TiC and SiC were somewhat indistinguishable as a result of both having the cubic structure with comparable lattice parameter. Some unidentified peaks in the composite are suspected to be α-SiC due to possible (β → α)-SiC transformation during sintering as indexed elsewhere [18].

4.2. Densification behaviour

Typical punch displacement curves of monolithic TiC (SPSed at 1400 and 2100 °C) and TiC-50 mol% SiC composite, which correlates temperature-ram displacement-time relationship of the powder during the SPS is shown in Fig. 4. As seen, the punch displacement has been divided into four distinct stages. These stages are classified based on the punch displacement curves with respect to temperature profiles obtained for monolithic TiC sintered at 1400 °C and 2100 °C as well as TiC-50 mol% SiC composite. During the stage (I), initial powder densification takes place due to particle rearrangement initiated by the sintering stress, as a result, the punch displacement of all the powders were observed in the positive direction. Whilst stage (II) marks the onset of the thermal expansion of the powder and here a negative direction punch displacement is observed. However, in stage (III) the punch displacement of all the powders increases linearly in the positive direction (that is, downward movement of punches). At this stage, intermediate powder densification is initiated owing to necking and plastic deformation of the powder particles. Lastly, in stage (IV), no significant punch displacement took place as this densification stage is where all pores are eliminated to obtain complete densification. During the stage (II), TiC-50 mol% SiC exhibited early initiation of intermediate densification. The SiC particles are suspected to have played a crucial role in initiating the early densification by inducing necking between the TiC grains followed by a short duration of particle rearrangement. The overall punch displacement which is recorded as the relative piston movement for TiC (1400 °C), TiC (2100 °C) and TiC-

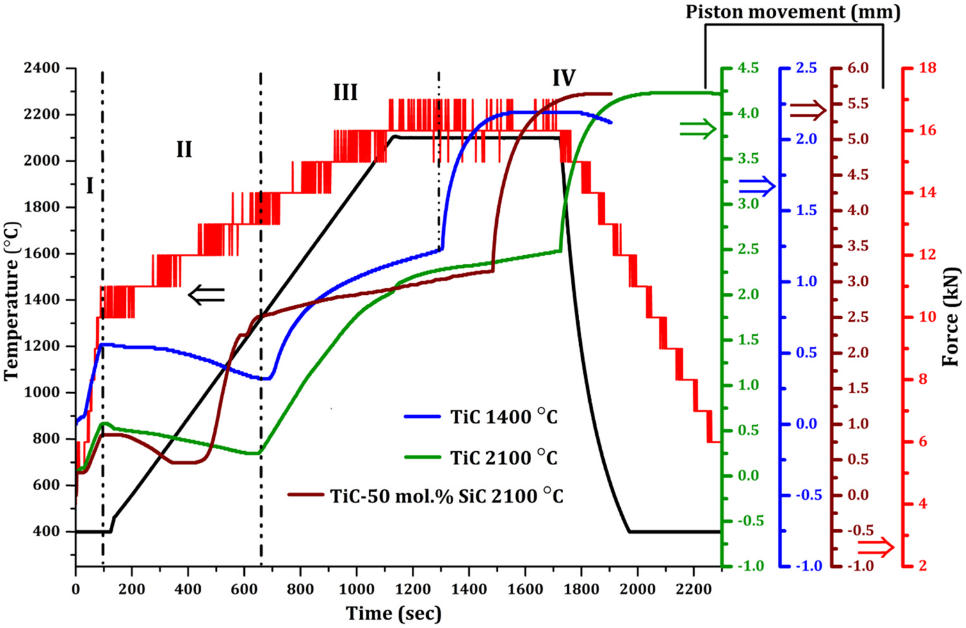

Fig. 4. Temperature – time – pressure – displacement profile recorded during SPS.

50 mol% SiC powder were 2.25 mm, 4.25 mm, and 5.75 mm, respectively. This indicates clearly that the addition of SiC resulted in greater compaction of the composite.

In the following and owing to high densification behaviour, friction and wear test will be carried out only on materials sintered at 2100 °C.

4.3. Microstructure

Fig. 5 shows the optical micrographs of unetched monolithic TiC as well as the TiC-SiC composites. The bright phase is TiC while the grey phase is SiC. A typical feature of the microstructure is the homogeneous distribution of both the TiC and SiC in the composite systems. Also, the optical micrograph revealed the grain sizes of both TiC and SiC in the TiC-50 mol% SiC were quite smaller and in overall grains were finer in comparison to TiC-30 mol% SiC that appeared bigger and overall the grains exhibits a coarse microstructure.

The morphology of the unetched samples, Fig. 6, confirms that the grains of the monolithic TiC were larger than that of TiC in the

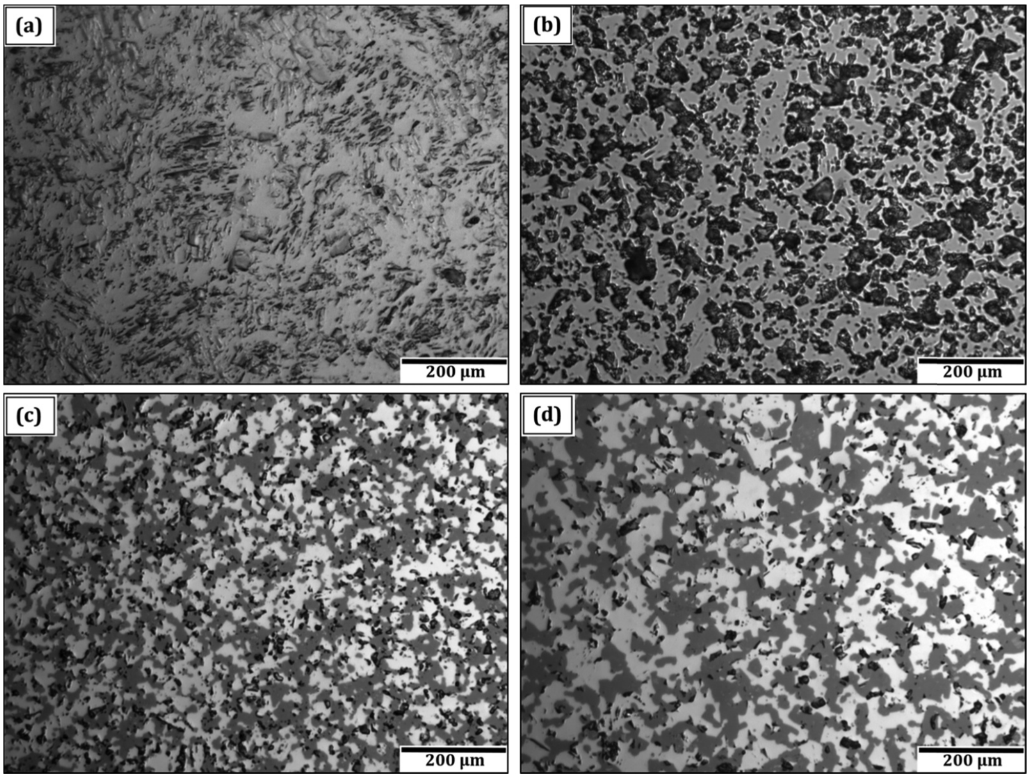

Fig. 5. Optical micrographs of polished unetched SPSed samples: (a) monolithic TiC at 2100 °C, (b) monolithic TiC at 1400 °C, (C) TiC-50 mol% SiC at 2100 °C, and (d) TiC-30 mol% SiC at 2100 °C.

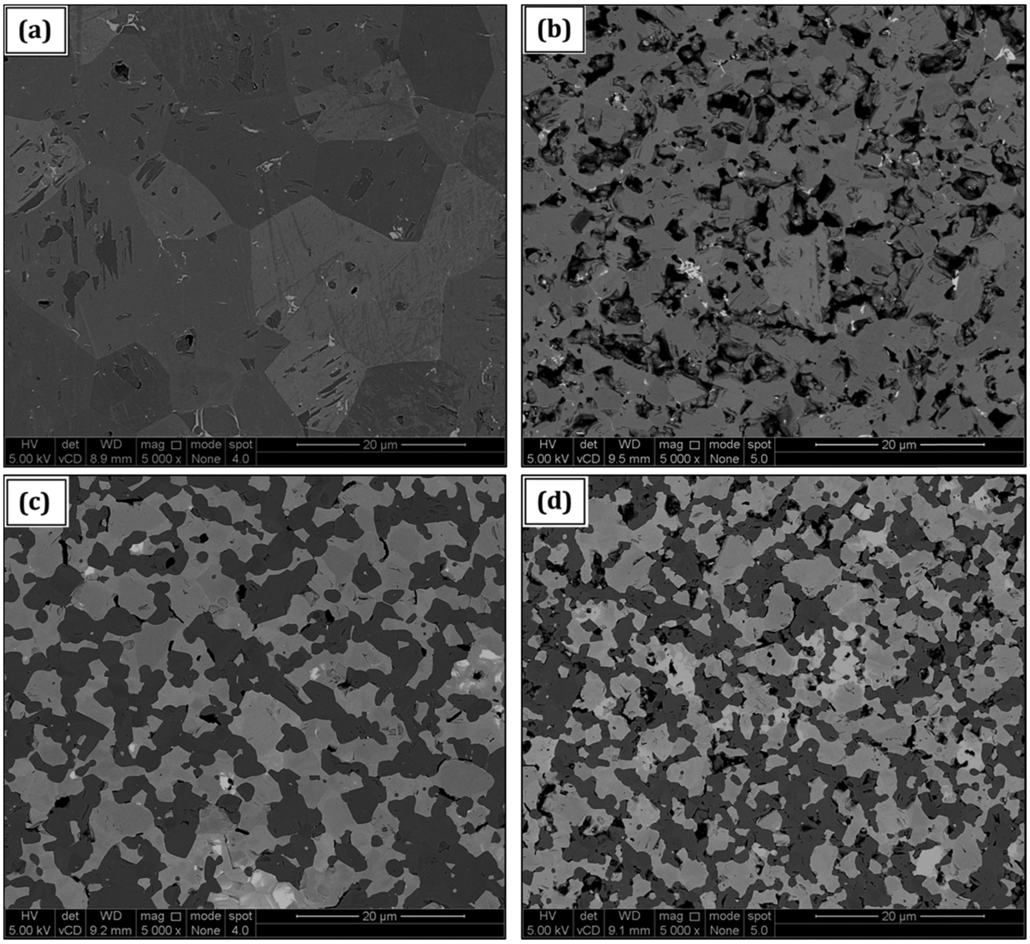

Fig. 6. Representative SEM microstructures of the SPSed TiC-based materials: (a) monolithic TiC 2100 °C, (b) monolithic TiC 1400 °C, (c) TiC-50 mol% SiC, and (d) TiC-30 mol% SiC.

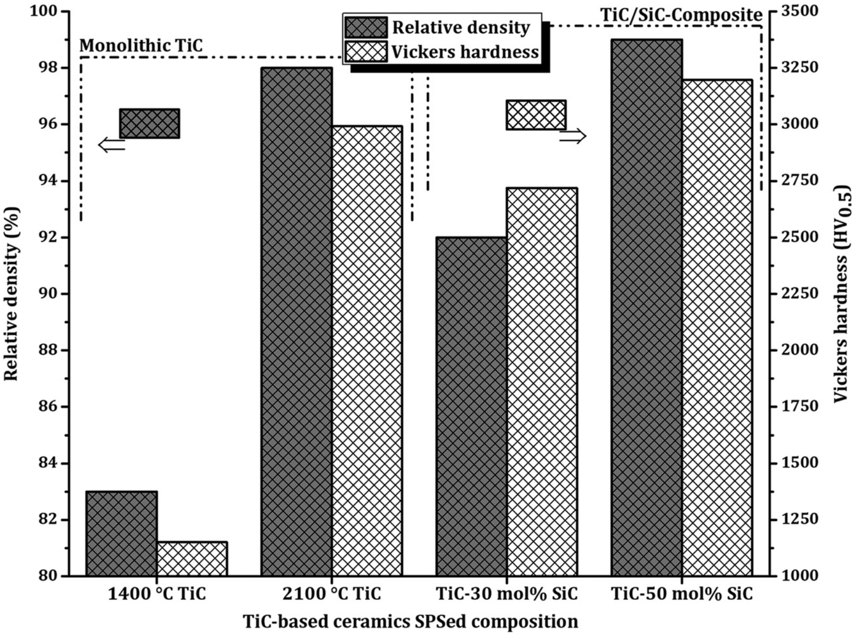

Fig. 7. Dependence of relative density and microhardness as a function of sintering temperature and composition.

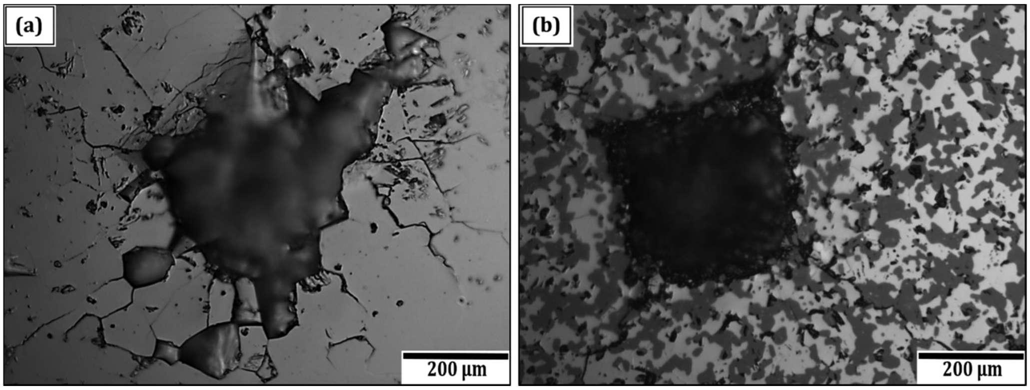

Fig. 8. Optical micrographs showing post-mortem analysis of Vickers indentation fracture behaviour of: (a) TiC-50 mol% SiC, and (b) monolithic TiC at 2100 °C.

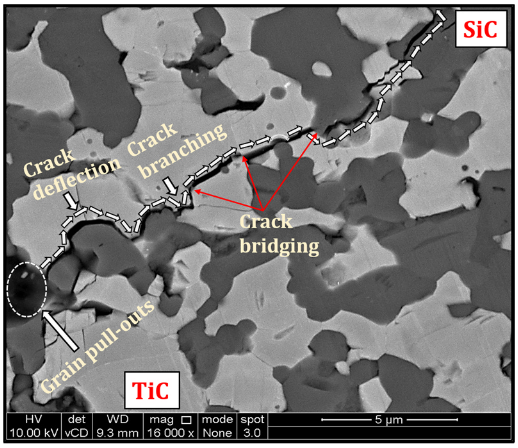

Fig. 9. SEM micrograph of contact damage and subsequent crack propagation initiated by Vickers indentation depiction crack deflection. Typical toughening mechanisms such as: grain pull-out, crack deflection, crack bridging, and crack branching are evident.

composites. This indicates that SiC particles inhibits the grain growth of TiC. Indeed, this observation is consistent with that reported by Wei et al. [6] who showed that SiC inhibited the growth of TiC by pinning and as a consequence restricts grain boundary movement.

The TiC grains grew with increasing sintering temperature. Indeed, this is particularly evident on comparing the microstructures of the monolithic TiC sintered at 1400 °C as well as 2100 °C. It appears that the TiC grains undergoes morphological change due to plastic deformation from equiaxed to matrix like, which is consistent with observation reported elsewhere [8]. The SiC grains on the other hand appears to be elongated as expected owing to the β → α phase transformation of SiC taking place as reported elsewhere [28].

4.4. Mechanical properties

Fig. 7 shows the evolution of relative density as a function of the composition. For monolithic TiC sintered at 2100 °C and TiC-50 mol% SiC, densification in excess of 99% was achieved. However, monolithic TiC sintered at 1400 °C was hardly densified with 82% theoretical density achieved. This is consistent with the small total displacement on

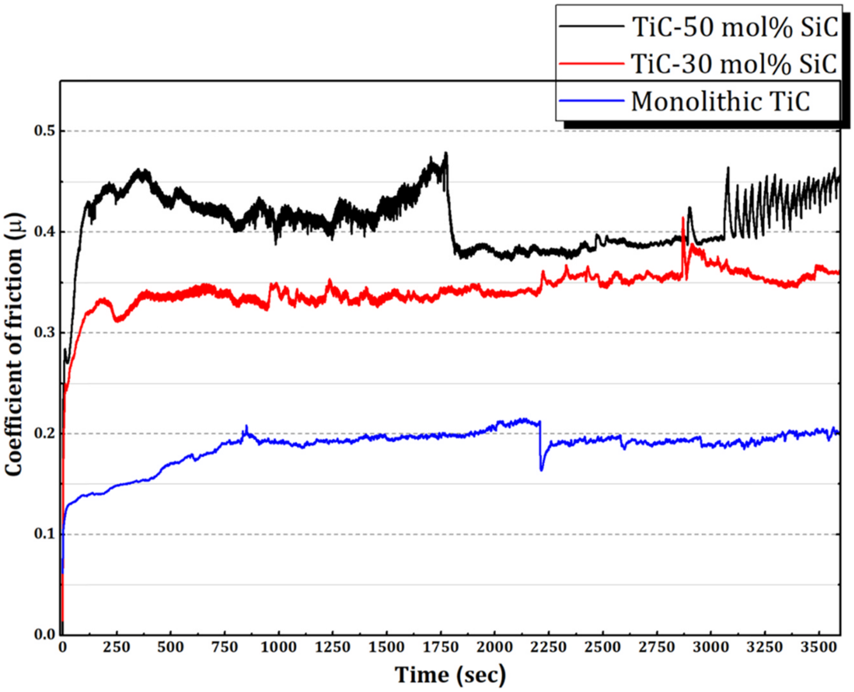

Fig. 10. Evolution of coefficient of friction during dry sliding TiC-based material slided against Al_2O_3 at room temperature.

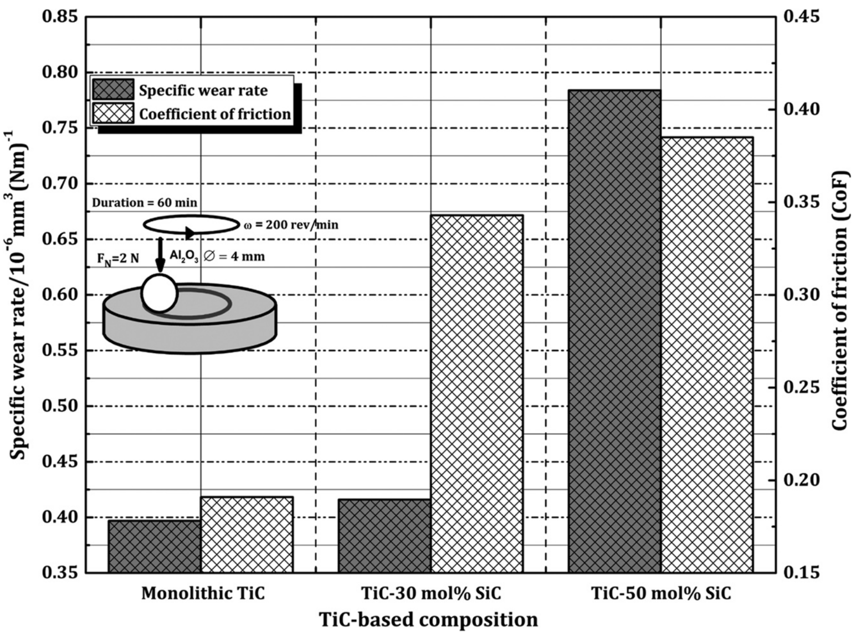

Fig. 11. The specific wear rates and mean COF's for the TiC-based materials – alumina ball tribocouples after dry sliding test.

the SPS ram, which indicates the shrinkage on sintering measurement (Fig. 4). Indeed the densification was incomplete for monolithic TiC sintered up to 1400 °C. In the case of TiC-30 mol% SiC, the relative density achieved was only 92% which is somewhat lower when compared to TiC-50 mol% SiC. The reason for differences in densification is not fully understood. It would be expected that an increase in volume fraction of TiC, which has a significantly higher density (4.92 g/cm^3) than that of SiC (3.21 g/cm^3), should bring about an overall increase in bulk density of the composite. Nevertheless, the density achieved for the TiC-30 mol% SiC is somewhat consistent with result obtained elsewhere [7]. The TiC and SiC grains in the TiC-30 mol% SiC both grew with increasing sintering temperature, which may have occurred due to coalescence that impeded its full densification.

The relationship between the Vickers hardness as a function of composition is shown in Fig. 7. The composite TiC-50 mol% SiC exhibited the highest hardness primarily due to the higher content of SiC. However, monolithic TiC sintered at 1200 °C had a higher hardness than the TiC-30 mol% SiC. The reason might be due to the lower density achieved in TiC-30 mol% SiC which has a direct influence on hardness achieved. It is no surprise that TiC SPSed at 1400 °C possessed the lowest hardness owing to incomplete densification.

Post-mortem assessment of the cracks initiated from Vickers indentations using optical microscope is presented in Fig. 8 for monolithic TiC and the TiC-SiC composite. It can be seen that (Fig. 8a) the cracks in monolithic TiC travelled predominantly along the grain boundaries. In monolithic TiC, the stresses on the TiC particle is mainly compressive whilst that on the grain boundary phase is tensile in nature due to thermal expansion mismatch [29]. As a result, cracks propagated easily via the weaker grain boundaries to bring about intergranular fracture behaviour [30]. On the other hand, cracking was mainly transgranular through the SiC grains (Fig. 8b) in the TiC-SiC composites, although occasionally intergranular fracture was also observed. Again, the main reason, as explained by Lixia et al. [29], is that the residual stresses in the TiC grains in TiC-SiC composite were predominantly compressive similar to monolithic TiC while the stresses in the SiC grains is tensile, promoting transgranular fracture through the SiC.

Furthermore, the residual stresses due to thermal mismatch between TiC and SiC was responsible for the crack deflection as well as crack bridging along the TiC-SiC phase boundary, as observed in Fig. 9. This is consistent with observations by Lixia et al. [29]. Hence, fracture mode transition from intergranular in monolithic TiC to transgranular in TiC-SiC composite as well as crack deflection and bridging events due to the elongated SiC grain is expected to bring about improved fracture toughness.

4.5. Frictional and wear measurement

The influence of material combination on the evolution of the characteristic coefficient of friction (COF) of the investigated TiC-based materials slid against alumina balls is shown in Fig. 10. For all materials, the COF initially increased sharply during the initial transient-state sliding period with steady state attained after about 100 s. However, there were significant differences in the friction behaviour observed. The monolithic TiC had the lowest average friction of ~0.2. As SiC was added, the friction coefficient increased such that for the TiC-50 mol% SiC the friction was double that of the monolithic TiC at ~0.4. In addition, there was a major differences in the stability of the friction. For monolithic TiC, the coefficient of friction appears to be relatively stable and smooth throughout the entire duration of the test. However, the coefficient of friction of the composites appears to be less stable and with some observed fluctuations especially for the TiC-50 mol% SiC. A possible explanation for these fluctuations might be linked to the formation of an unstable tribo-reaction layers that are unstable with time. In general upon comparing the steady-state COF values, the lowest friction was experienced by the monolithic TiC.

The specific wear rates calculated for the TiC-based materials as well as the mean COF's are presented in Fig. 11. Comparing the specific wear rate data, it is evident that monolithic TiC and TiC-30 mol% SiC exhibited somewhat similar wear rates with monolithic TiC slightly lower. The TiC-50 mol% SiC on the other hand suffered a significant higher wear loss when compared to TiC-30 mol% SiC. However, the wear rates appears to show no direct relationship with the mechanical

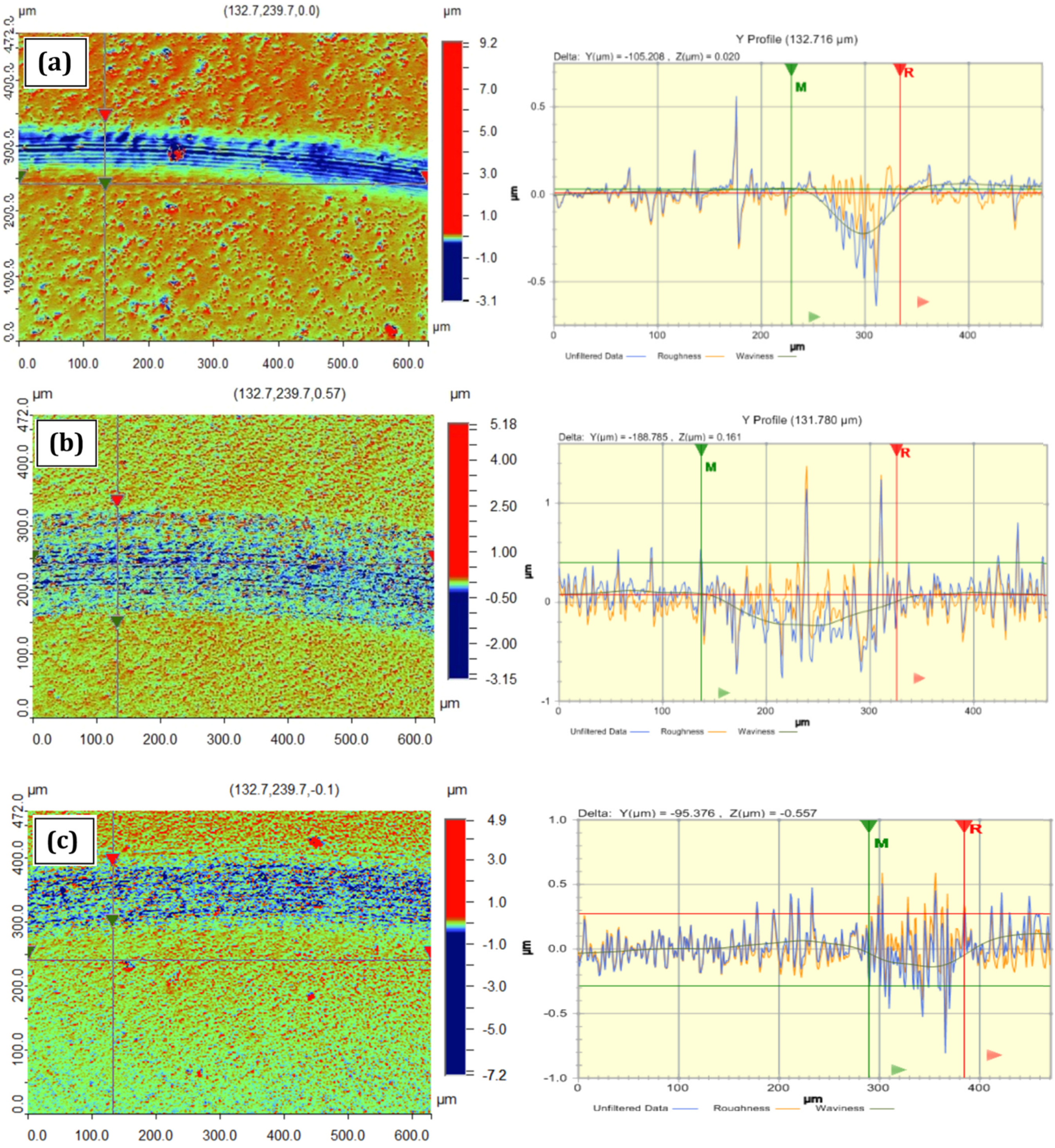

Fig. 12. 2D profiles of wear scars of the disks: (a) monolithic TiC, (b) TiC-30 mol% SiC, and (c) TiC-50 mol% SiC, respectively.

properties of the TiC-based materials (Fig. 7), which indicates that tribomechanical wear might not have played a crucial role in the wear mechanism.

4.6. Analysis of wear track

As shown in Fig. 12, 2D surface profilograms of the wear scars as well as their corresponding worn depth for the different material composition are presented. The micrograph depicts quantitatively the influence of the material composition on the wear behaviour based on the size of the wear scar. As seen from the profilometric micrographs, the worn surface of the monolithic TiC appears relatively smooth and polished whilst the composites shows a higher degree of roughness, possibly linked to wear debris entrapment. This would be consistent with the recorded coefficient of friction. The wear track appears to be wider and deeper on the worn surface of the TiC-SiC composites in comparison to the monolithic TiC.

4.6.1. Structural and chemical characterization of the wear track

Fig. 13(a-b) shows a typical Raman spectra acquired from the worn

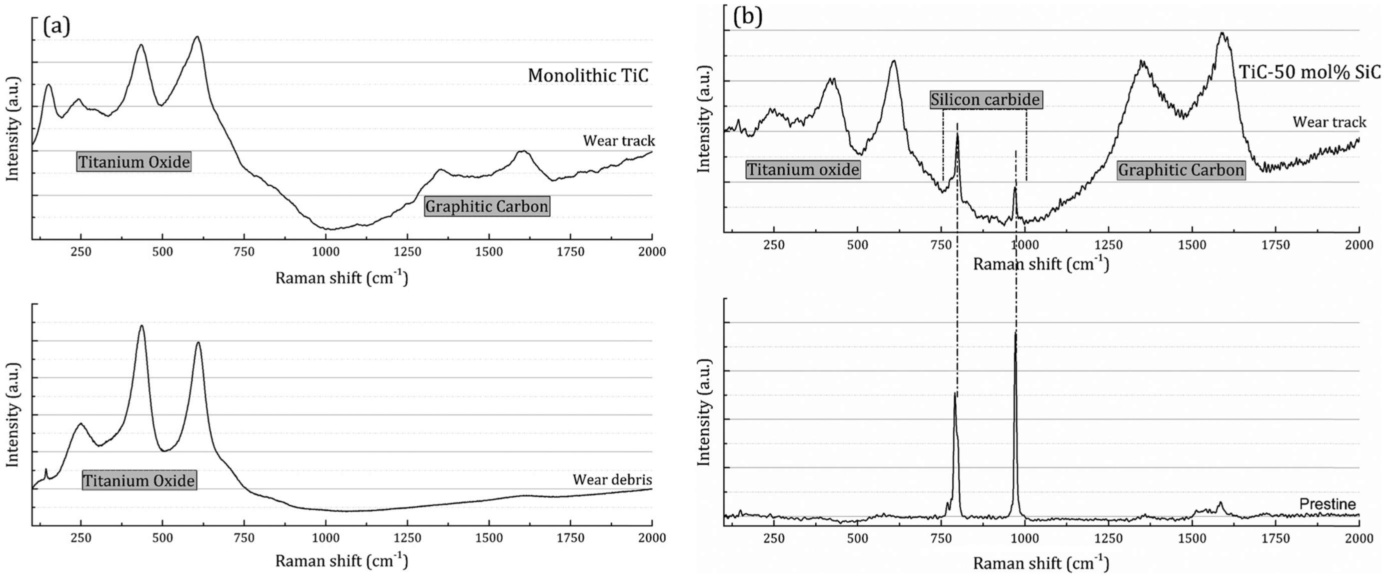

Fig. 13. a. Raman analysis of the wear track and generated debris of the worn surface of monolithic TiC. b. Raman analysis of the pristine surface and wear track of the worn surface of TiC-50 mol% SiC composite.

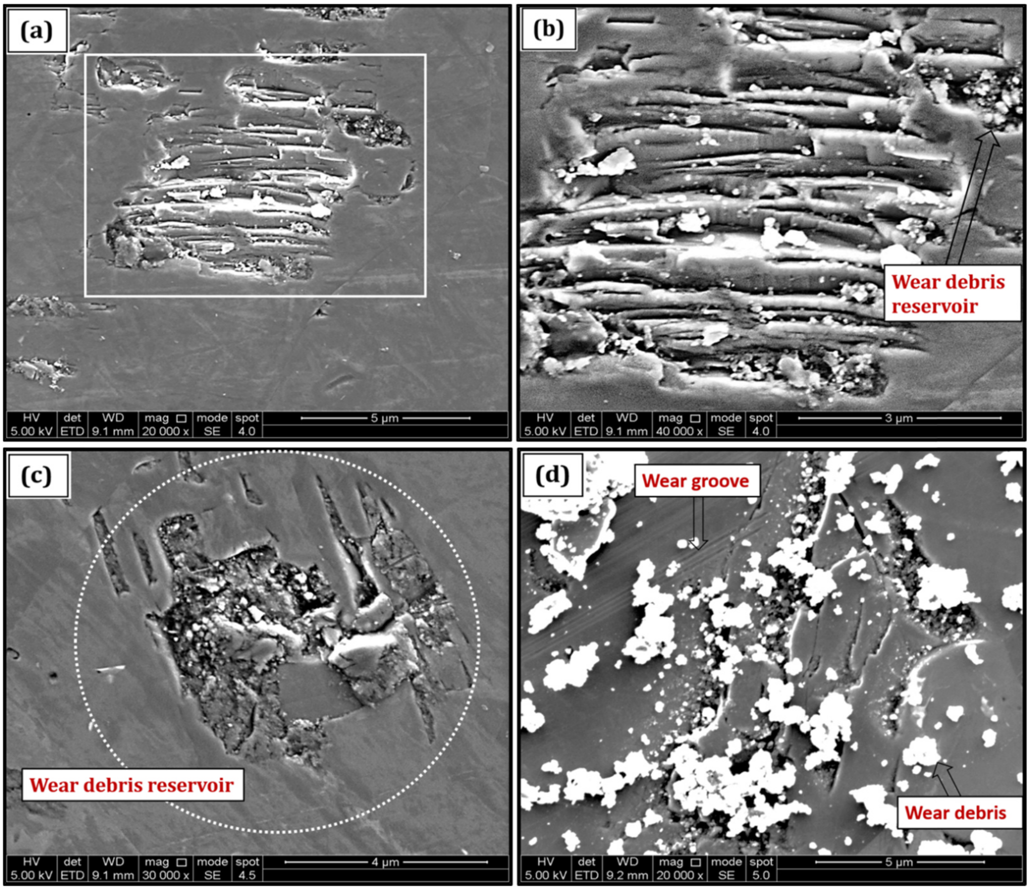

Fig. 14. SEM micrographs (a-d) of the worn surface of monolithic TiC acquired from different sections. Note the enlarged image of the with rectangle in (a) in (c).

surfaces of the TiC-based compacts. The phases were identified by comparison with data reported in the literature data [31]. Since stoichiometric TiC do not possess Raman active modes, no spectra was observed on the pristine monolithic TiC bulk surface. However spectra obtained from the debris detected predominantly rutile whilst the spectra from inside the wear track showed the coexistence of rutile and the evolution of graphitic carbon. The presence of TiO_2 indicates an oxidational wear probably due to possible frictional heating during the dry-sliding condition. Additionally, the evolution of graphitic carbon in wear track will beneficially provide easy-shear and low friction properties at the interface as observed in most carbon-based materials [32].

The Raman spectra on the other hand for the TiC-50 mol% SiC were

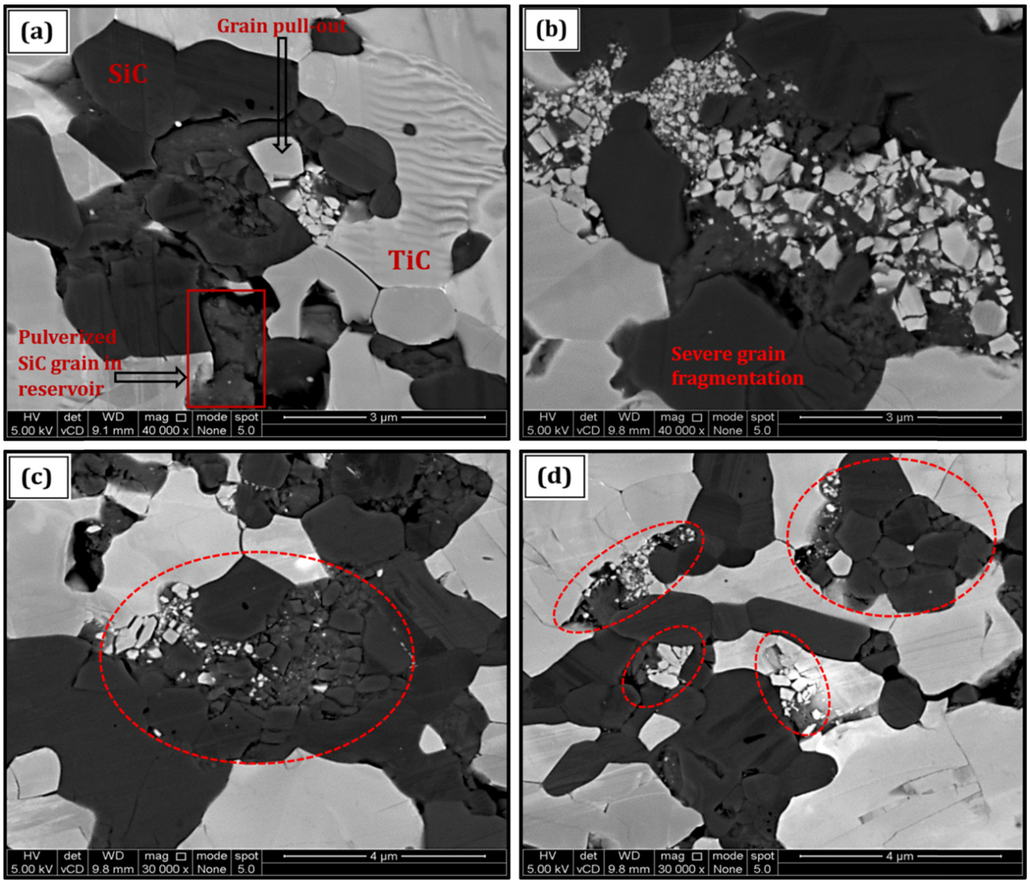

Fig. 15. SEM micrographs (a-d) of the worn surface of TiC-50 mol% SiC acquired from different sections.

acquired from the prestine surface as well as inside the wear track as shown in Fig. 13b. The acquired spectra from the prestine surface revealed the presence of vibrational modes of SiC. However, inside the wear track the spectrum exhibits typical vibrational modes of Ti-oxide, remnant of SiC, and graphtic carbon. The carbonaceous layers formed in the composite appears to be more intense as compared to the monolithic TiC. This is in agreement with the higher carbon content in the composite's composition as compared to the predominantly TiC composition. Since the composites exhibited similar Raman vibrational modes only the Raman data of the TiC-50 mol% SiC was reported.

SEM observations of the wear scars of the TiC-based material is shown in Figs. 14–16. For the monolithic TiC (Fig. 14), a relatively smooth surface with some abrasion grooves coupled with surface grain damage and transferred wear debris in the sliding direction can be observed. The TiC grains appeared to have been slightly fractured transgranularly with some grain pull-out evident. The grain pull-out leaves behind a cavity that serves as a reservoir for the wear debris. Furthermore, no visible tribolayer was observed in the wear scar on monolithic TiC even though severe oxidation was picked up by Raman analysis. A major reason might be that they are incorporated in the wear debris which have become trapped in the reservoir or worn off during the test.

The worn surfaces in TiC-SiC composites are shown in Figs. 15 and 16. The worn surfaces of both composites appears rather smooth with no visible wear grooves as compared to monolithic TiC. However, detailed microstructural investigation of the worn surfaces reveal severe micro-and macrocracking of both the SiC and TiC grains. The fractured grains seems to be trapped in a cavity left behind upon grain pullout and this creates a sort of microfractured grain reservoir which in part acts as abrasive third-body and further increasing the wear. A tribolayer was occasionally observed in the worn surfaces of the composites and forms predominantly on the TiC grains. This is consistent with the Raman analysis which revealed the presence of TiO_2, implying the SiC possesses a higher oxidation resistance than TiC as no traces of SiO_2 were found in the wear track. Furthermore, the tribofilm formed on the TiC-30 mol% SiC composite appears to cover larger area as compared to the TiC-50 mol% SiC, this in part may be attributed to higher TiC content.

Based on the SEM observation of the worn section of these TiC-based ceramics, it appears that the wear mechanism involves microcracking, grain pull-out, and eventual cavity formation which serves as a reservoir for the wear debris.

4.6.2. *EDX-analysis*

Further investigation of the wear scar of the TiC-based ceramics by EDX (Figs. 17 and 18) revealed that apart from the oxide layer generated in the sliding zone, elements of the disks or counterbody also coexists. In the case of the TiC-SiC composites, some Al also coexists. Although Al concentration was quite low, nonetheless, it indicates that some amount of counter material (alumina ball) was transferred to the wear scar during the sliding process. Detailed analysis of the wear scar indicates that the oxidation took place preferentially on the TiC grains as shown by elemental mapping and corresponding spectra which is consistent with Raman analysis revealing predominantly the presence of rutile with no indication of SiO_2. From the EDX analysis it can be deduced that selective tribo-oxidation is an active wear mechanism during the sliding process.

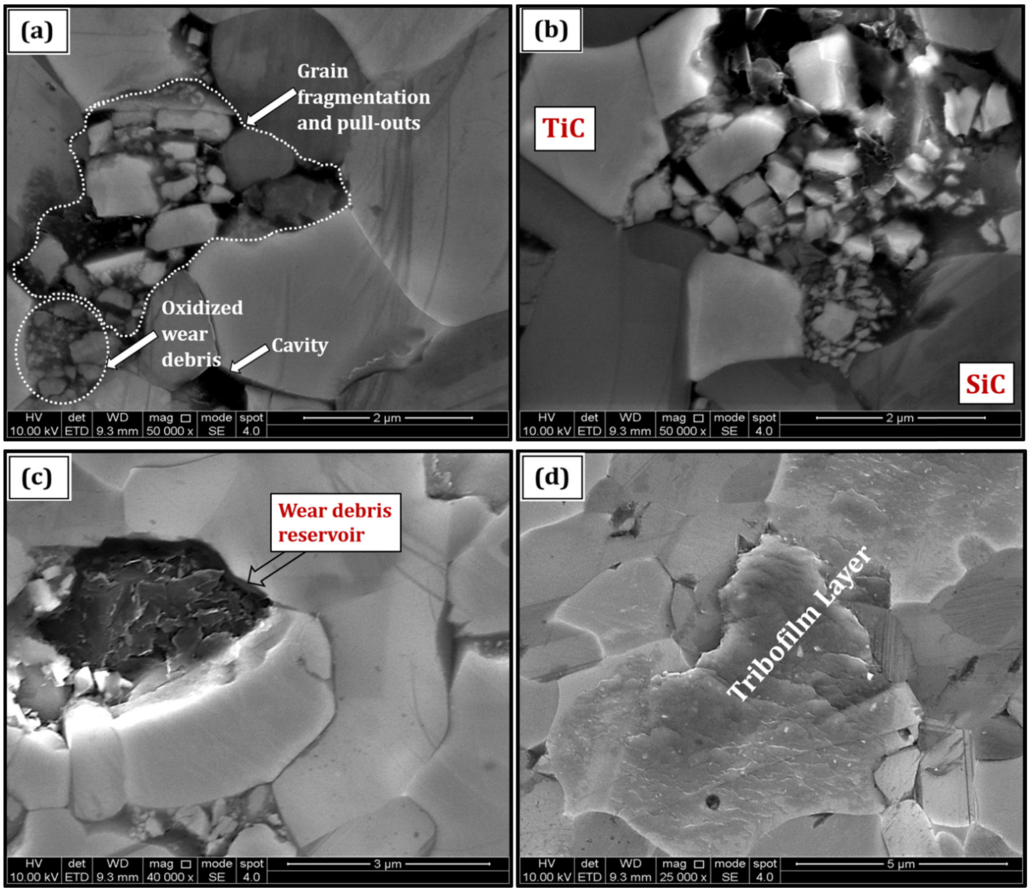

Fig. 16. SEM morphology (a-d) of the wear scar of TiC-30 mol% SiC after dry sliding against alumina ball.

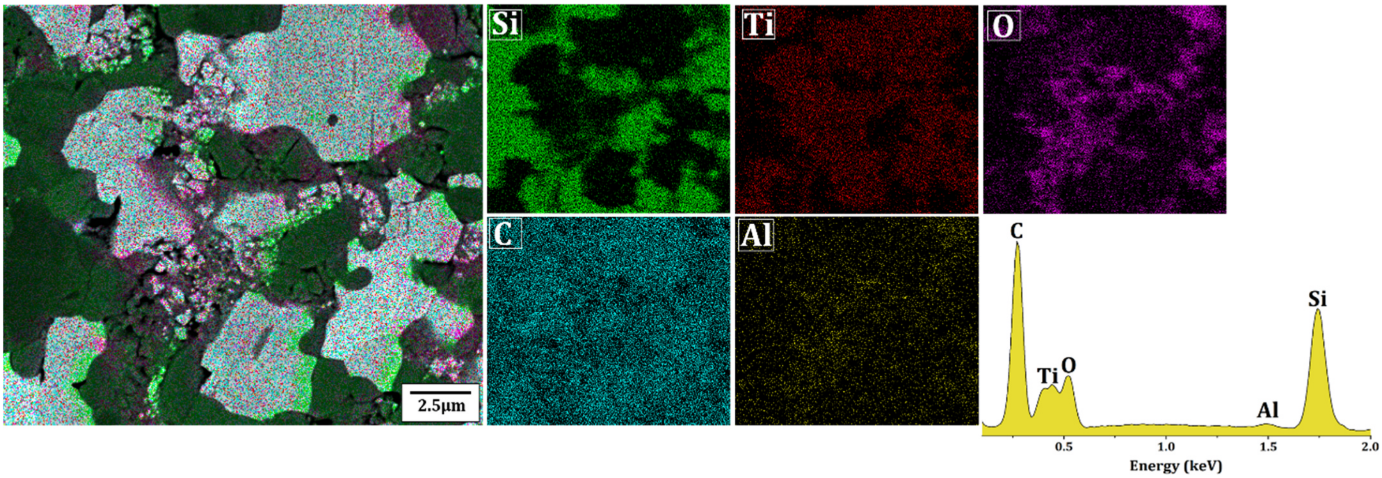

Fig. 17. EDX elemental mapping of the wear scar of TiC-50 mol% SiC and corresponding spectra. Note the oxygen formation preferentially on the TiC grains.

4.7. Wear mechanism

4.7.1. Comparison of wear behaviour of monolithic TiC and TiC-SiC composite

The operative wear mechanism based on the experimental results from these two systems are oxidative and mechanical in nature. It involves the tribologically induced oxidation of TiC possibly due to frictional heating owing to the dry-sliding friction test. The TiO_2 formed through tribo-oxidation then grows and the oxide layers grows as a function of composition i.e., TiC content. This is particularly true when taking into the consideration the COF plot (Fig. 10) where the coefficient of friction of the TiC-based materials increases with decreasing TiC content. However, owing to the brittle nature of the TiO_2 tribolayer, it breaks off periodically and thus leaves behind abrasive particle that acts as third-body. Additionally, as the tribofilm becomes worn off at the sliding zone, the ball makes direct contact with the disc material hence, the dominant wear mechanism is the mechanical failure of the material due to grain surface fracture and pull-out in the case of monolithic TiC whilst extensive micro- or macrocracking and eventual grain pull out leaving behind a cavity that either accommodates the

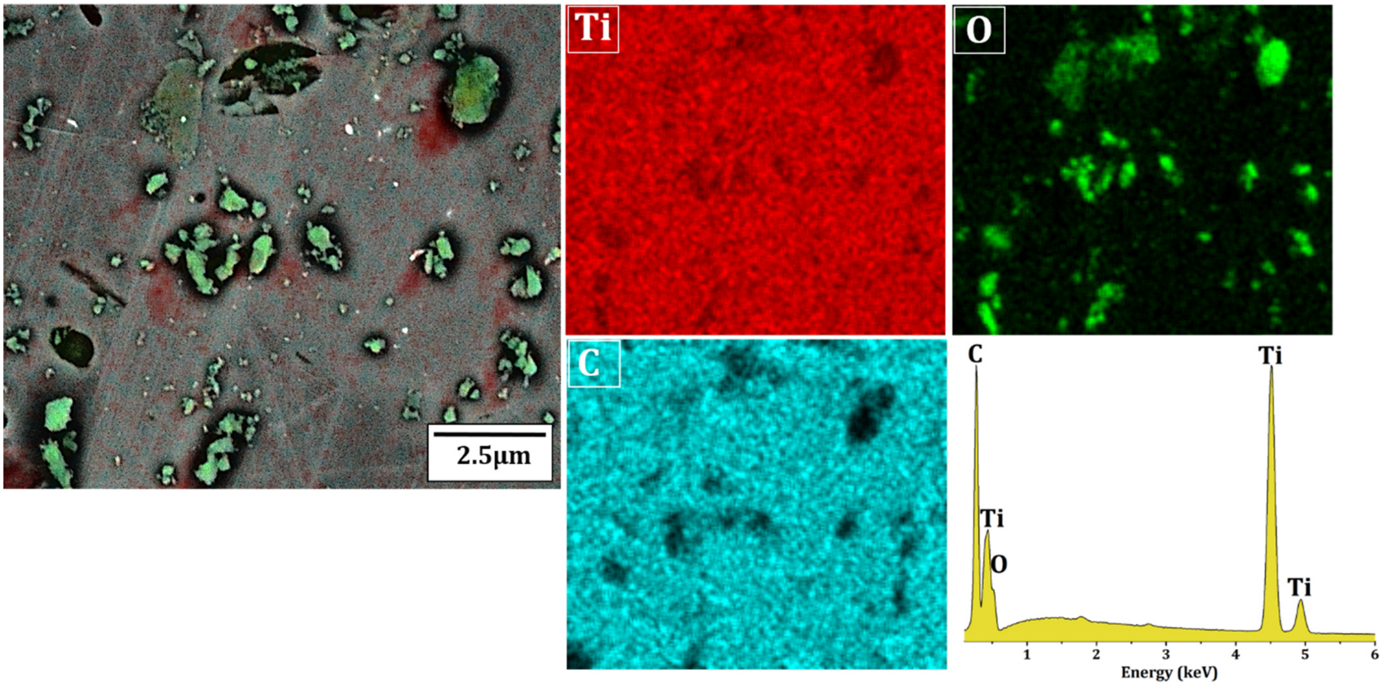

Fig. 18. EDX elemental mapping of the wear scar of monolithic TiC and corresponding spectra.

oxidized wear debris or the micro fractured grains which eventually becomes pulverized in the reservoir is observed in the case of the composites. As observed from the SEM images of the monolithic TiC, the grain undergoes macrofracture preferentially with cracks running intergranularly whilst the TiC-SiC composites on the other hand the composites undergoes microfracture intragranularly with the SiC grains appearing to have been pulverized preferentially in the wear zone. These micro and pulverized grains thus created act as third-body abrasives which explains the fluctuation in COF of the TiC-SiC in comparison to monolithic TiC.

4.8. Comparison of wear behaviour of TiC-30 mol% SiC and TiC-50 mol% SiC

The difference in wear behaviour between the TiC-SiC composites is essentially associated with the amount of SiC in the composition. With an increase in SiC content, tribofilm formation is limited due to depletion of TiC necessary for TiO_2 oxide formation in the sliding interface. As a result, the frictional heating based tribofilm provides inadequate shielding against the counterbody hence direct contact is made earlier between the pin and the disk as compared to TiC-30 mol% SiC composition. The trobofilm appears to form, be worn away and reform. This process is less efficient with the higher SiC content as the oxidation kinetic are slower for SiC than TiC. This manifest itself as an increase on friction coefficient and specific wear rate as shown in Fig. 11. Hence material removal mechanism is essentially mechanical fracture with increased SiC content as compared to tribochemical-to-mechanical fracture based material removal mechanism with increased TiC content as observed in TiC-30 mol% SiC composition.

4.9. Grain buckling and cracking

An intriguing phenomenon observed in TiC-SiC composites during dry sliding against alumina ball is the evolution of TiC grain buckling which has not been previously reported. Fig. 19 shows examples of this grain buckling. As mentioned earlier, mismatch in coefficient of thermal expansion and elastic moduli between TiC and SiC is essential to improve the fracture toughness of the resulting composite owing to beneficial compressive residual stresses [27]. At the same time the coefficient of thermal expansion mismatch between TiC and SiC detrimentally result in significant residual stresses in the composite after processing. The residual stresses in the TiC were tensile and this will have increased the chance of fracture during sliding contact. It is proposed that fracture occurs in the TiC along cleavage planes that is followed by surface plastic deformation that produces buckling effect. Similar evolution of residual stress induced fracture due to mismatch in the coefficient of thermal expansion (CTE's) in glass-sapphire composite have been reported [33].

Severe grain buckling was observed in the TiC grains. Scanning electron micrograph observation of the monolithic TiC compared to the composites showed that the TiC grain growth in the composite was inhibited due to the pinning action of SiC. This implies that high residual stresses will be trapped in the TiC grains and thus effectively supports the evolution of grain buckling during the wear test. In depth analysis of the evolution of grain buckling is beyond the scope of this work and further research will be needed to accurately explain this behaviour.

5. Conclusion

The present study on the in situ synthesis of TiC-based ceramics and subsequent tribological analysis has led to the following salient conclusions;

1. Monolithic TiC as well as TiC-SiC composites can be synthesized via SPS to full densification without sintering aid.
2. From the trend observed in the friction plots as well as SEM analysis, the COF decreases with increases in TiC content; simultaneously, the evolution of Ti-oxide and graphitic carbon at the sliding zone acts as an in situ solid lubricant and thus reduces the overall friction coefficient.
3. The formation of tribofilm reaction layers reduces both the wear rate as well as fluctuation in friction significantly.
4. Microcrack induced fracture alongside with grain pull-outs are

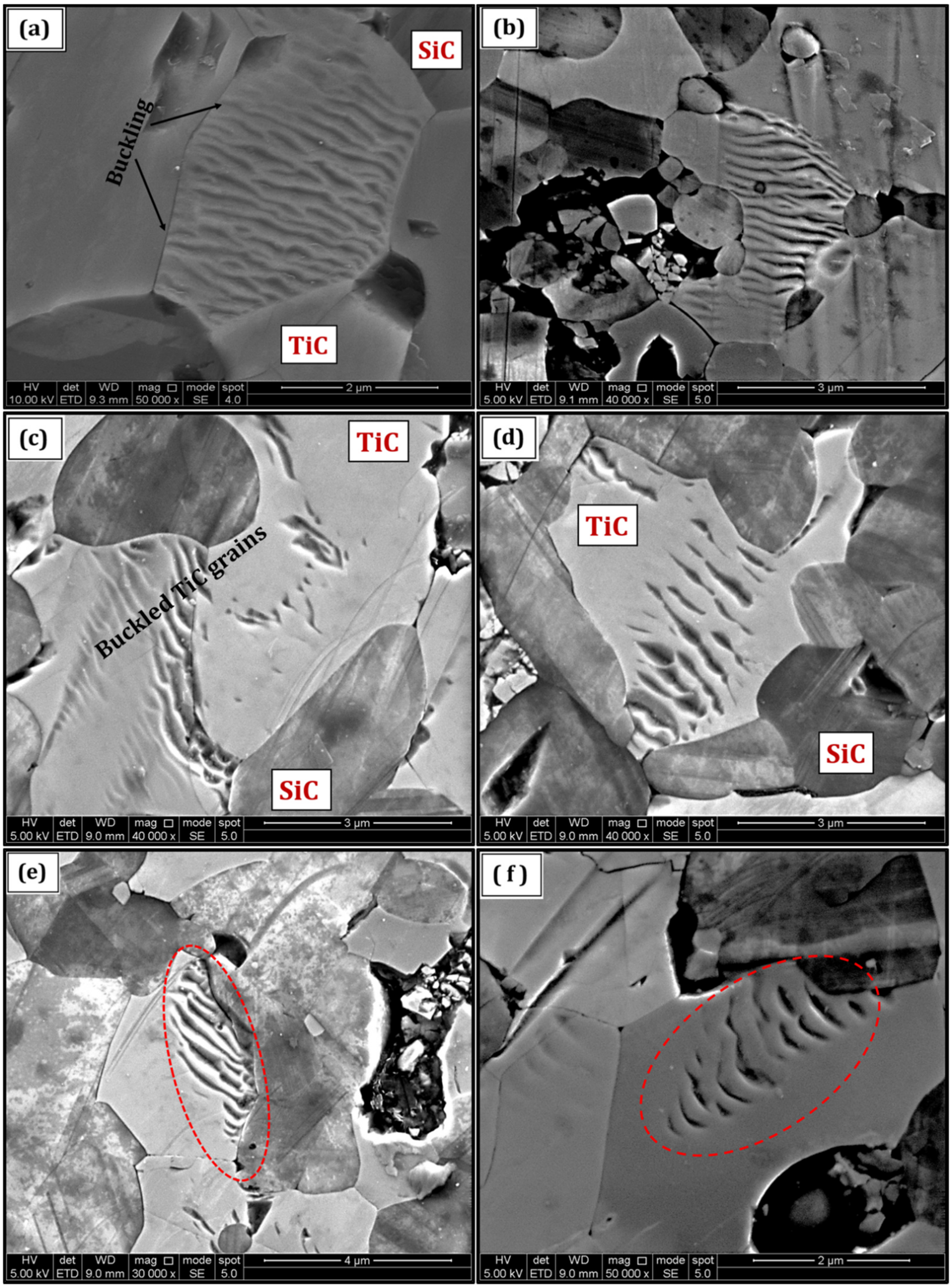

Fig. 19. Collection of SEM micrographs revealing extensive grain buckling as observed predominantly in the TiC-SiC composites wear track.

responsible essentially for material removal.

5. Severe wear arises due to grain buckling-induced cracking of grains due to wearing of beneficial compressive residual stress leaving behind detrimental tensile residual stresses which manifest as grain buckling.
6. Overall the main wear mechanism is identified as mechanical wear (micro-fracture) and frictional heating induced tribo-reaction.
7. Mismatch in coefficient of thermal expansion (CTE) between TiC and SiC induce beneficial compressive stresses into the composite system thus improving the fracture toughness. On the other hand, some residual tensile stresses are also locked up in the composite that brings about the evolution of grain buckling during the wear test.

References

[1] M.J. Gasch, D.T. Ellerby, S.M. Johnson, Ultra high temperature ceramic composites, in: N.P. Bansal (Ed.), Handbook of Ceramic Composites, Springer US, Boston, MA, 2005, pp. 197–224.

[2] L. Wang, W. Jiang, L. Chen, Rapidly sintering nanosized SiC particle reinforced TiC composites by the spark plasma sintering (SPS) technique, J. Mater. Sci. 39 (14) (2004) 4515–4519.

[3] W.G. Fahrenholtz, G.E. Hilmas, Ultra-high temperature ceramics: materials for extreme environments, Scr. Mater. 129 (Suppl. C) (2017) S94–S99.

[4] D.O. Moskovskikh, et al., Spark plasma sintering of SiC powders produced by different combustion synthesis routes, J. Eur. Ceram. Soc. 35 (2) (2015) 477–486.

[5] A. Lara, et al., Densification of additive-free polycrystalline β-SiC by spark-plasma sintering, Ceram. Int. 38 (1) (2012) 45–53.

[6] G.C. Wei, P.F. Becher, Improvements in mechanical properties in SiC by the addition of TiC particles, J. Am. Ceram. Soc. 67 (8) (1984) 571–574.

[7] J. Chen, W. Li, W. Jiang, Characterization of sintered TiC–SiC composites, Ceram. Int. 35 (8) (2009) 3125–3129.

[8] K.-S. Cho, et al., In S/Yu-toughened silicon carbide-titanium carbide composites, J. Am. Ceram. Soc. 79 (6) (1996) 1711–1713.

[9] L. Silvestroni, et al., Super-strong materials for temperatures exceeding 2000°C, Sci. Rep. 7 (2017) 40730.

[10] M.A. Janney, Mechanical properties and oxidation behavior of a hot-pressed SiC-15-vol%-TiB//2 composite, Am. Ceram. Soc. Bull. 66 (2) (1987) 322–324.

[11] A.P. Katz, et al., Mechanical behaviour of polycrystalline TiC, J. Mater. Sci. 18 (7) (1983) 1983–1992.

[12] H. Endo, M. Ueki, H. Kubo, Hot pressing of SiC-TiC composites, J. Mater. Sci. 25 (5) (1990) 2503–2506.

[13] H. Endo, M. Ueki, H. Kubo, Microstructure and mechanical properties of hot-pressed SiC-TiC composites, J. Mater. Sci. 26 (14) (1991) 3769–3774.

[14] K.W. Chae, K. Niihara, D.-Y. Kim, Improvements in the mechanical properties of TiC by the dispersion of fine SiC particles, J. Mater. Sci. Lett. 14 (19) (1995) 1332–1334.

[15] R. Alexandrescu, et al., Synthesis of TiC and SiC/TiC nanocrystalline powders by gas-phase laser-induced reaction, J. Mater. Sci. 32 (21) (1997) 5629–5635.

[16] L. Hultman, Materials science of wear-protective nanostructured thin films, in: A.A. Voevodin, et al. (Ed.), Nanostructured Thin Films and Nanodispersion Strengthened Coatings, Springer Netherlands, Dordrecht, 2004, pp. 9–21.

[17] M. Khodaei, et al., Effects of different sintering methods on the properties of SiC-TiC, SiC-TiB2 composites, Int. J. Refract. Met. Hard Mater. 70 (Suppl. C) (2018) S19–S31.

[18] M. Lodhe, et al., On correlation between β→α transformation and densification mechanisms in SiC during spark plasma sintering, Scr. Mater. 115 (Suppl. C) (2016) 137–140.

[19] E. Ghasali, et al., Preparation of silicon carbide/carbon fiber composites through high-temperature spark plasma sintering, J. Asian Ceram. Soc. 5 (4) (2017) 472–478.

[20] N.C. Ghosh, S.P. Harimkar, 3 - consolidation and synthesis of MAX phases by Spark Plasma Sintering (SPS): a review A2, in: I.M. Low (Ed.), Advances in Science and Technology of Mn + 1axn Phases, Woodhead Publishing, 2012, pp. 47–80.

[21] M. Zhou, et al., A novel approach for preparation of dense TiC–SiC nanocomposites by sol–gel infiltration and spark plasma sintering, J. Eur. Ceram. Soc. 34 (8) (2014) 1949–1954.

[22] R. Wäsche, D. Klaffke, In situ formation of tribologically effective oxide interfaces in SiC-based ceramics during dry oscillating sliding, Tribol. Lett. 5 (2) (1998) 173.

[23] R. Wäsche, D. Klaffke, Ceramic particulate composites in the system SiC–TiC–TiB2 sliding against SiC and Al2O3 under water, Tribol. Int. 32 (4) (1999) 197–206.

[24] R. Wäsche, et al., Tribological Tayloring of ceramic composites, Mater. Werkst. 34 (10–11) (2003) 1008–1013.

[25] R. Wäsche, et al., Oscillating sliding wear behaviour of SiC, TiC, TiB2, 59SiC–41TiB2 and 52SiC–24TiC–24TiB2 materials up to 750 °C in air, Tribotest 12 (2) (2006) 99–111.

[26] R. Wäsche, D. Klaffke, Wear of multiphase SiC based ceramic composites containing free carbon, Wear 249 (3) (2001) 220–228.

[27] D.L. Jiang, et al., Studies on the strengthening of silicon carbide-based multiphase ceramics I: the SiC TiC system, Mater. Sci. Eng.: A 109 (1989) 401–406.

[28] Y.W. Kim, et al., Effect of initial α-phase content on microstructure and mechanical properties of sintered silicon carbide, J. Am. Ceram. Soc. 81 (12) (1998) 3136–3140.

[29] L. Cheng, Z. Xie, G. Liu, Spark plasma sintering of TiC-based composites toughened by submicron SiC particles, Ceram. Int. 39 (5) (2013) 5077–5082.

[30] L. Wang, et al., Effect of starting SiC particle size on in situ fabrication of Ti5Si3/TiC composites, Mater. Sci. Eng.: A 425 (1) (2006) 219–224.

[31] R.V. Konakova, et al., Transformation of a SiC/por-SiC/TiO2 structure during rapid thermal annealing, Semiconductors 46 (9) (2012) 1221–1224.

[32] Tribology of Diamond-like carbon films, 2008, pp. 58–58.

[33] D.R. Clarke, Y.H. Chiao, Residual stress induced fracture in glass-sapphire composites: cylindrical geometry, Acta Metall. Mater. 38 (2) (1990) 259–267.

Paper H

Wear induced ripplocation during dry sliding wear of TiC-based composite

Wear 444-445 (2020) 203121

Contents lists available at ScienceDirect

Wear

journal homepage: http://www.elsevier.com/locate/wear

Wear induced ripplocation during dry sliding wear of TiC-based composite

Carl Magnus [a,b,*], Ali Mostaed [a], William M. Rainforth [a]

[a] *Department of Materials Science and Engineering, The University of Sheffield, Mappin Street, Sheffield, S1 3JD, UK*
[b] *Anton Paar TriTec SA, Rue de la Gare 4, 2034, Peseux, Switzerland*

ARTICLE INFO

Keywords:
Spark plasma sintering
High temperature ceramics
Dry sliding friction
Frictional heating
Residual stresses
Thermal expansion
Ripplocations
Exfoliation

ABSTRACT

Monolithic TiC and TiC particulate ceramic composite containing 30 and 50 mol.%SiC were consolidated and synthesized using spark plasma sintering (SPS) without sintering aids. The as-sintered bulk samples microstructural evolution and dry sliding room-temperature tribological properties against Al_2O_3 ball were characterized using X-ray diffraction (XRD), scanning electron microscopy (SEM), transmission electron microscopy (TEM) and Raman analysis. The role of coefficient of thermal expansion (CTE) mismatch between TiC and SiC as well as cubic to hexagonal SiC phase transformation on the evolution of residual stresses in the composite was also investigated. The friction and wear properties of the monolithic TiC were superior to that of the composite with frictional heating-induced tribo-oxidation playing a dominant role in the wear mechanism. The increase in friction and wear of the composite is attributed to wear-induced stress-relaxation of the previously trapped residual stresses in the composite leading to extensive ripplocation of the TiC grains and consequent SiC grain pull-outs. Herein, we report for the first time on the wear-induced mechanical exfoliation of carbon, its subsequent decomposition into graphite and eventual deformation by micromechanism involving nucleation and propagation of ripples.

1. Introduction

The brittleness and flaw sensitivity of TiC and SiC ceramics which have limited their use as structural material in monolithic state has led to the development of TiC–SiC particulate composite system with improved fracture toughness [1,2]. Silicon carbide exists in two forms, the α (hexagonal) and β (cubic), with the hexagonal form exhibiting many polytypes [3]. SiC possesses only three possible slip systems, as a result, dislocation motion is impeded and motion of dislocation occur only on a very limited scale [3], thus fracture toughness is much lower as compared to metals. Addition of TiC particles into a SiC matrix or SiC particles into a TiC matrix has been found to yield promising composite systems with significantly improved strength and toughness [2,4]. The increase in fracture toughness to about three or four times as large as that of monolithic states [5] has been associated predominantly with misfit of coefficient of thermal expansion (CTE) between the matrix and the second phase particle [6]. Misfit in thermal expansion introduces significant radial stresses at the phase boundaries and hoop compressive stresses inside the matrix. These residual stresses promote toughening mechanisms such as crack deflection, crack branching and stress-induced microcracking [6]. According to Wasche and Ajayi et al. [7,8], the incorporation of particles of a second phase into the matrix of monolithic ceramics can improve significantly their tribological behaviour in unlubricated conditions. The resulting composite system will enable the exploitation of the excellent wear property of SiC whilst simultaneously benefitting from toughening mechanism owing to the high thermal expansion coefficient mismatch between TiC and SiC [9].

Currently, a comprehensive understanding of the role of residual stresses due to misfit in coefficient of thermal expansion between the matrix and the particle phase in particulate ceramic composite on wear behaviour is lacking, even though it has been well established theoretically that internal residual stresses can influence the fracture and wear resistance of composites [10]. The objective of this work is to fabricate monolithic TiC and TiC–SiC composite systems using spark plasma sintering (SPS) and investigate their dry sliding tribological properties. In addition, the role of mismatch in thermal expansion coefficient between TiC and SiC upon synthesis on the wear behaviour of the resulting TiC–SiC composite will be explored.

---

[*] Corresponding author. Department of Materials Science and Engineering, The University of Sheffield, Mappin Street, Sheffield, S1 3JD, UK.
E-mail address: mcarl2@sheffield.ac.uk (C. Magnus).

https://doi.org/10.1016/j.wear.2019.203121
Received 26 April 2019; Received in revised form 17 September 2019; Accepted 8 November 2019

2. Experimental procedure

2.1. Ceramic material fabrication and characterization

Commercially available silicon carbide powder (cubic structure (β-SiC), 99.8% purity, 1 µm Alfa Aesar) and titanium carbide powder (99.5% purity, 2 µm Alfa Aesar) were initially mixed according to Table 1 and subsequently ball milled in isopropanol using a 1.0 mm diameter zirconia ball at room temperature for 24 h. The milled powder was then sieved using a 200 mesh sieve and synthesized by the spark plasma sintering (SPS) powder metallurgy method. Details of the sample composition and synthesis are summarized in Table 1.

Phase analysis of the SPSed polished unetched disc surfaces was carried out on a diffractometer (Bruker X/154 D2 Phaser, Germany) with Cu Kα radiation source using a step size of 0.02° and time per step 3 s over a 2Θ range from 5° - 80°. The microstructural evolution of the pristine and worn samples as well as toughening mechanisms were investigated by Vickers indentation (DuraScan 70 G5, emco-TEST), scanning electron microscopy (SEM), (FEI Inspect F50, The Netherlands) in conjuction with energy dispersive X-ray spectroscopy (EDS, Oxford Instrument X-Max/Aztec Nanoanalysis, UK) and transmission electron microscopy (TEM), (FEI Tecnai Spirit/JEOL 3100Z R005 aberration corrected high-resolution TEM). TEM samples were prepared using a focused ion beam, (FIB), (FEI Helios NanoLab G3 UC, FEI company, The Netherlands) by lifting out sections from the pristine and worn surface which were then further thinned down using FIB for TEM analysis. Raman analysis was carried out ex-situ on the pristine and worn surfaces by employing a Si-calibrated inVia Raman spectrometer (Renishaw plc, UK) with an Ar laser (λ = 514.5 nm, laser output power 20 mW) and a 50x objective lens (spot size of 2 µm). Optical microscopy was used to further analyse the alumina balls after each test to investigate any possible material removal, oxidation and/or transfer materials from the bulk sample.

Further details of the SPS synthesis and processing conditions are reported elsewhere [11].

2.2. Tribological behaviour

Unlubricated sliding wear tests were carried out using a ball on disk configuration (ball: Al_2O_3 (2 mm) and disk: monolithic TiC and TiC–SiC composite) in ambient conditions (25 °C and 38% RH) on a commercially available tribometer (pin-on-disc TRB, Anton Paar TriTec SA, Peseux, Switzerland). An Al_2O_3 ball was utilized as the counterface due to its relative inertness, as it would not be expected to react with the bulk sample and has been widely used in wear testing of TiC-based composites, thus the current results can better be compared to those in the literature. Tribological tests were conducted using a normal load of 2 N and rotational speed at 200 rpm which corresponds to a total sliding distance of 445 km for an hour. Schematic of the rotary configuration employed using the pin-on-disk tribometer is shown in Fig. 1. The frictional force and the normal load were continuously monitored by the load cell and the friction coefficient (CoF) was recorded in real time during the test. The specific wear rate was estimated by using Eq. (1) upon measuring the length and width of the wear track to determine the worn volume.

Table 1
Sample details and SPS sintering parameters.

Starting powder		SPS sintering details		
Sample details		SPS environment	Holding time	Temperature
Composition	(mol.%)	(gas)	(min)	(°C)
TiC	100	Argon	15	2100
TiC–SiC	50–50	Argon	15	2100
TiC–SiC	70–30	Argon	15	2100

*Pre-press load; 641 kg, graphite die; 20 mm, heating rate; 100 °C/min, sintering pressure; 50 MPa, and SPS unit (HP D 25 FCT Systeme, Germany).

$$K = V/F_N \times S_d \tag{1}$$

Where K = specific wear rate (mm^3/Nm), V = wear volume (mm^3), F_N = load (N), and S_d = sliding distance (m), respectively.

3. Results and discussion

3.1. Phase analysis, densification, hardness and microstructure

The XRD patterns of the synthesized TiC-based ceramic compositions are presented in Fig. 2. As seen in the diffraction patterns, TiC and SiC phases were the only crystalline phases present indicating no solid solution reaction between the TiC and SiC phases. Also, as TiC and β-SiC are cubic in nature, their phases were somewhat indistinguishable owing to similar lattice parameters. However, some distinct peaks of α-SiC were detected due to possible phase transformation from β → α – (SiC) at sintering temperature above 1800 °C.

SPS produced near-fully dense bulk samples for both the monolithic TiC and TiC–SiC composite compositions. The resulting SPS sintered compacts attained 98% density for monolithic TiC, 99% for TiC-50 mol.%SiC, and only 92% for TiC-30 mol.%SiC, upon taking into account the theoretical densities of TiC (4.92 g/cm^3) and SiC (3.21 g/cm^3), respectively. Vickers hardness measurement revealed that the hardness of the composite TiC-50 mol.%SiC was slightly higher than that of the monolithic TiC. For the measured values, the composite TiC-50 mol.%SiC exhibit the highest hardness ~3180 HV followed by the monolithic TiC ~3000 HV. The composite TiC-30 mol.%SiC exhibited somewhat the lowest hardness ~2750 HV which is quite surprising. According to the volumetric rule of mixtures, the hardness values of the composites are expected to be way higher than recorded [12]. However, due to thermal expansion mismatch between SiC and TiC, the work of indentation may have been reduced due to the distribution of residual stresses in the composite [13].

The microstructure (Figs. 3 and 4) of the TiC–SiC composite consist of two distinct phases of elongated particles of SiC (dark phase) homogeneously distributed in the TiC matrix (bright phase) as identified by EDS analysis (Fig. 5). The presence of only two major phases is in agreement with the lack of solid solutions found in the SiC–TiC pseudo-binary system [14]. It is noteworthy to mention that a possible reason for SiC grain elongation is linked to $\beta-(\text{SiC})\xrightarrow{1800\ ^\circ C}\alpha-(\text{SiC})$ phase transformation taking place during synthesis as explained elsewhere [15]. In comparison to the grain size of the monolithic TiC, the grain size of TiC in the TiC–SiC composite appears smaller. This can be attributed solely to the matrix grain-boundary pinning effect by the SiC particles during the sintering which inhibits the exaggerated TiC grain growth [16].

3.1.1. TEM of pristine surface of composite

Fig. 6 shows the TEM micrographs taken from the pristine surface of the TiC-50 mol.%SiC composite system. The TiC grain is essentially defect-free whilst profuse stacking fault can be seen in the SiC grain (1) (Fig. 6(a)). Higher magnification of the SiC grain (1) further highlights the extent of the planar defect (stacking faults) which has been linked to the low stacking fault of energy in SiC (Fig. 6(b)). Evidence of partial dislocation (arrow in Fig. 6(b)) can also be seen and represents the mechanism by which the growth of α-SiC nucleates (i.e., partial dislocation motion). This indicates that partial β→α phase transformation of SiC may have taken place during the SPS synthesis in consistent with the XRD analysis. To further verify the possible β→α phase transformation due to the SPS densification temperature above 1800 °C, TEM studies were done near the $<110>_\beta$ zone axis to reveal reciprocal lattice rows from which both the β and α patterns can be easily identified (i.e., extra spots are introduced into the β diffraction pattern due to the α polytype) as well as enabling the simultaneous visualization of the $\{111\}_\beta$ and

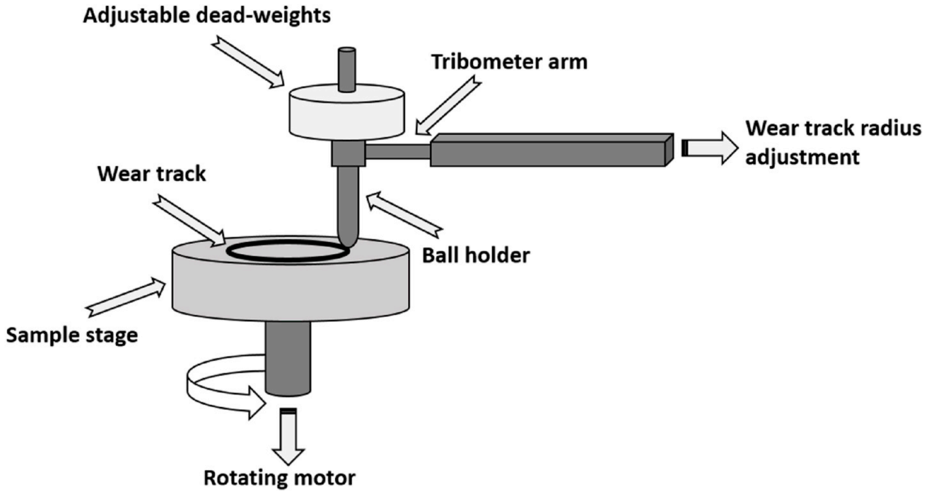

Fig. 1. Schematic of an Anton Paar pin-on-disc tribometer employed for friction and wear test.

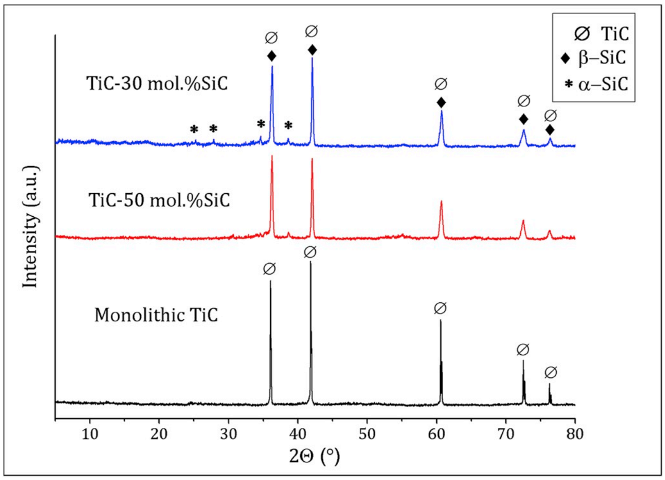

Fig. 2. X-ray diffraction patterns of the synthesized polished disc samples.

$(0001)_\alpha$ planes edge-on. Lattice fringe image obtained from a partially transformed plate-like SiC grain (2) is shown in Fig. 6(c-f).

3.2. Friction results

Fig. 7 shows the characteristic evolution of the coefficient of friction with sliding time. For the TiC/Al_2O_3 tribocouple subjected to sliding wear, the coefficient of friction was relatively stable throughout the entire test duration. This stable behaviour can be somewhat attributed to the formation of a triboreaction layer that tends to be stable as a function of time. On the other hand, the coefficient of friction of the TiC–SiC/Al_2O_3 tribocouples appear to be very unstable with repeated fluctuations observed for the entire test duration. The reason for this might be due to instability of the triboreaction layer formed, or because the tribo-reaction layer formed is repeatedly worn off upon formation. The steady state CoF mean value against Al_2O_3 was (0.19 ± 0.01) for TiC, (0.35 ± 0.02) for TiC-30 mol.%SiC, and (0.39 ± 0.01) for TiC-50 mol.%SiC composite, respectively.

3.3. Wear results

The specific wear rate of TiC and the TiC–SiC composites against Al_2O_3 ball is plotted in Fig. 8. In general, the corresponding wear measurements reveal a correlated behaviour that is consistent with the friction curve. The specific wear rate is lower for the TiC/Al_2O_3 tribocouple than for the TiC–SiC/Al_2O_3 composites, indicating a major role of tribo-oxidation product in the wear mechanism. The TiC–SiC composite exhibited approximately 3 times more wear against Al_2O_3 as compared to monolithic TiC. It is expected that TiC matrix reinforced with SiC particles would intrinsically exhibit higher fracture toughness, and thus mitigate mechanical fracture and/or grain pull-out during sliding contact [17]. However, the higher specific wear rate of the TiC–SiC composites as compared to monolithic TiC implies that enhanced fracture toughness due to toughening mechanisms was inactive or possibly inefficient during the shear sliding contact. Almost comparable data on

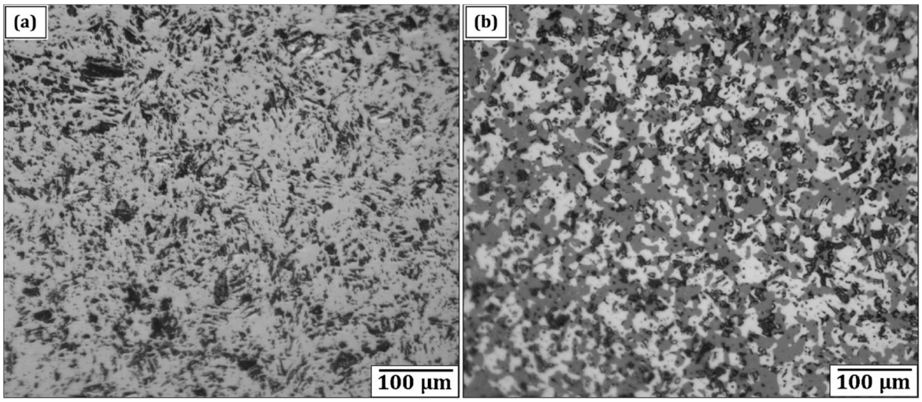

Fig. 3. Optical micrographs of the polished discs: (a) monolithic TiC and (b) TiC-50 mol.% SiC.

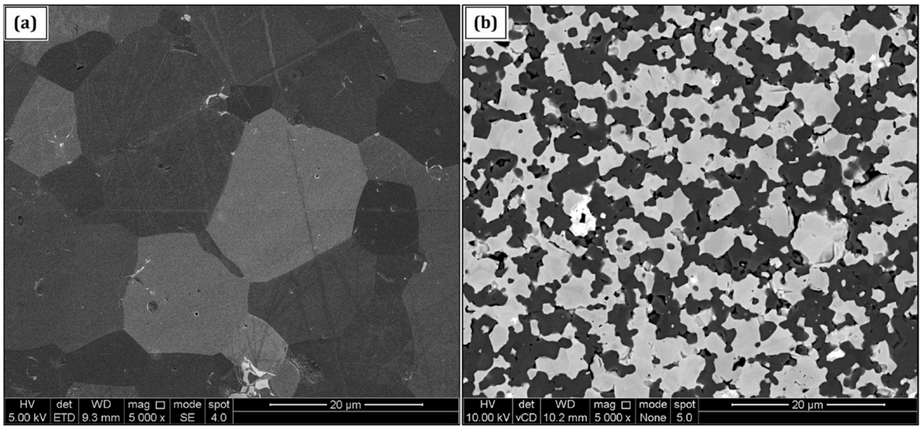

Fig. 4. SEM micrographs of the SPSed polished unetched surface of the discs: (a) monolithic TiC and (b) TiC-50 mol.% SiC composite. Note: white contrasts are artefacts from colloidal silica employed during sample polishing.

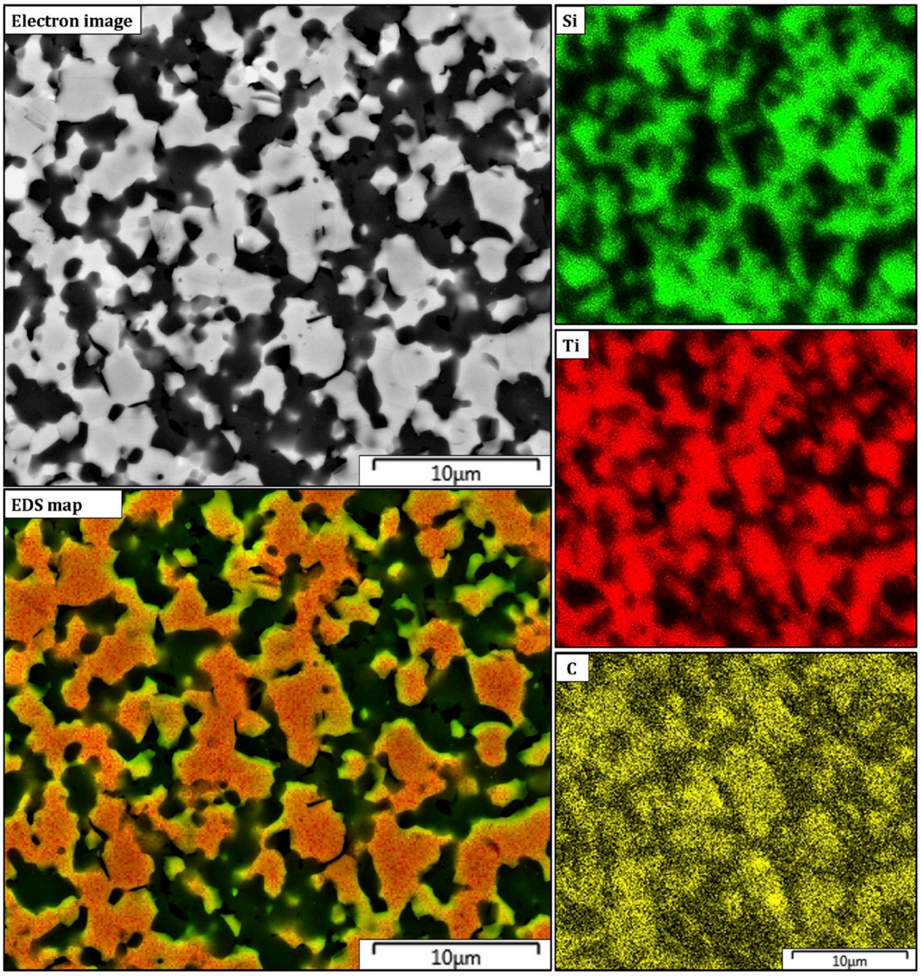

Fig. 5. EDS map analysis of the polished surface of the TiC-50 mol.%SiC showing the elemental distribution.

the friction and wear on a range of SiC–TiC composite system sliding against Al_2O_3 is presented elsewhere [18] albeit slight differences in testing parameters.

In the following and due to the scope of this work, microstructural analyses will be focused essentially on the TiC-50 mol.%SiC.

3.4. Raman analysis

Since no Raman active vibration modes are present in stoichiometric TiC [9,19], Raman spectra were collected from the β-SiC starting powder and the bulk SPSed TiC–SiC composite as shown in Fig. 9. The spectrum of the bulk TiC–SiC composite revealed characteristic peaks of the vibration mode of α-SiC indicating a phase transformation from cubic (β) → hexagonal (α) during SPS, especially with the presence of α-SiC

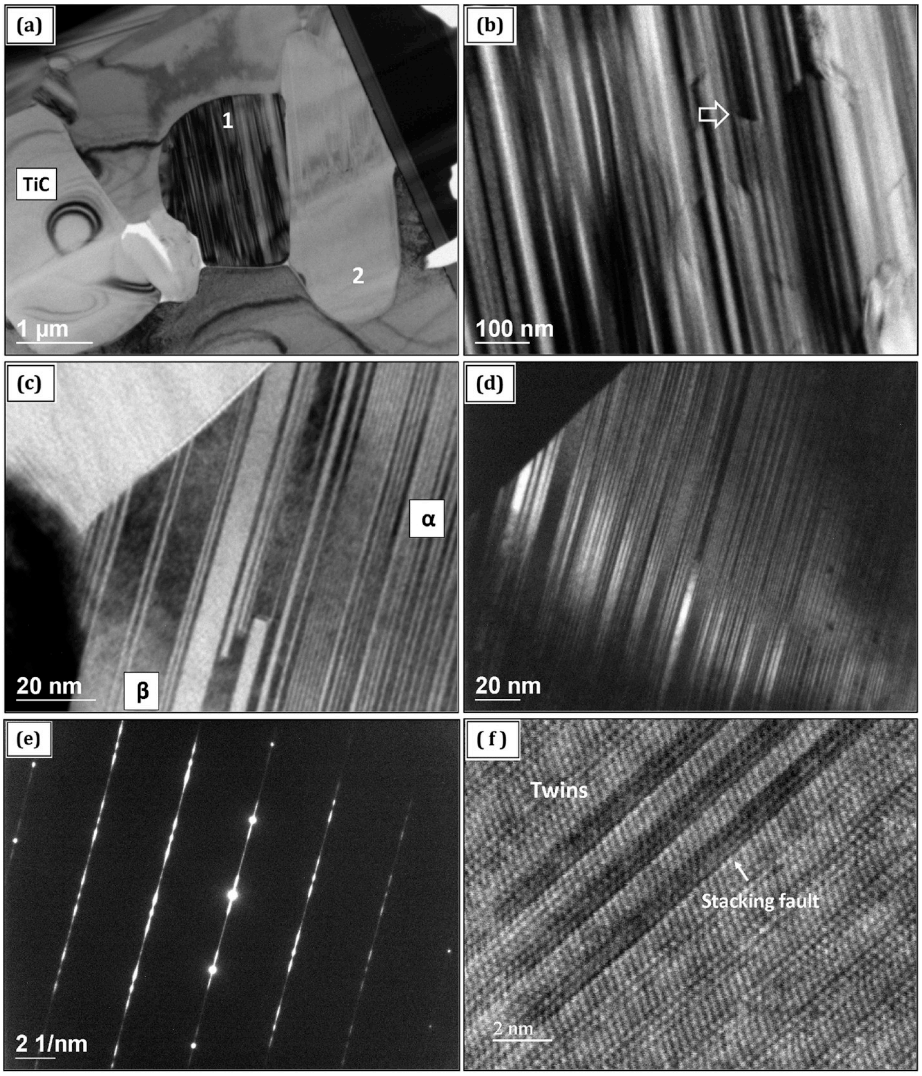

Fig. 6. (a) TEM bright-field (BF) image taken from the pristine surface of TiC-50 mol.% SiC composite, (b) higher magnification bright-field (BF) image taken from grain (1), (c-d) bright-field (BF) and dark-field (DF) lattice fringe image of β/α interface region in SiC grain (2) which has been partially transformed with an array of β twins evident at the centre, (e) SAED patterns showing extra spot due to twins and (f) HRTEM image in the <110> zone axis evidencing twins and stacking faults.

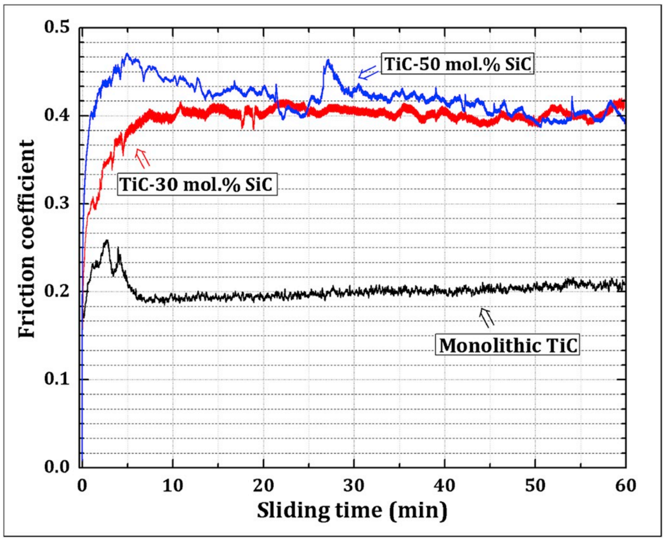

Fig. 7. Evolution of the friction coefficient with sliding time for rotational dry sliding contacts TiC/Al_2O_3 and TiC–SiC/Al_2O_3 composites at room temperature.

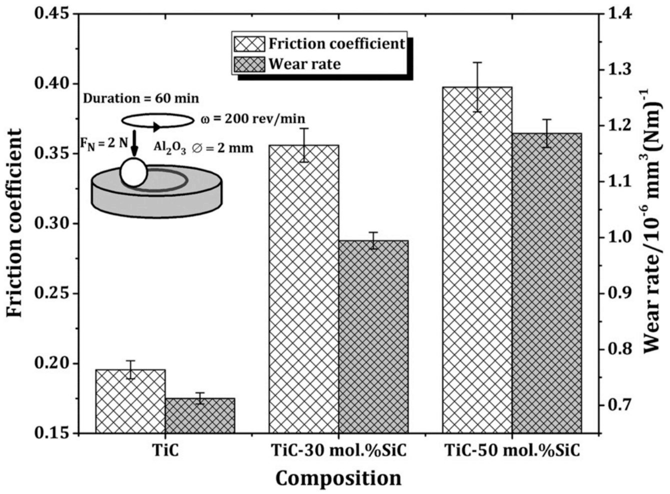

Fig. 8. Plot of the specific wear rate and friction coefficient as a function of composition.

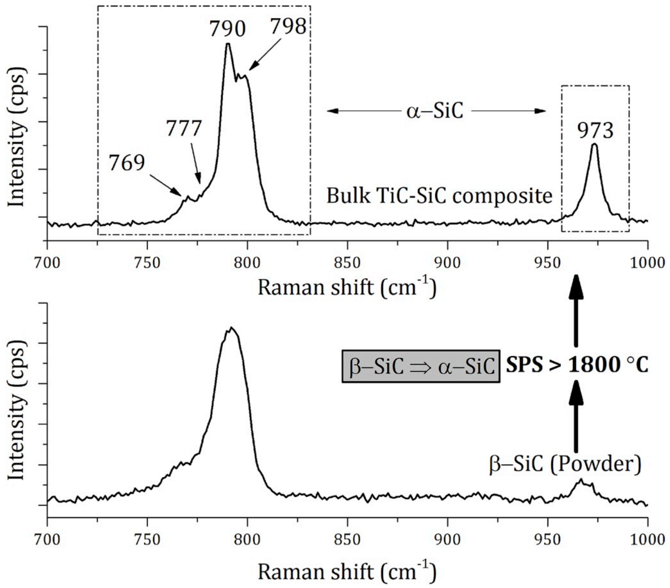

Fig. 9. Raman spectra collected from the β-SiC starting powder and the resulting SPSed bulk TiC-50 mol.%SiC composite pristine surface.

distinctive peak at 973 cm^{-1} consistent with results obtained elsewhere [9,20]. The implication of such transformation is evident as observed from microstructural evolution of the as-synthesized TiC–SiC composite in which equiaxed β-SiC grains transforms to plate-like α-SiC grains.

Raman analysis of the wear track of the TiC/Al_2O_3 and TiC–SiC/Al_2O_3 tribocouples are presented in Figs. 10 and 11. In both cases, the recorded Raman spectrum corresponded to vibrational modes of titanium oxide (typically rutile) and graphitic carbon upon comparing to literature data [21–23]. The formation of rutile implies that anatase TiO_2, whose formation temperature is around ~500 °C, transformed into rutile as the temperature of the sliding surface increased due to frictional heating in accordance with the phase transformation [24];

$$\text{Anatase}\quad (TiO_2)\xrightarrow{\sim 900\ ^\circ C}\text{Rutile}\quad (TiO_2)$$

The Raman spectrum collected from the composite worn surface showed lower intensity of TiO_2 peaks above the background in comparison to monolithic TiC. This could be attributed to the fact that the incorporation of SiC particles into the TiC matrix has reduced the amount of TiO_2 that can be formed due to frictional heating during dry sliding. On the other hand, the evolved graphitic layer in the wear track of the composite appear to be much more intense compared to the background than the graphitic carbon peaks in the Raman spectrum of TiC/Al_2O_3 wear track. The reason for this is not fully understood but it is conceivable that SiC is responsible for the increased graphitization of the TiC–SiC/Al_2O_3 tribocouple sliding interface.

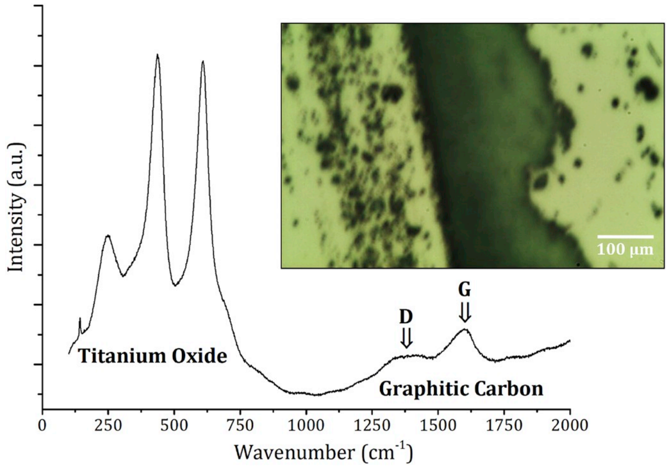

Fig. 10. Raman spectrum collected inside in the wear track of the TiC/Al_2O_3 tribocouple. Inset is an optical micrograph indicating the location on the wear track.

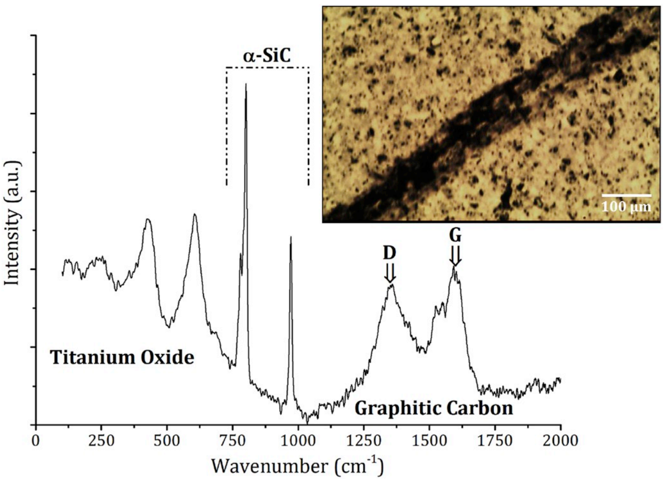

Fig. 11. Raman spectrum collected inside in the wear track of the TiC-50 mol. %SiC/Al_2O_3 tribocouple. Inset is an optical micrograph indicating the location on the wear track.

3.5. Post-mortem SEM-EDS analyses of wear track

Post mortem SEM and EDS assessments of the sliding interface of the TiC/Al_2O_3 tribocouple are presented in Figs. 12 and 13. The wear scar of the TiC/Al_2O_3 sliding surface appears to be moderately damaged with minimal grain fracture, pull-outs and subsequent pulverization evident. Wear grooves can also be seen running parallel along the wear track. Tribofilm(s) appear not to be visible inside the wear track even though Raman analysis revealed the evolution of tribo-oxidation products. This may be due to the fact that they have been worn off and/or incorporated and mixed with the wear debris. Nonetheless, EDS analysis of the worn surface (Fig. 12(b)) presented in Fig. 13 is quite consistent with Raman analysis in finding oxides on the surface.

SEM micrographs taken from the sliding surface of the TiC–SiC/Al_2O_3 tribocouple is presented in Fig. 14. Severe wear grooves (Fig. 14 (a)) running parallel across the wear track and grain fracture (Fig. 14(c-d)) are observed. In addition, tribofilms (Fig. 14(b)) as well as extensive rippling of the TiC grains (Fig. 14(e-f)) are evident in the wear track. The reason for the rippled TiC grains is not fully clear, however, it might be linked to the thermal expansion mismatch between TiC and SiC. In general, the extent of grain damage is surprising given the high content of easy-shearing graphitic material observed in the wear track of TiC–-SiC/Al_2O_3 tribocouple as confirmed by Raman analysis. Nonetheless, the observed microstructural damage seems to explain the higher coefficient of friction measured for the TiC–SiC/Al_2O_3 tribocouples as compared to the TiC/Al_2O_3 tribocouple.

Fig. 15 shows the comparative SEM-EDS elemental map analysis of an area inside the wear track of the TiC-50 mol.%SiC composite system. Preferential oxygen concentration around the TiC region is evident, which suggests possible TiO_2 formation in consistent with the Raman analysis. However, it is difficult using EDS analysis to distinguish between the intrinsic carbon content from the bulk sample composition and the evolved graphitic carbon layer due to the tribochemical reaction.

To further understand the wear mechanism, the surface of the alumina balls were analysed after each test. Analysis of the alumina ball after dry sliding against monolithic TiC disc (Fig. 16) showed evidence

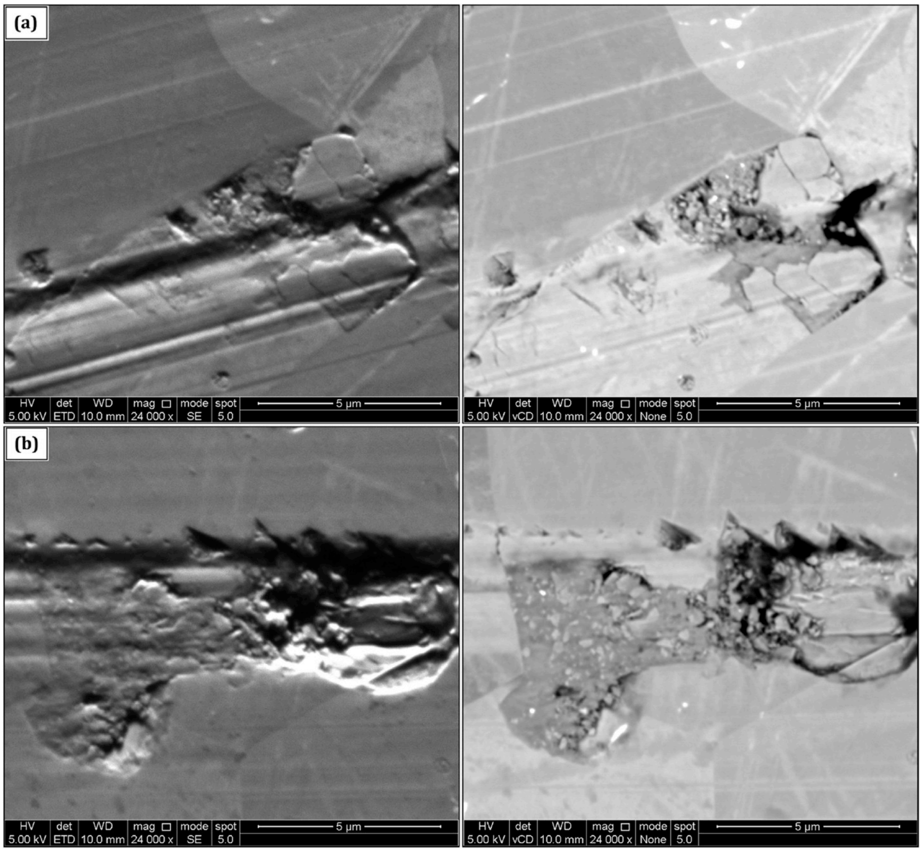

Fig. 12. Post-mortem topographical (SE-BSE) SEM micrographs of the sliding surface of TiC/Al_2O_3 tribocouple.

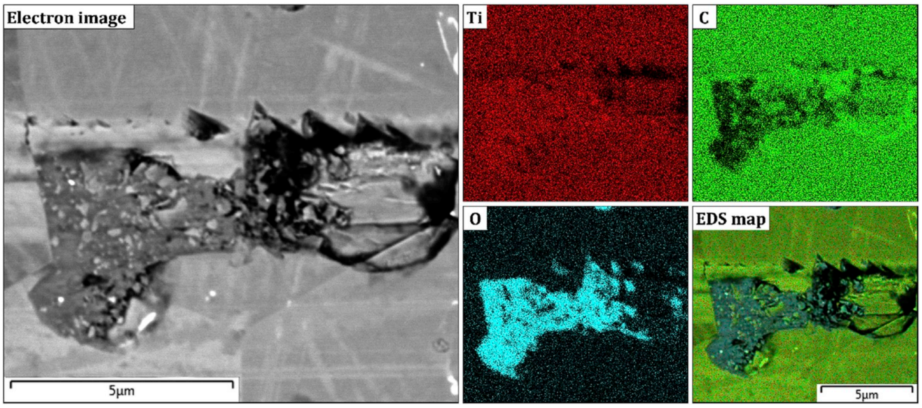

Fig. 13. EDS elemental map analysis taken at the sliding surface of TiC/Al_2O_3 tribocouple.

of some transfer film from the bulk material unto the ball surface as well as minor wear of the ball. The alumina ball surface after dry sliding against TiC-50 mol.%SiC disc (Fig. 17) showed that some wear debris was transferred to the ball surface from the bulk material. In addition, the ball surface appeared relatively rough and covered with compacted oxidized wear debris and/or smeared tribofilm. Wear grooves parallel to the sliding direction were also visible on the surface of the ball. It appears that debris accumulation on the surface of the ball grows as a function of time, and ultimately enough debris is entrapped between the ball and the disc which then acts as a load bearing third-body. As a consequence, there will be an increase in contact force due to point contacts with particles, thus bringing about fluctuations in friction behaviour and the eventual increase in friction coefficient as observed from the evolution of friction coefficient plot for the composites.

3.6. Toughening mechanism

As seen in Fig. 4, the presence of SiC particles in the TiC matrix inhibited the exaggerated grain growth of the TiC grains, thus a toughening mechanism will be initiated according to Refs. [1,25,26]. Furthermore, in addition to the SiC pinning-induced toughening, the mismatch in coefficient of thermal expansion between TiC and SiC will introduce an additional toughening mechanism [1,27]. This is because the thermal expansion coefficient of TiC is larger than that of SiC ($\alpha_{SiC} \approx 5.3 \times 10^{-6}\,^{\circ}C^{-1}$ and $\alpha_{TiC} \approx 7.4 \times 10^{-6}\,^{\circ}C^{-1}$, respectively [28]). As a consequence, hydrostatic compressive stress will be generated within the SiC grains [26], whilst at the same time, radial compressive stress and tangential tensile stress will be generated in the TiC matrix around the SiC particles [1,26]. Thus, if SiC is located on a crack

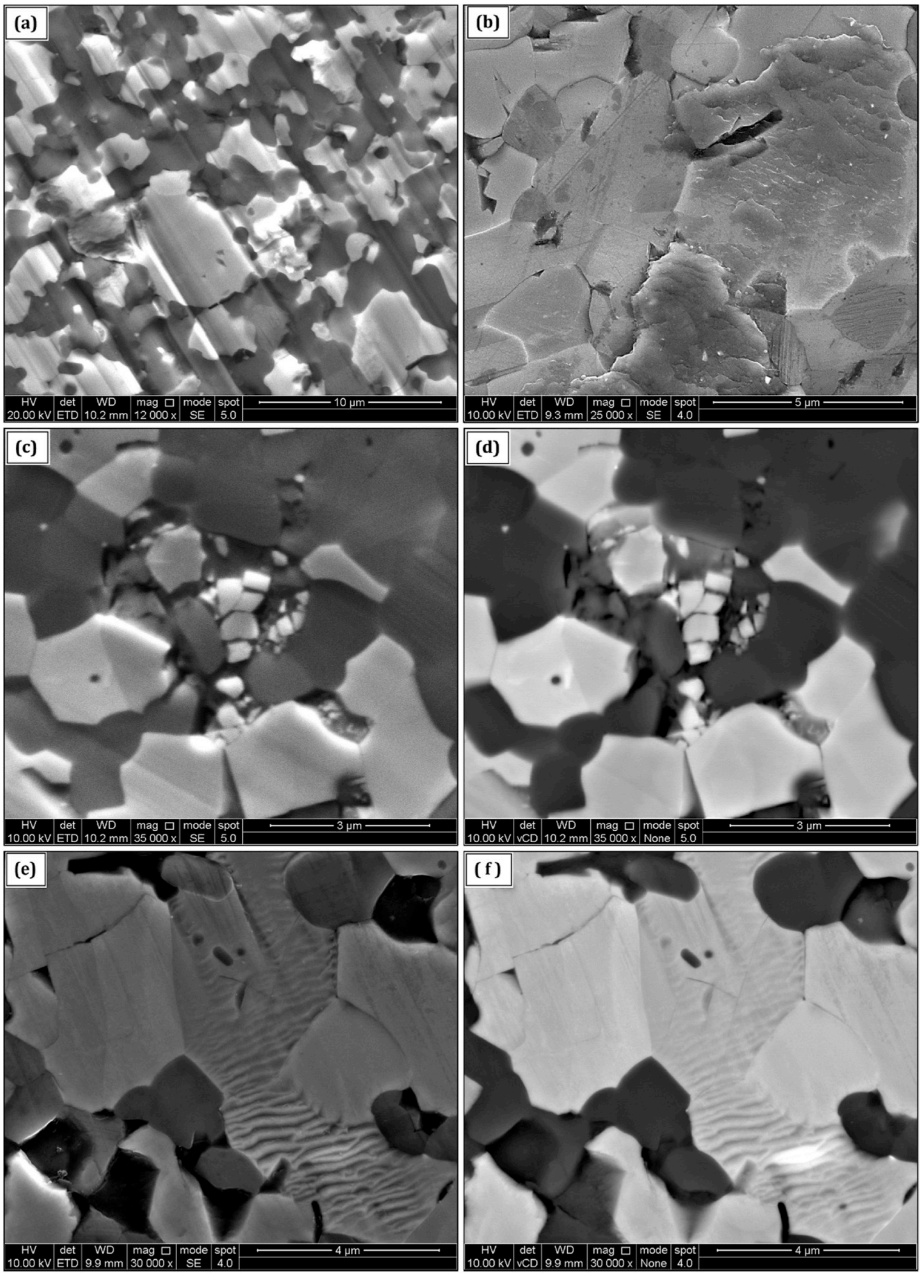

Fig. 14. Post-mortem topographical SEM micrographs of the contacting surface of the TiC-50 mol.% SiC/Al_2O_3 tribocouple. Note: (a and b) are SE-images whilst (c-d) and (e-f) are SE-images and their corresponding backscattered electron (BSE) images.

extension plane, the crack will preferentially first reach the boundary of the TiC and SiC grains, as the surface energy of the SiC grains is larger than the interface surface fracture energy of the TiC/SiC interface [29]. As a result, the crack will bypass the TiC matrix and SiC particle and instead propagate along the TiC/SiC interface [29]. However, occasionally, the crack will propagate through the particle if they possess an irregular shape and size [26,29]. Fig. 18 is a typical SEM micrograph of the trajectories of Vickers indentation cracks in the TiC-50 mol.%SiC composite. Energy absorbing toughening mechanisms such as crack deflection, crack branching and crack bridging are evident.

3.7. Thermal expansion mismatch and residual stress

It has been well established that particulate composites containing inherent residual stresses by virtue of the mismatch in thermal expansion between the matrix phase and the particle phase, is likely to initiate spontaneous microcracking when the second phase particle size attains a critical value [30,31]. SEM microstructural investigation of the as-synthesized SPSed TiC–SiC composite showed no evidence of neither microcracking nor fracture. This implies that the second phase SiC particle size distribution is below the critical size for the initiation of spontaneous microcracking [31]. The absence of cracks also indicates that stresses due to thermal expansion mismatch have not been relieved, thus strain due to the thermal cycling during the synthesis is retained in the composite (i.e., stress relaxation has not occurred). Post-mortem SEM observation of the TiC–SiC composite wear track, in contrast to the worn surface of the monolithic TiC, revealed evidence of stress relaxation upon dry sliding contact. The TiC grains in the TiC–SiC composite have undergone severe grain rippling preferentially (Fig. 19) with no grain rippling observed in the SiC grains. This strongly suggests that stress due to thermal mismatch was relieved (i.e., stress-relaxation) during the sliding contact. According to Luan et al. [32], residual

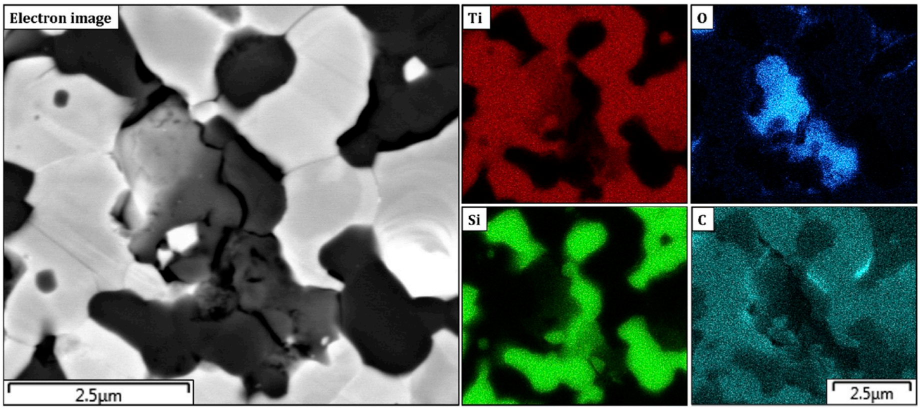

Fig. 15. EDS elemental map analysis taken from the worn surface of the TiC-50 mol.%SiC composite.

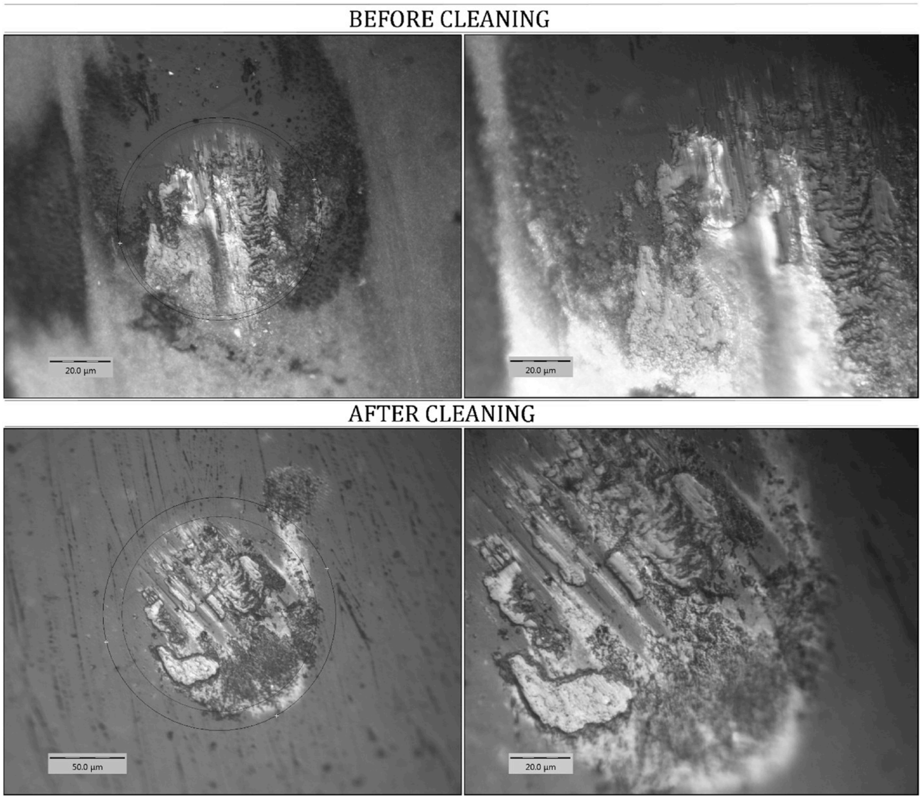

Fig. 16. Optical images of the alumina ball surface after dry sliding against monolithic TiC disc.

stresses trapped in composites could be relaxed significantly when there is a subsequent mechanical loading that causes superposition of the applied stress and residual stress via stress-induced microcracking [30, 33]. Such consequent stress-induced microcracking is expected to shield a propagating crack by the release of residual stress around the applied load [34,35] i.e., toughening effect. However, the beneficial compressive stresses appear to have been worn off during the wear process, rendering toughening mechanisms such as thermal residual toughening and microcracking inactive or inefficient against future loading. This is because detrimental tensile stresses are left behind in the matrix that promotes severe grain rippling and consequent microcracking of the surrounding grains.

In order to further provide detailed overview of the rippled TiC grains, 3D data were obtained from SEM images of the rippled section by employing a 3D image analysis software (MountainsMap® SEM Topo, Digital Surf, France) to reconstruct the backscattered SEM images. From the SEM 3D reconstruction (Fig. 20), extensive SiC grain pull-outs and subsequent fracture can be seen around the rippled TiC grains. It appears that the SiC grains are pulled out due to rippling of the TiC grains nearby and subsequently pulverized owing to the contact load. Whilst the TiC grains on the other hand undergo micro and macro-fracture due to the residual stress relaxation.

It is noteworthy to mention that similar TiC grain rippling was observed in the TiC-30 mol.%SiC composite system. This strengthens the fact the observed TiC grain ripplocation is not a one-off event in the TiC-50 mol.% SiC composite system.

3.8. TEM analysis of the rippled region

Focused ion beam (FIB) was used to prepare a cross-sectional TEM specimen containing the rippled TiC region (region of interest) inside the wear track. Fig. 21 shows the lift-out process for preparing the TEM

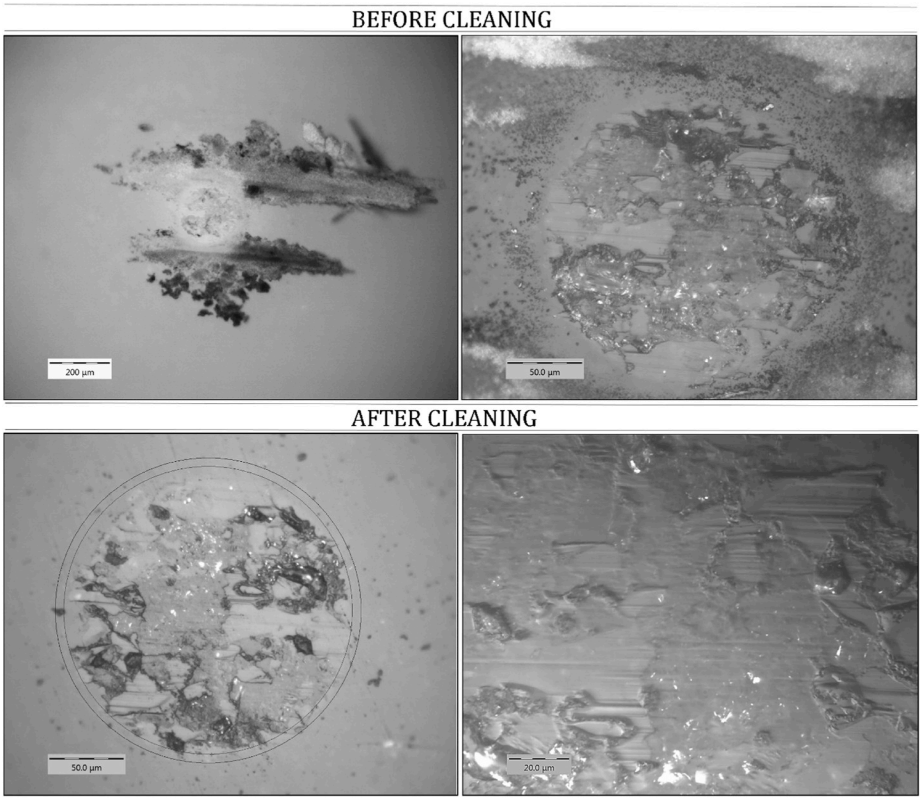
BEFORE CLEANING

AFTER CLEANING

Fig. 17. Optical images of the alumina ball surface after dry sliding against TiC-50 mol.%SiC disc.

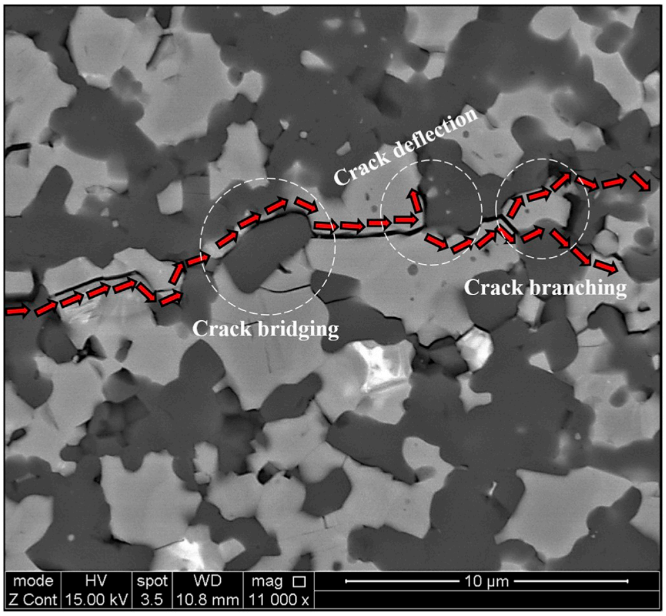

Fig. 18. Toughening mechanism in TiC–SiC composite showing crack propagating preferentially along the grain boundary and occasionally deviating into the TiC and SiC grains.

specimen.

Fig. 22 shows TEM images obtained from the rippled TiC grains. Upon careful observation of the TEM image (Fig. 22(a)) and EDS chemical maps (not shown here), a systematic exfoliation of carbon from the TiC grain is hypothesized. Further, judging from the HRTEM image and its corresponding selected area electron diffraction (SAED) pattern obtained from the TiC-graphite interface (position marked by a yellow rectangle in Fig. 22(a)), the rippled graphite layers formed on the TiC grain such that the graphite {001} are almost parallel to the TiC {100}. The ripples appear to be propagating along the {001} graphite plane which is manifested on the surface of the TiC grains along the {100} plane. This unquestionably highlights the crystallographic nature of this ripplocation micromechanism.

The observed TiC grain rippling is consistent with a new deformation mechanism termed bulk ripplocation (BR) as reported in 2D materials [36]. Recently, layered solids such as graphite, MAX phases, MoS_2 and mica have been reported to deform via a micromechanism involving the nucleation and propagation of ripplocations [36–39]. According to Kushima et al. [36], ripplocation implies surface ripples and crystallographic dislocations and are essentially different to dislocations as such that they possess no Burgers vector or polarity [36,37]. The formation of ripplocation is essentially associated to an atomic scale buckling which is not restricted to surfaces or near surfaces and can effectively occur in bulk in what was termed bulk ripplocations (BRs) [39].

3.9. *Mechanism of ripplocation formation*

Superimposition of the shear stresses originating from the contact sliding load on the inherent tensile residual stresses around the TiC grains will lead to possible weakening of the Ti–C bond [40], thus the systematic mechanical exfoliation of carbon unto the surface of the TiC grains. The exfoliated carbon then decomposes into graphite due to frictional heating and subsequently deforms via a micromechanism involving the nucleation and propagation of ripplocation as a result of the repeated sliding contact. Nonetheless, more work needs to be done to fully understand the underlying mechanisms leading to the exfoliation of carbon.

4. Wear mechanism

Upon microstructural and chemical characterization of the worn

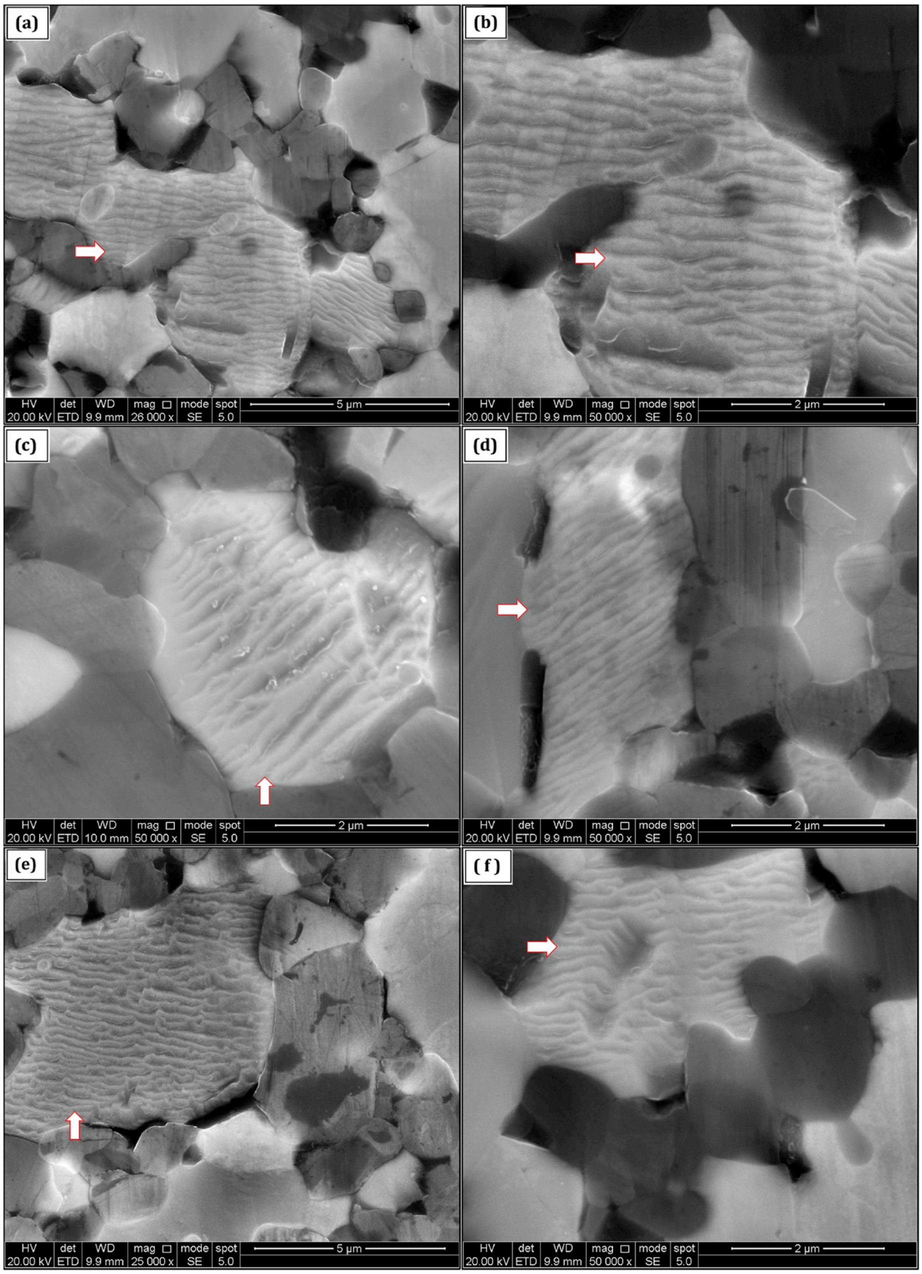

Fig. 19. SEM micrographs of the worn surface of the TiC-50 mol.%SiC composite showing evidence of extensive TiC grain ripplocation upon stress-relaxation. Note: (b) is a higher magnification of a section in (a).

surfaces of the bulk samples, the underlying wear mechanisms are elucidated as follows:

4.1. Tribo-oxidative wear

Tribo-oxidation appears is an operative wear mechanism according to the Raman and EDS analyses. The dry sliding nature of the tribological test seems to have generated enough frictional heating due to asperity temperature flashes to trigger selective oxidation of TiC in both ceramic compositions (i.e., monolithic TiC and TiC–SiC composite). The tribo-oxidatively formed TiO_2 alongside the graphitic layer acts as solid lubricant shielding the interface to prevent direct contact of the tribocouple. In the case of monolithic TiC, ‘oxidation-scrape-reoxidation’ appears to be taking place very rapidly such that limited contact is made between the tribocouple, thus the limited surface damage observed at the sliding surface of the TiC/Al_2O_3 tribocouple. For the composites, it seems that the oxidatively formed TiO_2 has a lower fraction as compared to monolithic TiC simply due to the lower volume fraction of TiC in the composition. Since silicon has higher oxidation resistance than titanium, the absence of silicon oxide in the Raman analysis of the composite wear track is not surprising. The limited TiO_2 formation will imply that repeated direct contact between the counterparts occurs faster, consistent with the instability observed in the friction plot of the TiC–SiC/Al_2O_3 tribocouples.

4.2. Abrasive wear

Abrasive wear is also an operational wear mechanism as evident by the evolution of horizontal grooves in the post-mortem sliding surfaces of both the monolithic TiC and the composite samples. The wear grooves

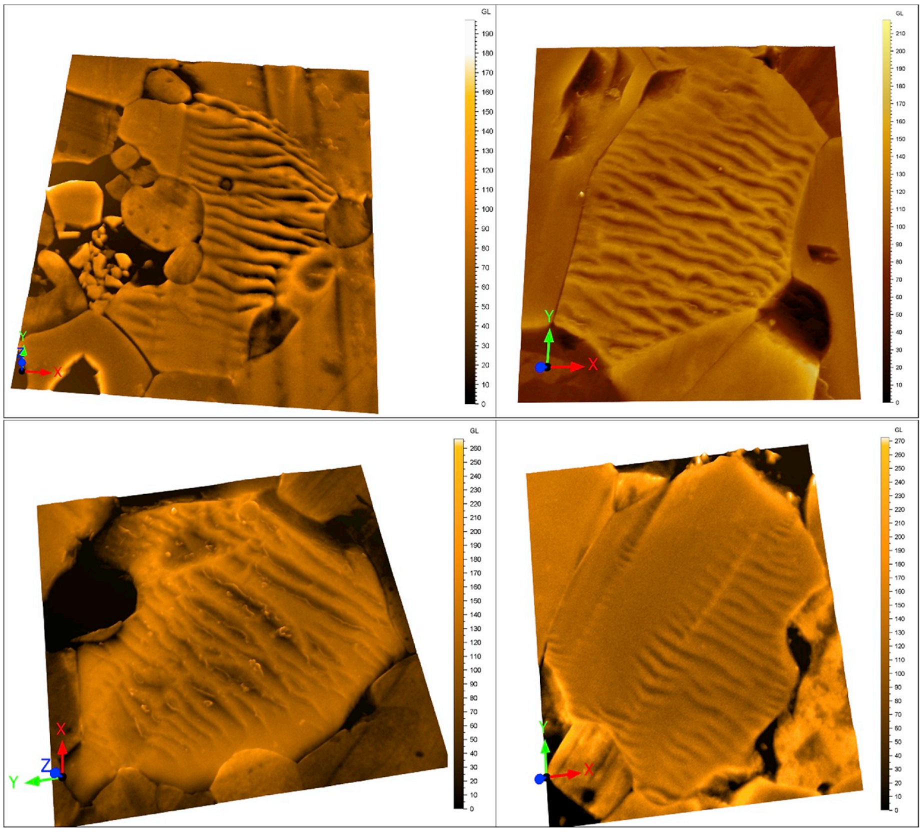

Fig. 20. 3D-SEM reconstruction of the rippled TiC grains from the wear track of the TiC-50 mol.%SiC composite.

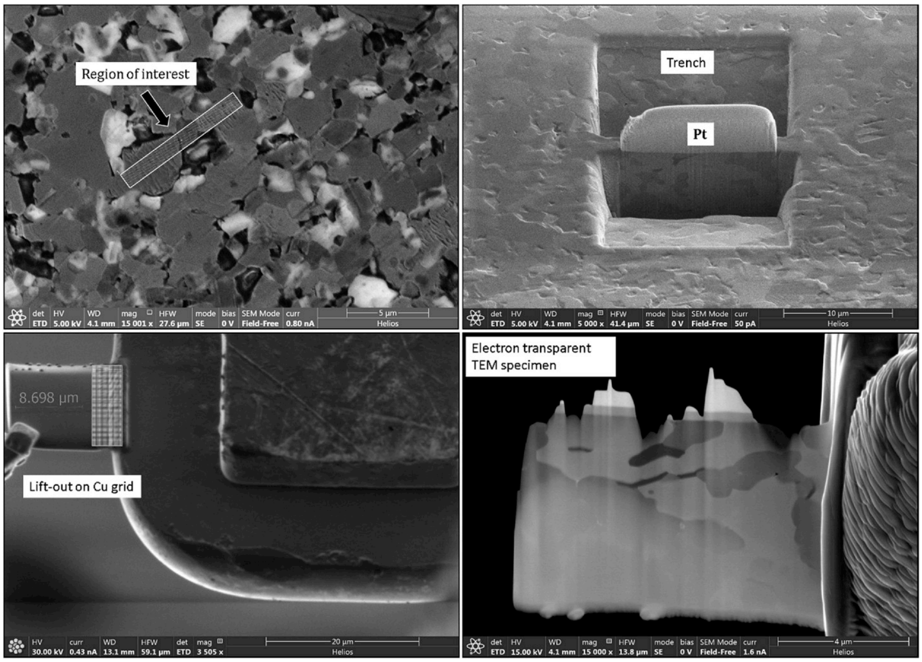

Fig. 21. Ion-induced secondary electron micrographs of FIB sample preparation showing location where the ripples were extracted inside the wear track and the final electron transparent TEM sample.

tends to be more pronounced in the composite sample as compared to the monolithic TiC due to the limited TiO_2 tribofilm formed at the sliding surface causing extended contact between the tribocouple. The origin of the wear grooves as seen on the surface of the Al_2O_3 ball may due to the fractured grains from the bulk material which detrimentally constitute an abrasive third-body. Fragments from the Al_2O_3 ball were however not found in the wear track possibly due to its very low content or the area mapped by EDS and probed by Raman did not contain the transfer material.

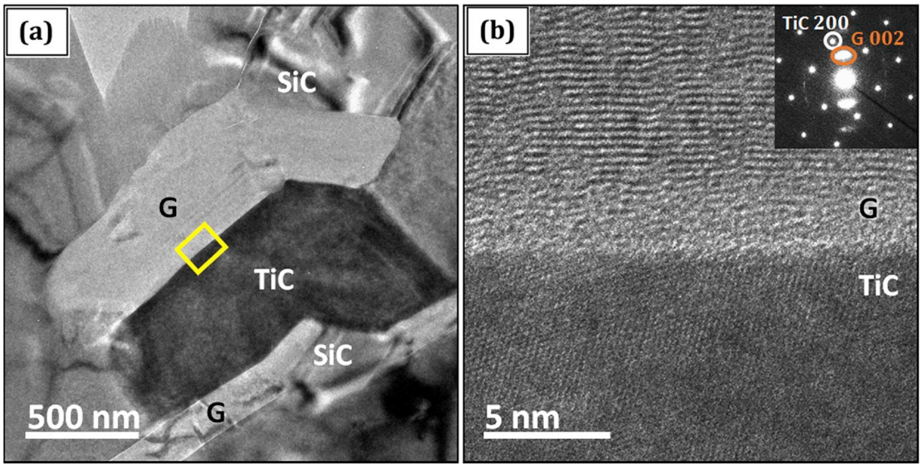

Fig. 22. (a) Bright-field TEM micrograph obtained from the rippled region inside the composite wear track. Here, graphite layers are marked by "G". (b) HRTEM image obtained from the TiC-graphite interface marked by a yellow rectangle in (a). (For interpretation of the references to colour in this figure legend, the reader is referred to the Web version of this article.)

4.3. Stress-relaxation induced wear mechanism

The simultaneous influence of the contact shear stress superimposed on the residual stress initiates the relieve of the residual stresses previously trapped in the composite after sintering during the wear test. The residual stress relieve led to the weakening of the interface (grain boundary) strength that causes grain pull-outs and microcrack formation. The weakening of the interface enabled easy pull-out of the SiC grains which is then subsequently fractured to constitute an abrasive third-body. This implies that the area in which beneficial compressive stresses prevail decreases, making toughening mechanism(s) less significant as wear progresses. As a result, detrimental tensile residual stress in the TiC grains will result in the rippling of the TiC grains due to the additional shear stresses imposed by the normal load during the sliding contact. The combination of SiC grain pull-outs due to stress relaxation and TiC grain rippling led to the high friction coefficient and specific wear rate of the composite system.

5. Conclusion

Monolithic TiC and TiC–SiC composite systems were successfully synthesized without sintering aids using SPS. The microstructure and tribological properties of the as-sintered samples were studied and the following conclusions can be drawn:

1. Mismatch in thermal expansion between TiC and SiC as well as β→α SiC phase transformation led to high residual stresses in the composite system.
2. Tribofilms formation due to frictional heating induced tribo-oxidation acts as a protective layer at the disc/ball sliding interface, thus reducing friction and wear of the counterparts.
3. Friction and wear behaviour of the monolithic TiC sample were superior to that of the composite albeit possessing better fracture toughness for the test condition. This is attributed to the incipient stress-relaxation and subsequent SiC grain pull-outs due to the shear stresses imposed upon sliding contact.
4. Mechanical exfoliation of carbon and its subsequent transformation into graphite due to frictional heating led to the deformation of the TiC grains via the nucleation of ripplocations.

Future exhaustive characterization will be needed to fully understand the combination of factors leading to the exfoliation of carbon from TiC as this is not fully understood at this time.

Declaration of competing interest

We the authors of this work hereby declare that there is no conflict of interest related to this work and this paper is an independent research carried out in our group at the department of engineering materials, University of Sheffield.

References

[1] G.C. Wei, P.F. Becher, Improvements in mechanical properties in SiC by the addition of TiC particles, J. Am. Ceram. Soc. 67 (8) (1984) 571–574.
[2] D.L. Jiang, et al., Studies on the strengthening of silicon carbide-based multiphase ceramics I: the SiC-TiC system, Mater. Sci. Eng. A 109 (1989) 401–406.
[3] R. Stevens, Dislocation movement and slip systems in β-SiC, J. Mater. Sci. 5 (6) (1970) 474–477.
[4] J. Chen, W. Li, W. Jiang, Characterization of sintered TiC–SiC composites, Ceram. Int. 35 (8) (2009) 3125–3129.
[5] C. Kawai, K. Suzuki, K. Tanaka, Fracture toughness of TiC-SiC composites fabricated by CVD and the mechanism of toughening, J. Ceram. Soc. Jpn. 100 (1162) (1992) 835–840.
[6] I.-W.C. Ralf Riedel, Ceramics Science and Technology : Materials and Properties, vol. 2, Wiley-VCH, Weinheim, 2010.
[7] R. Wäsche, et al., Oscillating sliding wear behaviour of SiC, TiC, TiB2, 59SiC–41TiB2 and 52SiC–24TiC–24TiB2 materials up to 750°C in air, Tribotest 12 (2) (2006) 99–111.
[8] O.O. Ajayi, et al., Sliding wear of silicon carbide—titanium boride ceramic-matrix composite, J. Am. Ceram. Soc. 76 (2) (1993) 511–517.
[9] H.J. L, et al., Microstructure, phase and thermoelastic properties of laminated liquid-phase-sintered silicon carbide–titanium carbide ceramic composites, J. Am. Ceram. Soc. 90 (7) (2007) 2189–2195.
[10] G. Gille, K. Wetzig, Investigations on mechanical behaviour of brittle wear-resistant coatings I. Experimental results, Thin Solid Films 110 (1) (1983) 37–54.
[11] C. Magnus, T. Kwamman, W.M. Rainforth, Dry sliding friction and wear behaviour of TiC-based ceramics and consequent effect of the evolution of grain buckling on wear mechanism, Wear 422–423 (2019) 54–67.
[12] T.S. Srivatsan, et al., Influence of TiB2 content on microstructure and hardness of TiB2–B4C composite, Powder Technol. 159 (3) (2005) 161–167.
[13] D.S. King, W.G. Fahrenholtz, G.E. Hilmas, Silicon carbide–titanium diboride ceramic composites, J. Eur. Ceram. Soc. 33 (15) (2013) 2943–2951.
[14] A. Sowmya, A.H. C, Synthesis of titanium silicon carbide, J. Am. Ceram. Soc. 78 (3) (1995) 667–672.
[15] Y.W. Kim, et al., Effect of initial α-phase content on microstructure and mechanical properties of sintered silicon carbide, J. Am. Ceram. Soc. 81 (12) (1998) 3136–3140.
[16] C.H. McMurtry, et al., Microstructure and Material Properties of SiC-TiB2 Particulate Composite, vol. 66, 1987, pp. 325–329.
[17] M. Woydt, A. Skopp, K.H. Habig, Dry friction and wear of self-mated sliding couples of SiC-TiC and Si3N4-TiN, Wear 148 (2) (1991) 377–394.
[18] R. Wäsche, D. Klaffke, In situ formation of tribologically effective oxide interfaces in SiC-based ceramics during dry oscillating sliding, Tribol. Lett. 5 (2) (1998) 173.
[19] P. Brüesch, Phonons: Theory and Experiments. 2, Experiments and Interpretation of Experimental Results, Springer-Verlag, London, 1986.
[20] P.V. Huong, Structural studies of diamond films and ultrahard materials by Raman and micro-Raman spectroscopies, Diam. Relat. Mater. 1 (1) (1991) 33–41.

[21] M.V. Klein, J.A. Holy, W.S. Williams, Raman scattering induced by carbon vacancies in TiCx, Phys. Rev. B 17 (4) (1978) 1546–1556.

[22] U. Balachandran, N.G. Eror, Raman spectra of titanium dioxide, J. Solid State Chem. 42 (3) (1982) 276–282.

[23] F. Tuinstra, J.L. Koenig, Raman spectrum of graphite, J. Chem. Phys. 53 (3) (1970) 1126–1130.

[24] W.K. Pang, et al., 12 - oxidation characteristics of Ti3AlC2, Ti3SiC2 and Ti2AlC. Advances in Science and Technology of Mn+1AXn Phases, Woodhead Publishing, 2012, pp. 289–322.

[25] Y.-W. Kim, S.-G. Lee, Y.-I. Lee, Pressureless Sintering of SiC–TiC Composites with Improved Fracture Toughness, vol. 35, 2000, pp. 5569–5574.

[26] D. Ahmoye, Pressureless sintering and mechanical properties of SiCComposites with in-situ converted TiO2 to TiC, in: Department of Mechanical and Materials Engineering, Queen's University Kingston, Ontario, Canada, 2010.

[27] H. Endo, M. Ueki, H. Kubo, Microstructure and mechanical properties of hot-pressed SiC-TiC composites, J. Mater. Sci. 26 (14) (1991) 3769–3774.

[28] K. Kornaus, et al., Mechanical Properties of Hot-Pressed SiC-TiC Composites, vol. 11, 2017, pp. 329–336.

[29] C. Qin, et al., Microstructure Characterization and Mechanical Properties of TiSi2-SiC-Ti3SiC2 Composites Prepared by Spark Plasma Sintering, vol. 47, 2006, pp. 845–848.

[30] W.H. Gu, K.T. Faber, Tensile behavior of microcracking SiC-TiB_2 composites, J. Am. Ceram. Soc. 78 (6) (1995) 1507–1512.

[31] D. Magley, R. Winholtz, K. Faber, Residual stresses in a two-phase microcracking ceramic, J. Am. Ceram. Soc. 73 (6) (1990) 1641–1644.

[32] W. Luan, C. Jiang, V. Ji, Residual stress relaxation in shot peened surface layer on TiB2/Al composite under applied loading, Mater. Trans. 50 (1) (2009) 158–160.

[33] D.J. G, Stress-induced microcracking at second-phase inclusions, J. Am. Ceram. Soc. 64 (3) (1981) 138–141.

[34] A.G. Evans, Y. Fu, Some effects of microcracks on the mechanical properties of brittle solids—II. Microcrack toughening, Acta Metall. 33 (8) (1985) 1525–1531.

[35] A.G. Evans, K.T. Faber, Toughening of ceramics by circumferential microcracking, J. Am. Ceram. Soc. 64 (7) (1981) 394–398.

[36] A. Kushima, et al., Ripplocations in van der Waals layers, Nano Lett. 15 (2) (2015) 1302–1308.

[37] J. Gruber, et al., Evidence for bulk ripplocations in layered solids, Sci. Rep. 6 (2016) 33451.

[38] M.W. Barsoum, et al., Ripplocations: a universal deformation mechanism in layered solids, Phys. Rev. Mater. 3 (1) (2019), 013602.

[39] J. Griggs, et al., Spherical nanoindentation, modeling and transmission electron microscopy evidence for ripplocations in Ti3SiC2, Acta Mater. 131 (2017) 141–155.

[40] A. Bartlett, A.G. Evans, M. Rühle, Residual stress cracking of metal/ceramic bonds, Acta Metall. Mater. 39 (7) (1991) 1579–1585.